Faculty of Civil Engineering Sciences

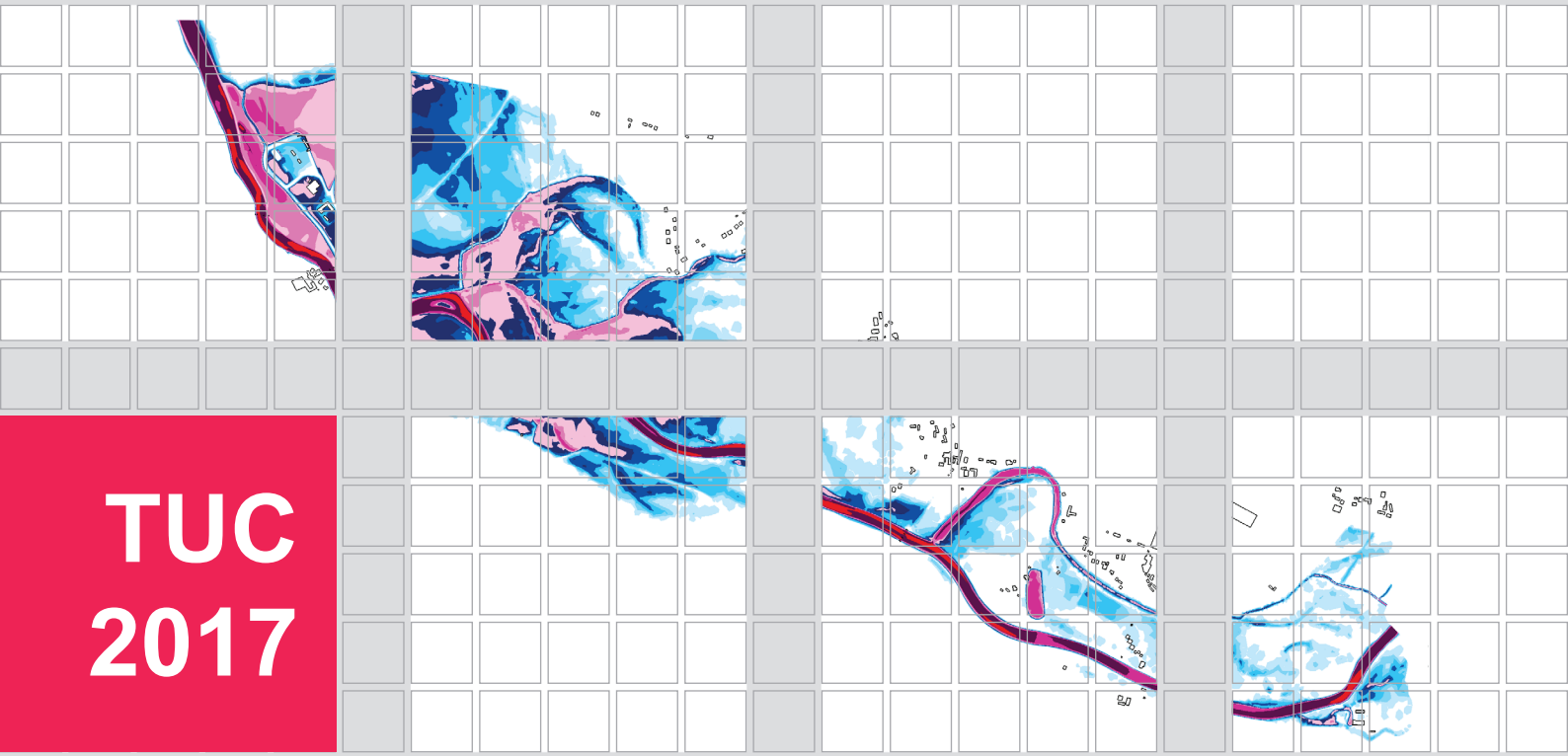

TUC 2017

Proceedings of the XXIVth TELEMAC-MASCARET User Conference

17 to 20 October 2017, Graz University of Technology, Austria

Editors: Clemens Dorfmann and Gerald Zenz

Proceedings of the

XXIVth TELEMAC-MASCARET User Conference

17 to 20 October 2017, Graz, Austria

Editors
Clemens Dorfmann and Gerald Zenz

Proceedings of the
XXIVth TELEMAC-MASCARET
User Conference

17 to 20 October 2017, Graz, Austria

Organized by
Graz University of Technology
Institute of Hydraulic Engineering and Water Resources Management
Stremayrgasse 10/II, 8010 Graz, Austria
Tel.: +43 316 873 8361
hydro@tugraz.at
www.hydro.tugraz.at

Edited by
Clemens Dorfmann and Gerald Zenz

Layout and Cover Design
Christina Fraueneder, Harald Breinhälter,
Clemens Dorfmann, Sebastian Gegenleithner

Published by

www.ub.tugraz.at/Verlag

Graz University of Technology
Rechbauerstraße 12, 8010 Graz, Austria
Tel.: +43 316 873 0, Fax: +43 316 873 6009

Printed by
Medienfabrik Graz - Wien

ISBN (print) 978-3-85125-544-7
ISBN (e-book) 978-3-85125-545-4
DOI 10.3217/978-3-85125-544-7

Foreword to the XXIVth TELEMAC-MASCARET User Conference

October 2017

Dear participant,

The Institute of Hydraulic Engineering and Water Resources Management - Graz University of Technology is delighted to host the XXIVth TELEMAC-MASCARET User Conference and welcomes you in Graz.

The TELEMAC-MASCARET User Conference follows a long and successful tradition of annual meetings. Since 2010, after the open source distribution, it attracts an increasing number of contributors and participants. The availability of free and open software, based on outstanding science, is indispensable for research as well as practical applications. It is a great commitment from the TELEMAC-MASCARET consortium to advance the software development, promote University's scientific research and support the engineering community.

At the TUC 2017 Conference, theoretical and practical aspects of water-related numerical simulations are presented and discussed. We have received 36 high quality papers and abstracts, which are presented and discussed during the conference. These contributions cover an exciting wide range of free surface flow modelling, from the ocean to the torrent catchment. They provide the scientific background for future users of the software suite. It needs to be emphasized that elaborated, discussed and published results by the scientific community – e.g. IAHR or ICOLD – are important resources, which enable the realization of major infrastructure projects for the society.

This year's conference is substantially supported by the TELEMAC-MASCARET consortium, which we gratefully acknowledge.

We wish all participants inspiring discussions throughout our TUC 2017 Conference in Graz and hope keeping the animating social contacts during our cultural and evening events in mind.

Gerald Zenz

Chair of the Local Organizing Committee

Organisation

International Scientific Committee

Christophe Coulet	Artelia Eau & Environnement
Olivier Bertrand	Artelia Eau & Environnement
Rebekka Kopmann	BAW
Kamal El Kadi Abderrezzak	EDF R&D
Riadh Ata	EDF R&D
Yoann Audouin	EDF R&D
Jacques Fontaine	EDF R&D
Thierry Fouquet	EDF R&D
Cédric Goeury	EDF R&D
Antoine Joly	EDF R&D
Agnès Leroy	EDF R&D
Chi-Tuân Pham	EDF R&D
Pablo Tassi	EDF R&D
Fabrice Zaoui	EDF R&D
Sébastien Bourban	HR Wallingford
Alan Cooper	HR Wallingford
Noémie Durand	HR Wallingford
Clemens Dorfmann	TU Graz
Josef Schneider	TU Graz
Shervin Shahriari	TU Graz
Gerald Zenz	TU Graz
Uwe Merkel	UHM River Engineering

Local Organizing Committee

Harald Breinhälter
Clemens Dorfmann
Sebastian Gegenleithner
Josef Schneider
Gerald Zenz

TELEMAC-MASCARET Core Group

Artelia
www.arteliagroup.com

Bundesanstalt für Wasserbau
Federal Waterways Engineering and Research Institute
www.baw.com

Centre d'études et d'expertise sur les risques, l'environnement, la mobilité et l'aménagement
www.cerema.fr

Électricité de France
www.edf.com

HR Wallingford
www.hrwallingford.com

Science and Technology Facilities Council
Daresbury Laboratory
www.stfc.ac.uk

Content

Coastal surges and tsunami waves

The Earth by TELEMAC 1
Sébastien E. Bourban, Michael S. Turnbull, Alan J. Cooper

An overview on the capabilities of the TELEMAC-MASCARET system to deal with tsunamis: feedbacks from TANDEM project 9
Riadh Ata, Marine le Gal, Damien Violeau

Validation of a TELEMAC-3D model of a seamount 17
Alan J. Cooper, Jeremy Spearman

Inundation Risk due to a Landslide-Generated Tsunami in the North Sea 23
Rohit Kulkarni, Nicolas Zimmermann, Thijs Lanckriet, Alexander Breugem

Development of a Hindcast Wave State Database in Northwest Pacific Ocean 31
Jian Shi, Antoine Joly

Numerical methods, code coupling and high performance computing

Development of a Large-Eddy- Simulation approach with Telemac-3D 35
Adrien Bourgoin, Sylvain Guillou, Jérôme Thiébot, Riadh Ata, Sofiane Benhamadouche

PyTelTools: Python scripts and GUI to automate Telemac post-processing tasks 41
Luc Duron, Yishu Wang

COURLIS: a new sedimentology 1D module for MASCARET 47
Eric Valette, Matthieu Secher, Philippe Ung, Nicole Goutal, Magali Jodeau

Performance Optimization for TELEMAC-MASCARET using GPU accelerators (only abstract) 53
Yoann Audouin, Hamza Belaoura, Frank Hulsemann

An experiment of adaptive mesh in hydraulics (only abstract) 55
Thierry Fouquet, Matthieu Secher, Gerald Nicolas

Data assimilation, optimization, risks and uncertainties

Interoperability applications of TELEMAC-MASCARET System 57
Y. Audouin, C. Goeury, F. Zaoui, R. Ata, S. El Idrissi Essebtey, A. Torossian, D. Rouge

Uncertainty analysis approximation for non-linear processes using Telemac-AD 65
Guilherme Dalledonne, Rebekka Kopmann, Jan Riehme, Uwe Naumann

Optimal calibration of TELEMAC-2D models based on a data assimilation algorithm 73
C. Goeury, A. Ponçot, J.-P. Argaud, F. Zaoui, R. Ata, Y. Audouin

Global Sensitivity Analysis applied to the Telemac2D numerical forecast model of high water levels in the Gironde estuary 81
Vanessya Laborie, Nicole Goutal, Sophie Ricci, Matthias de Lozzo, Philippe Sergent

River and urban floods, flood forecasting

Flood Wave Modelling and Risk Analysis of Overtopped Embankment Dams 91
Gabriele Harb, Hannes Badura, Wolfgang Troy

Mapping of Flood Dynamics Due to Sea Level Rise in Dyfi Estuary 99
Aasem Khatrush, Shunqi Pan

Modelling of river dike breach type physical test flow with Telemac-2D 107
Yohannis Birhanu Tadesse, Peter Fröhle

Hydraulic 2D Model of Landslide Generated Wave – Cases of Chehalis Lake and Chambon Lake ..113
Thomas Viard

Sensitivity analysis of urban flood flows to hydraulic controls (only abstract) 119
Shangzhi Chen, P.-A.Garambois, P. Finaud-Guyot, G. Dellinger, Abdelali Terfous, Abdallah Ghenaim

Comparison of 2D numerical models for the simulation of river flooding in a semi-urban area (only abstract) 121
Robert Stöffler, Clemens Dorfmann

River, estuaries, maritime, coastal sediment processes

Numerical estimation of bedform roughness 123
Frederik Folke, Sven Wurms

C-VSM-II: Large Scale and Long Time Simulations with Sisyphe's Continuous Vertical Grain Sorting Model 131
Uwe H. Merkel

Numerical modelling of the sediment dynamics in Saint-Martin-la-Porte reservoir, France.....139
Matthieu Secher, Aurélie André, Eric Valette, Anne-Laure Besnier, Pablo Tassi

A new gravity-driven runoff and erosion model for TELEMAC.....147
Florent Taccone, Germain Antoine, Nicole Goutal, Olivier Delestre

Temporal variability of contaminated sediments in a strongly regulated reservoir of the upper Rhine River (only abstract).....153
G. Antoine, T. Pretet, M. Secher, A. Clutier

Influence of hiding-exposure effect and vertical sorting of sediment on bars morphodynamics (only abstract) 155
F. Cordier, P. Tassi, N. Claude, A. Crosato, S. Rodrigues, D. Pham van Bang

Assessing the impact of Bulle-Effect on the morphodynamics of a laboratory-scale diversion using 3D numerical simulations (only abstract) 157
Som Dutta, Pablo Tassi, Dongchen Wang, Marcelo H. Garcia

Numerical assessment of the impact of climate change on the sediment yield in alpine catchments (only abstract).....159
Sebastian Gegenleithner, Clemens Dorfmann, Josef Schneider

NESTOR: Sediment management module of TELEMAC (only abstract).....161
Boris Glander

Water quality, ecology and environmental impact

Modelling potential drivers of fish kill events in Sulaibikhat Bay, Kuwait 163
John Bacon, David Haverson, Michelle Devlin, Roger Phillips

Analysis of time-step size and initial particle distribution effects on particle dispersal studies 169
Jonathan Demmer, Peter Robins

Assessment of nutrients and macroalgae growth in Poole Harbour, UK 175
David Haverson, John Aldridge, Karen Edwards

Oil spill modelling: A case study in the Gulf of Guinea 183
Anne Levasseur, Olivier Bertrand, Philippe Reveau

Waterworks and energy assessment

The Rance Tidal Power Plant Model 191
Christophe Cochet, Malo Lambert

3D modelling of the Lilla Värtan Bay in Stockholm to assess the impacts of an on-water housing project.....197
Pierre-Louis Ligier, Anders Söderström

Turbine array interactions and performance in TELEMAC-3D 207
Enda Murphy, Julien Cousineau, Mitchel Provan

The Earth by TELEMAC

Sébastien E. Bourban, Michael S. Turnbull and Alan J. Cooper
HR Wallingford, Coasts and Oceans,
Howbery Park, Wallingford, OX10 8BA, UK
s.bourban@hrwallingford.com

***Abstract*—This article describes the development of a highly detailed model of the Earth, based on the TELEMAC system, applied to modelling various physical processes including tides, storms, tsunamis and waves. Comparisons against known global datasets demonstrate the capability of the TELEMAC system to bridge the gap between environmental hydraulics and oceanography. Preliminary results in forecasting internal tides and 3D ocean currents are also presented.**

I. Introduction

A. *Mind the gap*

Numerical modelling for environmental hydraulics studies, whether for research or consultancy, has been historically focused on inland and coastal areas. It has been financed over decades by human activities as water affects, is sourced and is somewhat tamed by growing populations. Consequently, advanced solvers have been developed to provide scientists and engineers with flexible unstructured meshes fitting manmade or natural waterlines, interaction of physical processes such as hydrodynamics, waves, or sediment processes, as well as advanced mathematics and parallelised domain decompositions to greatly speed up computation for ever more detailed simulations. The TELEMAC system is one of those flexible, industry-driven, solvers that choose to open up its source code to further benefit from research and development carried out by growing communities of users worldwide.

Contrarily, numerical modelling for the oceans has mainly been restricted to the research arena, and is mainly used to represent decades or centuries of evolution mostly in the context of climate changes. While their global resolution and the complexity of their underlying density driven physical processes has increased with computer power to include coupling with atmospheric models, for instance, these developments have steered investments away from the underlying solvers: ocean models remain few in number, based on regular grid and legacy codes, with perhaps simpler mathematics compared to their shallow water counterparts.

With the rising costs of sourcing raw material such as oil, gas, bio-chemical compounds, human activities are gradually linking the shores to much deeper waters. It has, therefore, become essential for scientists and engineers to bridge the gap between environmental hydraulics and oceanography.

B. *Objectives*

In order to anticipate and meet the needs of its consultancy activities, it was essential for HR Wallingford to bridge the gap between environmental hydraulics and oceanography. The first of two objectives of the work presented here is to deliver the most comprehensive and detailed global modelling resources yet to support all sorts of shallow- and deep-water environmental hydraulics studies, providing hind-casts and forecasts at local, national or global scales.

The solution identified was to start a phased internal research project to demonstrate the capability of the TELEMAC system to model all physical processes present in these waters, whether independently or combined, and to develop a world leading global modelling resource: The Earth by TELEMAC.

The first four phases of the project were:

Phase 1. *Model setup and preliminary testing:* Finding the most efficient way to build a model of the Earth's waters and testing the capability of the TELEMAC system to run simulations over the entire globe. The existing functionality of TELEMAC-2D in modelling the propagation of Tsunami waves from source was selected for testing purposes.

Phase 2. *Modelling global tides and comparative validation*: Preliminary modelling of tides around the Earth based on the existing functionality of TELEMAC-2D to compute gravitational forces, which are accurately known. Resulting prediction of free surface elevations were compared against known global tidal datasets.

Phase 3. *Modelling storms through atmospheric parameters:* As a trivial application of the TELEMAC-2D component, temporally and spatially varying winds and pressure fields were derived for major known storms (large cyclones, typhoons and hurricanes) and used to predict surges.

Phase 4. *Modelling waves driven by atmospheric datasets:* As a trivial application of the TOMAWAC component, the model was driven by temporally and spatially varying, high resolution, wind data to compute waves propagation and transformation around the globe.

Subsequent development phases include the application of the Earth by TELEMAC to predicting internal tides (resulting from the combination of stratified waters and tides), computing mean dynamic topography (caused by temperature variations) and to forecasting ocean currents.

The second objective of the work presented here is to open up research and collaboration with national and international organisations, from around the world, to enhance the Earth by TELEMAC model with further knowledge, expertise and data. Already, separate research and development activities carried out by HR Wallingford in collaboration with renowned universities will be combined with this project to extend its capabilities. For instance, work done on Algorithmic Differentiation will be combined to extend the Earth by TELEMAC to possible data assimilation. Similarly, work done on Ice Modelling will help with the characterisation of the influence of the cold regions.

II. SETUP OF THE EARTH BY TELEMAC

The purpose of the model is to represent the entire Earth, more specifically its water bodies, at a higher resolution than the current state of the art, below the kilometre if possible. The first step in setting up a model with TELEMAC is to setup an unstructured mesh of the computation domain as defined by its extent and its resolution. The second step in setting up a model is to map the bathymetry. The third step is to define its temporally and spatially varying open boundary conditions. Luckily, the advantage of modelling the whole Earth is that there are no open boundaries!

A. *A scalable unstructured mesh of the Earth*

A data source often used to define the shoreline of coastal waters is the Global Self-consistent, Hierarchical, High-resolution Shoreline (GSHHS) database. GSHHS is a high-resolution shoreline dataset that has undergone extensive processing and is said to be free of internal inconsistencies (see [1]). It can be accessed from www.ngdc.noaa.gov or from www.soest.hawaii.edu/pwessel/gshhs.

Based on these shorelines, mesh generators can generate the unstructured mesh given a constant or variable resolution (triangle edge-length). At this stage, a constant mesh resolution is assumed, the value of which will depend on the computing resources available.

Unfortunately, currently available mesh generators are based on iterative methods that are too slow for extremely large number of vertices. Besides, most generator cannot deal with a round Earth, i.e. the fact that 0 deg = 360 deg.

The solution was, therefore, not to generate the mesh but to directly compute it, ignoring for a while the complication due to the presence of landmasses. Working on a full sphere, the main idea was to start from a known triangularly facetted 3D shape and to recursively refine it using the existing mesh refinement tools available within the python scripts of the TELEMAC system: the icosahedron, a 3D shape of 20 triangles (elements), was chosen.

Fig. 1 below shows the initial icosahedron rounding up the contours of the Earth, the first refinement (splitting each triangle into 4 smaller triangles) together with the re-projection of the new vertices on the sphere, and the subsequent refinement from iteration 2 through iteration 8.

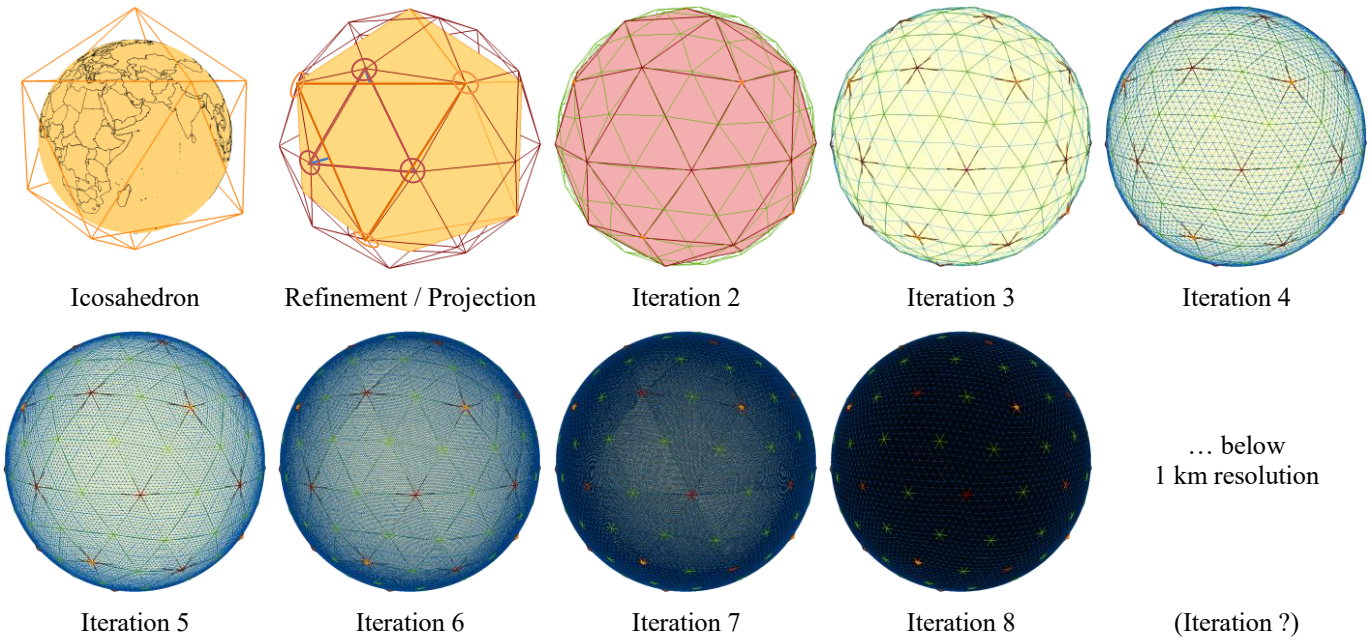

Figure 1. *Subsequent refinements of the icosahedron*

If we start with the 360 degrees of the circumference of the sphere based on a circle going through the poles, the icosahedron splits the sphere in 6 divisions, i.e. of 60 degrees for each foot of the triangle. The edge-length of a triangle is, therefore, slightly larger. If we now look at the circumference of the sphere based on a circle going along the equator after the first refinement, icosahedron splits the sphere in 10 divisions, i.e. 36 degrees for the first refinement, or 72 degrees for the icosahedron (5 divisions). In fact, depending on which pair of nodes, the edge length of the first refinement is either 31.72 or 36 degrees.

Let us chosen the longest of the edge lengths (i.e. 72 degrees), approximating the radius of the Earth, R, by 6,371,000 m, the circumference is $2\pi R = 40{,}030{,}173$ m. With that said, the "edge length" (distance when projected on the surface of the sphere) of the icosahedron is $(2\pi R/5) = 8{,}006{,}035$ km.

Subsequent refinements of the icosahedron multiply the number of elements by four while halving the edge length (following the curvature the sphere). TABLE 1 below shows the resulting metrics for subsequent mesh refinements.

TABLE 1 REFINEMENTS OF THE ISOCAHEDRON

Iterations	**Unstructured mesh characteristics**		
(sphere)	***360 (deg)***	***40,030,173 (m)***	***(elements)***
isocahedron	72	8,006,034.7	20
1	36	4,003,017.4	80
2	18	2,001,508.7	320
3	9	1,000,754.3	1,280
4	4.5	500,377.2	5,120
5	2.25	250,188.6	20,480
6	1.125	125,094.3	81,920
7	~ 1 / 2	62,547.1	327,680
8	~ 1 / 4	31,273.6	1,310,720
9	~ 1 / 7	15,636.8	5,242,880
10	~ 1 / 14	7,818.4	20,971,520
11	~ 1 / 28	3,909.2	83,886,080 *a*
12	~ 1 / 57	1,954.6	335,544,320
13	~ 1 / 114	977.3	1,342,177,280
14	~ 1 / 228	488.6	5,368,709,120

a. Current stage of the Earth by TELEMAC

b. Signed integers: 32bits = 2,147,483,647; 64bit = 9,223,372,036,854,780,000 Unsigned integers: 32bits = 4,294,967,295; 64bit = 18,446,744,073,709,600,000

Several comments can be made:

- It is noted that the current state of the art of global datasets and model results available are based on a resolution of about 1/12th of a degree. This is the case of global tidal harmonic dataset TPXO (see [20]), or the global 3D oceanic model HyCOM (see [21]).
- The highest resolution used so far to a compute an unstructured mesh for TELEMAC has been for Iteration 12. Higher iterations would require slight modifications to the existing python scripts to include long integers, as well as heavy modifications to the TELEMAC source code to allow long integer in appropriate places.
- Computation of the mesh for Iteration 11 takes about 10 minutes (on a standard computer) and 45 minutes for Iteration 12. This remains acceptable and far more efficient than generating the mesh. Iteration 13 (below the kilometre resolution) should not take more than 4 hours, although this was not tested.
- The chosen methodology (based on subsequent refinements) to compute the unstructured mesh of the Earth could be an advantage in the future to support multi-grid methods in order to accelerate further solutions for the TELEMAC system (although not part of the current research project). In any case, the approach taken has been beneficial to the project as testing of functionalities can be done on coarser meshes, while developing final results are based on the finer mesh.

B. Mapping Bathymetry and Topography

Having created an unstructured mesh of the Earth, the bathymetric and topographic datasets are then mapped using a trivial 3-point weighted interpolation method.

Using the software Blue Kenue (see [4]) Fig. 2 below shows a coloured rendering of the resulting mesh, with mapped values of bathymetry (in shades of blues) and topography (in shades of green).

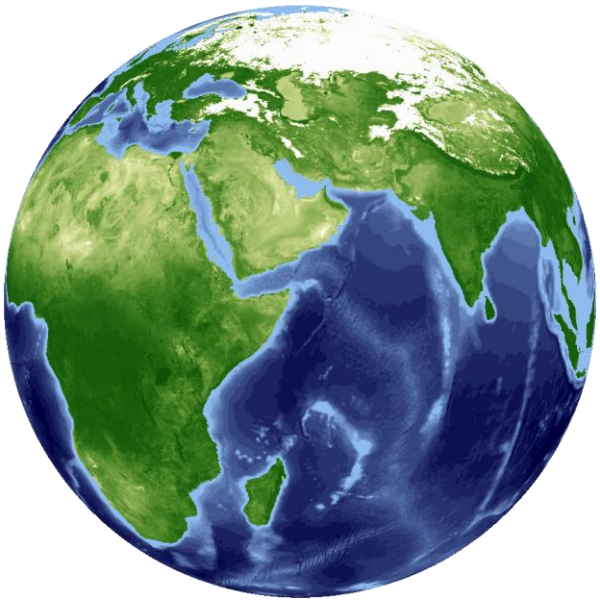

Figure 2. *The blue (and green) marble*

The GEBCO dataset was selected at this stage (see [2]). It has a resolution of about 1/16th of a degree. As the Earth by TELEMAC is refined further towards the kilometre, other sources of local bathymetries will have to be assembled for accurate results, particularly near the coasts. For instance, the marine data provider SeaZone (see [3]), can be put to the contribution by HR Wallingford.

The shades of green shown on Fig. 2 are here, in fact, not representing topography but were rather extracted from the "Blue Marble" satellite photo of the Earth surface (see [5]).

C. *Landmasses*

Having computed a mesh for the entire surface of the Earth imprinted with bathymetry and topography values, one can think of several approaches to deal with landmasses.

A first approach could consist in using TELEMAC's ability to deal accurately with wetting and drying. This approach implies that the mesh together with its mapped values remains untouched. However, this is not computationally efficient as all vertices on landmasses become dormant in a TELEMAC simulation.

A second approach could consist in using the shorelines of the GSHHS dataset (see [1], introduced in Section II.A), "checking" if a particular vertex is in one of the closed polygons defining landmasses, for every vertex in the mesh, and removing the vertex if so. Unfortunately, the "checking" step is also time consuming and would be prohibitive beyond Iteration 9.

Rather, the approach considered for the model of the Earth was to use the values (of bathymetry and topography) for the whole sphere, and simply / efficiently filter out values higher than a chosen mean sea level.

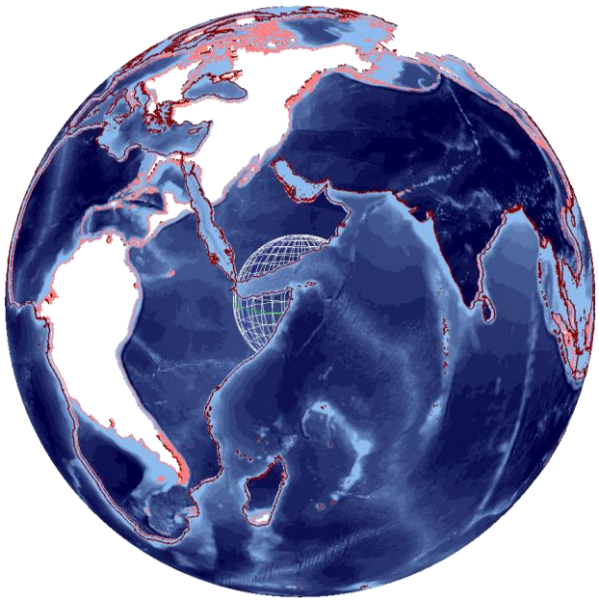

Figure 3. *The Earth by TELEMAC*

Fig. 3 above shows the resulting model: The Earth by TELEMAC in a see-through manner as the landmasses have been removed (the Pacific Ocean is visible through the Asian continent, South America through the African continent, …). The gridded sphere inside the Earth is only shown for perspective.

As previously said, several models of the Earth were developed in the course of this project, at various resolutions (mainly between Iteration 9 and 11), in order to effectively develop, test, validate and finally forecast various physical aspects of all water bodies.

III. Applications of The Earth by TELEMAC

A. *Propagation of Tsunami waves*

Having setup the model of the Earth, the first phase of the internal research project was to conclude on the ability of the TELEMAC system to deal with a complete sphere with no open boundaries. The application considered was to the propagation of tsunami waves, based on the TELEMAC-2D component. This application is one of the simplest to setup as all water bodies start at rest and the tsunami characteristics are provided through the steering file. It is important to note that the appropriateness of TELEMAC-2D to model the propagation of tsunami waves has been previously demonstrated in [6].

After corrections to the source code were made (in particular to account for the connection between 0 deg and 360 deg in the method of characteristics), model results were favourably compared with previous consultancy studies carried out at HR Wallingford. So far, local models had been setup for various projects in different parts of the world, including for the Lisbon 1755, Sumatra 2004, Tohuku 2011.

Unfortunately, because those consultancy study results remain confidential, they cannot be presented. Instead, the applicability of TELEMAC-2D to the propagation of tsunami waves over the entire globe was demonstrated through an animation posted on YouTube (see [7]), bringing 10 of the most devastating tsunami events together within a 24 hour simulation. Fig. 4 below shows two insets (two sides of the Earth), of snapshots of that animation.

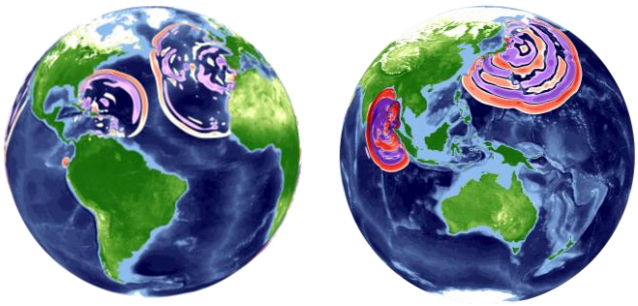

Figure 4. *Modelling tsunami waves over the Earth by TELEMAC*

Tsunami characteristics are set in TELEMAC through the Okada generator (see [8] and [9]). It is widely used in earth sciences to simulate seafloor deformation produced by local perturbation like earthquakes and was integrated within the TELEMAC system in 2012, by the authors of this article. The tsunami is characterised by its focal depth, its fault length and

width, its dislocation, its strike direction, its dip angle, and its slip (see illustrative Fig. 5 below).

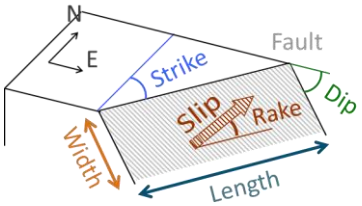

Figure 5. *Tsunami characterisation*

It should be noted that release v7p2 of the TELEMAC system only includes the possibility to define one tsunami source, using the keywords:

- ✓ OPTION FOR TSUNAMI GENERATION; and
- ✓ PHYSICAL CHARACTERISTICS OF THE TSUNAMI

It is anticipated, as a result of this internal project, that the keywords above will be extended in release v7p3 to the definition of multiple sources, whether combined to define one event, and / or triggered as separate events at different times.

For reference, the selected events shown in the animation posted on YouTube were: Solomon Islands 2007 (see [10]), Tohuku 2011 (see [11]), Sumatra 2004 (see [12]), Makran/Balochistan 1945 (see [13]), Greece 1956 (see [14]), Lisbon 1755 (see [15]), Dominican Republic 1946 (see [16]), Ecuador/Colombia 2016 (see [17]), Valvidia 1960 (see [18]) and Kamchatka 1952 (see [19]).

With a resolution of about 4 km (Iteration 11) and a time step of 1 minute, the 24 hour simulation was computed in less than 5 hours on 36 compute cores only. Higher speed up can be achieved with a higher number of cores, particularly for a possible forecasting mode.

B. *Forecasting tides*

In order to fulfil the first objective of this internal project (to deliver comprehensive and detailed global modelling resources to support environmental hydraulics studies anywhere in the world), the second phase looked at an important aspect of all coastal models: the forecasting of tidal information.

Typical of the setup of a coastal (hydrodynamic) model, one would extract tidal harmonic information from a global dataset or from a range of tidal gauge observations and re-synthetize a signal on its open boundary for various periods. The TPXO dataset (see [20]) is one such global dataset. It is widely used in earth sciences and was first integrated within the TELEMAC system in 2011, by the authors of this article. It provides several harmonic constituents computed from a best-fit of tidal levels measured along remote sensing tracks from the TOPEX/POSEIDON and its subsequent JASON satellite programs.

As previously noted, the Earth by TELEMAC has no open boundaries. Therefore, the forecasting of tides could not have been imposed but rather directly computed from known gravitational forces (relative rotations of the Sun, the Moon, the Earth and various corrections in orbit trajectories), a feature that is already available in the TELEMAC system, using the keyword:

- ✓ TIDE GENERATING FORCE

After calibration of the hydrodynamic model based on the TELEMAC-2D component (to account for 3D phenomenon such as internal tides), model results of surface levels and depth average velocities were favourably compared with the TPXO dataset.

In order to demonstrate the applicability of TELEMAC-2D to forecast tides over the entire globe, another animation was created and posted on YouTube (see [22]). For reference, an arbitrary 15-day period starting on January 13, 2017 was selected. Fig. 6 below shows two insets (two sides of the Earth), of snapshots of that animation of the Earth by TELEMAC. Colours represent the maximum tidal range computed over a spring tide (with red indicating the highest and blue the lowest variation in tidal range). For comparison purposes, Fig. 7 shows the same snapshots but extracted from the TPXO dataset.

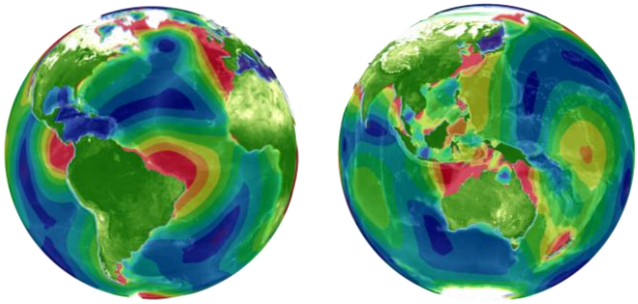

Figure 6. *Forecasting tides over the Earth by TELEMAC*

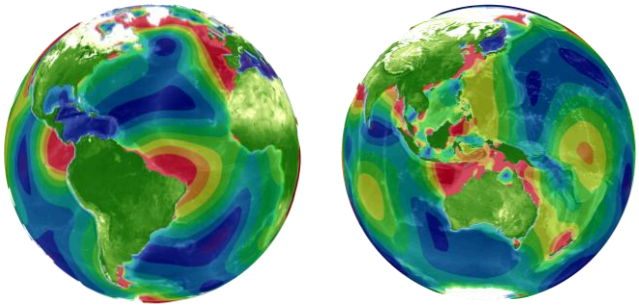

Figure 7. *Extraction of observed tides from the TPXO dataset*

While there are differences between the TELEMAC-2D forecast and the TPXO dataset, these could be explained by the absence 3D processes. It is expected that TELEMAC-3D, with an appropriate representation of ocean currents and internal waves / tides as well as a self-attracting force would provide a fairer comparison (see Chapter V).

C. *Forecasting storm surges*

In the continuation of Phases 1 and 2, the third phase of the project looked at atmospheric drivers, such as winds and atmospheric pressure. Atmospheric temperature and other aspects of the thermal balance would be tested later, before going 3D. Atmospheric drivers (whether drivers of the

hydrodynamic or the heat budget) are existing features of the TELEMAC system and are often used on a wide range of consultancy studies, particularly in metocean studies.

Therefore, similarly to the application of the Earth by TELEMAC to the propagation of tsunami waves, the applicability of TELEMAC-2D to predicting storm surges over the entire globe was simply tested and demonstrated through another animation posted on YouTube (see [23]).

The animation shows water surges (ranging from red: highs, down to purple: lows) driven by storms (shown by wind vectors) running across the globe for 11 known storms within an 85-day sequence. Fig. 8 below shows two insets (two sides of the Earth), of snapshots of that animation. Note that the winds are shown several hundred kilometres above the surface so that the surge and wind field can be seen more readily.

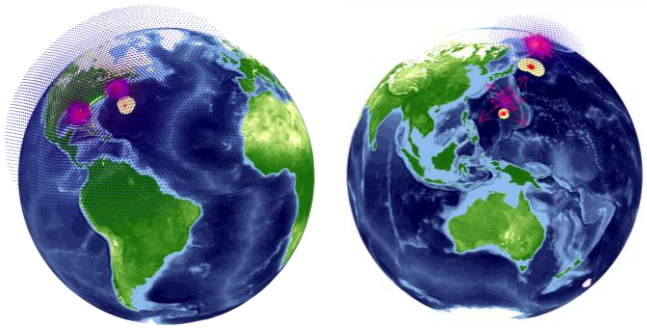

Figure 8. *Forecasting storms over the Earth by TELEMAC*

For reference, the selected storms shown in the animation posted on YouTube were: Cyclone Inigo 2003 (see [24]), Typhoon Haiyan 2013 (see [25]), Bangladesh Cyclone 1991 (see [26]), Cyclone Gonu 2007 (see [27]), Hurricane Allen 1980 (see [28]), Hurricane Ten 1924 (see [29]), Hurricane Katrina 2005 (see [30]), Hurricane Patricia 2015 (see [31]), Cyclone Pam 2015 (see [32]), Hurricane Ioke 2006 (see [33]) and Typhoon Tip 1979 (see [34]). Storm characteristics were extracted from the IBTrACS (see [35]) database for each of those, from which the wind and pressure field were computed (within TELEMAC) using the Holland model (see [36] and [37]).

D. Forecasting waves

Having demonstrated that the Earth by TELEMAC can be driven by atmospheric inputs, the fourth phase of the internal research project looked to forecasting waves on the entire globe, since these are resulting principally from winds.

Similarly to the tides, typical setup of coastal (wave) models would include the extraction of wave information from a global dataset or from a range of wave gauge observations and use these at its open boundary for various periods. The ERA-5 dataset (see [38]) available since July 2017 (or the ERA-Interim before then) is one such global dataset. It is widely used in earth sciences and often used in consultancy studies by HR Wallingford. The python scripts, developed for the TELEMAC system by the main author of this article, include a direct link to the dataset.

Again, the Earth by TELEMAC has no open boundaries. Therefore, the forecasting of waves has to be the sole results of winds. A simulation of the TOMAWAC component was, therefore, setup for the Earth by TELEMAC, with waves driven only by temporally and spatially varying winds. Winds were extracted from the ERA-5 dataset as well as waves for comparison purposes.

In order to demonstrate the applicability of TOMAWAC to forecast waves over the entire globe, another animation was created and should be posted on YouTube in early November 2017. For reference, an arbitrary 60-day period starting on November 1, 2016 was selected. Fig. 9 below shows two insets (two sides of the Earth), of snapshots of that animation of the Earth by TELEMAC. Colours represent the wave heights computed (with red indicating the highest waves blue the lowest waves). For comparison purposes, Fig. 10 shows the same snapshots but extracted from the ERA-5 dataset.

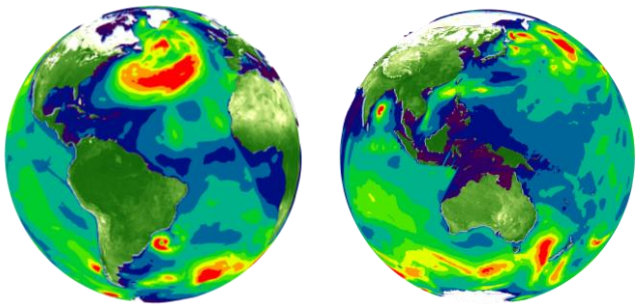

Figure 9. *Forecasting waves over the Earth by TELEMAC*

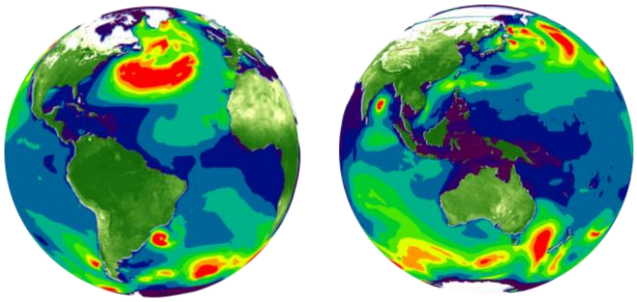

Figure 10. *Extraction of wave heights from the ERA-5 dataset*

While there are differences between the forecast and the ERA-5 dataset, the comparison remains favourable. A more detailed calibration and validation of TOMAWAC against observations at wave buoys should follow. Nonetheless, the applicability of the Earth by TELEMAC to model waves on the entire globe is here demonstrated.

For reference, with a resolution of about 15 km (Iteration 9), a time step of 5 minutes and a spectrum defined over 26 periods and 12 directions, the 60 day simulation was computed in a little more than 2.5 days on 36 compute cores only. Higher speed up can be achieved with a higher number of cores, particularly for a possible forecasting mode.

IV. Conclusions

HR Wallingford has setup the Earth by TELEMAC as an internal research project with the objective to demonstrate the

open source community that TELEMAC is capable to bridge the gap between environmental hydraulics and oceanography.

The first four phases of the project have already broken new ground, particularly in terms of resolutions both spatial and temporal, while providing forecasts comparable to often used global datasets. The absence of boundary conditions facilitates the modelling greatly; its parallelisation to great number of computing units makes the modelling possible.

However, this project will continue for another year as the two objectives set out remain to be fulfilled:

- While this project already provides a detailed and wide ranging platform of metocean data (tides, surges, extremes, waves, etc.) at high resolution over the entire globe, the project now needs to move to 3D processes.
- While the recipe of the Earth by TELEMAC is here published for everyone to copy, HR Wallingford is looking to focus and lead interests from national and international organisations from around the world, in order to create a larger pool of resources (computing, human, financial, observed data, …).

Future applications of the Earth by TELEMAC could include: forecasting activities (such as vulnerability to coastal flooding, or for the tracking and circulation of pollution, debris or plastics); engineering designs (for example for detailed 3D metocean analysis, extremes and climates); and resource assessments (such as for renewable energy, for deep sea mining, or for global environmental impact).

V. Preliminary 3D Applications

In anticipation to a follow-up article to be published at the user conference in 2018, the following shows two preliminary results of the Earth by TELEMAC based on TELEMAC-3D, further highlighting its potential to fulfil our objectives.

A. *Ocean currents*

The TELEMAC-3D component has been used here to investigate whether the Earth by TELEMAC can generate sensible ocean currents starting from still. The main driver to the model is a vertical density profile. The air temperature and the solar radiation extracted from the ERA-5 dataset (see [38]) are also imposed through the thermal exchange model, with the following keyword:

✓ ATMOSPHERE-WATER EXCHANGE MODEL = 2

Fig. 11 below shows the magnitude of the currents predicted at the surface, for the two sides of the globe. The simulation was run for a preliminary period of 30 days, starting with no water movements. The “coarse” mesh (based on Iteration 9) was used with only 4 planes in the vertical.

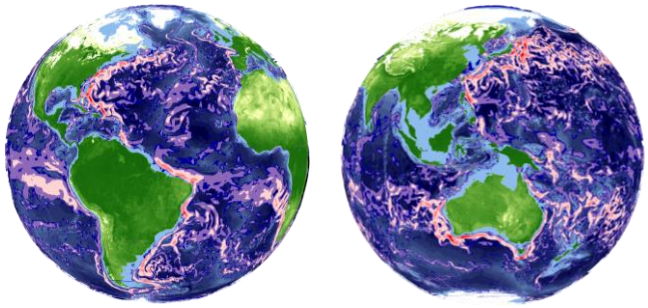

Figure 11. *Surface currents over the Earth by TELEMAC*

Despite the short duration and the coarse resolution of the model, some of the major ocean currents are formed in various places of the globe. While further calibration and validation of these results over much longer periods and finer meshes will be carried out in the next phases of the project, these results are extremely encouraging in TELEMAC ability to bridge the gap between environmental hydraulics and oceanography. Other 3D oceanic model such as HyCOM (see [21]) will be used as approximate hot-start conditions or at least for comparison purposes.

B. *Internal tides*

The TELEMAC-3D component has been used here to investigate whether the Earth by TELEMAC can generate a specific sort of internal waves: internal tides. These waves are particularly critical to offshore projects with risers or seabed facilities within the first kilometre of the water column. HR Wallingford has identified this phenomenon in several oil and gas and deep sea mining studies. These waves are the result of a combination of a strong stratification and the presence of tides, a combination of processes that is not available in any of the global models or datasets.

Fig. 12 below show a snapshot in time of the surface current (top plane) of a TELEMAC-3D results based on 10 planes.

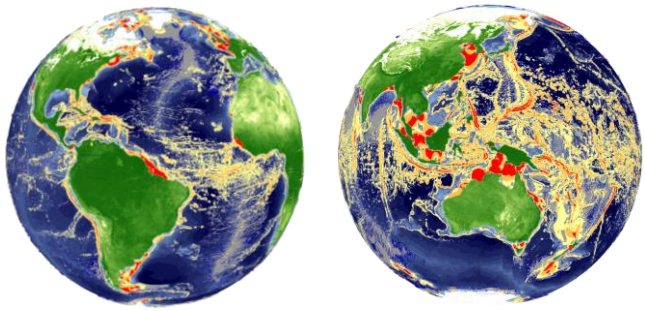

Figure 12. *Forecasting internal tides over the Earth by TELEMAC*

While high currents are predicted in places known for their high tidal energy the Earth by TELEMAC is able to also highlight places of internal tides. In fact, these results compare favourably with publish literature on the subject (see for instance [39]).

REFERENCES

[1] P. Wessel and W.H.F. Smith, "A Global Self-consistent, Hierarchical, High-resolution Shoreline Database", Journal of Geophysical Research, 101, #B4, pp. 8741-8743., 1996

[2] GEBCO, "The General Bathymetric Chart of the Oceans, the most authoritative, publicly-available bathymetry data sets for the world's oceans", 2017, http://www.gebco.net/

[3] SeaZone (part of HR Wallingford), "Developing marine maps for over ten years", 2017, www.seazone.com

[4] National Research Council, "Blue Kenue™: Software tool for hydraulic modellers", April 2017, https://www.nrc-cnrc.gc.ca/eng/solutions/advisory/blue_kenue_index.html

[5] NASA Earth Observatory, "The Blue Marble Next Generation - A true color earth dataset including seasonal dynamics from MODIS", August 16, 2017, https://visibleearth.nasa.gov/view.php?id=73751

[6] A.J.Cooper, G.Cuomo, S.E.Bourban, M.S.Turnbull, D.H.Roscoe, "Testing TELEMAC-2D suitability for tsunami propagation from source to near shore", Proceedings of the XIXth TELEMAC User Conference, Oxford, October 18-19, 2012, pp 89-92.

[7] S.E.Bourban, HR Wallingford YouTube Channel, "Watch tsunami waves propagating in this animation of 'The Earth' by TELEMAC", April 24, 2017. https://youtu.be/5mK-Ize2aY8

[8] Okada Y. (1985), Surface deformation due to shear and tensile faults in a half space, Bulletin of the Seismological Society of America, 75-4, pp. 1135-1154.

[9] Okada Y. (1992), Internal deformation due to shear and tensile faults in a half-space, Bulletin of the Seismological Society of America, 82-2, pp. 1018-1040.

[10] Solomon Islands 2007: N.Zamora, G.Franchello, A.Annunziato, "01 April 2007 Solomon Island Tsunami: Case Study to Validate JRC Tsunami Codes", European Commission, 2011.

[11] Tohoku 2011: P.K.Ravi, K.Satake, "A Research Report On Computer Simulation of 2011 East Japan Earthquake and Tsunami", University of Tokyo, July 2013.

[12] Sumatra 2004: A.Piatanesi, S.Lorito, "Rupture Process of the 2004 Sumatra–Andaman Earthquake from Tsunami Waveform Inversion" Bulletin of the Seismological Society of America, Vol. 97, No. 1A, pp. S223–S231, January 2007.

[13] Makran / Balochistan 1945: S. Neetu, S.Iyyappan, R.Shankar, S.C.Shenoi, "Trapped waves of the 27 November 1945 Makran tsunami: Observations and numerical modelling", Natural Hazards 59(3), December 2011

[14] Greece 1956: S.Beisel, et al, "The 1956 Greek Tsunami recorded at Yafo, Israel, and its numerical modelling", Journal of Geophysical Research, Volume 114, Issue C9, September 2009.

[15] Lisbon 1755: K.J.Horsburgh, C.Wilson, B.J.Baptie, A.J.Cooper, D.Cresswell, R.M.W.Musson, L.Ottemoller, S.Richardson, S.L.Sargeant, "Impact of a Lisbon-type tsunami on the U.K. coastline and the implications for tsunami propagation over broad continental shelves", Journal of Geophysical Research, Vol. 113, C04007, 2008

[16] Dominican Republic 1946: IOC, "Sources of tsunamis in the Caribbean with possibility to impact the southern coast of the Dominican Republic", Workshop Report No. 276, Dominican Republic, 6-7 May 2016.

[17] Ecuador/Colombia 2016: Lingling Ye, H.Kanamori, J.-P.Avouac, Thorne Lay, "The 16 April 2016, MW 7.8 (MS 7.5) Ecuador earthquake", Earth and Planetary Science Letters 454, September 2016.

[18] Valvidia 1960: A. Sanchez, Master of Science Thesis, "Tsunami Forecast using an Adaptive Inverse Algorithm for the Chile-Peru Source Region" at the University of Hawaii, December 2006

[19] Kamchatka 1952: Yoshiki Yamazaki, Master of Science Thesis, "Forecast of Tsunami from the Japan-Kuril-Kamchatka Source Region", at the University of Hawaii, August 2004.

[20] Oregon State University, "OSU Tidal Data Inversion Software and Atlas", TPXO-08 ATLAS, 2008, http://volkov.oce.orst.edu/tides/tpxo8_atlas.html

[21] National Ocean Partnership Program, of U. S. Global Ocean Data Assimilation Experiment, "The Hybrid Coordinate Ocean Model Overview", https://hycom.org/hycom/overview

[22] S.E.Bourban, HR Wallingford YouTube Channel, "The Earth by TELEMAC Simulation of Global Tidal Ranges", May 23, 2017. https://youtu.be/S2L0-p2Pi88

[23] S.E.Bourban, HR Wallingford YouTube Channel, "Watch our storm-tracker in this animation of 'The Earth' by TELEMAC", July 26, 2017 https://youtu.be/MRKtasKYQcQ

[24] "Cyclone Inigo 2003", Wikipedia page, 2017, https://en.wikipedia.org/wiki/Cyclone_Inigo

[25] "Typhoon Haiyan 2013", Wikipedia page, 2017, https://en.wikipedia.org/wiki/Typhoon_Haiyan

[26] "Bangladesh Cyclone 1991", Wikipedia page, 2017, https://en.wikipedia.org/wiki/1991_Bangladesh_cyclone

[27] "Cyclone Gonu 2007", Wikipedia page, 2017, https://en.wikipedia.org/wiki/Cyclone_Gonu

[28] "Hurricane Allen 1980", Wikipedia page, 2017, https://en.wikipedia.org/wiki/Hurricane_Allen

[29] "Hurricane Ten 1924", Wikipedia page, 2017, https://en.wikipedia.org/wiki/1924_Cuba_hurricane

[30] "Hurricane Katrina 2005", Wikipedia page, 2017, https://en.wikipedia.org/wiki/Hurricane_Katrina

[31] "Hurricane Patricia 2015", Wikipedia page, 2017, https://en.wikipedia.org/wiki/Hurricane_Patricia

[32] "Cyclone Pam 2015", Wikipedia page, 2017, https://en.wikipedia.org/wiki/Cyclone_Pam

[33] "Hurricane Ioke 2006", Wikipedia page, 2017, https://en.wikipedia.org/wiki/Hurricane_Ioke

[34] "Typhoon Tip 1979", Wikipedia page, 2017, https://en.wikipedia.org/wiki/Typhoon_Tip

[35] NOAA, "International Best Track Archive for Climate Stewardship", 2017, https://www.ncdc.noaa.gov/ibtracs/

[36] G.J.Holland, "An analytic model of the wind and pressure profiles in hurricanes." Monthly Weather Review, 108, 1212–1218, 1980.

[37] G.J.Holland, J.I.Belanger, A.Fritz, "A revised model for radial profiles of hurricane winds", Monthly Weather Review, 138, 4393-4401, 2010.

[38] ECMWF, Copernicus, "Climate Reanalysis, About ERA5", July 17, 2017, https://climate.copernicus.eu/products/climate-reanalysis

[39] S.D. Griffiths, "Global modelling of internal tides", 2nd Norway-Scotland Internal Waves Symposium, At The Royal Society of Edinburgh, UK, November 2011

An overview on the capabilities of the TELEMAC-MASCARET system to deal with tsunamis: feedbacks from TANDEM project

Riadh Ata, Marine le Gal and Damien Violeau
EDF R&D
6 Quai Watier
78400 Chatou, France

Abstract— **This paper gives an overview on the capabilities of the TELEMAC-MASCARET suite to simulate different steps of the tsunami phenomenon. The simulation of a full tsunami event includes generation, propagation, shoaling, run up and flooding. To deal with all these steps, a full set of benchmarks were identified with the TANDEM project [1]. Different numerical properties are required for these different steps. In this paper we summarize the final conclusions drawn from this project.**

I. INTRODUCTION

After the major tsunami events of Sumatra in 2004 and Japan in 2011, a lot of effort has been spent by the scientific community to understand phenomenon of tsunamis. Indeed, several physical aspects linked to tsunami are still under active investigation and represent open problems.

In the wake of the above tsunamis policy maker were confronted with criticisms about the readiness of their countries' defenses against major hazard. The fears on tsunami readiness are heightened in some areas where sensitive facilities could be impacted.

In this context, the French government approved the funding of a large research project dedicated to the study of tsunamis and the assessment of their risks on the French coast.

In the first part of the paper we will present the TANDEM project. The second part of this paper is dedicated to the assessment of the numerical features needed for the simulation of the tsunami generation, propagation and coastal flooding.

II. BRIEF PRESENTATION OF TANDEM PROJECT

TANDEM (Tsunamis in the Atlantic and the eNglish channel: Definition of the Effects through numerical Modeling) is a project funded by French government that includes a consortium of several research and consultancy institutions. Its main objective is the improvement of knowledge about tsunamis and the assessment of their risks on French coasts.

This project is organized in four work-packages:

- Work-package 1 (WP1): dedicated mainly to the qualification and validation of codes by handling several unitary benchmarks. These benchmarks will be described and discussed extensively in Section III.
- Work-package 2 (WP2): focuses on uncertainty quantification and propagation
- Work-package 3 (WP3): deals with simulation and lessons drawn from Tohuku event of 2011
- Work-package 4 (WP4): includes several cases linked to the French coasts

The subsequent section will not describe in detail the work-packages, however, we will cite some of their benchmarks when dealing with different steps needed to numerically describe the tsunami.

III. ASSESSMENT OF NUMERICAL FEATURES NEEDED FOR TSUNAMI SIMULATION

To reproduce a tsunami event, a numerical code has to be able to handle generation, propagation, run up, submersion and finally coastal impact and flooding. Very seldom all these features are captured with using a unique model. In a majority of past tsunami studies, the obtained results provide only few of the above-mentioned aspects. The main reason behind this is the overwhelming computation time needed to simulate all required aspects in a single numerical model run using a single mesh.

To overcome these difficulties, researches and practitioners use often different models with different mesh characteristics. In the best of cases, these meshes are nested in order to make easy chaining of models and boundary communications.

In the following we will focus on each feature of a typical tsunami and will discuss how the Telemac-Mascaret suite can represent each of them.

A. Generation

The generation of tsunamis can be the consequence of a fast movement of the earth crest (earthquakes, submarine landslides, etc) or the sudden fall of external bodies (meteorites, aerial landslide, any other body) in a mass of still or weakly moving water. Different source of tsunamis are:

1. Earthquake

The generation of tsunami source following an earthquake is an inverse problem which is far to be an easy task which explain the numerous ongoing works focusing on it.

The inversion problem recovers an initial distortion of the free surface and probably an initial velocity distribution by considering seismic and geodetic data (magnitude of the earthquake, its epicentre, slip amplitude, satellite and gauges measurements, etc.)

The most used seismic generation model in the literature is the one of Okada [2]. This latter computes the deformation of the ground using the theory of elasticity in an idealized homogenous medium. The deformation of the free surface is obtained with an instantaneous translation of the ground distortion. The initial induced velocity is assumed to be nil.

Seismic events include complex physics and can scarcely be reproduced by a single rectangular fault model (Okada). To better reproduce real scenarios, a patch of small faults (sub-faults) is preferred [3], [4], and [5].

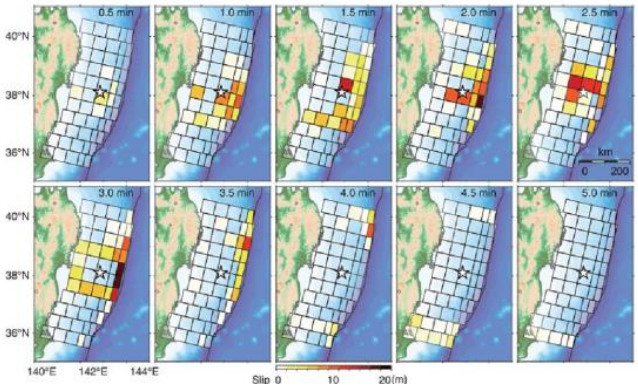

Figure 1. *Example of sub-faults used for the generation of the Tohoku event (Satake et al. [5]).*

Okada model was integrated to Teleamc-2D since version v6p2. It was widely used with in the Telemac community and overall, feedbacks are positive. However, based on the works of Hammack [7], Todorovska et al. [8] and more recently, Le Gal et al. [9], static generation (like the one of Okada) can in some cases be not sufficient to reproduce tsunami accurately. Indeed, instantaneous transmission of bed distortion can introduce non-physical behaviours that, even with heavy calibration efforts, cannot be avoided.

A more accurate generation should use "kinematic assumptions" which means to consider a finite transmission speed of the bed distortion in horizontal direction (rupture velocity Vp (Hammack[7])) and in the vertical direction (rise time tr (Todorovska [8])) or both (le Gal [9]). In the last case, the generation model reads (Fig. 2):

$$\xi(x,t) = H(L-x)H(x)\tau(t) \qquad (1)$$

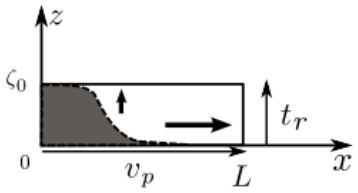

Figure 2. *Kinetic generation proposed by le Gal et al. [9]*

This new model was used to reproduce seismic generation source for the Tohoku event of 2011 and for the Gisborne-New Zealand event of March 25th, 1947. We focus in this section on the latter event.

Fig. 3 shows final free surface obtained at the end of the generation procedure of the Gisborne tsunami. For all these cases, a model with a set of 191 sub-faults. The rupture velocity Vp is considered equal to 300 m/s, which, based on seismic data, is the most probable value. Fig. 4 gives the maximum free surface obtained at the shoreline which are compared with data of Downes et al [10].

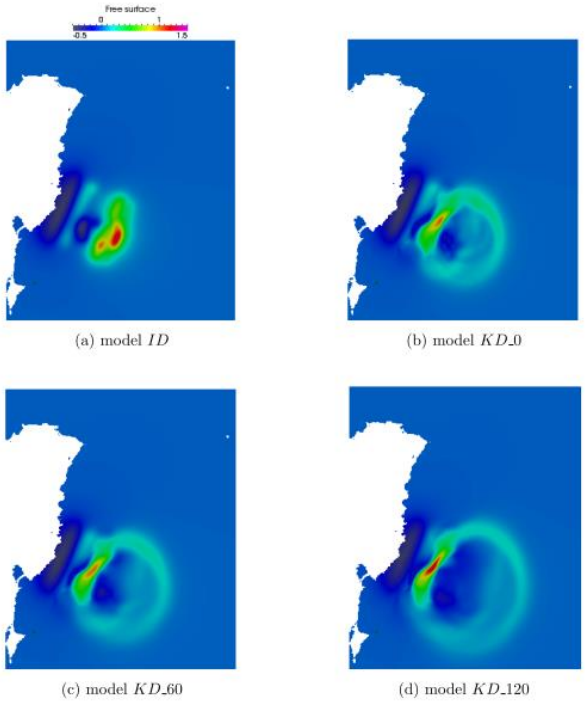

Figure 3. *the Gisborne tsunami (1947) tsunami: (a) instantenous generation, (b) kinematic generation with duration of 190s and tr=0s, (c) kinematic generation with tr=60s and (d) kinematic generation with tr=120s, by le Gal et al. [9]*

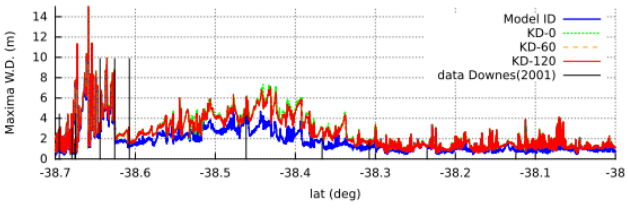

Figure 4. *maximum water elevation obtained at the shoreline. Comparison of different results with data of Downes et al. [10]*

The kinematic generation is an interesting option to be implemented in the Telemac-Mascaret suite. For more details about this topic, we refer to the PhD thesis of le Gal [9].

2. Landslides

Landslide induced tsunami is another open topic. Its complexity comes from the fact that it deals much more with soil mechanics than with hydraulics. The estimation of the volume of displaced soil and its velocity is the key point of an accurate generation of the induced tsunami. In a numerical point of view, it is safer to use a separate model to generate the initial starting state of the tsunami. Indeed, the dynamic behind a landslide is complex and the interaction between moving soil and neighbouring water is very rapid. This leads in most cases to the violation of most numerical assumptions (continuity, slow motion, homogenous media, etc.)

Within the TANDEM project, all the undertaken simulation of real case of La Palma, were based on the work of Abadie et al. [11]. This case supposes a slide of a huge volume of one mountain side due to volcanic eruption.

The nonlinear shallow water equation of Telemac-2D were used to simulate the propagation of the La Palmas event. The mesh is built using Blue Kenue using a density which varies with the bathymetry gradient. The extent of the mesh includes the major part of the North Atlantic Ocean (Fig. 5). The model consists of more 12.5 million elements and almost 6.5 million of nodes.

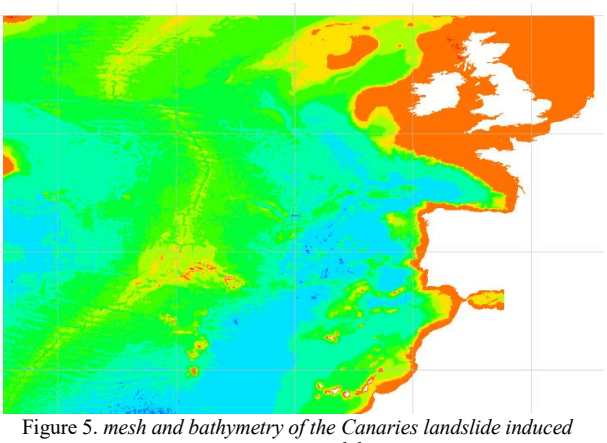

Figure 5. *mesh and bathymetry of the Canaries landslide induced tsunamis model.*

This mesh is used to reproduce four scenarios of landslide. The volume of the slide varies between 25 and 450 km^3. Fig. 6 gives snapshots of the water elevation in the case of a slide volume of 80 km^3.

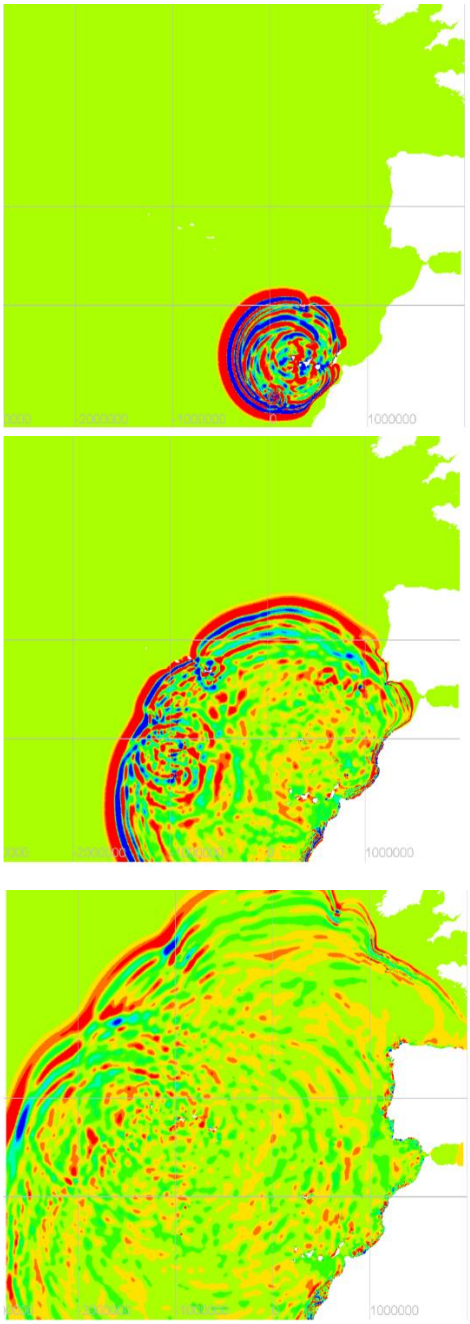

Figure 6. *Snapshots of Canaries Islands tsunami model*

Even though initial wave heights are overwhelming (around 100 m), tsunami reaches western European coasts (especially French ones) with an amplitude of several dozens of centimetres. For instance, at Brest, maximum water elevation is around 70 cm. At Bordeaux, maximum height is about 1.15 m reached by a secondary wave.

B. *Propagation*

To assess propagation, members of TANDEM project have identified several benchmarks with different ranges of complexity. In most of these cases, Telemac-2D with its

shallow water finite elements and finite volumes versions, as well as Boussinesq one has given satisfactory results. Telemac-3D also was used for several cases and results need to be improved especially when dealing with dispersive cases.

We cannot give in this paper a full reporting about these benchmarks. However, we give here the most challenging ones in order to discuss the efforts we need to improve the code in a near future.

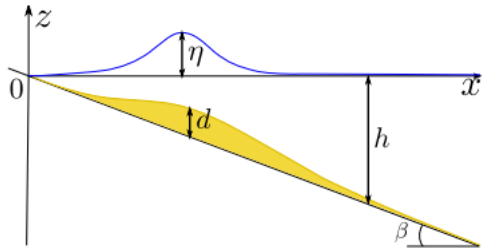

Figure 7. *Geometry and notation of analytical landslide*

1. Case GG01: analytical landslide

This case was proposed by Liu et al.[12]. This case describes an analytical tsunami generated by landslide in 1D (Fig. 7). The solution is obtained from linearized shallow water equations. The thickness of the landslide is defined by:

$$d(x,t) = \delta exp\left[-\left(2\sqrt{\frac{x\mu^2}{\delta tan\beta}} - \sqrt{\frac{g}{\delta}}\mu t\right)^2\right]$$

Where = 1m the maximum thickness of the slide and μ=δ/L and g the gravity, t the time and x the abscissa (Fig. 7).

The introduction of the sliding bed into Telemac-2D is done by varying the bathymetry during the time loop. A very small time step is used to verify the assumption that the movement is liner. The obtained results are given in Fig. 8 and shows very good agreement between numerical and analytical results.

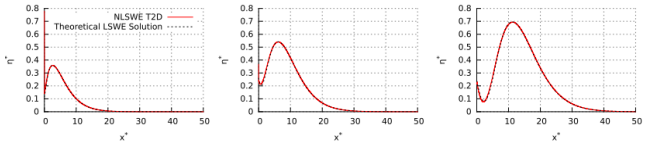

(a) $t^* = 0.5$ (b) $t^* = 1.0$ (c) $t^* = 1.5$

Figure 8. *Results of analytical landslide model*

2. Case P01: solitary wave

This case is one of the most challenging ones. It reproduces an analytical solution a solitary symmetrical wave. This case is very simple and the solution is the one obtained by a refined numerical discretization of Euler equations [13]. Fig. 9 describes this simple case where the wave travels with a velocity C which is the exact velocity of a solitary wave.

This case is challenging because it needs a fully dispersive model. Moreover, the non-linearity (ration of amplitude of the wave by the water height) is big which lays on the limits of the validity of Telemac-3D algorithm.

As it is known, solitary wave is not a solution of the shallow water equations. These latter tends to reshape the wave into a travelling sharp front (shock). In order to keep the original shape or the wave at least a Boussinesq model is necessary. The ideal mean should be a Navier- Stokes (Euler) model like the one of Telemac-3D.

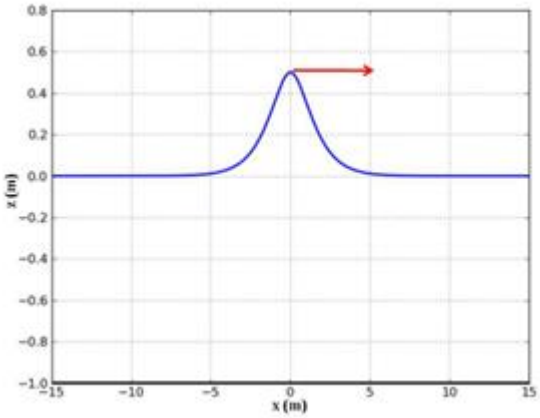

Figure 9. *Solitary wave benchmark*

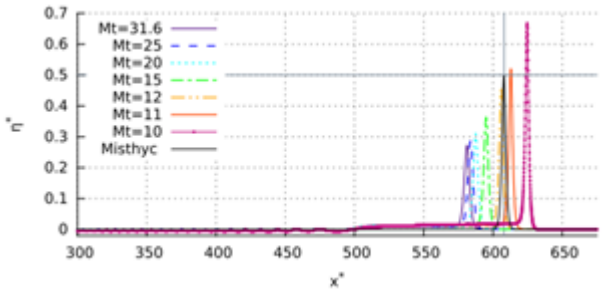

Figure 10. *Telemac-3D results for the solitary wave benchmark*

Within TANDEM project several dispersive codes were tested, among them Telemac-3D. The obtained results are shown in Fig. 10. The different curves represents different mesh refinements and different CFL values. Horizontal and vertical black lines gives the expected analytical wave height and location respectively.

The most striking conclusions from these results are:

- The extreme dependence of amplitude and location of the wave with mesh refinement and CFL values
- The shape of the solitary wave is almost conserved, however a spurious tailing wave appears and persists for most of numerical options.
- Amplitude of the wave can, for some cases, be amplified and goes over the initial value.

The question of conservation of momentum and of mechanical energy can come up.

- Compared to other codes, the results of Telemac-3D are not satisfactory. This can be explained in a major part by the fact the order in space and time of the used schemes are at best of second order. Whereas all the other codes are using very high orders
- A final explanation of the poorness of the results come from the moving mesh (Sigma transform) that introduces a non-negligible numerical diffusion but also spurious dispersion.

3. GS01: vertical movement on flat bottom [7]

This benchmark is a rectangular flume in which a wave is generated from a bed motion. The geometry and initial setting is described in Fig. 11. The bed motion is described analytically through an exponential or a sine based expression |7]. The obtained results are compared with the solution of the linear problem under an irrotational assumption. This solution can be found in [7].

This benchmark is useful to see the capabilities of Telemac-2D to deal with generation and propagation of waves due to bed motion.

The expressions of the initial bed motion are given by:

- Exponential motion :
$$\xi(x,t) = \xi_0(1-e^{-\alpha t})H(b^2-x^2)$$
- Sinusoidal motion:
$$\xi(x,t) = \xi_0\left[\frac{1}{2}\left(1-cos\left(\frac{\pi t}{t_r}\right)H(t_r-t) + H(t-t_r)\right)\right]H(b^2-x^2)$$

Where H is the Heavyside step function and ξ is the amplitude of the bed motion. Dimensionless varibles are defined as :

$$x^* = \frac{x}{h},\ b^* = \frac{b}{h},\xi_0^* = \frac{\xi_0}{h};\ t^* = t\sqrt{\frac{g}{h}};\ t_r^* = t_r\sqrt{\frac{gh}{b^2}}$$

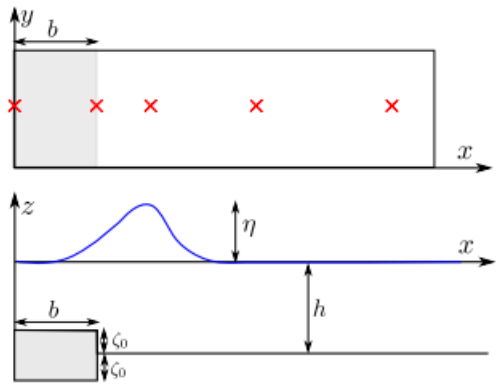

Figure 11. *geometry and initial setting of case GS01*

Three ranges of velocities has been identified:

- Impulsive motion: $t^* \ll 1$
- Creeping motion: $t^* \gg 1$
- Transitional motion where t* is in between.

This benchmark is clearly outside the range of assumption of shallow water equations. The Boussinesq version of Telemac-2D, as well as, Telemac-3D were used together with the code Mysthic (Euler equations with irrotational assumptions, Benoit et al. [14]). The obtained results are shown in Fig. 12.

As it can be observed, during the generation event, all models give good results which fit well reference solution. However, the propagation step, given by time profiles at x*=b* shows that Telemac-3D is still giving satisfactory results for the three types of flows. However, when transient effects are large, Boussinesq model fails to remain stable and shows spurious numerical wiggles. These observations are even worse for the case of sinusoidal generation motion.

This case shows clearly that the Boussinesq model needs to be improved.

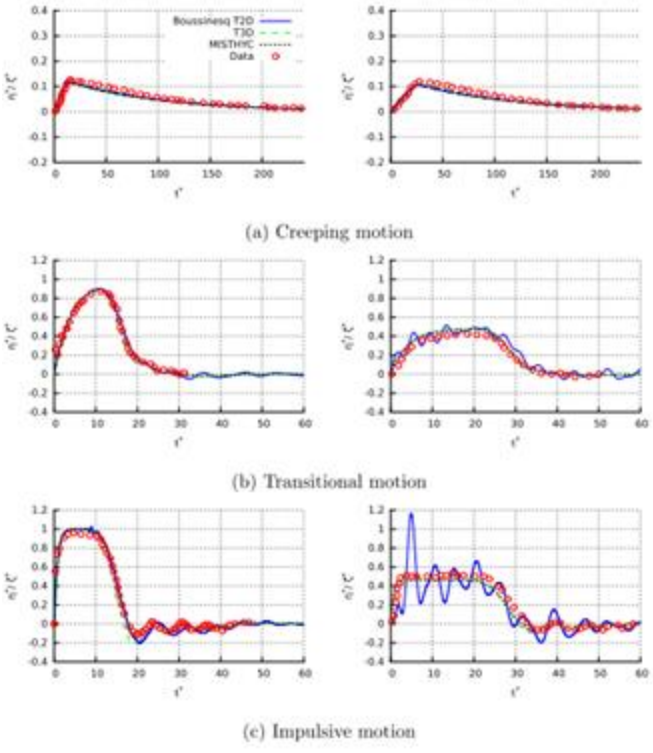

Figure 12. *Results of the exponential bed generation*

4. Case RS07: run up on a uniform beach [15]

This case aims at reproducing the run up of a solitary wave on an oblique beach is given in [15]. This benchmark allows to assess the numerical abilities of Telemac-2D to

handle propagation, shoaling, run up and finally flooding of dry beach.

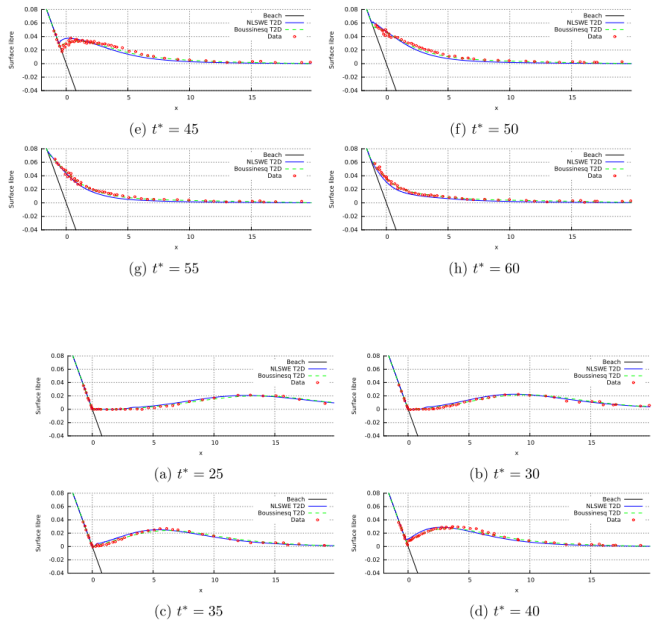

Figure 13. *Results for the case RS07:-part 1 (up), part 2 (down)*

The obtained results are partially shown in Fig. 13. It can be seen that overall behaviour of the code with its Boussinesq and shallow water versions, is really satisfactory. Shallow water equations overestimates arrival times and thus the draw-down phenomenon. Boussinesq model gives really good results for this case.

5. The Tohoku tsunami

The last case we present here, is the well-known tsunami of Tohoku (March 11th, 2011). This case is a very interesting one for plenty of reasons, among which the huge quantity of available data (bathymetry, hydraulics, gauges, seismic data, satellite data, flood marks, etc.). Moreover, all tsunami steps are represented in this events which makes it as one of most important validation cases for the Telemac-Mascaret suite.

In this paragraph we will present briefly the model and focus on the propagation aspects. The flooding part will be discussed in the next section.

The outline of the mesh represents the north-western quarter of the Pacific Ocean. It was originally proposed by the study of Sasaki et al. [16]. The finest mesh includes 680 000 nodes with an element edge length between 10 m in the bay of Iwate and 15 km at the eastern boundary. The density of the mesh is varying with the bathymetry gradient.

As for the Gisborne case, the generation of the Tohoku tsunami, several source techniques were tested (Shoa et al, Satake et al, classic Okada). The propagation step is computed using the nonlinear shallow water equations of Telemac-2D. Obtained results are compared to DART gauges located along of the eastern Japanese coast (Fig. 14) with gauge readings shown in Fig. 15.

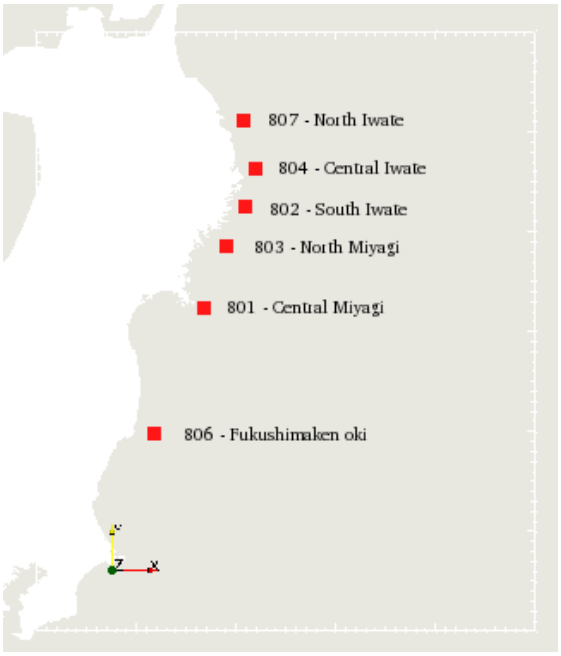

Figure 14. *DART gauge locations*

We can see that depending on the used source model, results fit more or less with data. Shao et al. generation gives nice fits in the far-field domain while it predicts the wave in the near-field. The Satake solution tends to under-estimate the wave amplitude in far-field but fits much better to data in the near-field. The CPU time for the propagation of this event is of 13 min on 48 processors which is really encouraging.

C. *Flooding*

To assess the coastal impact and flooding, several benchmarks were proposed. We will discuss only 2 of them to demonstrate the capabilities of the Telemac-Mascaret to deal with this important feature.

1. The Tohoku 2011 case:

To deal with flooding aspects at the end of a tsunami event, modeller often chooses to use separate model in order to alleviate computation costs. However, with the Telemac-Mascaret system, this reason is no more valid. In dead, in the framework of the thesis of le Gal, the built models includes both propagation and flooding aspects. This choice was applied both for the Tohoku and the Gisborne events.

Fig. 16, 17 and 18 show the used meshes which go behind the shoreline in order to take into account for the flooding aspects.

The computational time for the Gisborne model was of 21 min on 24 processors.

The final feedbacks show that advection schemes of the Telemac-Mascaret suite can handle both propagation and coastal flooding. However, it is important to indicate

that the method of characteristics can have some unstable behaviour when boundaries of the model have complex geometry, which was the case of the Japanese model. Addition optimization steps of the mesh were necessary to overcome these issues.

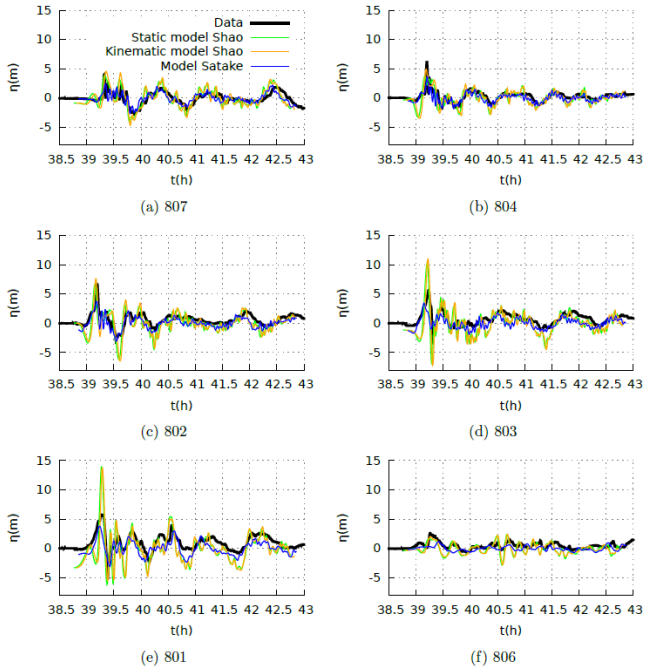

Figure 15. *Propagation results of the Tohoku tsunami- comparison with DART gauges*

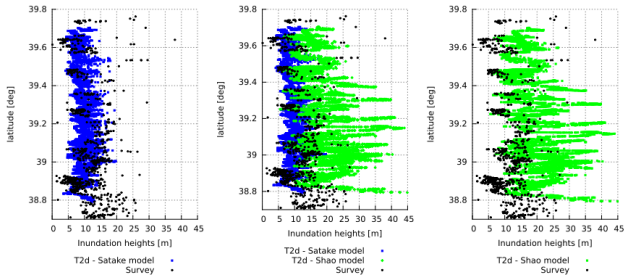

Figure 16. *The Tohoku tsunami: effect if the generation source.*

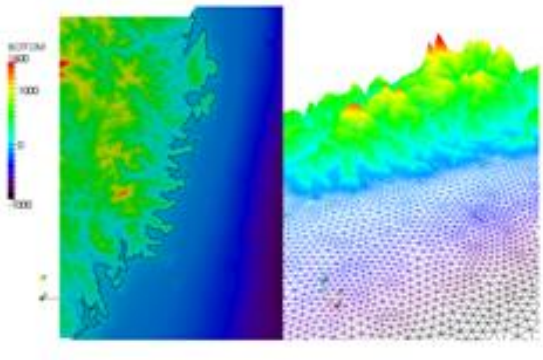

Figure 17. *used mesh for Tohoku tsunami- zoom on the coastal flooded area of the Iwate bay*

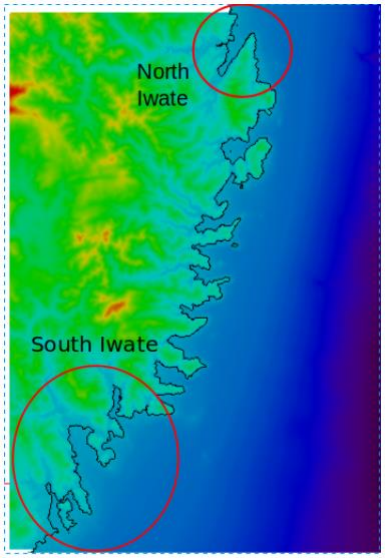

Figure 18. *coastal flooding of the Iwate bay.*

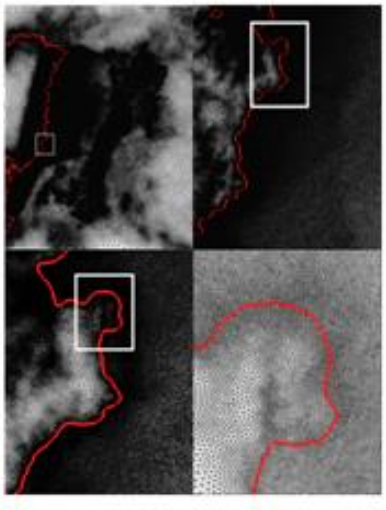

Figure 19. *mesh used for the Gisborne event of 1947. Zoom on the shore region.*

Lots of efforts have been done to improve capabilities of the Telemac-Mascaret system to tackle tsunami phenomenon. This have led to a wide use of this code throughout the numerical community. Several issues remains open and needs further investigations. Mainly:

- The Boussinesq version of Telemac-2D needs further improvements. In several cases, it shows unstable behaving.
- Advection schemes needs to be improved (in order, numerical diffusion, accuracy and stability). Schemes able to handle wetting and drying remains more expensive. In the other hand, the characteristic scheme, which is the most optimal in machine cost, reveals some weakness when mesh boundaries are complex.

- Telemac-3D needs to be improved to handle in a more accurate way the propagation of nonlinear solitary waves. Even though dispersive properties are well retrieved, the dependence of the results to the numerical parameters needs real investigation.
- To handle dispersive Boussinesq-type source terms with shallow water equations, schemes with high order in space are required. Besides, a refined time discretization is also needed.
- Coastal flooding which needs very often to include urban areas and dense vegetation, can benefit from porosity option in order to alleviate mesh refinement. This option is still not well assessed and thus needs further investigations.

ACKNOWLEDGEMENTS

This work is achieved with the Tandem project funded by the French government (projets investissment d'avenir) under the contract number ANR-11-RSNR-0023-01.

REFERENCES

[1] TANDEM: Tsunamis in the Atlantic and the eNglish channel: Definition of the Effects through numerical Modeling. http://www-tandem.cea.fr/

[2] Y. Okada. Internal deformation due to shear and tensile faults in a half-space. Bulletin of the Seismological Society of America, 82, No 2:1018–1040, 1992.

[3] D. Dutykh, D. Mitsotakis, X. Gardeil, and F. Dias. On the use of the finite fault solution for tsunami generation problems. Theoretical and Computational Fluid Dynamics, 27:177–199, 2013

[4] Y. Yagi. Source rupture process of the 2003 tokachi-oki earthquake determined by joint inversion of teleseismic body wave and strong ground motion data. Earth, Planets and Space, 56(3):311–316, 2004..

[5] K. Satake, Y. Fujii, T. Harada, and Y. Namegaya. Time and space distribution of coseismic slip of the 2011 tohoku earthquake as inferred from tsunami waveform data. Bulletin of the Seismological Society of America, 103(2B):1473–1492, May 2013..

[6] D. Violeau, R. Ata, M. Benoit, A. Joly, S. Abadie, L. Clous, M. Martin Medina, D. Morichon, J. Chicheportiche, M. Le Gal, A. Gailler, H. Hébert, D. Imbert, M. Kazolea, M. Ricchiuto, S. Le Roy, R. Pedreros, M. Rousseau, K. Pons, R. Marcer, C. Journeau, R. Silva Jacinto. IAHR Congress proceedings, August 2015.

[7] J. Hammack. A note on tsunamis: their generation and propagation in an ocean of uniform depth. Journal of Fluid Mechanics, 60:769–799, 1973.

[8] M. I. Todorovska and M. D. Trifunac. Generation of tsunamis by a slowly spreading uplift of the sea floor. Soil Dynamics and Earthquake Engineering, 21:151–167, 2001.M. le Gal. Influence des echelles de temps sur la dynamique des tsunamis d'origine sismique. PhD thesis (2017). https://pastel.archives-ouvertes.fr/tel-01529253

[9] G. Downes and M. W. Stirling. Groundwork for 2001. development of a probabilistic tsunami hazard model for New Zealand. In International Tsunami Symposium 2001, pages 293–301.

[10] Abadie, S., Morichon, D., Grilli, S., Glockner, S. (2010) Numerical simulation of waves generated by landslides using a multiple-fluid Navier–Stokes model. Coastal Engineering 57: 779–794.

[11] P. L.-F. Liu, P. Lynett, and C. E. Synolakis. Analytical solutions for forced long waves on a sloping beach. Journal of Fluid Mechanics, 478:101–109, 2003.

[12] D. Dutykh and D. Clamond. Efficient computation of steady solitary gravity waves. Wave Motion, 51(1):86–99, 2014.

[13] M. Benoit, C. Raoult, and M. Yates. Fully nonlinear and dispersive modeling of surf zone waves: Non-breaking tests. Coastal Engineering Proceedings, 1(34):15, 2014..

[14] C. E. Synolakis. The runup of solitay waves. Journal of Fluid Mechanics, 185:523–545, 1987.

[15] J. Sasaki, K. Ito, T. Suzuki, R. U. A. Wiyono, Y. Oda, Y. Takayama, K. Yokota, A. Furuta, and H. Takagi. Behavior of the 2011 Tohoku earthquake tsunami and resultant damage in Tokyo bay. Coastal Engineering Journal, 54(01), 2012.

Validation of a TELEMAC-3D model of a seamount

Alan J. Cooper and Jeremy Spearman
HR Wallingford, Coasts and Oceans,
Howbery Park, Wallingford, OX10 8BA, UK
a.cooper@hrwallingford.com

***Abstract*—A survey was carried out at Tropic Seamount off the Atlantic coast of Africa. This has allowed a TELEMAC-3D model to be constructed and validated using the measured data. The importance of internal tides at the site and possibility of a Taylor column have been assessed.**

I. INTRODUCTION

In late 2016 an extensive survey was carried out of the flows at and around Tropic Seamount. The data was to be used both to understand the flow regime and also to calibrate a flow model to be set up using TELEMAC-3D. TELEMAC-3D is the 3D hydrodynamic component of the open source, industry driven, TELEMAC system (www.opentelemac.org).

Fig. 1 below shows the bathymetry as coloured contours and the 2D spatial mesh used with TELEMAC-3D.

The observations have been analysed to understand the flow processes going on at Tropic Seamount with particular reference to internal tides at the seamount and the possibility of a Taylor column (rotating circulation pattern including closed streamlines) being observed here. The numerical model has been set up and calibrated using the observations. This has allowed the semi-diurnal internal tides to be seen and also to look for features of a Taylor column.

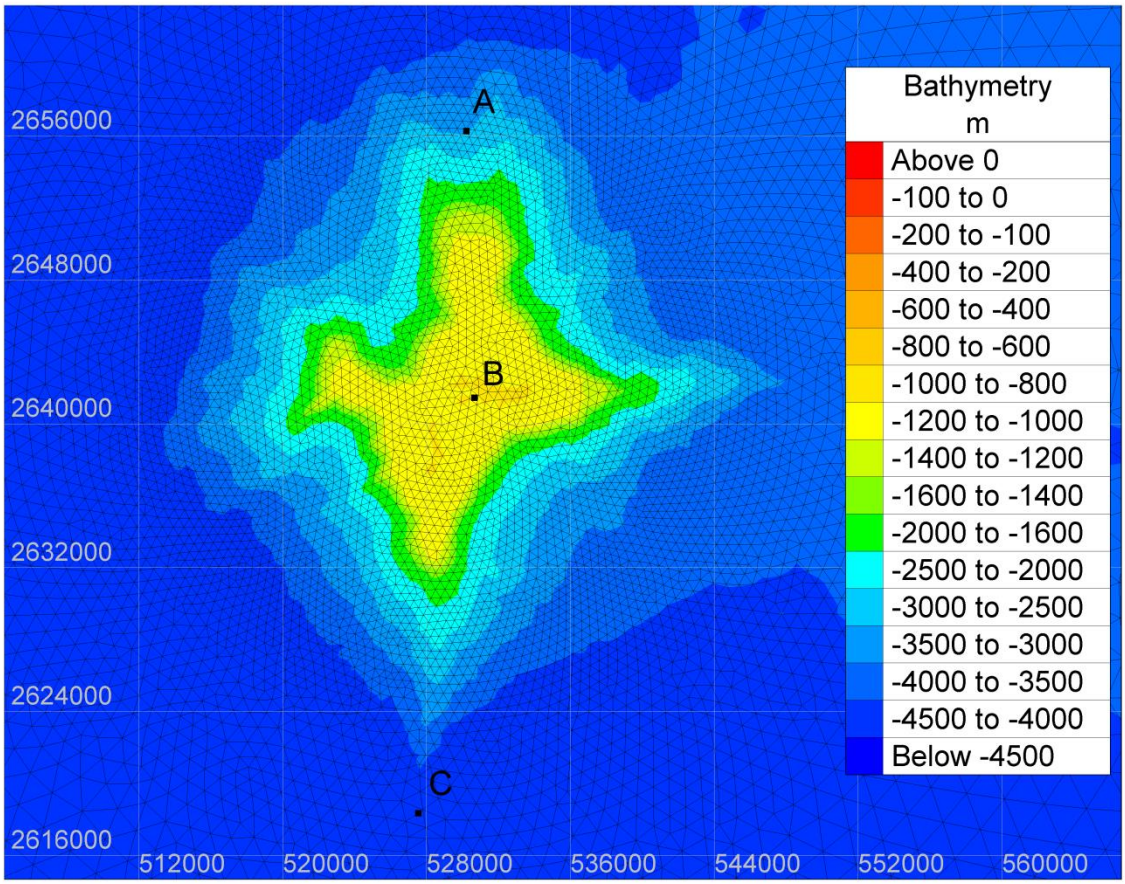

Figure 1. *Model mesh in area of the seamount*

II. Observed Currents at Tropic Seamount

Fig. 1 above shows the location of three instruments relative to the bathymetric contours of the Tropic Seamount.

A. *Yo-yo casts near the seamount summit*

During the survey (17-18 November 2016), a yo-yo set of casts at a location near the seamount peak in about 1,000 m of water was carried out over a 6.25 hour period at approximately hourly intervals while the vessel was stationary. The vessel also had two ADCPs attached to its hull measuring current at different frequencies.

Throughout the survey period at a close location B (see Fig. 1) there was an ADCP mooring attached to the sea bed and there was an ADCP at about 50 m below the surface attached to the bed by a 900 m long cable. The yo-yo currents cover almost the entire water depth over the seamount. The measured currents in the u and v directions are presented in Fig. 2 (top and bottom insets respectively).

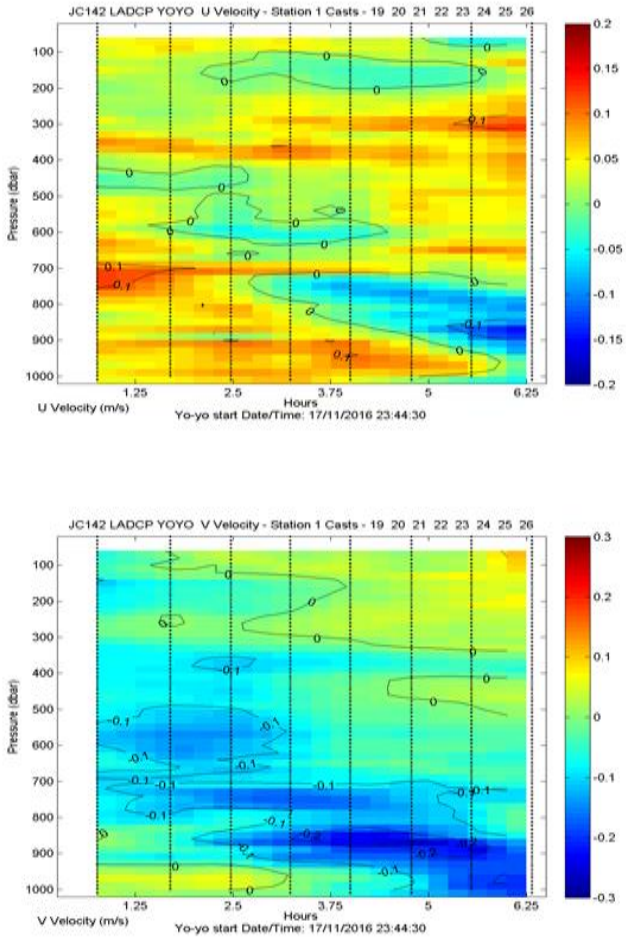

Figure 2. *Observed currents (above u-velocity, below v-velocity)*

As can be seen there is a semi-diurnal wave or "beam" (in blue) shown by both u and v currents travelling down from mid-depth to the bed over this half a semi-diurnal period. This is the expected behaviour of a semi-diurnal internal tide generated above the seamount as the surface tide carries the water up and down above the steep seabed topography.

However, what can also be seen are a quantity of narrow horizontal slices of both u and v slowly varying currents that last continuously for a period of nearly 6 hours.

It is not certain how accurate the currents from these casts are, as they are on a very long cable down from the ship and the ADCPs are falling and rising rapidly to get a cast completed in a fast enough time. However the following suggest that the currents are correct:

- The vessel's ADCPs give quite similar currents in the top 50 m or so of the water column;
- The moored current meter at 50 m depth gives a similar result to the casts near 50 m depth;
- The moored ADCP at the seabed gives a similar result to the casts near the bed; and
- The intrinsic consistency of the result indicates that the ADCP cannot have been rotating significantly as the u and v velocity components would then fade up and down and they do not greatly but they stay consistent for a long time.

All of this suggests that the narrow stripes of different current speed are actually real and not instrumental noise or error.

Similar results have been measured before (see [6] and [7]) and they signify the presence of diurnal currents in the signal with a high spatial wavenumber in the vertical. That is why they vary through a tidal period at only half the rate of change of the semi-diurnal current, but with strong spatial variation in the vertical.

To some extent this result is surprising as there is little apparent diurnal forcing that can cause these longer period currents. The barotropic tide here appears strongly dominated by semi-diurnal constituents (see Fig. 3).

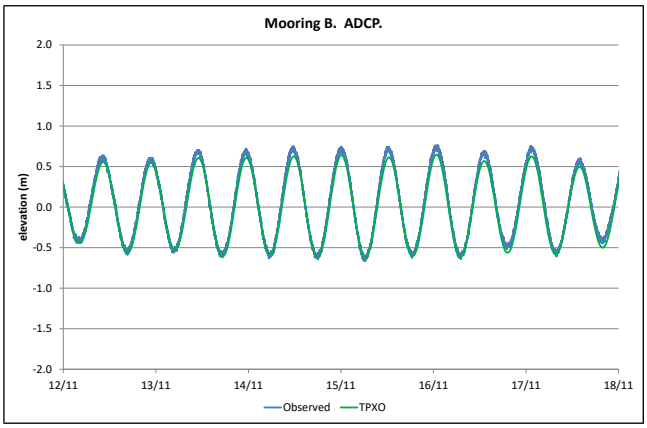

Figure 3. *Observed and modelled water level*

B. *Moored current meters*

Moored current meters were deployed for the survey period at location A (2 depths), B (2 depths) and C (1 depth), where locations are shown on Fig. 1. They operated continuously giving a high quality dataset enabling use of T-Tide, a freeware used for tidal harmonics analysis (see [10]). T-tide is written in the Matlab programming environment. It is based upon original FORTRAN program developed by M.G.G. Foreman (see [11] and [12]).

Tab. 1 below shows aspects of the statistics of the measured currents at the moorings.

TABLE 1 RESIDUAL CURRENTS AT MOORING LOCATIONS

Location + depth	u (m/s)	v (m/s)	Ratio
A1000	0.012	-0.027	0.18
A2000	0.005	-0.004	0.03
B50	0.010	-0.019	0.88
BADCP	0.005	-0.027	0.64
C3300	0.000	-0.009	0.35

The ratio is of minor to major M2 tidal ellipse, which indicates how linear or nearly circular the tidal ellipse is.

Clearly at all of the mooring locations and heights there is a general mean flow towards the east and towards the south. The strongest mean flow is about 0.03 m/s. At all the moorings the flow is dominated by tidal oscillations, mainly semi-diurnal.

Further, it is clear that the ellipse is closest to circular at the two B mooring locations representing a tendency for the current to rotate around the compass during each M2 tidal period. At A2000, by contrast, the ellipse is almost just a straight line with flows all going east or west.

Tab. 2 below shows which locations are more or less semi-diurnal dominated. Based on the tidal analysis of the observed currents at the moorings the degree to which the current is semi-diurnal (Ratio) is derived from the two largest diurnal and semi-diurnal constituents (O1+K1)/ (M2+S2) for the ellipse major axis.

TABLE 2 DEGREE TO WHICH CURRENT IS (SEMI-)DIURNAL

Location + depth	O1+K1	M2+S2	Ratio
A1000	0.028	0.078	0.36
A2000	0.021	0.052	0.40
B50	0.058	0.068	0.85
BADCP	0.061	0.129	0.47
C3300	0.013	0.053	0.25

This shows that greatest tendency towards diurnal variation is found at B50. Although the diurnal at 1,000 m depth at location B is almost the same, the semi-diurnal there is nearly twice as large and dominates.

At A1000 the current flows mainly north and south. As the meter is 1,000 m below the water surface, it is possible for the water to continue towards approximately north or south. This shows that the southward moving flow to the north of the seamount at 1,000 m depth is able to keep travelling south and sometimes flows north. During the measurement period the average u velocity is 0.01 m/s (to the east). The mean v velocity is 0.03 m/s south with periods of current greater than 0.15 m/s south.

III. 3D MODEL ASSUMPTIONS

A. *Model setup*

The model was set up to cover an approximately square area of side 450 km centred on the seamount.

The model was run using the hydrodynamic model TELEMAC-3D in hydrostatic mode. This open source model has the capability of a flexible mesh of triangles in the horizontal and a choice of meshing approaches for the vertical. In this case flat planes were used that drape the top of the seamount where they are lower than the peak.

Fig. 1 above shows the bathymetry as coloured contours and the 2D spatial mesh used over the seamount with TELEMAC-3D.

B. *Boundary conditions*

The model boundary conditions were taken from the Mercator Ocean global ocean circulation model (see [13]) with 52 horizontal layers with spacing closest near the surface and largest at depth. The model layers were taken the same as those in the Mercator Ocean model but with a spacing not greater than 20 m in the top 1,000 m. Initial conditions of salinity and temperature were taken from average conditions over the survey casts. Boundary conditions of water level were taken from the Mercator Ocean model added to the global TPXO levels (see [9]), the Mercator Ocean model not including tides. The currents on the boundaries were taken from the sum of the 3D currents from Mercator Ocean and those from TPXO, which were assumed to be uniform over the whole water depth.

As Mercator Ocean model outputs do not include tide variation they could not represent internal tide currents. The TPXO model does not include baroclinic variations so neither model allows boundary conditions representing internal tides to be applied. Although it was not possible to drive the model including actual internal tide motions at the boundaries, it was possible to absorb the internal tides generated inside the model by using sponge layer boundary conditions on the horizontal boundaries. However to ensure realistic water levels in the model the water level was imposed on the model boundaries without any sponge layer.

Model runs were carried out including different numerical recipes, different density formulations, and different winds (simulations reported here use the local measured wind). The Wu formula was used to specify the surface drag due to the wind.

IV. 3D Model validation

The 3D model result for the yo-yo period is shown in Fig. 4. The semi-diurnal beam from the middle moving downward can be seen but there is much less of the diurnal stripes in the upper part of the figure compared to what is observed.

A longer period presentation (Fig. 5) shows that the lower half of the water column at the yo-yo location is predominantly semi-diurnal and the top becomes diurnal after the first few tides. The reason for not reproducing better the diurnal detail could be due to:

- Diurnal internal tides propagating into the model area have not been reproduced;
- Semi-diurnal internal tides that propagate into the model and then change into diurnal stacked tides have not been reproduced; and / or
- The model has not been run with sufficient resolution to reproduce the detail of the stacked tides.

However the model clearly does reproduce the transition of the semi-diurnal beam into a diurnal one as the current at the surface is diurnal and no significant diurnal influence has caused this to happen.

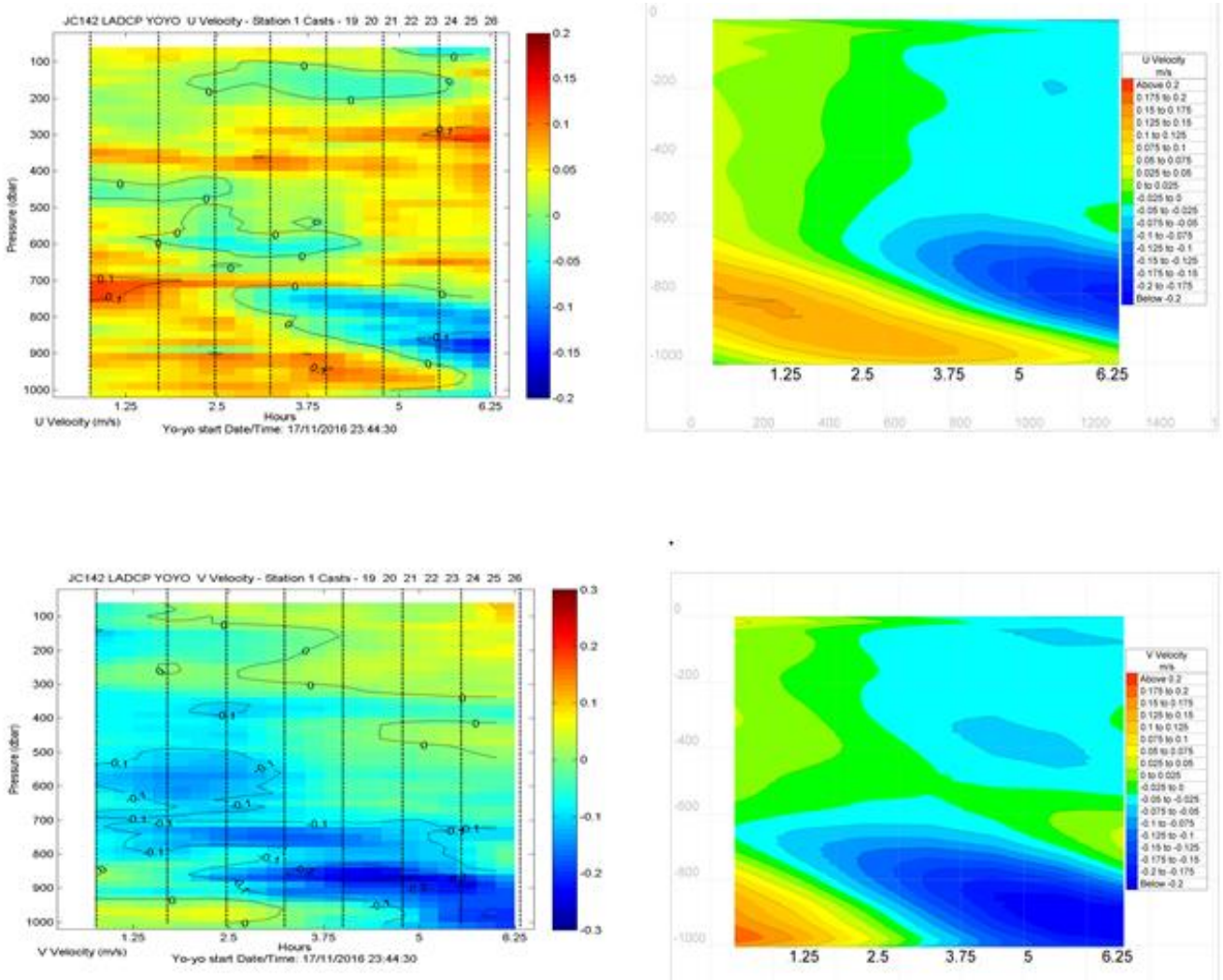

Figure 4. *Model yo-yo comparison (observed currents on left, model on right)*

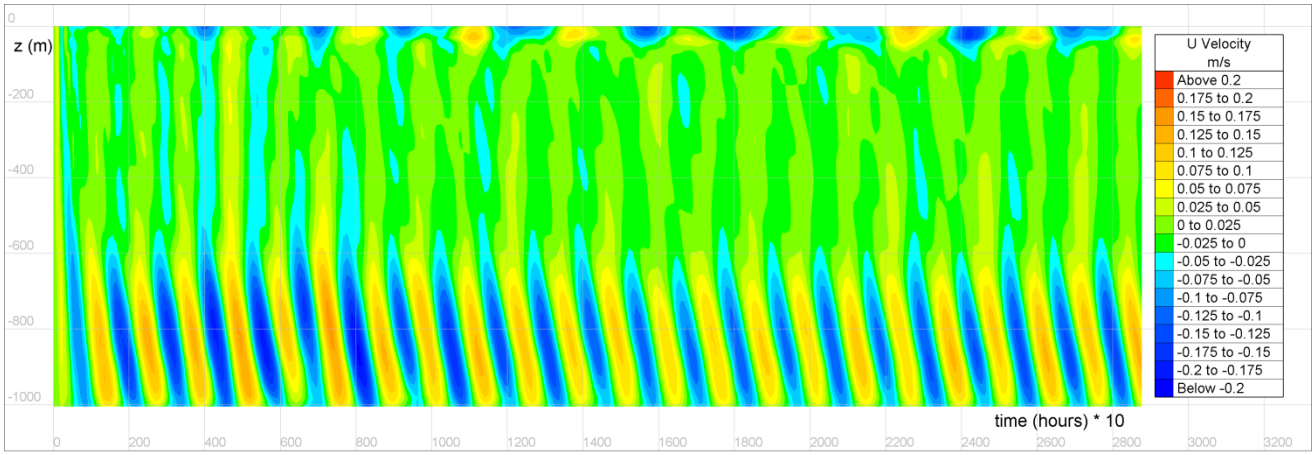

Figure 5. *Model u-velocity at yo-yo location, through tides*

Fig. 6 below shows a model result depicting the v velocity semi-diurnal magnitude (positive towards north) along a south to north section of the seamount. The propagation of the beam away from the top of the seamount towards the surface northward and southward can be seen, followed by its reflection back downward. The angle of the beam depends on the degree of stratification so it bends more near the surface where the density gradient is largest. The strongest semi-diurnal signal at the surface is about 60km from the seamount summit.

The data do not naturally lead to a conclusion that there is a Taylor column present at the seamount (this would be apparent in closed streamlines around the seamount).

The time averaged currents at 20 m above the sea bed are shown in Fig. 7 and they do show a tendency to a weak anti-cyclonic residual circulation around the seamount just above the bed (as has been seen at other sites). So it appears likely that there is a very weak Taylor column in the sea around the seamount close to the sea bed. This may be important in keeping material at the seamount.

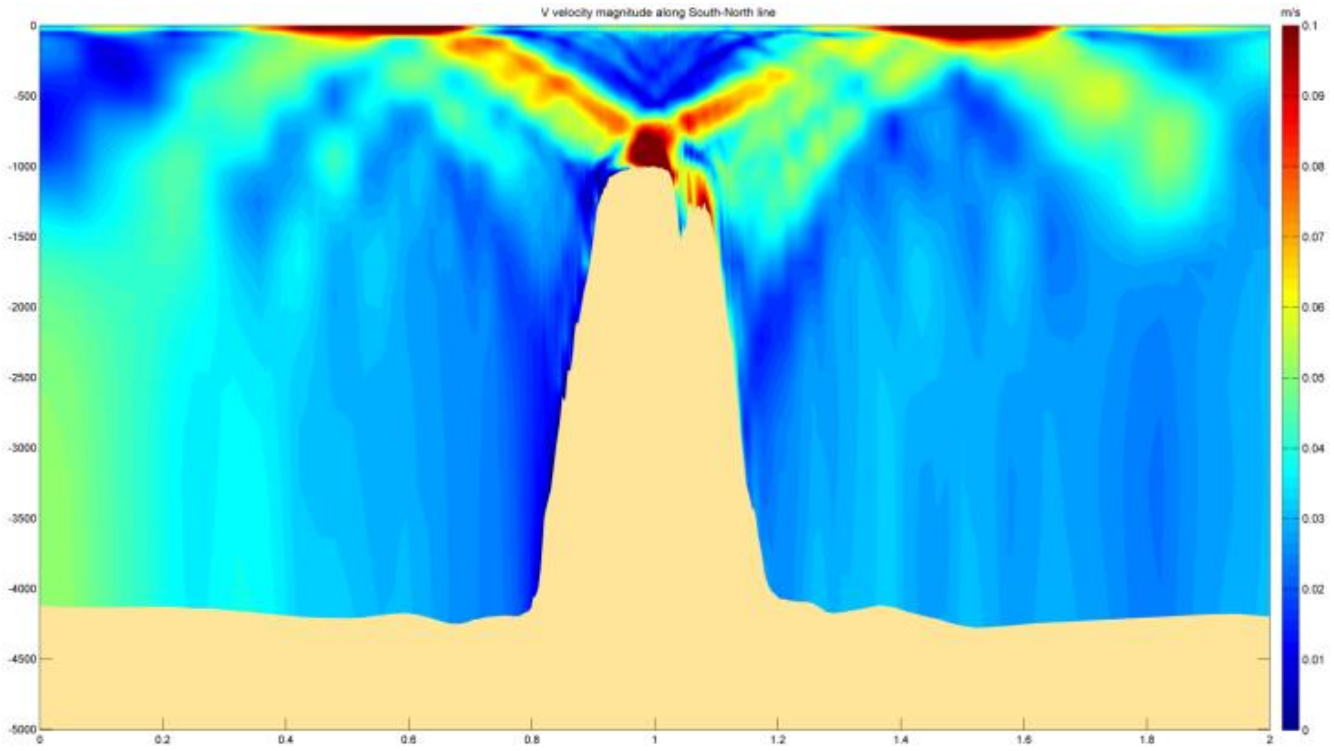

Figure 6. *Model v velocity (semi-diurnal) along a south-north section through the seamount (internal tidal beams)*

V. Conclusion

The observations show not only semi-diurnal internal tides but also a plethora of diurnal tides due to subharmonic instability. Because the area is bathed with internal semi-diurnal and diurnal tides arriving from further away, it is not readily possible to deduce the origin of all the observed flows.

The data do not naturally lead to a conclusion that there is a Taylor column present at the seamount. However, a 3D numerical model has been constructed and validated and it leads to the conclusion that there is a very weak Taylor column close to the sea bed.

References

[1] HR Wallingford, "Submarine Fe-Mn Crusts, Marine E-Tech, JC142 (Tropic Seamount)" – HR Cruise Report, 2017

[2] Gerkema, T., C. Staquet and P. Bouruet-Auberto, "Decay of semi-diurnal internal-tide beams due to subharmonic resonance." Geophys. Res. Lett., 33, L08604, 2006

[3] Hibiya, T., M. Nagasawa and Y. Niwa, "Nonlinear energy transfer within the oceanic internal wave spectrum at mid and high latitudes". J. Geophys. Res., 107, 3207, 2002

[4] MacKinnon, J. A. and K. B. Winter, "Subtropical catastrophe: significant loss of low-mode tidal energy at 28.9°N". Geophys. Res. Lett., 32, L15605, 2005

[5] Hans van Haren, Leo R. M. Maas and Theo Gerkema, "Patchiness in internal tidal beams", Journal of Marine Research, 68, 237–257, 2010

[6] Glenn S. Carter and Michael C. Gregg, "Flow and Mixing around a Small Seamount on Kaena Ridge", Hawaii Applied Physics Laboratory, and School of Oceanography, University of Washington, Seattle, Washington.

[7] Gerkema, T. and H. van Haren. "Internal tides and energy fluxes over Great Meteor Seamount", Ocean Science, 3, 441-449, 2007.

[8] White M and Mohn C, "Seamounts: a review of physical processes and their influence on the seamount ecosystem", Dept of Earth and Ocean Sciences, NUI, Galway, Ireland

[9] Oregon State University, "OSU Tidal Data Inversion Software and Atlas", TPXO-08 ATLAS, 2008, http://volkov.oce.orst.edu/tides/tpxo8_atlas.html

[10] R. Pawlowicz, B. Beardsley, and S. Lentz (2002), "Classical Tidal Harmonic Analysis Including Error Estimates in MATLAB using T_TIDE". Computers & Geosciences, Volume 28, Issue 8, 929-937.

[11] M.G.G. Foreman (1978, 2004 revision), "Manual for Tidal Currents Analysis and Prediction". Pacific Marine Science Report 78-6, Institute of Ocean Sciences, Patricia Bay, Sidney, B.C., 57 pp.

[12] M.G.G. Foreman (1977, 2004 revision), "Manual for Tidal Heights Analysis and Prediction". Pacific Marine Science Report 77-10, Institute of Ocean Sciences, Patricia Bay, Sidney, B.C., 58 pp.

[13] The European Commission's Copernicus Programme, in situ, satellite, and model output, http://marine.copernicus.eu

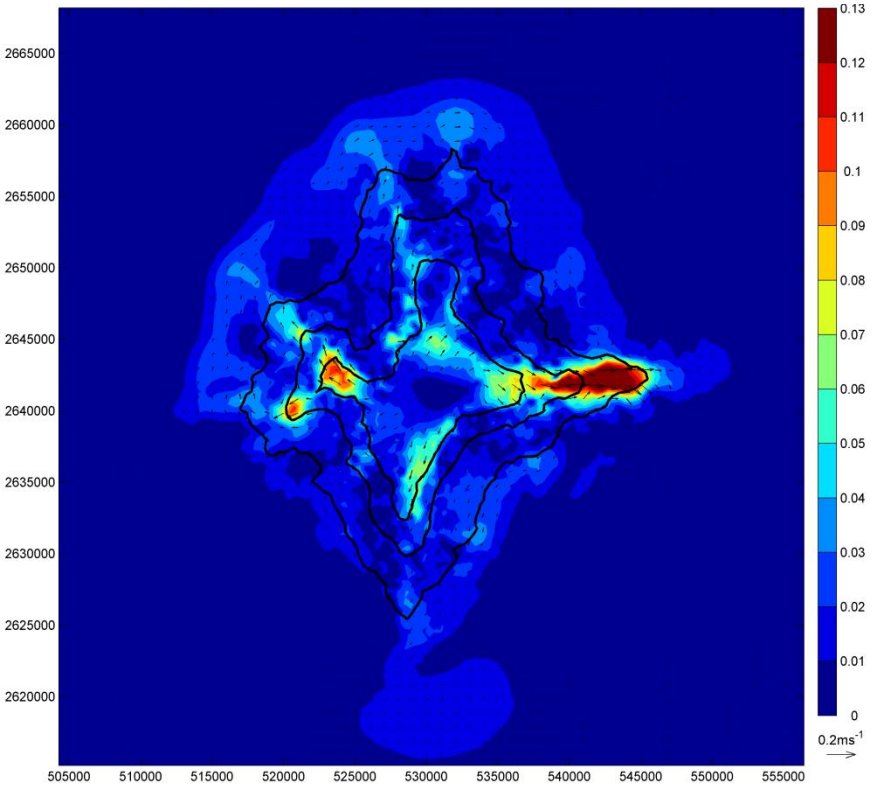

Figure 7. *Residual flow 20 m above sea bed*

Inundation Risk due to a Landslide-Generated Tsunami in the North Sea

Rohit Kulkarni, Nicolas Zimmermann,
Thijs Lanckriet, Alexander Breugem.
International Marine and Dredging Consultants
(IMDC nv)
Antwerp, Belgium
rku@imdc.be, nzi@imdc.be, thl@imdc.be, abr@imdc.be.

Abstract — A tsunami is a wave generated by the displacement of large volume of water. The water displacement can have different sources, such as earthquakes, asteroid impacts or underwater landslides. A series of massive landslides, known as the Storegga slides, occurred in the Norwegian Sea around 8000 years ago, leading to massive tsunamis in the North Sea basin. A study was performed, in which the inundation risk due to such a landslide-generated tsunami was determined for a sensitive industrial site situated behind the coastal dunes on the Dutch Coast. Thereto, two TELEMAC-2D models were setup. In a large-scale model, which includes the North-eastern Atlantic Ocean, the propagation of a tsunami up to the Dutch coast was simulated. A high-resolution small-scale model was nested in the large-scale model, to perform a detailed inundation study. Finite Element discretization was used for both the large-scale propagation and the small-scale inundation model.

The tsunami that was modelled is the so called Maximum Credible Event (MCE). The MCE is a concept introduced after the Fukushima disaster, to assure that no important changes in the plant status occur beyond the Design Basis Event-level (called margin assessment). It may correspond to a return period of 1 million years or more. It encompasses both the Design Basis Event (DBE) and the Beyond Design Basis Event (BDBE), which were already in use before Fukushima and corresponds to return periods of typically 10,000 years to 100,000 years. The MCE was selected from different potential landslide scenarios, and its magnitude was determined based on previous investigations. This leads to a Storegga-like slide at the entrance of the Norwegian trench.

The model is initially validated against propagated tsunami field of Hill et al. (2014) in the North Sea and to a time series of Harbitz (1992) offshore station in Aberdeen. The model results were found to be in good accordance with the peer reviewed results of Hill et al. [1] and Harbitz [2]. The results of the tsunami calculation are discussed which shows that in a MCE of a tsunami in the North Sea inundation is calculated on the coast of Netherlands through the dune openings.

Keywords: Tsunami model, TELEMAC 2D, inundation

I. INTRODUCTION

The two most studied types of tsunamis and most relevant for engineering purposes are earthquake- and (sub-aerial or submarine) landslide-induced tsunamis. These two types of tsunamis have clearly distinct characteristics and need to be treated differently. [6]

It is important to note that landslides are often co-seismic. Often a combination of an earthquake and an earthquake-triggered landslide is needed to explain the high tsunami run-up values observed, such as in Papua New-Guinea in 1998 and in Tohoku (Japan) in 2011.

Landslide-induced tsunamis can be particularly dangerous because the warning time is often too short for evacuation (unless in the case of a cataclysmic event generated farther). Initial free surface elevations of landslide-induced tsunamis can be up to an order of magnitude larger than most earthquake-induced tsunamis.

The current study focuses on a landslide-generated tsunami in the North Sea initiated off the coast of Norway. The model generated for the study is initially calibrated with the tsunami generated from the landslide at Storegga, 8000 years ago which was calculated to be a design event with a return period of 100,000 years. Currently, the Storegga slide is considered as stable, although there are certain locations around the northern Norwegian shelf, which can be considered as potential events which may affect the European coast.

For the propagation of the tsunami, dispersion becomes important when the wavelength is not much larger than the depth. This is the case for landslides with rapid acceleration or deceleration producing a large content of short wave length components [2]. For waves generated by large and subcritical submarine landslides with moderate acceleration or deceleration (0.005 m/s^2 – 0.033 m/s^2), such as the Storegga landslide, dispersion is of secondary importance.

For the purpose of this study, the calibrated hydrodynamic model is then used to calculate a Storegga-like slide further south of the coast of Norway which would generate a tsunami front incident directly through the North Sea. The inundation on the coast of Netherlands is further

[1]The Storegga submarine slide qualifies as cataclysmic event.

calculated with a smaller nested model which derives its boundaries from the larger domain.

The dune system on the coast of the Netherlands is seen to act as a barrier in case of any inundation. Although, there are certain gaps in the dune system to allow access to the beach area. The inundation study considers one of these 'openings' to demonstrate the risk of possible inland flooding.

II. Model Details

This section outlines the software used for the study, the model prepared and the various settings used for the simulations. The unstructured model TELEMAC-2D based on the shallow water equations is used. Dispersion is neglected, as justified previously.

The simulations are carried out in two steps. Initially a large domain (CSM - Continental Shelf Model) covering the North Sea and parts of Atlantic Ocean is simulated with the initial condition by applying the water levels depicting the start of the tsunami and subsequently the results from the large-scale model are used as a boundary condition for a smaller and detailed (local) model near the project area, to study the resulting coastal inundation.

The simulation results and model details presented in the report are in WGS84 geographic system (latitude/longitude). The bathymetry and water levels applied are relative to NAP (Normaal Amsterdams Peil).

A. *Grid and bathymetry*

In the initial step, the large-domain model was simulated with the design scenario of the tsunami. The CSM model is based upon an existing, calibrated hydrodynamic model of the North Sea continental shelf. The CSM model has been tested previously and has been shown to reproduce the tidal propagation quite accurately with a RMSE of 0.16 m near the coast of Netherlands. [3]

The model grid covers a part of North Atlantic Sea and extends to Iceland in the west and extends towards the north of Norway. The model also extends to the Bay of Biscay and covers the western coast of France. Fig. 1 shows the extents of the model which is 3300 km wide and 5500 km long along with the model grid and bathymetry. The model resolution decreases gradually from 75 km near the North Atlantic boundary to 5 km in the Norwegian Sea and the North Sea. The model resolution is increased to 1 km near the Norwegian coast, and around the tsunami source term to better capture the pattern of the initial waves. The maximum element size is restricted to 200 m near the Netherlands to facilitate nesting of the smaller local model with sufficient boundary points from the CSM model. The CSM model consists of close to 1.45 million elements. The independence of model results in the area of interest on resolution has been confirmed by a sensitivity test.

In a second step, nearshore results from the CSM model are imposed on a local nested model. This nesting allows to decrease the computation time of the CSM model, which is restricted by the size of the smallest element.

At each point along the offshore boundary of the local model, water levels and horizontal velocities derived from the large-scale model are prescribed (spatially varying boundary conditions), by linear interpolation from the large-scale model grid results. At the offshore boundary of the local model, the local and large-scale models have the same grid resolution.

The local model covers the northern part of the Dutch coast and contains around 360,000 elements. Fig. 2 shows the extent of the model grid which covers 5 km on land around the considered project site and also spreads out to 10 km offshore. The mesh of the local model domain varies gradually from 200 m offshore to 20 m on land. Fig. 2 also shows the mesh details near the study area and the opening in the dunes (inset) which are included in the model with a high resolution of 5 m to better calculate the propagation of the tsunami inundation front. The dune openings have a width of around 30 m.

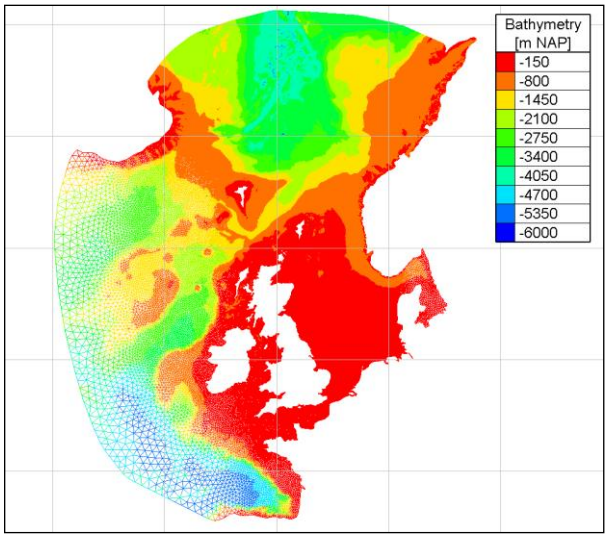

Figure 1. *CSM domain extent and mesh with bathymetry*

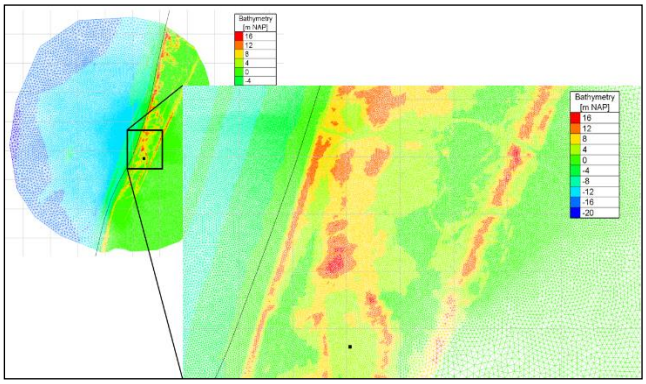

Figure 2. *Local mesh details*

B. *Model Settings*

For the CSM model, the time step was set to one second to resolve the initial tsunami propagation. A Manning's roughness coefficient of 0.02 was used for bottom friction. The model was simulated for a period of 24 hours to allow both the initial and secondary waves to reach the study site.

The initial water level is set to the design water level in the entire model domain. Non-reflecting boundaries are considered over the North Atlantic Ocean (Iceland to Spain) and Norwegian Sea (Iceland to Norway). The location of boundaries was based on the source term location and was kept far enough to minimize boundary effects on the tsunami propagation.

The local model is also run with a time step of one second, which is restricted by the smallest element size in the domain (5 m). The time steps between the models were kept same because for the larger model, the restricting criterion was to capture the reflected wave off the coast of Norway correctly whereas, for the local model, the time step was a requirement due to the small grid size. The maximum Courant number was always calculated to be below one, guaranteeing the numerical accuracy of the results. Similar to the CSM model, the initial water level is set to the design water level in the entire model domain, excluding land. After several tests, the advection schemes used for velocities was chosen as Characteristics and water levels were calculated using conservative PSI-scheme. A Manning's roughness coefficient of 0.02 was used for bottom friction, similar to the CSM model. No distinction has been made between the roughnesses at sea and on land. The land surface in the path of the tsunami is mostly covered by sand (which has approximately the same roughness as the sea bed), a narrow concrete / asphalt road (which has a similar roughness as sand) and dune grass. The dune grass has a higher roughness, creating additional dissipation of the tsunami run-up, and omitting the higher roughness of the dune grass is therefore conservative. However, it is expected that some of the dune grass will be removed by the tsunami flow, converting the bottom type at these locations to sand.

C. Tsunami Initialisation Source

The tsunami source term is derived from the analytical model of Grilli and Watts [4] and Watts et al. [5]. This semi-empirical formula has been derived from a large set of simulations with a near-field numerical model, itself validated on physical modelling results. The numerical implementation by IMDC of the analytical model of Grilli and Watts [4] and Watts et al. [5] has been validated based on test cases provided in the papers.

Due to its extreme nature, the selected scenario falls outside the applicability range of the analytical model for the slide kinematics. The depth-to-length ratio of less than 0.01 falls outside of the applicability domain (>0.06) resulting in an unrealistically high terminal slide velocity.

However, equation (1) of the model of Watts et al. [5] can be used with carefully selected parameters to manually define the shape of the initial surface elevation:

$$\eta(x,y) = -\frac{\eta_{0,3D}}{\eta_{min}}\,\mathrm{sech}^2\left(\kappa\frac{y-y_0}{w+\lambda_0}\right)\left(\exp\left\{-\left(\frac{x-x_0}{\lambda_0}\right)^2\right\} - \kappa'\,\exp\left\{-\left(\frac{x-\Delta x-x_0}{\lambda_0}\right)^2\right\}\right) \quad (1)$$

Where:

- $\eta(x,y)$ is the initial surface elevation [m]
- $\eta_{0,3D}$ is the maximum surface elevation [m]
- η_{min} is the minimum of the function on the right hand side of the equation, excluding the amplitude [m]
- κ is set to 3 according to Watts et al. [5]
- x_0 and y_0 are the coordinates of the slope bottom (end of slide movement)
- w is the landslide width [m]
- λ_0 is the characteristic near-field tsunami wave length [m]

κ' and $\Delta x = x_0 - x_g$ are parameters controlling the shape for given x_0 and λ_0 values.

Parameter values in TABLE 1 have been chosen such that the resulting initial surface elevation is comparable to that computed by Hill et al. [1] with a model including the dynamics of the slide (Fig. 3).

The initial maximum tsunami elevation has been selected to match that of Harbitz et al. [6], the slide width and characteristic tsunami length have then been chosen to match the displaced water volume of [1].

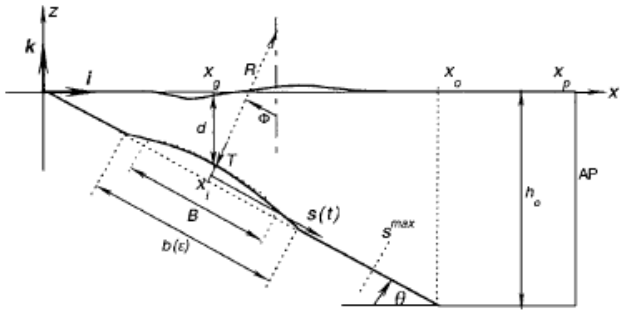

Figure 3. *Schematisation of slide in the analytical model of Grilli and Watts [4]*

In dynamic simulations such as in Harbitz et al. [6], Hill et al. [1], because the slide takes place over a long duration, the initial wave trough reflects against the coast of Norway and creates an asymmetric tsunami wave. Equation (1) however assumes a symmetric tsunami wave, i.e. equal minimum and maximum initial surface displacements.

This effect cannot be well corrected by varying parameter κ' which partly controls the asymmetry. It has hence been chosen to focus on the maximum surface displacement and to accept an error on the minimum surface displacement.

This approach is a pragmatic intermediate step between research models which generally include this dynamic coupling [2][7][1], and models more suitable for consultancy which generally impose a time series of water level along a

straight line between Scotland and Norway [8][9]. The model is validated in the next section.

TABLE 1. PARAMETER VALUES OF THE DESIGN TSUNAMI

Parameter	Value
$\eta_{0,3D}$	-8.19 m
w	750 km
λ_0	700 km
x_0 , y_0	150 km, 0 km
κ'	1
Δx	75 km

The tsunami initialization source, based on the tsunami sources of Hill et al. [1] and Harbitz et al [6] is deemed conservative, since these models from literature have inferred the initial tsunami characteristics by comparing the calculated *nearshore tsunami height* to observed geological tsunami deposits. The *tsunami run-up* on the other hand can easily be twice larger, as evidenced by the present study. Calibrating the initial tsunami characteristics on the tsunami run-up instead of the nearshore tsunami height, would have resulted in a smaller initial tsunami height.

III. MODEL VALIDATION

The model has been validated with the well-studied Storegga landslide event which occurred around 8000 years ago. Model results are compared to the propagated tsunami field of Hill et al. [1] in the North Sea and to a time series of Harbitz [2] offshore station in Aberdeen, two other model studies published in peer-reviewed scientific journals and using present-day bathymetry for the computation.

Fig. 4 shows the model results over the first hour as the imposed tsunami propagates from the source term. After around an hour, a part of the wave enters the North Sea, with a leading wave trough.

Fig. 5 shows that the tsunami propagation in the North Sea is fairly similar to that described in Hill et al. [1] in their simulation with the present day bathymetry. The model is able to capture the subsequent wave crest and trough propagation in the North Sea fairly accurately, which is important for the calculation of inundation at the Dutch coast.

Model results are also compared to the time series at Station 8 from Harbitz [2], located offshore Aberdeen, Scotland (Fig. 6). Results of Hill et al., [1] at that location are not available. This station is used as validation point in the study of Chacon-Barrantes [9]. Note that the time axis origin (t = 0 s) in the time series of Harbitz is at the moment of landslide initiation, whereas the time axis origin in the present model is at the moment when the initial water level begins to propagate outward. The model reproduces reasonably well the maximum water elevation and the wave period. The model calculates a water elevation of 3.44 m reaching the station while the Harbitz [2] model calculated a water elevation of 3.41 m at station 8. Results of Harbitz [2] at other stations show the same qualitative agreement. The model is hence suitable for inundation modelling.

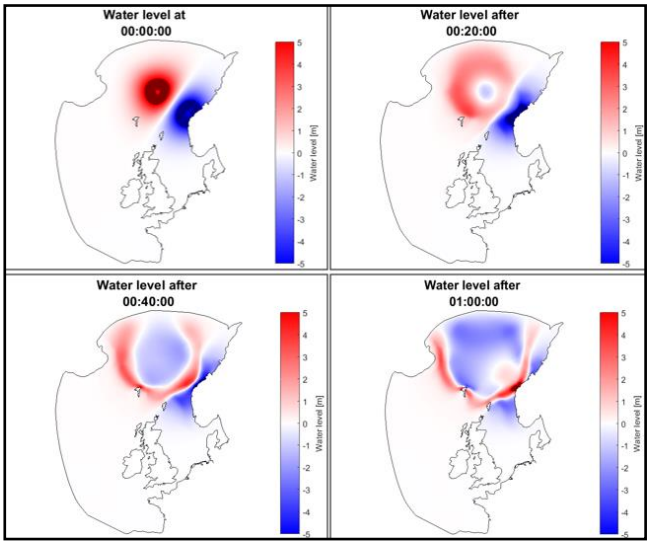

Figure 4. *Tsunami propagation over a period of 60 minutes for Storegga tsunami.*

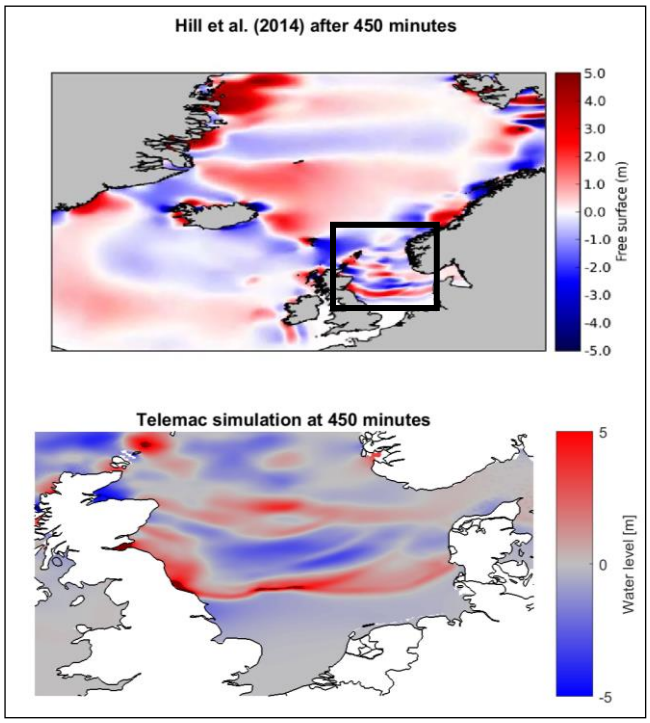

Figure 5. *Tsunami propagation after 7 h 30 min in Hill et al., [1] (top) and in the present study (bottom)*

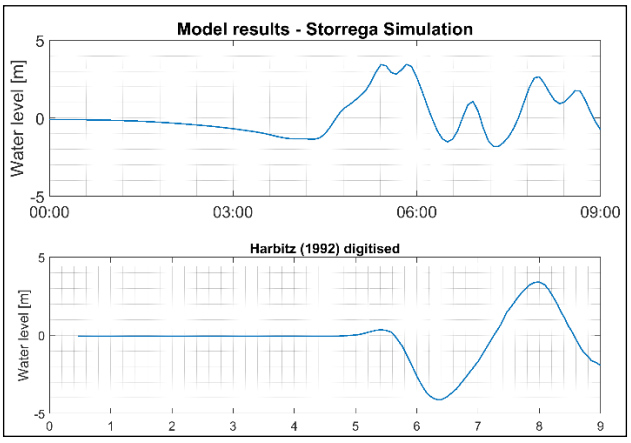

Figure 6. *Tsunami time series offshore Aberdeen in the present study (top) and at station 8 in Harbitz [2] (bottom).*

IV. Model Results

This section presents and discusses the simulation results for the Maximum Credible Event. It consists of a Storegga-like slide at the entrance of the Norwegian trench.

A. CSM Model

Fig. 7 shows the initial propagation of the tsunami until it enters the North Sea basin. The design scenario results in a larger wave front entering the North Sea compared to the Storegga tsunami. This is due to the fact that for the Storegga tsunami, a major part of the wave is blocked by the coast of Norway, whereas if the landslide occurs at the entrance of the Norwegian trench, the tsunami wave front propagates unobstructed.

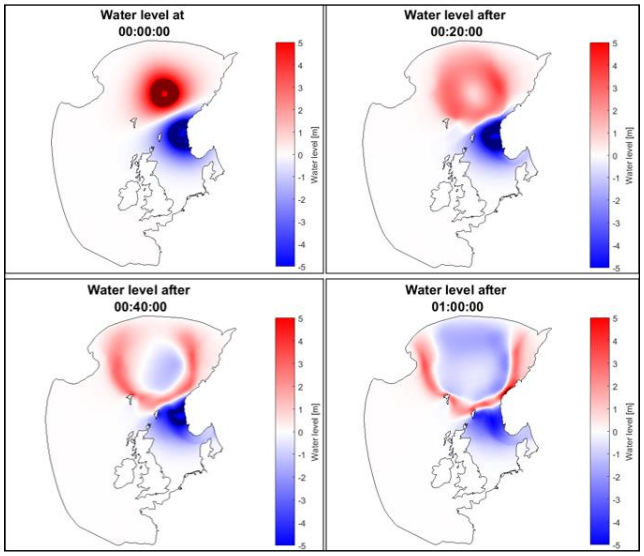

Figure 7. *Tsunami propagation over the first 60 minutes for the Maximum Credible Event (design scenario).*

Details of the tsunami propagating through the North Sea are shown in Fig. 8. The tsunami displays a similar pattern to the Storegga tsunami, although the wave length and wave amplitude are calculated to be larger. As the tsunami approaches the Dogger Bank area, its wave amplitude increases due to the shallow depth. The wave initially impacts the Wadden islands, the high waters then propagate along the Dutch coast.

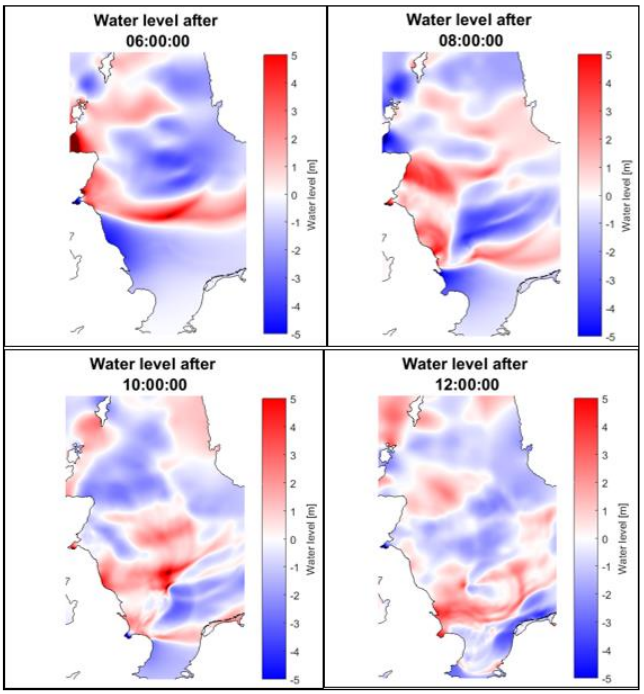

Figure 8. *Tsunami propagation in the North Sea for the Maximum Credible Event (design scenario) over a period of 6 hours. Initial water level subtracted from the results.*

B. Local Model

The Maximum Credible Event results in inundation at the coast, without significant impact on the infrastructure behind the first dune defence. Fig. 9 shows the time series of the water level near a gap in the dune system, including the run-up (initial water level subtracted from the results). The first effects of the tsunami become tangible about 6 hours after initiation. The second tsunami wave has the strongest impact and reaches the coast of Netherlands about 12 hours after initiation, with a maximum drawdown of 3.5 m over 2 hours and a maximum run-up of about 7.5 m over the next one hour (total water level close to 11 m). The run-up peak itself lasts about 20 min (Fig. 10). Secondary waves still reach the site during the next 12 hours due to the numerous reflections of the tsunami wave in the North Sea basin.

As seen in Fig. 11, the Maximum Credible Event results in a maximum flow depth of 3.5 m in a low lying area behind the dunes. Near the second row of dunes the maximum water depth is around 1 m. No overtopping of the dunes occurs and the inland areas are still safe from the inundation. The water inundates the hinterland via the opening in the dune field. It stops before it reaches the second row of dunes because entering water volumes are limited by the size of the opening. Note that the model does not take into account a

possible enlargement of this opening by erosional processes due to the high velocities involved, which may potentially increase the hazard at the project area.

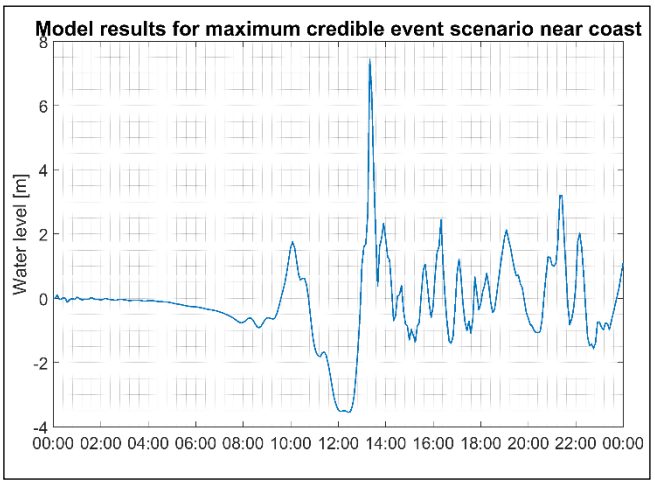

Figure 9. *Time series of water level near the project site (run-up included).*

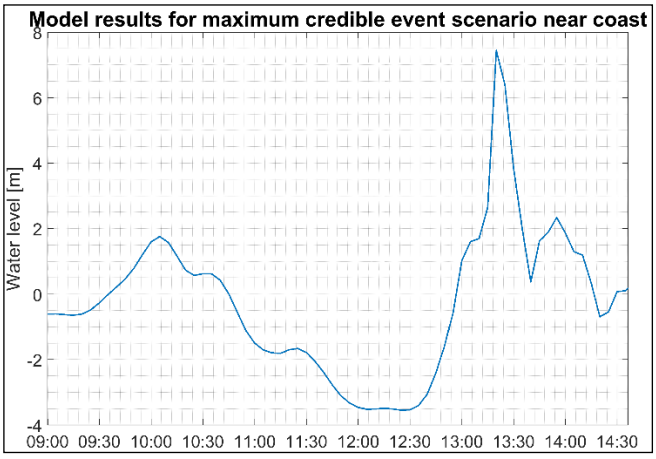

Figure 10. *Time series of water level near the project site (run-up included): zoom on the primary tsunami wave.*

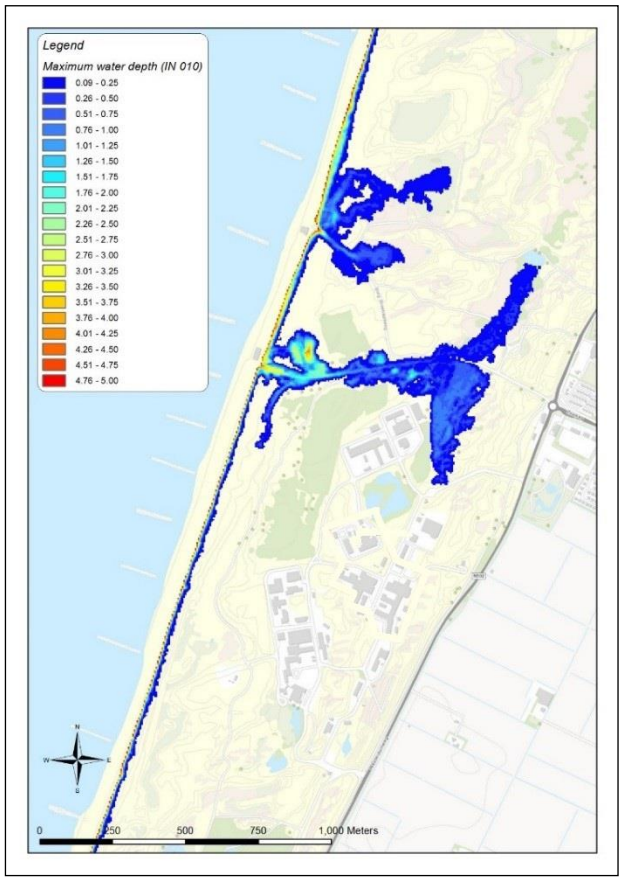

Figure 11. *Maximum water level in m NAP reached at each point for the Maximum Credible Event.*

V. CONCLUSION

The study outlines the efforts taken towards calculating propagation of tsunami generated in the North Sea and resulting inundation on the Netherlands coast. A previously validated model (CSM) is modified to better capture tsunami propagation through the North Sea. The model is validated against peer reviewed studies by calibrating the tsunami initialization source term and grid optimisations against the Storegga slide. A two model approach is taken to calculate the propagation of tsunami and inundation of the generated wave on the Dutch coast.

The results show a good correlation with the model studies published and also at measurement station in Aberdeen, Scotland. For the Storegga tsunami, the calculated tsunami wave front shows that a majority portion of the wave travelling towards the Netherlands is the wave reflected off the coast of Norway.

The maximum credible event (MCE) tsunami shows inundation on the coast of Netherlands through the opening in the coastal dune system. Although, the inundation is calculated to be restricted to the first line of coastal dune system. The total run-up during the MCE is calculated to be about 7.5 m. A maximum water depth of 3.5 m is calculated as a result of inundation behind the first dune system.

A coupled model simulating the landslide dynamics and its impact on the initial water motion, is expected to better reproduce the initial tsunami propagation reported in literature for the Storegga landslide, which was used for the model validation. However, considering the large uncertainty surrounding the initial landslide and tsunami characteristics, this approach is only expected to significantly improve the modelled tsunami drawdown.

Further improvements can be carried out by modelling the actual landslide separately which would generate the initial water level displacement to be modelled for further propagation.

ACKNOWLEDGEMENT

We would like to thank the project sponsors for the opportunity given to IMDC nv to showcase our expertise in applying research questions to practical problems and arriving at innovative solutions.

We thank our colleagues from IMDC nv, who helped during the project and assisted greatly in the research and finalising the study. We would especially like to extend our thanks to Gijsbert van Holland, Jon Kemp, Li Wang for their efforts in making this research possible. We would also like to show our gratitude to Boudewijn Decrop for his comments on the initial manuscript and helping to finalise the paper.

REFERENCES

[1] J. Hill, G. S. Collins, A. Avdis, S. C. Kramer, and M. D. Piggott, 'How does multiscale modelling and inclusion of realistic palaeobathymetry affect numerical simulation of the Storegga Slide tsunami?', *Ocean Modelling*, vol. 83, pp. 11–25, Nov. 2014.

[2] C. B. Harbitz, 'Model simulations of tsunamis generated by the Storegga Slides', *Marine Geology*, vol. 105, no. 1, pp. 1–21, Mar. 1992.

[3] W. A. Breugem, T. Verbrugghe, and B. Decrop, 'A continental shelf model in TELEMAC 2D', in *TELEMAC User Conference, Proceedings*, 2014.

[4] S. T. Grilli and P. Watts, 'Tsunami Generation by Submarine Mass Failure. I: Modeling, Experimental Validation, and Sensitivity Analyses', *Journal of Waterway, Port, Coastal and Ocean Engineering*, 2005.

[5] P. Watts, S. T. Grilli, D. R. Tappin, and G. J. Fryer, 'Tsunami Generation by Submarine Mass Failure. II: Predictive Equations and Case Studies', *Journal of Waterway, Port, Coastal and Ocean Engineering*, 2005.

[6] C. B. Harbitz, F. Løvholt, G. Pedersen, and D. G. Masson, 'Mechanisms of tsunami generation by submarine landslides: a short review', *Norwegian Journal of Geology*, vol. 86, 2006.

[7] S. Bondevik, F. Løvholt, C. Harbitz, J. Mangerud, A. Dawson, and J. I. Svendsen, 'The Storegga Slide tsunami—comparing field observations with numerical simulations', *Ormen Lange–an Integrated Study for Safe Field Development in the Storegga Submarine Area*, pp. 195–208, 2005.

[8] A. Dababneh, B. Ferguson, and D. Barton, 'Probable Maximum Tsunami Along the Dutch Coastline', *Proceedings of ISOPE, Rhodes, Greece, June 17-22, 2012*, 2012.

[9] S. Chacon-Barrantes, R. Narayanan, and Mayerle, 'Several tsunami scenarios at the North Sea and their consequences at the German Bight.', *Journal of Tsunami Society International*, vol. 32, no. 1, 2013.

Development of a Hindcast Wave State Database in Northwest Pacific Ocean

Jian Shi
Key Laboratory of Coastal Disaster and Defence (Hohai University), Ministry of Education
Nanjing, China
jianshi@hhu.edu.cn

Antoine Joly
EDF R&D
Laboratoire d'Hydraulique Saint Venant,
Chatou, France
antoine.joly@edf.fr

***Abstract*—In the Northwest Pacific zone, the extreme typhoon waves, which occur in summer and autumn, pose great risks on the nuclear facilities and related coastal infrastructures. To facilitate the assessment of the impact of typhoon waves over the whole Chinese coastal line, detailed data of the sea state over this region is necessary. For this reason, a numerical sea state data base, which includes the North-West Pacific Ocean is under construction. It will range over several decades, to provide long-term wave data in this area. An oceanic wave model with a triangular mesh covering the whole Pacific Ocean has been set up by using the third generation spectral wave model TOMAWAC. The wave state in 1999 is simulated and compared with observations of three oceanic buoy stations. The numerical result of significant wave height (SWH) shows a good agreement with the oceanic buoy observations. The minimum values of the average bias between prediction and measurement is around 4-7 cm. The prediction of mean period (MP), however, is less accurate than the results of SWH. The model underestimates the mean period with amplitudes of around 2 s. The numerical database is used to calculate seasonal mean wave energy density (WPD) in South China Sea. The results show that the values of seasonal mean WPD are larger in winter and spring due to the northeast monsoon in the period and the most energetic region is in the northeast part of the South China Sea.**

***Key Words*—Northwest Pacific Ocean; TOMAWAC; Wind-wave Simulation; Wave Power**

I. INTRODUCTION

Waves, occur everywhere in ocean, can destroy offshore facilities, coastal infrastructures and ships. But wave energy is one of the most potential energy among the renewable energy resources. It is estimated that there is about 2 TW energy all over the world, which can be derived from ocean waves [1]. In order to use the wave energy, the temporal and spatial distributions of wave characteristic are required. At present, this is done mainly through in situ observations and satellite data, which cannot provide the detailed sea state with high temporal and spatial resolutions needed in prediction of extreme events. A numerical database of sea state could provide the necessary details over a large temporal and spatial area. Due to the high computational efficiency, spectral wave models, such as TOMAWAC [2], SWAN [3] and WAVEWATCH III [4], have been widely applied in hindcasting models of ocean waves.

TOMAWAC, which is a third generation spectral wave model, will be used in this case as it has already been used successfully to construct sea-state atlas. An example of such a data base is ANEMOC-2, which provides wave information over 32 years from 1979 to 2010 along French coastline, the Atlantic Ocean, English Channel, North Sea and the Mediterranean Sea [5]. Motivated by the construction of ANEMOC-2, the establishment of a wave database for the Northwest Pacific Ocean is ongoing [6]. The final database will include detail wave parameters, such as significant wave height, mean period, peak period and mean direction, with a 1-hour resolution from 1979 to 2016. Based on this database, the distributions of sea-state, seasonal effects and estimation of extreme wave values can be analyzed.

Although various wave energy technologies are in development, none have reached an industrial stage yet due to the high cost. However, in some islands or reefs, electricity cannot be transmitted from mainland, thus, diesel power station is widely used in these areas. The cost of electricity generated by diesel and wave is comparable, and the increasing energy consumption demand in these areas make it wave energy converter an interesting alternative. There are plenty of reefs in South China Sea. Recently, many infrastructures have been constructed in these reefs, where the need for sustainable energy has become a concern. In this study, the wave energy density distribution in South China Sea is evaluated and analyzed based on a wave database. The introduction of the numerical model and wave database is shown in section 2. Then, section 3 is devoted to the method and results of wave energy density assessment. Finally, section 4 will include a conclusion and future work of the database.

II. CONSTRUCTION OF THE WAVE DATABASE

A. Model setup

TOMOWAC is developed by the EDF R&D's LNHE, and it is part of the Telemac-Mascaret system[1]. The governing equation of TOMAWAC is the action balance equation [7,8]:

[1] http://www.opentelemac.org/

$$\frac{\partial N(\sigma,\theta;x,y,t)}{\partial t}+\frac{\partial c_{g,x}N(\sigma,\theta;x,y,t)}{\partial x}+\frac{\partial c_{g,y}N(\sigma,\theta;x,y,t)}{\partial y}+\frac{\partial c_{\theta}N(\sigma,\theta;x,y,t)}{\partial \theta}+\frac{\partial c_{\sigma}N(\sigma,\theta;x,y,t)}{\partial \sigma}=\frac{S(\sigma,\theta;x,y,t)}{\sigma} \quad (1)$$

where σ is the radian frequency, θ is the propagation direction, c_g is the wave group velocity, c_θ and c_σ are the velocities in spectral space θ and σ. $N(\sigma,\theta;x,y,t)$ is the action density. The left-hand side terms in Eq. (1) represents wave shifting in x, y, t, θ, σ -space. Source term (S) in the right-hand includes the processes of wave generation by wind (S_{in}), quadruplet wave-wave interactions (S_{nl}) and white-capping (S_{ds}) in deep ocean. In shallow water, however, the triad wave-wave interaction (S_{tr}), bottom friction (S_{bf}) and depth-induced breaking (S_{br}) are also considered.

The numerical approach of TOMAWAC integrates the governing equation using the finite element method. The finite element method allows the ratio of the largest size to the smallest size of the grids to exceed 100, so TOMAWAC can be applied in cases simulating waves from deep water to coastal areas with complex geometry.

The wave model covers the whole Pacific Ocean, from 80ºS to 65º N in latitude, and from 100º E to 107º W in longitude (see Fig. 1). The spatial size of the mesh is variable as the mesh is refined in the area close to the Northwest Pacific Ocean. The maximum resolution is about 3° along the coastlines of South America and Antarctica. To capture the wave transformation induced by complex topography and bathymetry in coastal areas, the grid size is set to be about 1km along Chinese, Korean and Japanese coasts. In other areas, such as Australia and Southeast Asia, the grid size is about 50 km. The mesh comprises 28 343 nodes and 53 041 elements.

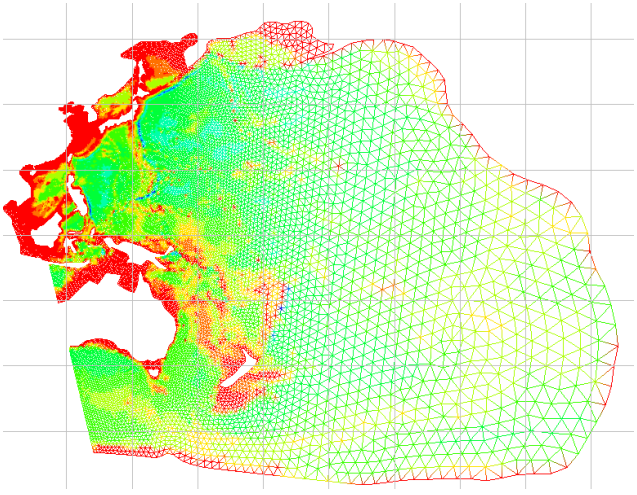

Figure 1. *Mesh of the wave simulation covering the Pacific Ocean.*

The time step for oceanic model is 300s. The frequency domain covers 36 bins from 0.0345 Hz with a growth ratio of 1.1. Direction is equally divided into 32 bins from 0° to 360°. The wind force is interpolated from the regular grid of CFSR onto the mesh every hour over 38 years from 1979 to 2016. Different combinations of physical terms have been tested in the calculation and the BAJ configuration shows the most accurate results of significant wave height (SWH)[6]. Therefore, the BAJ combination is used [9], which aims to improve the model's capabilities in simulating of wind-wave generation and dissipation [10]. By reformulating the mean wave parameters, the simulation with BAJ can take better into account the realistic interaction between wind sea and swell. The method used to calculate quadruplets wave interaction term is the Discrete Interaction Approximation (DIA).

B. Model validation

First, the validation of the oceanic model is conducted by comparing the SWH and mean period (MP) in 1999. Three ocean buoy stations from Japan Meteorological Agency (JMA) can provide observed SWH and MP in a time interval of 3h over this period. The locations of the three buoy stations, 21002, 21004 and 22001, are shown in Table 1. The main aim of this simulation is to assess the accuracy of the model in simulating ocean waves.

We compare the numerical results of SWH and MP with observations from January to April 1999. The time series of SWH are shows in Fig. 2, where it can be seen that the model can capture the variations of SWH during this period and the amplitudes of numerical results agree well with the observations. Fig. 3 shows the comparison of MP. It can be seen that the model underestimates the values of MP in this period.

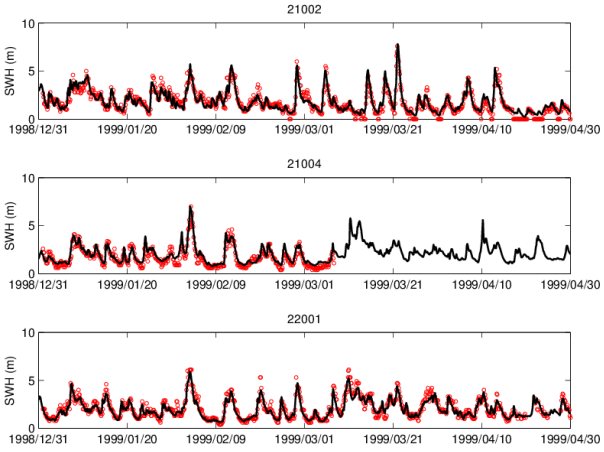

Figure 2. *Time series of Significant Wave Height (SWH). (Red circles: observation; Lines: numerical results)*

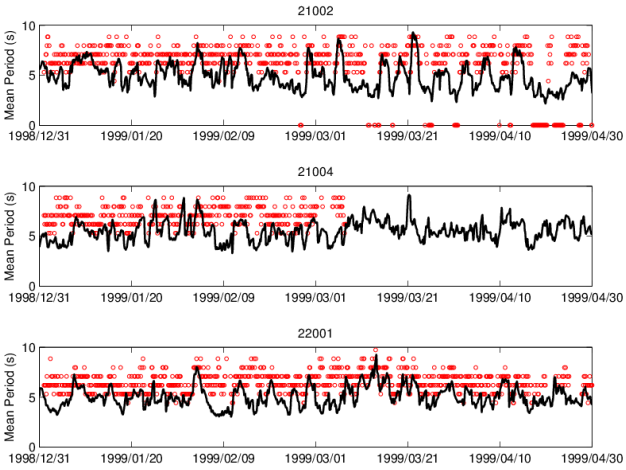

Figure 3. *Time series of Mean Period (MP). (Red circles: observation; Lines: numerical results)*

TABLE 1. THE LOCATIONS OF THE THREE OCEANIC BUOY STATIONS

Buoy Station	Longitude (°)	Latitude (°)
21002	134.533	37.917
21004	135.000	29.000
22001	126.167	28.333

Two statistical parameters are used to assess and quantify the differences between numerical simulations and observations:

$$\text{Bias} = \frac{1}{n}\sum_{1}^{n}(y_i - x_i) \qquad (2)$$

$$RMSE = \sqrt{\frac{1}{n}\sum_{1}^{n}(y_i - x_i)^2}$$

where y_i is the numerical results and x_i is the corresponding observed data.

TABLE 2. STATISTICAL PARAMETERS OF SIGNIFICANT WAVE HEIGHT (SWH) AND WAVE PERIOD(MP)

	Buoy	SWH (m)	MP (s)
BIAS	21002	0.04	-1.8
	21004	0.06	-2.0
	22001	0.07	-2.2
	21002	0.42	2.81
	21004	0.43	2.77
	22001	0.37	3.07

The statistical parameters of SWH and MP are shown in Table 2. The BIAS between observation and numerical results is less than 7 cm, which indicates the wave model can predict the variation of SWH accurately. However, the BIAS can only represent the average differences between observations and predictions. The Root Mean Square Error (RMSE) is also calculated, which is the square root of the differences. The RMSE is approximate 30-40 cm. The statistical parameters of MP are also shown in the table. The results show the simulation of MP is less accurate than that of SWH.

III. ESTIMATION OF WAVE POWER DENSITY

The wave power density (WPD) is calculated by integrating model spectra based on numerical results. The wave power density of a unit wave crest length is calculated by:

$$P = \rho g \int_0^{2\pi}\int_0^{\infty} c_g(f,d)S(f,\theta)dfd\theta \qquad (3)$$

where ρ is the density of sea water, g is the acceleration of gravity, c_g is the wave group velocity, $S(f,\theta)$ is the wave spectrum, f is frequency and θ is the direction.

The wave state in 1999 is selected to calculate the values of WPD in South China Sea. The resulting seasonal mean WPD is shown in Fig. 4. It can be seen the most energetic season is winter with the mean WPD of 9~10 kw/m. In contrast, the mean value of WPD in autumn is smallest, which is approximate 6~7 kw/m. The distribution of mean WPD in spring is consistent with that in winter, but the values are smaller. In winter and spring, the largest values of WPA are located at northeast part of the South China Sea, which is induced by the northeast monsoon during this period. The South China Sea is a marginal sea which is a part of the Pacific Ocean. In winter and spring, the northeast monsoon can increase wave energy and also the waves from Pacific Ocean can transmit into the northeast part of South China Sea, which increases the values of mean WPD. In summer and autumn, however, the intensity of wind is relative weak leading to much smaller values of mean WPD.

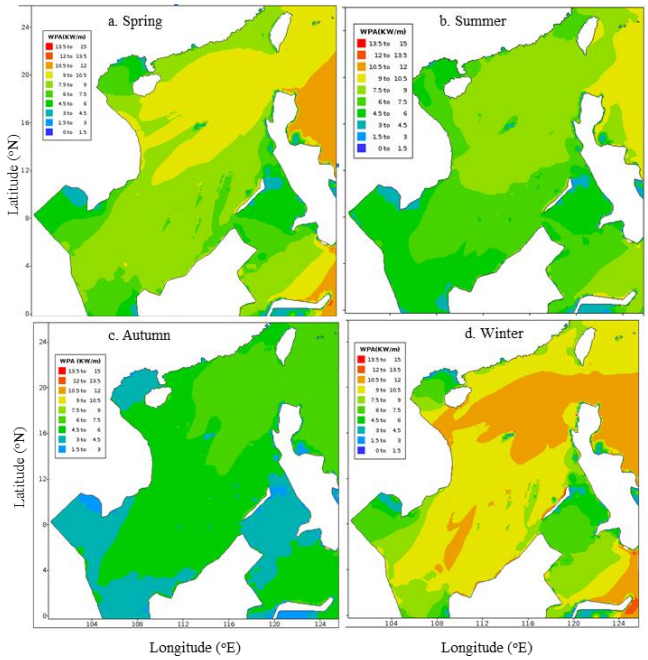

Figure 4. *Distributions of seasonal mean wave power density (WPD)*

IV. CONCLUSIONS

To provide accurate and detailled wave state in Northwest Pacific Ocean, a numerical sea state database is under construction. It will provide the sea state information during normal wave conditions as well as extreme conditions (such as typhoons). The database will include the wave parameters, such as SWH, MP, peak period and mean direction, over the period of 1979 – 2016.

Currently, the oceanic model covering the whole Pacific Ocean has been set up by using the spectral wave model TOMAWAC. The wave state in 1999 is simulated. The results show that the model can predict the variation of SWH well. The mean bias between numerical results and observation is 4-7 cm. The model underestimates the values of MP by about 2 s. The numerical results are applied to assess the seasonal variation of WPD in South China Sea. It can be seen that the intensity of wave energy is stronger in winter and spring, but it is relative weaker in summer and autumn. The most energetic part is located at the northeast part of South China Sea, which is induced by strong winter monsoon and waves transmitted from Pacific Ocean.

In future, the coastal model will be established with refined mesh in the coastal areas of China, Korea and Japan. The wave models will be calibrated by comparison with satellite data over a large spatial coverage, which will provide the necessary information to choose the best configuration of the source terms. Then, the model will be calculated during the period from 1979 to 2016 to establish the database. Finally, the wave climate analysis and extreme wave state will be assessed based on the simulated time series and spatial distributions of the wave parameters.

ACKNOWLEDGEMENT

The authors wish to thank the support by the collaborative research between Hohai University and EDF. This work was also supported by the National Natural Science Foundation of China (51339005, 41706087), the Natural Science Foundation of Jiangsu Province (Grants No. BK20170867) and the Fundamental Research Funds for the Central Universities (2016B13314).

REFERENCES

[1] Liang B, Shao Z, Wu Y, et al., (2017), Numerical study to estimate the wave energy under Wave-Current Interaction in the Qingdao coast, China. Renewable Energy, 101:845-855.

[2] Benoit, M., Marcos, F. and Becq, F. (1996). Development of a third generation shallow-water wave model with unstructured spatial meshing. Proceedings of 25th Conference on Coastal Engineering, Orlando (FL, USA), ASCE, 465-478.

[3] Booij, N.R.C. Ris, and L.H. Holthuijsen. (1999). A third-generation wave model for coastal regions, Part 1, Model description and validation. Journal of Physical Oceanography, 104:7649-7666.

[4] Tolman, H. (1991). A third-generation model for wind waves on slowly varying unsteady, and inhomogeneous depths and current. Journal of Physical Oceanography, 21:782-797.

[5] Tiberi-Wadier, A.-L., Laugel, A., Benoit, M. (2014) Construction of the numerical wave databases ANEMOC-2 on the Mediterranean Sea and the Atlantic Ocean by hindcast simulations over the period 1979-2010. Proceedings of SimHydro 2014, Sophia Antipolis (France).

[6] Shi, J., Joly, A., Zheng, JH., Zhang, JS., Chen, T., and Chen, GF., (2017), Development of a sea-state database in the Northwest Pacific Ocean by long-term numerical hindcast modelling, Proceedings of the 2017 25th International Conference on Nuclear Engineering, Shanghai, ASME, in press.

[7] Mei, C.C. (1983). The applied dynamics of ocean surface waves, Wiley, New York,740 p.

[8] Komen, G.J., Hasslemann, S., Hasselmann, K. (1984). On the existence of a fully developed wind-sea spectrum. Journal of Physical Oceanography 14, 1271-1285.

[9] Bidlot, J.-R., Janssen, P., Abdalla, S. (2007). A revised formulation of ocean wave dissipation and its model impact. ECMWF Tech. Rep. Memo., Reading.

[10] Laugel, A., Menendez, M., Benoit, M., Mattarolo, G., Mendez, F. (2014.) Wave climate projections along the French coastline: dynamical versus statistical downscaling methods. Ocean Modelling, 84: 35-50.

Development of a Large-Eddy-Simulation approach with Telemac-3D

Adrien Bourgoin, Sylvain Guillou and Jérôme Thiébot
Laboratoire Universitaire des Sciences Appliquées de Cherbourg, UNICAEN
60 rue Max-Pol Fouchet 50130 Cherbourg-en-Cotentin France
adrienbourgoin@gmail.com

Riadh Ata and Sofiane Benhamadouche
Laboratoire National d'Hydraulique et Environnement, EDF R&D
Saint-Venant Laboratory for Hydraulics
6 Quai Watier 78400 Chatou France

***Abstract*— Turbulence has a major impact on environmental flows. The complex seabed morphology combined with strong tidal flow gives rise to powerful turbulent structures that affect the different transport processes, such as heat or sediment transport. RANS modelling does not compute the turbulent variables, that is why a Large-Eddy-Simulation (LES) approach is developed in Telemac-3D. This method seeks to calculate the unsteady aspects of flows by modelling the largest turbulent structures. Thanks to the increase of calculation resources, the LES approach is nowadays applicable to simulate a large variety of environmental flows. This paper presents the implementation of new turbulence closures and the adjustment of the numerical schemes in Telemac-3D.**

The development of the method consists in implementing subgrid models and in introducing artificial turbulence in the computational domain with the Synthetic-Eddy-Method (SEM). In the meantime, we undertook efforts to reduce the numerical dissipation of the code. It was a prerequisite to propagate reliably the flow fluctuations.

This paper presents the validation of the developments in Telemac-3D considering simple flow configurations where both experimental and numerical data are available. The first results showed encouraging model behavior. The next step will consist in simulating the hydrodynamics of the Alderney Race (Raz-Blanchard in French).

I. INTRODUCTION

In environmental flows over complex bottom morphology, understanding turbulence is essential for studying processes such as sediment transport or heat transfer. In its original version, Telemac-3D uses a RANS (Reynolds Averaged Navier-Stokes) approach [4] where the averaged turbulent flow is modelled by using for example the famous $k-\epsilon$ model. Although such modelling is the most popular for natural flows, it does not provide accurate information as regards the fluctuating (instantaneous) quantities. The improvement of computational resources nowadays permits using Large-Eddy-Simulation for modelling environmental flows. This approach enables simulating the random aspect of turbulence, which plays an important role in transport phenomena. The method consists in introducing a subgrid model to mimic the smallest motion scales and in simulating the other scales by directly resolving the Navier-Stokes equations. The implementation of LES requires additional treatment, especially for the boundary conditions. In fact, contrary to RANS model, the velocity fluctuations have to be introduced in the computation domain. Moreover, near the solid boundaries, wall models are required to prevent an unaffordable mesh refinement. Finally it requires accurate and non-dissipative numerical schemes.

In this paper, several developments already done or being done in Telemac-3D are described. They are tested using a validation test case [11] representing an open channel flow over two-dimensional dunes.

II. LES METHODS

The concept of Large-Eddy-Simulation (LES) is to divide the energy spectrum [6] of the flow in two parts by using a numerical filter to separate the smallest turbulent length scales from the others. Then, these two parts are treated differently. As the smallest turbulent structures have a more universal behaviour and are hardly independent on the initial conditions, they can be modelled. Conversely, the biggest structures are directly solved by the motion equations. The filtering of the Navier-Stokes equations implies introducing a new unknown tensor called subgrid tensor. This tensor characterizes the interactions between the smallest turbulent scales and the others. It is evaluated by using a subgrid model. The filtered quantities, noted $\tilde{f}$, are computed by solving the filtered Navier-Stokes equations, written as:

$$\begin{cases} \dfrac{\partial \tilde{u}_i}{\partial x_i} = 0 \\ \dfrac{\partial \tilde{u}_i}{\partial t} + \tilde{u}_j \dfrac{\partial \tilde{u}_i}{\partial x_j} = -\dfrac{1}{\rho}\dfrac{\partial \tilde{p}}{\partial x_i} + \dfrac{\partial}{\partial x_j}\left(\nu \dfrac{\partial \tilde{u}_i}{\partial x_j}\right) - \dfrac{\partial \tau_{ij}}{\partial x_j} \end{cases}$$

where ν is the molecular viscosity and τ_{ij} is the subgrid tensor.

A. Subgrid modelling

To model the subgrid tensor, the most popular approach is named functional modelling [13]. It assumes that the interactions between the small and the big turbulent scales

can be treated as an energetic process. The action of the tensor is modelled by introducing a subgrid viscosity ν_t linking directly the subgrid tensor to the filtered velocity gradients $\tilde{s}$ with a Boussinesq assumption-like formulation:

$$\tau_{ij} = \frac{2}{3}\tau_{kk}\delta_{ij} - 2\nu_t\tilde{S}_{ij}$$

Then, the subgrid viscosity has to be evaluated with a more or less complex formulation, given by the subgrid models.

Several models have been implemented in Telemac-3D such as the Smagorinsky model [15], the dynamic Smagorinsky model [2] or the WALE model [9]. The latter model, which is retained here, was designed to provide a good asymptotic behaviour near the solid walls where the viscosity varies linearly with z^3, where z is the distance from the wall. The subgrid viscosity is written as:

$$\nu_t = (C_w\widetilde{\Delta})\frac{\left(S_{ij}^d S_{ij}^d\right)^{\frac{3}{2}}}{\left(\tilde{S}_{ij}\tilde{S}_{ij}\right)^{\frac{5}{2}} + \left(S_{ij}^d S_{ij}^d\right)^{\frac{5}{4}}}$$

with

$$S_{ij}^d = \frac{1}{2}\left(g_{ij}^2 + g_{ji}^2\right) - \frac{1}{3}\delta_{ij}g_{kk}^2 \ , \ g_{ij} = \frac{\partial\tilde{u}_i}{\partial x_j}$$

and C_w a constant evaluated to 0.325. In the formulation, $\widetilde{\Delta}$ is the filter width. It is a length scale directly linked to the grid size. Because of the prismatic shape of the elements used in Telemac-3D, two length scales have been defined to characterize respectively a vertical and a horizontal length.

B. Boundary conditions

The prescription of the LES boundary conditions is crucial as the inflow conditions have a strong influence on the flow characteristics in the calculation domain. In hydraulics, flows are mainly dominated by the advection. Thus, the prescribed values of the velocity must be as realistic as possible. The most popular approach is to prescribe Dirichlet boundary conditions over the inlet area. It is achieved by introducing a mean quantity and a fluctuating part. This technique is possible when the velocity fluctuations are known. For flows over simple bottom morphology, a common approach is to use a periodicity between the outlet and the inlet. However, when the complex geometry of a flow does not allow using periodicity, an artificial turbulence needs to be introduced at the inlet. In this section, two inlet boundary conditions (developed in Telemac-3D) are described, as well as an outlet boundary condition.

The recycling method is also called pseudo-periodicity. It aims at prescribing, at the time t^n, at the inlet ($x = x_0$) the velocity obtained at the outlet ($x = x_R$) at the time t^{n-1}. For each component of the velocity, it is written:

$$u_i(x_0, y, z, t^n) = u_i(x_R, y, z, t^{n-1})$$

This method is different from the real periodicity because it is explicit. Both recycling and periodicity are widely used but they have the drawback of introducing a spurious periodicity in the streamwise direction which can trigger instabilities as shown in [17]. To avoid this, a spanwise shift can be introduced at the inlet (a shift with respect to the outlet).

Moreover, for channel flows, the recycling method has the disadvantage of neglecting the friction loss. Near solid walls, the thickness of the boundary layer should be bigger at the outlet δ_R than at the inlet δ_0. This overvaluation at the inlet can be compensated by imposing:

$$u_i(x_0, y, z, t^n) = u_i(x_R, y, z\delta_R/\delta_0, t^{n-1})$$

For free surface flows, a source term has to be added to the streamwise Navier-Stokes equations in order to consider the friction loss of the flow [2]. This term is the mass density of force defined by:

$$F_x = -\frac{u_\tau^2}{h}$$

where u_τ is the friction velocity and h is the water depth.

The Synthetic Eddy Method (SEM) [5] consists in injecting an artificial turbulence in the computation domain. To do that, a virtual box around the inlet is introduced, where artificial eddies are created. The dimensions of the box in each dimension x_j are defined by:

$$\begin{cases} x_{j,min} = \min\limits_{x\in S}(x_j - \sigma(x)) \\ x_{j,max} = \max\limits_{x\in S}(x_j + \sigma(x)) \\ \Delta x_j = x_{j,max} - x_{j,min} \end{cases}$$

where S is the inlet surface and σ is a length scale for the virtual eddies, given by:

$$\sigma = \max(\min(\frac{k^{\frac{3}{2}}}{\epsilon}, \kappa\delta), \widetilde{\Delta})$$

with k the turbulent kinetic energy, ϵ the turbulent dissipation rate, κ the von Karman constant, δ the half of the water depth and $\widetilde{\Delta}$ the filter width.

The SEM consists in creating N virtual turbulent structures in the virtual box. Each of this structure has a random position and a random orientation in the three dimensions of space, noted $\epsilon_j^k \in \{-1,1\}$. Once the structures are created, the fluctuations at the inlet u_i' at the position $\boldsymbol{x}$ are computed from the characteristics of these eddies by using a shape function f_σ, such as:

$$u_i'(\boldsymbol{x}) = \frac{1}{\sqrt{N}}\sum_{k=1}^{N} c_i^k f_\sigma(\boldsymbol{x} - \boldsymbol{x_k})$$

where $\boldsymbol{x_k}$ is the position of the kth eddy, f_σ is the shape function that can be written as:

$$f_\sigma(\boldsymbol{x}-\boldsymbol{x_k})=\prod_{j=1}^{3}\sqrt{\Delta x_j}\sqrt{\frac{3}{2\sigma}}\left(1-\frac{|x_j-x_j^k|}{\sigma}\right)$$

and $c_i^k=a_{ij}\epsilon_j^k$ is the intensity of the k^{th} eddy in the ith direction, depending on the a_{ij} that is the Cholesky decomposition of a prescribed Reynolds tensor R_{ij}, expressed as:

$$\begin{pmatrix}\sqrt{R_{11}} & 0 & 0\\ R_{21}/a_{11} & \sqrt{R_{22}-a_{21}^2} & 0\\ R_{31}/a_{11} & (R_{32}-a_{21}a_{31})/a_{22} & \sqrt{R_{33}-a_{31}^2-a_{32}^2}\end{pmatrix}$$

At each time step, the eddies are transported by the mean flow in the virtual box. When an eddy leaves the box, it is reintroduced at the inlet of the box with new random spanwise and vertical positions as well as new intensities.

A particular outlet boundary condition is also required to perform Large-Eddy-Simulation. Theoretically, it is based on the prescription of the stress continuity [14] on each side of the domain written as:

$$\begin{cases}-p_{in}+\mu\dfrac{\partial u_n}{\partial n}=-p_{out}+\tau_n^{out}\\ \mu\dfrac{\partial u_t}{\partial n}=\tau_t^{out}\end{cases}$$

Where u_n and u_t are respectively the normal and tangential velocity, μ is the dynamic viscosity, p_{in} and p_{out} are the pressure inside and outside the domain and τ^{out} is the outside boundary stress. Telemac-3D assumes that there is no change of the velocity components across the outlet section, which yields to the set of boundary conditions:

$$\begin{cases}p=p_{out}\\ \dfrac{\partial u_n}{\partial n}=0\end{cases}$$

However this is too restrictive for Large-Eddy-Simulation since, for incompressible fluids, the tangential velocity is assumed to be null. Thus, a convective boundary condition has been implemented, written as:

$$\begin{cases}p=p_{out}\\ \dfrac{\partial u_n}{\partial t}+\vec{u}.\dfrac{\partial u_n}{\partial n}=0\end{cases}$$

where $\vec{u}$ is the advection velocity.

C. Numerical dissipation reduction

LES consists in adding a subgrid viscosity to the diffusion term of the Navier-Stokes equations. The implementation is similar to the adding of turbulent viscosity in a RANS method [7], [16]. However, the magnitude of the subgrid viscosity is much smaller than the turbulent viscosity. Using a too dissipative numerical scheme could therefore inhibit the subgrid modelling. High order and non-dissipative schemes are thus required in order to transport efficiently the flow fluctuations. Furthermore, refined grids and small time steps are also required. In [10], the recommended dimensionless grid sizes in the streamwise, spanwise and vertical dimension are respectively $\Delta x^+=50-150$, $\Delta y^+=15-50$ and $\Delta z^+<2$. Regarding the vertical discretization, larger cell sizes can be used thanks to a law of the wall.

In addition to the efforts in reducing the numerical dissipation, several approximations used in the original version of Telemac-3D have been corrected so that the fluctuations propagate in the flow. The SUPG advection scheme [1] has been modified to recover the vertical motion, through a redefinition of the vertical advection scheme and the building of finite element arrays without mass-lumping-type and zero vertical velocity approximations. Moreover, the projection step of the resolution does not involve the assumption of velocity constant per element used in Telemac-3D.

III. APPLICATION

A. Flow over a dune: presentation

The flow presented here describes a turbulent open channel flow over two-dimensional dunes of height k (see Fig. 1). This case has been studied experimentally by Polatel [10] who measured the flow over a train of 22 dunes using laser Doppler velocimetry. In those experiments, the dune height is $k=20\,mm$ and its length is $\lambda=400\,mm$. The maximum flow depth is fixed so that $h=4k$. The Reynolds number, based on the bulk velocity U_b and the maximum water depth, is approximately 25000.

B. Computational set up

This case has been reproduced with Telemac-3D using a computation domain covering a single dune. Indeed the use of the pseudo-periodicity condition (see section II.B) allows to reduce significantly the domain. It has been discretized with $161\times151\times40$ points, which corresponds respectively to the dimensionless grid spacing of $\Delta x^+\approx50$, $\Delta y^+\approx30$ and $\Delta z^+\approx20$. Those values are in line with the recommended values for LES according to [10], except for the vertical discretization where a Nikuradse wall law is used.

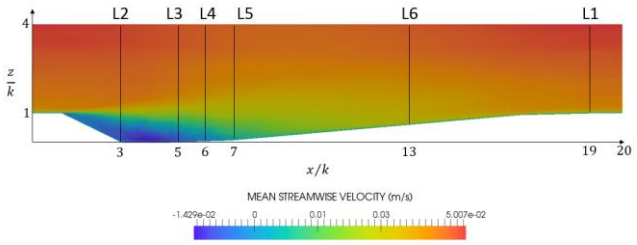

Figure 1. *Morphology of the open-channel, the six positions of measurments and mean streamwise velocity.*

As Telemac-3D clips several quantities (weak formulation), there is a minimum cell size. This limitation has been circumvented by multiplying all lengths by 4 (with respect to the experiments sizes) and by multiplying the bulk velocity by ¼ in order to keep the Reynolds number constant.

As boundary condition, the Synthetic-Eddy-Method is used for the first time steps of the calculation, in order to introduce fluctuations in the flow. An isotropic Reynolds stress tensor is prescribed. Its extra-diagonal components are null and the others are evaluated with:

$$R_{ii} = \frac{2}{3} k^+ u_\tau^2$$

where u_τ is the friction velocity and k^+ is the dimensionless turbulent kinetic energy. The latter is defined with a theoretical law [19] written as:

$$k^+ = 0.07(z^+)^2 e^{-\frac{z^+}{8}} + \frac{4.5\left(1 - e^{-\frac{z^+}{20}}\right)}{1 + \frac{4z^+}{Re_\tau}}$$

where $z^+$is the dimensionless distance to the wall and Re_τ is the turbulent Reynolds number ($Re_\tau = \frac{u_\tau h}{\nu}$). Moreover, a mean streamwise velocity profile is prescribed when using the SEM. It is dtermined using a Reichardt law [12], given by:

$$U^+ = \frac{1}{\kappa}\log(1 + \kappa z^+) + 7.8\left(1 - e^{-\frac{z^+}{11}} - \frac{z^+ e^{-0.33 z^+}}{11}\right)$$

An example of streamwise velocity prescribed at the inlet is given in Fig. 2. Once the fluid has passed through the computational domain, the Synthetic-Eddy-Method and the Reichardt law are replaced by the pseudo-periodicity method.

Regarding the numerical configuration of Telemac-3D, the modified SUPG advection scheme (see section II.C) along with Crank-Nicholson time integration scheme with a CFL of a magnitude of 0.3 are used. Finally the WALE model (see section II.A) is used as subgrid model. The velocities and the root-mean-square velocities are averaged over 5000 s, which represents a duration of about 250 flow recirculations. The calculation duration is 28h with 56 threads.

C. *Statistic results*

The averaged streamwise velocity and three components of the Reynolds stress tensor are extracted at six locations shown in Fig. 1, and compared with the experimental results from [11].

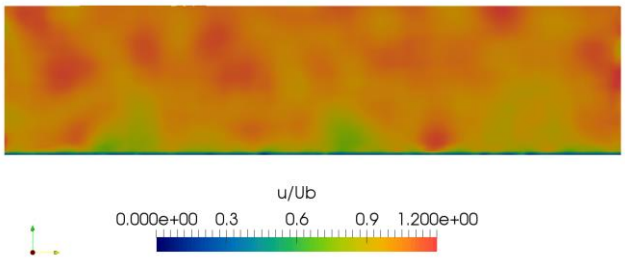

Figure 2. *Streamwise velocity prescribed at the inlet by using the SEM and the Reichardt law.*

The averaged streamwise velocity normalized by the bulk velocity profiles obtained with Telemac-3D are compared to the experimental results of [11] in Fig. 3. The agreement with experiments is good, except at the position L1 and L6 where a deviation is observed in the low part of the flow.

Fig. 4 and 5 show respectively the streamwise and the vertical root-mean square velocity along the six verticals. The agreement between the Telemac-3D results and the measurements are overall good for both of the turbulent intensities, despite a slight overestimation of the streamwise root-mean-square velocity at the location L3 and L4.

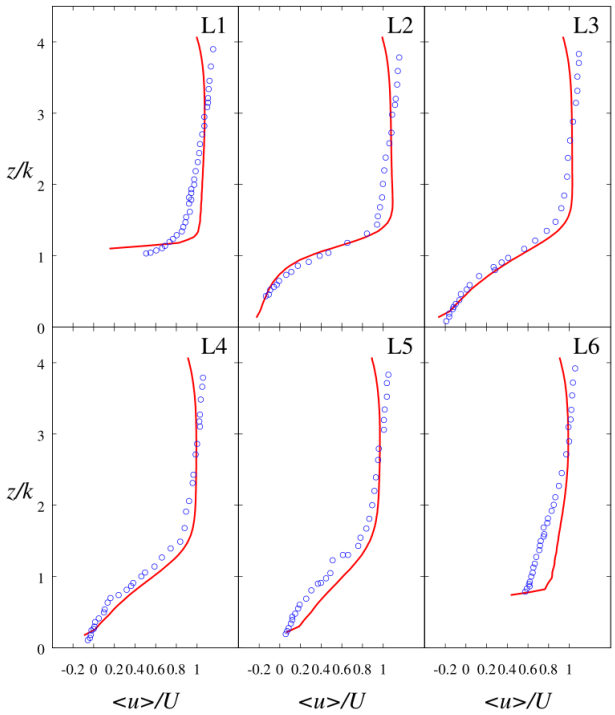

Figure 3. *Averaged streamwise velocity along the six measurement verticals, obtained with Telemac-3D (line) and the experiments of Polatel (symbol) [11].*

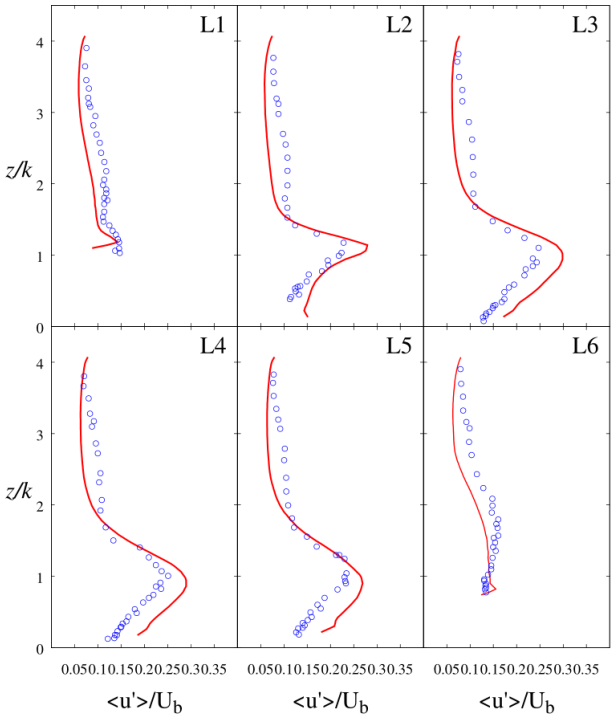

Figure 4. *Streamwise root-mean-square velocity along the six measurement verticals, obtained with Telemac-3D (line) and the experiments of Polatel (symbol) [11].*

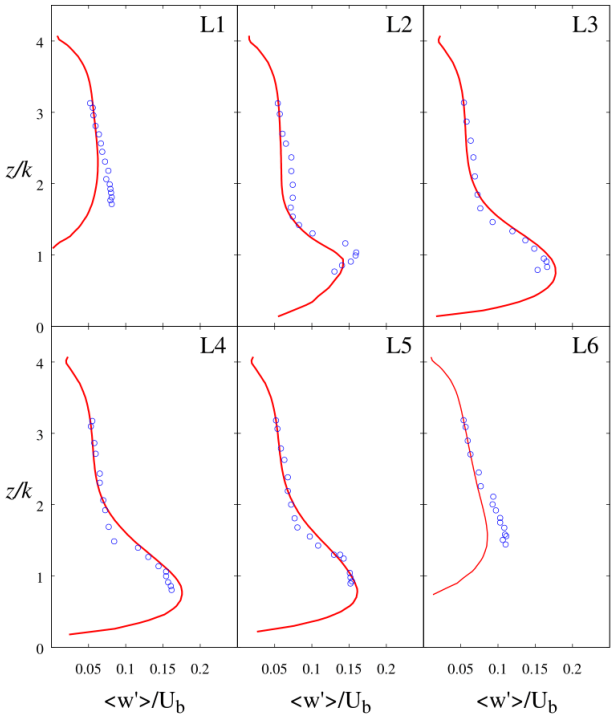

Figure 5. *Vertical root-mean-square velocity along the six measurement verticals, obtained with Telemac-3D (line) and the experiments of Polatel (symbol) [11].*

Fig. 6 shows the Reynolds shear stress profiles. The model-experiment comparison is also satisfactory. The maximum intensity is slightly overestimated at the locations L3 and L4.

The overall agreement between the model results and the measurements allows to validate the developments. Using LES now permits to analyse the dynamics of the turbulent structures. For instance, Fig. 7 shows some isosurfaces of pressure. This figure highlights the vortex generation at the foot of the dune and the transport of the vortex by the flow with an inclined orientation. The analyse of the instantaneous results indicate that spanwise vortices are generated in the separated shear layer and that they ascend up to the free surface.

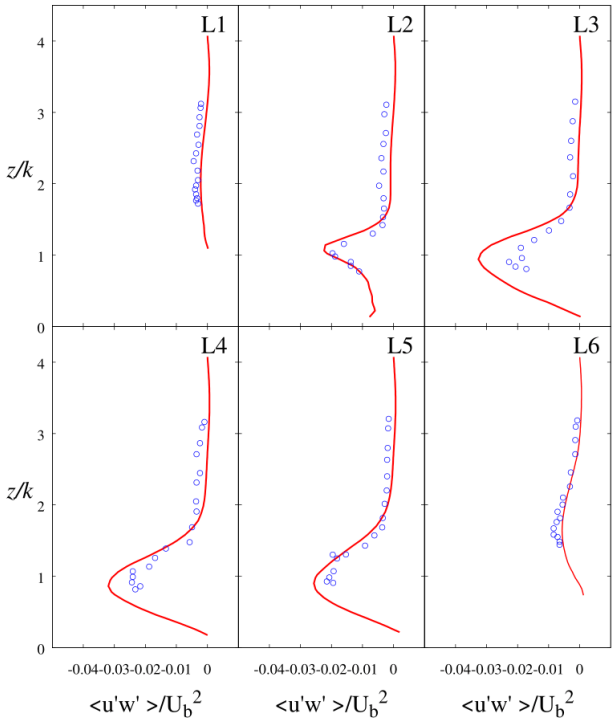

Figure 6. *Reynolds shear stress along the six measurement verticals, obtained with Telemac-3D (line) and the experiments of Polatel (symbol) [11].*

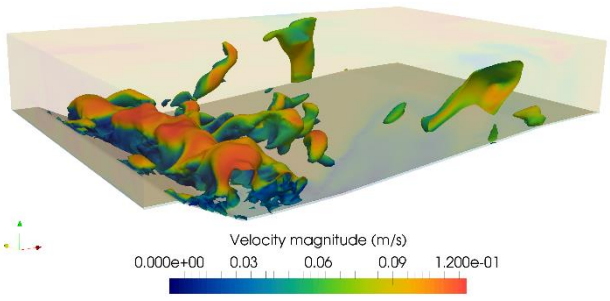

Figure 7. *Isosurfaces pressure colored by the magnitude of velocity*

IV. Conclusion

A Large-Eddy-Simulation approach is developed in Telemac-3D [4] for modelling free surface complex flows. After carrying out a state of the art of LES methods in hydraulics, several subgrid models are selected to be implemented. Since this kind of simulation requires specific boundary conditions, the Synthetic Eddy Method (SEM) [5] is used at the inlet boundary for generating the first velocity fluctuations and a recycling method is then used to introduce a realistic turbulence. Additional boundary conditions was also required for the stability of the calculation, such as a convective outflow boundary condition. A special care was at least required to reduce the numerical dissipation of Telemac-3D, mostly due to several assumptions on the vertical velocity in the advection step.

The results obtained by the LES model of Telemac-3D are in good agreement with experimental results of a flow over dunes. The turbulence indicators show satisfactory model performance. Both the averaged velocity and the Reynolds stress fit with the experimental results [11].

A final objective would be to perform regional simulations. Due to the high Reynolds number of environmental flows and the considerable computational cost of Large-Eddy-Simulation, a further investigation is currently in progress on the implementation of a DES method based on the Spalart-Allmaras [16] RANS model, which is a hybrid method between RANS and LES.

ACKNOWLEDGMENT

This work is funded by French Agence Nationale de la Recherche programme under a contract with a reference number ANR-10-IEED-0006-11

REFERENCES

[1] Brooks, A. N., & Hughes, T. J. (1982). Streamline upwind/Petrov-Galerkin formulations for convection dominated flows with particular emphasis on the incompressible Navier-Stokes equations. Computer methods in applied mechanics and engineering, 32(1-3), 199-259.

[2] Germano, M., Piomelli, U., Moin, P. & Cabot, W.H., (1991). A dynamic subgrid-scale eddy viscosity model. *Physics of Fluids A: Fluid Dynamics* (1989-1993), 3(7):1760–1765.

[3] Guillou, S. & Makhloufi, R., (2007). Effect of a shear-thickening rheological behaviour on the friction coefficient in a plane channel flow: a study by direct numerical simulation. *Journal of non-newtonian fluid mechanics*, 144(2):73–86.

[4] Hervouet, J.-M., (2007). *Hydrodynamics of free surface flows: modelling with the finite element method.* John Wiley & Sons.

[5] Jarrin, N., Benhamadouche, S., Laurence, D. & Prosser, R., (2006). A synthetic-eddy-method for generating inflow conditions for large-eddy simulations. *International Journal of Heat and Fluid Flow*, 27(4):585–593.

[6] Kolmogorov, A. N., (1941). Dissipation of energy in the locally isotropic turbulence. *Proceedings: Mathematical and Physical Sciences,* 434(1890):15-17.

[7] Launder, B. E. & Sharma, B. I., (1974). Application of the energy-dissipation model of turbulence to the calculation of flow near a spinning disc. *Letters in heat and mass transfers,* 1(2):131-137.

[8] Lilly, D.K., (1992). A proposed modification of the germano subgrid-scale closure method. *Physics of Fluids A: Fluid Dynamics* (1989-1993), 4(3):633–635.

[9] Nicoud, F. & Ducros, F.,(1999). Subgrid-scale stress modelling based on the square of the velocity gradient tensor. *Flow, turbulence and Combustion*, 62(3):183–200.

[10] Piomelli, U. & Chasnov, J. R.,(1996). Large-eddy simulations: theory and applications. *Turbulence and transition modelling*, vol. 2, pp. 269-336.

[11] Polatel, C., (2006). *Large-scale roughness effect on free-surface and bulk flow characteristics in open-channels flows.* ProQuest.

[12] Reichardt, H., (1951). Vollständige Darstellung der turbulenten. Geschwindigkeitsverteilung in glatten Leitungen, *ZAMM-J. Appl. Math. Mech./Z. Angew. Math. Mech. 31(7),* 208-219.

[13] Sagaut, P., (2006). *Large eddy simulation for incompressible flows: an introduction*. Springer Science & Business Media.

[14] Sani, R. L. & Gresho, P. M., (1994). Résumé and remarks on the open boundary condition minisymposium. *International Journal for Numerical Methods in Fluids,* 18(10): 983-1008.

[15] Smagorinsky, J., (1963). General circulation experiments with the primitive equations: I. the basic experiment. *Monthly weather review*, *91(3):99–164.*

[16] Spalart, P. R. & Allmaras, S. R., (1994). A one-equation turbulence model for aerodynamic flows. *Recherche Aerospatiale,* n/a(1):5-21.

[17] Spalart, P. R., Strelets, M. & Travin, A.,(2006). Direct numerical simulation of large-eddy-break-up devices in a boundary layer. *International Journal of Heat and Fluid Flow*, 27(5) :902–910.

[18] Stoesser, T., Braun, C., Garcia-Villalba, M. & Rodi, W., (2008). Turbulence structures in flow over two-dimensional dunes. *Journal of Hydraulic Engineering*, vol. 134, no. 1, pp. 42-55.

[19] Viollet, P.-L., Chabard, J.-P. & Esposito, P., (2003). *Mécanique des fluids appliquée: écoulements incompressibles dans les circuits, canaux et rivières, autour des structures et dans l'environnement.* Presses des Ponts.

PyTelTools: Python scripts and GUI to automate Telemac post-processing tasks

Luc Duron
Engineering department
Compagnie Nationale du Rhône (CNR)
Lyon, France
l.duron@cnr.tm.fr

Yishu Wang
Bioinformatics and Modelling department
Institut National des Sciences Appliquées (INSA)
Lyon, France
yishu.wang@insa-lyon.fr

***Abstract* — PyTelTools is a set of Python scripts recently developed by CNR Engineering department. Developed scripts are released as an open source software, which is intended to be accessible, extensible and customizable. An easy-to-use Python GUI was implemented to facilitate post-processing tasks on 2D or 3D TELEMAC-MASCARET computation results.**

A wide range of tools is offered to the modeller within PyTelTools. These tools include file conversions, interpolations, calculations, statistics and visualization. A workflow interface was developed to chain these unitary tasks. Indeed, after defining graphically a conceptual model representing the tasks nesting, runs can be performed on multiple simulations in parallel.

I. INTRODUCTION

A. CNR Engineering

CNR, the first producer of exclusively renewable energy in France, operates 18 hydroelectric facilities on the Rhone River, with an installed capacity of 3000 MW. Under the operation of these facilities, CNR has developed and uses specific hydro-informatics tools tailored to their individual needs, either for studies or for operational applications.

For engineering tasks requiring a fine resolution, TELEMAC-MASCARET is often used in connection with its associated pre and post-processing software. With the multiplicity of processing software along the modelling chain, some tools are required to interface them and to extend their possibilities.

B. Objectives and development guidelines

CNR Engineering recently decided to constitute a set of Python scripts which are intended to be robust, extensible, modular and accessible to the community. This project was named PyTelTools and stands for “Python Telemac Tools”. These scripts do not rely on Python scripts provided in the official openTelemac SVN repository, but were developed from scratch and are fully functional with Python 3.

A user documentation [1] and a developer documentation are provided online, with the source code. The developed scripts include some files parsers (Serafin, BlueKenue ...) and a collection of mathematical or spatial calculations based on 2D or 3D Telemac results. Moreover a graphical user interface (GUI) is provided to make them available, easy to use and to facilitate systematic exports and post-processing tasks.

These tools are extensible, thanks to a documentation, snippets and contributing guidelines. Additionally, a customization is possible and allows the user to change default behavior (e.g. the interface, I/O parameters, some calculations assumptions ...).

II. DESCRIPTION AND CLASSIFICATION OF POST-PROCESSING TOOLS

Main developed tools are described in this section in the different tasks items.

A. Compute variables tasks

“Extract (or Select) variables” is a tool whose aim is to compute derived variables from a Serafin input file. All the potential derived variables are suggested to the user depending on variables available in input file and equations implemented (more than twenty equations are implemented [2]).

Equations can be rather simple, but the tool handles multiple indirect computation of variables. For example, to compute Froude number, the equation states that it requires water depth and velocity magnitude variables. But if these variables are not already present in input Serafin file, they could be computed with other variables, such as bottom, free surface, velocity on X and velocity on Y.

Friction velocity can be recalculated depending on friction law and allows for example to compute Rouse numbers based on user defined settling velocities.

To compute complex and custom equations in 2D, the user has to use the tool named “Variable Calculator”. This advanced calculator allows to define successive conditions on variables or on zones defined spatially with polygons.

B. Compute fluxes tasks

Computation of fluxes in 2D through an arbitrary section is implemented with a generic integration of a product with one scalar, one vector field and eventually water depth (a particular second scalar). This allows computation of different types of liquid and solid fluxes, depending on

variables present in input Serafin file. An example for liquid fluxes is presented in Tab. 1 (with Telemac 2D variable names). For this example, among all the possibilities, the first computation (with velocities U and V) is more accurate because velocity vectors are projected on a normal vector to the cross-section, and it relies on a quadratic function integration. That quadric function is defined by parts.

(X, Y) Vector field	Height	Scalar
VELOCITY U VELOCITY V	WATER DEPTH	-
FLOWRATE ALONG X FLOWRATE ALONG Y	-	-
-	WATER DEPTH	SCALAR VELOCITY
-	-	SCALAR FLOWRATE

TABLE 1. EXAMPLE OF FLUX COMPUTATION POSSIBILITIES FOR LIQUID FLUXES

C. *Compute volume tasks*

Different kind of volumes can be computed in a set of 2D polygons defined by the user. Volumes are basically described by an upper and a lower surface. These surfaces are defined by values at nodes of the 2D mesh and for all frames. Upper values correspond to a scalar variable, whereas lower values can be zero, initial frame of same variable or another scalar variable. Typical applications with their upper and lower values are summarized in Tab. 2.

Upper values	Lower values	Interpretation
WATER DEPTH	0	Liquid volume
FREE SURFACE	BOTTOM	Liquid volume
BOTTOM	RIGID BED	Solid volume
BOTTOM	Initial values	Volume from beginning

TABLE 2. EXAMPLES OF TYPICAL VOLUME COMPUTATIONS (WITH TELEMAC-2D VARIABLE NAMES IN CAPITAL LETTERS)

Positive and negative volumes for each polygon can be computed in addition to the net volume. Exact volumes are computed, including pieces of elements which are cut by a polygon and/or by the lower surface defined by its values at nodes. The underlying theory is established on a document available online [3].

D. *Interpolate and project along lines tasks*

Interpolating a 2D variable along an open line provides a 1D view, with the x-axis being in general the cumulated distance. To have the exact evolution of the variable along the line, the initial line is populated with intersection points between it and the 2D mesh.

For fluvial applications, involving a long river reach, modellers often fall back on a 1D view along the hydraulics axis. Along this specific line, called reference line and drawn within the minor bed, a curvilinear distance (or kilometre point) is defined, starting from the first point.

The tool to project lines on the reference line interpolates variables along a set of lines and performs a projection to determine their curvilinear distance along the reference line. Fig. 1 shows on the left, the definition of the reference line (Line 1) and dykes (Lines 2 to 4) and on the right, the computed longitudinal profile mixing different variables (bottom elevation for dykes and free surface for the reference line).

E. *Compare two 2D results tasks*

Comparison of a variable of 2D results consists of a wide range of methods. Computation of differences between two meshes, which are eventually different, is one of simplest method and gives the spatial distribution of deviation.

For quantified comparison, modellers often compute criteria or turn to statistical analysis. However computation of deviation criteria or statistics are not direct because the triangular mesh is irregular. To overcome that, developed scripts do not rely on an intermediate regular grid, but compute the exact deviation thanks to some volume calculations [3].

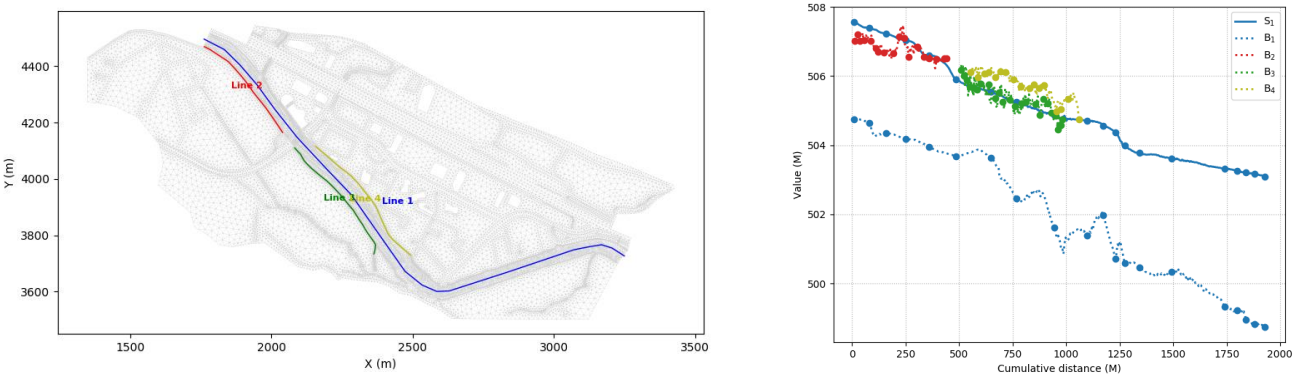

Figure 1. *Example of Project Lines application with the map (left) and longitudinal profile with bottom (dotted lines denoted Bi) and free surface elevation (continuous line denoted S_1) (right)*

Comparison criteria developed in PyTelTools are the following:

- Mean Signed Deviation (MSD)
- Mean Absolute Deviation (MAD)
- Root Mean Square Deviation (RMSD)
- Brier Skill Score (BSS)

The last criterion is mainly used for sediment transport issues, to compare bed evolution during two bathymetric campaigns.

Temporal evolution of criteria is interesting for analyse of the dynamic and can point out impacts (or even divergence) at specific time or during events. Some above-mentioned criteria can be visualized over time, as shown in Fig. 2 for the MAD criteria. This figure simply compares bottom elevation (on the whole domain) between a temporal 2D sediment result and the target (or reference). The reference, which is constant over time, is a bathymetric campaign, which should correspond to the last computed frame. In this example, MAD tends nearly to zero and shows some inflexion points corresponding to flood events.

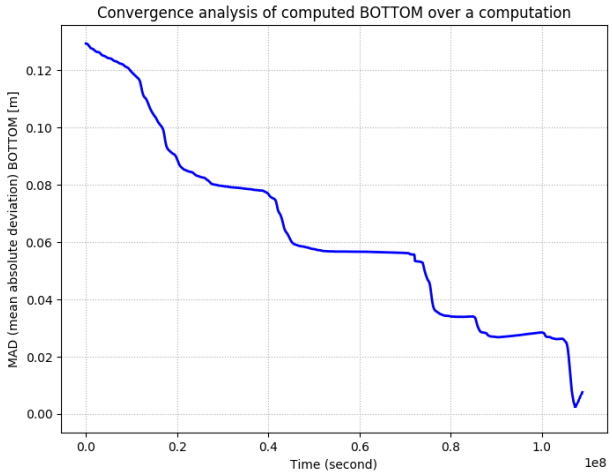

Figure 2. *Evolution of BOTTOM deviation from the target*

Moreover, all these criteria can be computed over the whole domain or in a set of polygons to study specific areas of interests.

III. BUILDING A WORKFLOW

A. *Context and notions*

Most post-processing tasks are not isolated, but are rather a part of a chain of operations. Using a tool handling workflow is more convenient and efficient, because these steps can be wrapped into a single operation, which can be modified later or repeated on other input data. This automation of post-processing tasks can save time, efforts, and avoid errors while repeating them manually. Some software already include their own automation tool:

- QGIS has his so-called graphical modeller,
- Paraview allows on-the-fly trace recording [4].

Developed scripts include a tailor-made graphical modeller, which is adapted and optimized to the hydraulic modeller needs. It is independent of any graphical post-processing, GIS or statistical software, but is not intended to replace any of them.

Conceptual Model Principle

PyTelTools offers an easy-to-use drag-and-drop interface that allows users to construct a series of computational tasks that can be chained up by drawing links between them. The resulting graph is a directed acyclic graph (DAG) and each node represents a unitary tool (or task).

The workflow graph not only represents graphically different steps of data manipulation, computation and visualization, it can also be executed within the software which also provides process monitoring in real time.

B. *Provided tools and specificities*

The conceptual model can include the post-processing tasks listed below. This list groups together tools by category.

- Load files
  - Load Serafin 2D or 3D
  - Load Reference Serafin
  - Load 2D Polygons
  - Load 2D Open Polylines
  - Load 2D Points
- Write files
  - Convert to LandXML, shp, vtk
  - Write Serafin 2D or 3D
- Basic operations
  - Select Variables
  - Select Time range or Single Frame
  - Add Rouse Numbers
  - Convert to Single Precision
  - Add Transformation
- Operators
  - Max, Min, Mean, SynchMax
  - Project B on A
  - A Minus B (or inversely)
  - Max(A, B) or Min(A, B)
- Calculations
  - Compute time of arrival and duration
  - Compute Volume
  - Compute Flux
  - Interpolate on Points
  - Interpolate along Lines
  - Project Lines
- Visualization
  - Show Mesh
  - Locate Points, Open Lines or Polygons
  - Visualize Scalars, Vectors
  - Point, Flux or Volume Plot
  - Project Lines Plot
  - Multiple variables or frames Line Plot
  - Vertical 3D Cross-Section
  - Vertical 3D Temporal Profile

C. *Two views for a more complete automation*

Two levels of automations can be performed by PyTelTools workflow.

The first one is intended to process a single simulation and is therefore called “Mono”. In the mono view, a run will go through the whole post-processing tasks defined in the conceptual model. It is in this view that the graph is built and each tool configured.

On the other hand, the “Multi” view in the workflow tool works on a level above and will apply a “Mono run” to a set of simulations.

IV. WORKFLOW EXAMPLES

A. *Typical Applications*

Common applications of a workflow for Telemac post-processing are mainly:

- sensitivity studies (on parameters, boundary conditions, ...),
- calibration processes,
- batch conversion or simplification of Telemac result files.

B. *Basic 2D hydraulic calibration*

A first application of PyTelTools workflow was led on a simplified 2D hydraulic model (only around 20 000 nodes for 39 000 elements). This example is based on a friction coefficient calibration process, for which 6 different roughness zonings were defined.

This kind of calibration process commonly includes several computations:

A. compute maximum of variables over flood duration,
B. interpolate along lines (and eventually project them on the hydraulic axis) and/or at points located at gauging stations,
C. compute fluxes through some cross-sections.

For each roughness zoning, a simulation was performed and the same post-processing tasks where applied. Post-processing tasks are described in the graph presented on Fig.3 (left panel).

C. *Sedimentary study*

For a study dealing with sediment transport issues on a large scale model, workflow tool was applied profitably. An example of some automated post-processing tasks is presented on Fig. 4. These different tools were defined to:

- compute liquid and solid fluxes,
- compute volumes of erosion and deposition,
- produce maps afterwards from shp and TIN files.

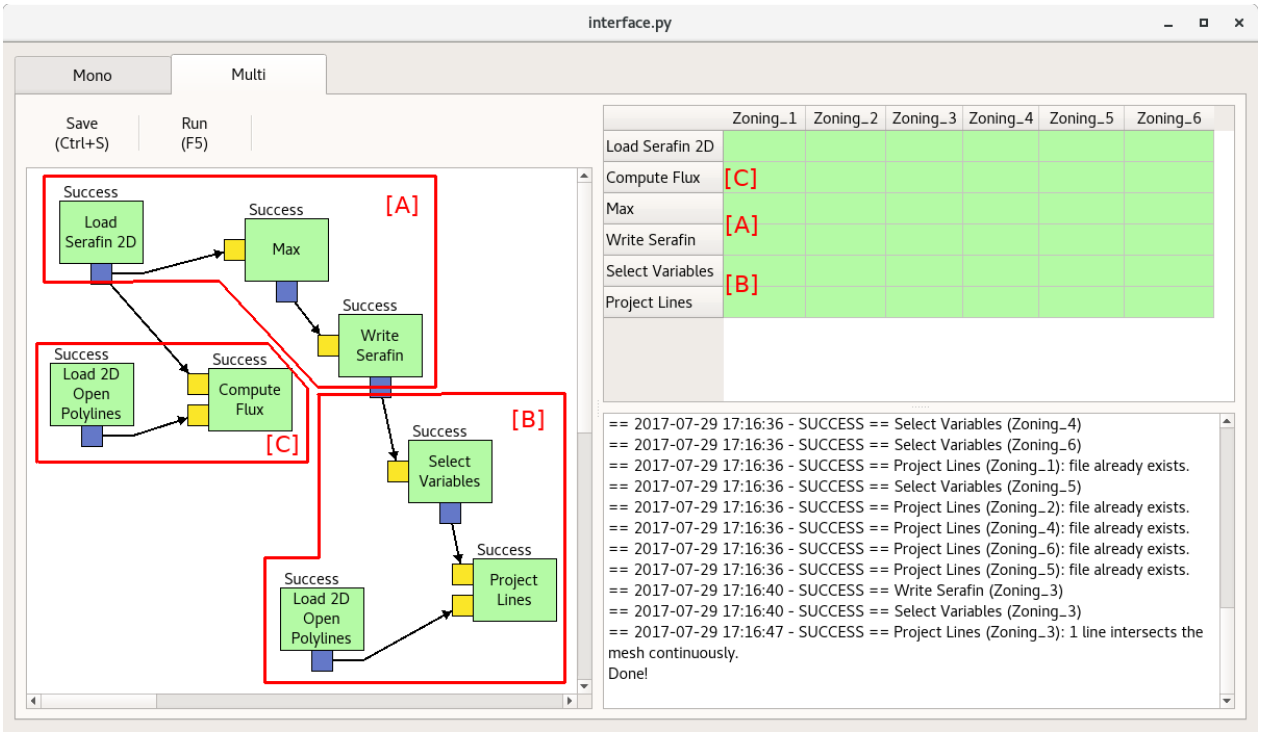

Figure 3. *Workflow graph (left panel) and process status after a successful run (right panel)*

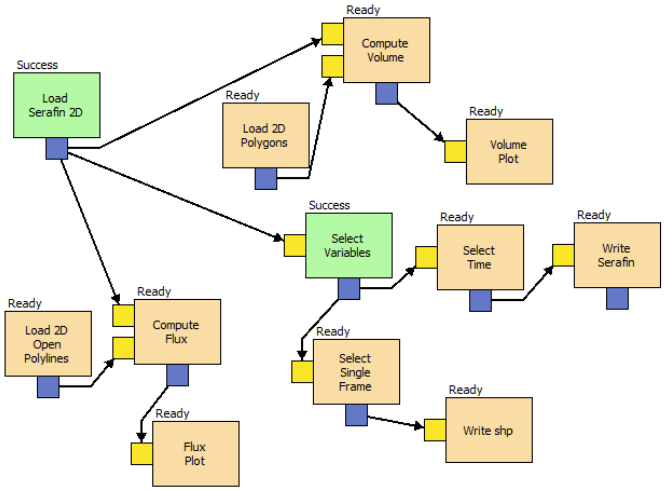

Figure 4. *Workflow graph with running status of post-processing tasks for a sedimentary study*

V. 3D VISUALIZATION

In addition to writing processed data, PyTelTools provides a set of visualization plots, which can be customized and exported in mass. Two visualization examples are presented hereafter and are dedicated to 3D results analysis on the vertical axis.

The first visualization plot (Fig. 5) shows vertical distribution of mud concentration over the time, at a single point. In this example, during the period representing two tidal cycles, high concentration of mud occurs at low tides.

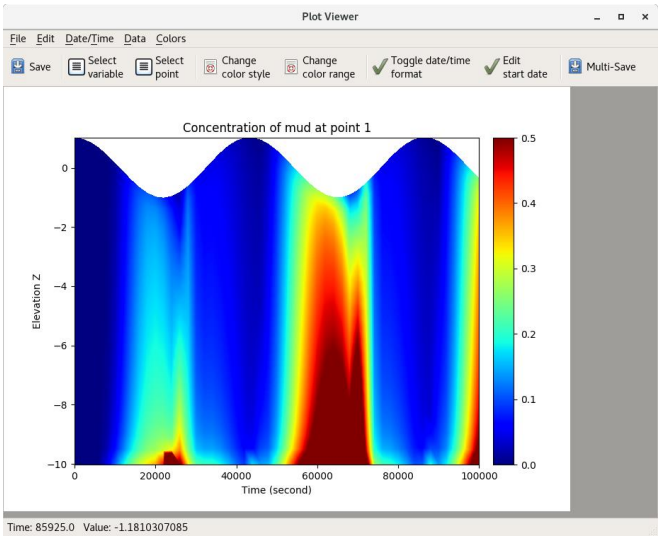

Figure 5. *Temporal vertical profile visualization of mud concentration at a specific location*

The second example deals with 3D velocity field through a cross-section. This data is often measured in situ (with a so-called ADCP instrument) and compared to 3D results.

Fig. 6 shows the superimposition of measurements and results on the same cross-section. ADCP measurements were processed with ADCPtool, which is developed by TU Graz, whereas TELEMAC-3D results post-processing was performed with PyTelTools.

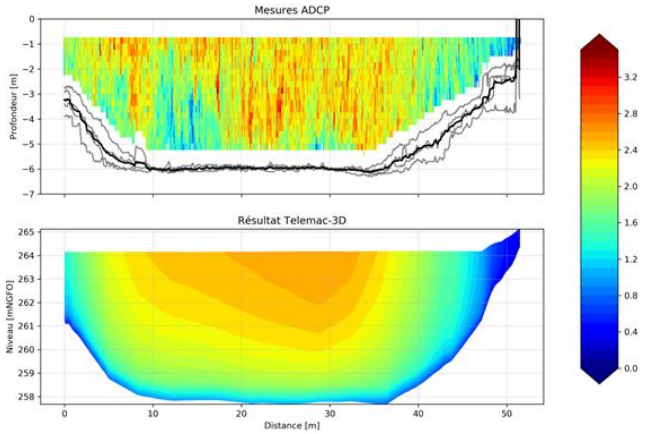

Figure 6. *Comparison of ADCP measurements (upper plot) and TELEMAC-3D results (lower plot) through a cross-section*

VI. MULTI-FOLDER PARALLEL EXECUTION

A. *Basic principles*

Default Python interpreter was designed with simplicity in mind and has a thread-safe mechanism. However some Python modules exist to spawn multiple subprocesses, and PyTelTools "Multi view" uses the library multiprocessing to distribute tasks on different data to multiple CPU cores.

Some performance tests were carried out in order to validate the proper functioning and efficiency of parallelism in PyTelTools.

B. *Performance test*

Local workstation

The computer used for the benchmark is a post-processing machine, whose performances are slightly higher than a typical PC workstation. Its characteristics are summarized below:

- Intel(R) Xeon(R) E5-2690, 2.90 GHz, 64 bits (8 cores, 16 threads),
- Windows Server with Python v3.6.1 64 bits

Test case

The example A, described in part IV, was used for the present benchmark. This simple and representative example includes only one bifurcation (just after "Load Serafin 2D" node), which leads to two independent chains of tasks for a single simulation (or folder). In this example, most of the computation time is spent on flux and interpolation calculations, which limit I/O bound state.

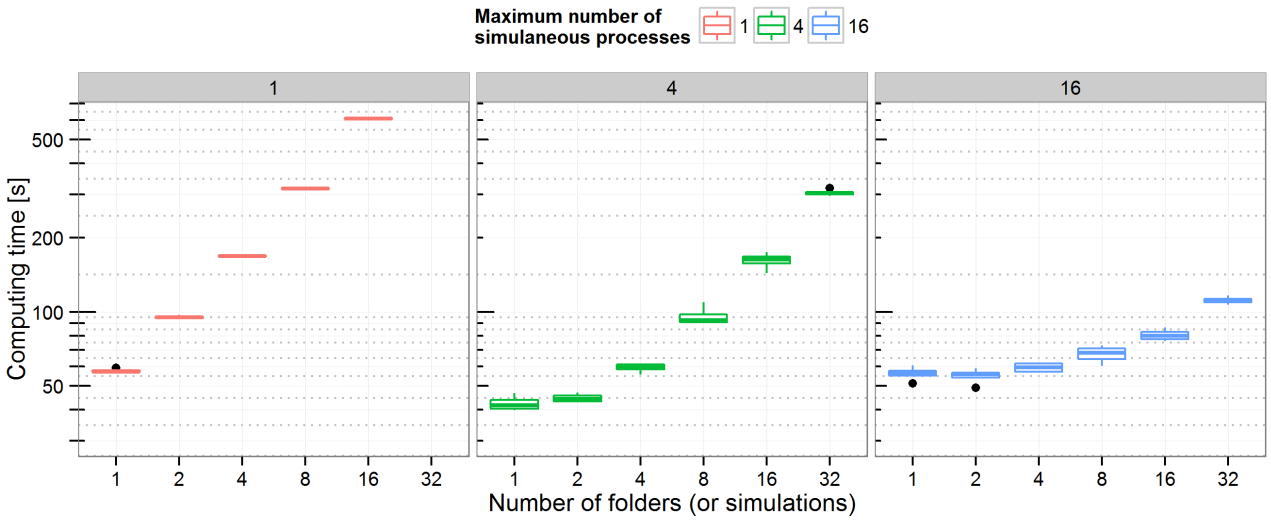

Figure. 7. *Computing time benchmark on example A, with different number of folders and CPU cores (1, 4 and 16, which corresponds to machine nproc)*

C. *Main outcomes*

The computing benchmark results are presented on Fig. 7 (with logarithmic axis). A sensitivity analysis was performed on two variables: the number of CPU cores (called maximum number of simultaneous processes) and the number of folders. For a given couple of these variables, each box plot includes at least 5 repetitions.

The different repetitions show that the results are well reproducible. The scaling is coherent with the number of folders and CPU limitations. Indeed, for a number of folders which is large enough (compared to CPU cores), the computing time increases linearly. Moreover, in this case, the slope of the curve is also proportional to the CPU cores number.

Because of the two independent chains of tasks in the graph, it is still interesting to have more CPU cores than the number of folders to process.

REFERENCES

[1] PyTelTools User Documentation (wiki based), https://github.com/CNR-Engineering/PyTelTools/wiki

[2] Equations integrated in PyTelTools, August 2017, https://github.com/CNR-Engineering/PyTelTools_media/raw/master/latex/equations.pdf

[3] Mathematical definitions for PyTelTools, August 2017, https://github.com/CNR-Engineering/PyTelTools_media/raw/master/latex/mathematical_definitions.pdf

[4] U. Ayachit, “The Paraview Guide, A Parallel Visualization Application”, Kitware

COURLIS: a new sedimentology 1D module for MASCARET

Eric Valette[1], Matthieu Secher[1]
[1] Centre d'Ingénierie Hydraulique (CIH)
EDF
Le Bourget du Lac, France
eric.valette@edf.fr , matthieu.secher@edf.fr

Philippe Ung[2], Goutal Nicole[2,3] Magali JODEAU[3]
[2] Saint Venant Hydraulics Laboratory
[3] EDF - LNHE
Paris, France

***Abstract*— COURLIS is a 1D sedimentology module coupled with MASCARET. The code has been developed by EDF R&D for many years. Recently, CIH identified the need to have a 1D bedload code to model the long term evolution of rivers and reservoirs (several decades).**

After a benchmark of existing and available 1D codes, we chose to develop an efficient version of COURLIS which calculates bedload transport. New numerical schemes were implemented, some improvements were done in the geometry evolution algorithms. In terms of performance and robustness, the best scheme implemented is a finite volume upwind/downwind scheme.

This new version of COURLIS was validated successfully on several test-cases (Soni, Newton ...). A real case of a river with a reservoir has been simulated during an 11 year period. These 11 years were reduced to 2 years after cutting flowrates lower than the sediment incipient flowrate. The calculation time on this real case is very similar to those obtained with codes tested in the benchmark and the results are in a good agreement with measurements and other code results.

The next step for COURLIS will be its integration into the TELEMAC-MASCARET system.

I. INTRODUCTION

Sediment management, sediment deficit or deposit in rivers and reservoirs are major issues:

- Environmental issue: Sediment continuity is required for the sustainable management and achievement of a good ecological state of the water resources mentioned by the Water Law (2006), French translation of the European Water Framework Directive (2000).
- Safety issue: Sediment deficit may lead to the alteration of the anthropic structures (bridge, dam ...) by scouring, and it may cause disturbance of drinking groundwater supply facility. Conversely, the presence of alluvial banks (mainly vegetated) can lead to an increase of flood risk and erosion of embankments due to the reduction of section caused by fixed bars.
- Tourism and economic issues: navigation can be affected by an increase in bed level and the visual impact (banks).

In addition, the hydraulic energy producer EDF also encounters production problems, for example, the reduction of the storage capacity of a reservoir. Fig. 1 illustrates the simplified issues that EDF is regularly confronted with: by reducing the flow velocities, the reservoir leads to the deposition of sediment (solid backwater due to the deposit of coarse sediment upstream and siltation close to barrage). Deposition leads to several problems: increased risk of flooding, reduced capacity of the reservoir, sealing of the bottom gate. In addition, the dam limits sedimentary continuity by limiting the solid supply downstream, causing a gradual erosion of the bed downstream of the reservoir.

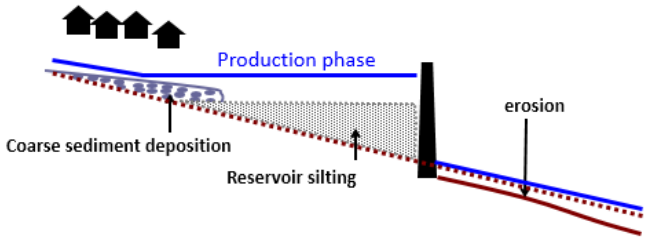

Figure 1. *Morphological evolution due to the dam*

To address these issues, EDF seeks to define optimized sediment management methods. This work should be done at the scale of its hydraulic valleys because in many rivers several reservoirs are managed together.

Numerical tools can be used to evaluate the consequences of several scenarios of sediment management (dredging, flooding, sluicing...). Among all available codes, 1D hydro-morphodynamic models allow the calculation of orders of magnitude concerning:

- total volumes transported and deposited,
- average bed level evolution.

Such results could be calculated for a period from some hours (floods) to several decades without large computation times.

In order to be able to lead sediment studies, CIH was looking for a 1D sediment transport code which would be stable with

low computation times. First a review of existing tools has been performed then specific developments have been done in MASCARET-COURLIS.

II. INVENTORY OF 1D NUMERICAL TOOLS AVAILABLE IN 2015

A. COURLIS

COURLIS is a one-dimensional numerical code originally developed at EDF (R&D) under the TELEMAC-MASCARET suite. A morphodynamic module is coupled with the MASCARET hydraulic code and allows to model the transport of the sediments and the bed evolution.

The first version of COURLIS modelled the transport of cohesive sediments in one-dimensional flows. The main applications were the optimization of flooding, emptying of reservoirs, and the study of settling basin [1], [2], [3], [4], [5].

The second version included the transport of sand by suspension.

And a third version of the software was developed to integrate the bedload transport (sands and gravels). Laboratory validation tests case had been successfully performed, but the code was unstable when used on real cases geometry. Moreover, the CPU time was too important for real applications.

B. 1D sediment transport software

Several 1D sediment transport software exist outside TELEMAC-MASCARET suite. After an initial selection, EDF CIH has selected two software to realize a benchmark (HEC-RAS, MIKE) in 2015.

Additional tests were performed by Artelia with their in-house developed software (CAVALCADE).

1)HEC-RAS:

It is a freeware but it presents too many problems which limit the calibration possibilities: many test cases failed due to the appearance of a non-physical diameter (3.048×10^{-8}m in the active layer).The transport formulas are limited and non-representative of the ones used in France.

The code is not open-source. Attempts to use the forum or contact a developer by mail have not been successful.

2)MIKE :

This software gave correct results for the chosen test cases. The customer service is good. However, the required formation time is significant.

The file formats between MASCARET and MIKE are not compatible and the integration of non-georeferenced geometries is problematic with a text file. As the CIH hydraulic studies are performed using MASCARET, the hydarulic and sediment files should be compatible.

Interpretation of results is sometimes difficult due to the limited number of available output data. The 'average bed level' result is not available whereas it is the data used for the calibration of the model. Otherwise the code is not open-source.

3) Conclusion

Following this benchmark, and taken into its needs, the CIH decided to continue the developments of the EDF-R&D software COURLIS. The new developments aim at adding a robust bedload module.

III. MODEL

COURLIS bedload is a sediment module and is coupled with MASCARET (same way as TELEMAC – SISYPHE):

$$\partial_t A_z(t,x) + \partial_x Q_s(t,x) = 0 \qquad (1)$$

with A_z (m^2) sediment volume in a cross-section and Q_s (m^3/s) volumetric sediment flux integrated along the transversal direction. The flow mean velocity is calculated by MASCARET and used by COURLIS to calculate the mean shear stress on the bed. The bottom evolution is calculated with the Exner equation (1) and a relation between A_z and Z the bottom elevation. This new bottom elevation is sent to MASCARET, and so on.

To close the Exner – shallow water equation system a bedload formula is required. Four different bedload formulas are coded:

- Meyer-Peter and Müller (1948);
- Engelund and Hansen (1967);
- Recking (2011);
- Lefort (2015).

To solve the Exner equation, a 1D finite volume discretization is adopted:

$$(A_z)_i^{n+1} = (A_z)_i^n - \frac{\Delta t}{\Delta x}\left((F^{Q_s})_{i+1/2}^n - (F^{Q_s})_{i-1/2}^n\right) \qquad (2)$$

with $(F^{Q_s})_{i+1/2}^n$ numerical flux evaluated at $x_{i+1/2}$ interface, Δt a timestep and Δx a space step ($X_i^n = X(n\Delta t, i\Delta x)$). Three different schemes were tested to solve numerical fluxes:

- a Roe scheme [6] (abandoned),
- a staggered scheme [7], [8] (named stag scheme in the following),
- an uncentered scheme, upwind or downwind according to the flow regime before and after the cells interface (critical and/or subcritical) [9], [10].

The third scheme was identified during the development as the most stable and robust.

In addition to the implementation of bedload formulas and numerical schemes to solve the Exner equation, a new method has been developed to optimize the update of the bottom elevation. Initially, the MASCARET subroutines calculating 1D geometric quantities from real geometry (1D profiles) were used to update the bottom from COURLIS

calculations ("to planimeter" refers to these calculations in the following). However, these routines slowed dramatically the simulations.

First, a threshold condition has been defined. The bottom is modified only when sediment erosion or sediment deposition were higher than a percentage of the water depth defined in the code. Before this modification, the "planimeter criterion" was a fixed value equal to 10^{-5} m.

Secondly, a new method to calculate deposition was implemented. Initially, deposition was done according to water depth. This definition is coming from COURLIS suspension, it allows to take into account a constant deposition on each node of the cross-section under the water level (named "delta constant planimeter method" in the following). It is not adapted to bedload sediment transport and so, constant elevation deposition was implemented (named "level constant planimeter method"). This method is *a priori* more suitable for bedload sediment transport and it is also more efficient. It allows to calculate the bed evolution easily and the1D quantities required by MASCARET like wetted areas.

Tests were also performed using either supercritical or subcritical kernels for the hydraulic solver.

IV. VALIDATION TEST CASES

A set of three experiments was selected to test the new developments.

A. *Dam Break Experiment*

The experiment of B. Spinewine and Y. Zech [11] reproduces a series of small-scale laboratory experiments of dam-break waves propagating over loose granular beds, established in a dedicated flume equipped with a fast downward-moving gate.

The sediment bed saturated with water is made of PVC, the grains are lighter than gravel or sand, in order to accentuate the geomorphological action of the dam break on the laboratory scale. To reproduce a dam, a 6 mm thick gate is placed in the center of the flume and retains a volume of water with a depth of 35 cm. When the gate is suddenly removed, a dam-break wave is formed and causes a strong sediment transport.

This test case allows us to verify the robustness of the numerical schemes. Therefore, the aim is not to reproduce the erosion rate because the bedload formula underestimates erosion (maybe because a part of sediment is transported by suspension). Furthermore, the evolution of the bed is very quick: the reference time for comparing the results to the observations is 1.4 second.

TABLE 1. DAM BREAK EXPERIMENTAL PARAMETERS

Length **width** **slope**	Lo=6 m L=0.25 m S=0
Upstream flowrate **Level upstream the dam** **Level downstream the dam**	Q=0 $m^3.s^{-1}$ h=0.35 m h=0 m
Sediment layer concentration **Mean diameter** **Sediment density**	C=1650 $kg.m^{-3}$ D_{50}=0.32 mm s=1.58 $g.cm^{-3}$

The result shows that the uncentered scheme is stable on this case while the stag scheme is not stable (see Fig. 2). This instability eliminated the stag scheme, and so the results for this scheme are not presented in the following test cases.

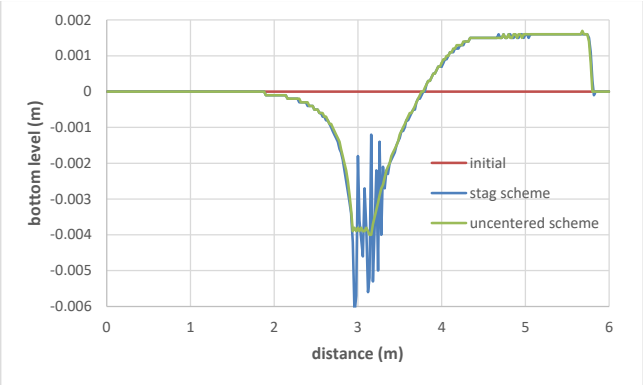

Figure 2. *Bottom evolution due to the dam break after 1.4s*

B. *Soni Experiment*

The aim of this experiment, carried out by J.P. Soni in 1980, is to study aggradation of sediment. The sediment supply is increased above the equilibrium sediment transport capacity of the flume [12], [13]. The evolution of the deposit is monitored during the experiment at 30, 60 and 90 min.

TABLE 2. SONI EXPERIMENTAL PARAMETERS

Length **width** **slope**	Lo=30 m L=0.2 m S=0.0051
Flow rate **water level** **velocity**	Q=0.0071 $m^3.s^{-1}$ h=0.072 m V=0.49 $m.s^{-1}$
Mean diameter **Grain size range** **Sediment density** **Upstream concentration**	D_{50}=0.32 mm σ=1.30 s=2.65 $g.cm^{-3}$ C_s=4.88 $kg.m^{-3}$

Results are presented in Fig. 3 for the uncentered scheme and the Meyer-Peter and Müller formula. The comparison shows a fairly good agreement with the 3 measurements (30, 60 and 90 min).

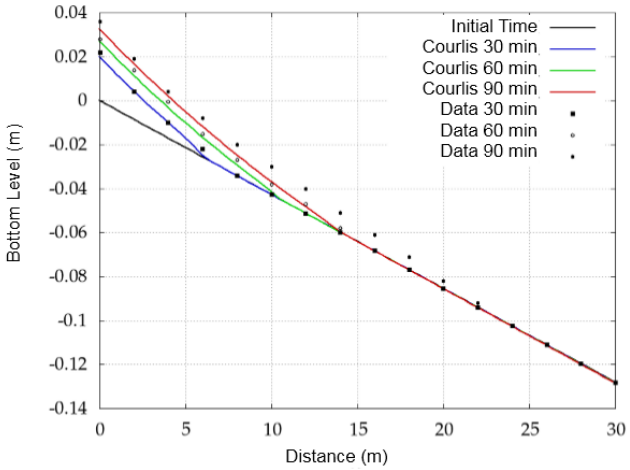

Figure 3. *Bottom evolution of the Soni experiment: measurement and calculations*

Tab. 3 summarize the calculation times. The uncentered scheme drastically reduces the calculation time. The subcritical kernel and the planimeter criterion reduce also this time. The new planimeter method does not increase performance in this case.

TABLE 3. SONI EXPERIMENT EXECUTION TIME

Scheme	***old vers.***	***ROE***	***Stag***	***Uncentred***			
Planim. Crit.	***10^{-5} m***				***5% of water level***		
Numérical scheme	***supercritical***						***subcritical***
Planim. method	***delta const.***					***level const.***	
Execution time	1h 43min	31min 22s	11s	39s	11	11s	1.4s

C. *Newton Experiment*

A degradation is often observed downstream of dams due to the interruption of sediment flow from upstream. The aim of the experiment, carried out by T. Newton in 1951 [14], is to study the erosion process in a flume in order to better understand this phenomenon. The evolution of the bottom of the flume following the interruption of the sediment supply is observed during 24 hours.

TABLE 4. NEWTON EXPERIMENTAL PARAMETERS

Length **width** **slope**	Lo=9.14 m L=0.3048 m S=0.00416
Flow rate **water level** **velocity**	Q=0.00566 m3.s-1 h=0.041 m V=0.45 m.s-1
Mean diameter **Sediment density** **specific weight of sediment**	D50=0.68 mm s=2.65 g.cm-3 C=1610 kg.m-3

Results are given on Fig. 3 for the uncentered scheme and the Meyer-Peter and Müller formula. The comparison show a fairly good agreement with the 3 measurements (1, 4 and 24h).

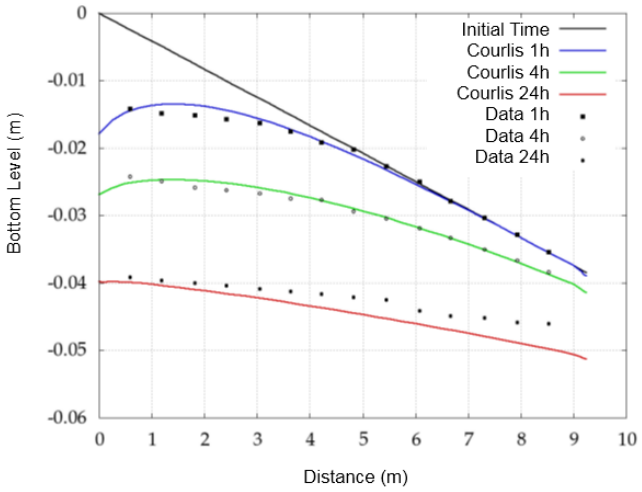

Figure 4. *Bottom evolution during the Newton experiment: measurement and calculations*

Tab. 5 gives calculation times. The conclusion are the same as for the Soni case except for the planimeter criterion that does not increase performance here.

TABLE 5: NEWTON EXECUTION TIME

Scheme	***old vers.***	***ROE***	***Stag***	***Uncentred***			
Planim. Crit.	***10^{-5} m***				***5% of water level***		
Numérical scheme	***supercritical***						***subcritical***
Planim. method	***delta const.***					***level const.***	
Execution time	1h 20min	1h 28min	4min 30s	4min 47s	4min 35s	4min 19s	30s

V. REAL RESERVOIR TEST CASE

This test case is based on an EDF reservoir. The study area is 3.9 km long (1.8 km of reservoir and 2.1 km upstream the reservoir). The objective is to simulate the bed evolution from the end of the year 2002 to the beginning of 2014. This period includes flushing events. Consequently, in different zones of the model, the bed alternates between periods of deposition and erosion of sediments generated by high flows (for this first step of calibration, flowrates below 20m^3/s are excluded). The river bed presents strong discontinuities (significant increase of the slope, variation of width). These discontinuities are a real challenge and the main difficulty of this test case in terms of modelling.

It is a well-documented reservoir with many campaigns of topographic and bathymetric surveys. The first step of the study addresses the robustness and the calculation time. This first step is presented hereafter. The second step, calibration and comparison with the measurement results will be carried out in the future.

Two meshes are used (fine and coarse), the geometric and physical parameters of the model are presented in Tab. 6.

TABLE 6. REAL TEST CASE PARAMETERS

Length **Width** **Slope**	Lo=3900 m around 150 m S=0.00416
Flow rate	0.8 < Q < 754 $m^3.s^{-1}$
Sediment diameter **Sediment density** **Sediment layer concentration**	D50=2.5 10^{-2} m s=2.65 $g.cm^{-3}$ C=2000 kg.m-3
Number of cross-sections	196 (fine mesh) 48 (large mesh)

Results are presented in Fig. 5 (the lowest point of the cross-section is plot). There are few differences between the two meshes (less than 10 cm).

The difference between the two planimeter methods is normal. The level constant method tends to suppress the trenches in the cross-section.

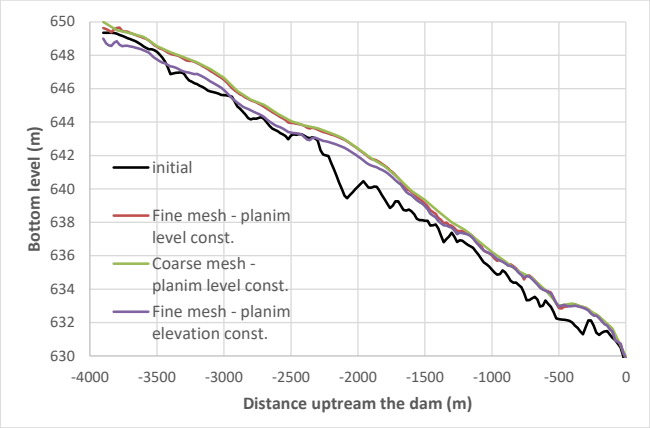

Figure 5. *Bottom evolution of the Real test case calculation*

Calculation times are given in the Tab. 7. The planimeter method does not decrease the calculation time. Important parameters are the mesh and the planimeter criterion. Improvement are still possible with the use of the subcritical scheme (unstable here with the old version of MASCARET currently being used in COURLIS).

TABLE 7. REAL TEST CASE EXECUTION TIME

Mesh	***Fine***			***Large***
Scheme	***Uncentred***			
Planim. Crit.	***10^{-5} m***	***5% of water level***		
Numérical scheme	***supercritical***			
Planim. method	***delta const.***	***delta const.***	***level const.***	***level const***
Execution time	> 100 day	17h 41min 54s	17h 15min 15s	2h 28 min 27s

The calculation times obtained with HEC-RAS and MIKE are respectively 30 min and 3h 15min (simulation of the whole duration with the flow rate under 20m^3/s). The calculation time obtained with CAVALCADE (Artelia software) is 1h 30 min (simulation with the hydrograph excluding flow under 20m^3/s).

VI. PERSPECTIVE

A. *Real test case calibration*

A calibration of the real test case reservoir will be carried out in 2018. COURLIS bedload version will be tested also on other test cases.

B. *Developments*

A post-doctoral work will start in 2018. The main objectives of this post-doctoral work will be to further develop the software by integrating new physical processes such as.

- Integration of several transport formulas,
- Integration of an extended granulometry model,
- Management of the transition from a rocky bottom to an alluvial bottom (adaptation of the friction law)

C. *TELEMAC-MASCARET trunk integration*

COURLIS should be integrated in the trunk in 2018 (possibly, with the suspension version). Some adaptations of the code have to be done because a lot of developments are still “hardcoded”.

Besides, MASCARET version currently used is an old one. Integration with the trunk version of MASCARET will allow us to have the last version of MASCARET coupled with COURLIS. Better stability and efficiency are expected with this update.

VII. CONCLUSION

Laboratory test cases (dam-break, Soni and Newton experiments) show that COURLIS (in its new bedload version) is giving results in a fairly good agreement with measurements. Moreover, several numerical schemes have been tested and the uncentered scheme showed good properties (stability, robustness, efficiency, etc.). Some developments have been done to reduce calculation times.

A real test case shows that developments carried out on the bedload version of COURLIS allow the software to simulate long term evolution of gravel bed rivers. This work will continue in 2018 to integrate COURLIS in the TELEMAC MASCARET open source system.

REFERENCES

[1] Bertier, C., Bouchard, J.-P. & Dumond, L. (2002) - One dimensional model for reservoir sedimentation management. Proc. River Flow 2002

[2] Valette E., Jodeau M., How to predict the sedimentological impacts of reservoir operations? Proc. ISCE-6 2012 unspublished

[3] Valette E., Villaret C., Tassi P., Jodeau M., Villaret C., St Egrève reservoir – Multi-dimensional modelling of flushing and evolution of the channel bed. Proc User Club TELEMAC-MASCARET 2013 unpublished

[4] Antoine G., Besnier A.-L., Jodeau M., Camenen B., Esteves M., Numerical modeling of suspended sediment transport during dam flushing : From reservoir dynamic to downstream propagation. Proc. River Flow 2014, published in Reservoir Sedimentation (crc Press) p175-184

[5] Valette E., Tassi P., Jodeau M., Villaret C., St-Egrève reservoir – Modelling of flushing and evolution of the channel bed. Proc. River Flow 2014, published in Reservoir Sedimentation (crc Press) p185-184

[6] C. Juez, J. Murillo, and P. Garcia-Navarro. A 2D weakly-coupled and efficient numerical model for transient shallow flow and movable bed. Adv. Water Resour., 71 :93–109, 2014

[7] P. H. Gunawan, R. Eymard, and S. R. Pudjaprasetya. Staggered scheme for the exner–shallow water equations. Computat. Geosci., 19(6) :1197–1206, 2015

[8] E. Audusse, S. Boyaval, N. Goutal, M. Jodeau, and P. Ung. Numerical simulation of the dynamics of sedimentaryriver beds with a stochastic exner equation. ESAIM : Proc., 48 :321–340, 2015

[9] S. Cordier, M. H. Le, and T. Morales de Luna. Bedload transport in shallow water models: Why splitting (may) fail, how hyperbolicity (can) help. Adv. Water Resour., 34 :980–989, 2011.

[10] P. Ung. Simulation numérique du transport sédimentaire : aspects déterministes et stochastiques. PhD thesis, Unversité d'Orléans, 2016

[11] B. Spinewine and Y. Zech. Small-scale laboratory dam-break waves on movable beds. Journal of Hydraulic Research, 45, 2007. pp. 73-86

[12] Soni J. P, (1981). Laboratory study of aggradation in alluvial channels. Journal of Hydrology, 49(1), 87-106.

[13] Soni J. P, (1981). Unsteady sediment transport law and prediction of aggradation parameters. Water Resources Research, 17(1), 33-40.

[14] Newton C.T, (1951). An experimental investigation of bed degradation in an open channel. Technical report, Boston Society of Civil Engineers, pp 28-60.

Performance Optimization for TELEMAC-MASCARET using GPU accelerators

Yoann Audoin[1], Hamza Belaoura[1], Frank Hulsemann[2]
[1] EDF R&D, National Hydraulics and Environment Laboratory (LNHE), 6 quai Watier, 78401 Chatou, France
[2] EDF R&D, Lab ParisSaclay,7 boulevard Gaspard Monge, 91120 Palaiseau, France
hamza.belaoura@edf.fr

Abstract: With the ever increasing size of numerical simulations, a major challenge for the HPC community is to take advantage of current hybrid architectures. The use of GPU computing appears most of the time as an efficient way to accelerate execution time and to obtain scalable applications.

One main difficulty of this type of computing is that it might be necessary to rewrite significant parts of the codes and sometimes to change the algorithm itself. However, the use of external HPC libraries offers the possibility to avoid redesigning all the code. MAGMA is a linear algebra library providing support for accelerators such as NVIDIA GPUs, Intel Xeon Phi (MIC), or any system that can work with OpenCL. Despite being originally focused on dense linear algebra problems, it also contains solvers, preconditioners and eigensolvers for sparse linear systems.

In the case of TELEMAC-2D, the code is based on finite element/finite volume method and a mesh of triangular elements to solve the SaintVenant equations. It deals mostly with sparse matrices and uses Krylov methods such as GMRES or the Conjugate Gradient to solve the large sparse linear systems resulting from the discretization.

In this study, we present preliminary results for the use of MAGMA in the case of the Malpasset simulation with different mesh sizes. We also describe the different steps and some issues encountered as well as the profiling results for the CPU and the GPU versions of the code.

An experiment of adaptive mesh in hydraulics

Thierry Fouquet[1], Matthieu Secher[2], Gerald Nicolas[1]
[1] EDF R&D
[2] EDF CIH
Thierry.Fouquet@edf.fr

Abstract: For a few years EDF has been working on the introduction of telemac in the simulation platform Salome, to produce Salome-Hydro. This platform has got many tools: geometry, mesh, post-processing, data assimilation and visualisation. In this paper we focus on one of those tools, Homard. This module allows to use mesh refinement automatically in a simulation to ensure the quality of the result without making too much calculation. Some technics are based on making a new mesh at each adaptation, some on mesh distortion. Homard uses a technics called h-refinement: i.e. the refinement is made by cutting the triangle. There are many strategies of mesh refinement, depending on the simulation one wants to do. For example, the strategy will be different in a steady case or in a transient case. One can also wish to reach a given error or might simply want to quickly have a mesh corresponding to his study. In general, a theoretical error indicator is better, but since Telemac does not have any indicator error, one can ask Homard to use the variation of field as a basis to the refinement. To set the parameters of refinement in Salome-hydro the user can do mesh refinement following different methods, manually refinement through the gui, use a coupling tool between Telemac and Tomard, or use some python tool to automatically refine.

We chose to present some uses of adaptive mesh in Salome-Hydro through a real test case, so that user can see how to use different strategies and different tools. This first example of a real study on a dam flushing shows how to better take into account the bathymetry, how to ensure the quality of the solution and how to follow the limit of the domain.

Interoperability applications of TELEMAC-MASCARET System

Y. Audouin[1], C. Goeury[1], F. Zaoui[1], R. Ata[1], S. El Idrissi Essebtey[1], A. Torossian[1], D. Rouge[1]
[1]EDF R&D National Laboratory for Hydraulics and Environment (LNHE)
6 quai Watier, 78401 Chatou, France
Email: yoann.audouin@edf.fr

Abstract*— This paper is focused on the application of the recently implemented TelApy module (www.opentelemac.org). TelApy aims to provide a python wrapper of TELEMAC API (Application Program Interface). The goal of TelApy is to have a full control on the simulation while running a case. For example, it must allow the user to stop the simulation at any time step, get values of some variables and change them. In order to make this possible, a Fortran structure called instantiation was developed with the API. It contains a list of strings pointing to TELEMAC variables. This gives direct access to the physical memory of variables, and allows therefore to get and set their values. Furthermore, changes have been made in TELEMAC main subroutines to make hydraulic cases execution possible time step by time step. It is useful to drive the TELEMAC-MASCARET SYSTEM APIs using Python programming language. In fact, Python is a portable, dynamic, extensible, free language, which allows (without imposing) a modular approach and object oriented programming. In addition of benefits of this programming language, Python offers a large amounts of interoperable libraries. The link between various interoperable libraries with TELEMAC-MASCARET SYSTEM APIs allows the creation of an ever more efficient computing chain able to more finely respond to various complex problems. Therefore, the TelApy module has the ambition to enable a new way of use for the TELEMAC-MASCARET system. In particular one can think about high performance computing for the calculation of uncertainties, optimization, code coupling and so on. The objectives of the paper are to present some examples of the TelApy module in the case of Uncertainty Quantification, Optimization, Reduced Order Model and Monitoring System.

I. INTRODUCTION

This paper will give a short explanation of the new Python module TelApy which is used to control the APIs of TELEMAC-MASCARET SYSTEM. The TELEMAC-MASCARET SYSTEM APIs are developed in Fortran. However, it is relatively easy to use these Fortran routines directly in Python using the "f2py" tool of the python Scipy library [7]. This tool will make it possible to compile Fortran code such as it is accessible and usable in Python. This compilation step is directly integrated into the compilation of the TELEMAC-MASCARET SYSTEM and is thus transparent to the user. Moreover, in order to make the TelApy module more user friendly, a python wrapper has been developed to encapsulate and simplify the different API Python calls. This set of transformation constitutes the TelApy module.

The first section of this paper is dedicated to a short description of how the APIs and TelApy are working, then four applications of that module are described.

II. TELAPY PACKAGE

A. *Fortran APIs*

An API (Application Programming Interface) is a library allowing to control the execution of a program. Here is part of the definition from Wikipedia:

"In computer programming, an application programming interface (API) specifies a software component in terms of its operations, their inputs and outputs and underlying types. Its main purpose is to define a set of functionalities that are independent of their respective implementation, allowing both definition and implementation to vary without compromising each other.

In addition to accessing databases or computer hardware, such as hard disk drives or video cards, an API can be used to ease the work of programming graphical user interface components, to allow integration of new features into existing applications (a so-called "plug-in API"), or to share data between otherwise distinct applications. In practice, many times an API comes in the form of a library that includes specifications for routines, data structures, object classes, and variables."

The API's main goal is to have control on a simulation while running a case. For example, it must allow the user to stop the simulation at any time step, retrieve some variables values and change them. In order to make this possible, a Fortran structure called instance was developed in the API. This structure is described later on. The instance structure gives direct access to the physical memory of variables, and allows therefore the variable control. Furthermore, modifications have been made in TELEMAC-MASCARET SYSTEM main subroutines to make hydraulic cases execution possible time step by time step. All Fortran routines are available in the directory "api" of TELEMAC-MASCARET SYSTEM sources.

In the rest of the paper we will make reference to the TELEMAC-2D part of the API but it is also available for other modules (so far for SISYPHE and soon TELEMAC-3D)

An instance is a Fortran structure that gathers all the variables alterable by the API. The definition of the

"instance" structure is made in a Fortran module dedicated to this purpose and is composed of:

- An indice defining the instance I.D.
- A string which can contain error messages.
- Some pointers to the concerned module variables. This is what makes it possible to manipulate the variables of the module by having a direct access to their memory location.

In addition to the instance definition, the module includes all routines needed to manipulate it (creation, deletion, and so on).

The way the instance is defined (pointers) allows manipulation of variables during the simulation. So, to get information on the variables the following set of functionalities has been implemented:

- get the list of variables reachable with the API.
- get the information on the variable :
    - type of a variable (integer, Boolean, real, string).
    - Access (read-only, read-write).
    - Number of dimensions.
    - …
- get the size of a variable for each of its dimensions.
- get/set the value of a variable for a given index.

The list of variables that can be accessed is given in Table 1. Not every variable within TELEMAC-2D is there. However adding a new variable is pretty easy, the 5 steps procedure is described in the TelApy user documentation [1].

MODEL.AT: Current time
MODEL.BCFILE: Boundary condition file name
MODEL.BND_TIDE: Option for tidal boundary conditions
MODEL.BOTTOMELEVATION: Level of the bottom
MODEL.CHESTR: Strikler on point
MODEL.FAIR: Fair on point
MODEL.COTE: Prescribed elevation value
MODEL.CPL_PERIOD: Coupling period with sisyphe
MODEL.DEBIT: Discharge on frontier
MODEL.DEBUG: Activating debug mode
MODEL.FLUX_BOUNDARIES: Flux at boundaries
MODEL.GEOMETRYFILE: Name of the geomery file
MODEL.METEOFILE: Name of the binary atmospheric file
MODEL.FO2FILE: Name of the formatted data file 2
MODEL.LIQBCFILE: Name of the liquid boundaries file
MODEL.GRAPH_PERIOD: Graphical output period
MODEL.HBOR: Boundary value on h for each boundary point
MODEL.IKLE: Connectivity table between element and nodes
MODEL.INCWATERDEPTH: Increase in the the depth of the water
MODEL.KP1BOR: Points following and preceding a boundary point
MODEL.LIHBOR: Boundary type on h for each boundary point
MODEL.LISTIN_PERIOD: Listing output period
MODEL.LIUBOR: Boundary type on u for each boundary point
MODEL.LIVBOR: Boundary type on v for each boundary point
MODEL.LT: Current time step
MODEL.COMPLEO: Graphic output counter
MODEL.NBOR: Global number of boundary points
MODEL.NELEM: Number of element in the mesh
MODEL.NELMAX: Maximum number of elements envisaged
MODEL.NPOIN: Number of point in the mesh
MODEL.NPTFR: Number of boundary points
MODEL.NTIMESTEPS: Number of time steps
MODEL.NUMLIQ: Liquid boundary numbers
MODEL.POROSITY: Porosity
MODEL.RESULTFILE: Name of the result file
MODEL.SEALEVEL: Coefficient to calibrate sea level
MODEL.TIDALRANGE: Coefficient to calibrate tidal range
MODEL.UBOR: Boundary value on u for each boundary point
MODEL.VBOR: Boundary value on v for each boundary point
MODEL.VELOCITYU: Velocity on u
MODEL.VELOCITYV: Velocity on v
MODEL.WATERDEPTH: Depth of the water
MODEL.X: X coordinates for each point of the mesh
MODEL.XNEBOR: Normal X to 1d boundary points
MODEL.Y: Y coordinates for each point of the mesh
MODEL.YNEBOR: Normal Y to 1d boundary points
MODEL.EQUATION: Name of the equation used

TABLE 1. ACCESSIBLE VARIABLES THROUGH THE API.

The computation control is carried out using some specific routines to launch the simulation. These actions constitute a decomposition of the main function of each TELEMAC-MASCARET modules considered corresponding to the following different computation steps:

- **Configuration setup.** This function initialises the instance and the output. The instance, characterised by the *ID* integer parameter, represents a run of TELEMAC-2D.
- **Reading the steering file.** This function reads the case file and set the variables of the TELEMAC-2D steering file accordingly.
- **Memory allocation.** This function runs the allocation of all the data needed in TELEMAC-2D. Any modifications to quantities of TELEMAC-2D should be done before the call to that function.
- **Initialization.** This function will do the setting of the initial conditions of TELEMAC-2D. It corresponds to the time-step 0 of a TELEMAC-2D run.
- Computation function that runs **one time-step** of TELEMAC -2D. To compute all time steps, a loop on this function must be done.
- **Finalization.** This function concludes the run of TELEMAC -2D and will delete the instance. To start a new execution of TELEMAC-2D the configuration step must be run again.

For each action defined above, the identity number of the instance is used as an input argument allowing all computation variables to be linked with the corresponding instance pointers. These actions must be done in that particular order to insure a proper execution of the computation in the API main program.

The API being entirely in Fortran the preparation for a parallel run that is done by the Python script in a standard TELEMAC-2D run is not done. The partitioning and merging can be done using the API with the “partel” and

"gretel" functions but the copying of files must be done elsewhere.

Fig. 1 presents the test case "gouttedo" written with the Fortran API.

```
PROGRAM HOMERE_API
  USE API_INTERFACE
  INTEGER :: ID, LU, LNG, COMM, IERR, VAR_SIZE, I
  INTEGER :: NTIME_STEPS
  CHARACTER(LEN=144) :: CAS_FILE = 't2d_gouttedo.cas'
  CHARACTER(LEN=144) :: DICO_FILE = 'telemac2d.dico'
  CHARACTER(LEN=144) :: DICO_FILE = 'r2d_test.slf'
  …
  CALL RUN_SET_CONFIG_T2D(ID,LU,LNG,COMM,IERR)
  CALL RUN_READ_CASE_T2D(ID,CAS_FILE,&
  DICO_FILE,IERR)
  ! Changing the name of the result file
  VARNAME = 'MODEL.RESULTFILE'
  CALL GET_VAR_SIZE_T2D(ID,VARNAME,VAR_SIZE,&
                        IDUM,IDUM,IERR)
  CALL SET_STRING_T2D(ID,VARNAME,RES_FILE,&
                      VAR_SIZE,0,0,IERR)
  CALL RUN_ALLOCATION_T2D(ID,IERR)
  CALL RUN_INIT_T2D(ID,IERR)
  !Get the number of timesteps
  VARNAME = 'MODEL.NTIMESTEPS'
  CALL GET_INTEGER_T2D(ID, VARNAME, &
                       NTIME_STEPS,&
                       0, 0, 0, IERR)
  DO I=1,NTIME_STEPS
     CALL RUN_TIMESTEP_T2D(ID,IERR)
  ENDDO
  CALL RUN_FINALIZE_T2D(ID,IERR)
END PROGRAM
```

Figure 1. *Example of a simple run of the gouttedo test case in Fortran*

B. *Python package*

It is relatively easy to use the Fortran API routines directly in Python using the "f2py" tool of the python Scipy library. This tool will make it possible to compile Fortran code such as it is accessible and usable in Python. For more details on this tool, the interested reader can refer directly to [7]. However, based on the advantage of the python language, it is possible to implement a wrapper in order to provide user friendly function of the Fortran API. Thus, a python overlay was developed in order to encapsulate and simplify the different API Python calls. The different python functions written to simplify the use of API are available in the directory "TelApy" withing the TELEMAC-MASCARET scripts folder. A doxygen documentation is available and allows the user to visualize python classes, functions that can be used as well as its input and output variables and so on.

The package follows the structure below:

- api
  - api_module: The generic python class for TELEMAC-MASCARET SYSTEM APIs.
  - generate_study: Automatic generator of a template for a run using the API.
  - hermes: Input and Output library allowing to write and read different mesh formats. Wrapper on the Fortran module.
  - sis: The SISYPHE python class for APIs.
  - t2d: The TELEMAC-2D python class for APIs.
- tools
  - genop: Optimization tool based on genetic algorithms.
  - newop: Optimization tool based on the SciPy minimizer function.
  - polygon: Function allowing to give point indices which are in a polygon defined by the user.

Fig. 2 displays all accessible classes of TelApy package.

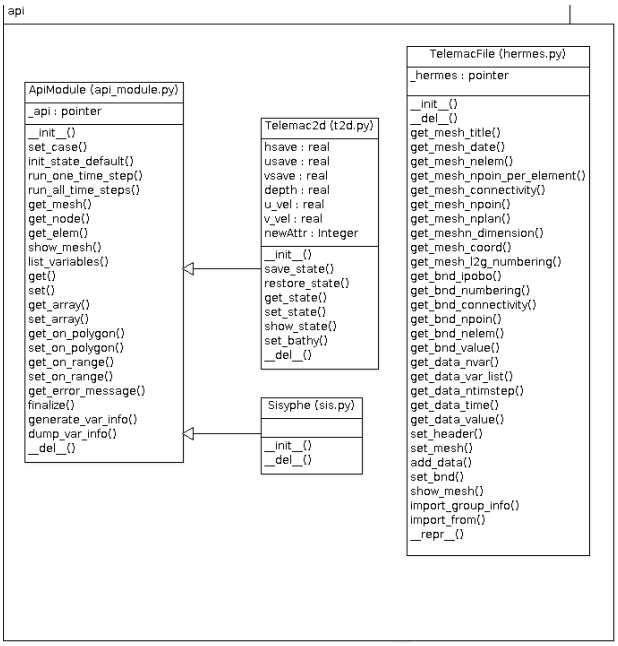

Figure 2. *Unified Modelling Language (ULM) of the classes in TelApy*

Fig. 3 presents the python scripting of the previous presented test case "gouttedo".

```
#!/usr/bin/env python
# Class Telemac2d import
from TelApy.api.t2d import Telemac2d
import shutil
# Creation of the instance Telemac3d
t2d = Telemac2d("t2d_gouttedo.cas")
# Running partel
t2d.set_case()
# Initalization
t2d.set("MODEL.RESULTFILE","r2d_test.slf")
t2d.init_state_default()
# Run all time steps
t2d.run_all_time_steps()
# Running gretel
t2d.finalize()
# Instance delete
del(t2d)
```

Figure 3. *Example of a simple run of the "gouttedo" test case in Python*

III. APPLICATIONS

The section below will describe different type of application of the new module TelApy.

A. *Uncertainties Quantifications*

Here we will describe two works done using TelApy and the software OpenTurns[4] to run a MonteCarlo study.

TelApy was used to create what will be called the study function in the form:

$$Y = f(X) \qquad (1)$$

Where X is the list of the input uncertain variables and Y the interest variable. In this study, the interest variable is the water depth in all computational domain.

1) *Study area*

The area chosen for this study extends over a reach of the Garonne river measuring about 50 km, between Tonneins (upstream), downstream of the confluence with the Lot river, and La Réole (downstream) (see Fig. 4).

Figure 4. *Study area of the Garonne*

This part of the valley was equipped in the 19th century with infrastructure to protect against floods of the Garonne river which had heavily impacted local residents. A system of longitudinal dykes and weirs was progressively built after that flood event to protect the floodplains, organize submersion and flood retention areas. This configuration is also similar to the characteristic of other managed rivers such as the Rhone and the Loire.

2) *The hydraulic model*

The TELEMAC-2D model, constituted by a triangular mesh of some 41,000 nodes with an extremely small mesh size around the dykes, has a constant discharge upstream imposed at Tonneins and downstream, a stage-discharge relationship corresponding to the stream gauge at La Réole. This model has been realized by Besnard and Goutal (2008) [1].

In this study, we investigate the effect of two uncertainty sources on water level calculation for extreme flood event, the roughness coefficient and the upstream discharge. In fact, the hydraulic roughness is uncertain because flow measures are not available or reliable for calibration and validation. Discharge is also uncertain because it results from extrapolation of discharge frequency curves at very low exceeding probabilities. Five different zones were defined for the roughness and two discharges. The figures below show the probability density functions that will be applied for the study.

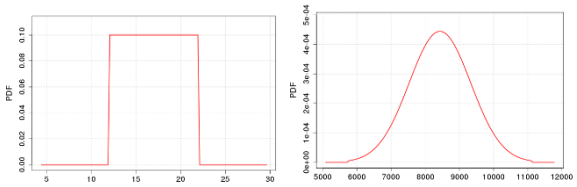

Figure 5. *Probability density function of the Strickler coefficient in the floodplain (left) and the upstream discharge*

3) *Results*

To handle the uncertainty with the Monte Carlo technique, it is important to run a lot of simulations in order to have reliable results. In this work, around 70,000 Monte Carlo computations have been carried out. EDF's cluster has been used to run these simulations. MPI library was used for launching and managing the uncertainty quantification study. Post-processing of the huge amount of results files is tackled through some Python scripts specifically developed within OpenTURNS.

The obtained results are analyzed twofold: On one hand, the effect of variability of random inputs is assessed at some specific points (assumed to be around an industrial plant, for example). On the other hand, a global statistical analysis all over the domain is done, as shown in Fig. 6.

A spatial distribution of the mean water depth and its variance is obtained. These results are of utmost importance for dimensioning of protecting dykes. Furthermore, there are very useful when establishing scenarios for flood managing.

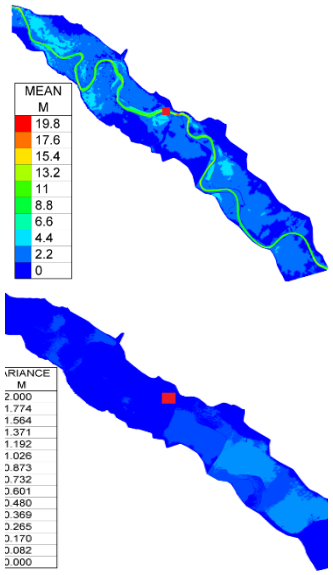

Figure 6. *Mean and variance all other the domain (■ node 37 242)*

To be sure that the obtained results are reliable, it is important to verify the convergence of them, especially by plotting the graph of the dispersion coefficient (σ/μ) as a

function of N: if the convergence is not visible, it is necessary to increase N or if needed to choose another propagation method to estimate the uncertainty [8].

Fig. 7 shows the convergence of the dispersion coefficient and the mean of the water depth at the node number 37 242 located on Fig. 6.

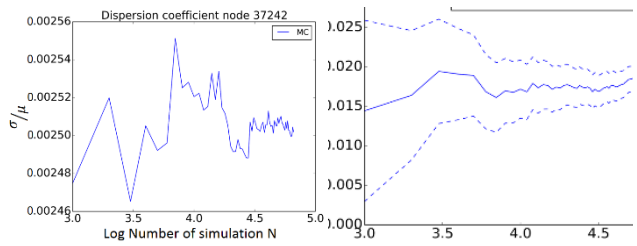

Figure 7. *Convergence graphs of the dispersion coefficient and the mean according to the logarithm of the number of simulations*

These graphics show that the convergence of results are guaranteed from 30,000 simulations of Monte Carlo Technique. These results are then used to provide reference statistical estimators in the comparison of the efficiency of the Monte Carlo-like methods.

For a more detailed explanation of the study you can read the article written by C. Goeury, et *al* [5].

B. *Automatic Calibration*

Two sensitive tidal parameters concerning the inflow conditions of a maritime case are optimized to better model the sea behaviour. The case is the Alderney race as described in [6].

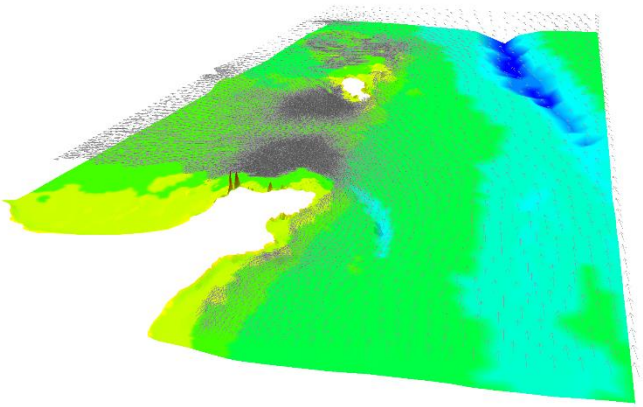

Figure 8. *Bottom and a velocity field in the strait between the Alderney Channel Island and Cap de La Hague*

The problem is mathematically formulated as given by (2). Here the boundaries are [-50, 50] for both parameters.

$$\min_{x\in\mathbb{R}^2} f(x) \quad s.t.\ \underline{x} \le x \le \overline{x} \tag{2}$$

Where x-components are tidal parameters and stand for the difference between the Telemac results and measurements:

$$f(x) = \|y(x)\|_2 \quad y(x) = \left(T_1(x) - M_1, T_2(x) - M_2, \dots, T_p(x) - M_p\right) \tag{3}$$

With T the Telemac operator, M the measurement for the water level and velocity, and p the number of time steps.

(2) is numerically solved with the help of the TelApy tools newop and genop for comparison. An important difference between these tools is that one requires derivative values and the other is a derivative-free optimizer. For the actual version of newop, derivatives are estimated only by numerical differentiation. Computations for successive evaluations of $f(x)$ or $\nabla f(x)$ are done automatically in parallel mode using the Python module *multiprocessing*.

As an example, Fig. 9 shows how using the TelApy tools on (2) is straightforward. The convergence of genop is presented in the Fig. 10 for a maximum number of 20 iterations. At the end of the convergence, 3,500 calls to TELEMAC-2D have been necessary. This large number can be easily divided by two with a stopping criteria of 10 iterations. Moreover, using a surrogate model for faster simulations, computational costs could also be reduced.

```
from TelApy.tools import genop
from TelApy.tools import newop

def genop_telemac():
    # the Python function computing the cost function f(x)
    my_function = alderney
    # the number of variables and bounds
    nvar = 2
    vbounds = np.zeros((nvar, 2))
    for i in xrange(nvar):
        vbounds[i, 0] = -50.
        vbounds[i, 1] = 50.
    # instantiate a genop problem
    mypb = genop.Genop()
    # change the verbosity mode
    mypb.verbose = True
    # initialize the problem
    error = mypb.initialize(my_function, nvar, vbounds)
    # do the optimization in parallel run mode
    fopt, xopt = mypb.optimize(nproc=24)
    # return all best found values for f and x
    return fopt, xopt

def newop_telemac():
    # the Python function computing the cost function f(x)
    my_function = alderney
    # the number of variables and bounds
    nvar = 2
    vbounds = np.zeros((nvar, 2))
    for i in xrange(nvar):
        vbounds[i, 0] = -50.
        vbounds[i, 1] = 50.
    # instantiate a newop problem
    mypb = newop.Newop()
    # change the verbosity mode
    mypb.verbose = True
    # the steps of FD (numerical derivatives)
    vdx = np.array([1.e-4, 1.e-4])
    # initialize the problem
    error = mypb.initialize(my_function, nvar, vbounds, vdx)
    # do the optimization in parallel run mode
    fopt, xopt = mypb.optimize(x0, 50, nproc=3)
    # return optimal values for f and x
    return fopt, xopt
```

Figure 9. *Example of an automatic calibration using TelApy on the Alderney TELEMAC-2D case*

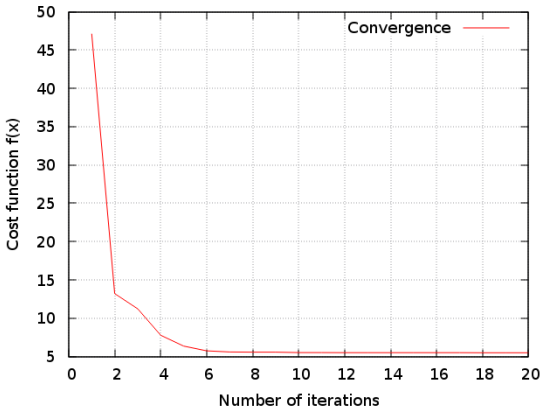

Figure 10. *Convergence of genop.*

C. *Surrogate model*

Many problems in the sciences and engineering require the determination of an unknown field from a finite set of indirect measurements. Examples include hydrology, oceanography, weather forecasts and hydraulic. In fact, numerical models are nowadays commonly used in fluvial and maritime hydraulics as prevention tools for example. Parameter estimation, also called inverse problem, consists of retrieving data of a problem from its solution. For free surface flow hydraulics, it involves assessing hidden or difficult-to-access parameters, such as bathymetry, bed friction, inflow discharge, tidal parameter, initial state and so on. In this work, an optimization process has been carried out to find initial state of a TELEMAC-2D computation. The fidelity of the optimized initial state is investigated with numerically generated synthetic data from so-called "identical-twin-experiments", in which true state is known. Thus, the test case "gouttedo" is studied in this work. This TELEMAC-2D model simulates the circular spreading of a wave. The domain is square with a size of 20.1 m x 20.1 m with a flat bottom. It is meshed with 8,978 triangular elements and 4,624 nodes. Triangles are obtained by dividing rectangular elements on their diagonals. The mean size of obtained triangles is about 0.3 m. The boundary conditions of the model are considered as solid walls with perfect slip conditions. The observation data used to retrieve the initial state are water depth synthetic data generated numerically. The water is initially at rest with a Gaussian free surface in the centre of a square domain such as the water depth is given by (4).

$$h_0^t(x) = 2.4e^{-\frac{[(x-10)^2+(y-10)^2]}{4}} \qquad (4)$$

So, the objective of this test case is to recover this initial state h_0^t constituent the true state using an optimization chain. The observations considered in this case are the water depth on all mesh nodes at different times in second $T = \{0.4; 0.8; \dots; 3.6; 4\}$. The initial guess of the initial state is set to a constant water depth of 2.4 m on each computational nodes. This inverse problem is solved computing variational data assimilation algorithm 3D-VAR. However, this algorithm consumes an important CPU time due to the large dimension of the system and the need for running it several times during the minimization of the cost function. Hence, we conclude the need to reduce the dimension of the initial model in order to alleviate the computational cost of the data assimilation process. The idea of order reduction is to search an optimal increment, not in the initial space of large dimension (dimension of nodes number), but in a space of reduced dimension. More precisely, we will look for an initial state $h_0(x)$ in the form given by (5).

$$h_0(x) = h_0^b(x) + \sum_{i=1}^{r} \alpha_i \Phi_i \qquad (5)$$

Where, $h_0^b(x)$ is a fixed reference state, and $(\Phi_1, \dots, \Phi_r)$ is the basis of the reduced space.
Then, the minimization process is done using the cost function $J\left(h_0(x)\right) = \tilde{J}(\alpha_1, \dots, \alpha_r)$.

Thus, the minimization takes place in a space of dimension r with $r \ll x$. The vector basis $(\Phi_1, \dots, \Phi_r)$ represents the modes of the system variability. The computation of this basis has been done in this work based on the classical Proper Orthogonal Decomposition method. By evaluating the energy captured by the proper vectors, only 7 modes are required to capture 99.9% of the total system variability. Thus, the truncation order of the approximation based of the proper orthogonal decomposition is fixed at $r = 7$. Generally, optimisation methods are used to solve minimisation problems. Many deterministic optimisation methods are known as gradient descent methods, among which the well-known BFGS quasi-Newton method, which is the approach used in this work. The inverse problem is solved in about 10 minimization iterations. Fig 8. displays the inverse problem results obtained when considering the minimization in the POD reduced space (green curve with circle markers) and in the initial space of large dimension (dimension of nodes number) (blue curve with square markers) over a slice along the axis x in the middle of the computational domain.

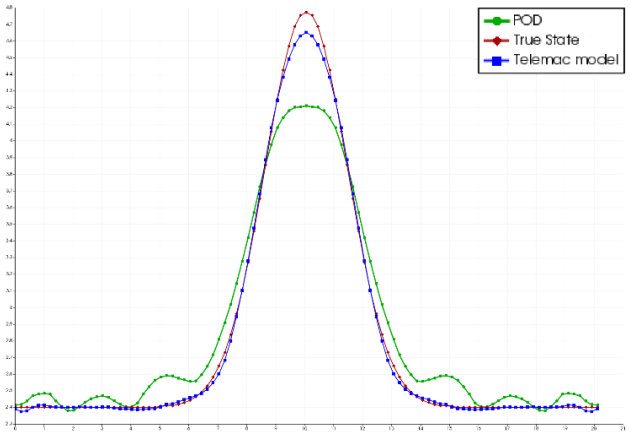

Figure 8. *Initial state results obtained by minimization process in the POD reduced space (green curve with circle markers) and in the initial space of large dimension (blue curve with square markers) over a slice along the x-axis in the middle of the computational domain. In comparison with the true state (red curve with diamonds)*

As shown in Fig. 8, the initial state obtained with the minimization in the initial space is close to the true state. Whereas the initial state obtained by solving the minimization in the reduced space presents more water depth oscillation, but the main behaviour is close to the true state. However, the computational cost is drastically reduced using the reduced space. In fact, the minimization process in the initial space takes about 5 days for 10 iterations. This is induced by the finite difference approximation of the observation operator adjoint. In the reduced space, this computational time is reduced to 17 minutes. This proves the efficiency of reduced order model when considering optimization in huge dimension problem.

D. Monitoring tool

The goal for that application was to create an autonomous software that will:

- Gather data to build the bathymetry of the model.
- Define the input parameters of the study.
- Run the TELEMAC-2D study.
- Display results informations.
- And a couple other functionalities such as automatic report generation, archives…

All these functionalities must be accessible through a user friendly GUI written in PyQt that could be used by someone not familiar with the TELEMAC-MASCARET system. The aim of this tool is to be able to control that the stream flows within the channels of the station are always fluvial. This taking into account the expected sedimentation and low water levels. If not, a dredging operation is required. So, the objective of this work is to provide a functional software able to analyse and forecast the water flow in order to anticipate the dredging operation. In order to evaluate this risk a simulation is ran to estimate the current number in the canal for the next months. Fig. 9 is an example of such a computation.

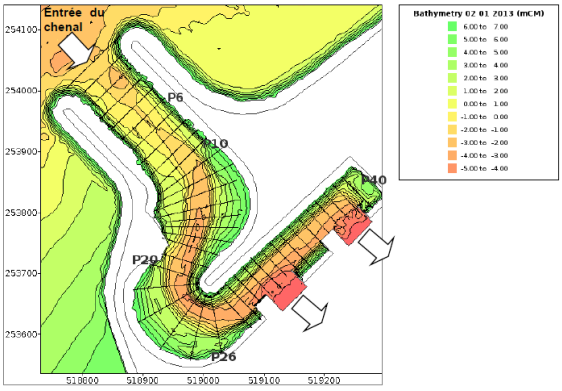

Figure 9. *Bathymetry estimation on the computational model*

TelApy is used here to have control on different computation parameters such as the date of the simulation, the sea level, the pump to take into account…

Fig. 10 displays a screenshot of the bathymetry built from the data available. Fig. 11 presents the GUI part where the study input parameters are defined. Finally, Fig. 12 displays simulation results of the Froude number on the computational model.

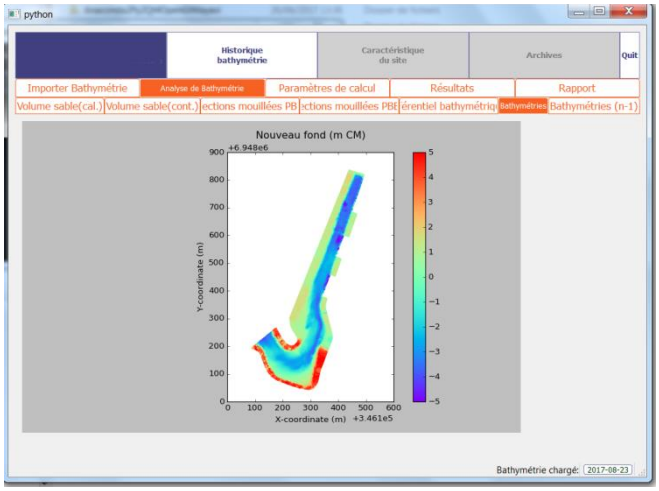

Figure 10. *Bathymetry on the model window*

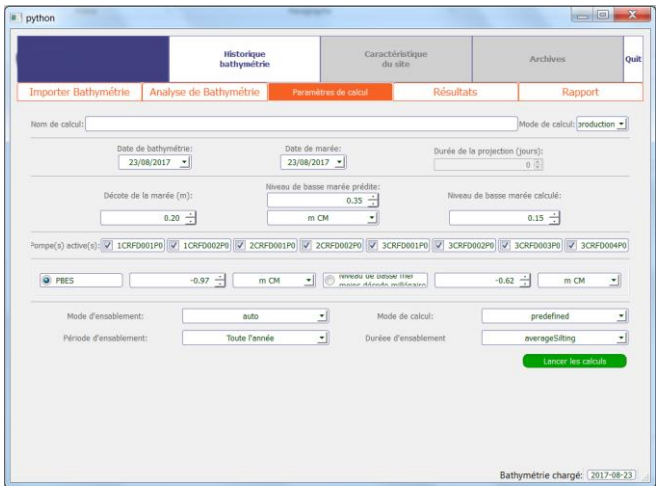

Figure 11. *Input parameters window*

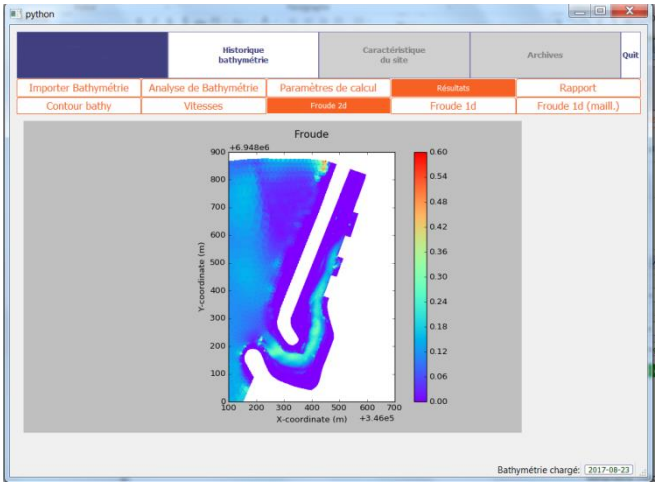

Figure 12. *Froude on the model window*

CONCLUSIONS AND OUTLOOKS

Interoperability has become an important factor for codes to evolve and interact with others. With this module we are beginning to scratch the surface of what it is possible to do. We have here four applications in multiple domains: Uncertainty Quantification, Optimization, Reduced Order Model and Surveillance System. Interaction with outside software is now facilitate with TelApy.

The documentations (Doxygen and user documentation) and examples will be available in the v7p3 release of TELEMAC-MASCARET. Examples can be found within the source code in notebook format, a practical interactive format to manipulate Python scripts[a].

This new tool will allow us, in the future, to remove "user fortran" because all the modifications can be done directly via the APIs. Also we could rewrite the coupling between modules using the APIs. In the next versions of the TELEMAC-MASCARET SYSTEM more complex examples will be added to the ones already available in notebook format.

REFERENCES

[1] A. Bernard and N. Goutal, "Comparison between 1D and 2D models for hydraulic modeling of a floodplain: case of Garonne river",proceedings of River Flow conference, 2008, in press.

[2] C. Goeury, Y.Audouin, F. Zaoui, "User documentation v7p3 of TelApy module", 2017

[3] J-M. Hervouet, "Hydrodynamics of Free Surface Flows", Wiley, 2007, pp. 83–130.

[4] EDF-EADS-PHIMECA, "Reference guide", OpenTURNS version 1.1, 2013.

[5] C. Goeury, T. David, R. Ata, S. Boyaval, Y. Audouin, N. Goutal, A-L. Popelin, M. Couplet, M. Baudin, R. Barate "Uncertatiny quantification on a real cas with TELEMAC-2D" Proceeding of the 2015 Telemac User Conference, October 2015

[6] C. Goeury, A. Ponçot, J.-P. Argaud, F. Zaoui, R. Ata, Y. Audouin, "Optimal calibration of Telemac-2D models based on a data assimilation algorithm", XXIVth Telemac & Mascaret User Club, Graz, Austria, October 2017

[7] PETERSON P. F2py: a tool for connecting fortran and python programs. International Journal of Computational Science and Engineering, 4(4):296–305, January 2009

[a]www.jupyter.org

Uncertainty analysis approximation for non-linear processes using Telemac-AD

Guilherme Dalledonne, Rebekka Kopmann
Department of Hydraulic Engineering
Federal Waterways Engineering and Research Institute
Kußmaulstr. 17, 76187 Karlsruhe, Germany
guilherme.dalledonne@baw.de

Jan Riehme
AdjointWare Jan Riehme
Dresden, Germany
adjoint@riehme.de

Uwe Naumann
Software and Tools for Computational Engineering
RWTH Aachen University
Aachen, Germany
naumann@stce.rwth-aachen.de

***Abstract*—The first-order second-moment (FOSM) is an uncertainty analysis method that assumes a first-order Taylor series expansion at the central value of the input variables to estimate the output variance. The expansion at central values with a first-order approximation might introduce large over- or underestimation when dealing with non-linearities. If the variance assumed for the input parameters is not small enough, the assumption of linearity or slightly non-linearity in this method might be violated.**

In FOSM the variance of the output variables is approximated by the product of the variance of the input parameters and the partial derivative of the model variable with respect to each parameter. In this study we propose to substitute the Gaussian distribution of a model input parameter with high variance by several Gaussian distributions with smaller variances. The weighted combination of the multiple distributions (Compound FOSM or CFOSM) represents nearly the same distribution as the original one (FOSM). In CFOSM the uncertainty analysis has to be carried out for each member of the compound distribution. For this reason the computing time is increased by the number of members considered. Yet, non-linearities can be better approximated and the new approach still requires much less computing time than the Monte Carlo method.

Uncertainty analysis based on the proposed approach will be carried out with validation test cases from the Telemac-Mascaret System. The partial derivatives will be calculated by means of Algorithmic Differentiation efficiently. Results from the analysis of each test case with FOSM and CFOSM will be compared to a Monte Carlo Simulation.

I. INTRODUCTION

Uncertainty analysis attempts to describe the entire set of possible outcomes of an event, together with their associated probabilities of occurrence. It can be very helpful to identify input parameters that produce the largest uncertainties in hydro- and morphodynamic modeling. Since the 1980's this technique has been employed to hydraulic and hydrological modeling ([1],[2],[8]) usually associated to structure and risk analysis in engineering. Since then the method is still found in use and its application has been extended also to sediment transport and morphodynamic modeling ([6],[7],[9],[10],[15]).

Especially in morphodynamic modeling the sensitivity analysis of relevant parameters and, finally, the determination of their uncertainty contribution on end results should be addressed. This recommendation is simply based on the mathematical formulations of sediment transport (e.g. initiation of motion, bedload). These are essentially empirical and might lead to significant errors depending on the time scale considered.

In this manuscript uncertainty analysis will be carried out by applying the first-order second-moment (FOSM) method. Hydrodynamic and morphodynamic processes are described by non-linear relations. However, the direct application of the FOSM method using a typical variation range for the input parameters, e.g. according to measurement uncertainties, could lead to excessive large variances. The main goal here is to properly address non-linearities by means of a new approach based on the FOSM. In order to test the proposed method, two test cases from Telemac-2D will be simulated applying both FOSM and Monte Carlo Simulations for uncertainty analysis.

II. UNCERTAINTY ANALYSIS

A. *First-Order Second-Moment (FOSM)*

- FOSM

The FOSM is given by the first order Taylor series expansion at the central values of the input variables, which is then truncated after the first-order term. Thus, if the

variables are statistically independent the output variance is given by

$$\sigma_Z^2 = \sum_i \sigma_i^2 \left(\frac{\partial Z}{\partial p_i}\Big|_{\mu_i} \right)^2 \quad (1)$$

where Z is the model output, p_i are the input parameters, μ_i are the mean values and σ_i^2 are the variances of the input parameters. All input parameters are considered here to be described by a Gaussian distribution, in which the variance represents the parameter uncertainty.

The partial derivatives of output Z with respect to parameter p_i in (1) has to be computed at the mean value μ_i of parameter p_i and can be calculated using Algorithmic Differentiation (AD)[14] up to machine accuracy (in contrast to numerical differentiation). The great advantage of using AD is that the derivatives of the model output with respect to an uncertain input parameter can be calculated by one single AD simulation. Several studies have been carried out with FOSM by means of AD ([4],[7],[10]), but there are still open questions regarding its applicability.

The drawback of the FOSM method lies on the linearity assumption. If deviations in the input parameters are not small enough, the output variance cannot be approximated well with the first-order terms in the series expansion. Since the partial derivative in (1) might change over the deviation interval considerably, both over– and underestimation of the true output deviation are possible.

- Compound FOSM (CFOSM)

Compound FOSM is an adaptation of the FOSM method for non-linear systems. Instead of considering a single value for the variance of each input parameter to represent its probability distribution, multiple values are taken into account. The Gaussian distribution of an input parameter with high variance is substituted by several Gaussian distributions with smaller variances. The weighted combination of the sub-distributions represents nearly the same distribution as the original one.

For a parameter p_i the mean value and variance of a compound distribution represented with j sub-distributions is given according to [11] by

$$\sigma_i^2 = \sum_j w_j(\mu_{ij}^2+\sigma_{ij}^2) - \mu_i^2 \quad (2)$$

$$\mu_i = \sum_j w_j \mu_{ij} \quad (3)$$

where w_j are the weights of the sub-distributions, μ_{ij}, σ_{ij} are the moments of the sub-distributions for parameter p_i.

In CFOSM we define the variance of model output Z by combining (1) and (2):

$$\sigma_Z^2 = \sum_i \sum_j [w_j(\mu_{ij}^2+\sigma_{ij}^2) - \mu_i^2] \left(\frac{\partial Z}{\partial p_i}\Big|_{\mu_{ij}} \right)^2 \quad (4)$$

given i input parameters and j sub-distributions.

In CFOSM the uncertainty analysis has to be carried out for each member (sub-distribution) of the compound distribution (the partial derivatives have to be computed at the mean values μ_{ij} of the sub-distributions).

The number of sub-distributions (j), their mean values (μ_{ij}) and deviations (σ_{ij}) will affect CFOSM results. Therefore, the mean and the standard deviation of each sub-distribution should be chosen carefully, so that the original distribution is well represented.

In order to apply the CFOSM method, w_j, μ_{ij}, σ_{ij} must be defined. For given moments (μ_i, σ_i) of the original probability distribution (Fig. 1a), the number of sub-distributions (j) and their moments (μ_{ij}, σ_{ij}) must be defined

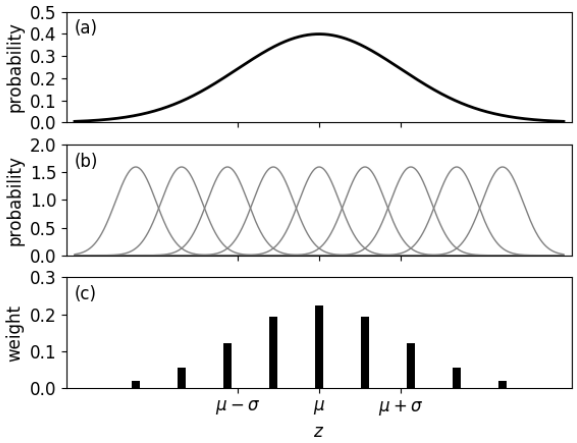

Figure 1*: Construction of a compound distribution.*

(Fig. 1b). After that, based on the cumulative density function of Fig. 1a, the partial areas relative to each sub-distribution (using the middle point between two successive μ_j) gives its corresponding weight (Fig. 1c). The final result for the compound distribution is then presented in Fig. 2.

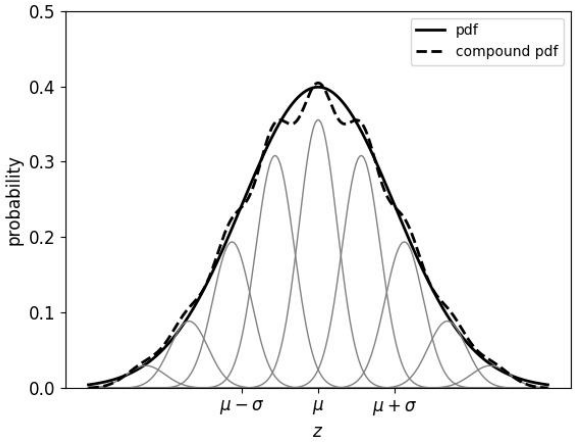

Figure 2: *Simple and compound probability distribution functions*.

B. *Monte Carlo Simulations (MCS)*

An alternative to the FOSM is to use the MCS approach for uncertainty analysis. A large number of model simulations (10^2-10^4) have to be carried out with different setups of uncertain parameters considered to be physically and statistically acceptable. Results will cover all possible outcomes if the statistical representation of input parameters is correct. However, this method requires much more computational effort and results might underestimate the true distribution of output values.

The confidence limits (CL) from the simulations can be derived from an empirical distribution function (EDF). From the cumulative EDF two points corresponding to the CL are chosen in order to get the function values. The absolute difference gives the CL.

The CL from the MCS method can be compared to FOSM and CFOSM results by calculating their corresponding CL as

$$CL_{FOSM} = 2 \cdot n \cdot \sigma_Z \tag{5}$$

where n is a factor corresponding to the level of confidence (e.g. n=3 means a 99% CL).

III. Applications

A. *Analytical example*

An analytical function will be used as test case, in which the derivative can be exactly determined. If we take the function

$$f(x) = c \cdot \arctan(b \cdot x - a) + d \tag{6}$$

with derivative

$$f'(x) = \frac{b \cdot c}{(b \cdot x - a)^2 + 1} \tag{7}$$

then the graphical representation of *f(x)* and *f'(x)* at $x = \mu$ is shown in Fig. 3.

The FOSM method applied to *f(x)* provides a confidence interval of the function, based on the derivative of the output at the mean value of the inputs. The confidence interval itself is represented by the projection of the tangent on the ordinate axis (light red) multiplied by a deviation related to the parameter uncertainty.

In Fig. 4 the same function is presented, but now evaluated with the CFOSM method. Instead of using just one point to calculate the derivative and estimate the confidence interval, several points are selected around the original one. A smaller value for the parameter deviation is now defined, and the confidence interval is now obtained by projecting all tangents on the ordinate axis. The total interval length depends on the underlying model. For the analytical example the constant b in (6) determines the reducing factor. The interval length in Fig. 4 is finally smaller than the one obtained in Fig. 3 (see Tab. 1).

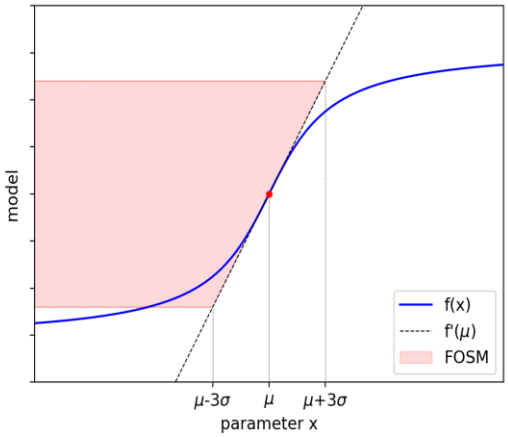

Figure 3: *FOSM concept applied to f(x).*

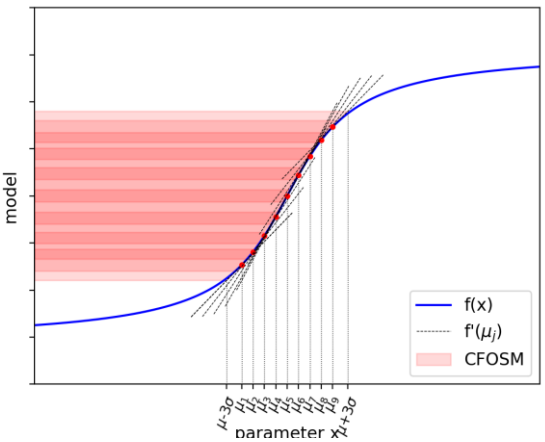

Figure 4: *CFOSM concept applied to f(x).*

TABLE 1: CONFIDENCE INTERVAL OF F(X).

x interval	f(x), b=1	FOSM	CFOSM
[μ-3σ , μ+3σ]	8.8	12.0	9.2

B. *The bump test case*

This test case also known as "bosse" is used as validation test case for SISYPHE, the sediment transport and bed evolution module from the Telemac-Mascaret Modelling System ([12],[13]). In the experiment a sinusoidal dune migrates during four hours due to a constant flow. The model topography is shown in Fig. 5.

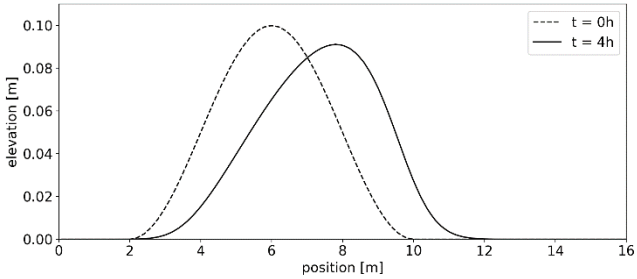

Figure 5: *Model topography.*

The parameters considered to contribute to the overall model uncertainty in this example are the bottom roughness, the slope effect and the median sediment grain size. The transport formula of Engelund-Hansen is applied. The bottom roughness is defined by the Strickler coefficient and the slope effect using the formula of Koch & Flokstra by the beta coefficient. The mean value μ and standard deviation σ for each parameter is presented in Tab. 2.

TABLE 2: STATISTICAL MOMENTS OF THE BUMP MODEL PARAMETERS.

	Median grain size (d_{50}) [m]	Roughness coefficient (k_s) [$m^{1/3}s^{-1}$]	Slope effect coefficient (β) [-]
μ	$3 \cdot 10^{-4}$	40	1.3
σ	$3 \cdot 10^{-6}$	0.5	0.3

The FOSM method is directly computed with AD in Telemac (Telemac-AD branch Foxface, based on Telemac-2D V7P2). Results from [9] already showed good agreement between the FOSM calculated and MCS methods. The new proposed method using j=9 and $\sigma_j = 0.25 * \sigma$ has been applied. Results from CFOSM also perform very similar to MCS with 1000 members, here presented for a 99% confidence interval (see Fig. 6).

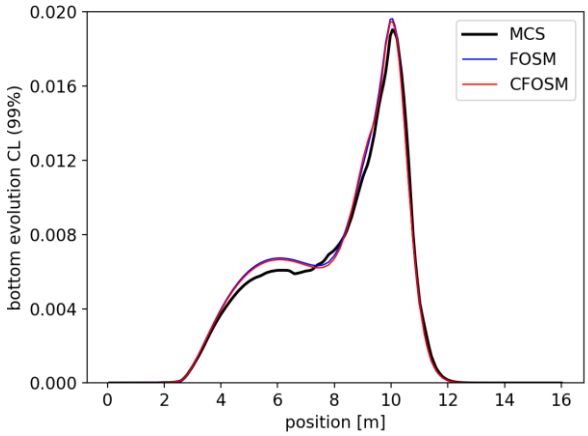

Figure 6: *Confidence limits of bottom evolution.*

Results presented so far do not add any improvement, as the linear approach already shows good agreement with the MCS method. With regard to computation times, FOSM (Telemac-AD) takes about 9 times longer than calculations with Telemac-2D for a single simulation. In total simulation time, FOSM took 2.7 min (1 distribution, 3 parameters), CFOSM 23.9 min (9 sub-distributions, 3 parameters) and MCS 100 min (1000 simulations).

However, a second test was carried out, in which a new set of parameters has been defined in order to consider more non-linearities (see Tab. 3).

TABLE 3: STATISTICAL MOMENTS OF THE BUMP MODEL PARAMETER SET 2.

	Median grain size (d_{50}) [m]	Roughness coefficient (k_s) [$m^{1/3}s^{-1}$]	Slope effect coefficient (β) [-]
μ	$3 \cdot 10^{-4}$	40	1.3
σ	$3 \cdot 10^{-5}$	4.0	0.3

In this second parameter set the median grain size and the roughness coefficient are considered to have a larger standard deviation, equals to 10% of the respective mean value. Results from the uncertainty analysis (see Fig. 7) differ among the three methods. Up to position 8 m the methods show a good agreement, but the peak around position 10 m happens before in FOSM and after in CFOSM. In general, assuming that the profile shape given by the MCS method is correct, the results of CFOSM approximate the true uncertainties better than FOSM. With respect to the number and deviation of the sub-distributions, a few tests showed that results differ very little for $j \geq 5$. However, the chosen standard deviation should be chosen accordingly. Therefore, further testing is still necessary on this topic.

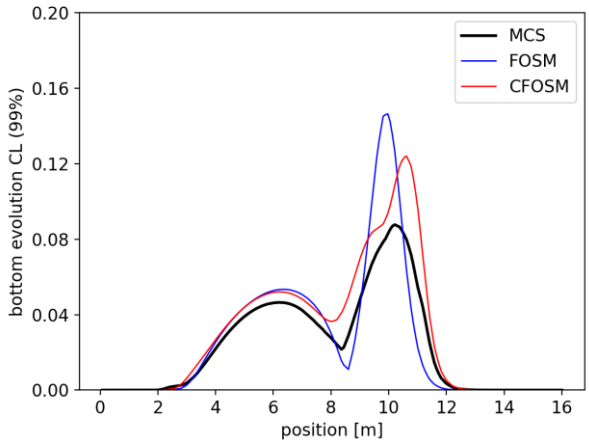

Figure 7: *Confidence limits of bottom evolution for parameter set 2.*

C. *The flume experiment test case*

In this example the new method can be tested in a less theoretical case. The numerical model is designed based on the experiment of [5], a 180° channel bend with a constant radius of curvature. The experiment is conducted during almost 6 hours with unsteady flow given by a hydrograph (see Fig. 8). The initial bottom is flat with a small slope downstream and it develops to a typical cross-section with sediment deposition near the inner side along the channel bend (Fig. 9). Also this example is used as validation test case for SISYPHE.

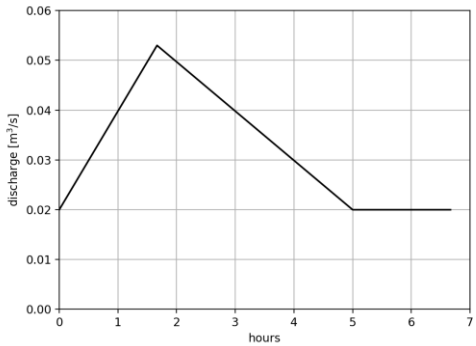

Figure 8*: Hydrograph used in the flume experiment.*

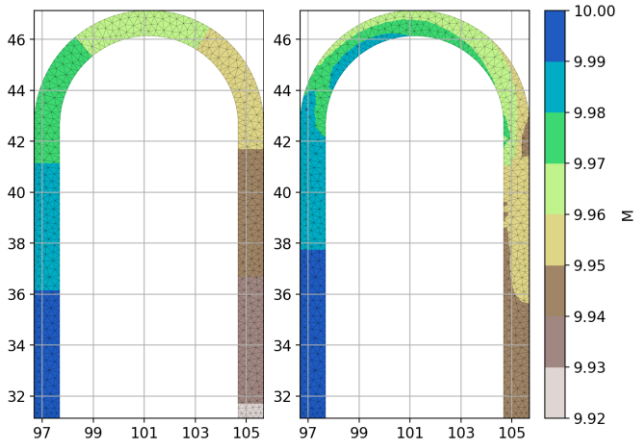

Figure 9: *Initial (left) and final (right) model topography.*

In this test case the same input parameters as in the bump test case have been considered, and additionally the α parameter related to secondary currents is taken into account. The transport formula of Meyer-Peter and Müller is applied and the roughness coefficient is defined after Nikuradse. In Tab. 4 the mean and standard deviation from each parameter are given.

TABLE 4: STATISTICAL MOMENTS OF THE FLUME MODEL PARAMETERS.

	Median grain size (d_{50}) [m]	**Roughness coefficient (k_s)** [m]	**Slope effect coefficient (β)** [-]	**Secondary currents coefficient (α)** [-]
μ	$1 \cdot 10^{-3}$	$3 \cdot 10^{-3}$	1.3	1.0
σ	$1 \cdot 10^{-4}$	$3 \cdot 10^{-4}$	0.3	0.1

Similarly to the previous test case, the CFOSM method has been applied using j=9 and $\sigma_j = 0.25 * \sigma$. The results from the uncertainty analysis are shown in Fig. 10. The confidence limits from the MCS with 1000 members indicate higher uncertainty at the outer side and at the exit from the bend on the right side (in flow direction). At the center of the flume along the bend results present a smaller deviation.

In general, the FOSM confidence limits agree well with the MCS results. Along the outer side, however, FOSM clearly underestimates the uncertainty. FOSM results before and after the bend are very similar to MCS results. With regard to computation times, FOSM (Telemac-AD) takes about 10 times longer than calculations with Telemac-2D for a single simulation. In total simulation time, FOSM took 20.5 min (1 distribution, 4 parameters), CFOSM 184.2 min (9 sub-distributions, 4 parameters) and MCS 516.7 min (1000 simulations).

The CFOSM confidence limits also agree qualitatively well with MCS results. Along the outer side CFOSM performs better than FOSM, and it produces an overall larger uncertainty.

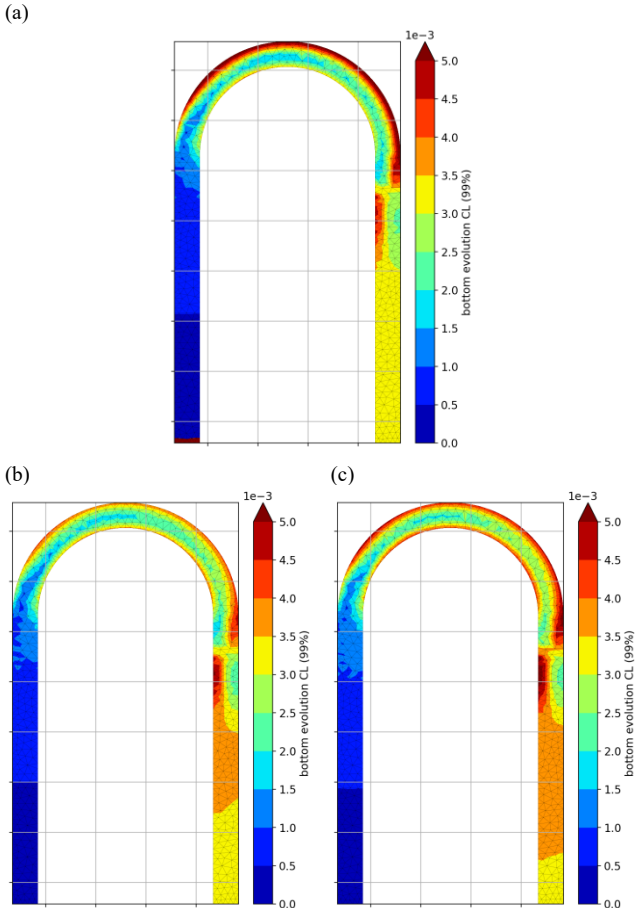

Figure 10*: Confidence limits (99%) of bottom evolution from the (a) MCS, (b) FOSM and (c) CFOSM methods.*

In order to have a clearer comparison among the three methods, a similar analysis to the bump test case has been carried out. For that, three profiles have been defined along the flume to evaluate the final bottom evolution (after 5.5 h): one at the center, one 40 cm to the left and one 40 cm to the right (Figure 11).

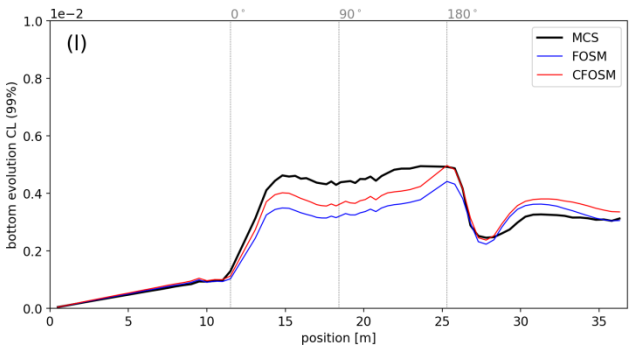

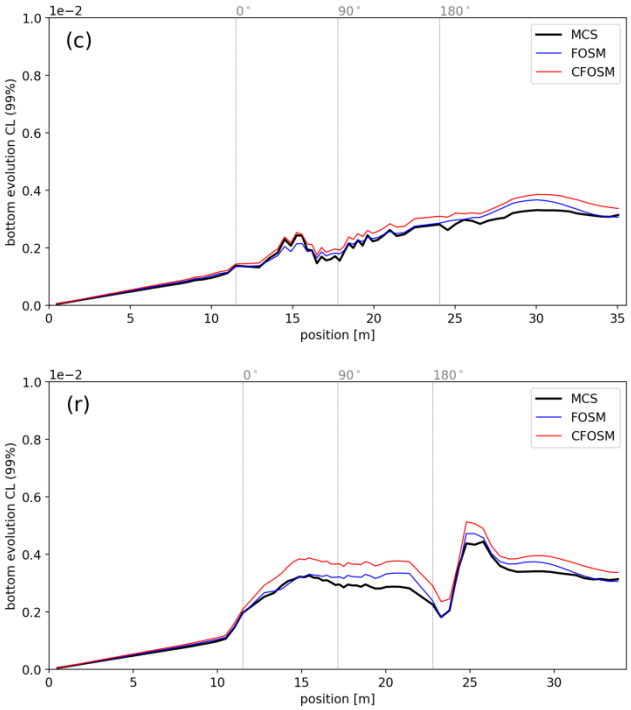

Figure 11: *Confidence limits of bottom evolution along the flume: (l) left, (c) center and (r) right profiles.*

Through this analysis it becomes clear that results are very similar before (0°) the bend among the three methods. Along the bend, FOSM agrees very well with MCS along the center and right profile, but shows a smaller uncertainty along the left profile (outer side). CFOSM reveals higher uncertainties at the center and right profiles, whereas at the left profile it gives a closer estimation to MCS along the bend.

IV. Discussion

In the analytical example (section III.A), the advantages of the CFOSM concept have been verified. The main idea is to improve the FOSM method and make it more robust for highly non-linear models and larger input variances.

In the bump test case (section III.B), results from the first simulation indicated that the proposed method does not improve the analysis of uncertainties. By considering larger deviations for the median grain size and bed roughness, however, new results showed a different situation. Because the first set of parameter deviations was relatively small, producing a quasi-linear variation in the bottom evolution, the use of the FOSM was good enough. In the second test, the larger deviations in the parameters led to a non-linear variation in the bottom evolution, which could not be fully determined by a single derivative. The CFOSM method indicated qualitatively better results taking the MCS method as reference, but with the benefit of computational costs 3 to 4 times lower.

Results from the flume experiment (section III.C), at first sight, indicated an overall increase in the confidence limits from the beginning until the end of the flume. This makes perfectly sense, as on a river usually downstream morphodynamic conditions depend on upstream conditions. Results before the bend given by the three methods agree very well, most probably due to linear and quasi-linear conditions found at those regions. Along the bend non-linear processes are probably dominant and should not be neglected.

V. CONCLUSION

A new uncertainty analysis method based on the first-order second-moment (FOSM) was proposed for non-linear processes. The compound FOSM (CFOSM) method was compared to FOSM and MCS methods.

The results from three test cases – an analytical, a bump and a flume bend – provided an insight on suitable conditions for using FOSM and CFOSM uncertainty analyses. According to those results, CFOSM showed its potential in the first two tests, but did not produce convincing better results in the 2D case. Although FOSM might work when dealing with small parameter deviations, it cannot approximate the true confidence interval of non-linear processes well.

Finally, there are still some open questions regarding the CFOSM method, such as the definition of the number of sub-distributions and their standard deviations, the performance of the method under more complex conditions, and covariance effects among parameters. Possible further development and tests still need to be discussed.

REFERENCES

[1] *B. C. Yen, "Engineering approaches to risk and reliability analysis", in Risk Analysis and Management of Natural and Man-Made Hazards, Y. Haimes and E. Z. Stakhiv, Am. Soc. Civ. Eng., New York, pp. 22-49, 1989.*

[2] *B. C. Yen, S.-T. Cheng and C. S. Melching, "First order reliability analysis", in Stochastic and Risk Analysis in Hydraulic Engineering, B. C. Yen, Water Resour. Publications, Littleton, pp. 1-36, 1986.*

[3] *C. S. Melching, "An improved first-order reliability approach for assessing uncertainties in hydrologic modeling", J. Hydrol., vol. 132, pp. 157-177, 1992.*

[4] *C. Villaret, R. Kopmann, D. Wyncoll, J. Riehme, U. Merkel and U.Naumann: "First-order uncertainty analysis using Algorithmic Differentiation of morphodynamic models", Computers & Geoscience, vol. 90, pp. 144-151, 2016.*

[5] *C. Yen and K. T. Lee, "Bed topography and sediment sorting in channel bed with unsteady flow", J. of Hydraul. Eng., vol. 121, pp. 591-599, 1995.*

[6] *C.-H. Chang, J.-C. Yang and Y.-K. Tung, "Sensitivity and uncertainty analysis of a sediment transport model: a global approach", Stochastic Hydrol. Hydraul., vol. 7, pp. 299-314, 1993.*

[7] *J. Riehme, R. Kopmann and U. Naumann, "Uncertainty quantification based on forward sensitivity analysis in Sisyphe", Vth European Conference on Computational Fluid Dynamics, Lisbon, 2010.*

[8] *N. Sitar, J. D. Cawfield and A. Der Kiureghian, "First-order reliability approach to stochastic analysis of subsurface flow and contaminant transport", Water Resour. Res., vol. 23, pp. 794-804, 1987.*

[9] *R. Kopmann and A. Schmidt, "Comparison of different reliability analysis methods for a 2D morphodynamic numerical model of River Danube", River Flow, pp. 1615-1620, 2010.*

[10] *R. Kopmann, U. Merkel and J. Riehme, "Using reliability analysis in morphodynamic simulation with Telemac-2d/Sisyphe", XIXth Telemac-Mascaret User Conference, Oxford, pp. 119-125, 2012.*

[11] *S. Frühwirth-Schnatter, "Finite mixture and Markov switching models", Springer Science & Business Media, 2006.*

[12] *Telemac Modelling System: Sisyphe Software – User Manual, v7.2, 2016.*

[13] *Telemac Modelling System: Telemac-2D Software – User Manual, v7.0, 2014.*

[14] *U. Naumann, "The art of differentiating computer programs – an introduction to algorithmic differentiation", SIAM, 2012.*

[15] *Y.-S- Jang, N. Sitar and A. Kiureghian, "Reliability analysis of contaminant transport in saturated porous media", Water Resour. Res., vol. 30, pp. 2435-2448, 1994.*

Optimal calibration of TELEMAC-2D models based on a data assimilation algorithm

C. Goeury[1], A. Ponçot[2], J.-P. Argaud[2], F. Zaoui[1], R. Ata[1], Y. Audouin[1]
[1]EDF R&D National Laboratory for Hydraulics and Environment (LNHE)
[2]EDF R&D Performance and prediction of industrial risks for park simulation and studies (PERICLES)
6 quai Watier, 78401 Chatou, France
Email: cedric.goeury@edf.fr

***Abstract* — Numerical models are nowadays commonly used in fluvial and maritime hydraulics as forecasting and assessment tools for example. Model results have to be compared against measured data in order to assess their accuracy in operational conditions. Amongst others, this process touches on the calibration, verification and validation. In particular, calibration aims at simulating a series of reference events by adjusting some uncertain physically based parameters until the comparison is as accurate as possible. Calibration is critical to all projects based on numerical models as it requires a very large proportion of the project lifetime. In this study, the Python module TelApy of the TELEMAC system (www.opentelemac.org) has been used with the ADAO library of the SALOME platform (www.salome-platform.org) to automatically calibrate a 2D hydraulic model. based on a 3D-VAR data assimilation algorithm. The algorithm combines mathematical information contained in the hydraulic model and physical information coming from observations in order to estimate the model input parameters (bathymetry, bed friction, inflow discharge, tidal parameter, initial state and so on).**

Keywords: Shallow Water Model, Data Assimilation, Calibration

I. INTRODUCTION

Many problems in sciences and engineering require the estimation of unknown parameters that will produce a solution that best fits a finite set of indirect measurements. Examples include hydrology, oceanography and weather forecasting. This is also true for fluvial and maritime hydraulics where numerical models are used as forecasting and assessment tools for example.

In all case, model results have to be compared against measured data in order to ascertain their accuracy in operational conditions. Amongst others, this process touches on the model calibration, verification and validation tasks. In particular, model calibration aims at simulating a series of reference events by adjusting some uncertain physically based parameters until the comparison is as accurate as possible. Calibration is critical to all projects based on numerical models as it lasts over a non-negligible proportion of the project lifetime.

The objective of this work is to implement an efficient calibration algorithm, based on data assimilation and coupled with TELEMAC-2D, capable of processing measurements optimally, to estimate the partially known or missing parameters (bathymetry, bed friction, inflow discharge, tidal parameter, initial state, etc.).

Section II and III introduce the principle of the calibration algorithm and the software tools used for this work respectively. Section IV is dedicated to model results obtained from different cases. Finally, Section V, offers some conclusions and outlook.

II. CONTEXT AND PRINCIPLE

A. Context

Parameter estimation, a subset of the so-called inverse problems, consists of evaluating the underlying input data of a problem from its solution. For free surface flow hydraulics, parameters that are often unknown or difficult-to-assess include bathymetry, bed friction, inflow discharge, tidal parameter, initial state etc. The calibration of two typical projects will be used here for demonstration purposes, one schematic river application (fluvial configuration) and one actual coastal site application (maritime configuration):

- *Fluvial configuration.* In 2D hydraulic solvers such as TELEMAC-2D, the nature of the bottom of a waterway is modelled by a roughness coefficient. In some occasion, this coefficient also takes into account the friction of the walls as well as other phenomena such as turbulence. Automatic calibration is a reverse method which is used to find an "acceptable" friction coefficient (here assumed constant by zone) leading to a computed water level close to the measured water level for a fixed flow [1].
- *Maritime configuration.* Calibrating a hydrodynamic model for tide is typically an engaged and difficult process due to the tidal flow interaction between shoreline, islands, meteorological conditions,... and the lack of a reliable tidal observation stations. Thus, in addition to the friction coefficients, the tidal amplitudes at boundary locations and the water depth are considered in this work.

If done manually, model calibration is time consuming. Fortunately, the process can be largely automated to reduce human workload significantly. In the following sections, the automatic calibration task is explained.

B. Automatic calibration algorithm

Thereafter, all model parameters constitute the n-components of the control vector $X = (X_i)^T, \forall \mathrm{i} \in [1, \dots \mathrm{n}]$.

Automatic calibration is a parameter estimation or reverse method used to simulate a series of reference events by adjusting uncertain physically based parameters contained in the control vector X to produce a solution that is as accurate as possible. Therefore, the optimal search for the control vector takes a minimization form of an objective or cost function $J(X)$ given in (1).

$$\begin{cases} \mathrm{J(X)} = \mathrm{J_b} + \mathrm{J_0} \\ \mathrm{J_b} = \frac{1}{2}(\mathrm{X} - \mathrm{X_b})^{\mathrm{T}}\mathrm{B}^{-1}(\mathrm{X} - \mathrm{X_b}) \\ \mathrm{J_0} = \frac{1}{2}\big(\mathrm{Y} - \mathrm{H(X)}\big)^{\mathrm{T}}\mathrm{R}^{-1}\big(\mathrm{Y} - \mathrm{H(X)}\big) \end{cases} \quad (1)$$

where the components of X represents parameters to be estimated / calibrated, X_b represents the prior knowledge about the control vector X, Y is the observation vector, H is the so-called observation operator enabling the passage of the parameter space (where the vector X lives) to the observation space (where Y lives) such that $Y = H(X)$ and B, R are the background and observation error covariance matrices respectively.

This is a formulation of the optimal search of control vector X, which must satisfy the background error statistics (J_b), and the equivalent observation error (J_o). Eq. (1) is known as the traditional variational data assimilation cost function, called 3D-VAR [2].

Generally, optimisation methods can be used to solve minimisation problems. The former can be very different according to the form of the cost function to be minimised (convex, quadratic, nonlinear, etc.), its regularity and the dimension of the space studied. Many deterministic optimisation methods are known as gradient descent methods, among which is the Broyden-Fletcher-Goldfarb-Shanno (BFGS) quasi Newton method [3], [4].

For these methods, the estimation of the optimal control vector X involves minimising the objective function $J(X)$ (or finding its extremes), which requires the computation of its gradient with respect to X, defined as follows.

$$\nabla \mathrm{J(X)} = \mathcal{H}^{\mathrm{T}}\mathrm{R}^{-1}\big(\mathrm{Y} - \mathrm{H(X)}\big) \quad (2)$$

with $\mathcal{H}$ the adjoint of the observation operator H that is to say the partial derivatives of the operator's component with respect to its input parameters. It is noted that the observation operator H represents a call to the hydraulic solver, which implies that $\mathcal{H}$ represent a call to the adjoint of the hydraulics solver.

C. Constrained BFGS Quasi Newton method

The optimisation method mentioned above (BFGS) is based on the application of the Newton method to the gradient of the functional $J(X)$, which involves the computation of the first and second derivatives of the cost function. The main disadvantage of this type of approach is the computation of the second derivative $\nabla^2 J(X)$ (or Hessian) and using it to solve a linear system at every iteration of the Newton algorithm. For large problems, this is computationally out of reach.

An alternative is to use algorithms such as the Quasi-Newton algorithm which provides Hessian approximations that improve as the iterations progress, for a reasonable cost. The method chosen to perform this work is the so-called constrained Broyden Fletcher Goldfarb Shanno Quasi-Newton method (c-BFGS-QN).

The optimisation problem is formulated as follows (Eq. (3), (4) and (5)), starting with the constrained minimisation.

$$\begin{aligned} &\min_{\mathrm{X}} \mathrm{J(X)} \\ &\mathrm{X_i^{min}} \le \mathrm{X_i} \le \mathrm{X_i^{max}}, \ \forall \mathrm{i} \in [1, \dots \mathrm{n}] \end{aligned} \quad (3)$$

If X^k is the solution at stage k, a direction d^k is obtained by solving the minimization process defined in (4).

$$\min_{\mathrm{d^k}} \nabla \mathrm{J}\big(\mathrm{X^k}\big)^{\mathrm{T}}\,\mathrm{d^k} + \frac{1}{2}\mathrm{d^{kT}M d^k} \quad (4)$$

where $d_i = 0$ if $X_i \approx X_i^{min}$ or $X_i \approx X_i^{max}$ and M is the approximate Hessian matrix.

A line search is then performed along the direction d^k to find a new feasible solution X^{k+1}. Then M is modified by the BFGS formula as follows.

$$\begin{aligned} \mathrm{M^{k+1}} = \mathrm{M^k} + \\ \left(1 + \frac{\gamma^{\mathrm{kT}}\mathrm{M^k}\gamma^{\mathrm{k}}}{\delta\mathrm{X^{kT}}\gamma^{\mathrm{k}}}\right)\frac{\delta\mathrm{X^k}\delta\mathrm{X^{kT}}}{\delta\mathrm{X^{kT}}\gamma^{\mathrm{k}}} - \frac{1}{2}\frac{\delta\mathrm{X^{kT}}\big(\mathrm{M^k} + \mathrm{M^{kT}}\big)\gamma^{\mathrm{k}}}{\delta\mathrm{X^k}\gamma^{\mathrm{k}}} \end{aligned} \quad (5)$$

with $\delta X^k = X^{k+1} - X^k$ and $\gamma^k = \nabla J(X^{k+1}) - \nabla J(X^k)$

Using a constrained optimisation method makes it possible to impose boundaries during the research process of the model parameters guaranteeing their physical values. Because the inverse problem (1) is often ill-posed and unstable with available data corresponding to more than one solution, small changes in model results can lead to very different estimates for the input (calibration) parameters. These problems are related to the issue of "parameter identifiability" [5].Still, the chosen optimisation method involves computing the adjoint $\mathcal{H}$ of the observation operator H (or the partial derivatives of the operator with respect to its input parameters). In this work, the partial derivatives are approximated by using a classical finite differences method. While this remains a simple solution, numerically sensitive and computationally costly, the observation operator can be written to make use of multiprocessor parallelism in order to provide an automatic calibration algorithm efficient in term of computational cost, practical for industrial applications.

III. SOFTWARE TOOLS

The automatic calibration algorithm presented in the previous section (section II) combines different skills such as optimisation, numerical analysis, parameter estimation, and

free surface flow hydraulics. The software implementation of the algorithm has to be based, therefore, on open source and flexible architecture with reusable components. This study was performed by coupling the hydrodynamic solver TELEMAC-2D and the data assimilation library ADAO within the SALOME platform, through the component TelApy of the TELEMAC system.

A. *The SALOME platform*

SALOME is an open source platform (www.salome-platform.org) for pre and post processing of numerical simulations, enabling the chaining or the coupling of various software tools and codes. SALOME is developed by EDF, the CEA and OPENCASCADE S.A.S. under the GNU LGPL license. It is based on an open and flexible architecture with reusable components, which can be used together to build a computation scheme assembling each module or external codes together through specific communication protocols. In our case, the TELEMAC-2D model is driven through the TelApy component and dynamically linked to ADAO within SALOME (See Fig. 1).

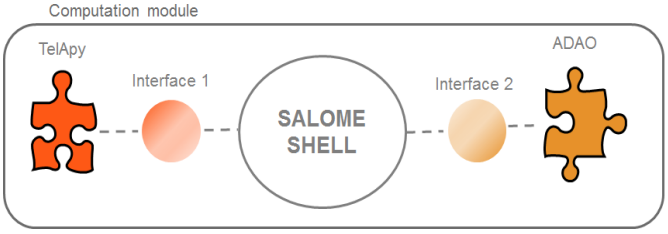

Figure 1. *The SALOME composition linking TelApy to ADAO*

B. *The TelApy component of the TELEMAC system*

The recently implemented TelApy component is distributed with the open source TELEMAC system (www.opentelemac.org). It aims at providing python source code that wraps and controls a TELEMAC simulation through a Fortran API (Application Program Interface) [6]. The API's main goal is to have control over a simulation while running a case. For example, it allows the user to hold the simulation at any time step, retrieve some variables and / or change them. The links between the various interoperable scientific libraries available within the Python language allows the creation of an ever more efficient computing chain able to more finely respond to various complex problems. The TelApy component has the capability to be expended to new types of TELEMAC simulations use including high performance computing for the computation of uncertainties, other optimization methods, coupling, etc.

C. *The Data Assimilation library ADAO*

The ADAO library provides modular data assimilation and optimization features within the SALOME platform [2]. It can be coupled with other modules or external simulation codes while providing a number of standard and advanced data assimilation or optimization methods. The ADAO library also covers a wide variety of practical applications, from real engineering to quick experimental methodologies. Its architechture and numerical scalability gives way to extend the field of application.

IV. APPLICATIONS

In the previous section, the software tools used to implement the computing chain of the automatic calibration algorithm have been presented. In order to demonstrate its application some case are presented in the following section.

A. *Fluvial configuration*

Within this fluvial configuration, the implementation within SALOME of the automatic calibration algorithm is applied to two of the standard TELEMAC-2D test cases: the so-called "estimation" and "verysimple" test cases. The aim of this configuration is to find optimal friction coefficients based on a numerically generated synthetic data from the so-called "identical-twin-experiment", in which true state is known.

1) *Parameter estimation: friction coefficient*

Friction comes into the momentum equations of the shallow water equations and is treated in a semi-implicit form within TELEMAC-2D [7]. The two components of friction force are given in Eq. (6).

$$\begin{cases} F_x = -\frac{u}{2h} C_f \sqrt{u^2 + v^2} \\ F_y = -\frac{v}{2h} C_f \sqrt{u^2 + v^2} \end{cases} \quad (6)$$

where h is the water depth, C_f a dimensionless friction coefficient and u and v are the horizontal x and y components of the current velocity.

The roughness coefficient often takes into account the friction by the walls on the fluid or other phenomena such as turbulence. Thus it is difficult to define directly from available data and must be adjusted using the water surface profiles measured for a given flow rate.

2) *Test case "estimation"*

This first test case is based on a schematic rectangular channel of varying mesh resolution. The channel is 500 m long and 100 m wide. The finite element mesh consists of 551 triangles (Fig. 2).

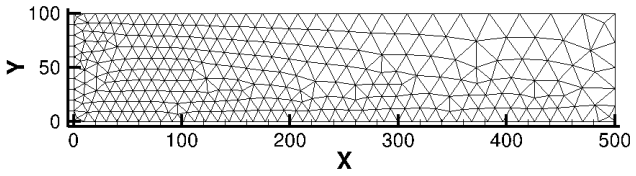

Figure 2. *Mesh and layout of the test case "estimation"*

Upstream and downstream of the model, the boundary conditions used are the imposed flow rate and water level, respectively set to 50 m^3s^{-1} and 1 m. A single Strickler friction value is set for the entire domain.

Regarding the automatic calibration, the initial guess of the Strickler is set to 15 $m^{1/3}s^{-1}$. The "observations" used to calibrate the model are synthetic water depth generated numerically with a Strickler coefficient of 35 $m^{1/3}s^{-1}$. The objective of this test case is to recover the synthetic value defined as the true state using the automatic calibration algorithm chain. The observation considered in this case are

the water depth on all mesh nodes at different times in second $T = \{2{,}000; 4{,}000;\ 6{,}000;\ 8{,}000; 10{,}000\}$.

Regarding the optimization search , the friction parameter is constrained between 5 $m^{1/3}s^{-1}$ and 90 $m^{1/3}s^{-1}$ and the differential increment is set to 10^{-4} for the computation of the observation operator approximated derivatives.

Fig. 3 shows the Strickler coefficient and the associated cost function evolution as a function of the number of iterations of the automatic minimization algorithm.

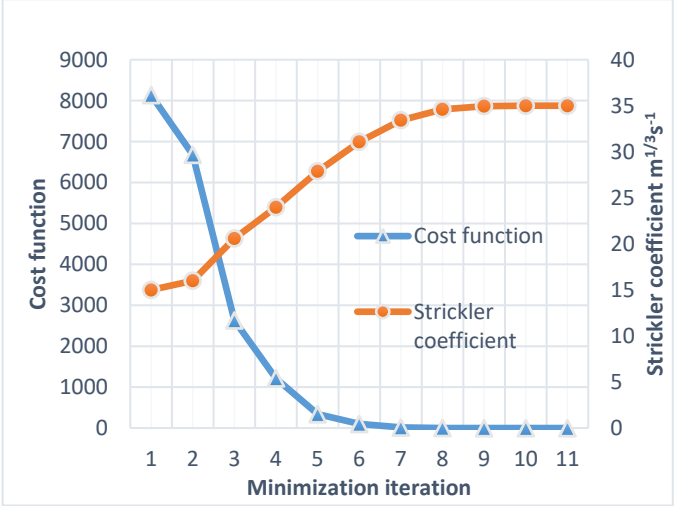

Figure 3. *Value of the cost function and the Strickler coefficient according to number of algorithmic calibration iterations*

Regarding the convergence speed of the automatic calibration method, Fig. 3 highlights a fast convergence and accuracy for the automatic calibration method developed in this work. The calibration tool finds an optimal solution in about 10 iterations with a cost function less than 10^{-2} corresponding to a Strickler coefficient of 34.998 $m^{1/3}s^{-1}$. This test case demonstrates that the data assimilation chain is well implemented.

3) Test case "verysimple"

For real applications, there are often a few measurements available at different locations. Additionally, bed properties often varies over the entire domain (rock, vegetation, sand, mud, etc.), for which a unique friction coefficient may not be appropriate.

This test case defines a limited number of zones (as many as the measurements), within which the friction coefficient is a constant parameter, independent of one another.

The "verysimple" test case is a rectangular channel of 50 m long and 1 m wide with a constant slope of 0.1 degree. The TELEMAC-2D model, constituted by a triangular mesh of some 5010 nodes (Fig. 4), has a constant discharge upstream and a water level downstream imposed, respectively set to 2.38 m^3s^{-1} and 1 m.

In this test case, 5 friction zones of equal sizes, numbered 1 to 5, are considered every 10 m of the channel. At the middle of each friction zone, one observation node is considered.

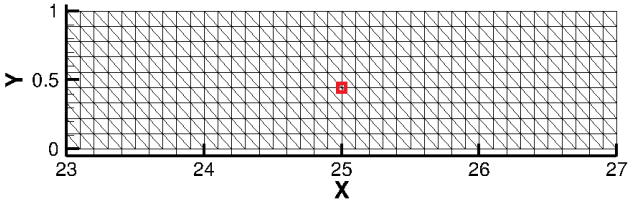

Figure 4. *Zoom of the test case "verysimple"(■observation node)*

Similar to the previous schematic application, the "observations" are water depth synthetic data generated numerically. The initial guess of Strickler (in $m^{1/3}s^{-1}$) is set to $[K_1^b = 25; K_2^b = 30; K_3^b = 35; K_4^b = 32; K_5^b = 28]$, whereas the value used to compute the synthetic data is $[K_1^t = 56.107 = K_2^t = K_3^t = K_4^t = K_5^t]$ (where the t and b exponents denote respectively true and background state).

This value of Strickler coefficient corresponds to a sub-critical flow with constant depth over the full length of the channel. The observation considered in this case are the water depth on observation nodes at different times in second $T = \{5{,}000; 10{,}000;\ 15{,}000;\ 20{,}000; 30{,}000\}$.

As for the previous test case, the optimal friction parameters are constrained between 5 $m^{1/3}s^{-1}$ and 90 $m^{1/3}s^{-1}$ and the differential increment is imposed to 10^{-4} for the computation of the observation operator approximated derivatives.

Fig. 5 shows the Strickler coefficients and the associated cost function evolution as a function of the number of minimization algorithm iterations.

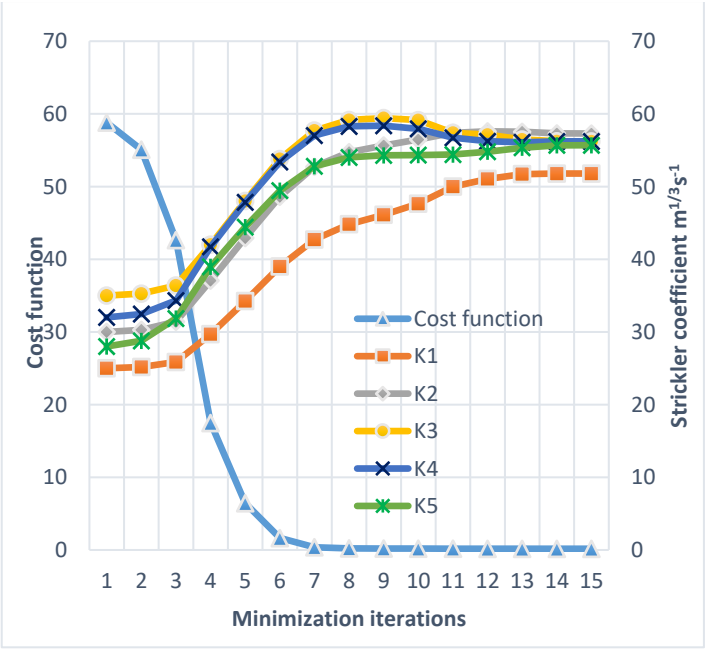

Figure 5. *Value of the cost function and the Strickler coefficients according to number of algorithmic calibration iterations*

As shown in the previous test case, the optimization process presents a fast convergence. In fact, the optimal solution is reached in about 15 iterations with a set of Strickler

coefficient values in $m^{1/3}s^{-1}$ such as $\left[K_1^{opt} = 51.79; K_2^{opt} = 57.3; K_3^{opt} = 56.21; K_4^{opt} = 56.215; K_5^{opt} = 55.69\right]$ corresponding to a cost function value less than 10^{-1}.

Furthermore, the results shown in Fig. 5 emphasise the complexity of determining a set of optimal friction coefficients. Indeed, the uniqueness of a solution of this type of problem is not mathematically proven and different sets of parameters can give analogous results. In fact, even in the framework of a simplify test case, the optimal friction parameters stabilize close but not exactly at the true state value. Thus it is important to set bounds on the search for optimal friction coefficients to avoid all the outliers and non-physical values [1]. This is why the automatic calibration method developed here uses a constrained optimisation approach.

B. Maritime configuration

A real maritime configuration is presented and calibrated using measurement data. Contrarily to the fluvial configuration, the identification of the most influential parameters was carried out through a sensitivity analysis. Indeed, it is essential to understand the relationship between the modelling inputs and the simulated variables which describe the system's dynamic. Subsequently, the automated calibration method was used for the estimation of those influential parameters.

1) Context and available data

The Alderney Race (also as known as "Raz Blanchard") is located between the Island of Alderney, UK, and the western tip of the Cotentin peninsula in Normandy, France. The maritime model includes Alderney and the tip of the Cotentin peninsula and covers an area roughly 55 km x 35 km. The finite element mesh is composed of 17,983 nodes and 35,361 triangular elements (Fig. 6). The mesh size varies from 100 m, at the shoreline and within the areas of interest, to 1.8 km offshore (western and northern sectors of the model).

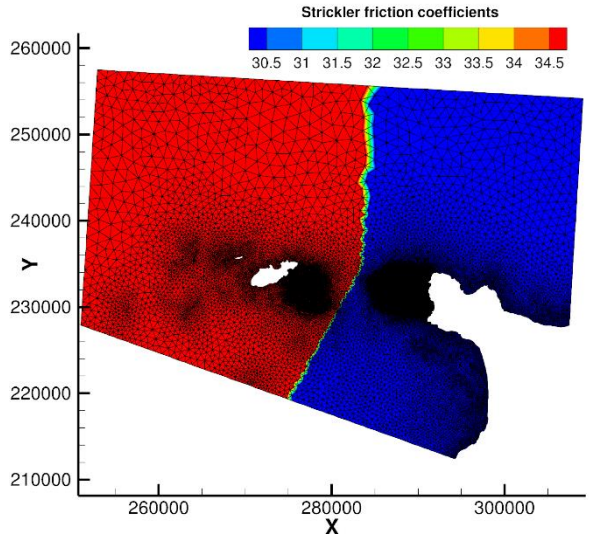

Figure 6. *Model mesh and friction coefficients (Lambert 1 North coordinate system)*

The boundary conditions of the model have been set up using depth-averaged velocities and water levels from the TPXO dataset (8 primary, 2 long-period and 3 nonlinear constituents). The TPXO dataset is an accurate global models of ocean tides based on a best-fit of tidal levels measured along remote sensing tracks from the TOPEX/POSEIDON satellite project in operation since 2002. Moreover, velocities and water depths are imposed along the marine borders of the model using Thompson-type boundary conditions that allows internal waves to leave the domain with little or no reflection.

Several measurement campaigns were carried out to the west of Cap de la Hague. For this study, only the results of one of these (a campaign lasting six months) are used over a 5 days period from October 15th to 20th. This six-month campaign was carried out during summer of 2009 (from the end of July to the end of January). Two ADCPs were deployed to measure flow velocity (magnitude and direction) and water depth with 1 measurement every 10 minutes and one hour respectively.

2) Sensitivity analysis

Calibrating a hydrodynamic model (here for a real tidal site) is typically an engaged and difficult process due to the complexity of the flows and their interaction with the shoreline, the bathymetry, islands, etc. Thus, it is essential to understand in depth the relationship between the modelling calibration parameters and the simulated state variables which are compared to the observations.

In this case, the identification of the most influential input parameters by sensitivity analysis has been led to target the calibration parameters when observations are available. In particular, both friction and tidal amplification were highlighted.

a. Friction parameter

As shown in Fig. 6, the model is composed of two friction zones, roughly along the French-UK border, where the Strickler friction coefficients are imposed to $K_1 = 30$ and $K_2 = 35$ m1/3s-1. The approach here is similar to that used in the schematic fluvial configuration.

b. Tidal amplification parameter

Tidal characteristics are imposed using a database of harmonic constituents to force the open boundary conditions. For each harmonic constituent, the water depth h and horizontal components of velocity u and v are calculated, at point M and time t by Eq. (7).

$$\begin{cases} \mathrm{F(M,t)} = \sum_i \mathrm{F_i(M,t)} \\ \mathrm{F_i(M,t)} = \\ \qquad \mathrm{f_i(t) A_{F_i}(M) \cos\left(\frac{2\pi t}{T_i} - \varphi_{F_i}(M) + u_i^0 + v_i(t)\right)} \end{cases} \tag{7}$$

where F is either the water level (referenced to mean sea level) z_S or one of the horizontal components of velocity u or v, i refers to the considered constituent, T_i is the period of the constituent, A_{F_i} is the amplitude of the water level or one of the horizontal components of velocity, $\phi_{F_i}$is the phase, $f_i(t)$ and $v_i(t)$ are the nodal factors and u_i^0 is the phase at the original time of the simulation.

The water level and velocities of each constituent are then summed to obtain the water depths and velocities for the open boundary conditions (8).

$$\begin{cases} h = \alpha \sum z_{Si} - z_f + z_{mean} \\ u = \beta \sum u_i \\ v = \beta \sum v_i \end{cases} \quad (8)$$

where z_f is the bottom elevation and z_{mean} the mean reference level.

In Eq. (8), the tidal amplitudes multiplier coefficient of tidal range and velocity, respectively α and β, at boundary locations and the sea level z_{mean} are assumed to be the tidal calibration parameters [8].

c. Analysis of variance

The sensibility analysis aims at quantifying the relative importance of each input parameter of a model. The variance-based methods aim at decomposing the variance of the output to quantify the participation of each variable. Generally, these techniques compute sensitivity indices called Sobol Indices. The definition of Sobol Indices is a result of the ANOVA (Analysis Of VAriance) variance decomposition. In fact, given a set of independent uncertain parameters $X = (X_1, \dots, X_n)$, the variance of the output $Y = M(X)$ can be expressed based on the total variance theorem by Eq. (9).

$$Var[Y] = \sum_{i=1}^{p} V_i(Y) + \sum_{i<j} V_{ij}(Y) + \cdots + V_{12\dots p}(Y) \quad (9)$$

where:

$$\begin{cases} V_i(Y) = Var[E(Y|X_i)] \\ V_{ij}(Y) = Var\left[E(Y|X_i, X_j)\right] - V_i(Y) - V_j(Y) \\ \vdots \end{cases} \quad (10)$$

The term $E(Y|X_i)$ represents the conditional expectation of the output Y under the assumption that the uncertain variable X_i remains constant. The resulting decomposition of the variance can then be used to compute the sensitivity indices called Sobol Indices. In the framework of this study, only the first order S_i and the total S_{Ti} Sobol sensitivity indices are studied. The definition of these two indices is given by Eq. (11).

$$\begin{cases} S_i = Var(E[Y|X_i]) \Big/ Var(Y) \\ S_{Ti} = Var(E[Y|X_{-i}]) \Big/ Var(Y) \end{cases} \quad (11)$$

where X_i is the uncertain variable i and X_{-i} refers to the set of uncertain input factors excluding X_i.

d. Polynomial Chaos method

In this work, a polynomial chaos expansion has been carried out to estimate Sobol sensitivity indices. This technique consists in looking for a functional representation of the output response of the system in the form of the development described by Eq. (12).

$$M(X(\zeta)) \approx M^{PC}(X(\zeta)) = \sum_{|j|<d} y_j \phi_j(\zeta) \quad (12)$$

where $\{\phi_j, j \in \mathbb{N}^p\}$ is a multivariate polynomial basis, d the maximum polynomial order and y_j adequate coefficients for the estimation of the model's response that can be determined using projection or least square methods.

In this work, the coefficients y_j are determined using the leat-square approach. In the following, the random variables in X defined in the input physical space are rescaled in the standard probabilistic space noted $\zeta \equiv \zeta(\omega) = [\zeta_1, \dots, \zeta_p]^T$ (0 mean and unit variance), to which the Polynomial Chaos framework applies. The fruitful link between Polynomial Chaos expansion and the formalism of Sobol indices has been established by [9].

e. Results

In this paper, we investigate the effect of three sources of uncertainty: the friction coefficients (K_1 and K_2), the tidal amplification coefficients along the marine boundaries (α and β) and the reference mean water level z_{mean}. All input parameters are described by uniform probability density functions such that $K_1, K_2 = U[15; 50]$ in $m^{1/3}s^{-1}$; $\alpha, \beta = U[0.7; 1.3]$ and $z_{mean} = U[-5; 5]$ in m.

To handle the sensitivity analysis with the polynomial chaos expansion, it is important to run a lot of simulations in order to have reliable results. In this work, around 2,000 Monte-Carlo computations have been carried out based on TELEMAC-2D through the SALOME platform described in [10]. Since, the sensitivity analysis results obtained for the water depth and velocity variables are similar to each other with a ranking variable without any time dependency, only the results for water depth at the last time step are presented here. Fig. 7 displays the first order and the total Sobol sensitivity indices (respectively S_i and S_{Ti}) obtained at the ADCP measurement point with a polynomial chaos expansion of degree 5.

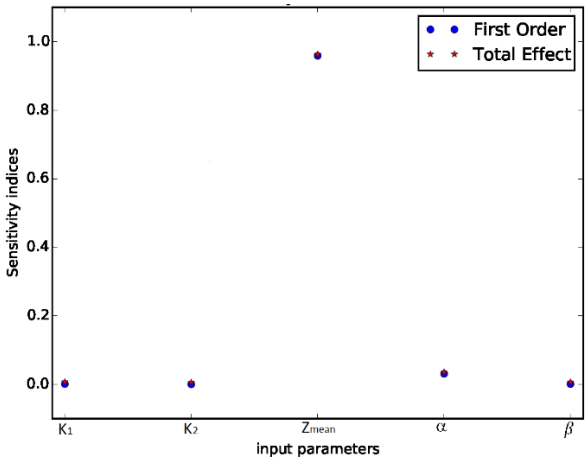

Figure 7. *First order and total Sobol sensitivity indices (respectively S_i and S_{Ti}) obtained by a degrees 5 chaos polynomial expansion*

As shown, the sea level calibration factor is by far the most influencing variable. This uncertain variable explains more than 95% of the output variation. Then, the tidal amplitude

multiplier coefficient α explains some percent of the output variation. The other variables can be considered negligible in comparison. These results depend, of course, on the hypothesis on the input random variables and especially on the choice of their distributions. Consequently, the calibration of the model is focused on these tidal parameters.

3) Tidal parameters estimation

The initial guess of the tidal parameters is set to the value $[z_{mean} = -1.6,\ \alpha = 1,\ \beta = 1]$ as prescribed by the original study with this model. The constrains of the search taken from the sensitivity analysis (section IV.B.2.e). Similarly to the fluvial configuration, the differential increment is set to 10^{-4} for the computation of the observation operator approximated derivatives.

The automatic calibration algorithm finds an optimal solution in about 16 iterations with the following set of parameters $[Z_{mean} = -0.995, \alpha = 1.112, \beta = 1.106]$.

Fig. 8 and Fig. 9 display the results of the automatic calibration over a 5 days period. As shown in Fig. 8, the water surface profiles calculated are much closer to the ADCP measurements than the original model calibration. The final results emphasises the efficiency of the automatic calibration tool in the framework of a maritime configuration.

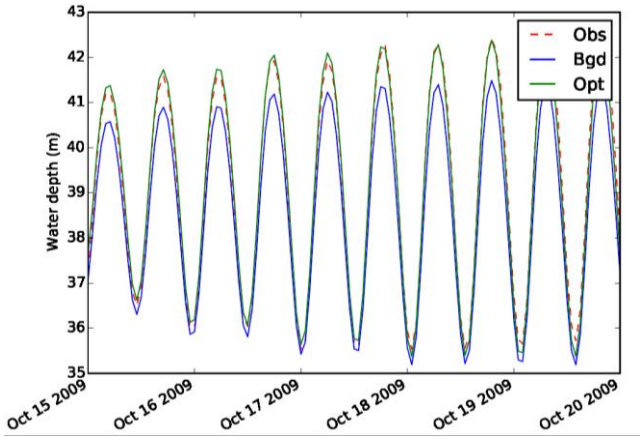

Figure 8. *Comparison of the water depth evolution with and without calibration (respectively - Opt and - Bgd) with respect to the ADCP measurements (- Obs)*

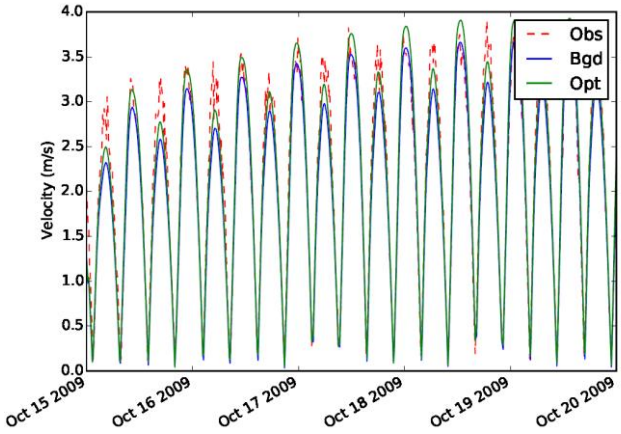

Figure 9. *Comparison of the water depth evolution with and without calibration (respectively - Opt and - Bgd) with respect to the ADCP measurements (- Obs)*

As expected, the velocity results are also closer to the measures but some differences can be observed (Fig. 9). These differences can be explained given the degree of uncertainty in the ADCP instrument or the influence of the bathymetry on the 3D structure of the flow with turbulent structure not well represented with 2D hydraulic model.

Finally, the computation time is a crucial point from operational point of view. Thus, the algorithmic calibration tool implemented in this work has been written to make use of multiprocessor parallelism in order to be efficient and compatible with industrial needs. Tab. 1 below summarizes the computation time in scalar and parallel modes obtained with processor Intel®Xeon®CPU E5-2620v3@2.40Ghz.

Number of processors	CPU time
1	9h6min26s
8	1h40min38s

TABLE 1. COMPARISON OF CPU TIME

Together with the chosen software tools and platform, the implementation of the automatic calibration algorithm remains efficient in term of computational cost for practical and industrial applications.

V. CONCLUSIONS AND OUTLOOK

Numerical models are nowadays commonly used in fluvial and maritime hydraulics as forecasting and assessment tools. Model results have to be compared against measured data in order to assess their accuracy in operational conditions. Amongst others, this process touches on model calibration, verification and validation. In particular, calibration aims at simulating a series of reference events by adjusting some uncertain physically based parameters until the comparison is as accurate as possible. However, if done manually, model calibration is time consuming. Fortunately, the process can be largely automated to reduce human workload significantly.

This article presented an automatic calibration algorithm and it implementation as a series of coupled tools. The optimal search for the parameters takes the form of minimising a cost function, which led to the implementation of a constrained BFGS Quasi-Newton method. Using a constrained optimisation method (setting bounds over the parameters) helped in finding an optimal friction coefficient in a complex, sometimes ill-posed problem for which different sets of parameters can provide analogous results.

In order to demonstrate the applicability of the automatic calibration method to converge to a known solution ("identical twin experiment"), tests on two fluvial schematic test cases were carried out. A real maritime configuration was also further calibrated against ADCP measurement with better results than originally obtained. Computation time also emphasised the efficiency of the automatic calibration tool in the framework of TELEMAC-2D.

Future works will include the replacement of the classical finite differences method, for the gradient computation of the cost function in the optimisation method, by a gradient based on algorithmic differentiation.

REFERENCES

[1] F. Demangeon, C. Goeury, F. Zaoui, N. Goutal, V. Pascual, L. Hascoet, "Algorithmic differentiation applied to the optimal calibration of a shallow water model", La Houille Blanche, n°4, pp.57-65, 2016.

[2] J.-P. Argaud, "User Documentation, in the SALOME 7.5 platform, of the ADAO module for Data Assimilation and Optimization", EDF R&D report, 2016.

[3] J. L. Morales, J. Nocedal, "L-BFGS-B: Remark on Algorithm 778: L-BFGS-B, FORTRAN routines for large scale bound constrained optimization", ACM Transactions on Mathematical Software, 38(1), 2011.

[4] C. Zhu, R. H. Byrd, J. Nocedal, "L-BFGS-B, FORTRAN routines for large scale bound constrained optimization," ACM Transactions on Mathematical Software, 23(4), pp. 550-560, 1997.

[5] I. M. Navon, "Practical and theoretical aspects of adjoint parameter estimation and identifiability in meteorology and oceanography", Dynamics of Atmospheres and Oceans, 27(1-4), pp. 59-79, 1998.

[6] C. Goeury, Y.Audouin, F. Zaoui, "User documentation v7p3 of TelApy module", 2017

[7] J-M. Hervouet, "Hydrodynamics of Free Surface Flows", Wiley, 2007, pp. 83–130.

[8] C. T. Pham, F. Lyard, "Use of tidal harmonic constants databases to force open boundary conditions in TELEMAC, Proceedings of the 19th Telemac-Mascaret User Club, 2012.

[9] B. Sudret, "Uncertainty propagation and sensitivity analysis in mechanical models. Contributions to structural reliability and stochatstic spectral methods", Accreditation to supervise research report, 2007.

[10] C. Goeury, T. David, R. Ata, S. Boyaval, Y. Audouin, N. Goutal, A.-L. Popelin, M. Couplet, M. Baudin, R. Barate, "Uncertainty Quantification on a real case with TELEMAC-2D", Proceedings of the 22nd Telemac-Mascaret User Club, 20

Global Sensitivity Analysis applied to the Telemac2D numerical forecast model of high water levels in the Gironde estuary

Vanessya Laborie[1,2], Nicole Goutal[2,3], Sophie Ricci[4], Matthias De Lozzo[4], Philippe Sergent[1]

[1] French Center For Studies and Expertise on Risks, Environment, Mobility, and Urban and Country planning (Cerema)
[2] Saint-Venant Laboratory for Hydraulics
[3] EDF R&D National Laboratory for Hydraulics and Environment (LNHE)
[4] CECI, CERFACS/CNRS

[1] Compiègne, France, [2,3] Chatou, France, [4] Toulouse, France
e-mail : vanessya.laborie@cerema.fr

***Abstract*—In the context of the development and the implementation of data assimilation techniques in Gironde estuary for flood forecasting, a Telemac 2D model is used to calculate water depths and velocity fields at each node of an unstructured mesh. Upstream, the model boundaries are respectively La Réole and Pessac on the Garonne and Dordogne river. The maritime boundary is 32 km off the mouth of Gironde estuary, located in Verdon.**

This model, which contains 7351 nodes and 12838 finite elements, does not take into account overflows. It has been calibrated on 4 non-overflowing events and then validated on 6 overflowing events.

In a first step, a propagation and quantification of uncertainties by an unidirectional analysis method (creation of a set of 2000 members perturbed for each parameter and input forcings and analysis of output water depths) was carried out on the numerical parameters (wind influence coefficient, Strickler friction coefficients for 4 zones) and forcings of the model (rivers discharges and maritime boundary conditions, meteorological forcings). The objective is to determine the variation coefficient of water depths for 13 major events between 1981 and 2016. The exploitation of 1981 event results shows a predominance of the influence of the maritime boundary conditions and the Strickler coefficient for the estuarine part and the confluence, to which must be added the Garonne discharge as a predominant parameter for the latter. Unsurprisingly, river zones are influenced primarily by the coefficient of friction and the respective river flows of Garonne and Dordogne rivers.

On the second hand, a Global Sensitivity Analysis (GSA) by variance analysis (ANOVA) was carried out, by calculating the total and partial Sobol' indices, integrating the time- and/or space dependent forcing variables. It has led to the identification of parameters and forcings to which the model is most sensitive, as well as their inter-dependencies, in order to choose the variables to assimilate. The GSA shows that the tidal signal imposed at the maritime boundary condition and provided by a more extended surge levels model is the key input variable. Moving from the mouth to the upstream part of the Garonne and Dordogne rivers, the influence of the friction coefficient increases and hydrological forcings have a very local influence upstream the rivers.

I. INTRODUCTION

Hydrodynamic numerical softwares based on shallow-water equations are commonly used for management and protection of urban infrastructures located near rivers or coasts. They are also used for operational flood forecasting with strong computational constraints. Yet, these numerical codes remain imperfect as uncertainties in the model (numerical schemes, time and space resolution, etc.) and its inputs (model parameters, boundary conditions, geometry, etc.) translate into uncertainties in the outputs. Quantifying uncertainties goes beyond the limits of deterministic forecast and represent a great challenge for Decision Support Systems for risk assessment of crisis management. This study presents a Sensitivity Analysis (SA) that aims at identifying the major sources of uncertainties for water level simulation. Once identified and quantified, these uncertainties can be reduced with data assimilation methods in further works, thus improving water level forecast in the context of flood forecasting on the Gironde estuary.

A wide range of SA methods are proposed in the literature [2] to explain the contribution of the uncertain model parameters to the uncertainty in the model Quantities of Interest (QoI). On the one hand, local SA approaches provide the sensitivity of the model outputs with respect to the model inputs around a reference value using the tangent linear of the model when available or finite differences techniques. A univariate global uncertainty propagation technique is first proposed here. It consists in perturbing uncertain inputs one at a time within physical ranges, computing the corresponding QoI and comparing the

associated relative variations. On the other hand, Global SA approaches (GSA) provide the contribution to the QoI's uncertainty from the uncertain input parameter when varying over the whole input parameter space. A multivariate GSA method (ANOVA) is then presented. It consists in the QoI variance decomposition in terms of elementary variances associated to the different parameters and their interactions.

This paper presents a SA study in the context of flood forecasting in the Gironde estuary. It aims at identifying which input variables should be better described for water levels to be better simulated and forecasted in the estuary. The structure of the paper is as follows: Sect. 2 presents the Gironde estuary hydrodynamic model implemented with TELEMAC2D. The experimental settings for the GSA (univariate and ANOVA) study is presented in Sect. 3. Results are given in Sect. 4. Conclusions and perspectives for the study are finally given.

II. HYDRODYNAMIC MODEL FOR THE GIRONDE ESTUARY

A. Shallow water equations in TELEMAC2D.

The non-conservative form of shallow water equations is derived from two principles: mass conservation and momentum conservation, after expansion of the derivatives. The equations are written in terms of water depth (h) and horizontal components of velocity (u and v).

$$\frac{\partial h}{\partial t}+\frac{\partial}{\partial x}(hu)+\frac{\partial}{\partial y}(hv)=0$$

$$\frac{\partial hu}{\partial t}+u\frac{\partial}{\partial x}(hu)+v\frac{\partial}{\partial y}(hu)=-gH\frac{\partial h}{\partial x}-\frac{1}{K^2}\frac{g|q|uH}{H^{\frac{1}{3}}}-\frac{h}{\rho}\frac{\partial P_{atm}}{\partial x}+\frac{\rho_{air}}{\rho}C_{Dz}U_{w,x}\sqrt{U_{w,x}^2+U_{w,y}^2}+hF_x+\nabla.\left(hv_e\vec{\nabla}(u)\right) \quad (1)$$

$$\frac{\partial hv}{\partial t}+u\frac{\partial}{\partial x}(hv)+v\frac{\partial}{\partial y}(hv)=-gH\frac{\partial h}{\partial y}-\frac{1}{K^2}\frac{g|q|vH}{H^{\frac{1}{3}}}-\frac{h}{\rho}\frac{\partial P_{atm}}{\partial y}+\frac{\rho_{air}}{\rho}C_{Dz}U_{w,y}\sqrt{U_{w,x}^2+U_{w,y}^2}+hF_y+\nabla.\left(hv_e\vec{\nabla}(v)\right)$$

where ρ / ρ_{air} [kg / m^3] are the water/air density , P_{atm} [Pa] is the atmospheric pressure, $U_{w,x}$ and $U_{w,y}$ [m/s] are the horizontal wind velocity components, C_{Dz} [-] is the wind influence coefficient, K [m$^{1/3}$/s] is the river bed and flood plain friction coefficient, using Strickler formulation [3]. F_x and F_y [m/s²] are the horizontal components of external forces (Coriolis force, for example), h [m] is the water depth, H [m NGF69] is the water level (h=H-z_f if z_f [m NGF69] is the bottom level), u and v [m/s] are the horizontal components of velocity, w [m/s] is the vertical component of velocity and v_e [m²/s] is the water diffusion coefficient. *g* is the gravity (9,814 m/s^{-2}). *t* [s] is time , *x* [m] and *y* [m] are the coordinates respectively along longitude and latitude axis.

This decomposition is obtained from an orthogonal decomposition of the uncertain QoI over the probabilized parameter space [1]. A set of sensitivity indices, called Sobol' indices, is estimated. They represent the contribution of each parameter and their interactions to the model output variance. This approach is efficient even for non linear and non monotonic models ([6], [13]).

To solve the set of equations (1), initial conditions $h(x,y,t=0)=h_0(x,y)$; $u(x,y,t=0)=u_0(x,y)$; $v(x,y,t=0)=v_0(x,y)$ are provided along with wall boundary conditions at the coastline (slip: $u=0$ and no normal flow: $u\frac{\partial h}{\partial x}+v\frac{\partial h}{\partial y}+w=0$) and at the upstream and downstream frontiers ($h(x_{BC}, y_{BC},t)=h_{BC}(t)$).

B. Gironde estuary numerical Model.

A hydrodynamics numerical model for the Gironde estuary (presented in Fig. 1) implemented with TELEMAC2D [4] is used to compute water depths and velocities in the estuary and on Garonne and Dordogne rivers. This model is used operationally by the Flood Forecast Service for Gironde Adour Dordogne watersheds (SPC GAD) and SCHAPI (Service Central d'Hydrométéorologie et d'Appui pour la Prévision des Inondations). The maritime boundary is located in the Gascogne Gulf, 35 km away from le Verdon. The upstream boundaries are located on the Garonne River (at La Réole) and on the Dordogne River (at Pessac). It should be noted that inflows from the Isle River and the Dronne are artificially injected at Pessac [5] and that flood plains are not taken into account. The model that covers about 125 km long from east to west features 12838 finite elements and is composed of 7351 nodes.

Surface forcing wind velocity and pressure fields from the regional meteorological model ALADIN are provided by Meteo-France at a 3-hour time step. Hydrological upstream forcing for the Dordogne and Garonne rivers are provided by DREAL (Direction Régionale de l'Environnement, de l'Aménagement des Territoires et du Logement) Nouvelle Aquitaine. Water levels at the maritime boundary, which are the sum of the predicted astronomical tide and surge levels, are also provided by Meteo-France at a 10 to 15 min time step.

The friction coefficient is described over 4 homogeneous areas as described in Fig. 1. The model calibration was achieved over 11 storm events using water level Root Mean Square Error (RMSE) and Nash criteria at high tides

(NASH_HT) computed between simulated and observed water levels where observations are available at the 26 observing stations shown in Fig. 1 (red stars). Two sets of friction coefficients were obtained from calibration and are presented in Tab. 1. The wind influence coefficient C_{Dz} formulates the wind shear stress at the free surface from the wind velocity [8]. A uniform and constant value was chosen here ($C_{Dz} = 2{,}1410^{-3}$) in coherence with the calibration of the surge levels numerical model for Atlantic Ocean, English Channel and North Sea [9].

TABLE 1. CALIBRATED STRICKLER (K) PARAMETERS COMPUTED FROM THE NASH_HT AND RMSE CRITERIA.

Input variable	Updated Strickler coefficients with NASH_HT criterion	Updated Strickler coefficients with RMSE criterion	Uniform distribution over
Ks_1	55	70	[50 ; 70]
Ks_2	70.	70	[45 ; 75]
Ks_3	75	65	[25 ; 75]
Ks_4	50	55	[40 ; 80]
C_{Dz}	$2.57.10^{-6}$	$2.57.10^{-6}$	$[0.678.10^{-6}$; $3.016.10^{-6}]$

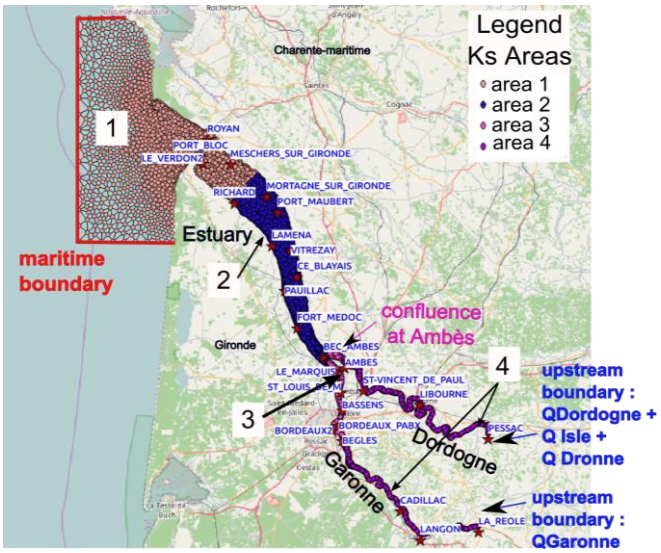

Figure 1. *extension and location of the numerical model of the Gironde estuary and delimitation of the Strickler coefficient areas 1 to 4. Circles represent the nodes of the numerical model based on on a mesh built with finite elements (in black). Red stars show the main measurement stations of interest for the water levels forecast.*

I. METHODOLOGY FOR GSA

A. Uncertain variables for SA

Eight uncertain input variables are considered for the univariate GSA and ANOVA in the following: the 4-zone distributed friction coefficients (K1, K2, K3, K4), the wind influence coefficient C_{DZ} and time-dependent boundary conditions at the hydrological limits (QDOR and QGAR for the Dordogne and Garonne rivers respectively) and at the maritime limit (CLMAR). The uncertain input vector is denoted by X, of components X_i with i in [1, 8]. The QoI is the water level at a specific node and a specific time, it is a scalar and it is denoted by Y in the following. The GSA is applied for water level at the 26 observing stations in Fig. 1, over time.

For each X_i, a Sobol' sequence is used for space filling in a normalized space and the sample is then mapped onto the physical space. Scalar uncertain variables are described by their Probability Density Function (PDF). Here, wind influence coefficient and friction coefficient PDFs are supposed to be uniform with ranges described in Table 1. The critical point is the description of the ensemble from which sensitivity indices are stochastically estimated. For ANOVA, all physical variables should be mapped onto a unit hypercube.

When uncertainty relates to time dependent variables (hydrological time vectors for this study), the dimension of the input space should be reduced for computational reasons. This applies to the time-dependent upstream discharge forcings (Dordogne and Garonne), downstream water level forcing and wind and pressure surface forcing (not treated in this paper). The sampling procedure for these quantities aims at preserving temporal correlation of errors. The discharge chronicles q_T are supposed to be Gaussian Processes with Gaussian correlation function f_T with a correlation length scale L_T, estimated from observed chronicles over the 1981-2016 period. L_T is assumed to depend on the event for the hydrological boundary conditions. It is set to 1.25 days and 3.6 days on the Dordogne and Garonne reaches for 1981. It is set to 1.21 days and 2.91 days for the 2003 event. For both events, L_T is set to 6 hours (half-tide) at the maritime boundary. q_T is written by a Karhunen-Loève decomposition, as the truncated sum of n_p orthogonal functions where ϵ_i coefficients (modes) are independent standard normal variables:

$$q_T(t) = \sum \sqrt{\lambda_i}\ {}_i(t)\ \epsilon_i \quad (2)$$

where $\sqrt{\lambda_i}$, ${}_i(t)$ are the eigen values and eigen functions for the Fredholm equation with *C* the Gaussian correlation function:

$$\forall i \in \int C(t_1,t_2)\ {}_i(t_2)dt_2 = \lambda_i\ {}_i(t_1) t_1 \in T \quad (3)$$

Eq. (3) is discretized:

$$C\psi_i = \alpha_i \psi_i \quad (4)$$

with $C_{i,j} = f(t_i, t_j)$, α_i and ψ_i (vector of size t_N) are the i^{th} eigen values and vectors of C, computed with a Singular Value decomposition (SVD). This leads to

$$q_T(t_1, \ldots t_N) = \sum \sqrt{\alpha_i}\psi_i\ \epsilon_i \quad (5)$$

From Eq. (5), a set of N_e boundary condition time dependent vectors are generated with a sampling of ϵ_i. The

amplitude of the perturbation is set proportional to the observed chronicle (1.04 multiplying factor for Dordogne and Garonne, 1.012 for the maritime boundary). This leads to a maximum discharge variance of 20 % and a maximum water level variance of 50 cm for the maritime boundary. A set of perturbed forcing for the Garonne boundary conditions are shown in Fig. 2.

The GSA is thus carried out in an uncertain space described by 20 variables: 4 Strickler coefficients, the wind influence coefficient Cdz, the 4 principal modes for each river discharge q(t) QDOR and QGAR and the 7 principal modes for the maritime boundary tide signal. However, for each time-dependent variables (river discharges and tide signal at the maritime boundary), perturbations for each mode are then aggregated by to the physical input space.

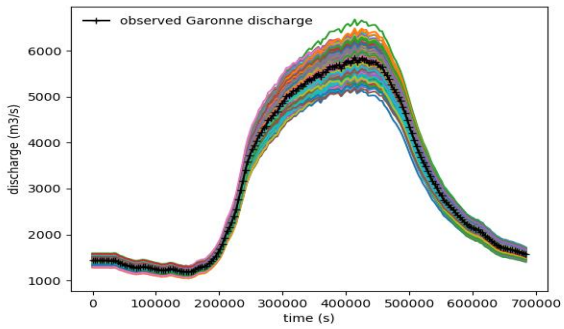

Figure 2. *Observed (in black) and Perturbed (other colors) Garonne discharge during 20030202 event.*

B. Coefficients of variation for univariate analysis

The coefficient of variation is defined with respect to each uncertain input variable X_i, at a given time step and at a given mesh node, as $CV=\frac{\sigma}{\mu}$, with σ and μ the standard deviation/ensemble-mean of the uncertain output Y (resp. uncertain input X_i) variable computed over the sample $E_u(X_i)$. The ratio $\frac{CV(Y)}{CV(X_i)}$ is then formulated.

C. ANOVA method and Sobol' indices

We consider a numerical model of the form $Y=f(X_1, X_2, \ldots X_k)$ with uncertain input vector X and uncertain output scalar variable Y. It is assumed in the following that the input parameters are scaled with respect to physical parameters. V_i is referred to as the "variance of conditional expectation" of Y given X_i and the subscript $X_{\sim i}$ denotes the vector X deprived from of all factors other than X_i.

The variance of the output Y is the sum of the contribution from the different input parameters:

$$V_{i,j}+\ldots+V_{1,2,\ldots,k} \quad (6)$$

where $V_i = V_{X_i}\left(E_{X_{\sim i}}\left(Y \mid X_i\right)\right)$ and

$$V_{i,j} = V_{X_i,X_j}\left[E_{X_{\sim i,j}}\left(Y \mid X_i, X_j\right)\right] - V_{X_i}\left(E_{X_{\sim i}}\left(Y \mid X_i\right)\right) - V_{X_j}\left(E_{X_{\sim ij}}\left(Y \mid X_j\right)\right)$$

Dividing Eq. (6) by V(Y) leads to:

$$S_{i,j}+\ldots+S_{1,2,\ldots,k}=1 \quad (7)$$

In Eq. (7), the S_i indices are the sensitivity coefficients (also called first order Sobol' indices) .The second order indices $S_{i,j}$ (second-order Sobol' indices) measure the variance in Y for higher orders. The S_{Ti} shows all contribution related to X_i: .

$$S_{Ti} = 1 - \frac{V_{X_i}\left(E_{X_i}\left(Y \mid X_i\right)\right)}{V(Y)} = \frac{E_{X_i}\left(V_{X_i}\left(Y \mid X_i\right)\right)}{V(Y)} \quad (8)$$

It should be noted that $S_i = 1$ for numerical models without interaction between the input parameters.

The main steps for the stochastic estimation of the Sobol' indices are described in the following. For more details, the reader can refer to [12] and [10].

1. Generation of an ensemble of size N_e (here N_e = 1000) for the normalized input parameters of size k. The (N_e, k) matrix is denoted by **A**. The space filling strategy is carried out with a Sobol' sequence rather than a classical Monte-Carlo strategy. The conditional probability computation requires the formulation of another sampling denoted by **B**:

,

$$A=\begin{bmatrix} x_1^{(1)} & x_2^{(1)} & \ldots & x_i^{(1)} & \ldots & x_k^{(1)} \\ x_1^{(2)} & x_2^{(2)} & \ldots & x_i^{(2)} & \ldots & x_k^{(2)} \\ \hline x_1^{(N-1)} & x_2^{(N-1)} & \ldots & x_i^{(N-1)} & \ldots & x_k^{(N-1)} \\ x_1^{(N)} & x_2^{(N)} & \ldots & x_i^{(N)} & \ldots & x_k^{(N)} \end{bmatrix}$$

$$B=\begin{bmatrix} x_{k+1}^{(1)} & x_{k+2}^{(1)} & \ldots & x_{k+i}^{(1)} & \ldots & x_{2k}^{(1)} \\ x_{k+1}^{(2)} & x_{k+2}^{(2)} & \ldots & x_{k+i}^{(2)} & \ldots & x_{2k}^{(2)} \\ \hline x_{k+1}^{(N-1)} & x_{k+2}^{(N-1)} & \ldots & x_{k+i}^{(N-1)} & \ldots & x_{2k}^{(N-1)} \\ x_{k+1}^{(N)} & x_{k+2}^{(N)} & \ldots & x_{k+i}^{(N)} & \ldots & x_{2k}^{(N)} \end{bmatrix}$$

2. Definition of k matrices C_i formed by all columns of A except the i^{th} column taken from B [12].
3. Computation of the model output for all the input values in the sample matrices A, B and the k matrices C_i, obtaining (k+2) vector outputs of

dimension N*1: $y_A = f(A)$, $y_B = f(B)$, $y_{C_i} = f(C_i)$ with i=1, …, k.

In this study, according to [12], [7] and [11] which describes the best practices for the simultaneous computation of S_i and S_{Ti} for each input variable, the following estimators have been chosen for the computation of:

- S_i ,
$$V_{X_i}\left(E_{X_{\sim i}}(Y \mid X_i)\right) = \frac{1}{N}\Sigma_{j=1}^{N} y_B^{(j)}\left(y_{C_i}^{(j)} - y_A^{(j)}\right)$$
- S_{Ti} ,
$$E_{X_i}\left(V_{X_i}(Y \mid X_i)\right) = \frac{1}{2N}\Sigma_{j=1}^{N}\left(y_A^{(j)} - y_{C_i}^{(j)}\right)^2$$
- $V(Y)$, $V(Y) = \frac{1}{N}\Sigma_{j=1}^{N}\left(y_A^j\right)^2 - f_0^2$ with $f_0^2 = \frac{1}{N}\Sigma_{j=1}^{N} y_A^j y_B^j$

II. GSA RESULTS

1. *Uni-variate GSA results*

The univariate GSA was carried for 12th-17th December 1981 event, characterized by a tide coefficient of [57 ; 106] and Dordogne (resp. Garonne) discharge of [1000 ; 2350] m^3/s (resp. [1700 ; 7050] m^3/s). In this study, for each input variable, a sample of 2000 perturbed realisations is generated.

The normalized variation coefficient is displayed over time in Fig. 3 for each uncertain variable X_i along the curvilinear abscissa from Royan to the confluence at bec d'Ambès (1st black vertical line), from the confluence to La Réole (Garonne river area located between both black vertical lines) and from the confluence to Pessac on the Dordogne river (Dordogne river area on the right of the 2nd black vertical line). The red vertical lines represent the limits between the 4 friction coefficients areas. The dashed lines represent the time-aggregated values for standardized coefficients of variation along the Gironde estuary.

Fig. 3a highlights the predominant influence of the maritime boundary condition.

This influence is strongly related to the tide periodicity over the estuary and beyond the confluence. When the influence of the maritime boundary condition decreases, the coefficient of variation for the friction coefficient increases especially in areas 1 to 3 (Fig. 3c, d, e).

This influence is strongly related to the tide periodicity over the estuary and beyond the confluence. When the influence of the maritime boundary condition decreases, the coefficient of variation for the friction coefficient increases especially in areas 1 to 3 (Fig. 3c, d, e).

The friction coefficient in area 4 has barely no impact on water level (with very low coefficient of variation in Fig. 3f) except upstream of the Dordogne river.

The hydrological boundary conditions have an impact that is limited to the extreme upstream part of the domain (Fig. 3g, h) for both Garonne and Dordogne rivers. The wind influence coefficient in Fig. 3c has a negligible influence on water level over the entire domain. It could thus remain fixed to a nominal value for further analysis. Overall, there is complementary behaviour between maritime boundary conditions and friction coefficients chosen for areas 1, 2 and 3 where Ks_1, Ks_2 and Ks_3 are applied.

This univariate SA only provides a qualitative feedback on the impact of each uncertain input variables on the water level uncertainty. A quantitative feedback is given by the ANOVA; it also describes how uncertainties in the inputs variables interacts.

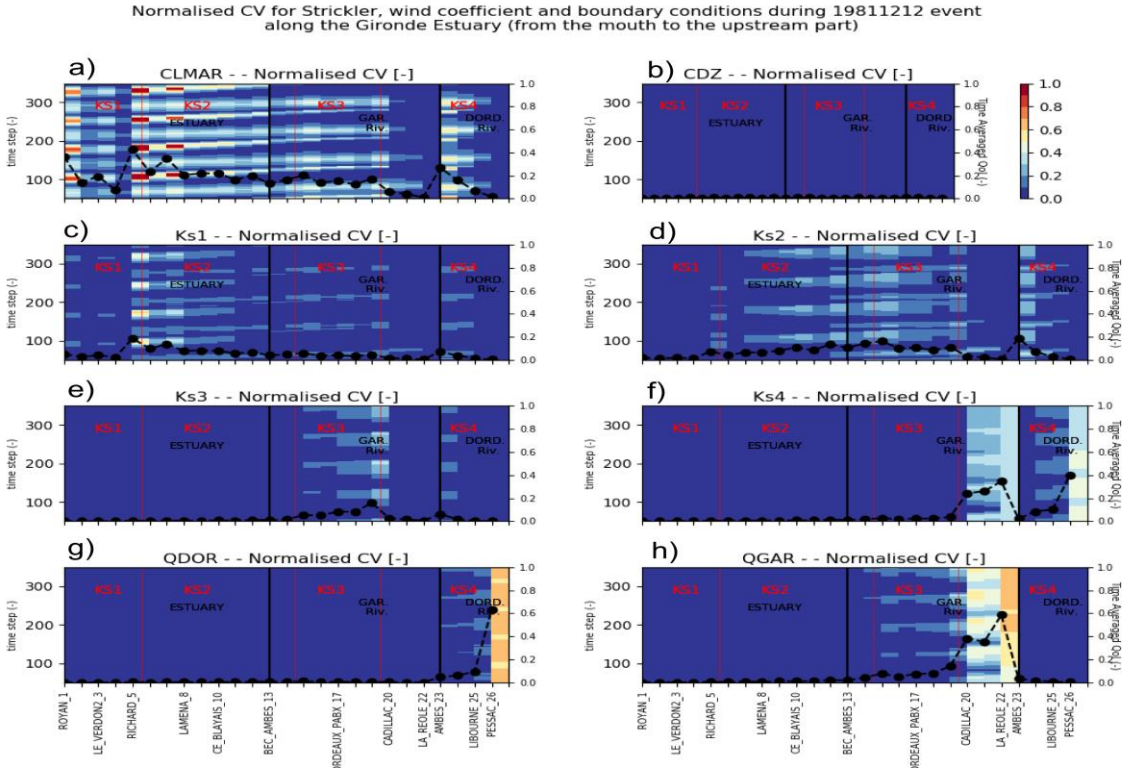

Figure 3. *Normalized coefficient of variation along the Gironde estuary during decembre 1981 storm for a) the maritime boundary conditions b) the wind influence coefficient c) friction coefficient in area 1, Ks1 d) friction coefficient in area 2, Ks2, e) friction coefficient in area 3, Ks3, f) friction coefficient in area 4, Ks4, g) the discharge of the Dordogne and Isle rivers at Pessac and h) the discharge of the Garonne river at La Réole.*

2. *ANOVA results*

The ANOVA GSA study was carried for 2nd-9th February 2003 event, characterized by a tide coefficient of [43 ; 90] and Dordogne (resp. Garonne) discharge of [600 ; 2200] m^3/s (resp. [1200 ; 5900] m^3/s). For each input variable, a sample of 1000 perturbed realisations is generated.

Sobol' indices are displayed in Fig. 4 with a blue-red color bar for the 8 uncertain inputs X_i, over time and along the curvilinear abscissa. The x-axis is similar to that of Fig. 2, with the 26 observing stations classified from left to right for downstream to upstream. The red vertical lines represent the limits between the 4 friction coefficients areas. The black vertical lines represent the limits between the estuary, the confluence and the Garonne and Dordogne rivers. For each input variable, the total Sobol' indices are plotted in panels –a and the difference between total and first order indices are plotted in panels –b. For panels –a, blue/red means small/large Sobol' indices; for panels –b, blue/red means small/large interactions of X_i with other uncertain variables. The thick dashed line represents time-averaged Sobol' indices. Fig. 5 provides a ranked interpretation of Fig. 4 where input variables are classified by order of predominance over time and over the curvilinear abscissa (1 for most significant to 8 for non-significant). Total Sobol' indices and rank are time-averaged and plotted in Fig. 6 for all X_i along the y-axis. along the Gironde estuary.

Fig. 4 clearly shows the predominance of the maritime boundary condition and the dependency of all variable impact on the tidal signal. As previously mentioned, the wind influence coefficient, the hydrological boundary conditions and the friction coefficient in area 4 have no influence on the water level variability except at the upstream location of Garonne and Dordogne.

Over area 1, the water level variance is explained by the variance in the boundary condition with Sobol' indices closed to 1 from Port-Royan (station 1) to Richard (station 5) near the mouth of the estuary. It should be noted the part of water level variance that is not explained by CLMAR is explained by Ks1.

Over area 2, CLMAR and Ks_2 are the most significant sources of uncertainty with a predominance of CLMAR at high tide. At low tide, the Sobol' index for Ks_2 reaches 0.8. The influence of the maritime boundary condition decreases from Fort-Medoc to the confluence between Garonne and Dordogne and the influence of Ks_2 and Ks_3 increases. At La Réole and Pessac, Sobol' index for Ks_4 reaches 0.8.

It should be noted that only the maritime boundary condition and Ks_3 have interactions with the other input variations, these cross-effects reach 30% for CLMAR.

Fig. 6 represents the time-averaged total Sobol' indices and corresponding ranks for each input variable. As expected, the maritime boundary conditions is predominant for the entire domain with significant influence of friction coefficients, while hydrological boundary conditions have a limited impact to the upstream locations of Garonne and Dordogne.

III. Conclusions

The numerical T2D model operationally used by SPC GAD to forecast water levels along the Gironde estuary was studied through a uni-variate uncertainty analysis and a global sensitivity analysis based of variance decomposition (ANOVA) to provide Sobol' indices. The uni-variate uncertainty analysis over December 1981 event leads to similar conclusions as the ANOVA over the 2003 event. However, it also enables to quantify the contribution of each variable during the storm and the part of the variance linked to interactions between variables. SA show that the tidal signal imposed at the maritime boundary condition and provided by a more extended surge levels model is the key input variable. Moving from the mouth to the upstream part of the Garonne and Dordogne rivers, the influence of the friction coefficient increases and the hydrological forcing have a very local influence upstream the rivers.

A perspective for this study is to use a bootstrap method to compute the confidence interval for Sobol' indices. Moreover, time and spatial dependent uncertain input variables such as the meteorological forcings associated to a tide signal should also be included in the SA.

Finally, this SA approach allows to identify the significant sources of uncertainty that should be reduced with data assimilation, for instance with an ensemble Kalman Filter, in order to improve the water level at key location on the estuary in simulation and forecast mode.

Acknowledgement

We would like to thank the service in charge of flood forecast on Garonne, Adour and Dordogne watersheds (SPC GAD), METEO-FRANCE and Greater Maritime Port Councils of Bordeaux (GPMB) for bathymetric and observation data they provided for the needs of this study. The sea level observations along Gironde estuary are the property of GPMB and of the French Ministry in charge of sustainable development (MEEM). A lot of thanks, too, to Yoann AUDOUIN (EDF/LNHE) for his support in the implementation and use of TELEMAC2D.

References

[1] [Efron & Stein, 1981] Efron, B.; Stein, C., (1981), *The Jackknife Estimate of Variance*. Ann. Statist. 9 ,no. 3, 586--596. doi:10.1214/aos/1176345462- http://projecteuclid.org/euclid.aos/1176345462.

[2] [Iooss & Lemaître, 2014] Iooss, B, Lemaître, P, (2014), *A Review on Global Sensitivity Analysis Method*s, Chapter Uncertainty Management in Simulation-Optimization of Complex Systems, Volume 59 of the series Operations Research/Computer Science Interfaces Series, pp 101-122

[3] [Gauckler, 1867] *Gauckler, Ph., (1867), Etudes Théoriques et Pratiques sur l'Ecoulement et le Mouvement des Eaux*, Tome 64, Paris, France: Comptes Rendues de l'Académie des Sciences, pp. 818–822

[4] [HERVOUET, 2006] Hervouet J.M. (2006) - *Hydrodynamics of free surface flows*. Ed. Wiley. 390 p.

[5] [Hissel, 2010] Hissel, F, (2010), *Projet Gironde – rapport final d'évaluation du modèle Gironde*, 70 p.

[6] [Homma & Saltelli, 1996] Homma, T, Saltelli. A, (1996), *Importance Measures in Global Sensitivity Analysis of Nonlinear Models*, Reliability Engineering & System Safety 52 (1), pp 1-17

[7] [Janssen, 1999] Janssen, M.J.W., (1999), *Analysis of variance designs for model output*, Computer Physics Communications 117, pp 35–43.

[8] [Levy, 2013] Levy, F., (2013), *Construction d'un modèle de surcotes sur la façade atlantique*, rapport provisoire

[9] [Levy & Joly, 2013] Levy, F., Joly, A., (2013), *Modélisation des surcotes avec TELEMAC2D*, rapport EDF à accessibilité restreinte, 79 p.

[10] [Nossent & al., 2011] Nossent, J., Elsen, P., Bauwens W., (2011,), *Sobol' sensitivity analysis of a complex environmental model*, Environmental Modelling & Software Volume 26, Issue 12, pp. 1515–1525

[11] [Saltelli, 2002] Saltelli, A., (2002), *Making best use of model evaluations to compute sensitivity indices*, Computer Physics Communications 145, p. 280–297

[12] [Saltelli, 2010] Saltelli, A., Annoni, P., (2010) How to avoid a perfunctory sensitivity analysis, Environmental Modelling & Software 25 (12), p. 1508-1517

[13] [Saltelli 2015] Becker, W, Saltelli, A, (2015), Design for Sensitivity Analysis, Handbook of Design and Analysis of Experiments, p. 627-673

[14] [Sobol', 1991] Sobol', I. M. 1993. *Sensitivity Analysis for nonlinear mathematical models.* Mathematical Modeling & Computational Experiment 1, p 407-414.

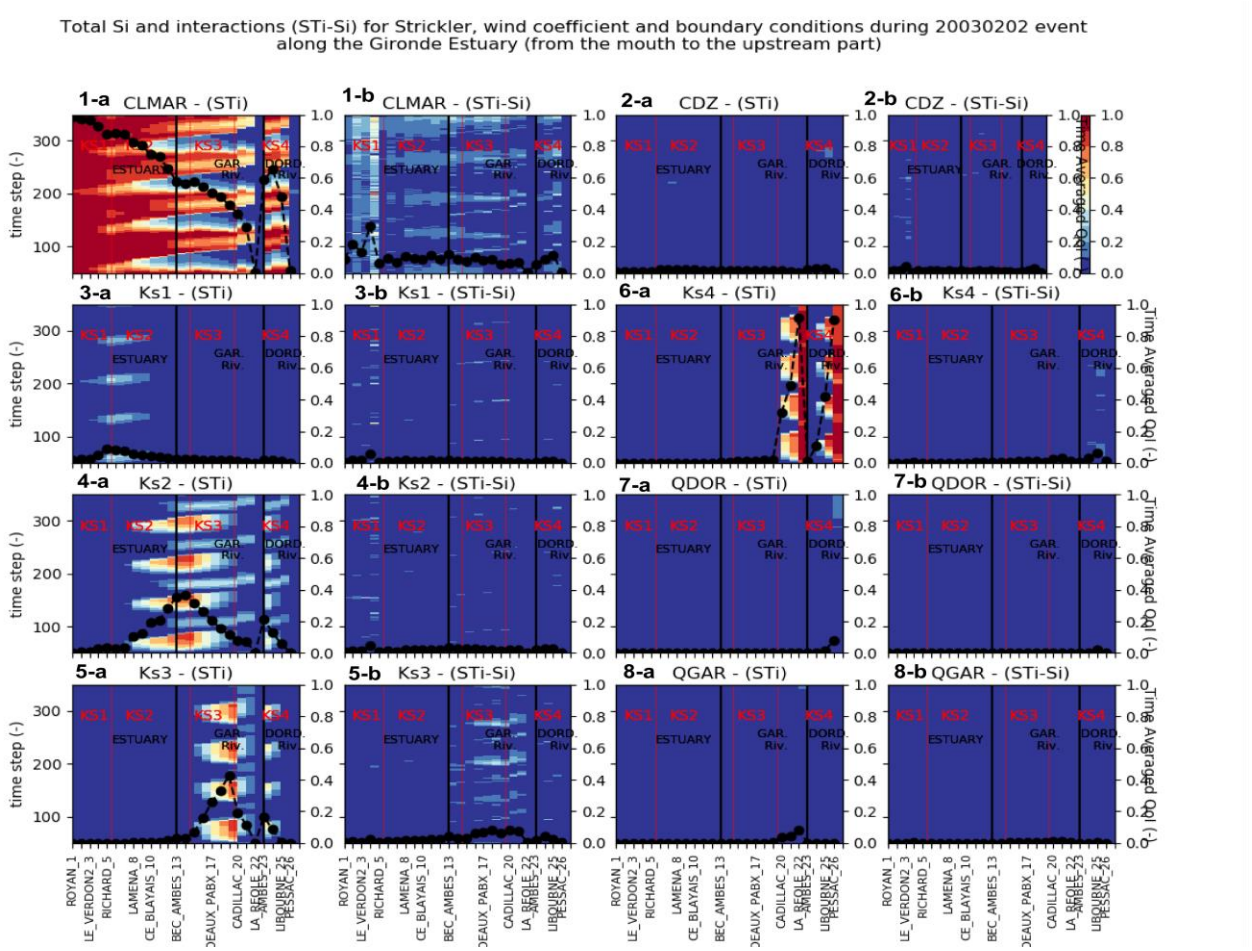

Figure 4. *Total Sobol' indices (ST_i) in panels a- (resp. interactions STi - S_i in panels b-) along Gironde estuary during february 2003 storm for 8 uncertain input variables (maritime boundary conditions (CLMAR), friction coefficients (Ks1, Ks2, Ks3, Ks4), the wind influence coefficient Cdz and hydrological boundary conditions (Dordogne river discharge: QDOR ; Garonne river discharge: QGAR).*

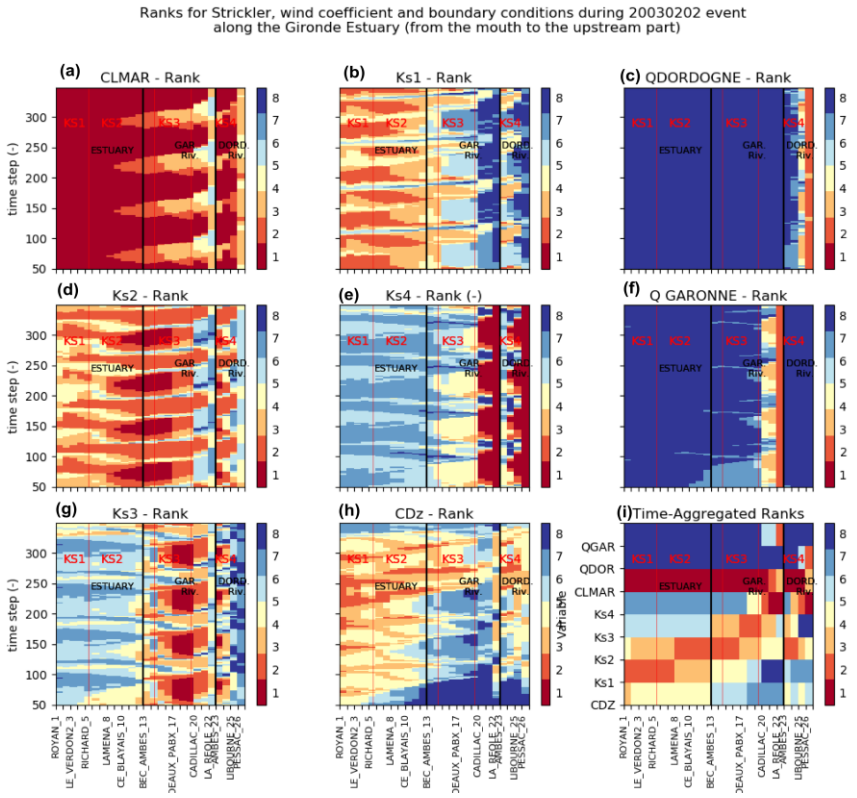

Figure 5. *Predominance rank of the 8 input variables over time along Gironde estuary during february 2003 storm for panel a- to h- (CLMAR, Ks1, Ks2, Ks3, Ks4, CDz, QDOR and QGAR) and time aggregated ranks (panel i-).*

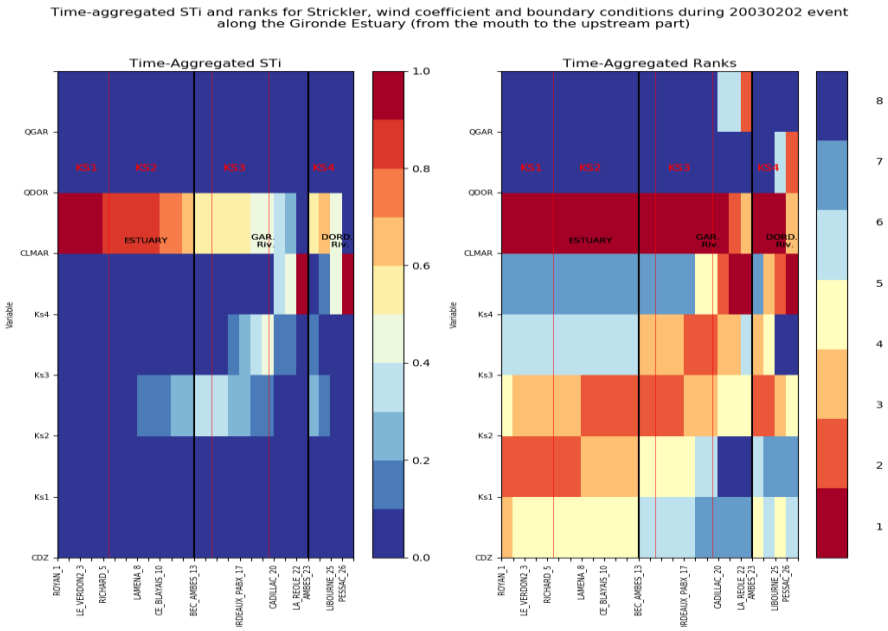

Figure 6. *representation of time aggregated Sti (on the left) and of the rank of the input variable with respect to Sti (on the right) along Gironde estuary during February 2003 storm.*

Flood Wave Modelling and Risk Analysis of Overtopped Embankment Dams

Gabriele Harb
VERBUND Hydro Power
Vienna, Austria
gabriele.harb@verbund.com
gabriele.harb@gmx.at

Hannes Badura, Wolfgang Troy
VERBUND Hydro Power
Vienna, Austria
hannes.badura@verbund.com
wolfgang.troy@verbund.com

***Abstract*— The paper presents the application of Telemac2D modelling 72h real-time of the design flood wave within a 40km river reach. Five reservoirs and flood plains up to 6km width are fully implemented in the geometry. The used meshes have an average edge length of 2-10m or 1.8 – 4.9 Mill elements within the whole domain. Time steps of 0.025-0.1s were used due to the full numerical modelling of the weir structure. The Elder model and the mixing length model were used for turbulence modelling. The application was contributed by a scientific project at the Vienna Science Cluster up to 128 core parallelized computation.**

The focus of the numerical investigation was i) the simulation of the steady and unsteady water levels and flow velocities in the river and on the flood plains, and ii) the risk analysis of the overtopped embankment dams. Several scenarios with artificial breaches in the embankment dams were simulated and the effect of the breaches analysed.

I. INTRODUCTION

Climate change affects the hydrological scheme of a river and - in order to rate discharges for flood protection - the Austrian province of Styria and the country of Slovenia decided to harmonize hydrological parameters along the Mur river. This leads to higher flood design values from Graz to the Slovenian boarder. As a consequence of higher design values, the safeness of embankment dams of this run-off river plant influenced river reach was no longer proved.

A simply increase of dam height would be the solution, but in last consequence, an elimination of flood plains leads to a downstream shift of flood wave propagation as well as higher discharge peaks. Therefore, preservation of designated flood plains as well as increasing flood wave propagation within the river reach is a must have for downstream urban areas. VERBUND Hydro Power, which is the operator of the hydro power plants (HPP) between Graz and the Slovenian border, decided to investigate the feasibility of conservation of overtopped embankment dams.

Due to the complexity of hydraulic exchanges between river and flood plains, TELEMAC was used to investigate the hydraulic conditions during flood wave, hydraulic parameters at the overtopped embankments as basis for structural safety measures of dams (small scale), and as a tool for confirmation of measures in large scale.

Additionally, reservoir sedimentation management measures were not permitted since the start of operation of the HPPs. The water level was kept at maximum operation level all the time, sediment particles settled in the reservoir. In further consequence the reservoirs have been “filling up”. Due to the relatively small reservoirs and low water depth in Alpine run-off river and diversion plants a large part of the suspended sediments is transported through the reservoir and the deposition of bed load fractions at the head of the reservoir is the main problem. A flushing strategy has thus been worked out and is currently permitted to solve this problem.

The focus of the project lies on the safety of the embankment dams against erosion caused by overtopping or seepage. The flood protection of urban areas in the flood plains is in the responsibility of the local authorities and thus not part of this project. Nevertheless, a general outlines of the possible flood protection for the communities in the flood plains have been carried out.

II. PROJECT AREA AND BACKGROUND

A. *Project Area*

The project area is a chain of five run-off-river hydro power plants (HPP) at the lower Mur in Styria, Austria (Fig. 1). Due to the flat landscape the leading embankment dams of the hydro power plant are up to 4 m high. This contribution focuses on the overtopping problems at the HPP Obervogau and the HPP Spielfeld.

The inflow data for the river Mur is shown in Tab. 1, the tributaries create the difference between inlet and outlet flow rate.

TABLE 1. HYDROLOGICAL CONDITIONS IN THE PROJECT AREA

Hydrology project area		
Flow condition	***Inlet [m3/s]***	***Outlet [m3/s]***
mean discharge	125.5	144
1-year flood	460	710
10-year flood	800	1200
30-year flood	1050	1460
100-year flood	1400	1750

B. *Background of the Flood Problems*

The HPP were designed and constructed in the 1950s to 1980s. At this time, the state of the art of HPP design included a manual backwater calculation, in the best case a HEC2 calculation of the water levels in the reservoir including the design flood events but neglect water exchange capabilities in the river-flood plain interaction. Due to less or inexistent water level gaugings at that time, hydraulic calculations were based on experience of experts. However, the low roughness values used back then give rather low water levels in the calculations. Since then, the used roughness values have been increased due to sediment transport, bed forms, and roughness of the geometry. This leads to higher water levels compared to the second half of last century.

Due to the rapid development of computational fluid dynamics (CFD), the increased computer power and the availability of clusters and parallel processing, the state-of-the-art in numerical modelling has changed completely in fields of hydraulics in the last decades. Nowadays, state of the arte 2d-models with accurate calibration data are used to model river reaches.

The lower Mur river in the province of Styria is next to the border to Slovenia. In this river Section, the design values for the flood events (30-year flood, 100-year flood, 300-year flood) were lower than in Slovenia, which led to flood problems in Styria, because the Slovenian embankment dams were higher. In the early 2000's, the governments of Styria and Slovenia harmonized the design flood values. This harmonization resulted in higher design flood values in the Austrian part of the Mur river. Together with no implemented reservoir sedimentation management in the last decades, this harmonization cause problems of the possible erosion of overtopped embankment dams and leads to a flood protection problem for the surrounding areas in the case of design floods.

III. OUTLINE OF THE PROJECT

The two main parts of the project were the modelling of the flood waves and the dam break scenarios.

A. *Design Flood Scenarios*

Basically two types of design flood scenarios were carried out:

- Steady scenario: Simulation of the design flood values until steady state, which is usually used in Austria to map the flood extent in terms of the Flood Directive 2007/60/EC
- Unsteady scenarios: Simulation of the design flood waves using the flood waves shown in Fig. 2 to indicate the flow path and the linking of the retention basins

The water levels and flow velocities at the air face of the embankment dams are important for the stability analysis of the dams. The complexity of hydraulic exchanges between river and flood plains is part of this analysis. Alternating water levels on both sides of the dams at different time steps of the flood have to been taken into account to analyse dam stress conditions.

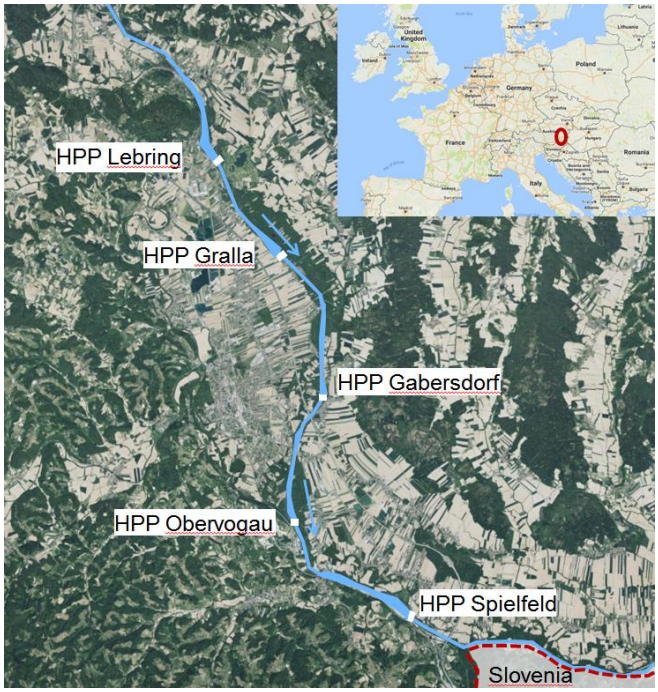

Figure 1. *Project area at the river Mur including five run-off river hydro power plants in Styria, Austria*

B. *Dam Break Scenarios*

The embankment dams are earth-fill dams mostly without special waterproofing measures, but their stress and piping stability is confirmed. The embankment dams of the reservoirs in the project area are not designed for any overtopping event, because the design flood values (100-year flood) have been increased since the start of power plant operation. The embankment dams are constructed as earth-fill dams. Overtopping events can lead to the erosion of the embankment dams. A dam break scenario analysis for the embankment dams was thus performed based on the results of the design flood

Several different dam break scenarios have been modelled and analysed. The scenarios can be divided into two groups:

- Small breach scenarios: Dam breach of 15-20 m in a section of the embankment dam, where overtopping starts (Fig. 4).
- Large breach scenarios: Dam breach over the whole overtopping section of the embankment dam, where overtopping starts. In these scenarios the breach length is between 0.9 – 1.2 km.

The breach depths are in both scenario groups approx.2/3 of the total dam height based on the embankment dam width and the water depths above dam crest.

IV. NUMERICAL MODELLING

A. *Design Flood Scenarios*

The paper presents the application of Telemac2D modelling 72h of the HQ30 and HQ100 flood waves in a 40km river reach with five reservoirs (weirs fully implemented in the geometry) and flood plain with up to 6km. Different meshes were used i) to ensure mesh independency and ii) to analyse flow processes in detail. For the analysis of the mesh independency analysis basically three smaller meshes (river Mur and smaller floodplain) were analysed (0.5; 2.0;8.0 Mill nodes). The results of the meshes showed no significant differences. For the flow analysis, the refinement of the mesh in the overtopping areas was necessary, also to prevent numerical piping.

The selected meshes have average edge lengths of 2-10m and 1.8 – 4.9 Mill elements. The edge lengths in the mesh is smaller in the river, in overtopping areas and next to urban areas than in the woods and meadows of the floodplains. The chosen time steps were rather low (0.025-0.5s) caused by the full geometrical implementation of the weirs in the mesh and the high flow velocities at the weirs. The turbulence was modelled using the Elder model and the depth-averaged mixing length model [2].

Why was the whole mesh used in the calculations and not split up? The most important reasons are: Due to the large flood plains, it was not straight forward to ensure a clear inflow and outflow sections. To avoid multiple interconnected inflow and/or outflow conditions especially for the unsteady simulations, the mesh was cut into two clear sections were the inflow and the outflow could be defined clearly. Additionally, we were not sure about the interconnection of the flood plains. We decided better to model the whole domain than to miss some relevant flow path or modify the unsteady flood wave by using wrong outflow conditions.

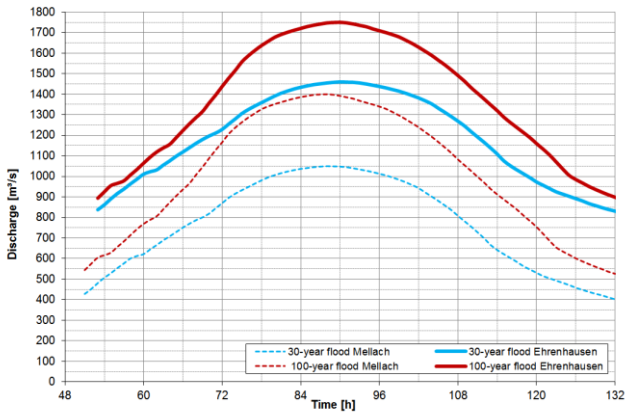

Figure 2. *30-year and 100-year flood wave at different sites in the project area*

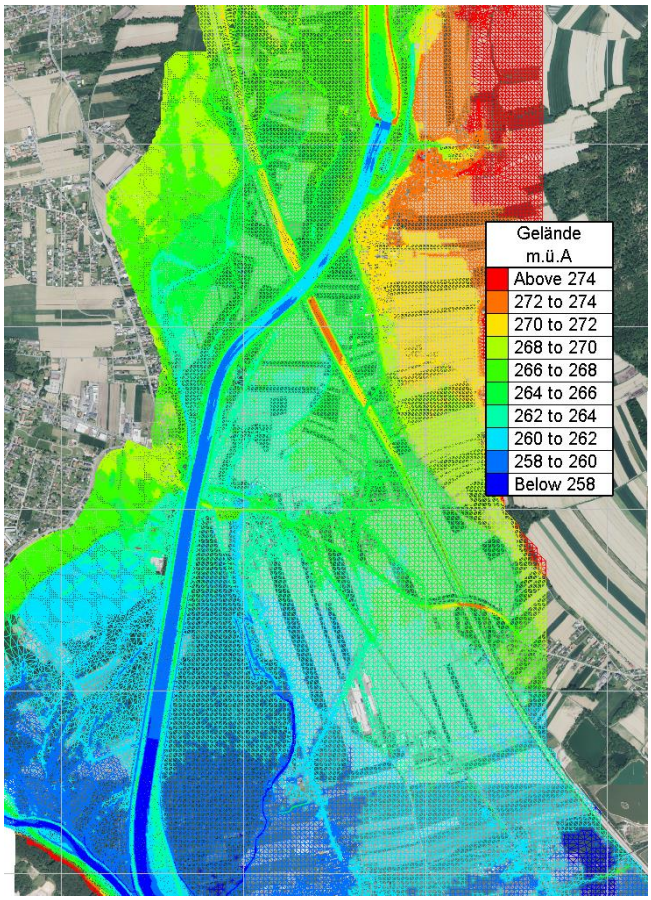

Figure 3. *Detail of the mesh next to the reservoir of the HPP Obervogau*

The simulations were mainly performed at the HPC cluster VSC3 in Vienna using 32 – 128 cores. The total used computation time for the calibration and validation of the model and the modelling of different bed levels and embankment dams are about 50.000 CPUh.

In the project area, there are three rivers feeding the river Mur: The river Kainach upstream of the reservoir Lebring, the river Stiefing downstream of the HPP of Gabersdorf and the river Sulm downstream of the HPP Obervogau. These rivers were fully implemented in the model within the floodplain area of the river Mur. The used flood waves are shown in Fig. 2. E.g., the simulation of the 100-year flood wave starts with a discharge of 650m3/s upstream of the reservoir Lebring and including the three feeding rivers 700m3/s at the outlet. A hotstart file was thus created to cut the first 50h of the flood wave, where no overtopping takes place. In total 72h of the flood wave were modelled, which reflects the peak of the flood wave between 50h and 122h in Fig. 2.

The mesh includes all geometrical relevant parts of the river bed and the flood plains, including over 14.000 buildings, highways, roads, culverts, and water bodies (ditches, etc.). A part of the mesh is shown in Fig. 3.

The calibration of the whole domain was done using the data of three gauges and the measured downstream water levels of the HPPs, which are located in the project area. The discharge-water level curves showed that the Elder model and the mixing length model gave the best results using constant roughness values over time. The used roughness values (Strickler) in the river bed were between 35 and 38$m^{1/3}/s$.

B. *Dam Break Scenarios*

All dam break scenarios based on the design flood scenarios and the same numerical parameters were used.

The dam break scenarios were also modelled with Telemac2D without any sediment transport module like Sisyphe, because the focus lied on the difference in water depth and flooded areas in the retention areas and not on the erosion process like in other studies (e.g., [1]). Due to the small dam heights compared with other dam break studies the wave height generated by the dam break would be very small. The simulations was thus running until overtopping in the defined section took place and after overtopping the simulations was stopped. Then the dam break was implemented in the geometry and the simulation contained (Fig. 4).

The breach width (small or large), the erosion time ($\Delta t=0$) and the breach depth (approx.2/3 of the total dam height) was fixed in the study, other dam breach parameters and their uncertainties, which are discussed in several studies (e.g., [3]) had been skipped. The water depth and the flooded area shortly after the dam break is thus a worst case scenario. However, the overtopping in the different retention basins takes place between hour 55 to hour 65 of the flood wave. The peak of the flood wave is between hour 90 to 92, depending on the river section. The wave effect of the dam break is thus smoothed out due to the massive flooding of the areas after.

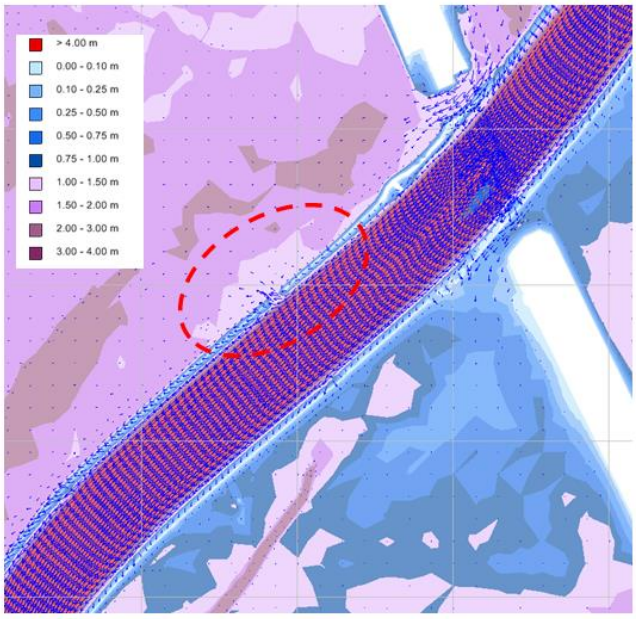

Figure 4. *Example of a small breach scenario (section R3)*

V. RESULTS

The first part of the analysis focused on the water depth and the flow velocities in the project area. In the next step, the overtopping sections were analysed and then the dam break scenarios created.

A. *Design Flood Scenarios*

The results of the design flood scenario of the 100-year flood show massive water depths in urban areas forms by the highway and roads together with the natural steps in the landscape. Retention basins are thus activated, which are filled up to 3 m with water depths after the overtopping of the embankment dams. There are also partly high flow velocities at the air face of the embankment dams and next to culverts or bridges (see Fig. 8 and Fig. 9).

As presented in Fig. 8 in all retention basins water depth with more than 2 m can be found. In the retention basins R3, R4, R6 next to HPP Spielfeld and R7 water depths reaches more than 3 m. Fig. 8 show the flow velocities. The flow velocities in the flood plains are usually lower than 1 m/s. However, in areas next to culverts, bearings of bridges or on road dams, the velocities can reach 2 to 3 m/s.

The flow path of the overtopping water are analysed using the unsteady flow calculations. The interlinkage of the natural retention basins is very important to understand the filling process and to find the “worst case scenarios” for different parts of the modelled river sections.

For the systematic analysis of the flood plains, the river domain in this area was classified into seven retention basins with different inflow and outflow characteristics as well as varying dam heights and urbanised areas. The retention basins are filled up after the overtopping of the embankment dams. The overtopping heights and the length of the overtopping sections vary over time.

In the project area several embankment dams are overtopped in case of floods. The water depths above dam crest are up to 1.2 m. A magenta solid line indicates the overtopped or bank full embankment dam sections in Fig. 8. The embankment dam sections can be roughly classified using the overtopping heights and the height of the embankment dam:

- low embankment dam height (<1.5 m), high overtopping (>0.5m); e.g. in retention basin R1, R7, R6 downstream of HPP Obervogau
- medium embankment dam height (1.5 m<h<3 m), medium overtopping (>0.3m); e.g. in retention basin R2, R3, R4, R6 upstream of HPP Spielfeld
- high embankment dam height (>3 m), moderate overtopping (<0.3m); e.g. in retention basin R5 and R6 upstream of HPP Obervogau

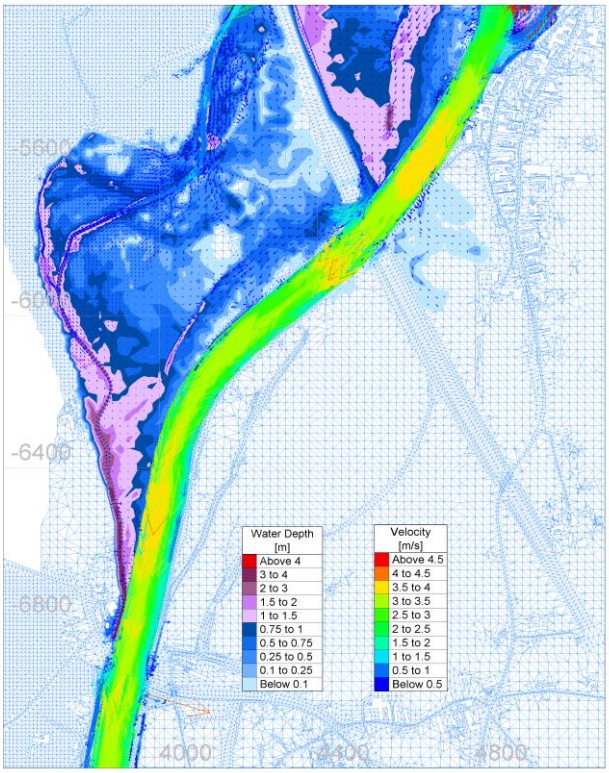

Figure 5. *Flow conditions in R3 shortly after start of overtopping – the upstream part of the embankment dams are overtopped and the retention basin R3 is filled up*

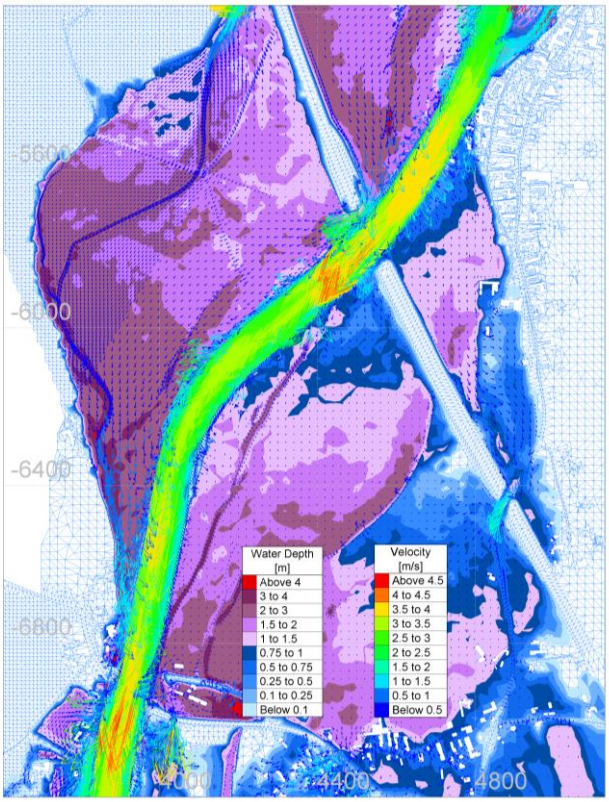

Figure 6. *Flow conditions in R3 when reaching the top of the 100-year flood wave – the upstream part of the embankment dams are still overtopped, the retention basin R3 is completely filled up and the water is flowing back in the river over the downstream embankment dams in R3*

As stated before, in some embankment dam sections the flow conditions vary over time. As an example, this is shown in retention basin R3 (R3). Fig. 5 presents the flow conditions in R3 shortly after the beginning of overtopping.

The upstream parts of the embankment dams are overtopped and R3 is filled up. When R3 is filled up completely, the water is flowing back into the river over the downstream embankment dams in R3 as shown in Fig. 6. Now the whole embankment dam section is overtopped; in the upstream part the water flows from the river in the retention basin and in the downstream part the water forced to flow from the retention basin back in the river due to a terrace in the natural terrain.

B. Dam Break Scenarios

The dam break scenarios showed that even a small breach may cause a significant change in the water depth in the flood plains up to 1.0 m.

The differences in water depths due to a small breach in the embankment dam section of retention basin R2 are shown in Fig. 7. The water depths are increasing in R2 next to the dam breach. The breach is also lowering the water level in the river itself and in the retention areas downstream of the breach. The small breach causes additional water depths of 0.15 – 0.5 m in case of a 100-year flood. The water depths without breach are between 0.5 -2.0 m in this R2. The embankment dams in sensitive areas will thus be protected against erosion in case of overtopping.

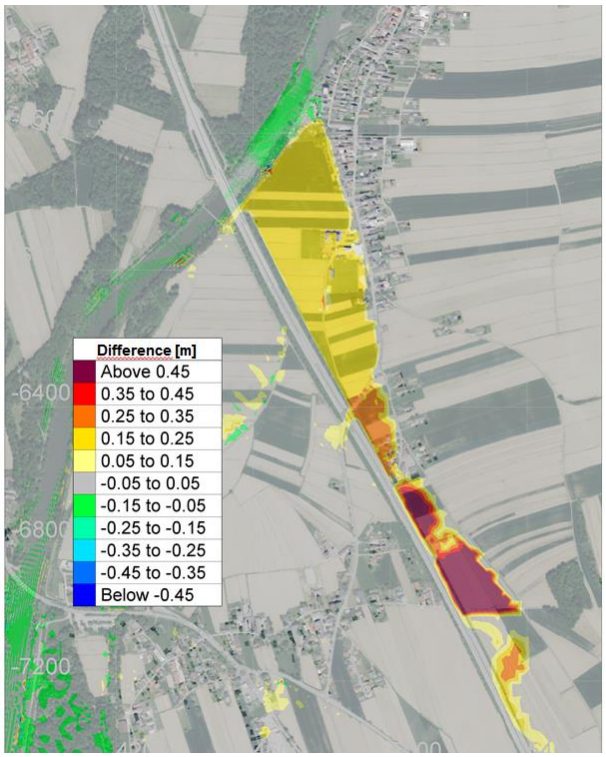

Figure 7. *Differences in water depths due to a small breach in the embankment dam in Section R2*

VI. CONCLUSIONS

In the project, Telemac2D was used to model the steady and unsteady design flood scenarios and dam break scenarios. The design flood scenarios were used to analyse the water depths and the flow velocities in the flood plains and on the air face of the embankment dams. Several section were found where the embankment dams are overtopped or bank full filled in case of the design flood events (30-year flood and 100-year flood).

Based on these results, different dam break scenarios have been analysed to quantify the impact of a dam break. The modelled dam breaks showed that even a small breach in the dam may cause significant changes in water depth.

The presented investigations and results are the basis data for the further design of erosion protection measures and training of embankment dams in this river reach.

ACKNOWLEDGEMENT

The computational results presented in this paper have been achieved using the Vienna Scientific Cluster (VSC3). We would like to thank the VSC team for the support.

REFERENCES

[1] Biscarini C., S. Di Francesco, and P. Manciola, 2010. CFD modelling approach for dam break flow studies. Hydrol. Earth Syst. Sci., 14, 705–718, 2010, www.hydrol-earth-syst-sci.net/14/705/2010/

[2] Dorfmann, C., and G. Zenz, 2016. The depth-averaged mixing length turbulence model for Telemac2D, Proceedings of the XXIIIrd Telemac User Conference, Paris, France. Published by HR Wallingford.

[3] Froehlich, D.C., 2008. Embankment dam breach parameters and their uncertainties. Journal of Hydraulic Engineering, Vol. 134, No. 12, P. 1708-1721.

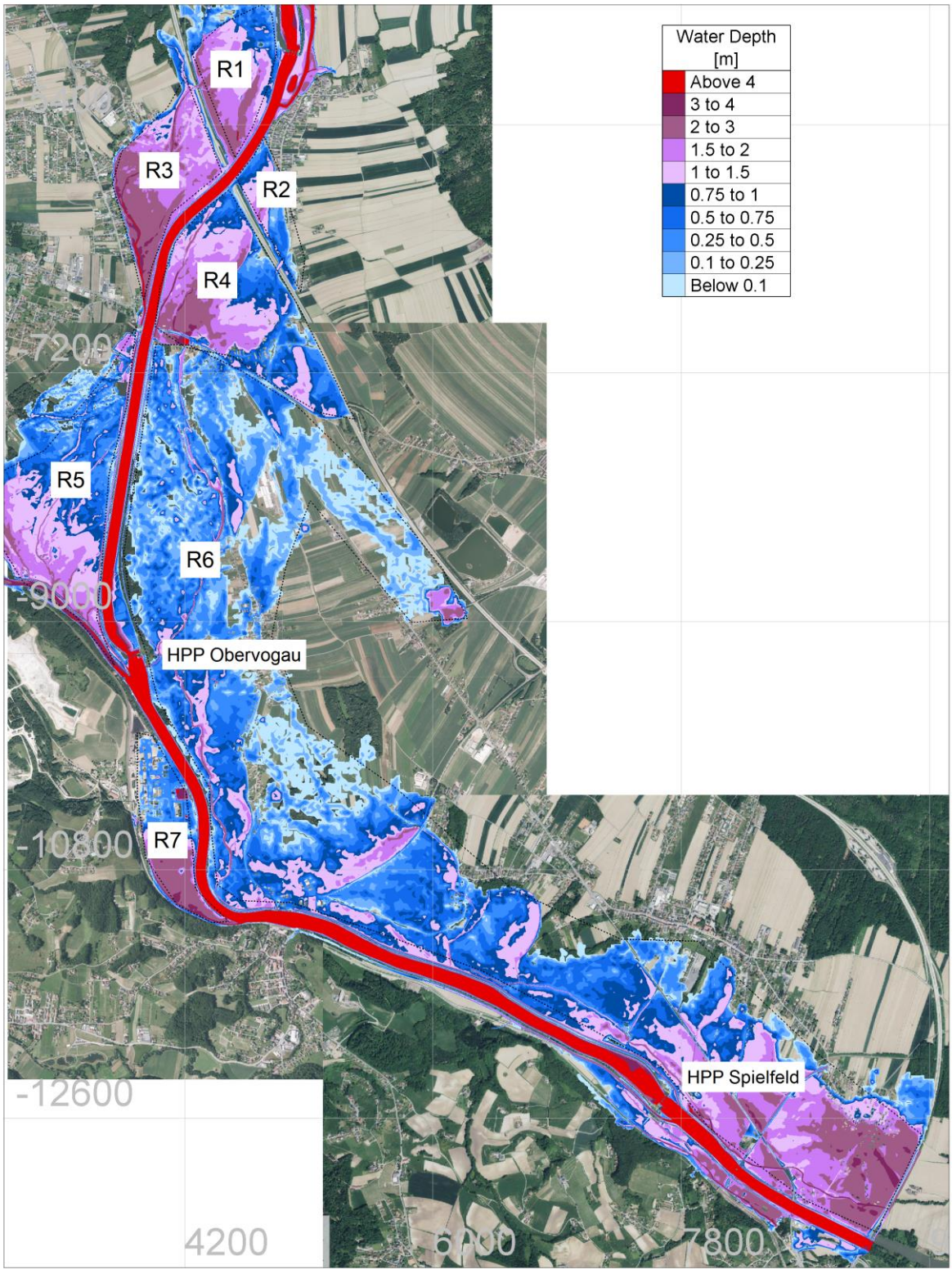

Figure 8. *Water depths at the 100-year flood in the lower part of the project area; the retention basins are numered from R1- to R7*

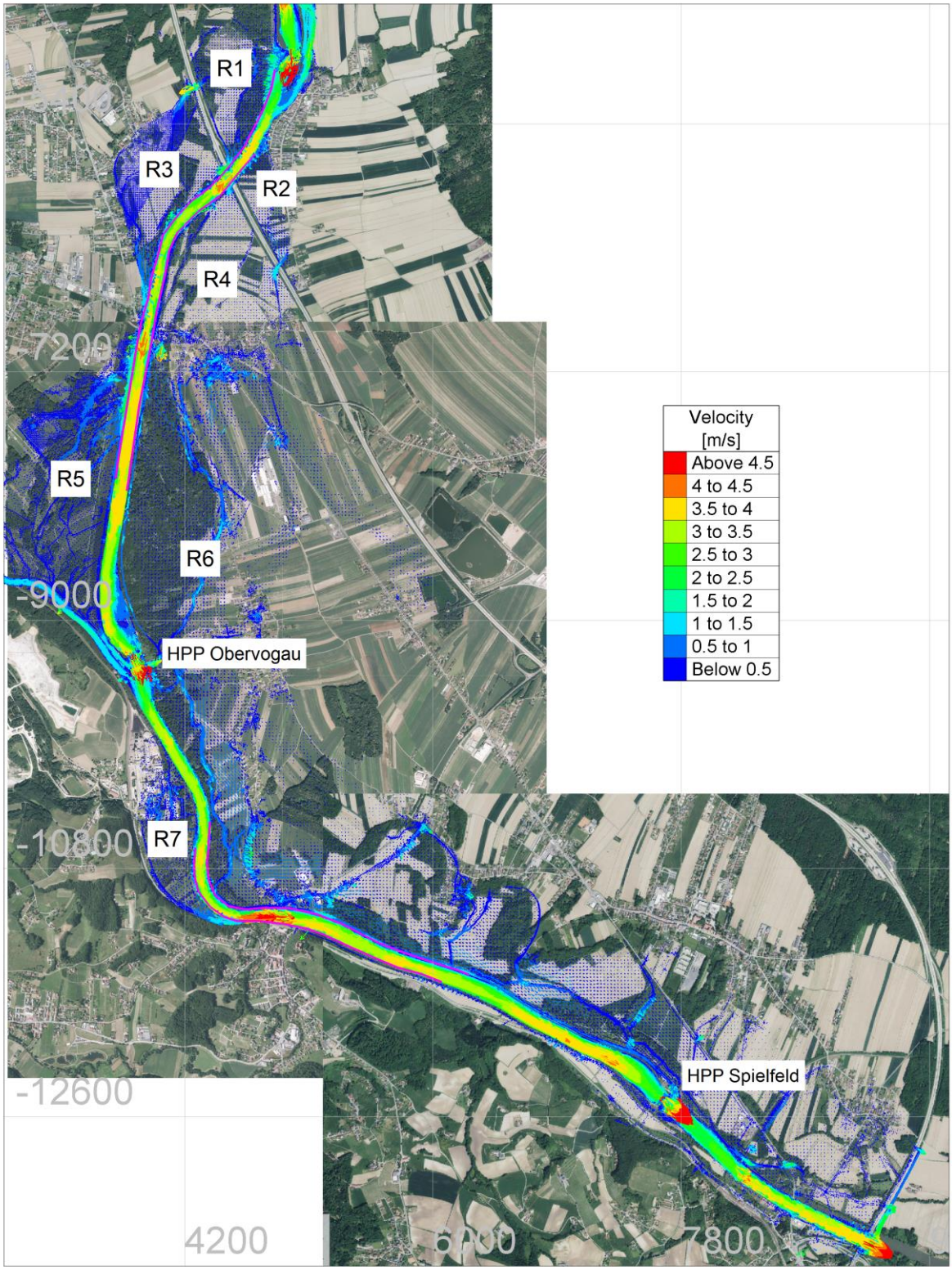

Figure 9. *Flow velocities at the 100-year flood in the lower part of the project area; the retention basins are numered from R1- to R7. The overtopped or bankfull embankment dam sections are marked with a magenta solid line.*

Mapping of Flood Dynamics Due to Sea Level Rise in Dyfi Estuary

Aasem Khatrush
Hydro-environmental Research Centre:
School of Engineering, Cardiff University
Khatrushas1@cardiff.ac.uk

Shunqi Pan
Hydro-environmental Research Centre:
School of Engineering, Cardiff University
pans2@cardiff.ac.uk

***Abstract*— Climate change and the resulting sea level rise are a serious threat to coastal zone in the world, including estuaries and coastal villages. The consequence of sea level rise (SLR) on the Welsh coast is still ambiguous, and updating of current flood risk tools is necessary to mitigate the potential damages arising from the future flood events along the Welsh coasts. This study focuses on hydrodynamic impacts of SLR on Welsh coasts, particularly in the Dyfi Estuary at Mid Wales, using an advanced modelling tool – TELEMAC2D. The analysis of flood dynamics is based on the time varying water depth and velocity from the model, so that flood index, flood duration and hazard rate can be more accurately predicted and assessed. In this study a high-resolution TEELAC2D model was setup, calibrated and validated for the Dyfi Estuary with a number of SLR and river discharge scenarios. Results showed that with the commonly accepted SLR quantities, a considerable area within the Dyfi Estuary is to be affected, but the flood duration and hazard rate vary widely within the study area, providing the insightful details of the flood risk in the region for better and sustainable future coastal management.**

I. INTRODUCTION

Estuary are simply tidal basins or "semi-enclosed coastal bodies of water which have free connection with the open sea and within as well as receiving great influences by tidal forces" as described by [1]. Estuaries are generally similar, in that they are influenced greatly by tidal forces [2] and are highly influenced by sediments transportation that play the major role in terms of estuary reshape [3]. Wales has over 1200 km coastline, along which many low-laid estuaries that are highly vulnerable to flooding and storm surge. A rise in the current mean sea level would increase flood severity and frequency of occurrence [4] and consequently affect the morphology of estuary and impact the environment and human life around estuaries and coastal zones. In such cases, coastal management becomes more difficult, because of the need to provide sufficient flood protection in such zones and more importantly to preserve nature of the coastal zone. The Dyfi Estuary which situated on the west coast of Wales at the center of Cardigan Bay, is remarkably one of the biggest, but most vulnerable estuary.

According to the Intergovernmental Panel on Climate Change's (IPCC) predictions on the sea level rise (SLR), the UK coastal zone in general will be subject to a SLR up to 0.98 m by 2095 [5]. With respect to the Welsh coasts, the SLR is expected to be between 0.32 to 0.76 m by 2095 due to global warming and thermal expansion of ocean based on the recommendation of the UK Climate Projection 2009 (UKCP09) [6]. The report further indicated that by including both ice sheets melting and vertical land movement, the estimated SLR could be between 0.93 m and 1.96 m by 2100. As a result, the low-lying lands in Wales including estuaries will be under increasing threats of coastal flooding. For such locations, urgent coastal management is required.

The Dyfi Estuary and neighboring villages were exposed tidal flooding and storm surges in the past [7,8] and a sea level will increase tidal flooding, surge severity, and reduce the efficiency of the soft sea defenses that are already present in Dyfi Estuary. Researchers have studied the impact of SLR on Dyfi Estuary flooding [8], and the expected future flood risk on coastal towns [9–11]. These studies have assessed flood risk depending on highest tidal level or peak flood within a short time serious; the outcome of these results is limited and does not sufficiently provide information about the contact of the flood on agricultures and secondly the short flood modelling period does not express the dynamic trend of flooding. In this paper, an approach based of flood dynamics and long computation run is applied on the Dyfi Estuary as example; the hydrodynamic model was based on Telemac-2D (v7p1r1). The combination of tidal forces and different river-flowrates under different SLR scenarios were used to plot flood map and flood dynamic maps in the Dyfi Estuary and surrounding locations. The main objective of this study is to enhance current knowledge about future flood caused by SLR and to suggest better coastal flood management in Welsh estuaries.

II. CASE STUDY

The Dyfi Estuary geographically is located in the center of Cardigan Bay Fig. 1, and is one of the biggest estuary in the UK; with main channel length being up to 19.6 km. The estuary is funnel-shaped and has maximum width of 2.4 km, with a sandy spit at its mouth. During spring tide, seawater submerges approximately 16 km² of the estuary, allowing of extensive development of intertidal sandbank and mudflat within the area. The estuary is connected with network of creeks, which are the pathway between the entrance and the southern estuary boundaries. This is because of being a shallow estuary where the estuary bed elevation is approximately 4.5 m above chart datum (CD), which steeply decreases outside the estuary mouth to become 10 m above CD.

The estuary and its surrounding beaches are located in active coastal zone, and subjected to macro tides. At the study site, semi-diurnal tides. The tide ranges are up to 4m for spring tides and 2 m for neap tides. Records show that human activity caused changes to the natural land formation, through the construction of a railway embankment, and the canalising and diverted of the Afon Leri to the southern of the estuary. The main purpose for these activities was to control high discharge inside the estuary, and protect the villages of Borth and Ynyslas from flooding, see Fig. 1. Despite these activities, the area is still subjected to regular coastal and

fluvial flooding, the combination of high spring tides, coinciding with high river discharges can result in flooding in coastal towns and hinterlands. The railway embankment has been considered as successful flood protection device, despite restricted existing salt marsh of moving back into land. If SLR, this area will see a reduction in salt marsh tidal creek networks because of the increased tidal prism in the estuary [12].

Current concerns about the Dyfi Estuary focuses on two main points: firstly, the aging nature of these defenses, and the low protection offered against flooding by a possible future SLR (and the subsequent future surges in Borth and Ynyslas). The second point concerns the preservation of conservation sites behind the hinterlands and the salt marshes to the south of the Dyfi Estuary. However, it is unclear how the estuary will respond to rise in sea level in the future, and how the conservation sites, such as Borth Bog, salt marsh will be maintained.

III. MODEL SETUP

Given the different spatial scales that were considered, the computer model was set up with coarser mesh to cover the entire Welsh coast and part of the English coast, including both Irish and Celtic Seas, and the refined local mesh to cover the details of estuary. Fig. 2 shows the computational domain, which was centered at the middle of Wales (Cardigan Bay), while the northern and western extremes of the model are located in the North Atlantic Ocean. In addition, the southern boundaries are located in the Celtic Sea. The computational domain consists of 81,993 cells that cover surface areas of 279,186 km². The mesh size decreases gradually toward the shoreline, the largest cell area is located within the open boundaries at 83.5 km²; and the minimum cell area is 90 m² near the shoreline. The bathymetry obtained from the Admiralty Digimap bathymetry data [13] and was plotted on the mesh.

To represent the details of the estuary and upstream river, it was necessary to for computational mesh to be refined in the estuary. Flood propagation onto land by the force of SLR was modelled by connecting a new mesh that shaped the Dyfi Estuary into the large model as described in previous section. Along the Dyfi Estuary, a new mesh that represents selected flood-prone areas was connected to the large model. The added areas are approximately 12 km along the domain beach centred by the Dyfi mouth and 28 km inside the estuary to the upstream boundaries, as shown in Fig. 2. The cell number of the new model increases from 81,326 to 257,158 cells and the smallest cell area becomes 6.35 m² inside the Dyfi Estuary Fig. 2.

Elevation data were provided by Admiralty Digimap bathymetry data [13] , the difference between bathymetry and topography datum (chart datum and ordnance datum) was resolved using the UKHO VORF dataset [14]. Assigning different friction values based on the land use of each cell is an essential task in flood modelling [15,16] to improve the accuracy of the model. Along the open boundaries, boundary forces were forced as water level and velocity The open boundary conditions were imposed with tidal levels using the date extracted from a TPXO database (the Global Ocean Tidal Model Database) [17]. The TPXO data provides amplitudes of tides concerning sea surface elevations of eight main tide amplitude types (M2, S2, N2, K2, K1, O1, P1, Q1), two long-period tides (Mf, Mm) and three non-linear tide (M4, MS4, MN4). The harmonic constituents and TPXO database http://volkov.oce.orst.edu/tides/global.html. The Manning values assigned for land use in the flooding area are as followed: riverbed friction was 0.02, arable land 0.04, bare earth 0.022, urban area 0.018, managed grassland 0.035 and salt marsh 0.035 and forest 0.045 [15]. Telemac-2D solves the non-linear shallow water equations, Saint-Venant equations (momentum and continuity), using the finite element methods [18]. Telemac-2D has been successfully used in hydrodynamic simulations in the recent years [19–21], and the effectiveness of Telemac-2D is clearly shown with its ability to simulate a closer tide range to the field data.

IV. MODEL VALIDATION

The model calibration and validation were carried out over 30 days, the computational output is 15-minute from the 1st to the 31st of January 2006, which covers two neap-spring tidal cycles. The model results were compared with the field measurements database at ten tidal gauges across both the English and Welsh coasts from tidal harmonic analysis (BODC – http://www.bodc.ac.uk) after removing of skew surge values from observed water level. However, in this paper we only illustrated results at of both tidal gauge stations in the Cardigan Bay closer to the Dyfi Estuary (Barmouth and Fishguard) for a shorter period of 9 days.

The overall validation shows a good agreement between the observed data and the model results in all locations in terms of tide levels and phase, as shown in Fig. 3. However, minor differences can be seen at the low tides at both sites, where the predicted sea levels are higher than those observed. This discrepancy may be attributed to inaccurate bathymetry in the target area. The validation of the model showed a good overall performance of the model and the model is capable for sea level simulation. To ensure that the modelled water level in the local area is accurate enough when compared to field measurements, Two sites were selected to fulfil this purpose, firstly the Aberdyfi harbour in the downstream, and secondly the Dyfi junction in the up upstream Fig. 4. In general, assessment showed a good agreement between the modelled and field data throughout the validation period in both locations. Although model results in the Aberdyfi pair showed shift in phase 25 min and lower water depth during the neap period, which is attributable to low accurate bathymetry inside the estuary. Within the Dyfi River, Telemac-2D predicted higher water levels than the observed date, as it is difficult to obtain accurate riverbed elevations, and therefore these errors are expected.

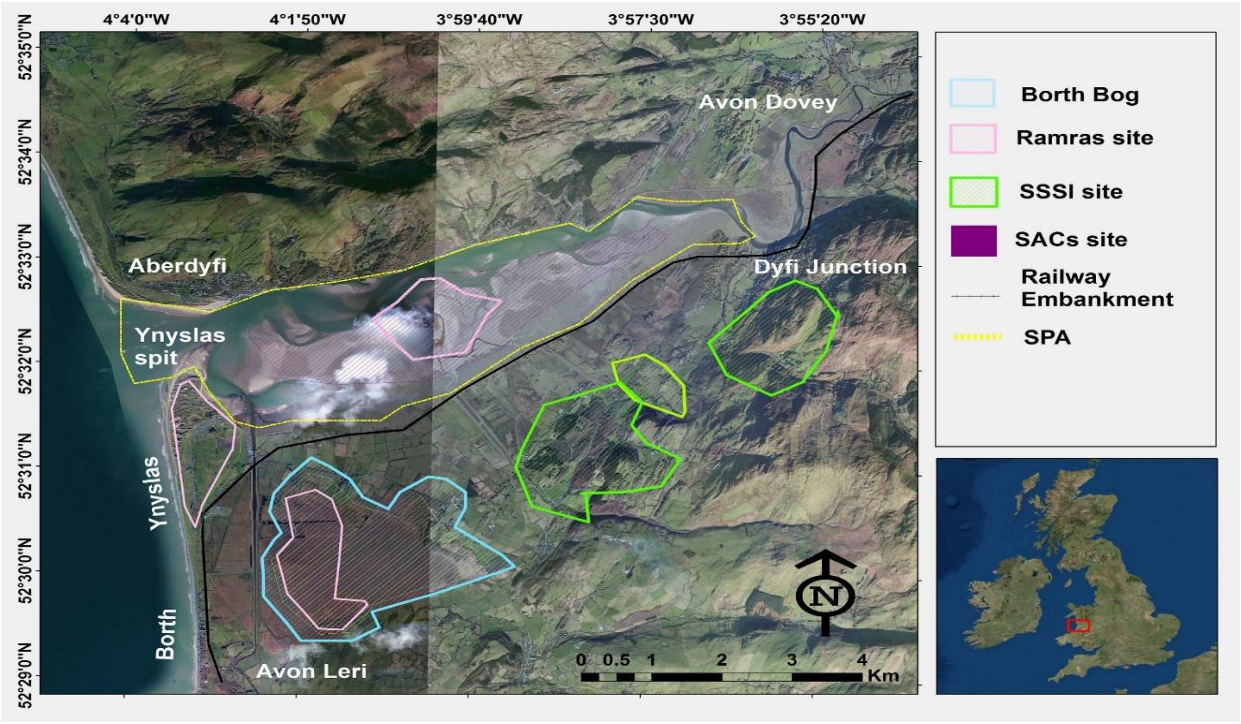

Figure 1. *Location of the Dyfi Estuary - the map shows the surrounding urban areas and the conservative sites located around the Estuary; SSSI (Special Scientific Interest); SACs (Special Areas of Conservation sites); (NNR) NationalNature Reserve; A Ramsar Site is a wetland site designated of international importance under the Ramsar Convention.*

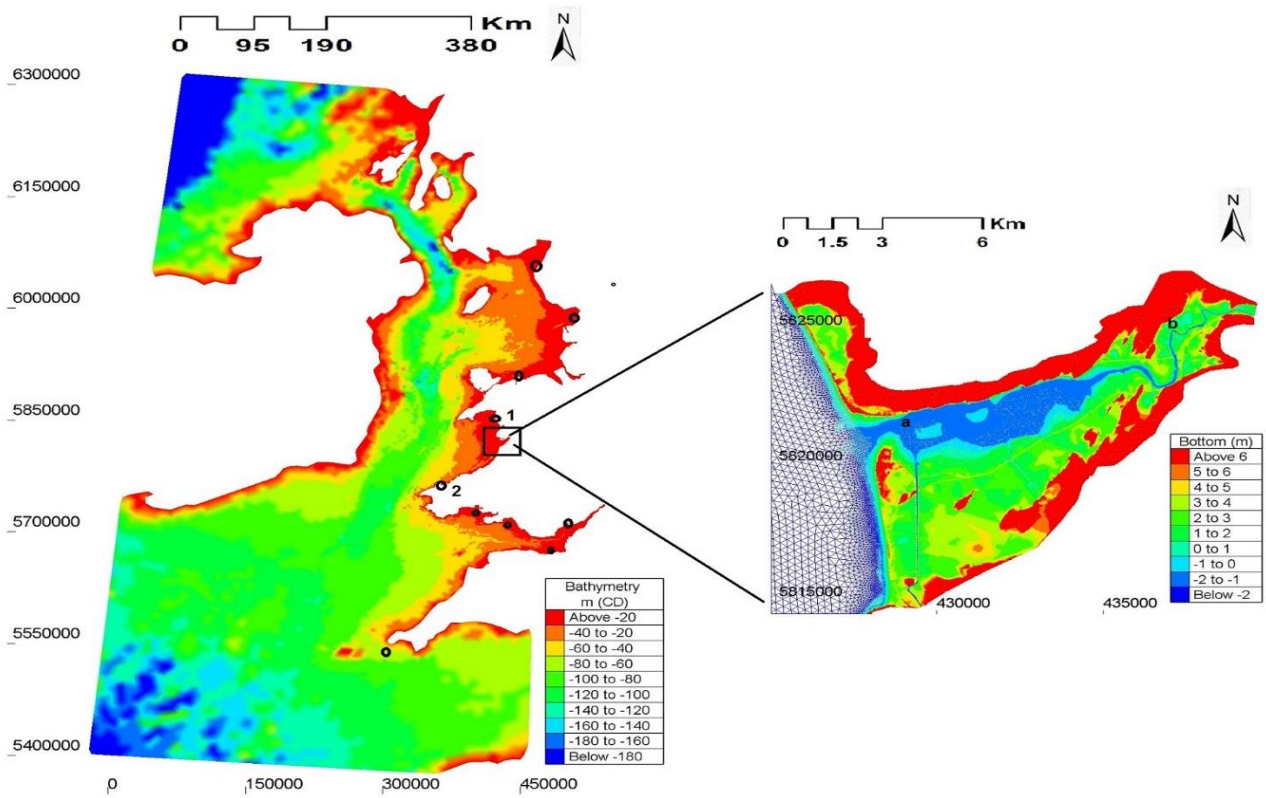

Figure 2. *Computational domain and bathymetry with tidal gauge stations (black circles); 1) Barmouth; 2) Fishgaurd (insert shows the refined mesh for Dyfi Estuary.*

Overall, the validation showed a good symmetry between the modelled and field data, and showed its suitability for use as a flood-modelling tool.

V. MODEL SCENARIOS

A set tidal forces combined with different fluvial discharges from the river's flowrate have been designed to simulate the most likely scenarios for today, the near and distant future. It is not expected that these conditions would occur at the same time. The simulation of the scenarios will illustrate the places most at risk of flooding in the future. SLR values were added as a linear increase of the selected sea water level as follows: 0.0 m, 0.5 m, 1.0 m, and 2.0 m as justified in previous sections. Other forces such as wind or waves were not included in this model, although Telemac-2D can simulate these parameters. While on the river boundaries, the scenarios were proposed to simulate different events, such as the following levels of river discharge: none, the mean, and the mean maximum. However, in this paper, only one case is show: the 1/100-years. All modelled scenarios are shown in Tab. 1 Telemac-2D ran this model for 31 days, from 1 - 31 July 2007, with one-hour time intervals and a 5-second time step.

TABLE 1. MODEL SCENARIOS ADOPTED FOR CURRENT STUDY

	SLR(m)	***River discharge (m³/sec)***	
		Avon Dovey	***Avon Leri***
Scenario 1	0.0		
Scenario 2	0.5		
Scenario 3	1.0		
Scenario 4	2.0		

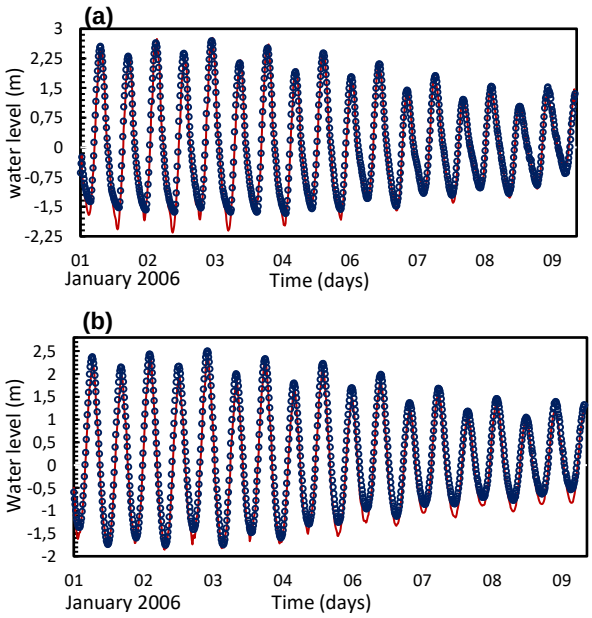

Figure 3. *Comparisons between Telemac-2D predicted water level and observed water levels in different tide gauges. (a) Barmouth; (b) Fishguard.*

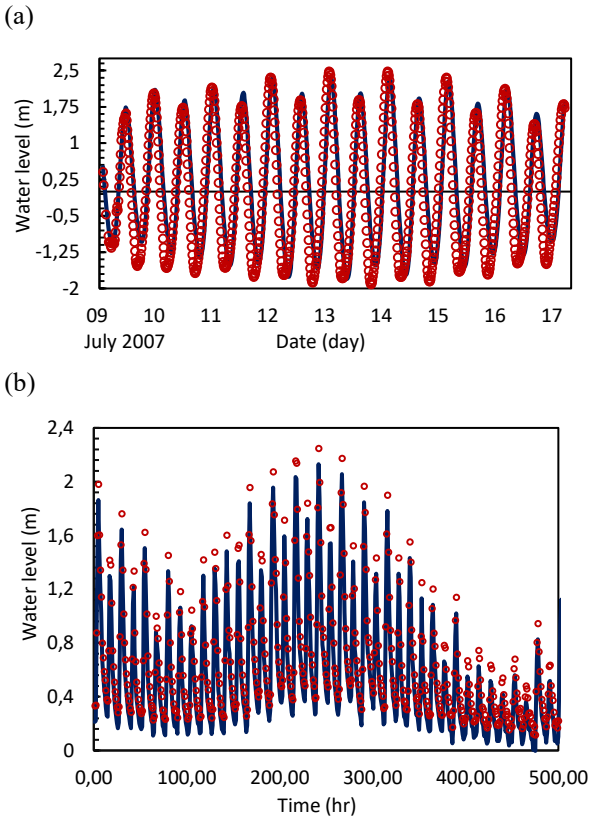

Figure 4. *Comparison between modelled water level by Telemac-2D and observed data at: (a) Aberdyfi Pier.form the 9th to the 17th of July2007; (b) Dyfi junction station, case was run using mean flow rate (23.8 m³/sec) for the period of 10th to the 25th October 2013.*

VI. RESULTS

Predicted water depth by Telemac-2D was used to outline flood maps of the domain. Water depth of each scenario was plotted over high-resolution satellite imagery. Plotting of all maps was during highest spring tide on July 2007. Fig. 5a shows modelling of current sea condition, in this scenario 1, water did not overtop the coastal defences and the embankment along the Dyfi Estuary. In opposite when adding the high-river flows of both Avon Leri and Avon dovey, where both caused flooding nearby both Dyfi junction and Borth Bog, to affect the A487 road and small part of the conservation sites. Fig. 5 shows the impact of SLR by 0.5 m above the current sea conditions. The most notable result from this scenario is the filling of estuary container by water and movement of water via small ditches into the Avon Leri and Afon Cletwrin in the south of the Dyfi. This caused limited flooding nearby channel's banks. However, filling of estuary by water will submersion significant part of salt marsh sites Fig. 5 that observed in this scenario with all cases, this increased concern about salt marsh future.

Fig. 5c shows flood map of modelling 1.0 m of SLR. The proposed scenario by the IPCC highlighted the weakness of the estuary against SLR; over-filling of the estuary with water during the high tide above 2.25 m depth. Consequently, water level in the upstream boundary increased sharply up to 2.75m

at many locations near by the A487 and B4353, to floods significant part of the forest and agriculture lands. In addition, the scenario showed that coastal flooding would occur if current coastal defence remain unchanged, mainly in the Borth village and south of Ynyslas, seawater movement extended to the south of Avon Leri traveling up to 800 meter further toward the river by the help of land topography. This flood extending is similar to mentioned reported after the 2013-2014 storm surge when the Borth town was flooded by high water level [22].

It should be mentioned that impact of 1.0 m of SLR influence is not restrained by flooding; it does even affect the beach of the Aberdyfi and other beaches around. As these beaches were submerged during the simulation with a high water depth, this may result in coastal receding and clear morphological changes. In addition, the spit in the mouth of the estuary were completely submerged over long time during the simulation. The possible changes of the beach area and shape would lead to a coastal squeeze and a limitation of future investments in this location. Fig. 5d shows flood map of 2 m SLR. The observable effects of this low probable scenario is massive flooding in the whole low land areas, and water propagated further inland to inundate Borth and south of Ynyslas villages inside land by 2 km approximately, the massive flood would submerge parts of A487, B4353 and the railway. This would make the evacuation and traveling into flood-prone very difficult task due to high water level. Adding 1 in 100-year river event to SLR scenario resulted in flooding 26.3 km² of lands, most of which with elevation below 6m above mean sea level. The major source of flooding is rivers flowing from the estuary filled with water that enters these rivers through the drainage holes and thus, flooded the surrounding lands.

Moreover, seawater overtopped coastal defences along the south boundary and massive flooding occur in Borth and Ynysals, and the high depth is because receiving of water is from two sources river and coastal. The flooded areas sharply increased from 2.5 km² during current conditions to 27.5 km² at the worst case scenario, this is because flooding by current condition and 0.5 m of SLR will influence the intertidal zone that is restricted by the estuary basin and the railway embankment. In opposite to other scenarios when over-contain of small channels flooding in surrounding green areas. The consequents of future SLR are severe. The agricultural spaces and conservative sites inside coastal zones are vulnerable to SLR; possible extensions of the tidal zone further into the hinterland may possibly alter coastal environments by causing land loss and coastal erosion in both Borth and Ynyslas especially in the Ynyslas sand dune and downstream of Dyfi Estuary.

VII. FLOOD DYNAMICS

The previous section showed how different SLR would result in more frequent tidal flooding. Although water depths commonly used to assess flood risk, other factors such as flood dynamics is rarely discussed by existing literature. Mapping of flood dynamics would give more realistic picture of future flooding risks than typical Flood maps, because flood dynamic will represent submerged period of each location, as SLR would increase the possibility of tidal flooding occurring more frequently. The illustration of the submersion time of each cell would point out the flood hazard on any element falling within the cell boundary. In addition, it would increase knowledge about possible evacuation routes, and helps to develop local flood management plans for emergency events.

The flood duration was achieved by using Telemac-2D to capture how many times each cell was flooded, while the accumulation of submerged time is the total inundation period of each single cell. The flood duration index was adopted from [23] who provided a methodology to show the impact of flood duration on communities. The duration index was divided into different periods. Periods of less than one day (2 / 12 / 24 hours) were seen to have a limited impact on a community. Periods of flooding that last between 1 - 4 days, shown to be a nuisance, and have limited impacts, including disrupting people's daily lives, affecting crops in farms, and causing the loss of assets. Finally, flooding periods that extend for longer than 5 days can cause the contamination of surface water, and outbreak of waterborne diseases.

Fig. 6 (a & b) shows flood dynamic maps of current sea conditions and a SLR of 0.5 m under different fluvial conditions, expressed as the number of hours flooded in July 2007. The most noticeable results of all scenarios showed that the longest inundation periods were located by the riverbanks of the Dyfi and Afon Leri rivers: of up to 240 hours spent submerged. This is as a result of water retention in land with an irregular topography around riverbanks with

Fig. 6 (c&d) shows the depth and duration of flooding in the cases of a SLR of 1.0 m and 2.0 m above current sea levels. The influence of a 1.0 m SLR increases flood duration in the southern bank of the estuary, while the 2.0 m rise submerges most of the lower lands for more than 240 hours per month. This longer flood duration (in the 2.0 m scenario) has a number of serious consequences, which are, flooding and both villages are totally submerged for a duration 240 hours (apart from the area to the north of Ynyslas). Although high sand dunes protect the area, the unflooded areas could be blocked by water, and evacuation processes might be difficult, as flooding will cause disruption on the roads that connect the countryside and the coast. Failure of existing coastal defenses is because they are designed to withstand against 1/100 year event (4.14 m); therefore, rise of sea level by 2 m increased mean sea level to 4.85 m (AOD), as follows. The Borth Bog and other conservation sites are submerged and potentially destroyed. In Aberdyfi, the lowland coastal area at the mouth of the estuary is under extreme risk due to the insufficient height of existing sea defenses.

Appropriate management of the estuary to face future challenges due to SLR is essential to maintain the environment value of the estuary. One of the Dyfi Estuary issues is the south boundary where salt marsh site appears along with total areas up to 421 ha [25].

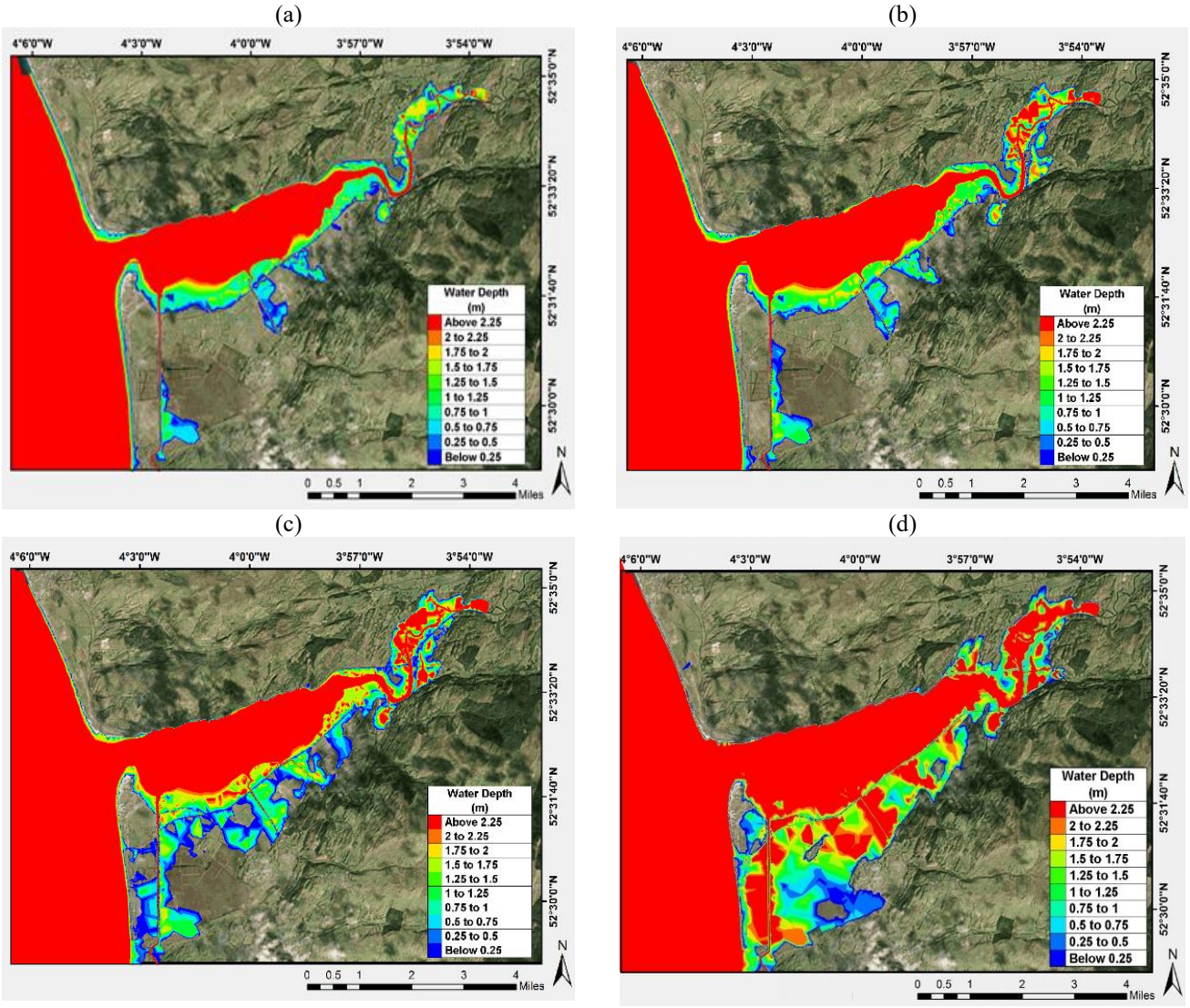

Figure 5. *flood map of the Dyfi Estuary (a) current sea condition. b) 0.5 m SLR. (c) 1.0 m SLR, (d) 2.0 m SLR. All scenarios are combined with 1/100 year fluvial event of both Avon Dyfi and Avon Leri.*

The railway has stopped the salt marsh sites expanding to further locations, and therefore, losing of salt marsh is expected because of being settled in low areas. As a result of SLR, the salt marsh may be submerged in water during flooding. Using flood dynamic to assess future of salt marsh is useful tool; this is because dynamic of the tidal cycle controls salt marsh vegetation distribution within the intertidal zone. Lowest salt marsh type is usually present in the bottom where it is submerged by seawater except during lowest tidal receding this is estimated to be submerged for around 40% of the tidal cycle time. Opposite to middle and high marshes submerged for 10% of tidal cycle time only during high spring tide [24].

The elevation of the southern estuary bank is fairly consistent; the elevation range of these sites is between 0 - 1.85 m AOD. A rise in sea level by 1.0 m would submerge 285 m towards the railway during the high tide. This could potentially submerge the pioneer and lower zones of salt marsh vegetation, and the middle marshes would move backward to the sea wall to cause coastal squeeze. The calculation of salt marsh reduction was based on the dynamic approach that was outlined previously. The results showed a significant loss of salt marsh sites. For example, in the highest sea-level rise scenario, water would dynamically cover 84.55% of salt marsh sites with a water depth of up to 2.5 m, to remain only 85 hectares. Environment agency [25] showed that there will be a reduction in salt marsh sites of 50% if the sea level rises by 0.3 m. While it was stated by [24] that all salt marshes will be wiped out if the sea level rises by 1.0 m, this discrepancy may be because this methodology is based on the dynamic approach while others have used the static approach. However, in the Dyfi Estuary, the main reason for salt marsh loss and the limited possibility for migration of marshes inland is the railway embankment, which restricts and constrains any further salt marsh growth.

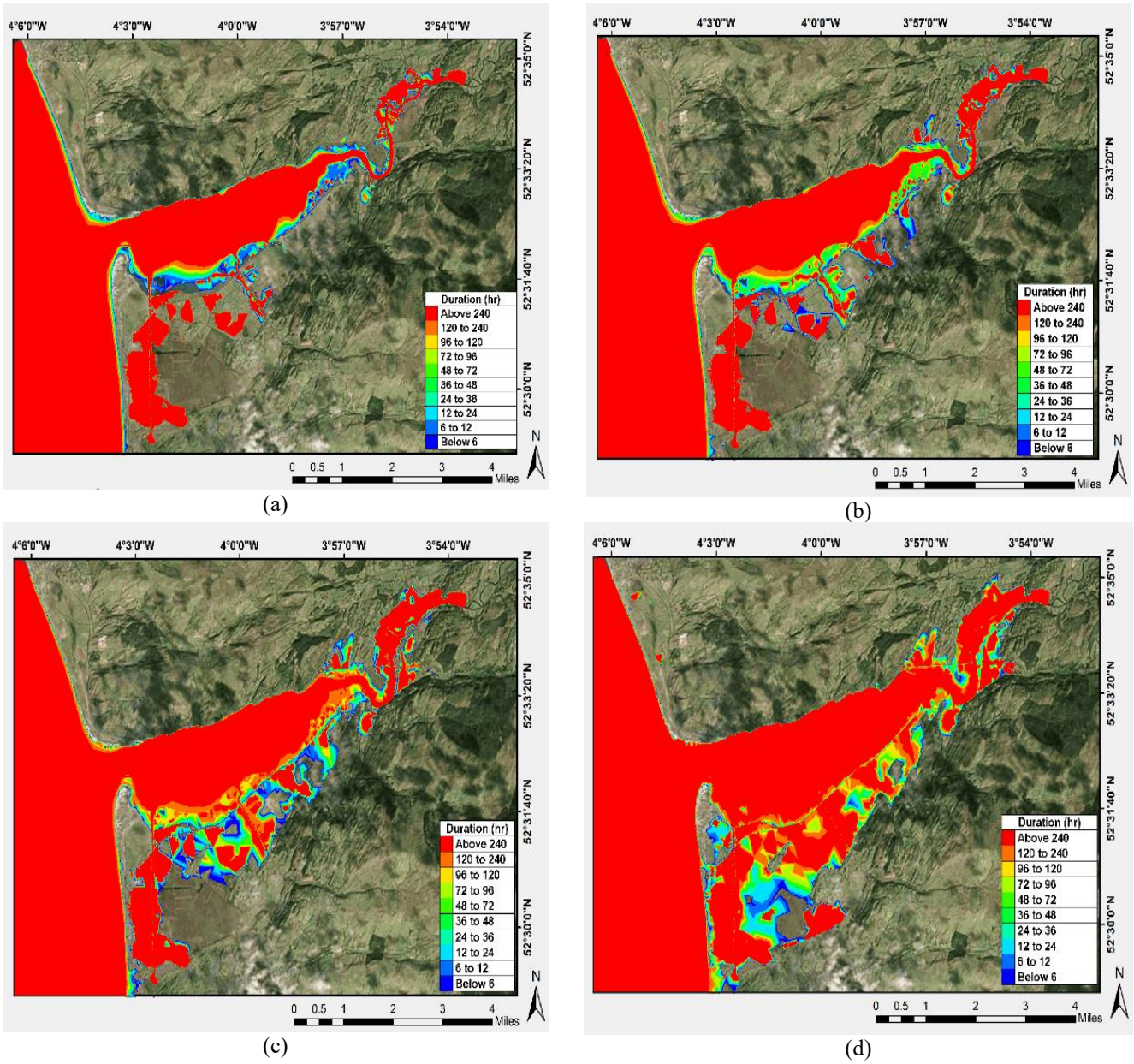

Figure 6. *Map of flood dynamic (Hours flooded/month) of the Dyfi Estuary and surrounding areas for different SLR scenarios modelled by Telemac-2D for: a) current sea condition; b) 0.5 m SLR; (c) 1.0 m SLR; (d) 2.0 m SLR. All scenarios are combined with 1/100 year flow discharges from Avon Dyfi and Avon Leri.*

VIII. CONCLUSIONS

A Telemac-2D hydrodynamic model was used to study the Dyfi Estuary and neighbouring low-elevation lands, including rivers and other side streams. The results show that Telemac-2D was capable of representing flood dynamic per cell. This concept is important to understand tidal flood stages, since it gives an insight into the tidal cycle rather than just giving the highest water level. The monthly flood dynamic maps illustrated that the most vulnerable areas in the domain are subjected to a medium flood duration of 48 -240 hours per month (case a, b, c). The longest flood duration occurred across most flooded areas during the worst-case scenario when combined with high river flow.

The flood dynamic was linked to other environmental issues around the Dyfi Estuary to gain a better understanding of the impact of a rise in sea level; for example, the future of the salt marshes in the domain. The current concern is that salt marsh spaces will be diminished if the sea level rises. The flood dynamic map showed the salt marsh sites are extremely vulnerable, as 0.5 m of SLR will reduce current sites by 59.45%. The worst-case scenario of a 2.0 m rise showed that

only 15% of current salt marsh would remain unaffected. It is recommended that the results of the model be used as a tool to further enhance the study of the region, such as prediction of flood hazard scale based on flood dynamics concept and investigate the future change of the shoreline under SLR.

ACKNOWLEDGEMENTS

The authors gratefully acknowledge the financial support from the Libyan government.

IX. REFERENCES

[1] D.W. Pritchard, Salinity distribution and circulation in the Chesapeake Bay Estuaries System., Journal of Marine Research. 11 (1952) 106–123.

[2] ME.G.Perillo, "Geomorphology and sedimentology of estuaries: an introduction." Developments in sedimentology 53 (1995): 1-16.

[3] D.M. Paterson, K.S. Black, Water Flow, Sediment Dynamics and Benthic Biology, Advances in Ecological Research. 29 (1999) 155–193. doi:10.1016/S0065-2504(08)60193-2.

[4] J.A. Lowe, J.M. Gregory, The effects of climate change on storm surges around the United Kingdom, Philosophical Transactions of the Royal Society A: Mathematical, Physical and Engineering Sciences. 363 (2005) 1313–1328. doi:10.1098/rsta.2005.1570.

[5] J. A. Church, P.U. Clark, A. Cazenave, J.M. Gregory, S. Jevrejeva, A. Levermann, M. A. Merrifield, G. A. Milne, R.. Nerem, P.D. Nunn, A. J. Payne, W.T. Pfeffer, D. Stammer, A. S. Unnikrishnan, Sea level change, Climate Change 2013: The Physical Science Basis. Contribution of Working Group I to the Fifth Assessment Report of the Intergovernmental Panel on Climate Change. (2013) 1137–1216. doi:10.1017/CB09781107415315.026.

[6] G.J. Jenkins, J.M. Murphy, D.M.H. Sexton, J.A. Lowe, P. Jones, C.G. Kilsby, UK Climate Projections: Briefing report, 2009. doi:ISBN 978-1-906360-04-7.

[7] A Cole, Ynyslas Storm Damage, (2014). https://www.alananna.co.uk/blog/2014/ynyslas-storm-damage/.

[8] P.E. Robins, A.G. Davies, R. Jones, Application of a coastal model to simulate present and future inundation and aid coastal management, (2011) 1–14. doi:10.1007/s11852-010-0113-4.

[9] M.J. Purvis, P.D. Bates, C.M. Hayes, A probabilistic methodology to estimate future coastal flood risk due to sea level rise, Coastal Engineering. 55 (2008) 1062–1073. doi:10.1016/j.coastaleng.2008.04.008.

[10] J. GE, D. Much, J. Kappenberg, O. Nino, P. Ding, Z. Chen, Simulating storm flooding maps over HafenCity under present and sea level rise scenarios, Journal of Flood Risk Management. 7 (2014) 319–331. doi:10.1111/jfr3.12054.

[11] M.P. Wadey, R.J. Nicholls, C. Hutton, Coastal flooding in the solent: An integrated analysis of defences and inundation, Water (Switzerland). 4 (2012) 430–459. doi:10.3390/w4020430.

[12] Z. Shi, H.F. Lambb, R.L. Collinb, MARINE Geomorphic change of saltmarsh tidal creek networks in the Dyfi Estuary , Wales, (1995).

[13] EDINA, “Marine Digimap Service,” [Online]. Available: http://digimap.edina.ac.uk. (Accessed 23 November 2016).

[14] United Kingdom Hydrographic Office, VORF Model VORF-UK08, UKHO, 2008.

[15] P.D. Bates, R.J. Dawson, J.W. Hall, M.S. Horritt, R.J. Nicholls, J. Wicks, M.A. Ali Mohamed Hassan, Simplified two-dimensional numerical modelling of coastal flooding and example applications, Coastal Engineering. 52 (2005) 793–810. doi:10.1016/j.coastaleng.2005.06.001.

[16] P.D. Bates, R.J. Dawson, J.W. Hall, M.S. Horritt, R.J. Nicholls, J. Wicks, M.A. Ali Mohamed Hassan, Simplified two-dimensional numerical modelling of coastal flooding and example applications, Coastal Engineering. 52 (2005) 793–810. doi:10.1016/j.coastaleng.2005.06.001.

[17] G.D. Egbert, A.F. Bennett, M.G.G. Foreman, TOPEX/POSEIDON tides estimated using a global inverse model, Journal of Geophysical Research. 99 (1994) 24821–24852. doi:10.1029/94JC01894.

[18] J. Hervouet, Hydrodynamics of Free Surface Flows: Modelling With the Finite Element Method, ISBN:04703 (2007).

[19] I. Flood, R. Analysis, M. Methodologies, R. Number, Benefits of 2D Approach for urban flood management TASK 19 : FRAMEWORK FOR FLOOD EVENT MANAGEMENT, (2007).

[20] M.S. Horritt, P.D. Bates, Evaluation of 1D and 2D numerical models for predicting river flood inundation, 268 (2002) 87–99.

[21] E.H.L. Fernandes, K.R. Dyer, O.O. Moller, L.F.H. Niencheski, The Patos Lagoon hydrodynamics during an El Ni no event (1998), 22 (2002) 1699–1713.

[22] BBC Wales, Wales flooding: Victims hoping for return to homes, 2012. http://www.bbc.co.uk/news/uk-wales-18384666.

[23] N.M. Dang, M.S. Babel, H.T. Luong, Evaluation of food risk parameters in the Day River Flood Diversion Area, Red River Delta, Vietnam, Natural Hazards. 56 (2011) 169–194. doi:10.1007/s11069-010-9558-x.

[24] L.A. Boorman, Salt marsh review. An overview of coastal salt marshes, theirdynamic and sensitivity characteristics for conservation and management, " REPORT-JOINT NATURE CONSERVATION COMMITTEE 334 (2003).

[25] N, Phelan, A. Shaw, and A. Baylis, The extent of saltmarsh in England and Wales: 2006-2009. Environment Agency, Bristol, UK (2011).

Modelling of river dike breach type physical test flow with Telemac-2D

Yohannis Birhanu Tadesse, Peter Fröhle
Institute of River and Coastal Engineering
Hamburg University of Technology
Hamburg, Germany
yohannis.tadesse@tuhh.de

Abstract— **Breaching of river dike / flood protection walls during flood events can cause devastating damages. Public authorities might often seek to find out flood inundation and damage that might be caused by a hypothetical dike breach. For such scenario simulations, 2D hydrodynamic numerical models such as Telemac-2D are indispensable tools. However, calibration and validation of scenario models is often impossible as river dike breach related data is usually unavailable. In this situation, river dike breach type laboratory physical test can be useful to evaluate the performance of the hydrodynamic numerical models for modelling dike breach type flows. This paper presents the performance of Telemac-2D for modelling a river dike breach type laboratory physical test flow. The physical test used here is carried out by Briechle and colleagues at Aachen University in the Institute of Hydraulic Engineering and Water Resources Management. Dike breach type flow is mimicked in the physical test by a sudden opening of a gate on the side of a channel with an attached propagation area. Telemac-2D model is set up for the different configurations of this physical test and the measured results were compared to Telemac-2D model results. The parameters breach discharge, wave front after breach, water level at selected points in the propagation area, and water level profile along the axis of the propagation area at semi-steady state are compared between the measurements and Telemac-2D results. For the optimum settings, Telemac-2D gives comparable results to the measurements. However, Telemac-2D underestimates the breach discharge and the semi-steady state water level in the propagation area by about 10% and 25% respectively. The wave front modelled by Telemac-2D deviates slightly from the measurements. The results show that Telemac-2D can be used for modelling river dike breach type flow by adapting appropriate parameters.**

I. INTRODUCTION

Many flood plains along rivers are reclaimed for human use such as agriculture, residence, manufacturing, industrial expansion and others. Such reclaimed flood plains are often protected from flooding during high river flows by flood defence structures such as dikes (also called levees) or flood protection walls. The flood defence structures, nonetheless, never guarantee absolute protection against floods. For example, the Elbe River floods in June 2013, which caused unprecedented damage, occurred after a lot of flood defence political discussion following the August 2002 Elbe River floods. This shows that flood defence structures even in the best design conditions can fail during extreme unprecedented events.

Thus, public authorities might often seek to know areas of flood risk, flood arrival time, flood flow direction in an event of failure of flood defence structure. Such information, which can be obtained from scenario simulation with 2D hydrodynamic numerical models such as Telemac-2D, are very useful not only for emergency response in case of flood disaster but also for land use planning [1].

However, calibration and validation of such scenario simulations is often impossible due to limitation of data. Here, river dike breach type laboratory physical tests can be used to assess the performance of the numerical models and necessary modifications can be implemented to improve their performance.

This paper presents the performance of Telemac-2D for modelling a river dike breach type laboratory physical test flow. The physical test used here is carried out at Aachen University in the Institute of Hydraulic Engineering and Water Resources Management ([2], [3]) and is described briefly in section II. Section III presents the Telemac-2D model set up and section IV presents the comparison of the physical test results and Telemac-2D simulation results for selected test configurations. Also, Telemac-2D simulation results are compared to the results of other hydrodynamic numerical models previously carried out by other authors.

II. THE PHYSICAL EXPERIMENT

The physical test used here is carried out at Aachen University in the Institute of Hydraulic Engineering and Water Resources Management and is published by [4] and [2]. [5], [6], [1] and [3] have further discussed the experiment and compared the test results with numerical simulation results. For the sake of completeness, the experiment is briefly discussed.

The experiment was set up in such a way that it mimics the conditions of river dike-breach type flow. As such, the physical model consists of a channel and an adjacent propagation area separated by a gate that can be opened suddenly with a pneumatically operated system. The channel, a sudden opening of the gate, and the propagation area – made of glass – adjacent to the gate serve as the representation of the river, the dike-breach phenomena, and flood plain protected by dike respectively.

The channel has a width of 1m, a length of about 8.50 m, no slope, and an adjustable sharp-crested weir at the outlet. The

weir serves to regulate the water depth in the channel. The gate is installed on the side of the channel connected to the propagation area. It can be set to three different widths: 30 cm, 50 cm and 70 cm. The centre of the gate is located 3.97 m from the channel inlet. The propagation area has a dimension of 3.5 m x 4.0 m and is made of glass. It has no slope and water can freely flow over its three edges. The schematic diagram of the experiment is shown in Fig. 1.

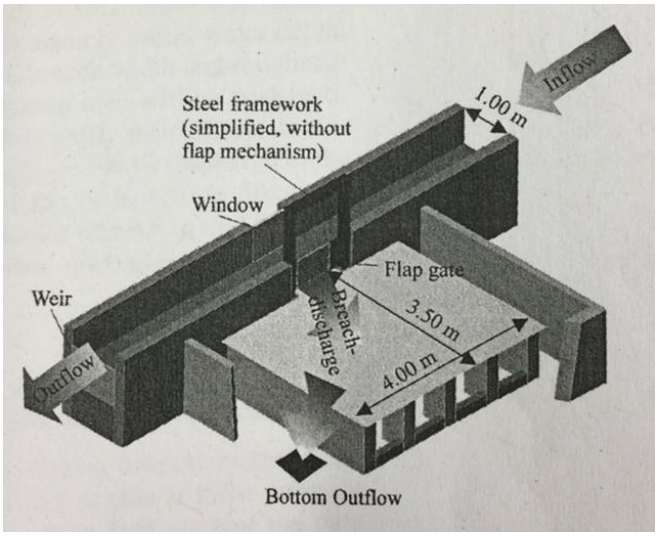

Figure 1. *Schematic diagram of the setup of the physical model, taken from [4]*

Dike-breach type flow is initiated by sudden opening of the flap gate. The flap gate is operated pneumatically with pull and rotation mechanism, which minimizes the disturbance on the water column in the channel during sudden gate opening.

III. TELEMAC-2D MODEL SET UP

A. *Introduction*

Telemac-2D model is set up for the physical test described above. The model is set up in such a way that the conditions of the physical test are replicated as correctly as possible. In the following sections, important aspects of the model set up are discussed.

B. *Computational mesh*

Computational mesh gives the geometric representation of the physical phenomena and need to be good enough to replicate the physical phenomena. Mesh used in this work is generated with the free software Kalypso1D2D. Kalypso 1D2D is pre-processing and post-processing module for hydrodynamic numerical models (2D, 3D) of Kalypso. Kalypso is an open source software developed by Björnsen Consulting Engineers (BCE) and the Institute of River and Coastal Engineering, Hamburg University of Technology (TUHH).

Mesh resolution of a model area have influence on the results of a numerical model. As a result, the computational mesh should be optimised to a mesh resolution that gives a mesh independent result. For this reason, a high resolutions mesh is used for the current work. The used mesh consists of about 46500 elements and 23700 nodes. The edge length of the mesh elements varies between 0.01 m and 0.03 m in the gate area and between 0.03 m and 0.05 m in the other parts of the model. The mesh resolution is chosen based on the sensitivity analysis of [3], who analysed mesh sensitivity for another finite element based hydrodynamic numerical model used to model similar physical test. Part of the computational mesh used in this work is shown in Fig. 2.

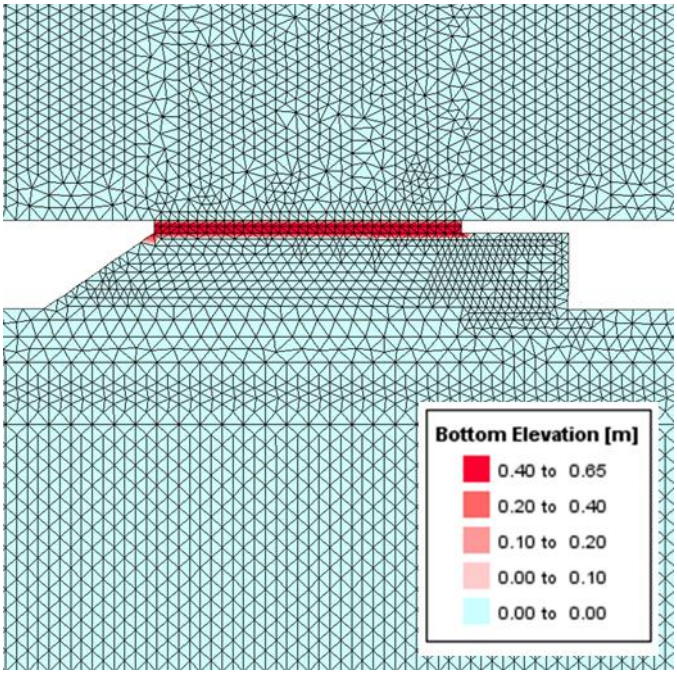

Figure 2. *Part of the mesh near the gate area used in the current investigation (not to scale)*

C. *Initial and Boundary conditions*

The initial condition of all the simulations in this work is dry condition, that is, the water surface is set to 0 (the bottom elevation of the channel and the propagation area is 0), except at the inflow boundary, where the elevation of the nodes are lowered to have some depth of water at the beginning.

The boundary conditions are discharge at the channel inlet, water level discharge relationship at the weir outflow, free overflow at the three sides of the propagation area, and solid boundary at the other parts of the boundary as shown in Fig. 3.

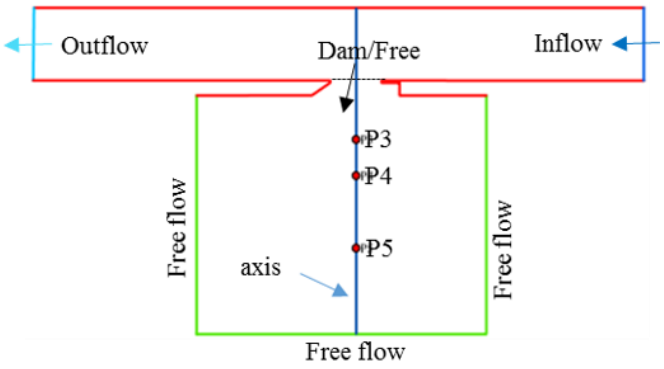

Figure 3. *Schematic diagram showing the boundary conditions of the model, three points in the propagation area at which point results were evaluated and an axis along which water level profile results were analysed.*

D. *Breach modelling*

The flap gate is represented in the numerical model by a sill of elevation 0.65 m. The gate opening is simulated by sudden dike breach. That is, the sill is lowered to the level of the channel instantaneously. For specifying the parameters of the breaching process, the dike breach model available in Telemac-2D is used.

E. *Test configurations*

In the current analysis, 12 test configurations are modelled with Telemac-2D. The test configurations differ from each other depending on the inflow discharge, the initial steady water depth in the channel before gate opening and the width of the gate opening. The configurations are named in the same manner as [3], in which the name indicates the breach width in cm, the inflow discharge in l/s and the initial depth in the channel before gate opening in cm. For example, test configuration name 'b50_Q300_h50' corresponds to configuration with gate opening of 50 cm, inflow discharge of 300 l/s and initial water depth in the channel before gate opening equal to 50 cm.

IV. CALIBRATION AND VALIDATION

A. *Calibration*

The numerical model is calibrated with the physical test configuration b70_Q300_h50.

First initial steady flow in the channel before the gate opening is calibrated for friction coefficient, boundary conditions, velocity diffusivity and free surface gradient compatibility. It is noticed the boundary condition at the outflow weir has the most significant influence on the steady water depth in channel before gate opening. Steady depth of flow in the channel equal to 0.50 m, equal to the physical test configuration, could be achieved by using stage-discharge relationship at the weir corresponding to a discharge of 90% of the maximum discharge at critical flow. Stage-discharge relationship boundary condition at the outflow weir determined experimentally by [6] for this configuration results in steady depth of flow in the channel equal to 0.53 m, which is higher than 0.5 m. Hence, the experimentally determined h-q relationship is not used.

The influence of friction coefficient on the steady water level in the channel before gate opening is not significant as can be seen from Tab. 1. Thus, a friction coefficient, ks = 0.01 m, corresponding to Nikuradse's friction formulation is used. Runs with different velocity diffusivity showed that with increasing values the steady state water depth in channel decreases. This is due to an implausible flow over the sill representing the gate in the numerical model. A velocity diffusivity equal to $1.0E^{-5}$ m²/s is adopted for further use. In addition, decreasing free surface gradient compatibility to 0 also improved the steady depth in the channel before the gate opening.

After successful calibration of the steady state flow in the channel before gate opening, further calibration of the model is carried out for the flow in the propagation area. Measured breach discharge and water levels at selected points in the propagation area are compared with Telemac-2D results. To obtain comparable results, boundary condition at free overflow boundary is varied. Best results were obtained with free flow boundary condition with Thomson option activated.

TABLE 1. STEADY WATER LEVEL IN THE CHANNEL FOR DIFFERENT SETTINGS

Varied Parameter	Parameter value	Simulated steady water level [m] in channel before gate opening
	0.1	0.5322
	0.01	0.5305
	0.001	0.5300
	0.0001	0.5298
	$1.00E^{-05}$	0.5305
	$1.00E^{-04}$	0.5320
	$1.00E^{-03}$	0.5294
	$1.00E^{-02}$	0.5162
	$1.00E^{-01}$	0.4521
	Free flow [4 4 4]	0.5368
	h-q (Max. Q)	0.4937
	h-q (90% Max. Q)	0.5078
	0.9	0.5078
	0.5	0.5058
	0.1	0.5045
	0	0.5043

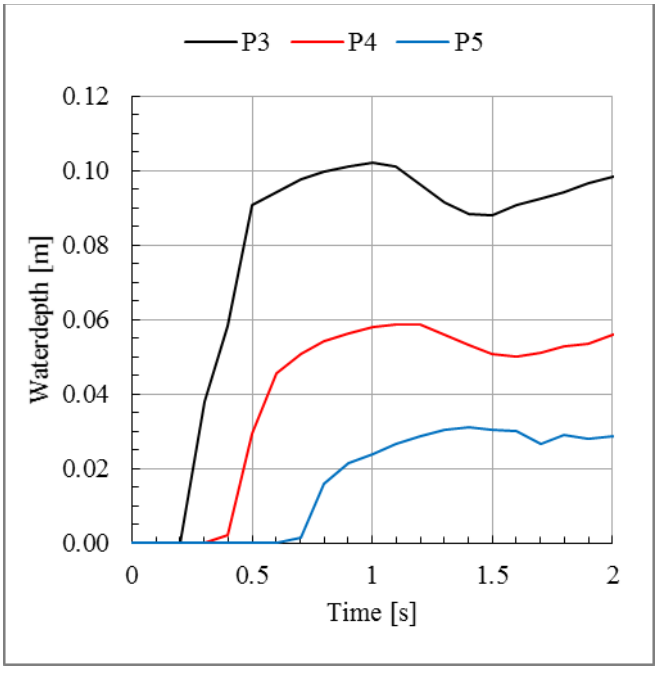

Figure 4. *Water level at three points in the propagation area (see Fig. 3 for the location of the points) over time for the configuration b70_Q300_h50 obtained with Telemac-2D (unsteady phase)*

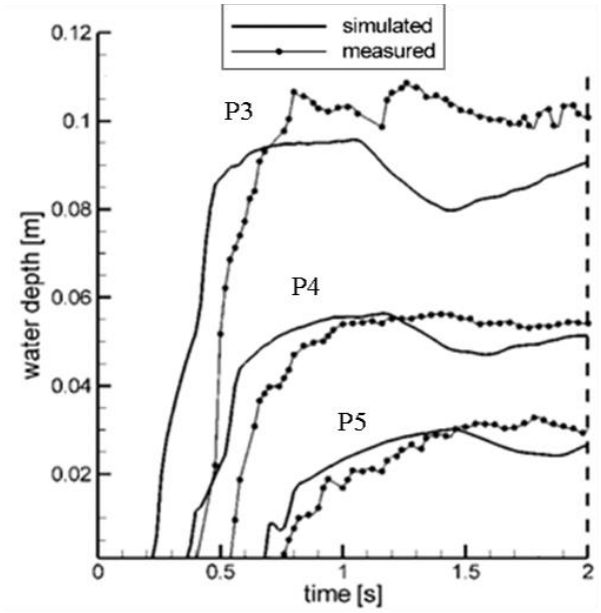

Figure 5. *Water level at three points in the propagation area (see Fig. 3 for the location of the points) over time for the configuration b70_Q300_h50 measured values compared to simulated values by [5] (unsteady phase)*

TABLE 2 STEADY WATER LEVEL AT THREE POINTS IN THE PROPAGATION AREA (SEE FIG. 3 FOR THE LOCATION OF THE POINTS) FOR THE CONFIGURATION B70_Q300_H50; MEASURED VALUES COMPARED TO TELEMAC-2D RESULTS AND SIMULATED VALUES BY [5]

Point	measured [m]	Telemac-2D [m]	Difference (%)	Simulated by [5] [m]
P3	0.085	0.079	7%	0.075
P4	0.045	0.046	-2%	0.044
P5	0.025	0.019	24%	0.023

B. *Validation*

The numerical model is validated with the physical test configuration b50_Q300_h50. The steady water level in channel before gate opening simulated with Telemac-2D is 0.5042 m and in the same accuracy range with the steady water level in the channel obtained during the calibration processes. Furthermore, the breach discharge computed with Telemac-2D is equal to 0.166 m³/s and the measured breach discharge was 0.182 m³/s.

The validation results show that the model parameters from the calibration give comparable results with measured values for an independent configuration. Hence, these settings are used for the remaining configurations.

V. COMPARISON OF TELEMAC-2D RESULTS WITH PHYSICAL EXPERIMENT RESULTS AND OTHER NUMERICAL MODEL RESULTS

A. *Wave front*

During the physical test, the wave front of the flood after the sudden gate opening was documented. The documentation was done at fixed time intervals. At similar time intervals, the wave front of the propagation simulated with Telemac-2D is extracted and compared with measurements.

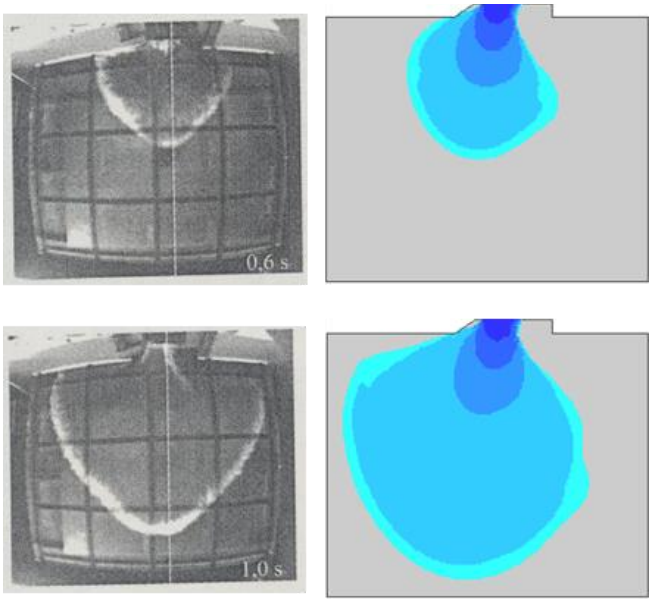

Figure 6. *Wave Front for configuration b50_Q300_h50; top left - wave front taken by CCD-camera 0.6 seconds after gate opening (adapted from [4]), top right - wave front as modelled by Telemac-2D, bottom left - wave front taken by CCD-camera 1 seconds after gate opening (adapted from [4]), and bottom right - wave front as modelled by Telemac-2D. Depths less than 1 mm are neglected.*

It can be seen from Fig. 6 that the model results are comparable to the measurements. However, slight differences are evident. The flow in the numerical model deflects more in the direction of the flow in channel compared to the measurements. These could be due to the difference in opening mechanism in the physical model and the numerical model. In the numerical model, the opening of the gate is achieved by sudden lowering of the bottom elevation of the nodes representing the gate (the sill) where as in the physical experiment sophisticated mechanisms were put in place not to influence the water column in the channel [4]. [5] and [3] also obtained similar results with other numerical models, which in the Authors view support the argument that the reason has to do with the mechanism of the gate opening.

B. *water level point results*

Water level measurements at fixed points over longer period in the propagation area are undertaken during the physical test. These measurements are very useful to compare the performance of the numerical model.

In Fig. 7 water level at three points in the propagation area (see Fig. 3 for the location of the points) obtained with Telemac-2D for the configuration b70_Q300_h40 are given. Corresponding results from the experiment and model run by [5] are given in Fig. 8. From the comparison of these figures, it can be seen that the measured and computed water levels at three points are quite comparable. However, flow arrived at points P3 and P4 earlier in Telemac-2D results compared to the measurements. The arrival time at point P5 is comparable between Telemac-2D result and the measurement. Similar behaviour in time of arrival of the flood at the three points can be observed in the numerical results of [5].

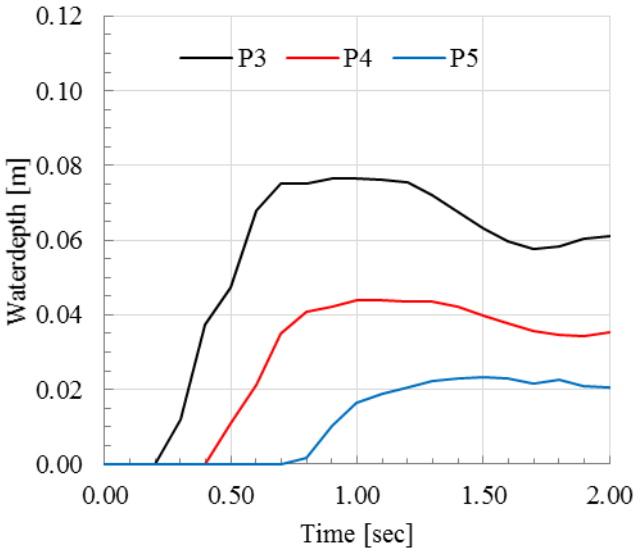

Figure 7. *Water level at three points in the propagation area (see Fig. 3 for the location of the points) over time simulated with Telemac-2D for configuration b70_Q300_h40 (unsteady phase)*

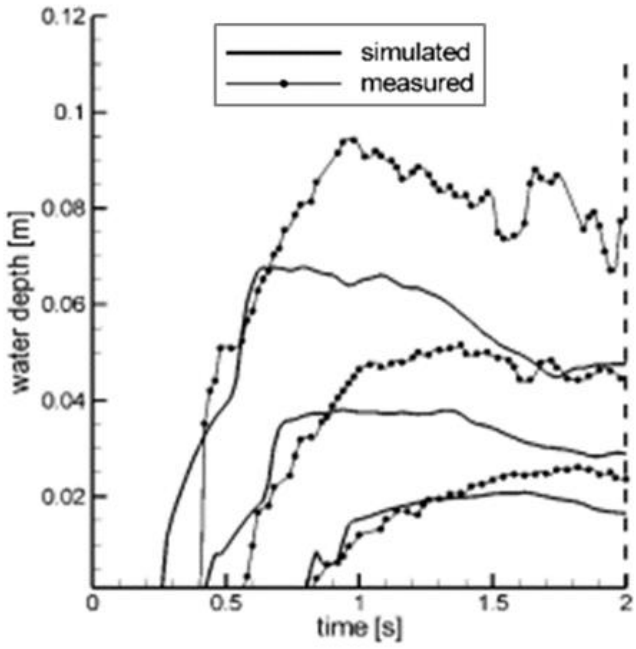

Figure 8. *Water level at three points in the propagation area (see Fig. 3 for the location of the points) over time for the configuration b70_Q300_h40 measured values compared to simulated values by [5](unsteady phase)*

Also, the final steady water level achieved by Telemac-2D is generally less than the measured values as can be observed from Tab. 3. The difference is higher for P5, which is further from the gate but nearer to the free boundary. Telemac-2D performed better than the numerical model results of [5] for points P3 and P4.

TABLE 3. STEADY WATER LEVEL AT THREE POINTS IN THE PROPAGATION AREA (SEE FIG. 3 FOR THE LOCATION OF THE POINTS) FOR THE CONFIGURATION B70_Q300_H40; MEASURED VALUES COMPARED TO TELEMAC-2D RESULTS AND SIMULATED VALUES BY [5]

Point	measured [m]	Telemac-2D [m]	Difference (%)	Simulated by [5] [m]
P3	0.075	0.059	21%	0.047
P4	0.036	0.031	15%	0.028
P5	0.017	0.011	34%	0.15

C. *Steady breach discharge*

During the physical test, the steady breach discharge, that is, the discharge through the gate opening after steady flow, is computed from the difference of the inflow discharge and the outflow discharge at outflow weir. The same is computed for Telemac-2D simulation results and is presented in Tab. 4 together with breach discharges determined with other numerical models by [3].

The breach discharges computed by Telemac-2D for the different test configurations agree very well with the measurements. However, Telemac-2D underestimated the breach discharge for the test configuration b50_Q300_h50 by about 9% and overestimated for the test configuration b50_Q200_h30 by about 4 %. For the rest test configurations the error in breach discharge by Telemac-2D is in between these two test configurations.

In addition, Telemac-2D computed the breach discharge better than the 2D-models DGFlow and WOLF 2D for most of the test configurations. Nevertheless, Telemac-2D performed inferior to the 3D-model STAR-CD with respect to breach discharge.

TABLE 4. BREACH DISCHARGE FOR DIFFERENT TEST CONFIGURATIONS

configuration	*measured (l/s)*	Telemac-2D		Numerical results of [3]	
		Simulated (l/s)	*diff (%)*	*DGFlow (l/s)*	*STAR-CD(l/s)*
b50_Q300_h50	182	166	8.8	164	174
b50_Q300_h40	127	124	2.4	114	130
b50_Q200_h50	171	158	7.6	156	163
b50_Q200_h40	130	120	7.7	118	122
b50_Q200_h30	79	82	-3.8	74	81
b50_Q100_h30	81	75	7.4	74	72
b70_Q300_h50	218	203	6.9	200	211
b70_Q300_h40	159	150	5.7	141	153
b70_Q200_h50	194	185	4.6	183	190
b70_Q200_h40	154	144	6.5	143	148
b70_Q200_h30	98	99	-1.0	92	99
b70_Q100_h30	91	88	3.3	87	90

D. *Water level Profiles*

Water level profile along the axis of the propagation area extracted from the results of Telemac-2D for four test configurations are given in Fig. 9. The corresponding water level profiles from the physical test results are shown in Fig. 10.

Comparison of the water level profiles between the measurements and the results of Telemac-2D show that Teleamc2D reproduced the water surface profiles very well. However, free surface near the free outflow boundary shows strong oscillation in the results of Telemac-2D. This should be related to the boundary condition prescribed as free outflow with Thomson option at this boundary.

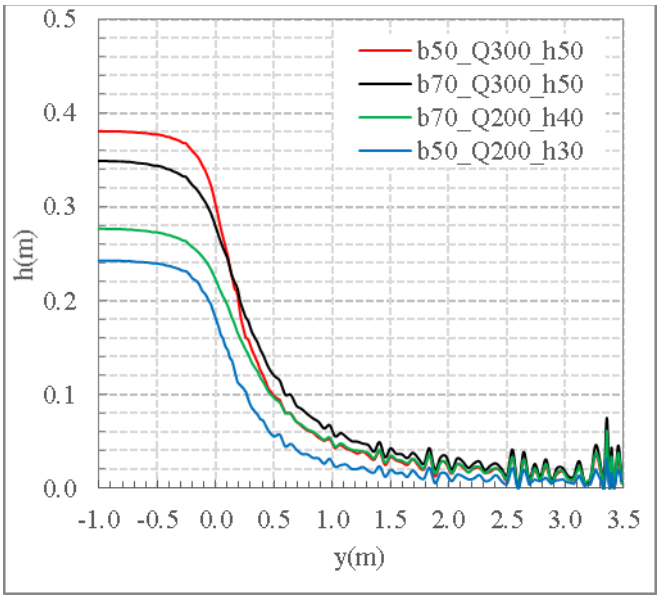

Figure 9. *Water level profile along axis shown in Fig. 3 after steady flow conditions are reached (1 minute after gate opening)*

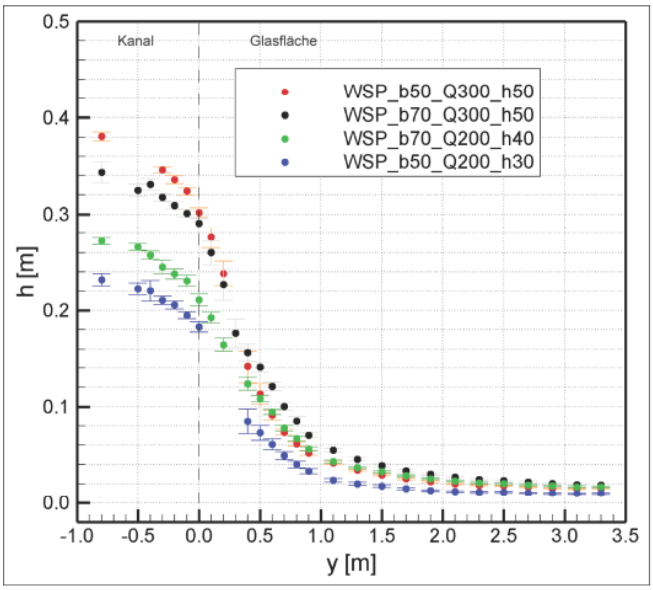

Figure 10. *Measured water level profile along axis shown in Fig. 3 after steady flow conditions are reached (1 minute after gate opening) (taken from [3])*

VI. Conclusions

The presented results show that Telemac-2D reproduced the measurements in the physical test. In particular, Telemac-2D replicated the breach discharge very well. As breach discharge is the most important factor in hinterland inundation resulting from dike breach, it can be concluded that with appropriate parameters, Telemac-2D is a suitable tool for assessing flood inundation resulting from dike breaching.

References

[1] S. Roger, J. Köngeter, H. Schüttrumpf, S. Erpicum, P. Archambeau, M. Pirotton et al., "Hybrid modelling of dike-break induced flows," *River flow 2010: Proceedings of the Fifth International Conference on Fluvial Hydraulics,* Braunschweig, Germany. 8 - 10 June, pp. 523–531.

[2] S. R. Briechle, "Die fächenhafte Ausbreitung der Flutwelle nach Versagen von Hochwasserschutzeinrichtungen anFließgewässern," Doctoral Thesis, RWTH Aachen University, Aachen, 2006.

[3] S. Roger, "Hybride Modellierung deichbruchinduzierter Strömungen für ein idealisiertes Breschennahfeld an Fließgewässern," Doctoral Thesis, RWTH Aachen University, Aachen, 2011.

[4] S. Briechle, A. Joeppen and J. Köngeter, "Physical model test for dike-break induced, two-dimensional flood wave propagation," *River flow 2004: Proceedings of the Second International Conference On Fluvial Hydraulics,* Napoli, Italy. 23-25 June, pp. 959–966.

[5] S. Roger, E. Büsse and J. Köngeter, "Dike-Break Induced Flood Wave Propgation," *Hydroinformatics 2006: Proceedings of the 7th International Conference,* Nice, France. 4 - 8 September, 2006.

[6] S. Roger, B. J. Dewals, S. Erpicum, D. Schwanenberg, H. Schüttrumpf, J. Köngeter et al., "Experimental and numerical investigations of dike-break induced flows," *Journal of Hydraulic Research*, Vol. 47, No. 3, 2009, pp. 349–359. doi:10.1080/00221686.2009.9522006.

Hydraulic 2D Model of Landslide Generated Wave – Cases of Chehalis Lake and Chambon Lake

Thomas Viard
Hydro Engineering Centre,
EDF
Le-Bourget-du-Lac, FRANCE
Thomas.viard@edf.fr

***Abstract*— In 2015, a landslide began to fall above Chambon Lake in France. This event reminds us that this phenomenon stands as one of the main risks for dam safety. Risks associated to generation and propagation of landslide-induced impulse waves in reservoirs might have dramatic consequences around the lake shores, for the dam itself, and also downstream as the Vajont catastrophic event showed in 1963. Recent research and permanent improvement of models have provided better risk evaluation tools by linking geology and hydraulic physics.**

Since 1998, EDF has been using Telemac to model landslide-induced waves. The first work was a comparison between numerical and physical models for the Billan landslide above Grand'Maison Lake. The landslide was defined as a hydrograph with very high flow.

In 2010, EDF started using Telemac in a different way to model landslide entering into a lake: a landslide is now represented by a dynamic vertical deformation of the bathymetry. This approach used Chehalis Lake landslide as validation case: in 2007, a landslide of 3 000 000 m^3 occurred in Chehalis Lake with a wave run-up going up to 40 meter high. Run-up leaves were collected all around the lake.

This way to model landslide-induced impulse waves gives good results and can be apply in safety management. However we have to keep in mind that numerical results only provide orders of magnitude as uncertainties inherent to landslide forecast (velocity, volume ...) remain high.

In 2015, this approach was applied to evaluate risks of "Berche" landslide at Chambon Lake with good confidence in the results.

I. INTRODUCTION

Landslides in reservoirs and lakes are a major potential problem for dam safety. Waves induced by landslides can cause [1]:

- damage to shoreline structures and boats,
- overtopping of dams by waves with resulting damages and downstream flooding,
- failure of dams,
- upstream flooding due to river blockages,
- loss of usage of the water body due to the final position of slide material.

Interest to study landslide is evident in terms of security.

In 2007, a 3 000 000 m^3 landslide occurred in Chehalis Lake, a natural lake near Vancouver in Canada. The maximum run-up height of the wave induced by the landslide reached about 40 meters. Damages were limited as it occurred in winter when the two campsites located on the lake sides were closed.

Electricité de France (EDF) was interested to test the efficiency of tools used to model landslide in reservoir. Chehalis landslide was a good opportunity to test this efficiency since a lot of information about the Chehalis landslide itself, topography (bathymetry) and run-up (wave marks: trash lines, tree scars…) were collected. EDF studied the wave induced by the landslide in the lake, its generation and its propagation. Two different methods were tested: empirical equations from Heller's studies [2] and [3], and a 2D model with TELEMAC-2D.

In 2015, "Berche" landslide began to move above Chambon Reservoir in the Alps. Tests done with Chehalis Lake Landslide allowed EDF to manage risks induced by Berche Landslide with good confidence using both methods Heller's empirical equations and TELEMAC-2D

II. GENERAL METHODOLOGY

A. *Heller's study*

The main topic of this article is the use of TELEMAC-2D to model wave induced by landslides. But, most of the time, before building a complex model, it can be useful to know the order of magnitude of wave that can be induced by a landslide.

Here is a short summary of Heller's work [3]. It follows works of Fritz [4] and Zweifel [5]. A lot of experiments were made on a unique channel. Fritz and Zweifel carried out 223 runs and Heller added 211 runs. From results of these 3 works, Heller provided empirical equations which allow predicting the wave height considering all relevant parameters of the landslide at impact on water surface.

Heller determined a set of governing parameters that allow calculating wave near field characteristics: slide impact velocity V_s slide thickness s, bulk slide volume $\forall_s$ bulk slide porosity n, slide density ρ_s, slide width b, slide impact angle α, still water depth h, gravitational acceleration g and water density ρ_w.

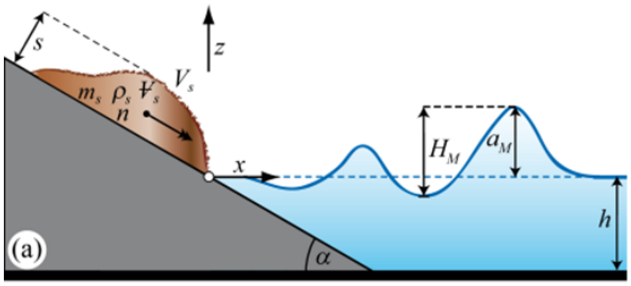

Figure 1. *Wave generation governing parameters*

From these parameters, Heller calculated 3 dimensionless numbers:

F	:	Froude number	$F = \frac{V_s}{(g*h)^{\frac{1}{2}}}$	(1)
S	:	Relative slide thickness	$S = \frac{s}{h}$	(2)
M	:	Relative slide mass	$M = \frac{V_s*\rho_s}{\rho_w*b*h^2}$	(3)

From these 3 dimensionless numbers and the governing parameter α, Heller defined another dimensionless number: *Impulse product parameter* P.

$$P = F * S^{0.5} * M^{0.25} * \left(cos\left(\frac{6\alpha}{7}\right)\right)^{0.5} \quad (4)$$

From this impulse product parameter, Heller determined empirical equations to calculate near field characteristics and wave characteristics on a given point of the propagation zone in a channel ("2D") or in a basin ("3D"). Water height maximal value H_m (5), or at a point in a channel ("2D") *H(x)* (6) or in a basin ("3D") *H(r;γ)* (7) and run-up wave height (8) are given by equations below:

$$H_m = \left(\frac{5}{9} * P^{\frac{4}{5}} * h\right) \quad (5)$$

$$H(x) = \left(\frac{3}{4}\right) * (P * X^{\frac{-1}{3}})^{\frac{4}{5}} * h \text{ with } X = \frac{x}{h} \quad (6)$$

$$H(r,\gamma) = \frac{3}{2} * P^{\frac{4}{5}} * (\cos(\frac{2*\gamma}{3}))^2 * (\frac{r}{h})^{\frac{-2}{3}} * h \quad (7)$$

$$R = 1.25 * (\frac{H}{h})^{\frac{5}{4}} * (\frac{H}{L})^{\frac{-3}{20}} * (\frac{90°}{\beta})^{\frac{1}{5}} * h \quad (8)$$

Other equations such as wave celerity or wave length are detailed in Heller's study.

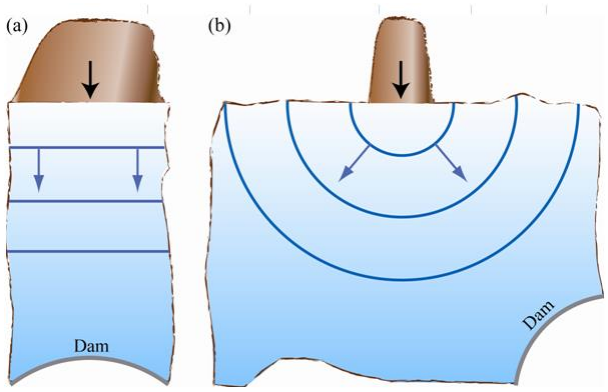

Figure 2. *"2D" (a) and "3D" (b) configuration*

B. TELEMAC-2D

When wave and run-up heights induce risks for population or dam, a TELEMAC-2D model can be implemented to have a better assessment of wave height by taking into account effect due to topography (island, complex shore shape, reflection effects…).

TELEMAC-2D cannot model a real landslide entering a lake. Therefore, 3 ways to simulate a landslide were tested on Chehalis Lake case:

1. The landslide is replaced by a hydrograph,
2. The landslide is replaced by a dynamic vertical deformation of bathymetry,
3. The landslide is replaced by a block of water in the area from where landslide begun.

The first hypothesis is a natural input for the software but landslide behaviour after impact and effect of a "shock" cannot be simulated. The third hypothesis is interesting but many parameters such as density cannot be taken into account and there are not many possibilities to adapt initial conditions.

Therefore the second hypothesis is deemed the best way to simulate the landslide and the induced wave. But it is not the easiest way to use TELEMAC-2D. Subroutine Corfon.f can be used to modify bathymetry, but this subroutine is only called at the first time step. The use of an application programming interface (API) would be useful but such a tool did not exist in 2010. Therefore a program using a loop was created modifying corfon.f and calling TELEMAC-2D for only few time step. Two time step are defined:

- Time step of TELEMAC-2D,
- Time step of the loop (modifying corfon.f therefore moving the landslide).

Another difficulty had to be overcome: when option "computation continued" is used, corfon.f is called only if the geometry was not recorded in the previous computation file. And when corfon.f is called, it is adapted to sediment transport calculation (Sisyphe), keeping surface elevation and adapting water height, whereas we need the opposite. Therefore TELEMAC-2D have to record only water heights and velocities but no geometry and no water surface elevation.

The landslide shape under water can have an impact on waves and wave reflexion. Therefore 3 ways of underwater landslide behaviour were tested:

1. Landslide stopping (constant shape): The simplest way of modelling the landslide is to let it move at constant speed without distortion and stop it at the deepest point of the lake;
2. Landslide vanishing: When the landslide reaches the bottom of the lake, it continues underground until it vanishes totally. It is as if the landslide is disintegrated when it touches the bottom of the lake (there is no conservation of landslide's volume);
3. Landslide scattering: When the landslide has totally entered water, its thickness decreases and its width increases, conserving the total volume of the landslide.

The third hypothesis gave the best results and is always used for new cases (Berche case).

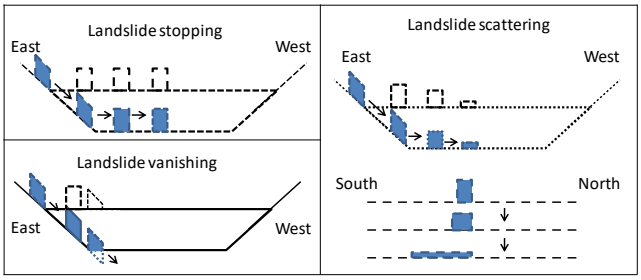

Figure 3. *Different ways to model landslide progression underwater*

When bathymetric deformation is used to model a landslide, the landslide kinetic energy is transferred to the water body by potential energy (elevation) and the initial water volume moving at impact is equal to the landslide volume.

When a real landslide occurs, depending on Froude number of the landslide, the initial water volume moving at impact can be much bigger than the landslide volume (up to 8 times [4]) and wave generation is due to different phenomena:

1. Physical displacement of water by the landslide,
2. Viscous drag and pressure drag (not modelled by TELEMAC-2D).

Therefore 2 verifications are needed before using TELEMAC-2D: the initial water volume moving should be similar to the landslide volume and the predominant force at impact should be the physical displacement. The first condition is obtained when Froude number is below 2 and the second condition when wave celerity is higher than landslide celerity, therefore when Froude number is not significantly higher than 1.

These conditions can seem restrictive but when the lake depth is between 30 and 40 m, landslides with a velocity up to 20 $m.s^{-1}$ can be modeled and when the lake depth is around 100 m, landslides with a velocity up to 30 $m.s^{-1}$ can be modeled.

III. CHEHALIS LAKE CASE

A. *Model*

The lake

Chehalis is located in the North-East of Vancouver in British Columbia, Canada. Chehalis Lake's main axis is South-North. On this axis, the lake is 8.2-km long. On the East-West axis, the lake is around 1-km long. There is a 450-m wide neck dividing the lake in two parts:

- North part, 2.8-km long (where the landslide occurred),
- South part, 5.4-km long.

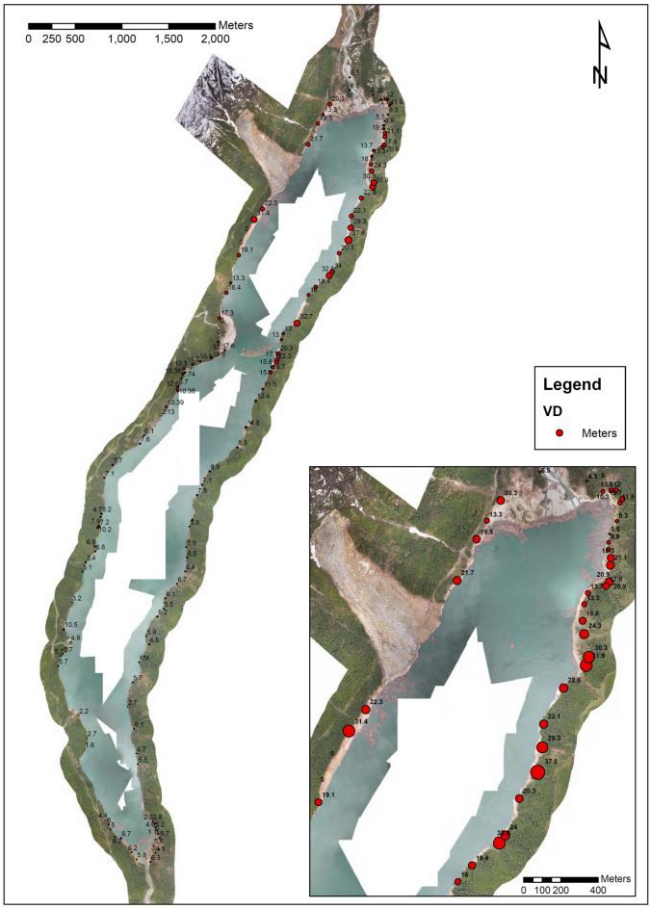

Figure 4. *Chehalis Lake and run-up recorded*

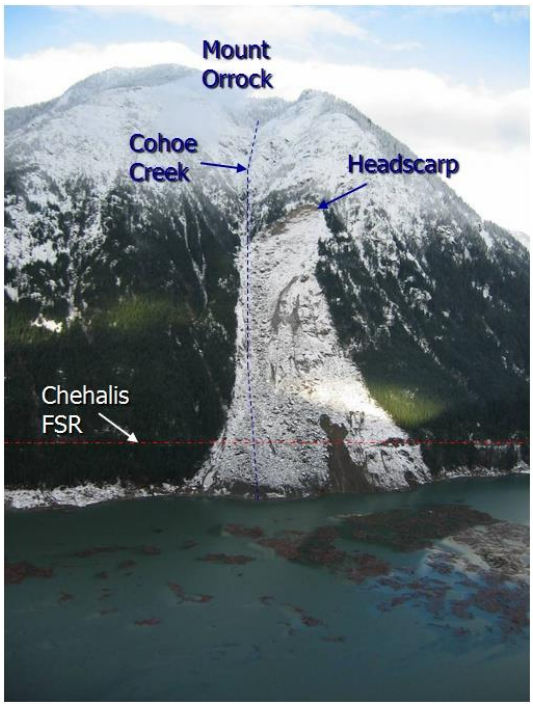

Figure 5. *Chehalis Lake landslide*

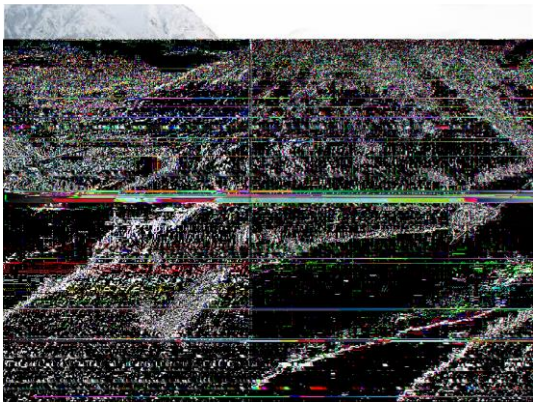

Figure 6. *Chehalis Lake and landslide*

The landslide

The landslide occurred on December 4th, 2007. Around 3 000 000 m^3 of rockslide fell into the north part of Chehalis Lake. The wave induced by the landslide uprooted many trees on shores creating many woody debris. It occurred during a storm flood event that masks any possible surge wave signature in Chehalis River.

Velocity of the landslide was estimated around 20 $m.s^{-1}$.

Topography / bathymetry

In June 2009, a bathymetric and side scan sonar survey was conducted to assist in evaluation of the lakebed conditions at Chehalis Lake. The objectives were to generate data sets which could be used to model the wave, examine the lake bed features generated in the proximity of the failure, develop volume estimates as well as look for evidence of prior failure events.

On top of this bathymetric survey, topographic data of slide area and shores were obtained by LIDAR

Equation and scheme used

In 2010, simulations were done with V5P9 of TELEMAC-2D. Using Boussinesq equations seemed naturally more adapted to the present problem since it is a wave. But the first tests led to very long computation times or errors due to tidal flats.

Therefore the choice was to use shallow water equations with finite volume (in the version V5P9 of TELEMAC-2D used, the finite elements code uses the method of characteristics in its calculations and this method did not work well on a resting lake or on tidal flats).

Mesh

4 mesh sizes were used depending on location:

- In the north part of the lake (near the landslide)
  - 15 m in the centre and
  - 5 m on shores and in the impact area
- In south part of the lake (south of the neck),
  - 25 m in the centre
  - 15 m on shores.

B. Results

Many simulations were done to test a lot of hypothesis: different ways to simulate the landslide, underwater landslide behaviour, shallow water or Boussinesq…

Here is presented the simulation corresponding to the best recorded run-up all around shorelines: with a bathymetric landslide scattering, using shallow water equations with finite volume scheme, a good correlation between simulation results and recorded run-up were found. Results were analysed area by area.

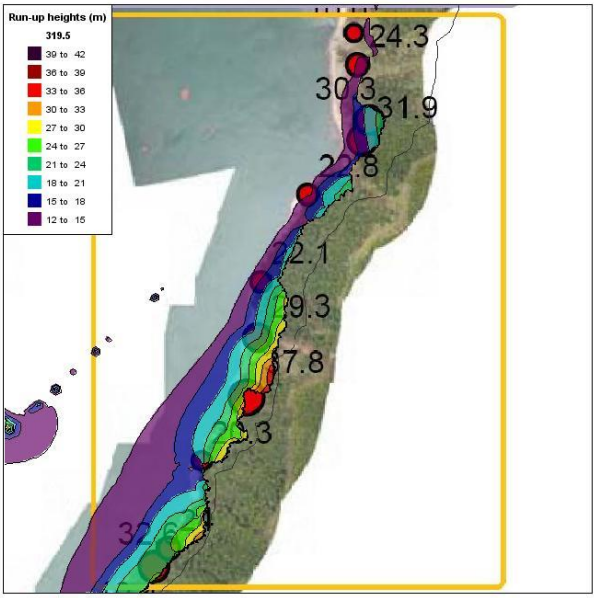

Figure 7. *Simulated run-up facing landslide*

Calculated and observed run-up heights on the shore facing the landslide were similar. The south part of this area gave really good results, but the north part seemed a little under estimated. Maximum calculated run-up height was 38 m for a 40 m observed run-up.

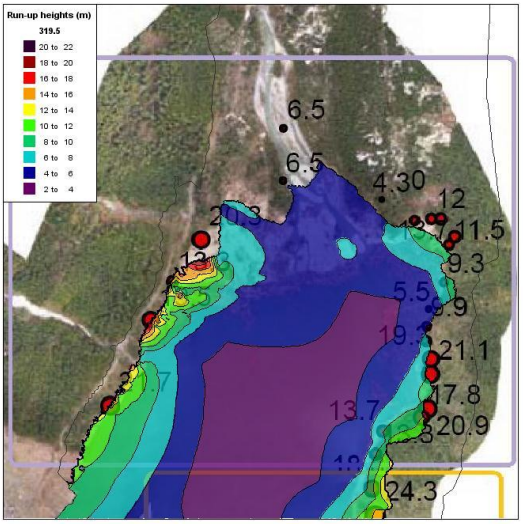

Figure 8. *Simulated run-up in North part of the lake*

In the north part of the lake, the east shore results seemed a little bit under estimated and the west shore results good.

Near the landslide impact, results were really close to observed run-up heights, but maxima of calculated run-up heights were located a little bit more south than maxima of observed run-up heights

In the south part of the lake, average, minimum and maximum run-up heights were good, but calculated run-up heights decrease from north to south a little bit quicker than observed run-up heights.

C. Feedback

This case gave a good confidence in the numerical method implemented. Comparison of results from TELEMAC-2D, Heller equations and run-up recorded showed a good correlation between results of the 2 methods and reality. Therefore it was concluded that these methods can be used for risk assessment (if conditions on Froude number are fulfilled for TELEMAC-2D).

IV. BERCHE CASE

In 2015, Berche landslide began to move above Chambon Lake. Geotechnical studies concluded that the landslide should remain with low velocity, but 2 scenarios could not be totally excluded:

1. Fall of 50 000 m^3 at 20 $m.s^{-1}$ into the lake,
2. Fall of 150 000 m^3 at 10 $m.s^{-1}$ into the lake.

First estimations of run-up heights on shores and at the dam were done with Heller's equations. But to have better confidence in results and take into account particular shape of the lake, a TELEMAC-2D model was developed to simulate both scenarios.

A. Chambon Lake

Chambon Lake is located between Grenoble and Briançon in the French Alps. Chambon Lake's main axis is East-West. On this axis, the lake is 3-km long. On the South North axis, the lake width varies between 250 m and 1km with an average of 400 m. Just like Cheahlis Lake, there is a 250m wide neck dividing the lake in two parts (the dam and the landslide are in different parts). Depth at impact area is around 34 m.

B. Model

Software version and equations

Between 2010 and 2015, TELEMAC-2D improved a lot. For this case, version V7P1 of the software was used. Boussinesq equations could be used without difficulties.

Figure 9. *Berche landslide*

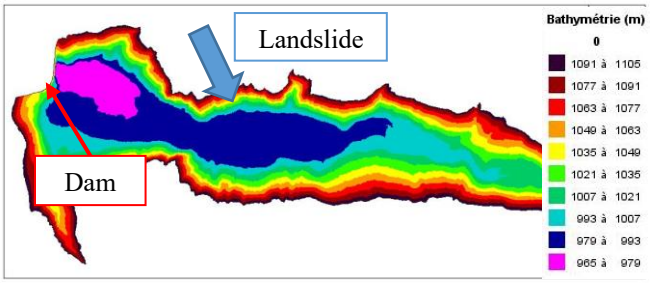

Figure 10. *Chambon Lake topography and bathymetry (French reference altitudes)*

Topography / bathymetry

A lot of information about bathymetry was available because lake sedimentation is monitored.

A LIDAR survey was undertaken during summer 2015.

Mesh

2 mesh sizes were used depending on location:

- 2 m in impact area and on shoreline,
- 5 m everywhere else.

Landslide shape and underwater behaviour

Taking into account Chehalis Lake feedbacks, a landslide scattering underwater was studied and its shape was chosen to maximise energy transfer between landslide and water.

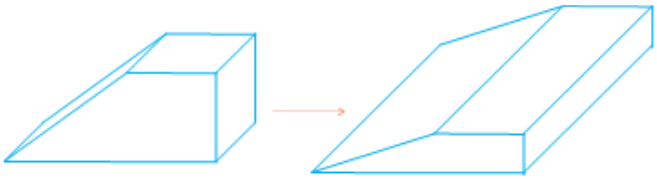

Figure 11. *Landslide shape in model and underwater behaviour (scattering)*

C. Results

Both scenarios were simulated.

Water depths at impact area are around 34 m. The first tests for scenario 1 yielded a wave celerity between 18 and 21 $m.s^{-1}$ for a landslide velocity of 20 $m.s^{-1}$ (Froude number of the landslide around 1). These results were used for risk assessment, therefore, to avoid any risk on security, a safety factor was applied to all run-up heights of scenario 1.

This factor was chosen by comparison between Heller's equation and TELEMAC-2D first results. Both methods gave similar wave heights (around 8 m), but TELEMAC-2D gave for this scenario lower wave length (lower energy transfer) and lower run-up heights facing the landslide (12 m vs. 16 m).

For each scenario results were studied on shores facing the landslide and at the dam.

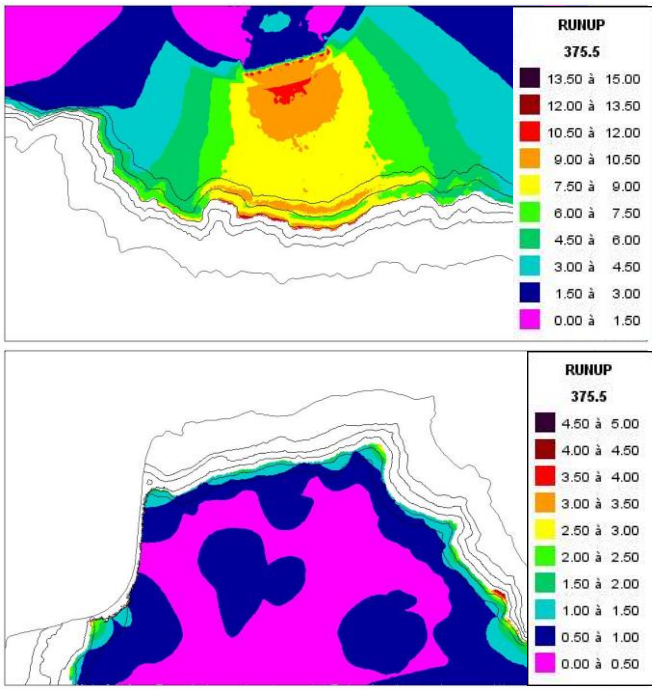

Figure 12. *Run-up heights (m) facing the landslide and around the dam for scenario 1*

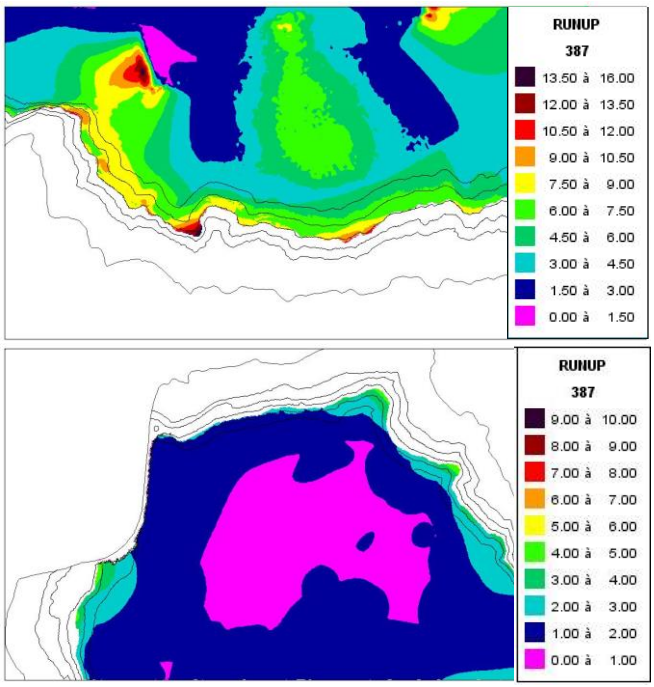

Figure 13. *Run-up heights (m) facing the landslide and around the dam for scenario 2*

These simulations allowed to manage risks all around the lake. The water level of the lake was adjusted during all studies depending on the knowledge about the landslide and risk induced.

Around the dam, it showed that there was no risk of overtopping and no risk of dam breaking

Facing the landslide, a road was built to allow car traffic from one side of the lake to the other (the landslide forced to close the tunnel that was used for traffic before). Risk assessment with TELEMAC-2D modelling allowed to have a safety road construction site.

V. Conclusion

Nowadays, thanks to Heller's equations, EDF can manage a landslide crisis with a good confidence in risk assessment. But a n additional safety factor is most of the time needed since this method does not take into account lake shape particularities.

Thanks to TELEMAC-2D modelling, with time, it is possible to take into account lake shape particularities and try to lower the safety factor used with Heller's method if Froude number of the landslide is not higher than 1.

The program implemented to model landslides should be improved by the use of the API. If another study must be carried out on this subject, the program will be rewritten with the API.

Special cases still remain such as landslide with high Froude number or really narrow lakes where wave induced by landslide cannot be fully generated before reaching opposite shore. For these special cases, TELEMAC-3D, Smoothed particles hydraulic (SPH) modelling or scale model should be used.

Acknowledgement

I would like to thank geologists and Chambon dam operators who help us to have the best risk assessment and Denis Aelbrecht for help and control of these studies.

References

[1] Kofoed-Hansen H., Cifres Giménez E., Kronborg P. (2001). *Modelling of landslide generated waves in MIKE 21*. 4th DHI Software Conference, Helsingør, Denmark, 21p.

[2] Heller, V., Hager, W. H., Minor, H.-E. (2009). *Landslide generated impulse waves in reservoirs: Basics and computation*. VAW-Mitteilung 211, ed. ETH Zürich, Zürich.

[3] Heller, V. (2008). Landslide generated impulse waves: Prediction of near field characteristics. Dissertation 17531, ETH Zürich, Zürich.

[4] Fritz, H. M. (2002). *Initial phase of landslide generated impulse waves*. Dissertation 14871, ETH Zürich, Zürich.

[5] Zweifel, A. (2004). *Impulswellen : Effekte der Rutschdichte und des Wassertiefe*. Dissertation 15596, ETH Zürich, Zürich.

Sensitivity analysis of urban flood flows to hydraulic controls

Shangzhi Chen[1], P.-A.Garambois[1], P. Finaud-Guyot[2], G. Dellinger[2], Abdelali Terfous[1], Abdallah Ghenaim[1]
[1]ICUBE-UMR 7357, fluid mechanics team, INSA Strasbourg,
24 Boulevard de la Victoire, 67084 Strasbourg cedex, France
[2]ICUBE-UMR 7357, ENGEES, fluid mechanics team, 2 rue Boussingault, 67000 Strasbourg cedex, France
shangzhi.chen@insa-strasbourg.fr

Abstract: Flooding represents one of the most significant natural hazards on each continent and particularly in highly populated areas. Improving the accuracy and robustness of prediction systems has become a priority. However, in situ measurements of floods remain difficult while a better understanding of flood flow spatiotemporal dynamics along with dataset for model validations appear essential. The present contribution is based on a unique experimental device at the scale 1/200, able to produce urban flooding with flows corresponding to frequent to rare return periods. The influence of 1D Saint Venant and 2D Shallow water model (Telemac2D) input parameters on simulated flows is assessed using global sensitivity analysis (GSA). The tested parameters are: global and local boundary conditions (water heights and discharge) and spatially uniform or distributed friction coefficient tested around their calibrated values thanks to accurate experimental data and related uncertainties, where the outputs of interest are spatially distributed water height and outlet discharge. For various experimental configurations a variance decomposition method (ANOVA) is used spatially to calculate distributed Sobol' sensitivity indices (Si's). The sensitivity of water depth and discharge to input parameters on the whole experimental device is presented here. Results show that the closer from the downstream boundary condition on water height, the higher the Sobol' index as predicted by hydraulic theory for subcritical flow, while interestingly the sensitivity to friction decreases. The sensitivity indices of all lateral inflows representing crossroads in 1D are also quantified in this study along with their asymptotic trends along flow distance. The relationship between lateral discharge magnitude and resulting sensitivity index of water depth is investigated. The spatially distributed Sobol' index in 2D configuration show similar trends as in 1D with except for a sub-critical flow zone where coupling effects between the tested parameters is highlighted. The role of street width and obstruction on discharge distributions is also analyzed using GSA. This methodology could be applied to any urban flood configuration in order to better understand flow dynamics and distribution but also guide model calibration in the light of flow controls.

Comparison of 2D numerical models for the simulation of river-flooding in a semi-urban area

Robert Stöffler[1], Clemens Dorfmann[2]
[1] Government of Styria, Hydrographic department
[2] flussbuero
robert.stoeffler@stmk.gv.at

Abstract: The study deals with the comparison of three 2D depth-averaged numerical models for the simulation of a flood event. In the comparative study the numerical models MIKE21 FM, HYDRO_AS-2D, RIVERFLOW2D and TELEMAC-2D are used. The four numerical models differ in the spatial and time discretization of the shallow water equations. For a transparent comparison, in the setups of the four models it has been aimed at applying the same parameters in terms of mesh, roughness and turbulence closure. Two flood scenarios have been investigated: unsteady flood hydrograph and steady 100-year-flood. The analysis of the results consisted mainly in the comparison of the computed water depths and the quantitative evaluation of the differences. Although the numerical models produce somewhat similar flood inundation areas, the computed local water depths can differ significantly especially in the flood plains. The study shows the high impact of the chosen numerical discretization scheme on the simulated flow processes. It highlights the required steps and the associated difficulties when comparing different 2D numerical models quantitatively. As a side product, the computation times of the numerical models are compared, too.

Numerical estimation of bedform roughness

Frederik Folke and Sven Wurms
Department of Hydraulic Engineering
Federal Waterways Engineering and Research Institute
76187 Karlsruhe, Germany
frederik.folke@baw.de

***Abstract*— An appropriate a priori estimation of the bed roughness for numerical river models is still challenging. For gravel river beds various approaches exist based on the grain-size distribution curve. But there is still a lack to estimate the roughness effect of geometrical bed structures such as rock peaks which are not resolved by the numerical grid, so-called sub-grid structures. The aim of the ongoing investigation is to provide a general method to capture sub-grid structures for individual numerical models using both TELEMAC-3D and TELEMAC-2D.**

A numerical test-bench to evaluate the roughness effect of geometrical bedform structures is introduced. For the calibration and validation a three-dimensional hydrodynamic-numerical (3D-HN) model is set up. All structures of the underlying geometry are resolved properly. For the investigation both a digital elevation model of natural rock peak structures of a shallow river bed and an artificial elevation model are used.

The coarse grid two-dimensional hydrodynamic-numerical (2D-HN) model is calibrated via the high-resolved 3D-HN model. Furthermore a statistical roughness approach for steep streams is applied to model shallow open-channel flow. The suitability of this method to capture the roughness effect of sub-grid structures is tested. Subsequently the flow over different elevated rock peaks is investigated. Beside the global water level local effects are compared and discussed.

I. INTRODUCTION

The hydraulic resistance of river flow is affected by various factors. Beside bed roughness [2] identified vegetation, channel irregularity, channel alignment, silting and scouring, obstruction, size and shape of channel, stage and discharge, seasonal change, suspended material and bedload as the factors with the greatest impact. These mechanisms do not act isolated but interact resulting in a complex physical behaviour. In all engineering applications of open-channel flow the estimation of the bed roughness is of prime importance; as it can be seen as the major calibration factor for all hydrodynamic-numerical models.

The bed roughness is influenced both by the grain size of the occurring sediments and by the geometrical structure of the bed surface. According to [3] the total hydraulic resistance of bed roughness, τ, can be interpreted as a sum of the drag force of the grain roughness, τ', and the drag force of the form roughness, τ'',

$$\tau = \tau' + \tau''. \quad (1)$$

An appropriate a priori estimation of the bed roughness for numerical river models is still challenging. For the grain roughness various approaches exist based on the grain-size distribution curve assuming a linear behaviour between a representative grain diameter and the roughness coefficient (here: equivalent sand roughness of Nikuradse, k_s) as shown in Tab. 1.

TABLE 1. GRAIN ROUGHNESS APPROACHES

Author (year)	Approach
Garbrecht (1961)	$k_s = d_{90}$
Engelund & Hansen (1966)	$k_s = 2 \cdot d_{65}$
Hey (1979)	$k_s = 3.5 \cdot d_{84}$
Kamphius (1974)	$k_s = 2 \cdot d_{50}$
Van Rijn (1984)	$k_s = 3 \cdot d_{90}$
Mertens (1997)	$k_s = 2.5 \cdot d_{50}$
Dittrich (1998)	$k_s = 2.5 \cdot d_m$ (gravel)
	$k_s = 3.5 \cdot d_{84}$ (coarse gravel)

In mobile sand and gravel bedded rivers the roughness can be significantly affected by pattern formation. For example ripples and dunes can occur in sand and sand dominated river beds acting as a roughness on the flow. To account for these geometrical shapes three different bed roughness predictors are implemented in SISYPHE to account for flat beds, rippled beds or dunes and mega ripples [6].

But there is still a lack of knowledge to estimate the roughness effect of geometrical bed structures such as rock peaks which are not resolved by the numerical grid. To investigate the effect of a modification of such sub-grid structures on the flow field an appropriate model is necessary. Up to now most researchers dealing with this subject concentrated on steep streams. Beside various approaches of other authors [5] and [1] introduced the standard deviation of the bottom elevation, s, to capture the roughness effect in steep streams

$$s = \sqrt{\frac{1}{n-1}\sum_{i=1}^{n}(z_i - \bar{z})^2}\,. \quad (2)$$

In this paper we focus on the estimation of bed roughness in large slightly sloped rivers due to geometrical structures. A numerical test-bench to evaluate the roughness effect of sub-grid structures is introduced. The aim of the ongoing investigation is gaining a deeper insight into the roughness effect of geometrical bedform structures and to provide a general method for the determination of the calibration parameter for individual numerical models using both TELEMAC-3D and TELEMAC-2D. As a first step the roughness approach of [5] and [1] for steep streams is applied to model shallow open-channel flow. Furthermore the suitability of this method is tested.

For the calibration and validation of the coarser models a high-resolution three-dimensional hydrodynamic-numerical (3D-HN) model is set up. All structures of the underlying geometry are resolved properly. The standard k-epsilon model is used to capture the turbulent structures. For the vertical velocity components the non-hydrostatic approach is used. The effect of roughness is taken into account by the implemented approach of Nikuradse. All models are operated with stationary boundary conditions. For the investigation both an artificial elevation model and a digital elevation model of natural rock peak structures of a shallow river bed are used.

After calibrating the smooth bottom case subsequently the flow over different elevated rock peaks using the above mentioned roughness model (cf. equation 1) for the sub-grid structures is investigated. Beside the global water level local effects are compared and discussed.

II. Bottom friction

A. *Definition of bottom friction in 2D and 3D*

The bottom shear stress in both horizontal directions (parallel to the bottom) is described for depth-averaged flow as (cf. [4])

$$\vec{\tau} = -\frac{1}{2} \cdot \rho \cdot C_f \cdot \vec{u} \cdot \sqrt{u^2 + v^2} \tag{3}$$

with the fluid density, ρ, the dimensionless friction coefficient, C_f, and the horizontal depth-averaged flow velocities, u and v. According to the depth-averaged formulation the bottom shear stress in 3D is described as

$$\vec{\tau} = -\frac{1}{2} \cdot \rho \cdot C_f \cdot \vec{U} \cdot \sqrt{U^2 + V^2} = \mu \frac{\partial \vec{U}}{\partial n} \tag{4}$$

with the horizontal flow velocities, U and V, the dynamic viscosity, μ, and the bottom normal vector, n.

Both in TELEMAC-2D and TELEMAC-3D various laws of bottom friction are implemented to account for the shear force at the bottom. In this paper only the formulation of Nikuradse is considered.

B. *Nikuradse law in TELEMAC-2D and TELEMAC-3D*

The friction law of Nikuradse is based on the equivalent sand roughness, k_s. Assuming a logarithmic velocity profile over the whole depth in TELEMAC-2D the bottom friction is determined by Nikuradse law as

$$\vec{\tau} = -\rho \cdot \left(\frac{\kappa}{\ln\left(\frac{H \cdot 11.036}{k_s}\right)} \right)^2 \cdot \vec{u} \cdot \sqrt{u^2 + v^2} \tag{5}$$

with the water depth, H, and the von Kármán constant, κ. In TELEMAC-3D the logarithmic velocity profile is constrained only for the bottommost layer resulting in the following assumption for the bottom shear stress

$$\vec{\tau} = -\rho \left(\frac{\kappa}{\ln\left(\frac{30 \cdot \Delta z}{k_s}\right)} \right)^2 \cdot \left(U^2 + V^2\right) \tag{6}$$

with the height of the first layer, Δz. The velocity profile in the layers above is part of the 3D solution.

III. Numerical Model

To investigate the effect of geometrical bedforms a numerical test-bench is introduced. In a slightly sloped rectangular channel different bedform structures are inserted in a defined test section. The elevation of the structures will be modified by a scaling factor to evaluate their impact on the flow field. In the reference model all geometrical structures are resolved using TELEMAC-3D with the non-hydrostatic approach and the standard k-epsilon turbulence model. For a proper representation of the turbulent flow structures the widely-used two-equation k-epsilon model is used instead of an algebraic model or defining a constant viscosity.

Different cases both in TELEMAC-2D and TELEMAC-3D with representative mesh size values for numerical models of German waterways, such as River Rhine, Danube etc. at BAW are setup. The bottom elevation is defined by a mesh dependent patch averaging.

In a first step the smooth channel case will be calibrated for the particular variants. Subsequent different bedforms are investigated using the reference setup. The influence on the water level differences of the geometrical structures are compared and discussed. Finally the statistical approach of [5] and [1] is applied to the present cases with different geometrical structures. Both with TELEMAC-2D and TELEMAC-3D the method is evaluated according to capture the non-resolved geometrical structures.

A. *Geometry and boundary conditions*

The channel has a horizontal size of 2000 m x 50 m and a slope of 0.63‰ (illustrated in Fig. 1). The sidewalls are modelled with the slip-boundary condition. The section with the geometrical roughness elements starts and ends with a

distance 500 m of each inlet and outlet to minimize the effect of the upstream and downstream boundary conditions.

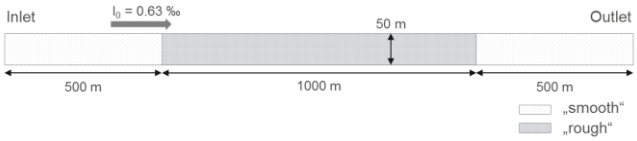

Figure 1. *Test channel geometry (topview)*

Three different discharge events are investigated according to low water level, mean water level and a high-water level of the Middle Rhine (cf. Tab. 2). The relevant flow is analytically determined using the empirical Darcy-Weisbach equation.

TABLE 2. BOUNDARY CONDITIONS

Event	Water depth	Flow
Low water	H = 3 m	Q = 320 m³/s
Mean water	H = 5 m	Q = 750 m³/s
High water	H = 7 m	Q = 1295 m³/s

B. Bottom elevation / geometrical structures

Beside a complete smooth channel two different geometrical structures as shown in Fig. 2 are investigated. The rock peak structures are extracted from the riverbed of the Middle Rhine in the slate mountains with a maximum elevation of -0.84 m and +0.68 m and with a standard deviation of 0.23 m. The “artificial” structures are generated by a superposition of two sinusoidal waves

$$z = A \cdot \left(\sin\left(\frac{x \cdot 2\pi}{\lambda}\right) \cdot \cos\left(\frac{y \cdot 2\pi}{\lambda}\right) \right) \quad (7)$$

with the amplitude, A, and the wavelength, λ.

The mean bottom level of all cases is the same. The inlet and outlet sections are smooth (Fig. 1). The overall grain roughness in the reference case is 0.075 m.

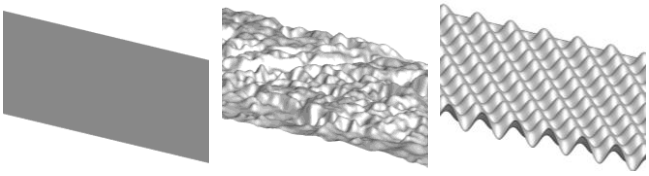

Figure 2. *Bottom elevation, 5x superelevated (left: smooth, center: rock peaks, right: artificial)*

To investigate the influence of the height and the slope of the peaks the structures are both scaled (a) only vertically (z-direction) and (b) in all directions (uniform) as sketched in Fig. 3.

In Tab. 3 all geometrical variants of the presented study are listed leading to a total number of 12 channel bed structures – the smooth case, 4 rock peaks variants and 7 variants with an artificial geometrical structure.

Figure 3. *2D-sketch of rock peaks (left: original, center: scaled in vertical direction (a), right: scaled in vertical and horizontal direction (b))*

In Tab. 3 all geometrical variants of the presented study are listed leading to a total number of 12 channel bed structures – the smooth case, 4 rock peaks variants and 7 variants with an artificial geometrical structure.

TABLE 3. OVERVIEW OF GEOMETRICAL VARIANTS

Structure Case	Scaling factor (FS) / Wavelength (λ) and amplitude (A)
Smooth	FS = 0 / A = 0
Rock peaks	FS = 1 FS = 0.8 (z-direction) FS = 0.5 (z-direction) FS = 0.5 (uniform)
Artificial	λ = 4, A = [0.25, 0.5] λ = 8, A = [0.25, 0.5] λ = 12, A = [0.25, 0.375, 0.75]

C. Meshes

In the reference case (TELEMAC-3D) the geometrical structures are resolved with an average horizontal mesh size of 0.3 m. For the vertical direction 30 sigma-layers are used resulting in a large mesh size of approximately 77 million 3D-elements.

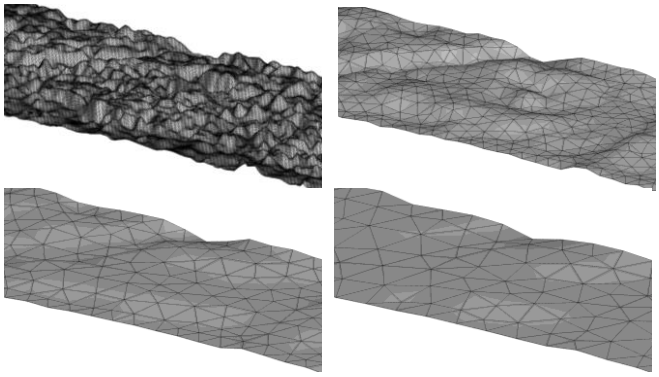

Figure 4. *Bottom elevation (rock peaks) for different mesh resolutions, 5x superelevated (topleft: reference, topright: grid 3 m, bottomleft: grid 5 m, bottomright: grid 7 m)*

For the variants an average mesh size of 3 m, 5 m and 7 m is chosen, according to mesh size values for numerical models of large rivers such as River Rhine at BAW. Geometrical information of sub-grid structures – structures smaller than the mesh size – is getting lost. This phenomenon is illustrated in Fig. 4. The bottom elevation is defined by a mesh dependent patch averaging. For the evaluation of the bottom elevation of a cell node all points of the elevation model within the adjacent elements are considered. The

method is not explained in detail here. An overview of all three meshes including the number of elements is given in Tab. 4.

The Elder turbulence model in the TELEMAC-2D cases is chosen analogously to preceding study. For "grid 5 m" at low water level no difference in the water level was observed comparing the Elder and k-epsilon turbulence model in TELEMAC-2D. These results are not shown in here. Further investigations of the influence of the turbulence modelling approaches are not part of the present study.

TABLE 4. OVERVIEW OF MODELS AND MESH SIZES

	Dim.	Turb. model	2D-Elements	Sigma-Layers	3D-Elements
Reference	3D	k-epsilon	2'560'704	30	76'821'120
Grid 3 m	2D	Elder	19'496	-	-
Grid 5 m			6'454	-	-
Grid 7 m			3'590	-	-
Grid 3 m	3D	k-epsilon	19'496	10	194'960
Grid 5 m			6'454	10	64'540

IV. RESULTS

To compare the results the free surface is extracted along the x-axis (with x in direction from inlet to outlet) in the middle of the channel. For a quantitative comparison the water level difference, ΔH_{1200m}, 100 m before and after the rough section is evaluated

$$\Delta H_{1200m} = H_{x=400m} - H_{x=1600m}. \quad (8)$$

The location with a certain distance to the rough section is chosen to avoid local roughness effects without averaging the results over the channel width.

A. *Calibration (smooth bed)*

In a first step the TELEMAC-2D and TELEMAC-3D with an average mesh size of 3 m, 5 m and 7 m (latest only TELEMAC-2D) are calibrated via the highly resolved TELEMAC-3D reference results.

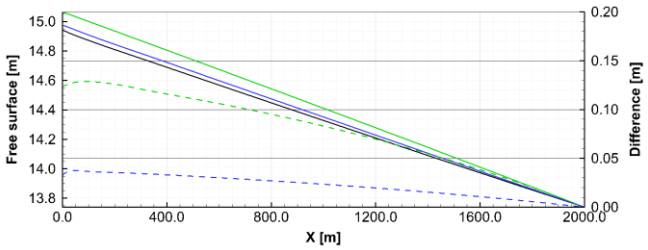

Figure 5. *Free surface along mean flow direction at mean water level with a grain roughness of 0.075 m (solid lines; black: reference, green: grid 3m 2D, blue: grid 3m 3D) and water level difference to reference case (dashed lines)*

In Fig. 5 the free surface at mean water and the water level differences of the reference case and of the variants with an average mesh size of 3 m, both TELEMAC-2D and TELEMAC-3D are shown with a grain roughness of 0.075 m. The TELEMAC-2D case shows the highest free surface elevations which can be concluded in the highest energy losses along the x-axis. For a fitting of cases a reduction of the grain roughness is necessary. The results for the calibration of all cases are summarized in Tab. 5.

The TELEMAC-2D cases can be fitted to the reference results with a grain roughness of 0.047 m and the TELEMAC-3D cases with a grain roughness of 0.065 m for all three discharge events. The influence of the average mesh size between 3 m and 7 m is negligible both for the TELEMAC-2D and the TELEMAC-3D cases (cf. Tab. 5).

TABLE 5. RESULTS OF GRAIN ROUGHNESS CALIBRATION (SMOOTH BED)

	Dim.	Grain roughness	Deviation $(\Delta H_{1200m}-\Delta H_{1200m,ref})/\Delta H_{1200m,ref}$		
			Low	Mean	High
Reference	3D	k_s = 0.075 m	-	-	-
Grid 3 m	2D	k_s = 0.075 m	+8 %	+11 %	+12 %
		k_s = 0.047 m	±0 %	±0 %	+1 %
Grid 5 m		k_s = 0.075 m	+8 %	+11 %	+12 %
		k_s = 0.047 m	±0 %	±0 %	±0 %
Grid 7 m		k_s = 0.075 m	+8 %	+11 %	+12 %
		k_s = 0.047 m	±0 %	±0 %	±0 %
Grid 3 m	3D	k_s = 0.075 m	+2 %	+3 %	+3 %
		k_s = 0.065 m	±0 %	±0 %	±0 %
Grid 5 m		k_s = 0.075 m	+2 %	+3 %	+3 %
		k_s = 0.065 m	±0 %	±0 %	±0 %

The considerable difference between the highly resolved TELEMAC-3D reference case and the TELEMAC-2D case is beside numerical impacts such as numerical diffusion mostly due to the different vertical velocity profiles. The assumption of a logarithmic profile in TELEMAC-2D cannot be verified within the TELEMAC-3D reference case. Fig. 6 shows the vertical velocity profiles of the TELEMAC-3D reference case (k_s=0.075 m) and the TELEMAC-2D case with an average mesh size of 5 m (k_s=0.075 m and k_s=0.047 m) at mean water level extracted at approximately x=1200 m. The logarithmic velocity profiles for the TELEMAC-2D cases are determined based on the friction velocity, U^*, and the grain roughness, k_s (cf. [4])

$$\frac{U}{U^*} = \frac{1}{\kappa} \cdot \ln\left(\frac{y}{k_s}\right) + 8.5 \quad . \quad (9)$$

The assumption of hydraulically rough flow is in all cases valid.

With the reduced grain roughness the water level and thus the depth-averaged velocity of the TELEMAC-2D cases can be calibrated via the reference results but with different values for the bottom shear stress and the maximum values of the velocity at the free surface. This is due to the non-matching vertical velocity profiles.

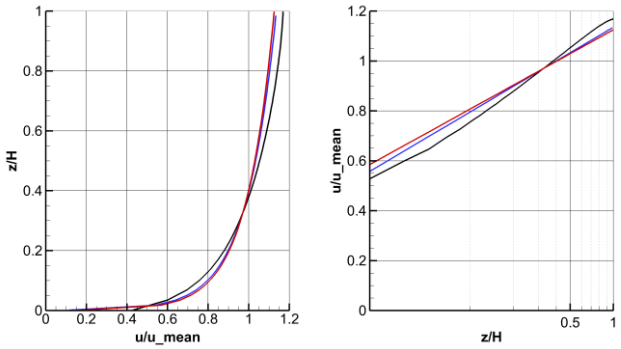

Figure 6. *Vertical velocity profiles at mean water level (black: reference, , k_s=0.075 m; blue: TELEMAC-2D, grid 5 m, k_s=0.075 m; red: TELEMAC-2D, grid 5 m, k_s=0.047 m)*

B. Resolved bedform roughness (reference model)

The influence of the geometrical bedform structures is both investigated for the rock peaks and for the artificial structures using the highly resolved reference setup.

The shape of the channel bottom has a significant impact on the velocity field which can be observed by both geometrical structures. In Fig. 7 and Fig. 8 the depth-averaged scalar velocity distribution at mean water level is shown for the rock peak structures and the artificial geometry, respectively. The scaling is chosen analogue to the mean depth-averaged velocity in the smooth case. In both cases the shape of the bottom geometry can be found also in the velocity field. With higher bottom elevations this influence is getting more significant.

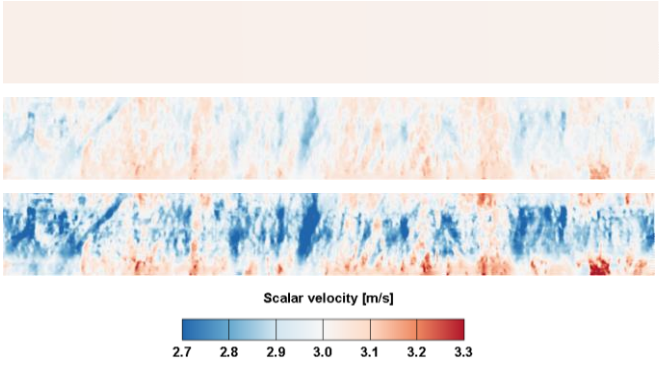

Figure 7. *Depth-averaged scalar velocity at mean water level of reference cases "rock peak structures", section x = 800 m to x = 1200 m (top: FS = 0 (smooth), center: FS = 0.5, bottom: FS = 1.0)*

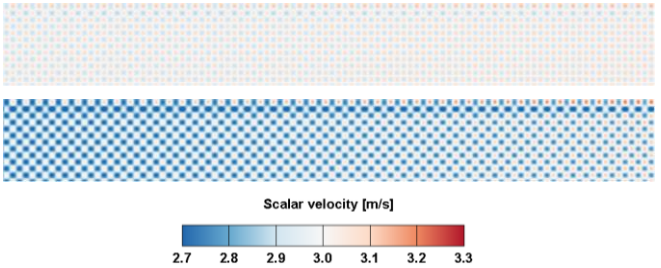

Figure 8. *Depth-averaged scalar velocity at mean water level of reference cases "artificial structures" with λ=12 m, section x = 800 m to x = 1200 m (top: A = 0.25 m, bottom: A = 0.5 m)*

In Fig. 9 the resulting water level difference, ΔH_{1200m} , for the rock peaks structures is plotted against the vertical scaling factor. The scaling factor FS=0 describes the smooth bed case. With an increasing scaling factor the water level difference, ΔH_{1200m} , is getting larger. This can be explained by the corresponding behaviour of the ratio, e,

$$e = \frac{\Delta z}{H} \tag{10}$$

with the elevation of the bedform structures, Δz, and the water depth, H. For constant discharge conditions the ratio, e, is increasing with an increasing scaling factor.

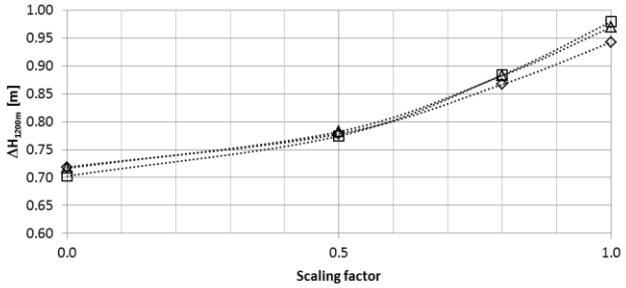

Figure 9. *Water level differences, ΔH_{1200m}, of the resolved "rock peak structures" with different geometrical scaling factors in vertical direction (◇ low water, △ mean water, □ high water)*

Differences associated with different discharge conditions are relatively small. The maximum deviation occurs for the original rock peaks structures without scaling.

The results show a non-linear behaviour between the water level difference, ΔH, and the elevation of the rock peaks structures for all water levels– especially for scaling factors greater than 0.5.

Due to the vertical scaling of the bedform structures the local gradient in the horizontal directions of the rock peaks is changing (cf. Fig. 3). The influence of the scaling only in vertical direction compared to a uniform scaling in all directions – without changing of the gradients – is shown in Fig. 10 for a scaling factor of 0.5. For all water levels the change is relatively small.

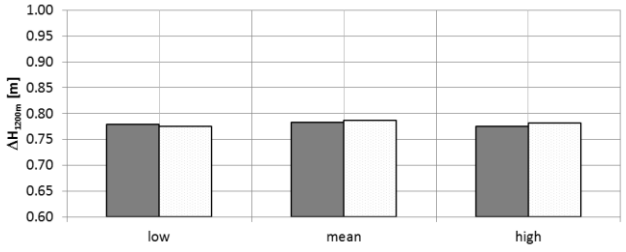

Figure 10. *Water level differences, ΔH_{1200m}, of reference cases "rock peak structures" with geometrical scaling factors of 0.5 (filled: scaled in vertical direction, hollow: scaled in all directions)*

The non-linear behaviour between the differences of the water level, ΔH_{1200m}, and the bedform elevation is also observed for the artificial structures as shown in Fig. 11.

For the artificial structures, composed of sinusoidal waves, the scaling only in vertical direction compared to a uniform scaling has an impact. The variants "λ=4 m, A=0.25 m", "λ=8 m, A=0.50 m" and "λ=12 m, A=0.75 m" result all in a similar water level difference (cf. Fig. 11). All three cases have the same gradients in horizontal directions but different elevations. This phenomena can also be observed comparing the variants "λ=8 m, A=0.25 m" and "λ=12 m, A=0.375 m".

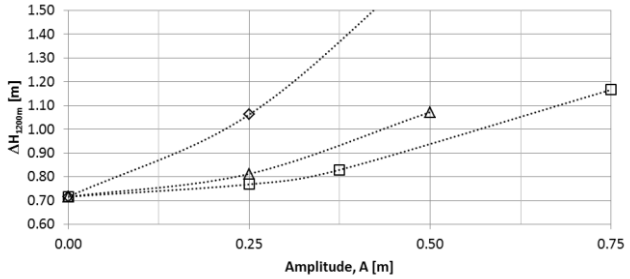

Figure 11. *Water level differences, ΔH_{1200m}, of reference cases "artificial structures" at mean water level with different amplitudes (◇ λ=4 m, △ λ=8 m, □ λ=12 m)*

Contrary to the rock peaks the bedform structure of the artificial elevation model is homogeneous and steady over the whole region. This might lead to different behaviour of the influence of the local gradients and the total elevation.

Similar to the results of the rock peaks structures the influence of the discharge on the water level differences is small for the artificial bedform structures as shown in Fig. 12 for a wavelength, λ, of 12 m.

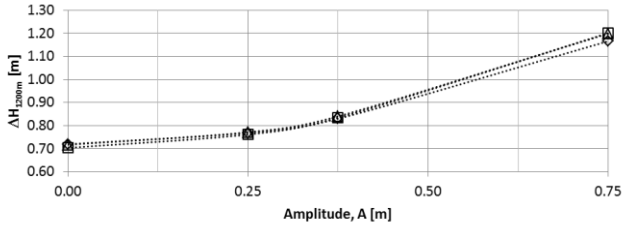

Figure 12. *Water level differences, ΔH_{1200m}, of reference cases "artificial structures" with λ=12 m and different amplitudes (◇ low water, △ mean water, □ high water)*

C. *Statistical roughness approach*

For the coarser meshes with an average size of 3 m, 5 m and 7 m effects of non-resolved geometrical structures have to be represented via the roughness model. Based on the approach of [5] and [1] the total Nikuradse roughness, $k_{s,sum}$, is determined as the sum of the calibration grain roughness, $k_{s,cal}$, and the grid dependent standard deviation of the bottom elevation, s, multiplied by a weighting factor, w,

$$k_{s,sum} = k_{s,cal} + w \cdot s. \qquad (11)$$

Fig. 13 shows the resulting water level differences, ΔH_{1200m}, for both the TELEMAC-2D and TELEMAC-3D cases compared to the reference case at mean water. The applied approach of the standard deviation of the bottom elevation shows a linear behaviour between the water level difference and the bottom elevation. With increasing weighting factor the slope is getting steeper.

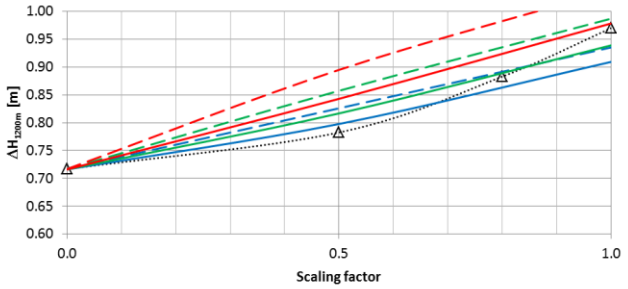

Figure 13. *Water level differences, ΔH_{1200m}, for case "rock peak structures" at mean water with different geometrical scaling factors in vertical direction (△ reference case, solid lines: TELEMAC-2D, dashed lines: TELEMAC-3D) and different weightening factors of the standard deviation of the bottom (red: s·0.5, green: s·0.7, blue: s·1.0)*

Due to its linear behaviour the approach of [5] and [1] cannot capture the roughness effect of the non-resolved geometrical rock peaks with a single weighting factor for the different scaling factors of the geometrical bedform structures.

V. Summary and Conclusion

To gain deeper insight into the roughness effect of geometrical bedform structures a numerical test-bench is successfully introduced. With a highly resolved mesh in both horizontal and vertical direction using TELEMAC-3D with the standard k-epsilon turbulence model and the non-hydrostatic approach different geometrical structures are investigated. Two different elevation models are investigated – natural rock peaks and an artificial structure composed of sinusoidal waves.

For the smooth highly resolved TELEMAC-3D reference case a non-logarithmic velocity profile was observed. The coarser resolved TELEMAC-2D and TELEMAC-3D cases could be calibrated both with a single grain roughness for all three water levels.

Vertical scaling of geometrical structures with a constant mean bottom elevation shows both for the rock peaks and for the artificial bedform structures a non-linear dependency between the bottom elevation and the differences in the water level. The influence of a uniform scaling of the geometrical structures on the water level differences appears different in the two cases.

The non-linear behaviour of geometrical roughness versus the water level difference could not be modelled using the roughness approach based on the standard deviation of the bottom elevation with a single weighting factor for the different scaling factors. Further investigation is necessary to provide a general method for the modelling of sub-grid structures. An obvious approach would be to introduce a

weighting exponent for the standard deviation of the bottom elevation. But this would lead to non-conformity in units between form and grain roughness values.

For numerical investigations in river engineering it is of great importance to capture the occurring roughness effects. The current study illustrates the complexity of geometrical bedform structures and their modelling. For an appropriate a priori estimation of these effects further research is necessary.

There is a need to bear in mind that the capability of TELEMAC-3D for such highly resolved meshes is to the authors' knowledge up to now not tested and validated in detail. Furthermore, the influence of numerical effects like numerical diffusion and the influence of the turbulence models were not evaluated in the present study.

ACKNOWLEDGEMENT

The authors thank Rebekka Kopmann for the fruitful discussions and reading the manuscript.

REFERENCES

[1] J. Aberle, "Untersuchung der Rauheitsstruktur zur Bestimmung des Fließwiderstandes in Gebirgsbächen unter Klarwasserabfluss", Mitt. des Instituts für Wasserwirtschaft und Kulturtechnik, Univ. Karlsruhe, Heft 207, 2000

[2] V.T. Chow, "Open-channel hydraulics", McGraw Hill International Book Company. Tokyo, Japan, 1983

[3] H.A. Einstein, and N. Barbarossa, "River channel roughness." Transactions ASCE, 1952, Vol. 117, Paper no. 2528, pp.1121-1146

[4] J.-M. Hervouet, "Hydrodynamics of free surface flows: modelling with the finite element method", Wiley, Chichester 2007

[5] M. Rosport, "Fließwiderstand und Sohlstabilität steiler Fließgewässer unter Berücksichtigung gebirgsbachtypischer Sohlstrukturen", Mitt. des Instituts für Wasserwirtschaft und Kulturtechnik, Univ. Karlsruhe, Heft 196, 1998

[6] P. Tassi and C. Villaret, "Sisyphe v.6.3 User's Manual", EDF R&D, 2014

C-VSM-II: Large Scale and Long Time Simulations with Sisyphe's Continuous Vertical Grain Sorting Model

Dr. Uwe H. Merkel

UHM River Engineering Karlsruhe
Ritterstr. 42, 76137 Karlsruhe, Germany
info@uwe-merkel.com

***Abstract*— The stratigraphy of a river bed is of essential influence on the development of the bathymetry and the resulting flow patterns. Sorting of sediment grains results in armouring layers, sand lentils, dunes, antidunes, ripples, scours and deposits. Furthermore the tracking of sediments is a necessary functionality for sustainable sediment management on waterways, especially for dredging and dumping.**

Like most hydro-morphodynamic software packages Telemac & Sisyphe calculate sediment transport, sediment sorting and development of bed forms depending on the sediment distribution and the assumption of a fully mixed "active layer" of the river bed. The empirical active layer concept has been developed in 1971 by Hirano and expanded by Ribberink among others to fit the numerical models and demands of their time. Nowadays long time and large scale models reach the limit of this mean value theory. The presented "Continuous Vertical Grain Sorting Model" (CVSM) and its dynamically estimated active layer thickness overcomes several limitations of this meanwhile 40 years old concept.

Results of this new vertical sorting model were compared to the classical Hirano-Ribberink implementations on 3 laboratory flumes during the CVSM-I project, which was finished in 2012. In the second project CVSM-II (finished in 2016) the algorithms robustness was enforced for industrial strength and proofed by the simulation of two large scale and long term projects along a large shippable river. It is now implemented in the new version of Sisyphe V7P3. Additionally, the new CVSM-II is now extended to work with the new dredging module called "Nestor" which can be coupled to Sisyphe. The article gives a short overview about the implemented algorithms. It mainly focuses on a real world example and lists configuration recommendations for Sisyphe users.

I. Introduction

Vertical grain sorting is one of the leading processes for many hydrodynamic and morphodynamic simulations. Like most hydraulic & morphological software packages Telemac & Sisyphe calculate sediment transport, sediment sorting and development of bed forms depending on the active layer of the bed. The empiric active layer thickness concept has been developed in 1971 by Hirano [1] and expanded by Ribberink [3] among others to fit the numerical models and demands of their time. Todays long run and wide range models reach the limit of this mean value theory. With new high performance computers the here presented continuous vertical grain sorting model and its dynamically estimated active layer thickness overcome several limitations of this meanwhile 40 year old concept.

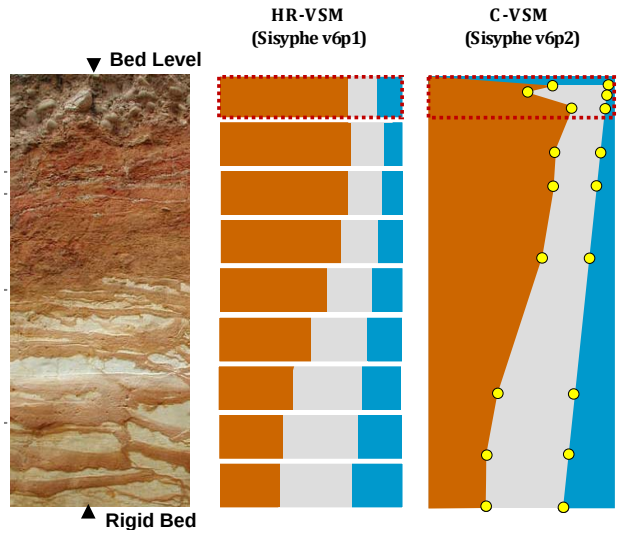

Figure 1. Stratigraphy abstraction models with Active Layer (red dotted): Measured profile (left); Hirano/Ribberink model, also known as "Layer" model (middle), Continuous model based on polylines (= probability density functions) as implemented in Sisyphe (right).

The complete theoretical description of the CVSM Sisyphe implementation, which might be necessary to understand the following pages, is given in [4]. This document focuses on the algorithm updates, practical experiences and new usage recommendations.

With the C-VSM-II project came the clear project target to make the C-VSM algorithms as robust as possible for practical applications. The BAW provided two wide range and long time scale models from pending projects. Both models are very well known and are in use already since several years with the classic HR-CVSM. Both models include dredging and dumping rules with time and dynamic triggers (handled by the new Nestor module).

II. Interaction with Nestor

As the combination of dredging and dumping with C-VSM was run for the first time, a new academic flume case "Flume 4" was necessary to proof the expected functionality

and especially the mass conservation at the interfaces between Sisyphe, Dredgesim, Nestor and the C-VSM.

A. *Model Properties*

- Points = 1 111
- Triangles = 2 000
- Time Step = 0.25s
- Number of Time Steps = 240 000
- Coupling Period = 10 = 2.5s
- Grain Size Classes = 3

The following figure 2 shows a simulation with 3 grain size classes over ~16.6 hours. One dredging area in the upper (green) half and 3 dumping events are time triggered. Additionally, all grain sizes are chosen to move under different conditions, to produce a new stratigraphy which is disturbed by dredging and disposal. The figures are snapshots from a set of videos which show the described effects more precise.

B. *Results*

Figure 2 shows some results of the Nestor <-> CVSM interaction tests. The four pictures, from top to bottom, show

- the mean grain size before flooding the flume,
- the first dredging (in the upper flume half) and dumping (lower half) procedures. As expected, immediately after starting the flume, the surface sediments start to sort, especially blue (very fine) material leaves the flume in an early stage.
- the deformed sediment heap after 16.6h.
- a cut through the sediment heap, which developed over time. It is over formed by incoming sediments and erosion effects at the same time. It shows the stratigraphy (as mean diameter) in 500 sections.

The tests on Flume 4 resulted in various minor changes in Sisyphe and Dredgesim / Nestor with the result, that the share of volume errors can be reduced to less than 10^{-15}, if all thresholds are chosen to that accuracy. For practical purposes, where CPU time matters, the thresholds are set to 10^{-8}.

III. Large Scale and Long Term Simulations

The following case is the largest case calculated so far with the C-VSM. The model itself was developed at the *"Bundesanstalt für Wasserbau"* in Karlsruhe over several years for multiple sediment surveys on a shippable river in Germany. The river bed is up to 2 kilometres wide and 30 km long. The original version includes a 3-layer Hirano-Ribberink stratigraphy model and 9 grain size fractions. The old implementation of Dredgesim was converted to the new Nestor module. Dredging occurs demand driven.

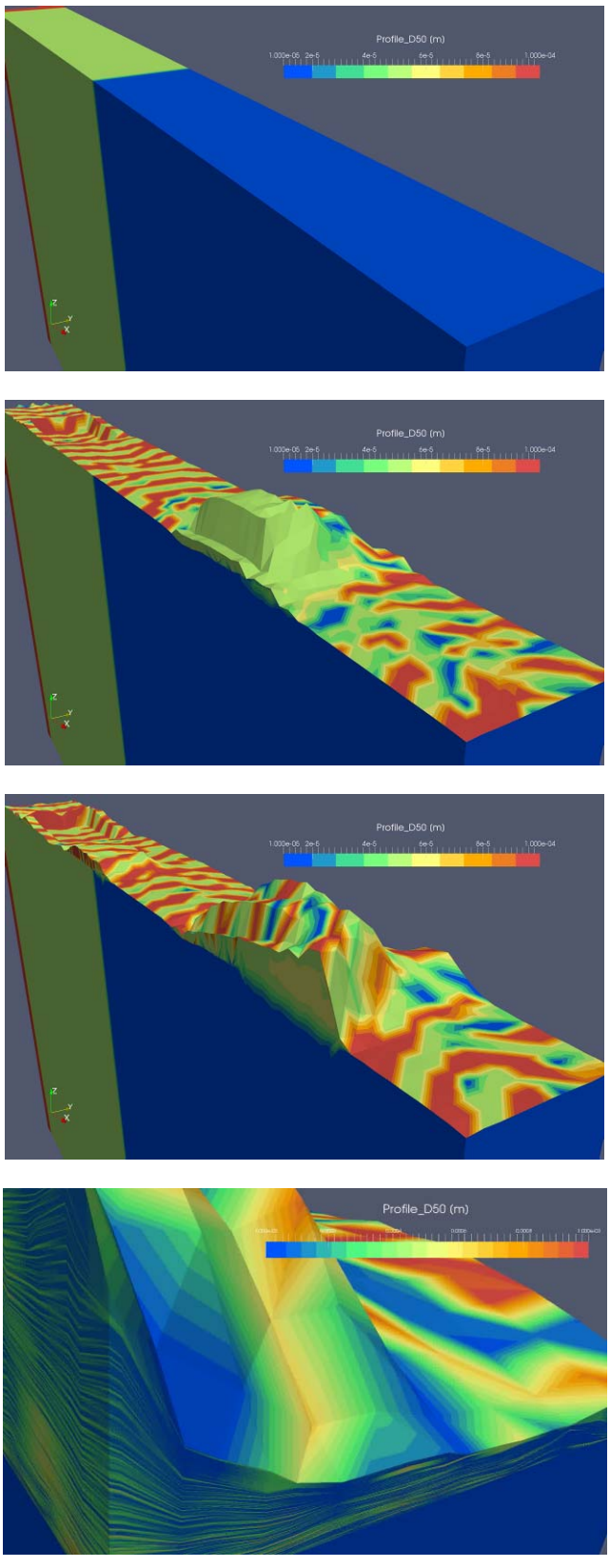

Figure 2. Development of a new stratigraphy which is disturbed by dredging and dumping events. (Color: Mean Diameter D50 [m])

A special focus is laid on a sediment trap, islands, groynes, bridge piers and confluences which affect the development of the morphology. (Overview: Fig.3)

Even though this river stretch is well known to the BAW from many surveys, a large uncertainty remains for the initial grain distribution, and therefore for the development of the bed.

Special to this model is the usage of the "Morphological Factor (MOFAC)". This means, that evolution in every time step is magnified through the MOFAC, which was chosen to be 10 here. The hydraulic simulation time, and therefore the CPU hours are cut to 1/10th. The price is an excessive sediment movement. The MOFAC should be handled with great care, especially for unsteady simulations. This project was not meant to observe the MOFAC advantages and disadvantages, but on many smaller issues the impression shall not be suppressed, that already the Hirano-Ripperink original model can only be seen as a generalized sediment movement theory. One shall not take every nodes value as certain. It is the coarse spatial context, which shows the sediments main moving path.

From this point of view it is questionable and needs to be observed if a strong 2D and 3D smoothing MOFAC and a very high 3D resolution makes sense, if used together.

From the technical point of view, which had robustness of the algorithm as another main goal, the MOFAC does not disturb the C-VSM. Without the MOFAC, the results are even more plausible.

A. *Model Properties*

- Points = 314 963
- Triangles = 625 097
- Time Step = 4 s
- Number of Time Steps = 5 523 120
- Coupling Period = 30 = 2 min
- Morphological Factor = 10
- Layers for Hirano = 3
- Grain Size Classes = 9

The C-VSM is technically hard to visualize, due to its excessive memory consumption. One time step of the model consumes: 314963 points * 500 depth sections * 10 fractions * 16 byte ~ 24GByte RAM

The values are normally overwritten by the next time step. The recommended usual output is automatic reconversion to the HR-VSM layers. It is written as common Sisyphe Selafin file, which needs only 3/500th memory of the C-VSM. Today's computers can handle this amount of data for calculations, especially clusters. But it is difficult to render the 3D stratigraphy as volume, like Figure 2 of the before mentioned "*Flume 4*". The following Figure 4 renders only 1 of 200 domain parts to illustrate the general development of the stratigraphy.

B. *Interpretation*

- Figure 4 (top): This cut is 10 times vertically exaggerated to make the armouring layer visible. The C-VSM model starts from the previous HR-C-VSM computation. Therefore the 3 layer stratigraphy can still be seen after the first 30 days (x10 MOFAC). Especially the former boundary between L2 and L3 is still visible, as they are untouched by the C-VSM algorithms until the displayed time. This L2 / L3 layer boundary was originally 1m below the bed level. The armouring layer is 3 to 10 cm strong and covered in an average of 4 cm (but up to 40 cm) of moving fine sediments. The given values of this illustration example are only valid for this setup and not calibrated to natural data.

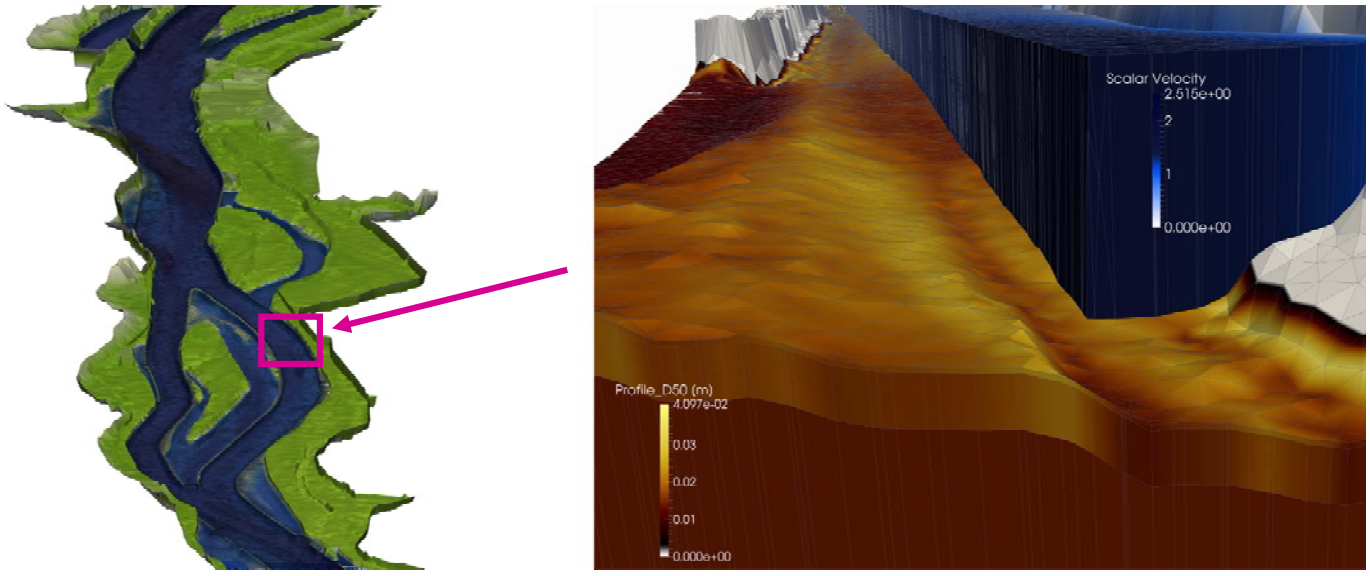

Figure 3. Left: Perspective view of the river and slice of the initial sediment stratigraphy. Flow direction top to bottom.
Right: A 2D hydraulic model drives the sediments in 3 depth layers (HR-VSM).

- More interesting is the dark layer below the bright surface layer. This is a clear proof that the moving fines are separated from the coarse grains. In some places, e.g. the front corner, the initial L2 was eroded and the new armouring layer covers the former L3.
- Figure 4 (bottom) shows a cross section through the same river section.

C. *Dynamic Active Layer Thickness*

The original Hirano idea assumes the active layer bottom as the limit of the moving part of the bed. It is clear that a fix active layer thickness can not account for changing hydraulics, morphology and grain sorting.

This empirical mean value is hard to measure and

- has growing uncertainties the coarser the spatial steps get (mesh width),
- is sensitive to the length of the observed morphological activity (time step),
- and is dependent on the shear stress magnitude.

Replacing these influence factors with mean values increases the morphological uncertainties. A collection of formulas for dynamic ALT approximations during a simulation is available in Malcherek [2] and implemented in Sisyphe. Some formulas use the bottom shear stress τ_B, the critical shear stress τ_C, the characteristic diameters d_{50}, d_{90}, d_{MAX} or the transport stage parameter D^*.

Their implementation in Sisyphe v7p3 divers from the old implementation. The formula can be chosen by the following keyword:
"C-VSM DYNAMIC ALT MODEL"

- Option 0: Constant Active Layer Thickness (uses additional keyword "Active Layer Thickness")

$$ALT = const.$$

- Option 1: Hunziker & Günther

$$ALT = 5 * d_{MAX}$$

- Option 2: Fredsoe & Deigaard

$$ALT = \frac{2 \cdot \tau_B}{(1-n) \cdot g \cdot (\rho_S - \rho) \tan \phi}$$

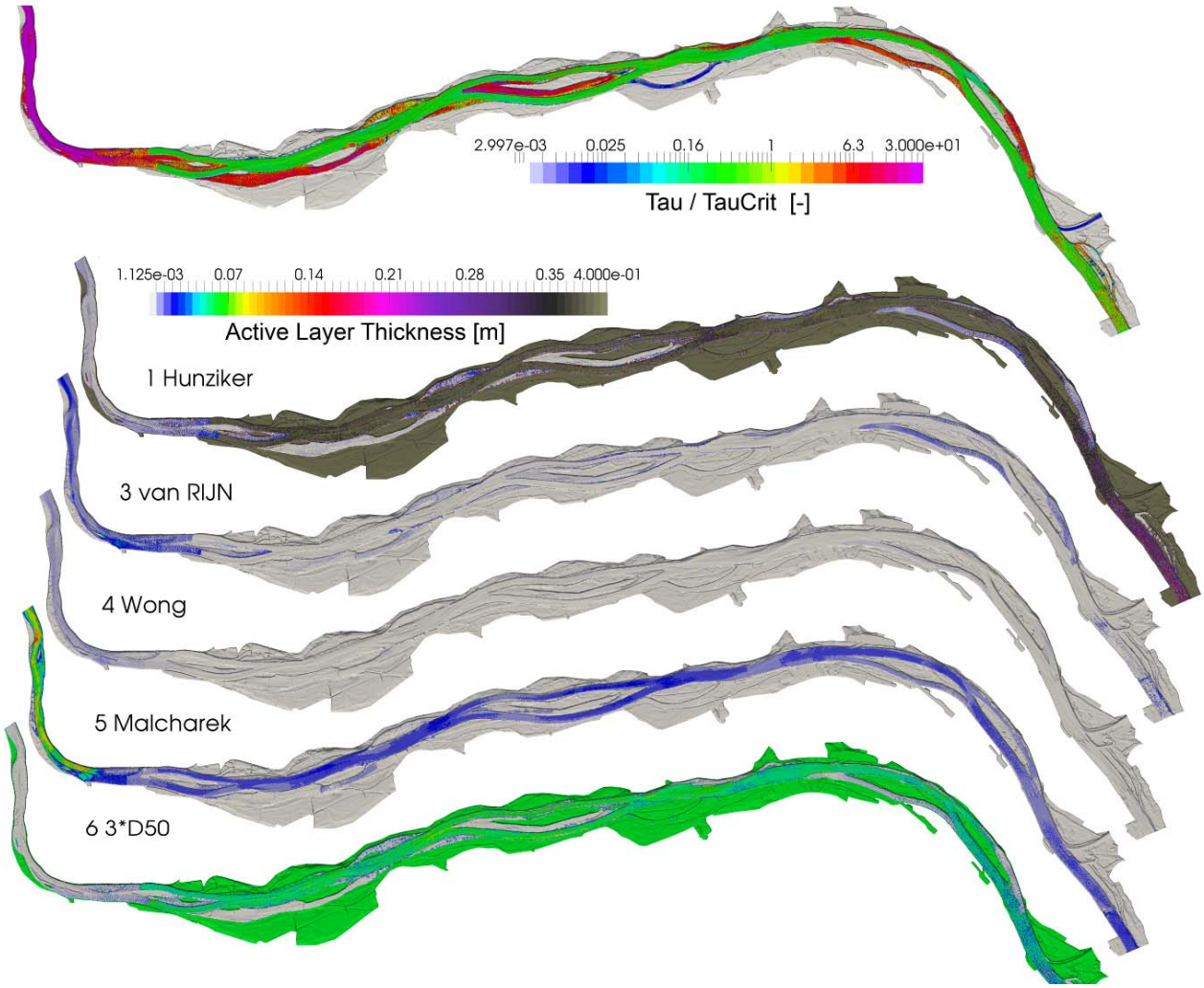

Figure 5. The implemented Active Layer Thickness (ALT) estimation formulas produce very different results. Not every formula seems to be transferable from laboratory scale to every river.

- Option 3: van RIJN

$$ALT = 0.3 \cdot D_*^{0,7} \cdot (\frac{\tau_B - \tau_C}{\tau_B})^{0,5} \cdot d_{50}$$

- Option 4: Wong

$$ALT = 5 \cdot (\frac{\tau_B}{(\rho_S - \rho) \cdot g \cdot d} - 0{,}0549)^{0,56} \cdot d_{50}$$

- Option 5: Malcherek

$$ALT = \frac{d_{90}}{1-n} \max(1, \frac{\tau_B}{\tau_C})$$

- Option 6: $3*d_{50}$

$$ALT = 3 * d_{50}$$

Other used parameters: ρ_S … density solid; ρ … density water; n … porosity; $\tan\phi$ … friction angle.

The implementation of these formulas would be possible for HR-VSP with very long morphological time steps. But it is limited, due to the smearing problem shown in Figure 2. Especially in pulsating eddy zones the ALT changes by several 100% within few time steps instead of the above shown 0.0001%. This increases the smearing problem.

With the new C-VSM this problem is obsolete and the formulas for a dynamic ALT can be used over longer simulation periods in coupled morphodynamic and hydrodynamic models. No further recommendation is given on these formulas, as their usability is strongly dependent to the project.

Figure 7 (top) shows as an example for the last time step the relation shear stress to critical shear stress. Figure 7 (others) shows, that the implemented dynamic Active Layer Thickness estimation formulas have strongly varying values.

- Option 1, Hunziker & Günther, is just 5 * d_{MAX}, and therefore does not reflect the shear stress. In places, where only a single grain of the biggest grain fraction is found in the last time steps active layer, the new ALT will be automatically the maximum possible size, here 40cm. Therefore, the original formula was changed to use $5*d_{99}$ instead of $5*d_{MAX}$. Then thinner active layers are possible in parts with moving fines on the surface.

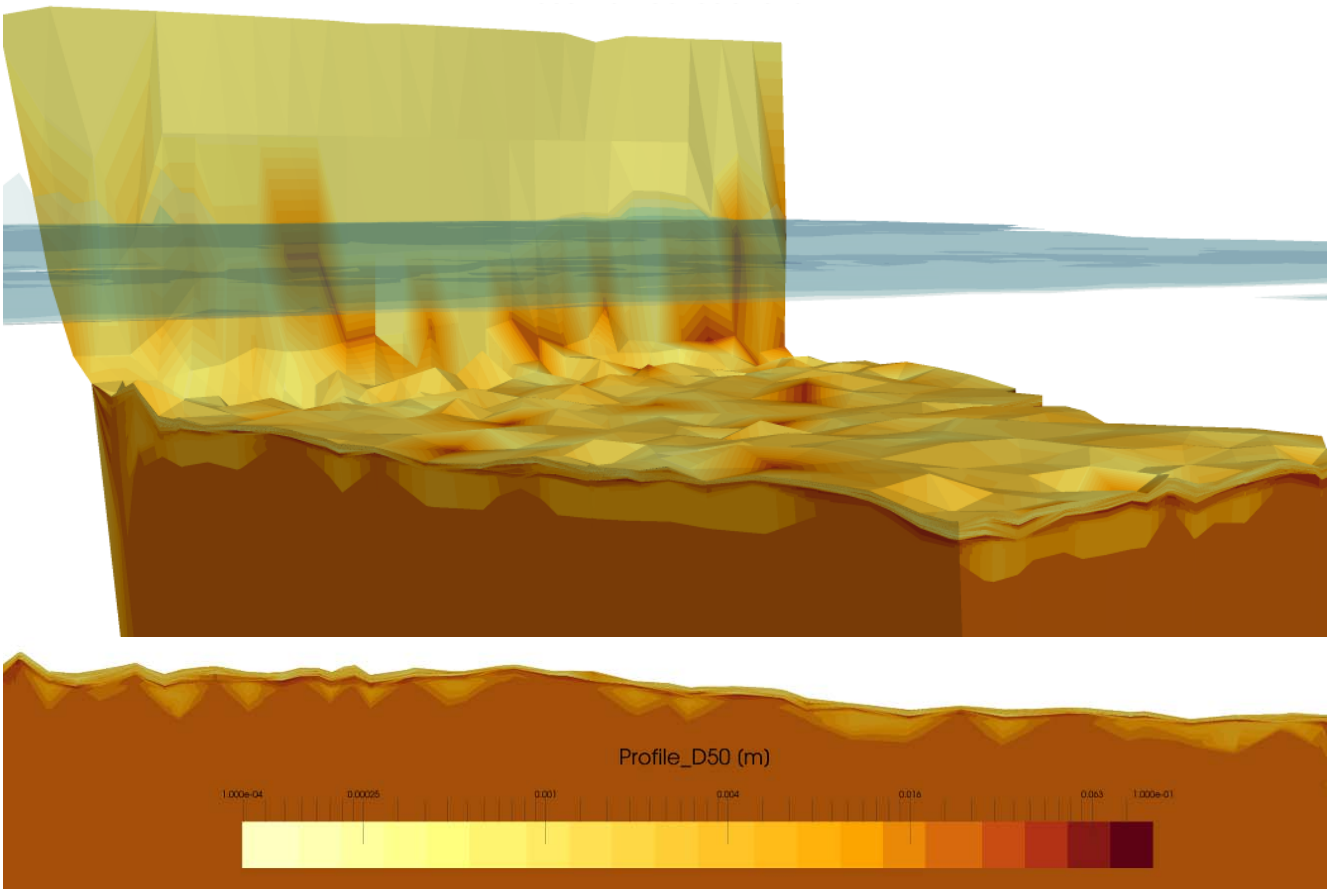

Figure 4. CVSM with 500 vertical sections and an Active Layer Thickness of 5 x d_{Max}. Color: Mean grain size d_{50}. An armouring layer covers sand lentiles and fine sediments are moving above the armouring layer.

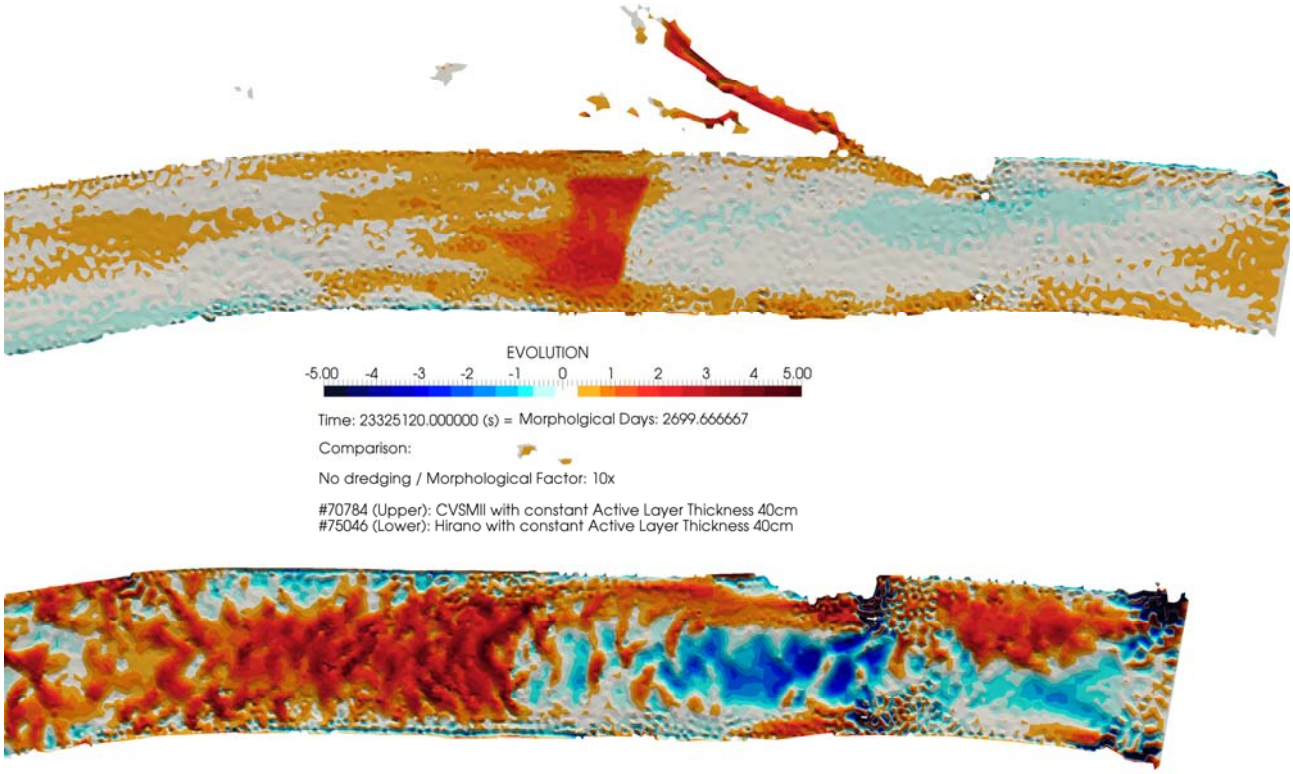

Figure 7. Model inflow (flow from right to left), sediment trap in the picture middle. No dredging.

- The Fredsoe option 2 does not bring any useful results and is not displayed.
- The van Rijn option 3 leads to generally very thin ALTs which can not be trusted. It seams that the formula, which worked better for the flume cases is out of range for this setup.
- The same applies to the Wong option 4.
- Malcherek's option 5 reflects the shear stress / critical shear stress ratio and the grain size. In general the relative ALT characteristics are good, but with a tendency to underestimate the ALT. This behaviour of Malcherek's formula was observed for any tested model so far. It can be recommended to investigate more in this direction, as it seams to be the most promising of all formulas.
    - Tweaking porosity, critical shear stress and shear stress approximations can easily multiply the ALT.
    - An easy, less physical way, is to implement a magnification factor.
- Option 6 again is just a grain size based formula like formula 1. Both are very robust in comparison to shear stress and critical shear stress based formulas, which are difficult to calibrate as the quotient τ_B / τ_C can easily make a change by some 100%. It is confusing that these formulas deliver the strongest ALT on the flood plains. Explanation:
    - The sediment volume on the flood plains is 0. In those cases, for consistency reasons each fraction is set to 1 / "Number of Fractions". A d_{50} is assigned to zero volume.
    - This is not a problem, as erosion will not take place if there is no free material.

D. *Discussion of results*

1) *Full model*

An analysis over the full model (fig. 6) shows clearly less strong evolution effects of the C-VSM. The following detail figures 7,8 & 9 give an impression of the general behaviour.

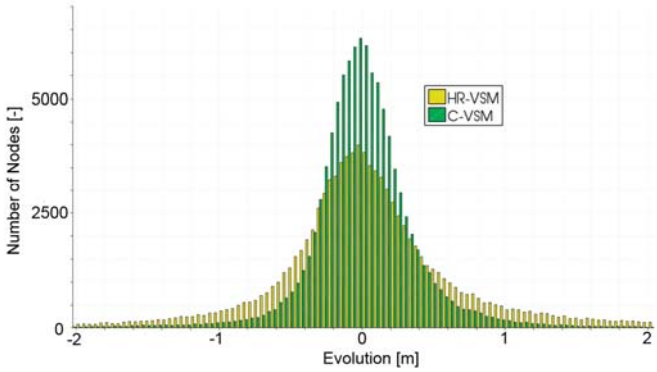

Figure 6. Comparison of evolution values between HR-VSM and C-VSM (250 sections, both constant ALT=40 cm)

2) *Inflow and sediment trap*

Right after the inflow, when flow patterns are still biased by the imposed velocity direction vectors, heavy erosion and deposition effects with amplitudes of up to 5 meters

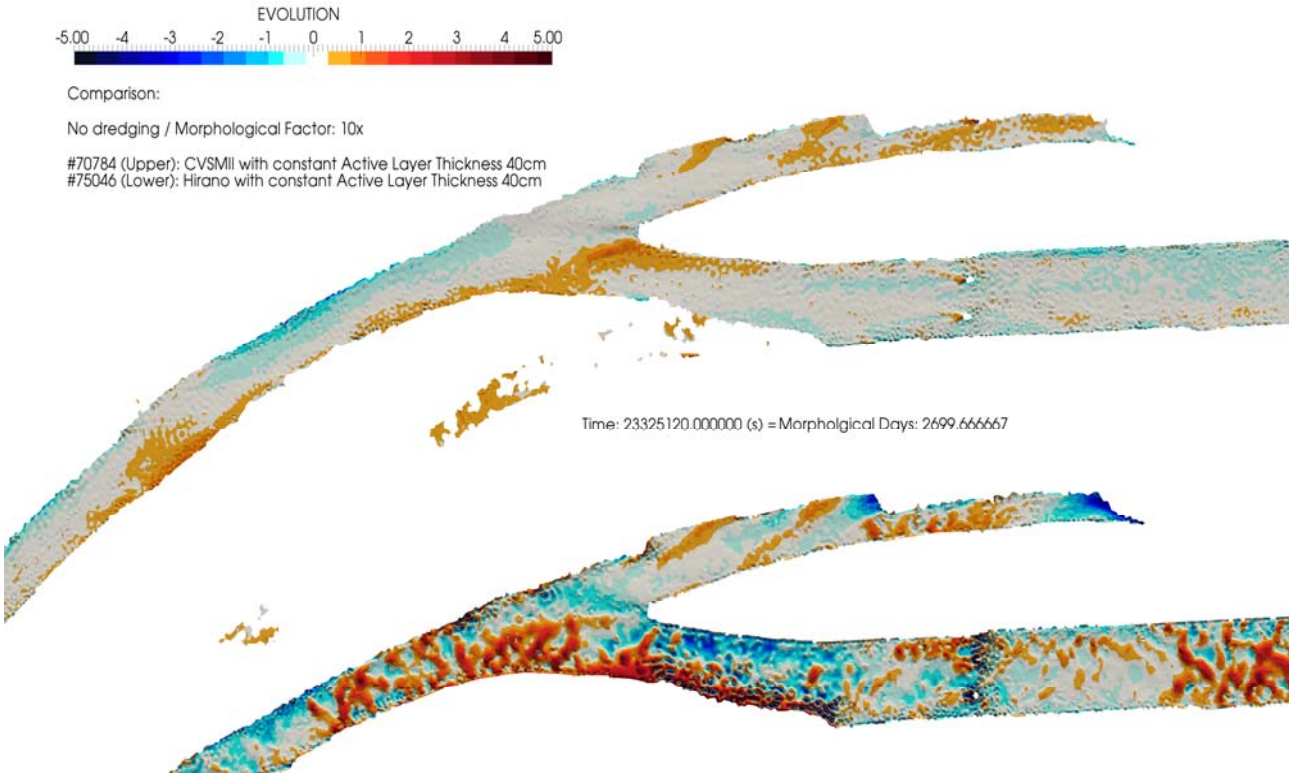

Figure 8. Confluence and bend, (flow from right to left)

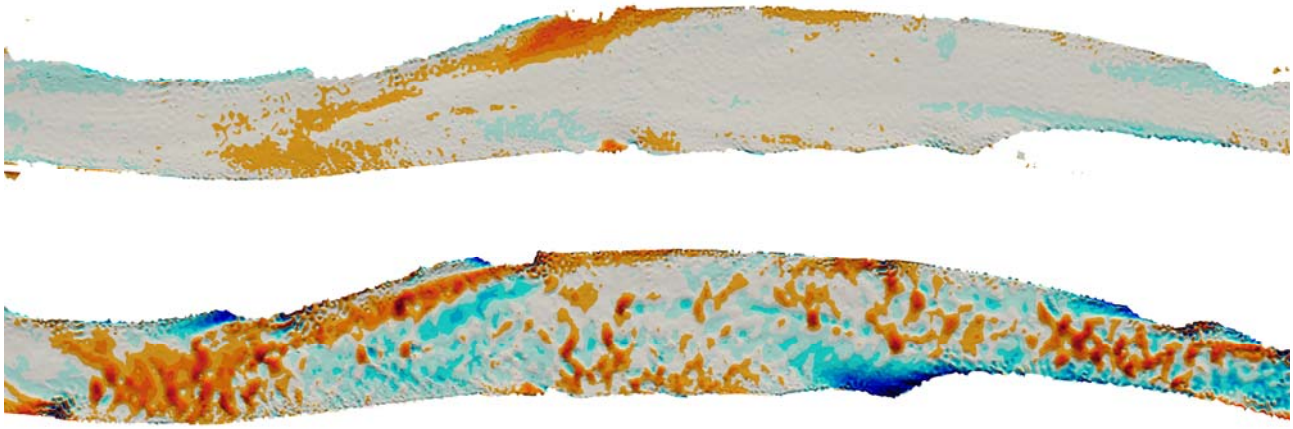

Figure 9. Moving sediment bodies and scours do not appear in the C-VSM. This leads to a generally narrower histogram of the evolution (valid only for the above printed stretch)

characterize the HR-VSM (fig. 7). A funnel develops through erosion in the middle and deposition on the right bank. This funnel presses accelerated flow in the next hundred meters, where deeper scours develop.

The C-VSM on the other hand shows a much smoother behaviour, for this setup, with a 40 cm constant strength active layer. 40 cm equals 5 times the theoretical $d_{MAX,}$ which should not be mixed up with the real local d_{MAX} at a certain point in time. All active layer formulas approximated less strength and produced varying evolution patterns.

The sediment trap is filled, after a certain time and not dredged in this example. Even though the compatibility to Nestor is given, the right configuration of Nestor is possible after a calibration of the sediment transport model.

Without comparison to measured values, a final conclusion cannot be given. Too short is the work period and the number of models run with C-VSM to judge from experience. However, for the here presented section, the slope and variability of the newly developed bed is much too steep in the HR-VSM, compared to the exiting river bed.

3) Patterns of transported sediments

Figure 8 shows a confluence area with excessive evolution patterns in the HR-VSM. Especially in the main branch some areas show strong red blue pattern, which have to be interpreted with up to 8 m elevation difference between two single model nodes. C-VSM misses these patterns, but shows depositions and erosion in right the areas where the engineers experience would expect them. The maximum

```
/************************************************************************ ****
/ New keywords for the Continuous VERTICAL SORTING MODEL by Uwe Merkel
/************************************************************************
/
VERTICAL GRAIN SORTING MODEL = 1
/         0 = Layer = HR-VSM (HIRANO + RIBBERINK = SISYPHE Standard)
/         1 = C-VSM
C-VSM MAXIMUM SECTIONS        = 250
/         Should be at least 4 + 4x Number of fractions,
/         better > 100, tested up to 10000
C-VSM FULL PRINTOUT PERIOD    = 0
/         0 => GRAPHIC PRINTOUT PERIOD
/         Anything greater 0 => Sets an own printout period for the C-VSM
/         useful to save disk space!!!
C-VSM PRINTOUT SELECTION    = 0|251|3514|1118|1750|2104|3316
/           Add any 2D Mesh Point numbers to produce .CSV-Ascii output
/           of the C-VSM
/           Add 0 for a full C-VSM output as Selafin3D files
/           (called VSPRES + VSPHYD)
/           expects: "C-VSM FULL PRINTOUT PERIOD" > 0
/           All files are saved to your working folder and
/           in /VSP & /LAY folders below
C-VSM DYNAMIC ALT MODEL       = 5
/         'MODEL FOR DYNMIC ACTIVE LAYER THICKNESS APROXIMATION'
/         0 = CONSTANT (Requires Keyword: ACTIVE LAYER THICKNESS)
/         1 = Hunziker & Guenther 5*d99
/         2 = Fredsoe & Deigaard (1992)
/         3 = van RIJN (1993)
/         4 = Wong (2006)
/         5 = Malcherek (2003)
/         6 = 3*d50 within last time steps ALT
```

Figure 10. Keywords and recommended standard values, starting from Sisyphe v7p3

secondary bed slope change (left to right bank) is approx. 3.5 m. As for the other figures and examples, a final conclusion cannot be given without calibration to measured values. Figure 9 shows the same effects in a straight river section.

E. Computational cost of the C-VSM

Based on the parameter sets of figures 6-9, a performance test has been run over 10000 time steps to show the general cost of the C-VSM. These results are only roughly transferable to other projects, as they depend strongly on the size of the model, the number of MPI processes and the hardware (e.g. RAM size, bandwidth and frequency, CPU) a.o. From the software side, thresholds and the number of fractions affect the performance.

Table 1 gives an impression of necessary extra CPU times for the shown model.

Table 1: Runtime comparison

Type	HR-VSM	C-VSM	C-VSM	C-VSM	C-VSM	C-VSM	C-VSM	Only T2D
ALT Formula	0	0	0	0	0	0	5	
Coupling Period	30	30	30	30	30	10	30	
Sections / Layers	3 Lay.	100	250	500	1000	250	250	
Runtime [s]	125	163	352	695	3619	1230	363	66
Extra Time over HR-VSM [multiples]	1	1.3	2.8	5.5	28.9	9.8	2.9	0.53

IV. How to use C-VSM II in Sisyphe

Add the lines of Figure 10 to a Sisyphes.CAS file. The full C-VSM output can be found in the Selafin files VSPRES & VSPHYD in the tmp-folders, they are erased after the calculation if the option –t is not used. As the higher resolution of the C-VSM needs resources, one can reduce the print output period, or suppress the output at all. The common Sisyphe result files only show the Hirano output. Even more disk space can be saved, if only few points are printed out as .VSP.CSV files in the subfolder /VSP/. It is recommended to use between 200 and 500 vertical sections. More will not improve the accuracy much, and less will lead to increased data management, as the profile compression algorithms are called more often.

Acknowledgement

The project and the necessary developments were financed by the Bundesanstalt für Wasserbau (BAW). All raw data was provided and belongs to the BAW.

References

[1] Hirano, M. River bed degradation with armouring. Proceedings Japan Soc. of Civil. Engineers 195. 1971

[2] Malcherek, A. Sedimenttransport und Morphodynamik, Scriptum Institut für Wasserwesen, Universität München, 2007

[3] Ribberink, JS. Mathematical modelling of one-dimensional morphological changes in rivers with non-uniform sediment. Delft University of Technology. 1987

[4] Merkel, U.H, Kopmann, R. Continuous Vertical Grain Sorting for Telemac & Sisyphe v6p2. In: XIXth TELEMAC-MASCARET User Conference, Oxford, UK, 2012.

Numerical modelling of the sediment dynamics in Saint-Martin-la-Porte reservoir, France

Matthieu Secher[1], Aurélie André[1], Eric Valette[1], Anne-Laure Besnier[2], Pablo Tassi[2,3]
[1]EDF CIH
[2]EDF R&D
[3]Saint-Venant Hydraulics Laboratory
matthieu.secher@edf.fr

Abstract— **The Saint-Martin-La-Porte reservoir is located on the River Arc in the French Alps. Launched recently, an operational plan seeks to optimize its sediment management and to study the opportunity of restoring its storage capacity.**

This work presents two models: the first model is built in order to reproduce the evolutions induced by annually flushing operation; the second model is built to simulate deposition in the reservoir during an 8 months period while the reservoir is operated normally. Results of these two models are both compared with measurements, bathymetries realized before and after a flushing operation for the first one, and measurements of sediment concentrations for the second one.

Best results for the flushing model were obtained using bedload transport model with a non-uniform sediment grain size distribution, whereas the deposition processes were simulated using suspended load transport model. The results of the two models are in good agreement with the measurements. In the case of the flushing model, numerical results indicated a very realistic mixing of the different sediment grain sizes modelled. For the deposition model, flow recirculation zones are well reproduced and led to deposition zones identified on the bathymetries.

I. INTRODUCTION

The Saint-Martin-La-Porte (SMLP) reservoir is located on the River Arc in the northern French Alps. This river is a main tributary of the Isère River, which is a tributary of the Rhône River (see Fig. 1).

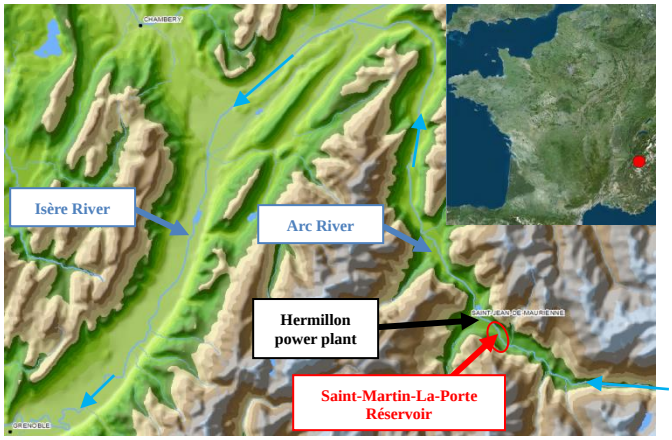

Figure 1. *The Saint-Martin-La-Porte reservoir location in Arc River valley (northern French Alps).*

The SMLP dam, built in 1986, has a storage capacity around 100,000 m^3 and receives drainage from an area of 1,167 km^2. It consists of three wide river gates with a water intake located on the right side of the dam (see Fig. 2). It allows diverting 90 m^3/s to the Hermillon hydro-power plant.

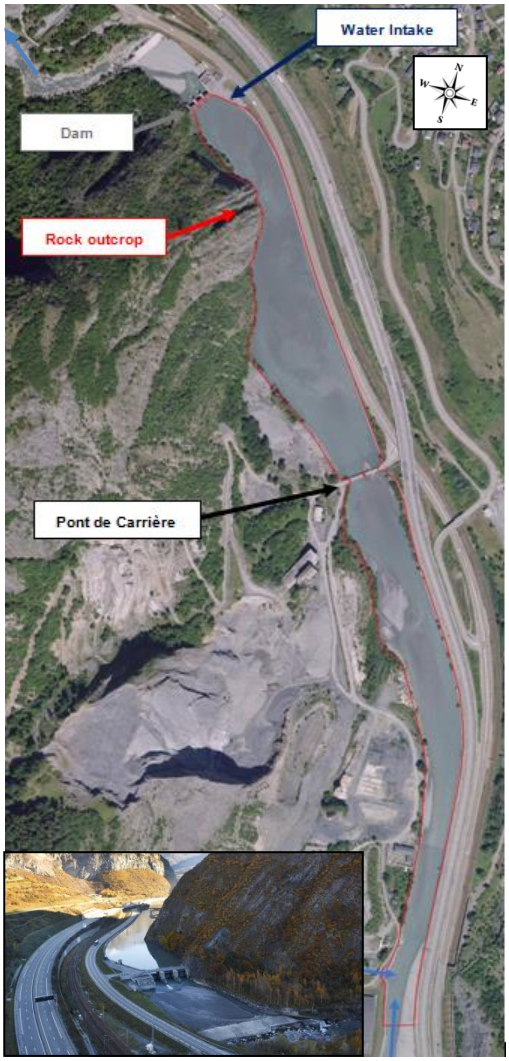

Figure 2. *Orthophotography of the reservoir (with the area of the model in red) and picture of the dam from downstream point of view.*

Suspension sediment transport is important on the Arc River with around 100,000 tons per year. There is also bedload sediment transport on this river, since the grain size distribution is large (from silt to gravel, including sand). There is also bedload sediment transport on this river but it is complicated to estimate an order of magnitude (probably less than suspension sediment transport).

The SMLP dam is trapping a significant part of this sediment transport. To manage these deposits, once a year the dams of the Arc River are flushed for around 12 hours in order to evacuate as much sediments as possible. These annually operations are done in June, unless a strong enough flood of the Arc River to clear reservoirs happen before the planned date.

In order to better understand sedimentation processes in the SMLP reservoir, two Telemac-2D-Sisyphe models have been implemented:

- one to model a flushing event ;
- one to model an 8 months period while the reservoir is operated normally.

The aim of this work is to provide a better understanding of the sediments processes in order to optimize the management of sediments in this reservoir and to study the opportunity to restore its storage capacity.

II. MODELLING OF FLUSHING EVENT

A. *Input data*

A hydraulic model (Telemac-2D) has been built using a bathymetry survey done in 2015. This model has been calibrated (friction coefficient mainly) using current surveys (LSPIV[1] and velocity profiles). The hydrodynamic model is used as a basis for the development of the sediment transport model using Sisyphe.

The flushing event of June 2012 is used to calibrate the model as this event is well monitored:

- measurements of the inflow discharge and water elevation in the reservoir during the event (see Fig. 3);
- bathymetries before and after the event (see Fig. 4);
- measurements of the suspension sediment concentration upstream and downstream the dam.

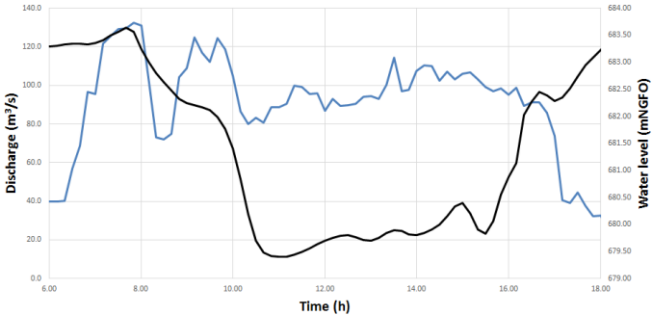

Figure 3. *Upstream hydrograph and water level at the dam during the flushing of 2012*[2]

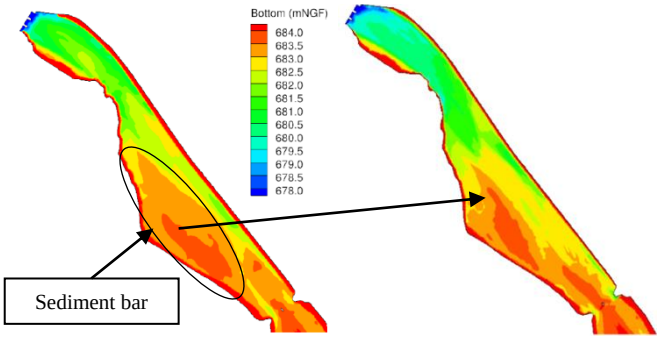

Figure 4. *Bathymetry before the 2012 flushing event (left); bathymetry after the flushing of 2012 (right)*

A grain size survey in the reservoir was also completed in 2012. It shows the grain size sorting along the reservoir with coarse sediment upstream (13 mm) and fine sediment downstream (<300 µm), with sands in-between (from 0.3 to 2 mm).

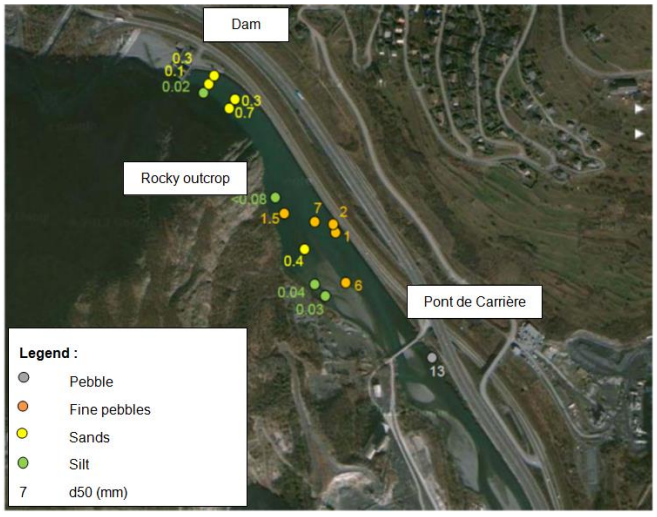

Figure 5. *Map of the grain size survey of 2012.*

[1] LSPIV : Large-Scale Particle Image Velocimetry

[2] NGFO : stands for "Nivellement Général Orthométrique de France" (Orthometric height system of France)

B. Model

The hydraulic model is a Telemac-2D [1] [2] [3] model using the V7P0 version. For sedimentology part, Sisyphe module [4] of the same version is used.

Mesh

The model area (see Fig. 2) is approximately 1.5 km long and in average 80 m wide. The convergence of the model and the mesh dependence were studied by analyzing the velocity distribution at selected profiles. Sensitivity tests for mesh resolution showed that a discretization of 114,000 elements (58,000 nodes), with medium mesh size ranging from 2 m (downstream) to 3 m (upstream) is a good compromise between model efficiency and simulation time.

Boundary conditions

The boundary conditions are indicated on Fig. 6 and the different characteristics and values used through this study are summarized in the table below.

TABLE 1. BOUNDARY CONDITIONS

N°	Boundary conditions	
	Prescribed variable	***Values***
1 (Arc River)	Inflow discharge	[0 – 140] m^3/s
2 (water intake)	Water level	[682.5–684] mNGFO
3 (river gate)	Outflow discharge	~0 m^3/s
4 (outflow)	Outflow discharge	1.1 m^3/s
5 (river gate)	Outflow discharge	~0 m^3/s
6 (river gate)	Outflow discharge	~0 m^3/s
7 (tributary)	Inflow discharge	~0 m^3/s

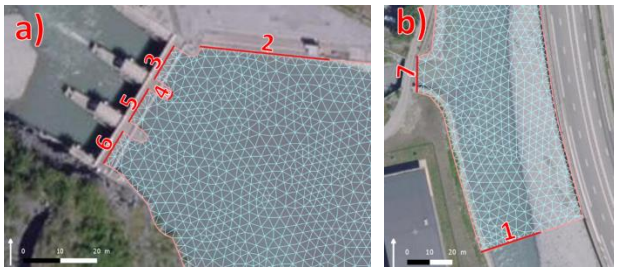

Figure 6. *Downstrem boundary conditions (left), upstrem boundary condition (right).*

To model normal management conditions, the three river gates are closed and all the flow is diverted through the water intake. These boundary conditions are described in Tab. 1.

During the flushing event, all the flow passes through the river gates which are opened alternatively (see Fig. 7). To represent this sequence in the model, the Telemac-2D subroutine *bord.f* has been modified to change the type of river gates boundary condition (N°3, 5 and 6) during simulation. When the gates are opened, the prescribed state on their boundaries is *water level prescribed*. The boundary condition for the water intake is also changed from *water level prescribed* to *outflow discharge prescribed* equal to 0 m^3/s (there is no hydroelectric production during a flushing event).

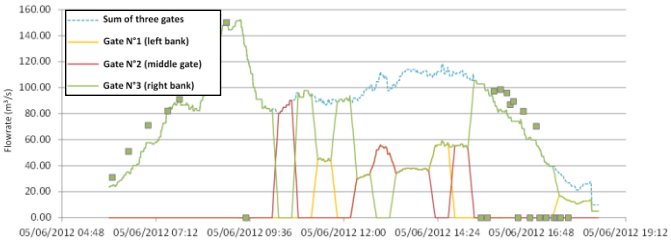

Figure 7. *Opening gates sequence during the 2012 flushing of SMLP reservoir (green squares are theortical discharge of the dam calculated with the water level measured) .*

Sediment model

It was initially assumed that the sediments eroded in the reservoir were mainly transported by suspension. Preliminary results with this transport model were very far from reality. A bedload sediment transport model turned out to be much better (suspended + bedload model were not tested here).

The first lesson from this model is that bedload transport during flushing event in SMLP reservoir is significant and more importantly, that the reservoir morphology is mainly modified by bedload sediment transported.

For the bedload sediment transport model, sediment boundaries conditions are set on equilibrium sediment discharge on boundaries n°1 and 7 (LIEBOR = 5) and on free sediment outflow discharge (LIEBOR = 4).

The bedload transport formula which provides the best results in this case is the Engelund-Hansen formula (bedload formula 30 in Sisyphe). This transport formula, appropriate for non-uniform sediment distribution, was calibrated on a total transport physical model, with bedload and suspension transport on sand [4].

The Meyer-Peter and Mueller formula initially tested yielded inferior results, especially downstream in the fine sediment areas.

The sediment slide module was used with an equilibrium angle of 30 degrees and others slope effects were activated with the default values (correction of direction of bedload transport and intensity of bedload transport rate, but no secondary currents effect). Finally, in this case, the best results were obtained with no skin friction correction ($\mu = 1$).

To get a realistic sediment model of this reservoir with highly variable grain sizes, four zones have been defined

with four representative mean diameter classes by simplifying and interpolating the grain size survey of 2012. These zones are applied in the code with the *inpoly* function in *init_compo.f* Sisyphe subroutine. Several grain sizes were tested in the different areas to try to calibrate the model to obtain a bottom elevation as close as possible to measurements. The best results were obtained with the configuration shown in Fig. 8.

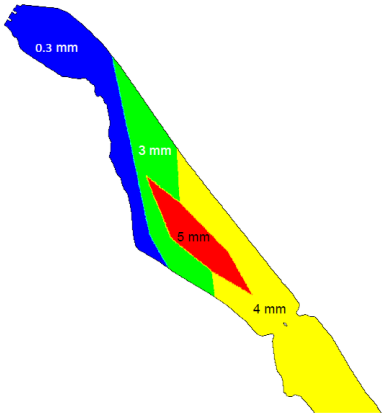

Figure 8. *Map of the grain size allocation defined in the model drawn from simplification of 2012 grain size survey*

The moveable bed has been defined 3 m thick below the initial bathymetry, constant in the entire model but only in zones where the bottom is constituted of sediment. It is done by the modification of *noerod.f* Sisyphe subroutine.

Finally, main fixed parameters of the simulations are resumed in the Tab. 2.

TABLE 2. MAIN MODEL PARAMAETERS

Parameters	Values
Time step	0.1s
Simulation duration	45 000s
Strickler coefficient	40 $m^{1/3}.s^{-1}$
Hydraulic numerical scheme	Characteristics method
Sediment numerical scheme	Edged-based N-scheme
Sediment transport formula	Engelund-Hansen
Sediment slide	Yes (slope stability of 30°)
Secundary currents	No
Slope effects	No
Tidal flats	yes

C. Results

The best results obtained with this model are shown in Fig. 9 and for two cross sections in Fig. 10. The comparison between the bathymetry after the flushing event of 2012 and the numerical results shows that the simulated final bottom level is close to the measurements, especially downstream the reservoir (see cross section C1 in Fig. 10).

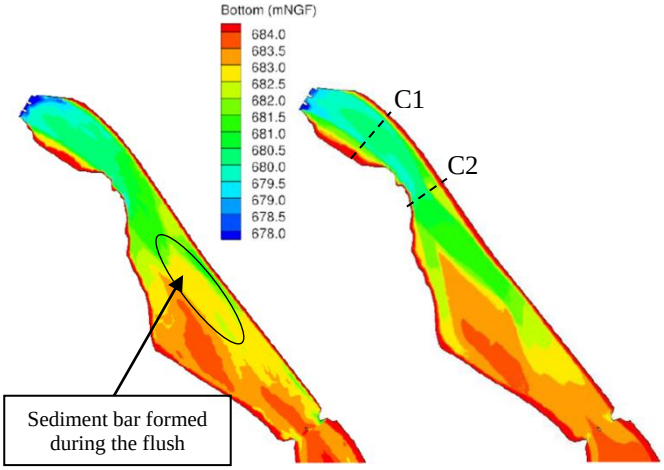

Figure 9. *Measured bathymetry after the flushing of 2012 (left); final numerical results of the Telemac-2D-Sisyphe model (right).*

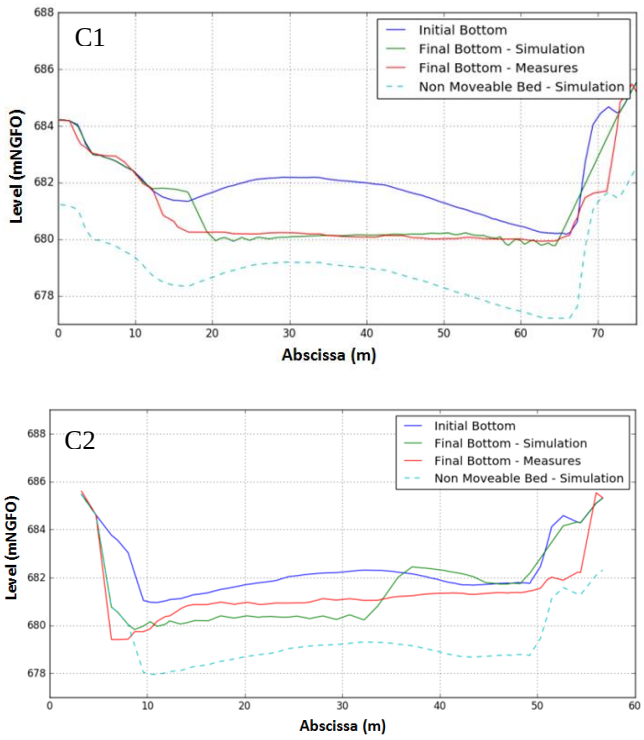

Figure 10. *Initial bottom, non-moveable bed of the model and simulated and measured final bottom after the flushing event for cross-section C1 around 100 m upstream the dam (top) and cross-section C2 around 250 m upstream the dam (bottom).*

400 m upstream of the dam, the agreement between the results and the measurements is not as good. First, in the main channel, a sediment bar formed during the flush (see

Fig. 9) is not captured by the model. Otherwise, the top of the bar present before the flush on the left of the reservoir is moving from the left to the right of the bar during the flush (see Fig. 4). This reconfiguration is not captured either.

Several hypotheses can explain these differences:

- There are not enough grain sizes zones and their initial distribution is not precise enough;
- the definition of only one grain size per zone is highly unlikely and cannot capture complex evolution;
- no suspension sediment transport is modelled, especially for upstream suspension influx which can deposit during and after the flush;
- the final bathymetry was realised several days after the flush. Some reconfigurations and deposits may have happened between the end of the flush and the measurements.

However, the simulated sediment volume balance between before and after the flush is very close to the measurement:

- Simulated: -18,800 m^3;
- Measured: -19,500 m^3.

Another interesting result is the mean diameter distribution at the end of the simulation (see Fig. 11). These results show that coarse sediment can progress in the reservoir and can exit the reservoir with several flushes. It also shows that there is a mix of grain size sediment during the flush and consequently, validates the hypothesis that the initial grain size allocation is too simple.

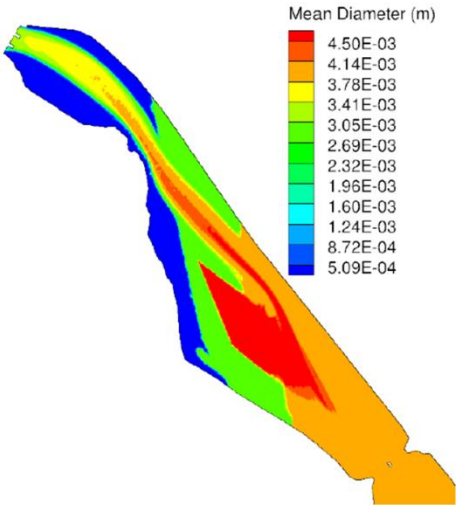

Figure 11. *Map of the grain size allocation at the end of the simulation*

D. Comparison with 1D results

A 1D-model of SMLP has also been constructed at CIH with Cavalcade, a software developed by Artelia. Cavalcade is a 1D hydraulic and sediment transport model. The geometry is constituted of cross-section profiles simplified with one bottom level value for each cross-section calculated from the average of the river bed for the initial geometry. The same cross-section average has been done on the Telemac 2D-Sisyphe results. The comparison between Cavalcade model calibrated on the 2012 flush and the Telemac 2D-Sisyphe is shown in Fig. 12 on a longitudinal profile. The Cavalcade results were obtained with Engelund-Hansen formula and a mean grain size of 4.4 mm (no multi grain approach).

The results are very close and it shows that, even if the Telemac-2D-Sisyphe model is not in perfect accordance with the measurements on transversal sediment evolution, it is in very good agreement and as good as Cavalcade 1D-model for the longitudinal bottom level evolution.

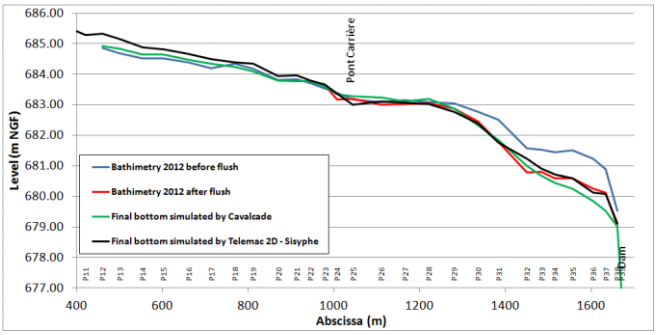

Figure 12. *Longitudinal profile of bathymetries of SMLP before and after the flush of 2012, and Cavalcade and Telemac 2D-Sisyphe simulated final bottom.*

III. MODELLING OF STANDARD MANAGEMENT OF THE RESERVOIR

Another model of SMLP reservoir was built, with the aim to model the sediment dynamic during standard management of the reservoir (without flush). One of the objectives was to specify the sedimentation rate inside the reservoir, which is estimated to be lower than 5% of the sediment influx according to experts.

A. Input data

The same hydraulic model is used for this model. Only the geometry is modified and, no treatment of boundary conditions like in the flushing model is performed, since gates are kept closed during the simulation.

The measured bathymetry from 2013 of the reservoir is used. This bathymetry was chosen because it is the only one with a long period before the next flush (8 months) and with relatively complete upstream measurements of sediment influxes (turbidity prone), inflow discharge and reservoir water level.

B. Model

For this model, the sediment transport is modelled using the Sisyphe suspension sediment transport model. In standard management of the reservoir without drawdown of the reservoir level, the shear stress is not sufficient to significantly move gravels or sands.

Hence, this model is mainly a sediment deposition model. Thus, the bottom of the model is defined as non-moveable with the *noerod.f* subroutine.

During standard management period of the reservoir a non-cohesive behaviour of the sediments in suspension is assumed. Hence, the Partheniades formula is used for erosion and the Krone formula is used for deposition. The settling velocity of the sediments is set according to measurements of the Arc sediments [5].

The main issue with this model was the accuracy of discharge and water level boundary conditions. For many periods during the simulation period of 8 months the upstream measured discharge was not high enough to actually sustain the measured water level rising in the reservoir. Due to these input data problems, simulation crashed. The modelling of the bed evolutions even increased this issue.

The principal reason was a problem of synchronism between the different measured upstream discharges combined to get the main discharge imposed at the upstream boundary condition. Errors in these different measured discharges or in bathymetric data are also an explanation. Finally, some small tributaries are not taking into account because their discharges are not measured and they can contribute to this disequilibrium.

The only solution found to solve this problem was to increase manually the upstream inflow discharge when it was not sufficient.

The eight month simulation was performed on EDF R&D cluster named Porthos. On 56 cores, the run lasted about 40 hours.

C. *Results*

Fig. 13 shows the final simulated bed evolution. This calculation highlights 3 major zones of sedimentation. Two of these zones are due to hydraulic recirculation zones. The third one corresponds to slow currents just upstream the sluice gates of the dam.

These deposits zones were obvious from bathymetries analysis and the model was able to correctly capture them.

The calculated deposits along the limit between dried and wet mesh (relatively large because of the water level fluctuations) is less obvious on the bathymetry analysis.

The simulated sedimentation rate during these eight months is 4.6 % of influx sediment; this rate confirms the expert estimation.

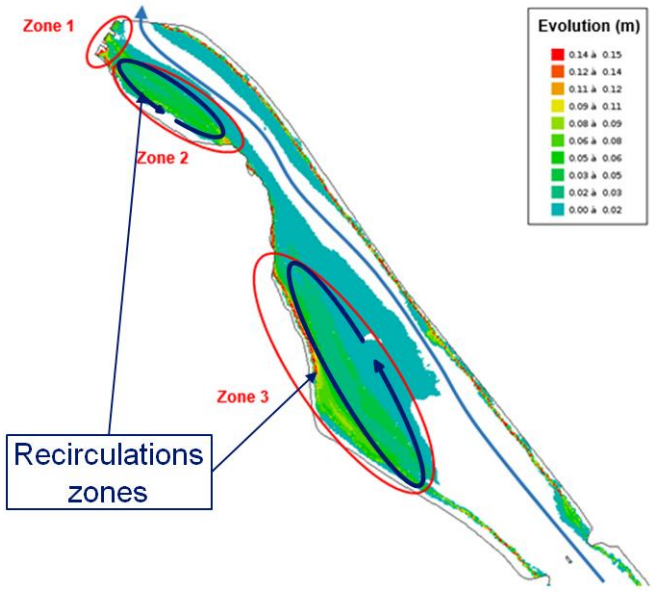

Figure 13. *Final bed evolution (initial bottom level minus final bottom level) of 8 month simulation.*

IV. CONCLUSION AND PERSPECTIVES

Two Telemac-2D-Sisyphe models have been developed, one to simulate sediment dynamics during a flushing event and the other one, to model sediment dynamics during a period of standard management of the reservoir.

The model of the flushing event yields to results in good agreement with the bathymetric measurements. It proves that bedload sediment transport mode is the dominant process during a flush of the SMLP reservoir. This model allows simulating the mixing of different sediment grain sizes in the reservoir and indicates that gravel can pass through the dam with several flushes.

However, the model shows that the initial description of the grain size distribution must be very precise to get good results in the transversal directions.

Results obtained with the second model, developed to study deposition in a standard period of time with no flush, are *a priori* good. It strengthens the expert evaluation on the sedimentation rate and it helps to understand sediment dynamics in the reservoir. It allows anticipating sedimentations problem in the reservoir like for example deposits in front of gates which can compromise there opening.

These models can now be used to optimize sediment management of the SMLP reservoir (dredge plan, opening sequence of gates during flush, etc.).

ACKNOWLEDGEMENT

The authors thank Artelia for their permission to use Cavalcade results in this article.

REFERENCES

[1] Hervouet J.-M. (2007) Hydrodynamics of Free Surface Flows. Modelling with the finite element method. John Wiley & Sons, Ltd.

[2] Open-Telemac webpage (2017) www.opentelemac.org

[3] Ata R. V7P0 Telemac 2D User Manual

[4] Tassi P. V7P0 Sisyphe User Manual

[5] Antoine G. (2013) Dynamique des matériaux en suspension (MES) le long des rivières aménagées ; exemple de l'Arc en Maurienne et de l'Isère, PhD Thesis, Université de Grenoble

A new gravity-driven runoff and erosion model for TELEMAC

Florent Taccone, Germain Antoine and Nicole Goutal
Laboratoire National d'Hydraulique et Environnement,
EDF R&D
Saint-Venant Laboratory for Hydraulics
6 Quai Watier 78400 Chatou France
florent.taccone@gmail.com

Olivier Delestre
Laboratoire de Mathématiques J.A. Dieudonné
UMR 7351
Ecole Polytech Nice-Sophia Antipolis
Université de Nice-Sophia Antipolis
Parc Valrose 06108 Nice France

Abstract— **With the aim of representing hydraulic transfers and upstream erosion sources on mountain watershed, the representation of the infiltration, immature debris flows and shallow landslides is important because it can be the largest contributor to the amount of sediment exported at the outlet. To model these phenomenon, a hydrological and a gravity-driven erosion model have been implemented in TELEMAC2D. The infiltration is a 1D vertical model. The motion of the granular flows is described with a fully dynamic system. A Coulomb like bottom friction treatment, more adapted to the properties of the flow, is also added. These new developments are complementary to the use of SISYPHE for the erosion, deposition and transfers in the hydraulic network.**

The infiltration model is confronted to field data on a real catchment (Draix, in the Southern French Alps). Then, the new erosion model is qualitatively evaluated on a theoretical test case: a plot with a steep slope upstream and a break in slope to evaluate the form of the erosion and deposition. Then, on a real catchment, the upstream hillslope erosion and the deposition in the hydraulic network is observed.

I. INTRODUCTION

In mountain watersheds, extreme events can lead to the exportation of a large amount of sediment at the outlet. Indeed, the combination of steep slopes and highly erodible soil in badlands is responsible for this phenomenon. The presence of a large mass of sediment in the river flows can fill the dam reservoirs which affects the hydro-electricity production and causes safety issues. At the outlet of small watersheds, the filling of tunnel built to bypass water channels is also observed. The prediction of the sediment transfers is important to dimension some structures or to prevent erosion by hillslope management. A physically based modeling gives explicit values of the hydraulic and sedimentary parameters distributed in time and space. It offers the possibility of identifying the critical erosion zones but also anticipating watershed responses to a management strategy like slopes revegetation or dike construction.

There are several processes involved in the sediment dynamics at the catchment scale. The erosion and deposition processes being heavily reliant on the flow characteristics, the choice of the hydraulic model is crucial. In a precedent paper [18], the selection of the numerical scheme used in TELEMAC2D has been justified. The hydrology of a watershed needs to be taken into account to represent the correct hydraulic transfers. Concerning the sedimentary processes, the model used by SISYPHE is well adapted in the hydraulic network. However, the upstream erosion sources on the hillslopes are not well represented in the code. Then, a focus is on these gravity-driven erosion mechanisms, and particularly the immature debris flows. Plenty of models can be found in the literature to represent the detachment, deposition and dynamic of muddy or granular flows [6, 19, 16, 13], but none of them is integrated to a global model with a hydraulic and hydrological description. The key is to build a model capable of representing the hydrology of a watershed with TELEMAC2D, the upstream gravity-driven erosion sources that supply the classical erosion and sedimentation model in the hydraulic network already present in SISYPHE.

In this paper, the modelling of all the processes above-mentioned and the coupling method are presented. Then, a theoretical test case and a field application are used to assess qualitatively the model.

II. MATERIALS AND METHODS

A. Presentation of the test cases

The first test case is a straight channel with a length of 5 m and a width of 1 m. This channel is divided in two parts: an upstream part with a 50% slope and a downstream part with a 5% slope. The break in slope is in the middle of the channel. On this domain, a steady rain, with an intensity of 100 mm/h, is applied during 10 s. The spatial discretization of the channel is a triangular mesh with a mean space step of 10 cm. The upstream and lateral boundaries are considered as walls. The flow being supercritical at the outlet, the boundary is treated with a free condition.

Thanks to data provided by [11], it is possible to evaluate the model by comparing the results to measured discharges from field campaigns on a real catchment. The Laval watershed is a sub-catchment of the Bouinenc watershed, located on the Draix site in the Southern French Alps. Its total area is about 86.4 ha and the mean slope is 58%. The soil is mostly constituted of black marls and 68% of the surface is a bare soil. At the outlet of the catchment, the discharge are available for many rainfall events with a time step of 60 s. The rainfall intensity associated to the discharge is also measured every 60 s. Two different events are selected, one spring rain following three rainy days with a high soil moisture initial condition, and a summer storm with a dry initial soil state.

B. Overland flow simulation

To simulate rain induced runoff, TELEMAC2D solves the Shallow Water equations which are

$$\partial_t U + \partial_x F(U) = S,$$

where $U = \binom{h}{hu}$, $F(U) = \binom{hu}{hu^2+gh^2/2}$ and $S = \binom{R-I}{-gh(\partial_x z+S_f)}$ with h the water height in m, u the flow velocity in m/s, g the gravity constant in m/s², R the rain intensity in m/s, I the infiltration in m/s, z the bottom elevation in m and S_f the friction slope. For that, the following explicit finite volume scheme is used:

$$U_i^{t+1} = U_i^t - \frac{\Delta t}{\Delta x}\left(F^t_{i+\frac{1}{2}} - F^t_{i-\frac{1}{2}}\right) + \frac{\Delta t}{\Delta x} S_i,$$

where $F^t_{i+\frac{1}{2}} = F(U_{i+\frac{1}{2}+}, U_{i+\frac{1}{2}-})$ is the numerical flux calculated at the interface $i+\frac{1}{2}$ with the HLLC method [20] and $S_i = \begin{pmatrix} R_i - I_i \\ s_{i+\frac{1}{2}-} - s_{i-\frac{1}{2}+} \end{pmatrix}$ are the source terms. The intermediate states $U_{i-\frac{1}{2}+} = \begin{pmatrix} h_{i-\frac{1}{2}+} \\ h_{i-\frac{1}{2}+} u_i \end{pmatrix}$, $U_{i+\frac{1}{2}-} = \begin{pmatrix} h_{i+\frac{1}{2}-} \\ h_{i+\frac{1}{2}-} u_i \end{pmatrix}$, $s_{i+\frac{1}{2}-}$ and $s_{i-\frac{1}{2}+}$ are defined as:

$$z_{i+\frac{1}{2}} = \min(\max(z_i, z_{i+1}), \min(h_i + z_i, h_{i+1} + z_{i+1})),$$

$$h_{i-\frac{1}{2}+} = \min(h_i + z_i - z_{i-\frac{1}{2}}, h_i),$$

$$s_{i-\frac{1}{2}+} = \frac{g}{2}(h_i - h_{i-\frac{1}{2}+})(z_{i-\frac{1}{2}} - z_i),$$

$$h_{i+\frac{1}{2}-} = \min(h_i + z_i - z_{i+\frac{1}{2}}, h_i),$$

$$s_{i+\frac{1}{2}-} = \frac{g}{2}(h_i + h_{i+\frac{1}{2}-})(z_i - z_{i+\frac{1}{2}}),$$

according to the Chen and Noelle's scheme [3].

The friction slope, defined as:

$$S_f = \frac{q|q|}{C^2 h^3},$$

with $q = hu$, is then added to the scheme by a semi-implicit treatment (like in [1]), with a Chézy coefficient $C = 30$ m$^{1/2}$/s.

This scheme correspond to the 5th finite volume scheme with the 2nd hydrostatic reconstruction option of the V7P2 version of TELEMAC2D.

C. Infiltration model

A derivation of the Green and Ampt's [8] model, presented in [5] and [4] is used to represent the infiltration in the model. It is a vertical 1D model computed at each cell of the domain. The infiltration velocity is discribed like

$$I = K\left(1 + \frac{h_f + h}{z_f}\right),$$

with K the soil conductivity under less than 1 cm of hydraulic head in m/s, h_f the capillarity head in m and z_f the wetting front in m. Then, the wetting front is updated following the equation:

$$z_f = \frac{I_c}{\theta_s - \theta_i},$$

where I_c the cumulated height infiltrated since the beginning of the event, θ_s the saturated soil moisture or the porosity and θ_i the initial soil moisture. The soil is vertically divided in two layers, a first with an associated width Z_C and conductivity K_C and a second with a width considered as infinite and a conductivity K_s. The conductivity K varies with the wetting front evolution according to this equation:

$$\begin{cases} K = K_C \text{ if } z_f \le Z_C \\ K = \dfrac{z_f}{\dfrac{z_f - Z_C}{K_s} + \dfrac{Z_C}{K_C}} \text{ else.} \end{cases}$$

D. Debris flow modelling

The detachment criterion is calculated in accordance to [19]. At each cell interface, the slope of the ground ϕ between two nodes of the mesh is calculated. Then, depending on the water depths and the soil properties of these nodes, a stability angle ϕ_1 is evaluated and compared to ϕ. The soil is considered stable if $\phi_1 < \phi$ and unstable if $\phi_1 \ge \phi$. The formula to calculate the critical angle is:

$$\tan\phi_1 = \frac{F_0}{F_1}\left(1 + \frac{c\sqrt{1 - c^2k^{-2}F_1^{-2}g^{-2}h^{-2} + F_0^2F_1^{-2}}}{kF_0gh(1 - c^2k^{-2}F_1^{-2}g^{-2}h^{-2})}\right),$$

where:

$$F_0 = C_*(\rho_s - \rho)\tan\varphi,$$

$$F_1 = C_*(\rho_s - \rho) + \rho\left(1 + \frac{1}{k}\right),$$

with c the apparent cohesive strength of the sediment layer in Pa, k a numerical coefficient near unity, C_* the maximal volumetric concentration allowed in the flow, ρ_s the sediment density in kg/m^3, ρ the water density in kg/m^3 and φ is the internal friction angle of the sediment. The Fig. 1 shows the behaviour of the detachment criterion depending on the slope and the water depth for $C_* = 0.65$, $c = 35$ Pa, $\rho_s = 2650$ kg/m^3, $\rho = 1000$ kg/m^3 and $k = 0.85$. If the rainfall intensity is large enough to generate a runoff with a water depth in the unstable zone, a layer with a thickness e is eroded. This thickness is proportional to the water depth following

$$e = \frac{C_e}{C_* - C_e}h,$$

with $C_e = \frac{\rho\tan\phi}{(\rho_s - \rho)(\tan\varphi - \tan\phi)}$ the equilibrium concentration.

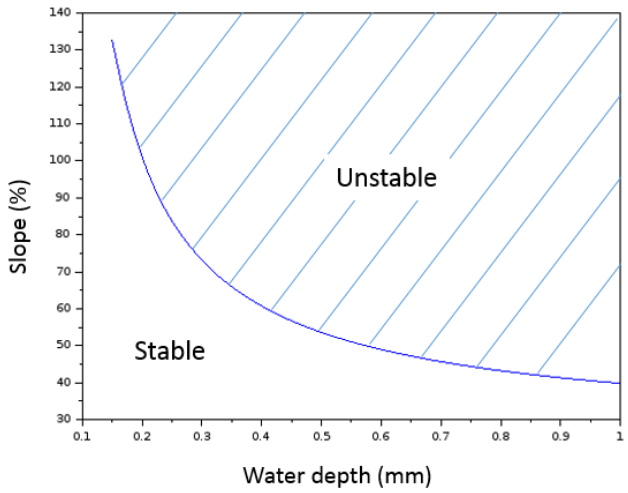

Figure 1. *Detachment criterion for the debris depending on the slope and the water depth*

Concerning the deposition velocity, the formula is similar to the one used for the cohesive sediment deposition in SISYPHE:

$$D = \left(1 - \left(\frac{u_s}{u_c}\right)^m\right)_+ CV_s,$$

where u_s is the debris flow velocity in m/s, u_c is the critical deposition velocity in m/s, m is a coefficient less than 1, C is the sediment concentration in the flow, V_s is the settling velocity in m/s and $(.)_+ = \max(0,.)$.

The debris flow motion is described by its velocity u_s in m/s and depth h_s in m. The evolution of these variables is governed by the shallow water equation with $U = \begin{pmatrix} h_s \\ h_s u_s \end{pmatrix}$, $F(U) = \begin{pmatrix} h_s u_s \\ h_s {u_s}^2 + g {h_s}^2/2 \end{pmatrix}$ and $S = \begin{pmatrix} E-D \\ -g h_s(\partial_x z + S_f) \end{pmatrix}$. The source term is modified with the erosion $E = e/\Delta t$ and deposition velocities, and the friction becomes:

$$S_f = \frac{q|q|}{C^2 h^3} + \cos\phi \frac{|u|}{u},$$

the turbulent part is treated semi-implicitly and the coulomb friction is added explicitly to the scheme (see [15]).

E. *Coupling method*

The coupling between the infiltration and the runoff is made through the source term I in the mass conservation equation. Concerning the debris flow dynamic, it interact with the runoff equations by modifying the bottom elevation like:

$$(1 - \theta_s)\partial_t z = E - D.$$

The entire model is presented in the Fig. 2. The available eroded layer is limited by the wetting front calculated with the infiltration model. Indeed, only the saturated part of the soil is considered available for the debris flow simulation.

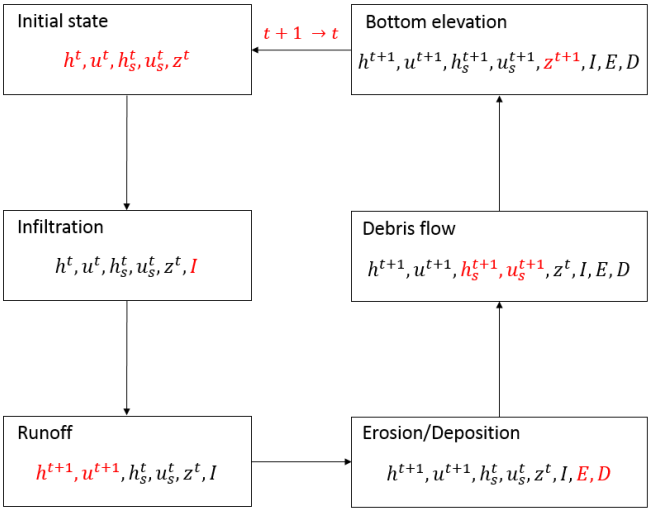

Figure 2. *Schematic representation of the model*

III. RESULTS

A. *Channel test case*

To fulfill the condition of instability, we set $c = 1$ Pa, $k = 0.85$, $\rho_s = 2650$ kg/m^3, $\rho = 1000$ kg/m^3, $C_* = 0.65$, $\tan\varphi = 0.8$, $u_c = 1$ m/s, $m = 0.3$ and $V_s = 0.01$ m/s. The saturated zone is initially set at the constant value 0.1 m and the infiltration is not considered. The Fig. 3 presents the bottom profile along the channel at the end of the simulation. In the upstream part, the erosion starts after 20 cm, when the depth of the water is sufficient to reach the unstable state. Then, a fully eroded zone is observed until the deposition starts, when the velocity decrease with the gentlest slope. This results are consistent with what is expected from the model. Moreover, the shape of the deposition is close to the experimental observations of [19] shown in Fig. 4.

B. *Watershed hydrology*

The hydrological model is confronted to field data by comparing the measured and simulated outlet discharges on two events. The events are selected because they are the most erosive of the 2012 year, in terms of sediment volume exported at the outlet. The first event is recorded the 29th of May succeeding six rainy events from 21st to the 27th of May. The maximal value of the rain intensity is 84 mm/h and the peak discharge is 3 m^3/s. Concerning the other event, it is a summer storm of the 25th august with an initial dry state because the last recorded event is the 25th July. The maximal intensity of the rain is 156 mm/h and the peak discharge is 6.6 m^3/s.

To simulate these events, we set the properties of the soil constant, modifying only the initial soil moisture (θ_i in the infiltration model). The calibration gives the following soil parameters:

- first layer thickness: $Z_C = 8$ cm,
- first layer porosity: $\theta_1 = 0.35$,
- first layer conductivity: $K_C = 20$ m/s,

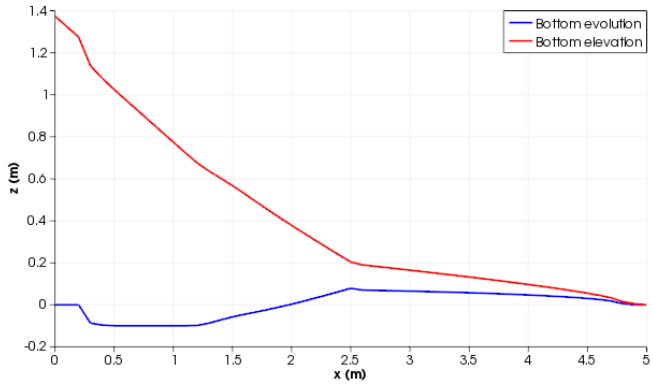

Figure 3. *Bottom elevation and total evolution at the end of the simulation*

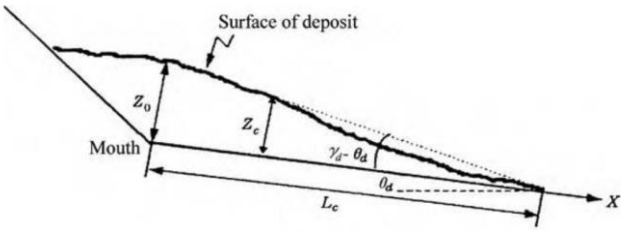

Figure 4. *Side view of the shape of the deposition, experimental results from [19]*

- second layer conductivity: $K_s = 1$ m/s,
- second layer porosity: $\theta_2 = 0.15$,
- capillarity head: $h_f = 5$ cm.

Inspired by [12], the parameters are chosen to have a porous surface layer and a more structured base layer. The initial soil moisture is set to $\theta_i = 0.22$ for the spring event and $\theta_i = 0.03$ for the summer storm. The Fig. 5 presents the measured and simulated outlet discharges for the spring event and the Fig. 6 shows the results for the summer event.

The simulated results are in good agreement with the observations. Despite some important simplifications of the model, the outlet hydrograph are well represented. Indeed, the soil properties are considered as uniform in space, as well as the friction coefficient. In addition, the exfiltration is not represented and compensated by a low conductivity of the base layer. The representation of the vertical structure of the soil is sufficient to have a satisfactory reproduction of the hydrographs.

C. *Watershed gravity-driven erosion*

The debris flow model is now applied to the Laval watershed. The goal is to observe quantitatively if the upstream sources are well represented and if the sediment are deposited in the hydraulic network. The model is tested on the summer event, because of its high rain intensity. The parameters used for the detachment and deposition are:

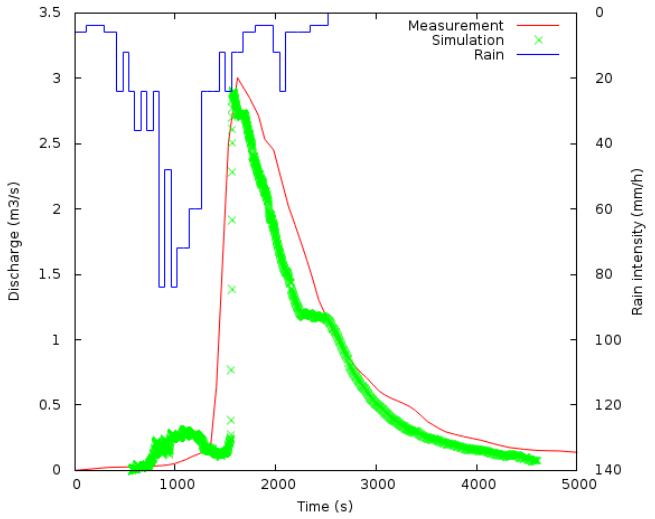

Figure 5. *Discharge at the outlet of the Laval catchment, 29 May 2012 event: measurement vs simulation*

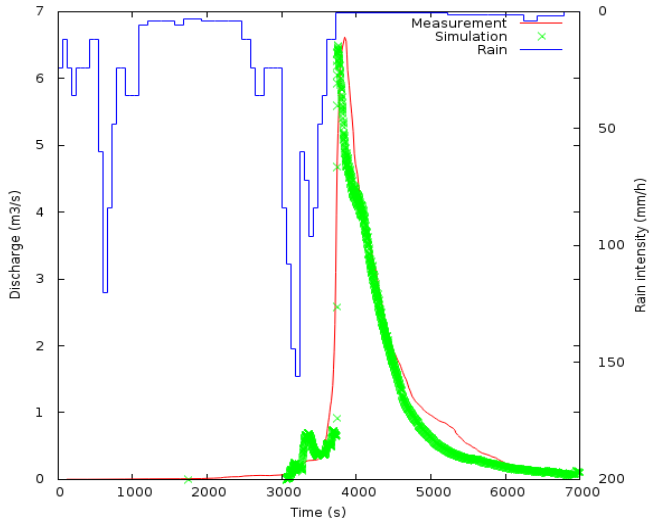

Figure 6. *Discharge at the outlet of the Laval catchment, 25 August 2012: measurement vs simulation*

- cohesive strength of the soil: $c = 35$ Pa
- density of the sediment: $\rho_s = 2650$ kg/m^3
- density of the water: $\rho = 1000$ kg/m^3
- parameters: $k = 0.85$ and $m = 0.3$
- internal friction angle: $\tan\varphi = 0.8$
- maximal concentration: $C_* = 0.65$
- critical deposition velocity: $u_c = 1$ m/s

The Fig. 7 shows the erosion and the deposition in the Laval catchment. The erosion is mainly localized at the upstream of the watershed, in the small gullies. Then the sediments are deposited in the main channels, distributed in the entire watershed.

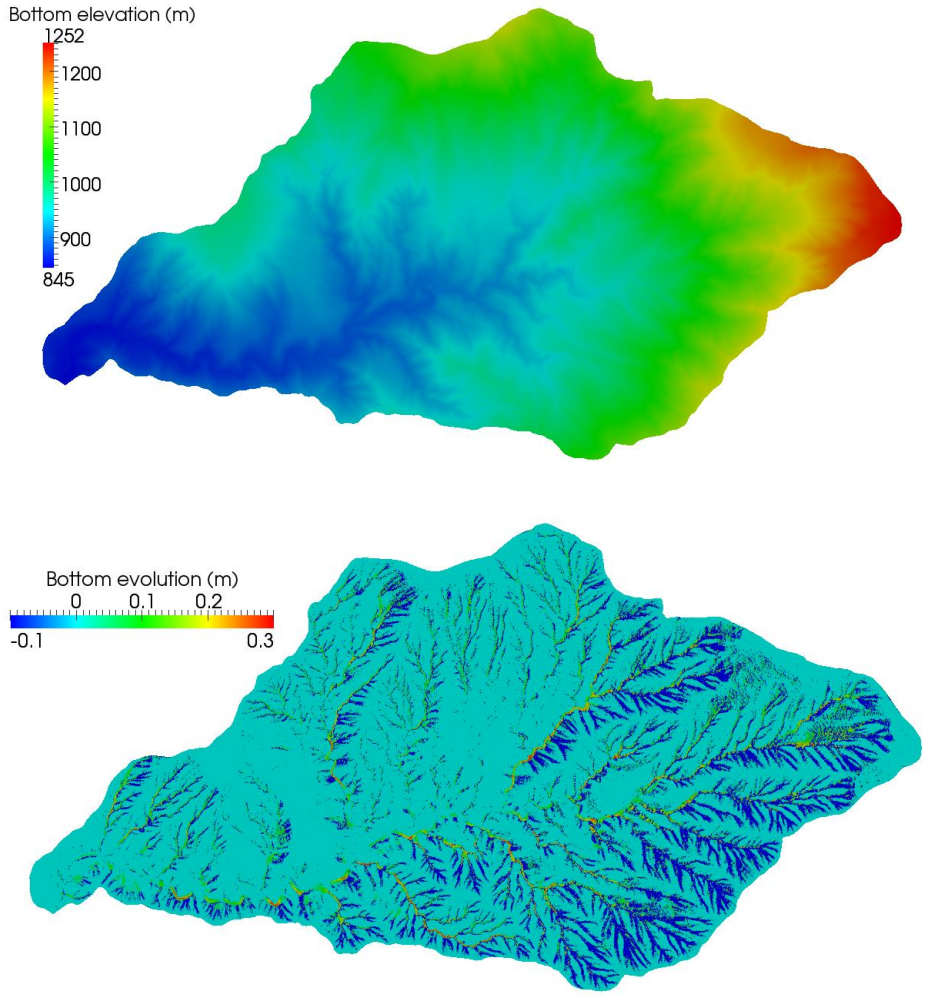

Figure 7. *Bottom elevation and evolution at the end on the simulation in the Laval catchment*

IV. Discussion

The model presented above has many benefits to represent the erosion in mountain watershed. It is composed of models widely used, whose efficiency has been proven. The Green-Ampt infiltration model [8] can be found in a lot of physically-based hydrological models: CASC2D [10], WASIM [17], FullSWOF2D [4]. Furthermore, the accuracy of this model has been demonstrated at the plot scale [5], but also at the catchment scale, in comparison with other infiltration formulas [2]. Concerning the gravity-driven erosion model, the detachment formula is based on experiments with immature debris flows, which is the main phenomenon observed in small mountain watersheds [14]. Indeed, this study shown that for events with a rain intensity greater the 55 mm/h, it can contribute to more than 60% of the total erosion in the Draix catchments, including the Laval watershed. The shallow water equations have also shown their efficiency to simulate the motion of muddy or granular flows ([21], [7]), adding a Coulomb term to represent the friction of the solid fraction of the flow with the bottom. The coupling method between the water runoff and the debris flow ensures that the hydrology of the watershed is slightly affected, and the infiltration and overland flow model stay efficient. Indeed, the system has the same properties as the Saint-Venant/Exner one, with a different dynamic in the solid discharge formulation. Another advantage of this method is that the deposition is located in the hydraulic network and can be provided to SISYPHE as amount susceptible to be eroded.

However, the main assumption of the model is the fact that the runoff on the upstream and the debris flows are moving in the same theoretical volume. Indeed, the bottom elevation considered for the water and the muddy flow is the same. This approximation raises a question concerning the validity of this hypothesis. This is justified by [9], saying that the aquifer responses can be described with the shallow water approximation. The shallow water equations are governing the aquifer responses while the debris flows is considered as a surface process on the upstream slopes. This approach still needs to be validated with the concentration measurement on the Draix watersheds.

V. Conclusion

The TELEMAC computation code is adapted to river simulations and need to be adapted to simulate hydraulic and sedimentary transfers in mountain watersheds. In a precedent paper [18], a numerical scheme has been proposed to simulate the runoff on steep slope.

A derivation of the Green-Ampt hydrological model [8] is first presented. It is a 1D vertical model which give a precise representation of the properties of the soil. This model have been tested on the Laval watershed, on two different rainy events. The simulated and measured outlet discharges are in good agreement, keeping the same parameters of the soil properties and modifying only the initial soil moisture between the two events.

Then, a gravity-driven erosion model has been tested. It consists in simulated the debris flow formation, evolution and deposition in the model. On a simple test case, the behaviour of the debris flow is expected and the form of the deposition is close to what can be observed in the experiments. Then, on the Laval watershed, it is interesting to see that the debris flows are generated in the gullies upstream and deposited in the hydraulic network. The amount deposited can be consider as an input for SISYPHE to model erosion and sedimentation in the network.

This model still need to be validated. The concentration at the outlet are available on several events on the Laval watershed. Data on other catchment can also be used, like tracking of deposition and erosion on the main river event by event.

References

[1] M.-O. Bristeau and B. Coussin, “Boundary conditions for the shallow water equations solved by kinetic schemes,” INRIA technical report, 2001.

[2] N. Chahinian, “Comparison of infiltration models to simulate floos events at the field scale,” Journal of Hydrology, vol. 306, pp. 191-214, 2005.

[3] G. Chen and S. Noelle, “A new hydrostatic reconstruction scheme based on subcell reconstructions,” SIAM Journal on Numerical Analysis, vol. 55, pp. 758-784, 2017.

[4] O. Delestre, S. Cordier, F. Darboux, M. Du, F. James, C. Laguerre, C. Lucas, O. Planchon, “FullSWOF: a software for overland flow simulation,” 2014.

[5] M. Esteves, X. Faucher, S. Galle, M. Vauclin, “Overland flow infiltration modelling for small plots during unsteady rain: numerical results versus observed values,” Journal of hydrology, vol. 228, pp. 265-282, 2000.

[6] D. L. George and R. M. Iverson, “A depth-averaged debris flow model that includes the effects of evolving dilatancy. II. Numerical predictions and experimental tests,” Proceedings of the Royal Society A, vol. 470, 2014.

[7] J. M. N. T. Gray, M. Wieland and K. Hutter, “Gravity-driven free surface flow of granular avalanches over complex basal topography,” Proceedings of the Royal Society A, vol. 455, pp. 1841-1874, 1999.

[8] W. H. Green and G. A. Ampt, “Studies on soil physics,” The Journal of Agricultural Science, vol. 4, pp. 1-17, 1911.

[9] A. Guerin, O. Devauchelle and E. Lajeunesse, “Response of a laboratory aquifer to rainfall,” Journal of Fluid Mechanics, vol. 759, 2014

[10] P.-Y. Julien and B. Saghafian, “CASC2D user’s manual: a two-dimensional watershed rainfall-runoff model”, 2016.

[11] C. Le Bouteiller, S. Klotz, F. Liébault and M. Esteves, “Observatoire hydrosédimentaire de montagne Draix-Bléone,” 2017.

[12] N. Mathys, “Analyse et modélisation à différentes échelles des mécanismes d’érosion et de transport de matériaux solides. Cas des petits bassins versants de montagne sur marne (Draix, Alpes-de-Haute-Provence),” INP Grenoble, 2006.

[13] J. S. O’Brien, P.-Y. Julien and W. T. Fullerton, “Two-dimensional water flood and mudflow simulation,” Journal of Hydraulic Engineering, vol. 119, pp. 244-261, 1993.

[14] D. J. Oostwoud Wijdenes and P. Ergenzinger, “Erosion and sediment transport on steep marly hillslopes, Draix, Haute-Provence, France: an experimental field study,” Catena, vol. 33, pp. 179-200, 1998.

[15] J. Paik, “A high resolution finite volume model for 1D debris flow,” Journal of Hydro-environment Research, vol. 9, pp. 145-155, 2015.

[16] S. P. Pudasaini, “A general two-phase debris flow model,” Journal of Geophysical Research: Earth Surface, vol. 117, 2012.

[17] J. Schulla, “Model Description WaSiM,” 2012

[18] F. Taccone, G. Antoine, O. Delestre and N. Goutal, “Improving TELEMAC on a simple test case to simulate runoff and erosion generation,” TELEMAC-MASCARET User Conference, 2016.

[19] T. Takahashi, “Debris flow: Mechanics, prediction and countermeasures,” Taylor & Francis, 2007.

[20] E. F. Toro, “Riemann solvers and numerical methods for fluid dynamics,” Springer, 2009

[21] C. Wang, S. Li and T. Esaki, “GIS-based two-dimensional numerical simulation of rainfall-induced debris flow,” Natural Hazards and Earth System Sciences, vol. 8, pp. 47-58, 2008

Temporal variability of contaminated sediments in a strongly regulated reservoir of the upper Rhine River

G. Antoine[1, 2], T. Pretet[1,3], M. Secher[3], A. Clutier[3]
[1] National Laboratory for Hydraulics and Environment (LNHE), EDF R&D, Chatou, France.
[2] Saint Venant Laboratory for Hydraulics, Chatou, France.
[3] Engineering Center for Hydraulics (CIH), EDF, Chambery, France.
germain.antoine@edf.fr

Abstract: The upper Rhine River is a highly harnessed and regulated river. Its main channel is navigable and its water is used for agriculture, drinking water supply and electricity production. EDF (a French electricity company) is in charge of eight dams on the upper Rhine River for producing hydro-electricity. In order to increase the safety and the competiveness of the installations, but also to reduce their environmental impact, the sediment dynamic in these reservoirs has become a key factor to control and predict. In this study, we focused on the Marckolsheim reservoir, which is located 50 kilometres upstream the city of Strasbourg. Since its construction in 1961, this reservoir has been filled continuously with cohesive sediments, partially contaminated.

To keep the water level suitable for navigation, the dam is regulated with a high-frequency repositioning of its gates. This regulation, combined with the bifurcation configuration of the channel, leads to a complex and unsteady hydrodynamic in the reservoir. Furthermore, the high temporal variations of suspended sediment supply makes the deposition in the reservoir even more difficult to predict. Two field campaigns were performed in 2015 and 2016 under two different discharge conditions, with the objectives of estimating hydraulic and suspended sediment transport variables.

The numerical codes TELEMAC-2D and SISYPHE were used to simulate in 2D (integrated along the water depth) the hydrodynamic and the suspended sediment transport on this site. A ten kilometres long model was built and calibrated with the measured data of the 2015 and 2016 field campaigns, but also with measurements of sediment parameters that have been done previously, like erosion tests (Westrich, 2010). The originality of this model consists in an explicit 3D representation of the dam gates. An algorithm was implemented in TELEMAC in order to adapt the gates position at each time step, in conformity with the real regulation rules followed by the dam operator. By using upstream measured data of discharge and suspended sediment concentration as boundary conditions, a six months period was simulated thank to the EDF R&D clusters. The comparison of the simulated results with bathymetric surveys shows good agreements if specific properties of sediments related to settling processes are taken into account.

Finally, a new method is proposed in order to simulate the dynamics of the contaminated sediments. The SISYPHE code has been modified for allowing the simulation of two cohesive sediment classes: one class for contaminated sediment, one class for the non-contaminated ones. A 3D spatial distribution of the contaminated sediments in the reservoir has been defined in the layer representation of SISYPHE. The long-term simulation gives interesting highlights of the effect of flood events on the resuspension conditions of the contaminated sediments.

Influence of hiding-exposure effect and vertical sorting of sediment on bars morphodynamics

F. Cordier[1,2], P. Tassi[1,2], N. Claude[1], A. Crosato[2], S. Rodrigues[3], D. Pham van Bang[4]
[1] EDF – R&D – LNHE, Chatou, France
[2] IHE Delft and Delft University of Technology, Netherlands
[3] École polytechnique de l'université de Tours, UMR CNRS 7324 Citeres, France
[4] Cerema – Laboratoire Saint-Venant – ENPC, Chatou, France
florian.cordier@edf.fr

Abstract: Gravel-bed rivers inherently show a certain degree of variability in Grain Size Distribution (GSD), which strongly alters the characteristics and dynamics of alluvial bars at the macro-scale (Lanzoni, 2000b; Singh *et al.*, 2017). However, the understanding and the modelling of the impact of sediment grading on bar morphodynamics remains limited (Siviglia and Crosato, 2016). In order to investigate the impact of grain size heterogeneity on bar morphodynamics, a set of two-dimensional fully-nonlinear morphodynamics numerical models, based on the laboratory experiments of Lanzoni (2000a,b), have been implemented in the Telemac modelling system (TMS).

Morphodynamic processes are modelled with the 2D depth-averaged hydrodynamics solver of the TMS (TELEMCAS-2D), internally coupled to the sediment transport and bed evolution module (SISYPHE). Three bedload formulas are adopted in the present study: the original formula proposed by Meyer-Peter and Müller (MPM) (1948) used for uniform sediment transport, the MPM formula modified with the hiding/exposure factor proposed Egiazaroff (1965) for modelling graded sediment transport, and the formula of Wilcock and Crowe (2003) used for the transport of graded sediment. The model is based on the active layer concept of Hirano (1971) for sediment mass continuity, with an improved algorithm for vertical sediment sorting based on the work of Reisenbüchler *et al.* (2016). The numerical models simulate sediment recirculation from downstream boundary to the upstream boundary, which was used in the laboratory experiments. Two distinct laboratory experiments of alternate bar formation carried out by Lanzoni (2000a,b) are reproduced numerically, one using uniform sediment, the other one using graded (bimodal) sediment.

The results of the numerical simulations show that taking into account hiding-exposure effects is necessary to mimic the same patterns of sediment sorting as observed in the laboratory, with the accumulation of coarse sediment on the top of the bars and the presence of finer sediment in the pools. These effects appear to enhance the stability of the numerical simulations with a smoother (more realistic) topography on the bars and a more coherent spatial distribution of the different grain sizes in the riverbed. On the other hand, the results suggest that depending on the configuration of the morphodynamic system (*e.g.* sediment transport mode), the vertical sorting of sediment (*i.e.* formation of distinct sediment layers) can affect the bar properties such as amplitude, wavelength or celerity.

References:

Hirano, M. (1971). River bed degradation with armoring. *PhD thesis*, JSCE.
Lanzoni, S. (2000a). Experiments on bar formation in a straight flume 1. Uniform sediment. *WRR*, 36(11).
Lanzoni, S. (2000b). Experiments on bar formation in a straight flume: 2. graded sediment. *WRR*, 36(11).
Meyer-Peter, E. and Müller, R. (1948). Formulas for bed-load transport. In International Association for Hydraulic Structures Research. *IAHR*.
Reisenbüchler M., Bui M.-D. and Rutschmann P. (2016). Implementation of a new Layer-Subroutine for fractional sediment transport in SISYPHE, XIIIrd TELEMAC-MASCARET User Conference.
Singh U., Crosato A., Giri S., Hicks M. (2017), Sediment heterogeneity and mobility in the morphodynamic modelling of gravel-bed braided rivers, *Advances in Water Resources*, Volume 104, June 2017, Pages 127-144, ISSN 0309-1708, https://doi.org/10.1016/j.advwatres.2017.02.005.
Siviglia, A. and Crosato, A. (2016). Numerical modelling of river morphodynamics: latest developments and remaining challenges. *Advances in Water Resources*, 90:1–9.
Wilcock, P. R. and Crowe, J. C. (2003). Surface-based transport model for mixed-size sediment. *Journal of Hydraulic Engineering*, 129(2):120–128.

Assessing the impact of Bulle-Effect on the morphodynamics of a laboratory-scale diversion using 3D numerical simulations

Som Dutta[1,3], Pablo Tassi[2], Dongchen Wang[3], Marcelo H. Garcia[3]
[1] Dept. of Computer Science, UIUC, Urbana, 61801, USA
[2] Electricite de France Research & Development - Laboratoire National d'Hydraulique (LNHE) and Saint-Venant Hydraulics Laboratory, Chatou, France
[3] Dept. of Civil and Environmental Engg., UIUC, Urbana, 61801, US
dutta5@illinois.edu; pablo.tassi@edf.fr

Abstract: The phenomenon in which disproportionately higher percentage of near-bed sediment enters the later-channel of a diversion, compared to the flow, is often referred to as the Bulle-Effect. Previously 3D numerical simulations at experiment-scale diversions have been used to study the mechanism behind the phenomenon (Dutta et al., 2017), though in all the studies the bottom of the channel was assumed to be non-erodible. The current study explores the impact of Bulle-Effect on morphology of the bed at an experimental diversion, while further evaluating how the changing morphology impacts the hydrodynamics of the flow at the diversion. The non-hydrostatic version of Telemac-3D has been used for modelling the hydrodynamics, and SISYPHE has been used for modelling the evolution of the channel bed. Results show scouring at the high-flow zone in the diversion channel, along with deposition at the flow-separation zone. The study also explored the dependence of the bed morphdynamics on the size of the sediment and different sediment loading.

Reference:

Dutta, S., Wang, D., Tassi, P., and Garcia, M. H. (2017). Three-Dimensional Numerical Modeling of the Bulle-Effect: the non-linear distribution of near-bed sediment at fluvial diversions. Earth Surf. Process. Landforms

Numerical assessment of the impact of climate change on the sediment yield in alpine catchments

Sebastian Gegenleithner[1], Clemens Dorfmann[2], Josef Schneider[1]
[1] Institute of Hydraulic Engineering and Water Resources Management, Graz University of Technology, Austria
[2] flussbüro, Graz, Austria
sebastian.gegenleithner@tugraz.at

Abstract: Sediment-laden torrential floods are among the most important natural hazards in Austria. Ongoing climate change in the Austrian Alps will make it necessary to expand and reassess protection measures. Climate change projections for the Alpine region show increasing precipitation during winter and stronger convective precipitation events in summer, even if the aspired warming thresholds of the Paris Agreement were reached. In the research project RunSed-CC one module aims at numerical modelling the current and future sediment transport based on runoff and sediment availability in the Schöttlbach catchment in Styria (Austria). The 2D depth-averaged numerical models Telemac-2D & Sisyphe will be implemented, calibrated and validated by linking the simulated runoff from a hydrologic model and the observed sediment data. The high variability of boundary conditions in a torrent leads to significant uncertainties. Minimum and maximum calculations of sensitive input parameters will allow to assess the possible bandwidth of the results. Different algorithms for the sediment transport in mountain streams will be adapted or implemented to enhance the capability of the numerical model. The calibrated sediment transport model will be used to generate sediment-discharge functions related to the given parameter range in the catchment. This enables the analysis of the possible impact of climate change on the sediment yield in alpine catchments including a scenario coming close to the Paris Agreement (rcp4.5) and a high-end emission scenario (rcp8.5). The calibrated numerical sediment transport model will be applied for estimating the changes of sediment transport in the catchment due to different climate scenarios and modified boundary conditions (e.g. different flood hydrograph, sediment availability). The research will include further sensitivity analyses of key parameters for sediment transport processes and flood hazards in the climate change scenarios.

NESTOR: Sediment management module of TELEMAC

Boris Glander
Department Hydraulic Engineering in Inland Waterways
Federal Waterways Engineering and Research Institute (BAW)
Kußmaulstr. 17, 76187 Karlsruhe, Germany
boris.glander@baw.de

Abstract: Since version V7P1 NESTOR is the new sediment management module of the TELEMAC modelling system. The functionalities of NESTOR were motivated by the sediment management activities at the German Federal waterways. With NESTOR a lot of actions can be defined e.g. dredging and dumping at a specified time, dredging if a water depth is less than a specified value or dumping the just dredged material at a dumping area. The actions will be presented using three applications to show the capabilities of NESTOR.

Application-1: Calibration of a morphodynamic model considering human intervention in the sediment budget (e.g. dredging, dumping and sediment supply).

Application-2: Test model for the prognosis of annual dredging volume dependent on various maintenance depths of a navigation channel.

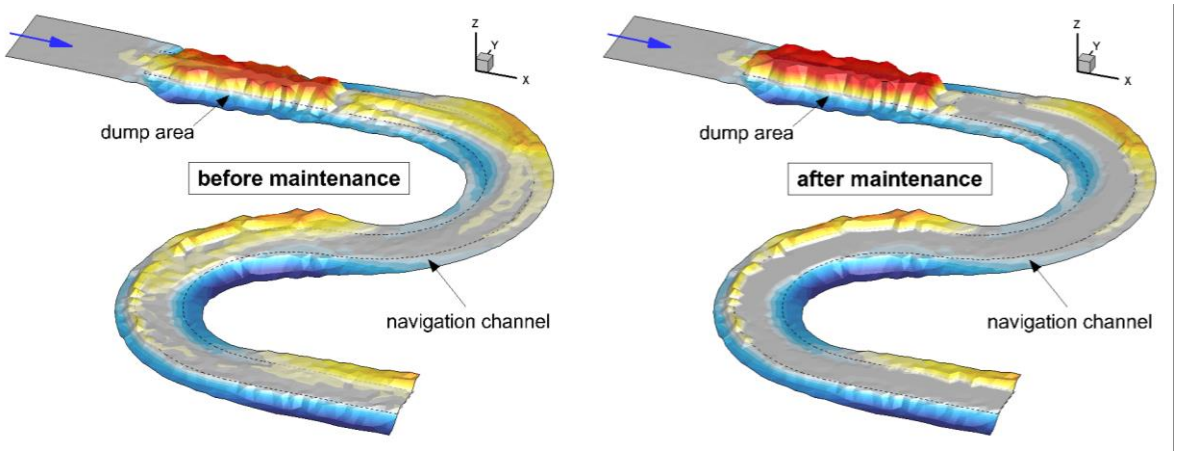

Figure 1: Bottom evolution before (left) and after (right) a maintenance measure at a navigation channel.

Application-3: Iterative determination of the level of a new navigation channel relative to a reference level. The reference level is the water level that belongs to a defined discharge. Because the water level will change due to changes in the bottom geometry the new navigation channel will change the reference level. This leads to an iterative process to find the right level of the new navigation channel. Using NESTOR we are able to go through the whole iterative process in one single simulation.

Modelling potential drivers of fish kill events in Sulaibikhat Bay, Kuwait

John Bacon, David Haverson,
Michelle Devlin
Centre for Environment, Fisheries and Aquaculture Science
Pakefield Road
Lowestoft, UK
john.bacon@cefas.co.uk

Roger Phillips
Marine Science Support Ltd
Chudley, Devon UK

Abstract—**The marine environment of Kuwait Bay, a shallow, tidally dominated area at the margin of the northern and westernmost extreme of the Gulf of Arabia is one of the harshest on the planet. Air temperatures have been known to reach 52 °C, with water temperatures above 30 °C in the summer months. Stratification and mixing in the shallow bay is influenced by freshwater input of the Shaat-al-Arab waterway to the east, by exceptionally high rates of evaporation, and mixing driven by the periodic "Shamal" winds, blowing over the Bay from the north west.**

Coupled with the harsh physical conditions, are the impacts from discharging domestic and industrial waste pollutants and thermal or hypersaline plumes from industrial plants into the Bay, which severely impact marine biota.

In recent years, several catastrophic "fish-kill" events have occurred when physical and anthropogenic conditions have contrived to demonstrate the frailty of the marine system. The most recent of these, in Sulaibikhat Bay, an embayment at the western end of Kuwait Bay, occurred in April 2017 and demonstrated further fragility in the local marine system.

The UK's Centre for Environment, Fisheries and Aquaculture Science (Cefas) developed a Telemac-2D tidal model of Kuwait Waters, coupled with the Telemac integrated water quality module (WAQTEL) to simulate the conditions which may cause such lethal events. Whilst a full water quality modelling process of the region relies on comprehensive knowledge of initial conditions, the modular application of Telemac-2D with the O_2 modules of WAQTEL re-create the likely conditions in Sulaibikhat Bay when the fish kill events occur. We demonstrate how the potential build-up of pollutants coupled with high temperature, salinity and poor flushing of the Bay, partly due to the wide diurnal inequality experienced at the site, reduce levels of dissolved oxygen close to and in places exceed critical thresholds at times. Whilst some species have greater tolerance to these events, other populations are devastated when exposed to such conditions for any length of time. The management and eradication of these events can be effected when they can be accurately simulated and the hazards closely defined.

Introduction

The coastal zone of Kuwait, in keeping with many of its Gulf neighbours has a densely populated and developed coastal zone where residential and industrial land-use exist close to one another. The southern coastline of Kuwait Bay, where Kuwait City has expanded inland and southwards along sandy eastern coastline over the last 5 decades, represent the modern city today and increasing stress is placed upon the marine domain from many quarters. Anthropogenic activities, creating discharges of pollutants which impact the marine biota, have increased significantly during this time and the design and management of procedures to monitor and maintain high water and sediment quality systems need to be considered with great care to ensure the effects of discharges are mitigated [4].

Kuwait Bay is situated at the north-western tip of the Arabian Gulf. It is characterised by a semi-enclosed shallow body of water, about 35 km wide with a mean depth of 5 m, a strong semi-diurnal tidal regime and a maximum depth of about 20 m, covering an area about 750 km^2 [5].

Physical and environmental conditions causing sporadic loss of marine biota have occurred with increasing regularity; in 2001 an estimated 3000 tonnes of fish were killed during the hot August and September period, and as recently as April this year when less severe, but similar fish-kill occurred generating some condemnation of marine management systems and the environmental authorities in the local media [3].

Objectives

Kuwait's extreme marine conditions, particularly in the embayment of Sulaibikhat Bay, are brought about by several physical phenomena which combine to maximise their impact at certain times of the year. Air temperatures around 50 °C; high rates of evaporation contributing to high salinity; low rates of precipitation and limited freshwater input; wind driven mixing, are the natural drivers which contribute to reducing the capacity of the water column to hold oxygen. There are several anthropogenic influences, including industrial scale and domestic waste outfalls distributed along the Kuwait City frontage, contributing to the chemical and biological oxygen demand. Numerous outfalls from power station cooling waters, de-salination plants, refineries and major industrial plants also contribute to the degradation of water quality on the coastal zone.

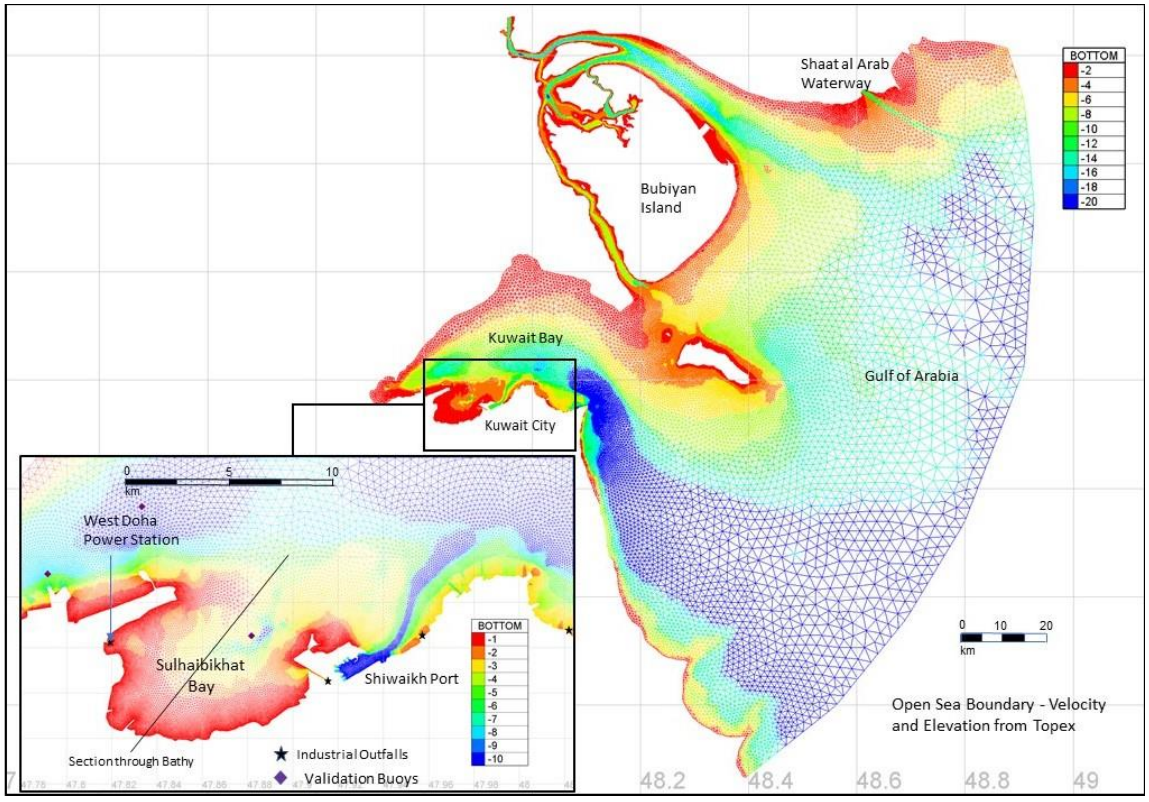

Figure 1. *Telemac2D regional model of Kuwaiti Waters and inset showing the detailed model area of Sulaibikhat Bay; the outfalls at Al Ghazali, Al Bida'a either side of the Port, and Power Station outfalls are shown in relation to the Bay.*

Water temperatures in Kuwait Bay range from an average value of 15.5 ºC in February to a high of 32.3 ºC in August. These values, coupled with high salinity driven by high evaporation and reducing fresh water inputs from the Shaat-al-Arab, reduce the saturation value for dissolved oxygen in the water column even further.

The objective of this study was to create a depth averaged hydrodynamic solution (adequate in the shallow, well mixed zone under investigation), to demonstrate the factors which combine to inhibit circulation and physical attributes which reduce and deplete dissolved oxygen in the embayment at times when physical stressors are at a maximum. However, the amount and quality of data available to validate inputs and outputs of various components in the model is sparse and the results obtained from the present study are only considered qualitative. They do however suggest that during the periods when these conditions align, dissolved oxygen values in the water column are likely to be below the value needed to support fish species.

TELEMAC-2D MODEL – KUWAIT WATERS

A Model Setup

The Telemac-2D model developed for this study covers the area of Kuwaiti National Waters, at just over 12,000 km^2 and is driven by tidal harmonics derived from satellite sensed sea-surface elevations, at its open sea boundary. Whilst 3D models have been successfully applied to demonstrate the importance of the freshwater inputs at Shaat-al-Arab waterway for altering circulation and residence times in the Northwest Gulf [1], for this study a Telemac-2D model was considered suitable. The principal area of interest, Sulaibikhat Bay, at the western end of Kuwait Bay is a shallow embayment (mostly <5m depth) bounded by tidal flats to the west and south and the industrial development of Shuwaikh Port to the east. On its western shore, the cooling water outfalls of Doha Power Station release a hot water plume of approximately 50 m^{3}s^{-1} and flows into the embayment. The plume exhausts from the cooling function of the power station release water with a relative temperature elevation estimated to be 11ºC higher than the intake water temperature.

The model mesh uses bathymetry synthesized from the General Bathymetric Chart of the Oceans (GEBCO) (30 sec), UK Hydrographic Office and augmented by the author's single beam surveys made in 2014 during the Mishref Study [5]. The model is relatively simple in operation employing constant viscosity and options for tidal flats which ensure the large drying regions are included in this tidally dominated region of the Gulf. Details of the Telemac2D model mesh are shown in Fig. 1.

The model resolution increases to a density of 50m along the shoreline of Sulaibikhat Bay and the developed frontage of Kuwait City where the six major releases of treated effluent and industrial waste into the Bay occur.

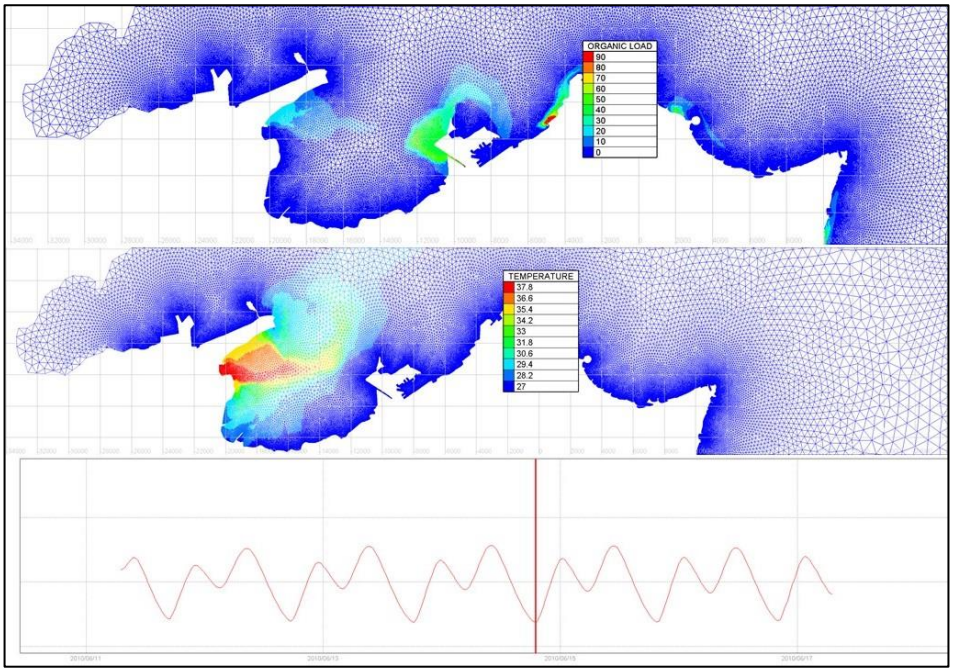

Figure 2. *Organic load from Al Ghazahli outfall and heated water from the power station trapped against the coast at a low spring tide.*

B Local Conditions

The embayment at Sulaibikhat provides a challenging environment for marine animals. At this end of Kuwait Bay, a tidally dominant coastline exists, with a spring range of ~3.2m and neap range reducing to ~1.5m. The embayment itself is shallow (maximum depth of ~4m) and a submarine sill exists across the mouth of the embayment. During each intermediate tide, high diurnal inequality in the local tidal regime severely inhibits flushing of the embayment and as a low spring tide coincides with the top of the sill then flushing is prevented or partially inhibited during each tide. The combination of high sill level and tidal regime can entrap potentially harmful pollutants and waste in the embayment. The sill also traps heated water from the Doha Power station, released at the extreme west end of the Bay, such that heat cannot dissipate freely. The effect of the hot water is detrimental to dissolved oxygen saturation in the embayment and some elevation of temperature exists until the bay can be flushed on the next tide. These effects are shown in Fig. 2 where pollutants and heated water are trapped and lie close to the coast.

C Validation

Validation data for hydrodynamic models are difficult to obtain locally. However, time series of observations provided by the Kuwait Meteorology Department provided enough data to calibrate and validate the Telemac-2D model against elevations and velocities. The Kuwait Environment Public Authority is currently working to develop the Environmental Monitoring Information System of Kuwait (eMisk), a modern GIS based, information system. One aspect of this is for the marine region and in time, as this becomes more fully operational a fully integrated marine monitoring and regulatory process will be at its core and will provide calibrated ocean management, monitoring and modelling systems.

For this study the model's performance was evaluated using the method of [8] (Relative Mean Absolute Error – RMAE). The final parameters used for the Telemac2D hydrodynamics used a Nikuradse friction method with K_s=0.05; Kinematic Viscosity=10^{-4} ; Amplitude Coefficient = 1.1;. These values achieve a RMAE of 0.25 for Elevation and 0.29 for Velocity.

D Waste Inputs – Sources and Tracers

The six waste outfalls which serve the sewerage treatment plants in Kuwait, processing waste from 3.6 million inhabitants of Kuwait's metropolitan area, have been beset with reliability issues for periods of time during recent decades. Much work has been carried out to upgrade the system but at times up to 150,000 m^3 of raw, untreated waste has been released into the Kuwait coastal zone, in this instance from the Mishref pumping station breakdown in 2009 [5], [7].

Precise measurements of the outfall discharges and concentrations of tracers are not available at present and assessments of likely values have been made by colleagues at site. The total discharge at each outfall was assessed to be 60% of the output during the periods when unprocessed material was released (1.736 m^3s^{-1}). Tab. 1 shows the concentrations used at the sources in the model and the tracer inputs to the WAQTEL module.

The O_2 module of WAQTEL will trace sources of Organic Load (Biological Oxygen Demand), Ammoniacal Load (Ammonium NH_4) and Dissolved Oxygen. Background

values for these source inputs were set as 3 mgl^{-1} and 0.01 mgl^{-1} each. For environmental conditions prevailing in Kuwait Bay, water temperature at a mean value of 28 ºC and salinity of 40 ppt, a background value for dissolved oxygen of 6 mgl^{-1} was used. A comprehensive study in 2008 [2], reported a slightly lower average value in Kuwait bay for dissolved oxygen of 5.3 mgl^{-1} however gradients exist between conditions nearer to Bubiyan Island and less developed coasts on the north of the Bay where wide expanses of shallow tidal flats act to reduce the average.

E Water Quality – WAQTEL

Water Quality Processes are invoked in the Telemac-2D code with a call to WAQTEL, controlled by a separate steering file. The O_2 module of the WAQTEL system is used to compute the density of dissolved oxygen in the water. The methodology is designed to be simple [9] and computes the

residual quantity of an O_2 tracer based on relatively simple methods to evaluate sources and sinks which control the evolution of O_2 in the water column. It does not consider the full complexity of biological interaction and uses co-inputs of Organic Load (BOD) and Ammoniacal Load (NH_4), the elements which represent typical treated waste from sewage treatment plants.

The residual dissolved oxygen value is computed by reconciling the following sources and sinks for O_2:

$$F([O_2]) = K_2(C_s-[O_2])—K_1[L]—K_4[NH_4]+P—R—\frac{ben}{h} \quad (1)$$

Where: Cs = O_2 Saturation density of water; K1 =Constant of Degradation of Organic Load (L) ; K2 =Reaeration Coefficient; K4 = Constant of Nitrification; P = Photosynthesis; R = Vegetal Respiration; ben = Benthic Demand; h=depth of water.

The separate components of (1) should be calibrated and several options are available to effect this within the steering files or directly within the calc_o2.f source code. Without alteration, the simplistic method of summation of values can result in negative values for O_2 concentration.

In Kuwait, the harsh physical conditions affect some of these components such that the default values are not valid and need to be adjusted.

The default values of K1, Constant of degradation of Organic Load and K4, Constant of Nitrification were used in the model. Values of 0.25 and 0.35 degrade the tracers in time and are independent of other factors.

K2, the coefficient of Re-aeriation, offers options for method of computation. Firstly, a variety of empirically derived parameterisations can be selected to determine a value. These are strongly dependent upon flow velocity and depth, but valid for a water temperature of 20 ºC. Therefore, a second adjustment is made to consider the high-water temperature in the Bay (average value of 28 ºC in June). This adjustment increases the re-aeriation coefficient by a factor of 20%, in the mostly shallow conditions with moderate tidal strength in the Bay, re-aeriation is likely to be stronger than that set by default.

Values for Photosynthesis and Vegetal Respiration, which are a source and a sink of oxygen respectively, were kept at default values. Both values are relatively low in the Kuwait conditions. Poor water clarity degrades light availability although shallow conditions in the embayment are likely to boost photosynthesis. There is sparse vegetal growth on the tidal sand flats and in the embayment and related respiration is likely to be at a minimum.

Benthic Demand, also dependent upon water depth, is evaluated at 20 ºC and an increased coefficient is used which for a temperature of 28 ºC, enhances demand by up to 65%.

RESULTS

A Deployments

In each case in this section where point values are presented they are considered at a point coincident with the location of a smartbouy deployment made by the Environment Protection Authority of Kuwait and located at the centre of the Sulaibikhat Bay, the location indicated on Fig.1. The location is in the deepest part of the embayment before the sill rises to create shallow conditions again. Whilst this deployment forms one of twelve new monitoring stations incorporated into the eMisk programme it is not yet fully operational. Sensors for dissolved oxygen and CTD have not yet been calibrated in-situ and data are not yet telemetered.

B Hydrodynamics

The model was run for a relatively brief period (6 days) given the caveats for the operation of the O_2 module, of it being valid for a period of several days only. The hydrodynamics were validated for a month-long period and validation statistics showed that in its 2D form, the Telemac hydrodynamic performance is good to excellent [4].

TABLE 1. TRACER LOCATIONS AND INPUTS TO THE MODEL

Name	Lat	Lon	Q	O_2	Org. Load	NH_4	Temp
			m^3s^{-1}	mgl^{-1}	mgl^{-1}	mgl^{-1}	^oC
Al Ghazali	29.34	47.90	1.0	6.0	125	125	28
Al Bida'a	29.32	48.09	1.0	6.0	125	125	28
Al Khitabi	29.30	48.08	1.0	6.0	125	125	28
Al Messela	29.27	48.09	1.0	6.0	125	125	28
Chin. Rest.	29.36	48.02	1.0	6.0	125	125	28
Sher. Hot.	29.36	47.95	1.0	6.0	125	125	28
Pwr Stat. o/fall	29.36	47.81	50.0	0	0	0	39

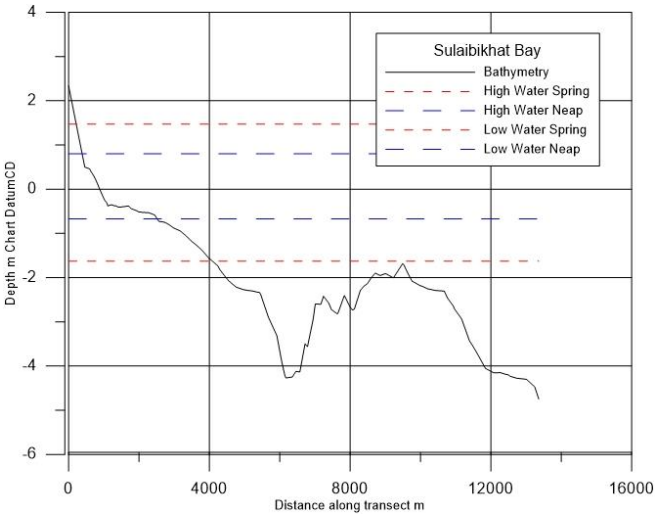

Figure 3. *Relationship between the embayment bathymetry and Spring, Neap High and Low water levels.*

C Dissolved Oxygen Concentration

The impact of natural diurnal inequality is a dominant factor inhibiting polluted water from flushing out of the embayment. Fig. 3 shows the relationship between HW and LW Spring and Neap tidal conditions and their absolute levels in relation to a transect along the seabed for 13.5km from shoreline of Sulaibikhat Bay out into Kuwait Bay (shown in Fig.1). Whilst over 50% of the area of the embayment dries to tidal flats on low water of a spring tide, the sill prevents exchange of water at tidal levels above this also.

Whilst temperature was added as a tracer in the discharge from the power station outfall it was not included in the computations of the model for this study. The model was run in a barotropic mode, without the effect of salinity, and the final evaluation of dissolved oxygen, which includes the effect of salt on dissolved oxygen concentration, was post-processed. A factor of 80% was applied to the computed values of dissolved oxygen to allow for a salinity of up to 40ppt and temperature of 28^{o}C [3].

The effect of temperature on the dissolved oxygen concentration is linear in this model and to improve the results, temperature should be included as a direct variable in the O2_calc.f subroutine. However, the elevated temperatures in this model were applied in the WAQTEL module and the hot water plume effect reduces dissolved oxygen values by up to 0.87 mgl^{-1} with these at their maximum at low water when flushing is prevented.

Absolute values of dissolved oxygen measured by the Kuwait EPA buoy deployment in the centre of the embayment reduce to levels of 4.89 mgl^{-1} at low water of a spring tide. During the low neap tide condition, this degrades further to a value of 4.28 mgl^{-1}.

Fig. 4 shows the value of dissolved oxygen across the embayment at a low Neap tide, values close to the source outfalls at negligible levels but in the centre of the embayment the extent of the lowered values ~4.2 mgl-^{1} is clear.

DISCUSSION

The objective of the study was to highlight factors which combine under certain conditions to inhibit circulation and flushing and degrade dissolved oxygen levels when pollution and elevated water temperatures are trapped in Sulaibikhat Bay. This occurs for particular durations of the tidal cycle, and for much of the time the model does not show reductions in the level of dissolved oxygen of such severity to cause the rates of mortality in fish species observed in recent years.

Whilst the power station (in this case) and other industrial plants add plumes of hot or hyper saline water to the marine environment of the embayment, the discharge of the plumes act to invoke strong re-aeriation due to turbulence generated in the outfall. The design of this structure takes the form of a spillway and mixing, dissipation and re-aeriation are strong in this case. The model simulates this by the relative dimensions of the discharge boundary and strength of the discharge rate applied.

The embayment is generally sheltered, its location at the extreme southwest of Kuwait Bay means that the prevailing “Shamal” winds from the northwest determine that wave activity in the area is relatively low. Waves would act to reaerate the water column strongly but the surface conditions of the embayment are calm for much of the time.

The embayment has a mostly natural shoreline formed of tidal sand flats and few structures exist to add turbulence to the flow. However, the new development of the Sheikh Jaber Al Ahmed Causeway will add a line of twin ~5m diameter support columns, at approximately 25m centres. The structure will cross the entire 10 km long mouth of the embayment. The bridge will then continue to the northeast, extending across Kuwait Bay to the new Silk City Development on the northern coast of the Bay. One effect of the substructures of this construction will be to generate further turbulence from the mesa-tidal flows which can also act to improve re-aeriation.

The rates of mortality observed in the fish-kill events which have occurred in the embayment, are not likely have been driven solely by catastrophic reductions in the levels of dissolved oxygen. A combination of several factors should be attributed.

The levels of pollution emitted in the area, whilst fixed in the model are likely to change significantly over the period of a day and recorded events such as the Mishref crisis [4] indicate that at times, the failure of treatment plants and emergency measures invoked to prevent build-up of untreated waste at these times, can result in the release of much higher concentrations of organic and ammoniacal load than used in this simulation.

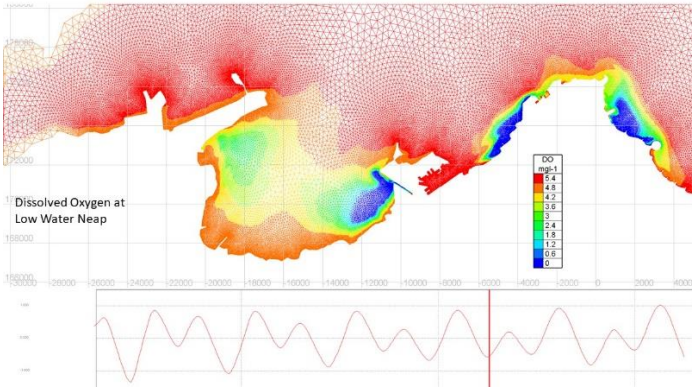

Figure 4. *Absolute values of dissolved oxygen computed at Neap low water, the condition at which values are at their minimum in the embayment where the fish kill events have occurred.*

The range of minimum dissolved oxygen concentrations for cold water and warm water fish species is wide; warm water fish are generally more tolerant to lower oxygen levels, reflected in Water Quality Standards around the world. For salt water fish in the warm and salty water conditions of this embayment, tolerance to lower oxygen levels is likely to be high. Levels of 7-5 mgl^{1} are considered normal whilst levels which drop to 4 mgl^{-1} will generate stress in some species and fatalities at oxygen levels at 50% of this [5].

The model demonstrates that these conditions could certainly exist at times when the stressors of oxygen depletion coincide.

When the fully developed eMisk marine monitoring system is implemented much higher quality and validated datasets will be available to calibrate these type of model simulations.

CONCLUSIONS

The study provided an opportunity to implement a trial of the Telemc2D-WAQTEL, O_2 module although its application in this setting is complex and presents challenges in attaining the correct values for the calibrating coefficients which ultimately control the computation of dissolved oxygen.

The work demonstrates the fragility of the marine system to maintain safe levels of dissolved oxygen in the environment of Sulaibikhat Bay, at the west end of Kuwait Bay. Whilst these were not proven to be at fatal levels during the short periods simulated, the elements which control dissolved oxygen levels in the model are those which can inform the causal effects of harmful low levels in the environment.

ACKNOWLEDGEMENTS

The authors thank the Environment Protection Authority of Kuwait with their assistance in providing data for the work and also the Research Computing Department of the University of East Anglia, Norwich for use of their Hitachi High Performance Computing Cluster.

REFERENCES

[1] Alousari Yousef, Tanuspong Pokavinich, Residence and transport time scales associated with Shatt-Al-Arab discharges under various hydrological conditions estimated using a hydrodynamic model, 2017 marine Pollution Bulletin, In press.

[2] Al-Ghadban, A.N., Uddin, S., Beg, M. U., Al-Dousari, A. M., Gevao, B., Ecological Consequences of River Manipulation and Drainage of Mesopotamian Marshes on the Arab Gulf Ecosystem: Investigations on changes in Sedimentology and Environmental Quality, with Special Reference to Kuwait Bay, Report submitted to Environmental Public Authority and Kuwait Institute for the Advancement of Sciences, 2008

[3] Editorial Article, Kuwait Times, 05/05/2017.

[4] B.P. Lyons, M.J. Devlin, S.A. Abdul Hamid, A.F. Al-Otiabi, M. Al-Enezi, M.S.Massoud, A.S. Al-Zaidan, Smith, A.J., Morris S., Bersuder, P., Barber, P., Papachlimitzou, A., H.A. Al-Sarawi, 2015, Microbial water quality and sedimentary faecal steroids as markers of sewage contamination in Kuwait, Marine Pollution Bulletin 100, p689-698.

[5] Lyons, B., Smith, A., Morris, S., Devlin, M., Evaluation of existing conditions and health of biota in marine and coastal areas impacted by violations (raw sewage and industrial water discharges) from Mishref pumping station, Al Ghazali sewer and El-Esheirij Coastal industrial area, Report to KEPA, 2015.

[6] Fondriest Environmental Inc, Dissolved Oxygen – Fundamentals of Environmental Measurements, 2013. http://www.fondriest.com/environmental-measurements/parameters/water-quality/dissolved-oxygen/

[7] Saeed, T., Al-Bloushi, A., Abdullah, H.I., Al-Khabbaz, A., Jamal, Z., 2012. Preliminary assessment of sewage contamination in coastal sediments of Kuwait following a major pumping station failure using fecal sterol markers. Aquat. Ecosyst. Health Manage. 15, 25–32.

[8] Sutherland, W. J., A. S. Pullin, P. M. Dolman, and T. M. Knight. The need for evidence-based conservation. 2004, TRENDS in Ecology and Evolution 19(6):305-308.

[9] Telemac2D User Manual Version 7.2, 2016, EDF

Analysis of time-step size and initial particle distribution effects on particle dispersal studies

Jonathan Demmer
Bangor University
School of Ocean Sciences
Menai Bridge, U.K.
osp816@bangor.ac.uk

Peter Robins
Bangor University
School of Ocean Sciences
Menai Bridge, U.K.
p.robins@bangor.ac.uk

***Abstract*— Telemac-2D/3D is used here to understand larval dispersal of mussels in the Irish Sea. Mussels (*mytilus edulis L.*) represent 40 to 50 % of the total gross turnover of Welsh shellfish industries and the industry has been operating sustainably for over 50 years in North Wales. In this context, it is in the interest for Mussels companies to understand where the larvae go in order to manage their stocks efficiently. We study the interactions between physical (e.g., tides, currents, temperature, weather conditions…) and biological (e.g., vertical migration, pelagic larval duration) processes experienced by the larvae. We created a variable mesh density for the Irish Sea: very fine scale at mussel seed source in the Menai Strait to coarser scale in the north and south Irish Sea. The aim was to simulate: 1) a range of larval dispersal under present-day natural variability (from a calm and cold year to a windy and warm year); and 2) dispersal patterns in the future (impact of sea-level rise and temperature warming). Telemac in baroclinic mode for the Irish Sea will be compared to existing data and models. A range of larval behavioural traits will also be simulated (e.g. passive vs. active swimmers). Model results will be fed back to the Mussel companies, who will then survey the likely settlement regions identified by the model, and so help validate the model.**

I. Introduction

The accuracy of an oceanographic model is the key to explain the best the impact of physical parameters (tide, wind, temperature…) on larvae dispersal. However, such model may be long to generate and/or to produce files which are too big. Furthermore, the creation of a model in a complex environment as the Irish Sea (shallow water vs deep water; stratified water or not…) can imply a variation of the particle dispersal from an area to another (Parker-Humphreys, 2004; Hill *et al.*, 1997).

The aim of this study is to model the mussel larvae dispersal in the Menai Strait and the Irish Sea. The TELEMAC-2D software was used to simulate the hydrodynamics and a Matlab program was used for the particle dispersion, modelling only the advection. A sensitivity analysis with regards to the time-step size and initial particle distribution was performed in order to determine optimal parameters for futures simulations.

II. Material and Methods

A. *Mesh generation in Blue Kenue*

A variable unstructured triangular mesh density, from 30 meters to 5000 meters, has been created for the Irish Sea on Blue Kenue. The finest scale (30 meters) is in the Menai Strait where mussel companies farm *Mytilus edulis*. The scale is getting coarser to the extreme south and north of the Irish Sea (5000 meters). Furthermore, several areas of interest, such as Morcambe Bay or Liverpool Bay, have a scale of 50 meters. Bathymetry has been downloaded from Digimap, changed into mean sea level (MSL) and mapped to the mesh (Fig. 1).

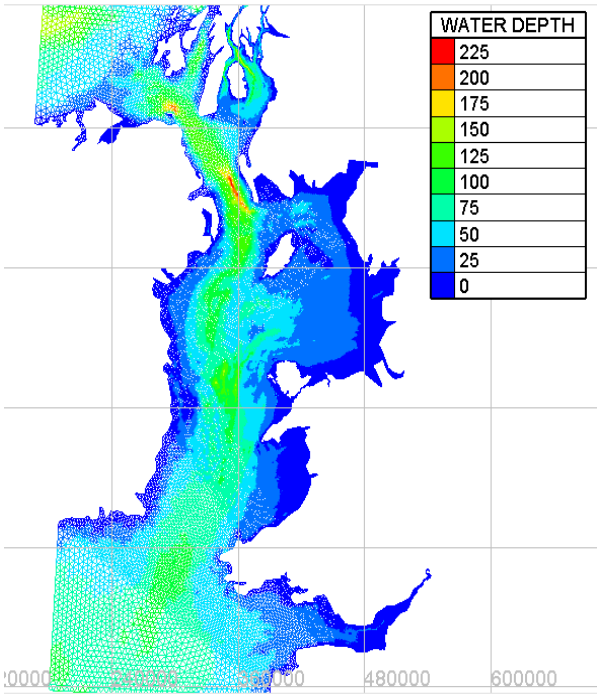

Figure 1. *Variable density of the two-dimensional unstructured triangular mesh of the Irish Sea with bathymetry*

B. *Telemac modelisation and validation*

The model has been run with TELEMAC-2D v7p2r2 with only the tide component. It ran during 4 days from the 1st of March 00:00:00 to 5th of March 00:00:00 during a neap tide. Only the time step has been modified in order to understand if there is an impact on the particle tracking model. The time steps tested are: 5, 10, 15, 30, 45, 60, 90, 120 and 180 minutes. The water elevation validation has been made using tide gauge data from the British Oceanographic Data Centre (BODC) on 14 sites scattered everywhere on the Irish Sea coasts. We also take into account the residuals on the validation results for each month of the year 2015 by calculating the Root Mean Square Error (RMSE). The residuals are the observed elevation of the water minus the predicted elevation of the water. Basically, the residuals are the effect of the weather on tides. In our case, we subtracted the residuals to the observed water elevation in order to validate our model only on tide effect on water elevation.

C. *Particle tracking model (PTM)*

The PTM has been run on Matlab for 5000 particles located between the Isle of Man and Llyn Peninsula for the north and the south boundary respectively (Fredj *et al.* 2016). The east and the west boundary are Anglesey (North wales) and Ireland coast respectively. Particles have been disposed either perpendicular or parallel to the flow (Fig. 2 and 3 respectively). The PTM was run only with the advection equations in order to minimize the random dispersal from the diffusion equations. We used a Lagrangian model and the same time-step for the PTM as the one in TELEMAC-2D.

Only the last position of each particle of the 5000 particles was recorded for all time steps. Then, we calculated the distance between the results from the 5 min time-step output (most accurate) and the other output by using Pythagoras theorem.

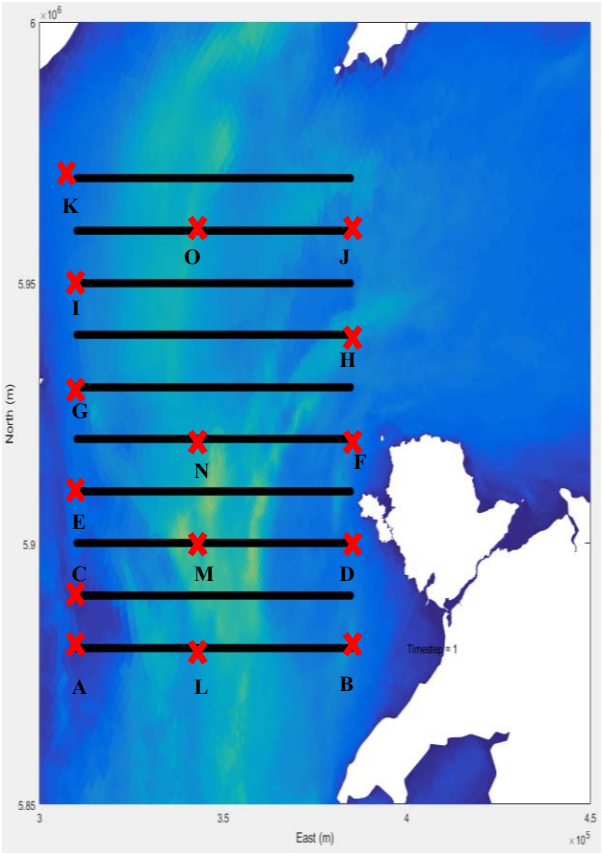

Figure 2. *Position of 5000 particles perpendicular to the flow, red crosses correspond to 15 individual particles of interest labelled from A to O.*

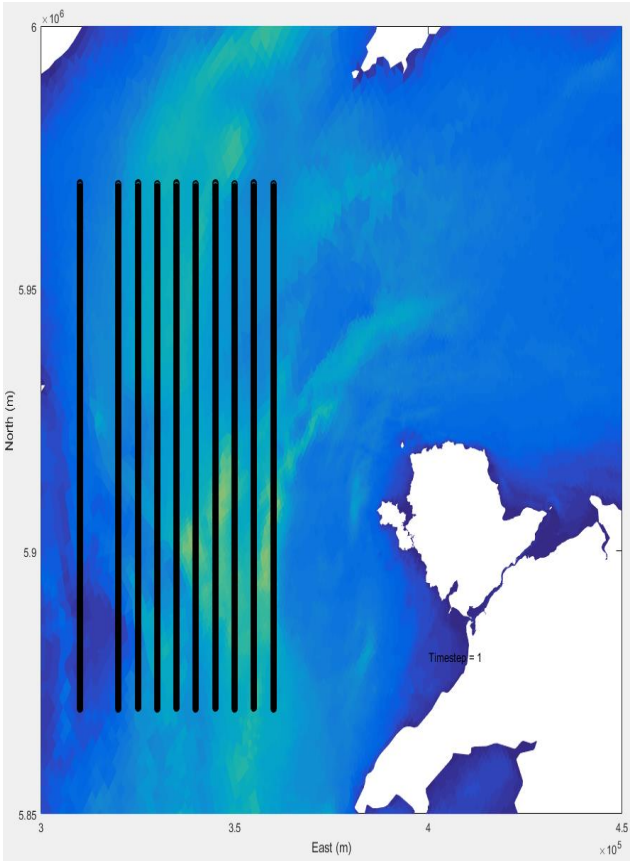

Figure 3. *Position of 5000 particles parallel to the main flow*

III. RESULTS

A. *Validation results*

The RMSE stays the same with a changing time step for each month. When the residuals were used for the water elevation validation, we observed an amelioration of the results. That means the value of the RMSE are more similar between the observed data and the model data. The summer and spring months were less impacted than the autumn and winter months by the residuals as we noticed an improvement of the validation results of 8.89 % and 32.99 % respectively (Tab. 1).

B. *PTM results*

The results showed that bigger is the time step and bigger is the distance with 5 min time step in average for both parallel and perpendicular situation (Fig. 4). However, the difference looked less important in average when particles are disposed parallel to the main flow. We also saw the emergence of a gyre in the south west of the Irish Sea as the time step is finer (Fig. 5).

By looking at individual particle, we noticed a difference of response between several areas (Fig. 2). We observed the biggest distance between the model run with a time step of 5 min and the time step of 180 min for the particle D and the smallest for the particle K (Tab. 2 and Fig. 6).

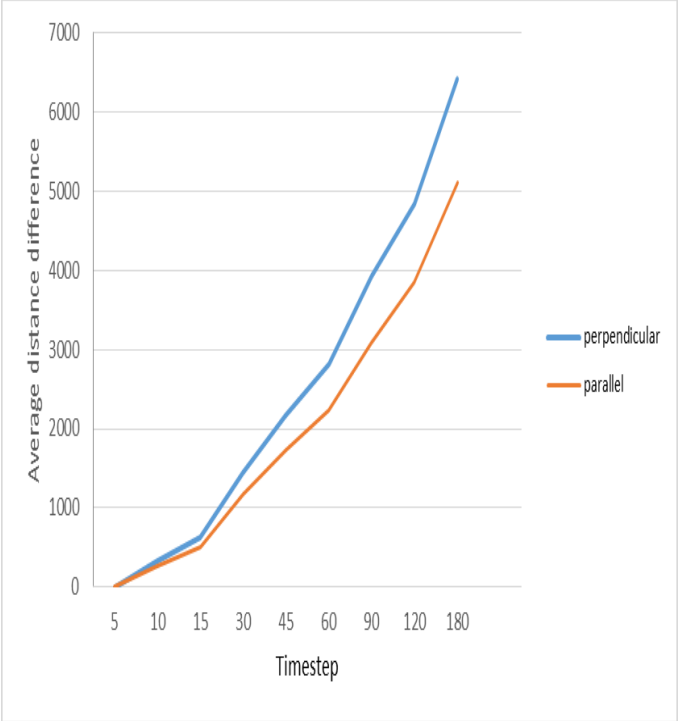

Figure 4. *Average difference distance for both situations when particles are parallel (orange curve) and perpendicular (blue curve) to the main flow.*

TABLE 1. ELEVATION VALIDATION FOR THE YEAR 2015

Month		*January*	*February*	*March*	*April*	*May*	*June*	*July*	*August*	*September*	*October*	*November*	*December*
	No residuals	6,39	5,68	5,51	4,86	4,70	4,68	4,24	4,69	4,93	5,02	5,56	5,38
	With residuals	4,74	4,67	4,59	4,42	4,08	3,95	4,20	4,46	4,74	4,38	4,30	3,92
Amelioration (%)		34,78	21,60	20,10	9,84	15,07	18,54	0,91	5,17	3,87	14,47	29,50	37,22

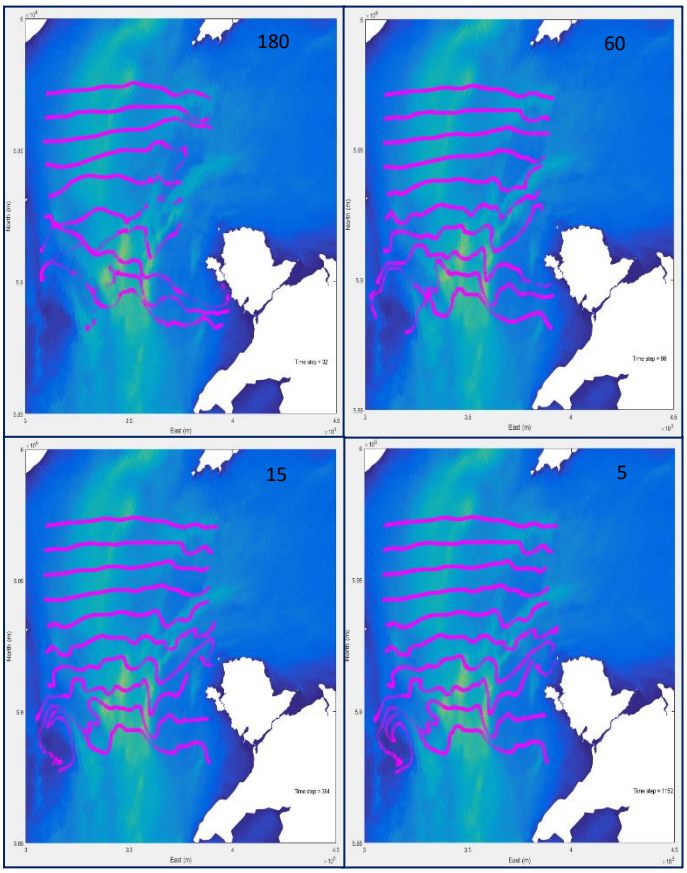

Figure 5. *Final position of 5000 particles distributed perpendicular to the main flow for 5, 15, 60 and 180 min time step after running a PTM.*

TABLE 2. DISTANCE BETWEEN THE 5 MINUTES TIME STEP OUTPUT AND 180 MINUTES TIME STEP OUTPUT FOR THE LAST POSITION OF 15 PARTICLES WITH IN RED THE BIGGEST DISTANCE AND IN BLUE THE SMALLEST DISTANCE.

Particle name	*Distance (m)*
A	15133,84
B	7002,60
C	22960,79
D	**24676,39**
E	4270,42
F	18503,45
G	867,31
H	11386,18
I	1371,81
J	2897,81
K	**777,05**
L	6192,52
M	3780,48
N	1787,28
O	1145,71

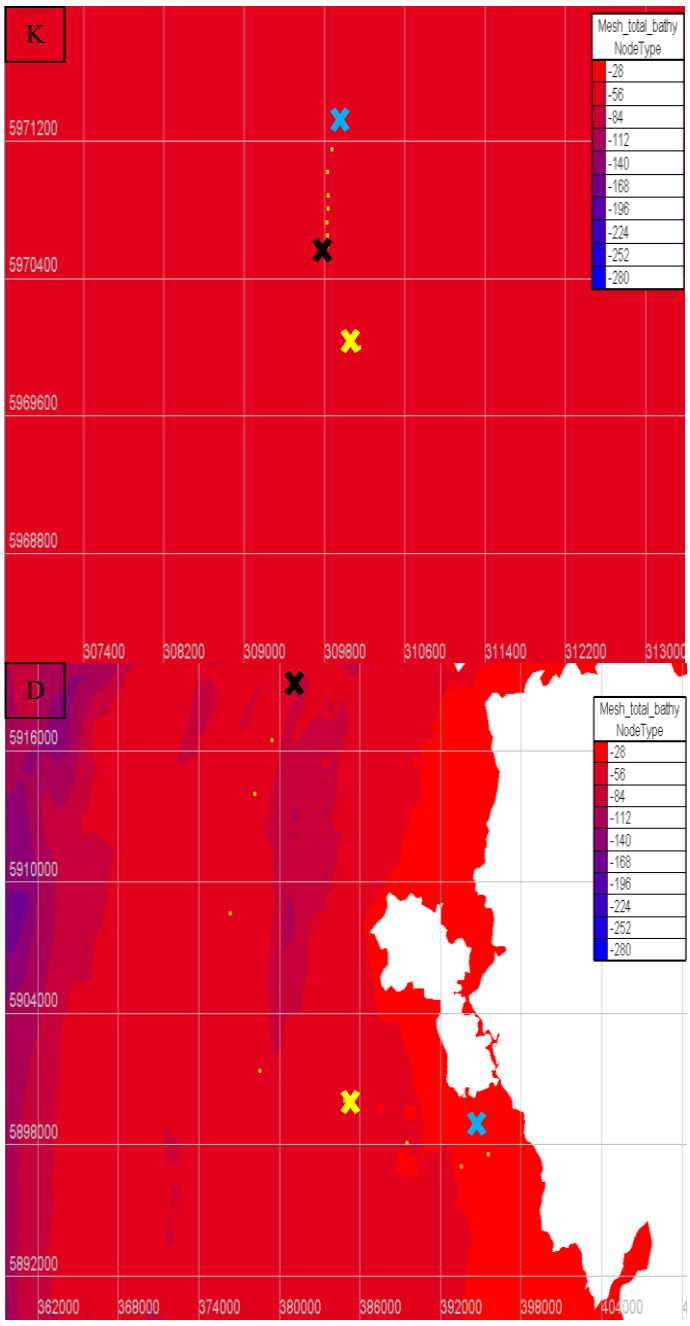

Figure 6. *Representation of the dispersion of particle D and K. The initial position (yellow crosses) and the last positon for 5 minutes output (black crosses) and 180 minutes output (blue crosses) are represented.*

IV. DISCUSSION

The difference in results between particles distributed parallel and perpendicular to the flow (20.27 % in average) could be explained by the absence of particle around Anglesey which is on area of high dispersal due to the velocity of the current as shown in Fig. 6.

As shown in the Fig. 5, it seems that variation of time step impact more the south part of the Irish Sea than the north part. This could be explained by in the west part of the Irish Sea by the gyre formation which occurs every year during the spring

and the summer (Hill *et al.,* 1997) and in the east part by the current velocity and/or direction along the north coast of Anglesey (Borthwick *et al.*, 2013). The next step would be to study the residuals to consolidate those results. The evaluation of the model accuracy will be done by different kind of surveys 1) by the mussel company by recording observations like date and places of spawning and settlement during spring/summer period (data are already available) and 2) by water sampling of different areas around Anglesey and in the Menai strait to identify the larvae present in the water.

V. Conclusion

This paper showed the difficulty to run a particle tracking model in a variable environment such as the Irish Sea. The creation of a varying time step model depending on the physical marine conditions (velocity, water depth and/or seasonal effect) could be a solution to avoid both heavy files problematic and wrong results interpretation.

VI. Acknowledgments

This research is supported by Knowledge Economy Skills Scholarships (KESS 2) in collaboration with the commercial partner Extramussel ltd.

VII. References

[1] M. Parker-Humphreys, “Distribution and relative abundance of demersal fishes from bean trawl surveys in the Irish Sea (ICES Division VIIa) 1993-2001. Sciance Serie Technical Report, vol. 120.

[2] A.E. Hill, J. Brown and L. Fernand, “The summer gyre in the western Irish Sea: shelf sea paradigms and management implications”, Estuarine, Coast and Shelf Science, vol. 44, pp. 83-95, 1997.

[3] E. Fredj, D.F. Carlson, Y. Amitai, A. Gozolchiani and H. Gildor, “The particle tracking and analysis toolbox (PaTATO) for Matlab”, Limnology and Oceanography: Methods, vol. 14, pp.586-599, 2016.

[4] A.E. Hill, J. Brown and L. Fernand, “The summer gyre in the western Irish Sea: shelf sea paradigms and management implications”, Estuarine, Coastal and Shel Science, vol. 44, pp. 83-95, 1997.

[5] A. Borthwick, S. Serhadlioglu,TAA Adcock,G.T. Houlsby and S. Draper, “Tidal stream energy resource assessment of the Anglesey Skerries”, International Journal of Marine Energy, vol 3-4, pp. e98-e111, 2013.

Assessment of nutrients and macroalgae growth in Poole Harbour, UK

David Haverson, John Aldridge
Centre for Environment, Fisheries & Aquaculture Science
Pakefield Road, Lowestoft, NR33 0HT, UK
david.haverson@cefas.co.uk

Karen Edwards
Environment Agency
Manley House, Kestrel Way, Exeter, EX2 7LQ, UK

***Abstract*— A high-resolution depth-averaged hydrodynamic model was developed for Poole Harbour, UK, with the aim to test water quality scenarios for reducing nutrient levels. These scenarios were developed from a separate Combined Macroalgae and Phytoplankton (CPM) model, a simple linked box model that can be used to calculate nutrient concentrations and the biomass of phytoplankton and macroalgal communities. For the CPM model to function, exchange rates between the different parts of the water body are required. The flushing rates of Poole Harbour are calculated from the hydrodynamic model. Furthermore, as there is uncertainty in what leads to the spatial distribution of macroalgae growth, the hydrodynamic model was used to investigate any links between environmental conditions, nutrient concentrations and macroalgae growth.**

I. Introduction

Poole Harbour is a water body, located on the south coast of the UK, whereby high nutrient concentrations have led to large growth of macroalgae along the shorelines and mud flats. Large macroalgae mats can have negative environmental impacts by reducing the total area of mudflats available to wading birds [1], in addition to reducing dissolved oxygen leading to anoxia in benthic communities within the sediments and lead to nitrogen loading within Poole Harbour waters [2]. Investigations into the feasibility of the removal of macroalgae as a mitigation measure to reduce nutrients and improve water quality is ongoing [3]. Nutrients are fed into the harbour via farm run offs into a number of rivers, notably the River Frome and River Piddle, in addition to a number of outfalls from sewage treatment works at Wareham, Lytchett and Holes Bay. Historically, very high levels of nutrients were found within the harbour. Within the last few decades water quality controls were implemented reducing nutrient inputs from point sources. However, the trend of the amount of nutrients from ground water diffuse sources is increasing as historic run off and land use is still slowly working through the surrounding water table. As such, the aim of the study was test a range of water quality scenarios to investigate how nutrient levels could be further reduced. Furthermore, there is a degree of uncertainty as to what leads to the spatial distribution of macroalgae growth within Poole Harbour. Therefore, the secondary aim was to identify possible links between environmental conditions, nutrient concentrations and macroalgae growth.

II. Hydrodynamic Model

A. Model Domain

A high-resolution depth-averaged model of the Poole Harbour, UK, was built with an unstructured triangular mesh, using the hydrodynamic software Telemac-2D (v7p1). The model domain extends between 1.646°W – 2.239°W and 50.362°N – 50.737°N. The unstructured mesh was discretised with 76,448 nodes and 145,947 elements. Along the open boundary, the mesh has a resolution ranging between 200m to 5km, reducing to 100m along the coastline. Within Poole Harbour the resolution is further refined to 30m. Bathymetry of the outer domain was sourced from the Department for Environment, Food & Rural Affair's UKSeaMap 2010 [4]. The resolution of the bathymetry points from this dataset are 1 arc-second (~30m). Within Poole Harbour, bathymetry was provided by Environment Agency with a resolution of 20m. The hydrodynamics are forced along the open boundaries using 11 tidal constituents (M2, S2, N2, K2, K1, O1, P1, Q1, M4, MS4 and MN4) from the OSU TPXO European Shelf 1/30° regional model. After a spin up period of 5 days, the model was run for 30 days to cover a full spring-neap cycle. Four fresh water inputs are included within the model domain, representing the Rivers Piddle, Frome, Sherford and Corfe. The model uses a k-ε turbulence model with velocity diffusivity set to 1×10^{-6} m^2/s, representing the kinematic viscosity of water. In the absence of accurate wide spread sediment data, the Nikuradse law for bottom friction was used, with a constant value of roughness length, k_s =0.04, applied to the whole model domain.

B. Validation

Validation data have been obtained from the British Oceanographic Data Centre (BODC) for surface elevation at the Bournemouth tide gauge, whose location is shown in Fig. 1. After a spin-up period, the model was run for 30 days from 19/05/2012 00:00 to 19/06/2012 00:00. Comparisons of the modelled free surface elevation and observed tidal elevations, at Bournemouth, is shown in Fig. 2.

To validate the free surface elevations, three statistical tests have been applied: the coefficient of determination, the root mean squared error (RMSE) and the scatter index. The scatter index is the RMSE normalised by the mean of the observations. It is widely used in the validation of wave models [5-7], meaning there is a wide source of literature for

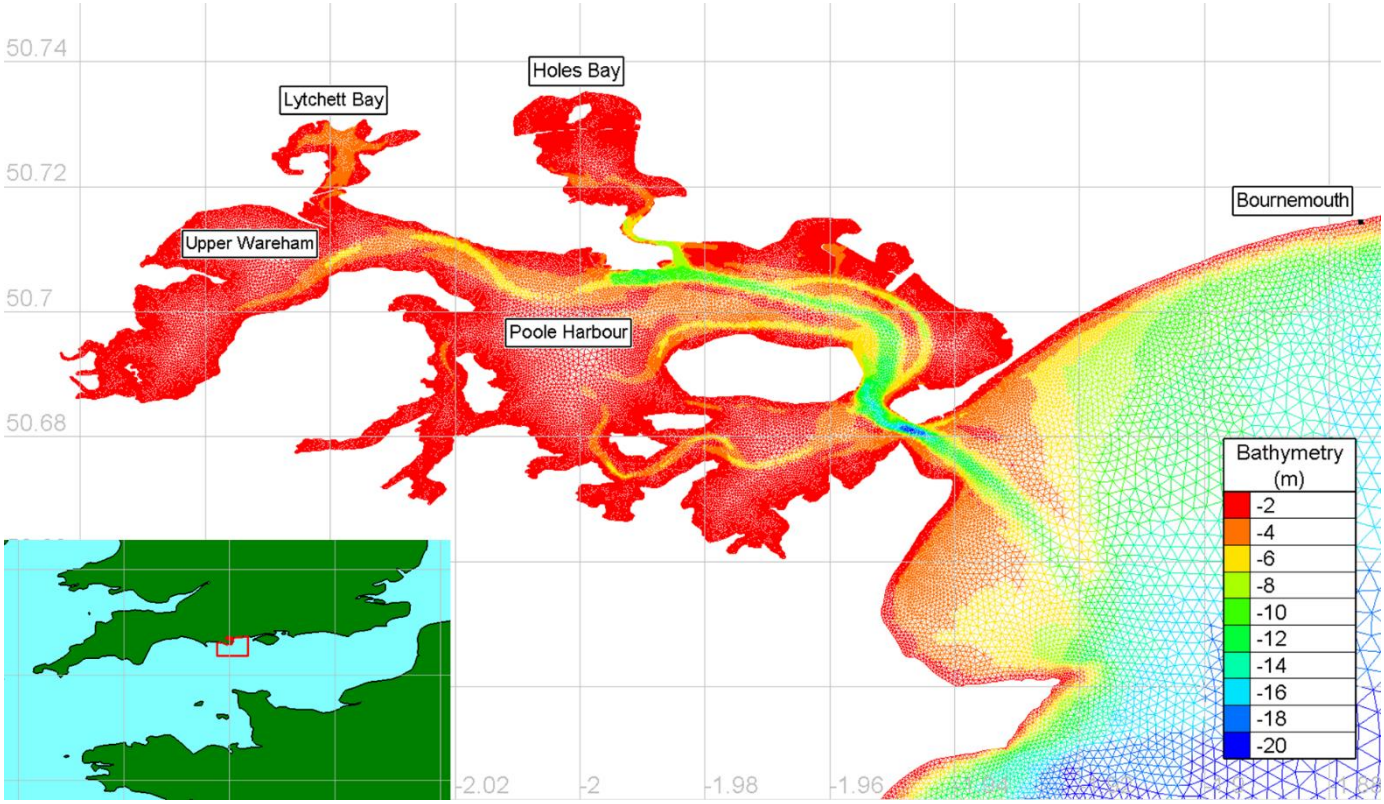

Figure 1. *Model computational domain with the location of tide gauge, used for validation.*

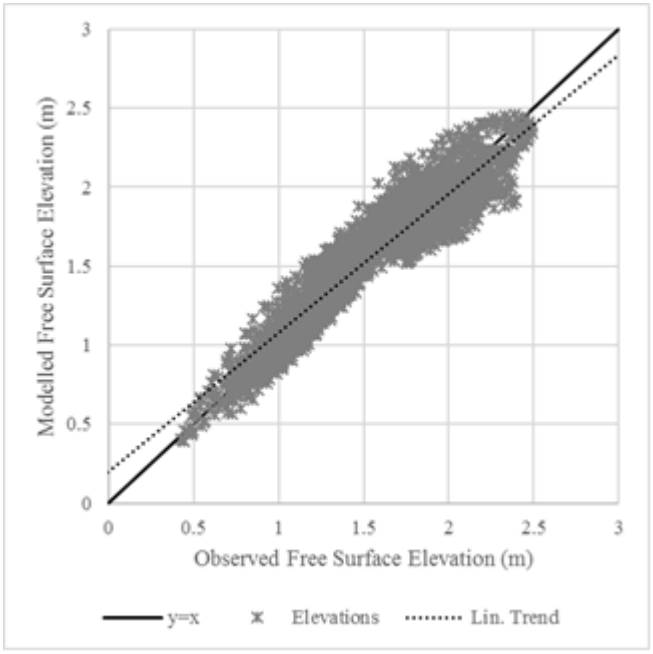

Figure 2. *Comparison of modelled free surface elevation and observations from BODC tide gauge. The black line represents a y=x relationship.*

comparable values. However, there is no comparison for validating tidal elevations. For this study, a scatter index of less than 10% will be considered a good validation. Tab. 1 summarises the validation statistics of the Bournemouth tide gauge. The presented validation represents the preliminary assessment of the model's performance whilst other sources of data are obtained to validate the model beyond a single tide gauge.

TABLE 1. VALIDATION STATISTICS OF THE BOURNEMOUTH TIDE GAUGE.

Tide Gauge	R^2	RMSE (m)	Scatter Index (%)
Bournemouth	0.83	0.15	9.08

C. *Modelling nutrients*

To investigate the spatial distribution of nutrients, specifically the total dissolved inorganic nitrogen (DIN), the nutrients have been introduced as a single passive tracer. There are two types of sources: riverine inputs and sewage treatment works (STW). The riverine inputs include the River Frome (6.54 m^3/s), Piddle (2.47 m^3/s), Sherford (0.57 m^3/s) and Corfe (0.51 m^3/s). There are three STWs: Wareham, Lytchett and Poole East. The location of the source inputs is shown in Fig. 3. As the Wareham STW flows into the River Piddle, the concentrations of both the river and the STW are combined as a single source. The coefficient for diffusion of tracers was set to 0.1.

Before the tracer initial conditions were applied to the model, the hydrodynamics were spun-up for a period of 5 days, after which the model was run with the tracer for 30 days to ensure a steady state was reached. This 30-day period

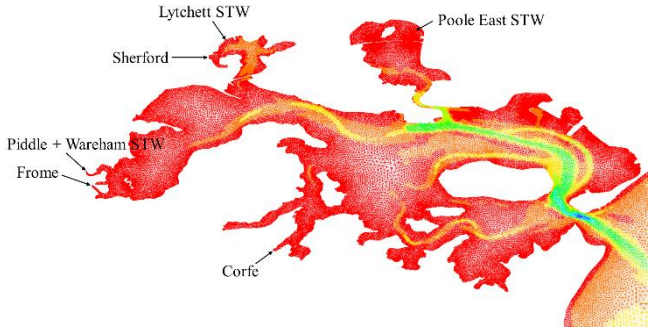

Figure 3. *Nutrient riverine sources and sewage treatment works.*

provided the starting point for a 30-day base case reference. Based on observations provided by the Environment Agency, the initial background concentration of DIN in Poole Harbour and the English Channel was 0.75 mg/l, with 0.94 mg/l applied to Holes Bay.

III. Combined Phytoplankton & Macroalgae Model

A. Model Description

The Combined Phytoplankton and Macroalgae (CPM) model v2.0 is a simple linked box model that can be used to calculate nutrient concentrations and the biomass of phytoplankton and macroalgal communities as a function of nutrient inputs, light climate and physical characteristics of a given water body. The model is best viewed as a tool to aid interpretation of the data and as a means of exploring the factors affecting growth in a given water body – rather than as providing a single predictive 'answer'. In principle, the CPM model uses mechanistic, theory-based, descriptions of the physical and biological processes involved in the growth of seaweeds and planktonic micro-algae. For this paper, the CPM model has been used to assess and provide water quality scenarios for boundary conditions of further Telemac models. The CPM model is a separate model and does not couple with Telemac.

The model algorithms are programmed in the Matlab language but the package is not required for the model to be run by an end user. The CPM model is installed on a Windows PC as an executable file along with a free runtime library that allows the model to be run independently of Matlab. The original CPM model combined two earlier models developed for the Environment Agency (EA): one for phytoplankton, based on the CSTT model [8-11] and one for macro-algae [12,13]. A schematic summary of the main features of the model is shown in Fig. 4.

Several kinds of primary producers are found in estuaries. Micro-algae are found in the water column, as the phytoplankton, and in or on the sea-bed, as the microphytobenthos. Attached larger producers include seaweeds (macro-algae) and aquatic macrophytes (such as seagrasses and salt-marsh plants). The current CPM model simulates phytoplankton and macro-algae. In a given water body, the total biomass of these producers is assumed to be controlled by the least available, or limiting, resource. This

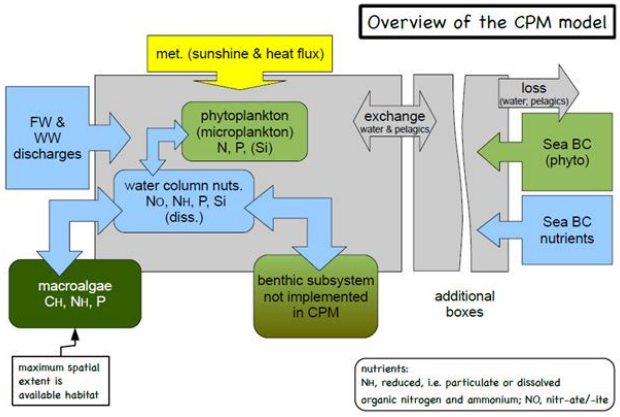

Figure 4. *Overview of the Combined Phytoplankton & Macroalgae (CPM) model.*

can be a nutrient (nitrogen or phosphorous), light or, for macroalgae, available space. If nutrients are controlling biomass then the total biomass of primary producers stops increasing when the rate of nutrient input equals the rate of consumption. The biomass achieved when this occurs is the 'equilibrium' biomass value and is the maximum attainable for a given loading of the limiting nutrient.

Ignoring all complicating factors, this maximum biomass (B) is simply given by:

$$B = q\,S/L \qquad (1)$$

where q is the yield of biomass from unit assimilated nutrient, S (mg/day) is the input rate of the limiting nutrient coming from both direct inputs and coastal waters and L (/day) is the loss rate. For estuarine phytoplankton, L is a combination of the estuary flushing rate and grazing losses; for macroalgae, it is less clear exactly what L relates to but is a general loss term that includes predation and storm-driven removal of fronds.

For the static equilibrium model, predictions are ultimately based on this simple relationship. For the case of light limitation an analogous equilibrium relationship can be derived. The dynamic model solves the underlying equations for the rate of change of phytoplankton and macroalgae biomass without requiring assumptions of equilibrium. As Eq. 1 suggests, the equilibrium prediction can be made with a minimum of information about the water body, whereas the dynamic model requires additional input data reflecting the requirement to simulate a seasonal cycle.

The model allows a water body to be split into an arbitrary number of linked compartments. The division is constrained to be a 'tree' structure, so that each box is linked to a single upstream downstream box (although a given box can have many upstream boxes linking to it). For a multi-box setup, the transports between boxes need to be specified in the form of an average exchange rate in a similar manner to the exchange rate with outside waters.

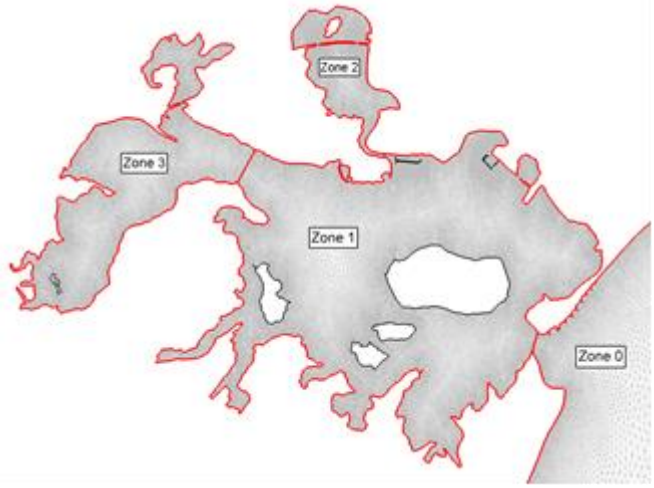

Figure 5. *Delineation of Telemac model domain into CPM box zones*.

B. Calculating flushing rates

To calculate nutrient concentrations and the biomass of phytoplankton and macroalgal communities, the Poole Harbour water body has been split into four distinct zones, as shown in Fig. 5. Zone 1 is Poole Harbour, Zone 2 is Holes Bay, Zone 3 is Upper Wareham and Zone 0 is the English Channel or the 'open sea'.

The methodology as described by [14] been used to calculate the flushing rates between the four zones. Each zone is filled in turn with a uniform value of a non-decaying tracer. A decay curve can then be fitted to the total mass of the tracer in the start zone over the course of the simulation run as it leaves and exchanges with the rest of the model domain. Zone 2 and 3 are filled in isolation to calculate the exchange between Zone 2 to Zone 1 and Zone 3 to Zone 1.

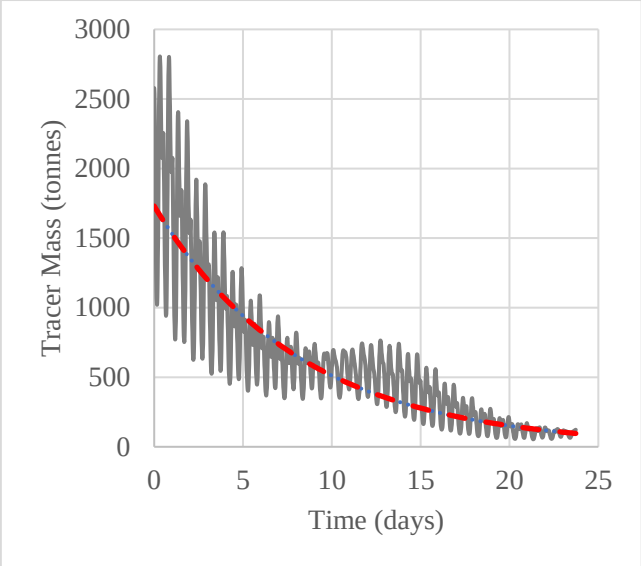

Figure 6. *Decay curve fitted to the total tracer mass in Zone 3, Upper Wareham.*

Whereas, Zone 1, 2 and 3 are filled together to calculate the exchange between Zone 1 and Zone 0.

Fig. 6 shows the decay curve fitted to the total tracer mass calculated in Zone 3, Upper Wareham. Based on the fitted decay curves, the daily net volumetric exchanges between the four zones was:

- Zone 3 to Zone 1 (Upper Wareham to Poole Harbour): 11.47%
- Zone 2 to Zone 1 (Holes Bay to Poole Harbour): 0.55%
- Zone 1 to Zone 0 (Poole Harbour to open sea): 3.48%

C. Water quality scenarios

Based on the calculated exchanges rates five scenarios were developed, using the CPM model, to test the impact of different water quality control measures.

- Case 1 – 1730 tonnes/annum Nitrogen
- Case 2 – No Poole East STW to Holes Bay
- Case 3 – Reduction in average rural STWs
- Case 4 – CMP algal density < 1 kg/m^2
- Case 5 – CPM algal density < 0.5 kg/m^2

Case 1 represents a 20% reduction in the total annual nitrogen, through a reduction from riverine inputs. The inputs from the STWs remain the same as the base case. Historically, Holes Bay is an area of high occurrence of algal growth along with high nutrient loads. As such, Case 2 investigates the impact of removing the STW input into Holes bay. Case 3 investigates the impact of reducing the nutrient inputs from the Wareham and Lytchett STWs. Case 4 and 5 represent the reduction in nutrient inputs from both riverine and STW sources, as calibrated by the CPM model, to achieve the respective algal densities.

The modelling of the water quality scenarios is a two-stage process. The CPM model is used to provide the boundary conditions for nutrient levels which are then modelled using the separate Telemac model. The CPM model assesses the nutrient loads over an annual period to encompass the life cycle of the macroalgae and phytoplankton. Whereas, the Telemac model represents the nutrient distribution over a spring-neap cycle, as detailed in Section II. Fig. 7 shows the mean concentration of DIN over 30-day model period, for the reference base case and the five scenarios.

The concentrations in Poole Harbour are dominated by the combination of the River Piddle and the Wareham STW sources. This is clearly seen in Case 3 which has a lower input concentration, meaning the concentration within Poole Harbour is significantly lower compared to the base case. This is in part due to the large flow rate, as the tracer mass in the model domain is the multiplication of input volume and concentration.

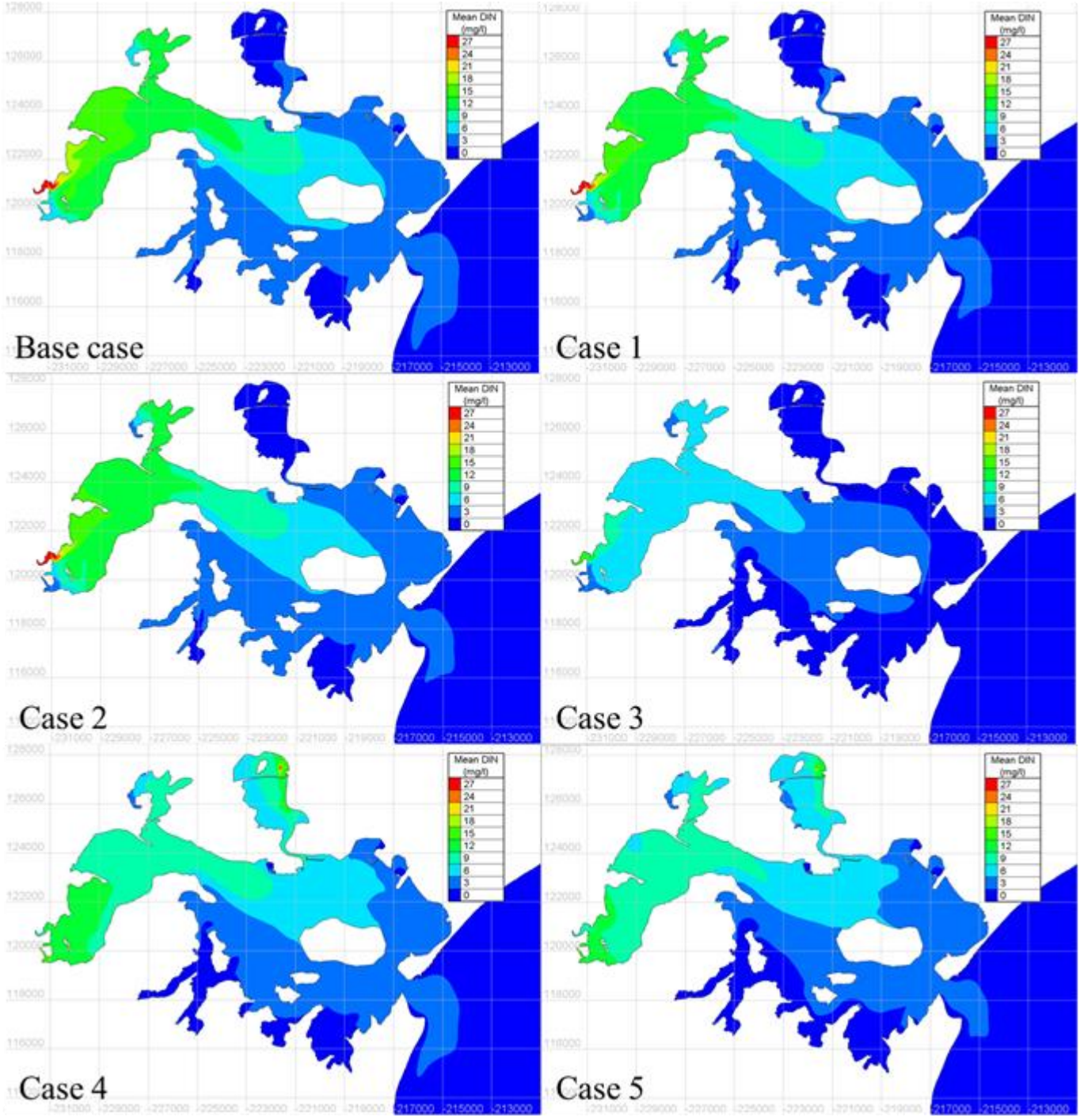

Figure 7. *Mean concentration of DIN (mg/l) over 30-day model period, for the reference base case and the five scenarios.*

Whilst concentrations from the STW are larger, their corresponding input flow rates are much smaller meaning their influence is much smaller. Despite this, one surprising result was the low concentration of DIN in Holes Bay. Field measurements suggest the bay has a high background concentration due to the presence of the STW outfall meaning algae mats are frequently observed. However, the model suggests the influence is much smaller. Due to the very low flushing rate and source input, the high concentrations may be due to historical nutrients stored within the sediment from a previous outfall from a power station, which was decommissioned in 1993. Only in Case 4 and 5 are higher concentrations seen in Holes Bay, due to a higher than current source input.

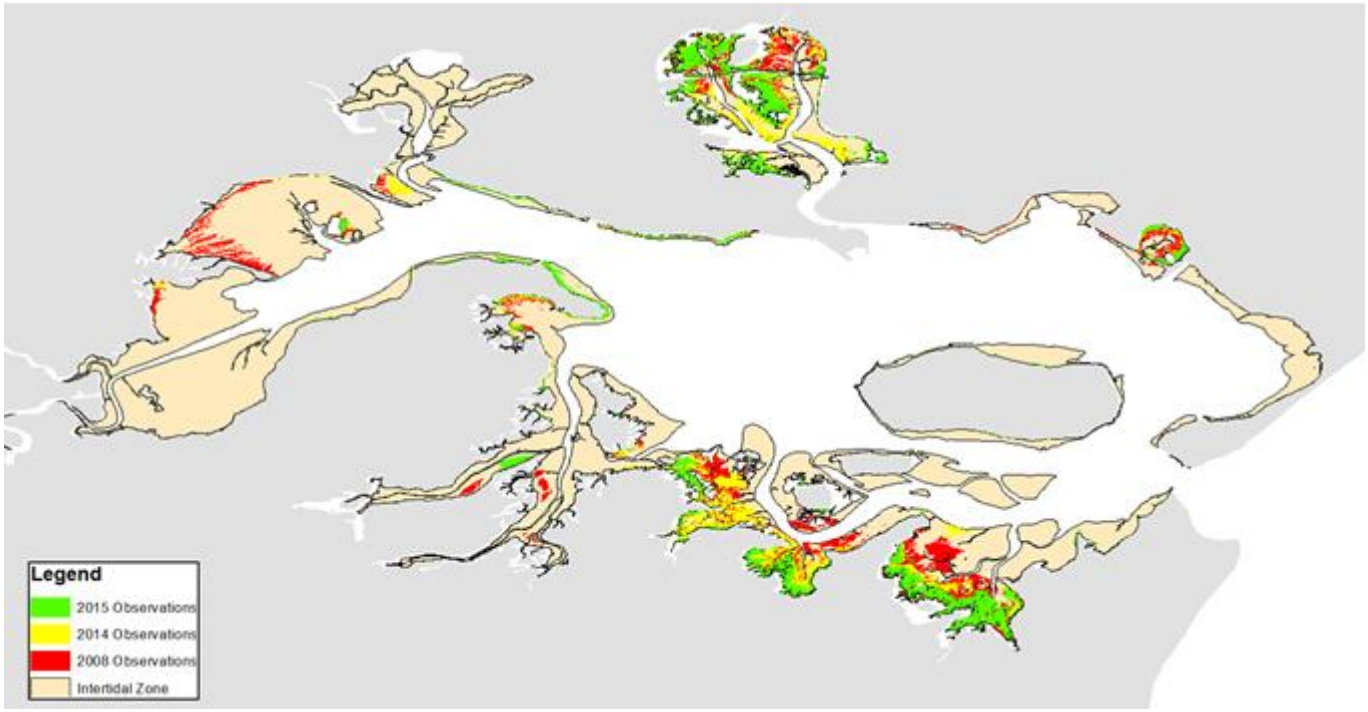

Figure 8. *Spatial distribution of observed macroalgae growth, in 2008, 2014 and 2015.*

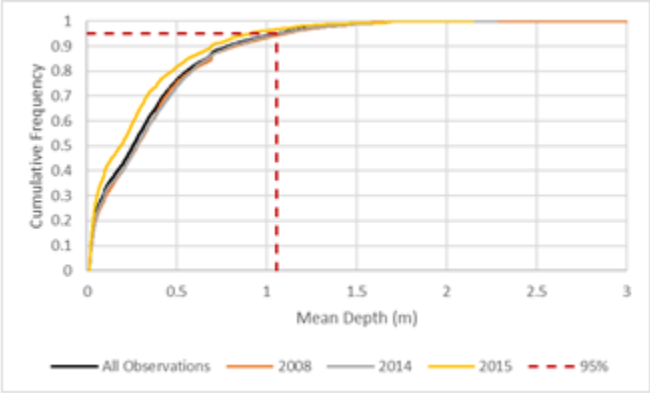

Figure 9. *Cumulative frequency distribution of mean depth at the location of observed macroalgae growth.*

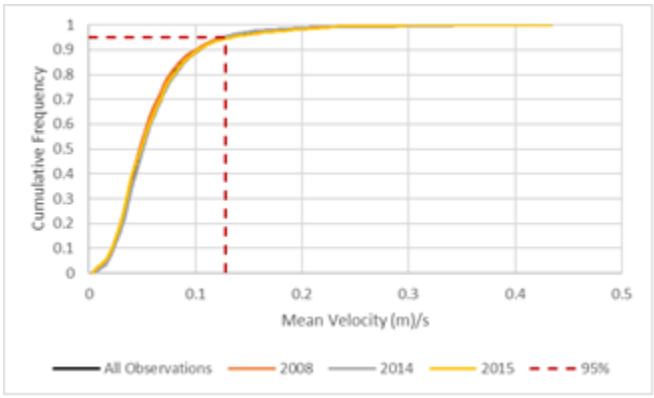

Figure 10. *Cumulative frequency distribution of mean velocity at the location of observed macroalgae growth.*

IV. Spatial Distribution of Macroalgae

A. Initial assessment

Three of the model variables were considered as potential indicators for macroalgae growth: mean water depth, mean velocity and mean winter DIN concentrations. To assess the variables, the model values were extracted from the model base case at the locations of known macroalgae growth. A cumulative distribution of the extracted variables was then plotted. As the nutrient concentrations are highest in the winter, the nutrient levels modelled in the five scenarios and base case represent a winter concentration, as distributed of a spring-neap cycle. Field assessments, mapping the spatial distribution of macroalgae growth within the Poole Harbour water body, were conducted during 2008, 2014 and 2015 and are shown in Fig. 8. The modelled base case represents the winter levels of DIN with the present water management controls before any new control measures have been implemented, meaning the single model should be representative of the spatial distribution of DIN for 2008, 2014 and 2015. However, to assess any potential temporal variation, cumulative distributions were plotted for all the observed locations combined, as well as the individual field campaigns. Results shown in Fig. 9 and 10 shows that mean water depth and velocity are good indicators with 95% of the observations found below 1.05m depth and 0.13m/s velocity. This can visually be seen in the spatial distribution, in Fig. 8, where the macroalgae growth is restricted to the intertidal zone. The use of mean winter DIN concentrations was less clear as an indicator. Whilst 85% of the observations were between

1 and 4.5 mg/l, macroalgae was located in areas with concentrations over four standard deviations from the mean. Similar conclusions were found for a study of macroalgae growth in the Medway Estuary, UK, where bed shear stress was a controlling factor and nutrient supply a limited role [15].

Further work is required to assess potential indicators of macroalgae growth as it is clear there are other controlling factors. Whilst depth and mean velocity were good indicators, it does not explain why then it is not more prevalent in the Upper Wareham region and Lytchett Bay, which has extensive intertidal regions. Factors such as sediment composition, light penetration and grazing should be considered. Furthermore, there may be climatic variables, such as temperature and rain fall, that are indicators. These might explain why there is a 50% reduction in the total area of macroalgae growth from the 2008 and 2015 field observations.

V. Summary & Conclusion

A depth-average hydrodynamic model was developed for Poole Harbour, UK, to test water quality scenarios for reducing nutrient levels. The scenarios were developed from a Combined Macroalgae and Phytoplankton model, tuned by flushing rates calculated from the Telemac model. The hydrodynamic model was a useful tool in providing insight into the dominant sources of nutrients into the water body and most effective solutions for reduction nutrient loads.

Furthermore, the hydrodynamic model was used to identify model outputs could be used as indicators for spatial distribution of macroalgae growth. Mean water depth and velocity were shown to be good indicators. However, mean winter concentrations of nutrients were less important. Further work is required to identify other controlling factors as field observations suggest water depth and velocity are not the only indicators.

Acknowledgements

This work was carried out on the High-Performance Computing Cluster supported by the Research and Specialist Computing Support service at the University of East Anglia.

References

[1] Lewis, L.J. and Kelly, T.C., 2001. A short-term study of the effects of algal mats on the distribution and behavioural ecology of estuarine birds. Bird Study, 48(3), pp.354-360.

[2] Jones, M. and Pinn, E., 2006. The impact of a macroalgal mat on benthic biodiversity in Poole Harbour. Marine pollution bulletin, 53(1), pp.63-71.

[3] Taylor, D., 2015. Review of potential to remove harmful algae and reduce nitrogen load in Poole Harbour. Commissioned by Dorset Local Nature Partnership.

[4] McBreen, F. and Joint Nature Conservation Committee, 2011. UK SeaMap 2010: predictive mapping of seabed habitats in UK waters.

[5] Cox, A.T. and Swail, V.R., 2001. A global wave hindcast over the period 1958-1997- Validation and climate assessment. Journal of Geophysical Research, 106(C2), pp.2313-2329.

[6] Niclasen, B.A. and Simonsen, K., 2007. Validation of the ECMWF analysis wave data for the area around the Faroe Islands. Societas Scientiarum Færoensis.

[7] van Nieuwkoop, J.C., Smith, H.C., Smith, G.H. and Johanning, L., 2013. Wave resource assessment along the Cornish coast (UK) from a 23-year hindcast dataset validated against buoy measurements. Renewable energy, 58, pp.1-14.

[8] CSTT, 1994. Comprehensive studies for the purposes of Article 6 of DIR 91/271 EEC, the Urban Waste Water Treatment Directive. Published for the Comprehensive Studies Task Team of Group Coordinating Sea Disposal Monitoring by the Forth River Purification Board, Edinburgh.

[9] CSTT, 1997. Comprehensive studies for the purposes of Article 6 & 8.5 of DIR 91/271 EEC, the Urban Waste Water Treatment Directive, second edition. Published for the Comprehensive Studies Task Team of Group Coordinating Sea Disposal Monitoring by the Department of the Environment for Northern Ireland, the Environment Agency, the OAERRE page 40 version of July 4, 2002 Scottish Environmental Protection Agency and the Water Services Association, Edinburgh.

[10] Painting, S.J., Devlin, M.J., Parker, E.R., Malcolm, S.J., Mills, C., Mills, D.K. and Winpenny, K, 2003. Establishing Practical Measures for the Assessment of Eutrophication Risks and Impacts in Estuaries: Biological Response to Nutrient Inputs in different estuary types in England and Wales. CEFAS contract for the Environment Agency, Countryside Council for Wales and English Nature.

[11] Painting, S.J. Devlin, M.J. Malcolm, S.J. Parker, E.R., Mills, D.K., Mills, C., Tett, P., Wither, A., Burt, J., Jones, R. and Winpenny, K., 2007. Assessing the impact of nutrient enrichment in estuaries: susceptibility to eutrophication. Marine Pollution Bulletin, 55(1-6): 74-90.

[12] Cefas, 2003. Investigation of Factors Controlling the Presence of Macroalgae in some Estuaries of South East England. Cefas contract C1642 contract for the Environment Agency.

[13] Aldridge, J.N., Trimmer, M., 2009. Modelling the distribution and growth of 'problem' green seaweed in the Medway Estuary, UK. Hydrobiologia. 629: 107-122.

[14] Hartnett, M., Dabrowski, T. and Olbert, A.I., 2011. A new formula to calculate residence times of tidal waterbodies. Water Management, 164, pp.243-256.

[15] Aldridge, J.N. and Trimmer, M., 2009. Modelling the distribution and growth of 'problem'green seaweed in the Medway estuary, UK. Hydrobiologia, 629(1), pp.107-122

Oil spill modelling: A case study in the Gulf of Guinea

Anne Levasseur, Olivier Bertrand
Numerical Hydraulics Unit
ARTELIA Eau et Environnement
Echirolles, France
Anne.LEVASSEUR@arteliagroup.com

Philippe Reveau
Risk, Society and Environment Unit
ARTELIA Eau et Environnement
Lyon, France

***Abstract*— As part of Environmental Impact Assessments (EIAs), accidental oil spills are modelled to identify potential impacts on the marine environment. These applications require first to construct and calibrate a hydrodynamic model using metocean data, and then to define the scenario of the oil spill (type of release, volume, oil type, physical properties of the oil). A case study off the Gabonese coast is presented. It includes two cases of predefined risk: a vessel collision and a subsurface blowout during offshore drilling. Results are analysed by means of oil slick trajectories, maps of nearshore area impacted and mass evaporated.**

I. INTRODUCTION

The project under assessment is the drilling of one exploration well. The main purpose of the well is to confirm the presence of hydrocarbon reservoirs, previously identified during a seismic acquisition campaign. Drilling operations are done using an ultra-deepwater dynamically positioned drillship. The drilling block is located in the Gabon Sea. The oil spill module included in the TELEMAC-MASCARET suite is used to simulate the impact of an accidental vessel collision and a subsurface blowout. It represents the oil slick, its transport by currents and wind, its spreading, and its evaporation. Firstly, the construction and calibration of the hydrodynamic model are described. Then the characteristics of the oil spill model and its results are presented.

II. HYDRODYNAMIC MODEL

A. Model Grid and Bathymetry

The horizontal model grid is composed of 2078 grid nodes and 4011 triangles (Fig. 1). Model grid size ranges from 20km offshore to 7km along the coast. The model covers a rectangular domain parallel to the Gabonese coast, south of Cap Lopez. It is approximately 550km long and 300km large. Two datasets are used for the bathymetry:

- General Bathymetric Chart of the Oceans (GEBCO): used in area deeper than 200 meters;
- Data from marine charts: used in area shallower than 200m.

Model geographical coordinates are in UTM 32S. Vertical coordinates are relative to Mean Sea Level (MSL).

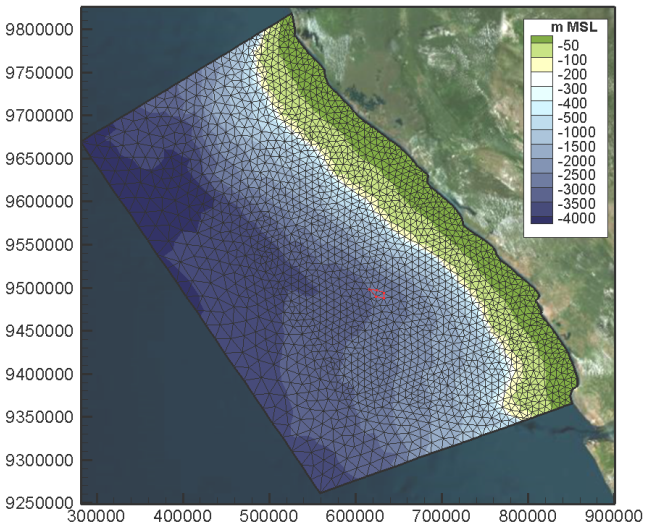

Figure 1. *Model grid and bathymetry, location of the project in red*

B. Forcing data

The regional model presented above is forced at its boundaries with inputs from the following available datasets:

- Wind datasets from the French Research Institute for Exploitation of the Sea (IFREMER) and available from the Copernicus marine environment monitoring services [1]. The IFREMER Global Blended Mean Wind Fields include wind components (meridional and zonal), wind module, and wind stress. The associated error estimates are also provided. They are estimated from the Advanced SCATterometers (ASCAT) and Oceansat-2 scatterometer (OSCAT) retrievals, and from the European Centre for Medium Range Weather Forecasts (ECMWF) operational wind analysis with a horizontal resolution of 0.25x0.25 degrees, and available at synoptic time 00:00; 06:00; 12:00; 18:00 since 1 January 2013.
- Results from a numerical model of the global ocean, namely products PSY4V2R1 with a resolution of 1/12° degree [2], from the Copernicus marine environment monitoring

services. The 50-level vertical discretization retained for this system has a resolution of 1 m at the surface, decreasing to 450 m at the bottom. It includes 22 levels within the upper 100 m. This product makes use of data assimilation of Sea Surface Temperature (SST), sea level and in situ temperature and salinity profile. This product includes daily mean files of temperature, salinity, currents, sea level, mixed layer depth and ice parameters from the top to the bottom over the global ocean.

- Tidal elevations from the FES2012 atlas [3]. FES2012 is based on the resolution of the tidal barotropic equations in a spectral configuration using T-UGO model, developed by the French research laboratory LEGOS, in collaboration with the companies NOVELTIS and CLS. The numerical solution is improved by assimilating long-term altimetry data (Topex/Poseidon, Jason-1, Jason-2, ERS-1, ERS-2 and ENVISAT) through an improved assimilation method. FES2012 provides 32 tidal constituents distributed on a grid with a resolution of 1/16°.

C. Model setup and configuration

The hydrodynamic model accounts for variations of the sea surface elevation due to the astronomical tides, and variations of horizontal and vertical seawater velocities. The water column is divided in 30 vertical levels. Among them, 6 levels are fixed at a constant depth: -1m, -5m, -10m, -140m, -500m, and -800m. Other vertical levels are distributed uniformly at equal distance between these fixed vertical levels.

Spatial fields of temperature and salinity are prescribed in the model using results of the large-scale model PSY4V2R1. Temporal variations of temperature and salinity are not modelled, to reduce computational time and under the approximation that they are negligible over monthly timescale.

The model is forced on the lateral boundary by the zonal and meridional components of the daily velocity from PSY4V2R1, varying in time and space, and the predicted sea surface elevation from FES2012, using the methodology developed by ARTELIA [4].

The horizontal velocity field at the surface is constantly adjusted to fit the outputs from the global model PSY4V2R1. PSY4V2R1 provides accurate and robust oceanic parameters as it uses data assimilation and state-of-the-art numerical methods. This method ensures to get a realistic surface velocity field in TELEMAC-3D, representative of seasonal trends at the regional scale, and representative of the coastal circulation.

At the surface, the momentum flux induced by wind at the sea surface is accounted for. The Gabon Sea is under the influence of the trade winds, relatively constant in direction and of small intensity throughout the year. Wind statistics on the drilling site show a constant wind field directed towards the Gabonese coast (westerly wind) with intensity mostly from 3 to 6 m/s.

D. Calibration and validation

A simulation is made, starting with initial conditions (temperature, salinity and horizontal velocity) from 30 September 2015.

The tidal elevation at Pointe-Noire is compared with the tidal prediction from SHOM (Service Hydrographique et Océanographique de la Marine, which is the French National Hydrographic Service). The results show the capacity of the model to represent the amplitude and phase of the tide at Pointe-Noire, which vary in amplitude from 1m to 1.8 m between spring tide and neap tide (Fig. 2). The model shows a discrepancy of less than 10cm on the amplitude at spring tide, and less than 2 cm on the amplitude at neap tide.

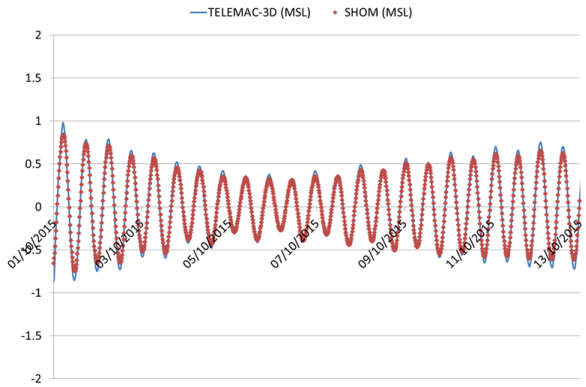

Figure 2. *Comparaison of the modeled tide and the SHOM tidal prediction at Pointe-Noire.*

Results of the horizontal velocity at several depths are analysed and compared with the velocity field from PSY4V2R1 on 13 October 2015 12:00.

At the surface and subsurface (Fig. 3), TELEMAC-3D represents the differences of the ocean circulation between the shelf and the area offshore (depth over -500m): a current flows northward along the coastline, with velocity up to 0.6 m/s. Offshore conditions are characterised by slower motion of the water masses, with velocity less than 0.4 m/s. Ocean currents direction varies but shows a flow entering at the North-western boundaries, flowing broadly to the South-East direction before exiting the model through the southern boundary. Flow pattern and direction are in agreement with PSY4V2R1 flow velocity. TELEMAC-3D shows a slight underestimation of the peak flow in two areas: along the coast from the southern boundary of the model domain to Nyanga, and offshore at the location X=650000m Y=9400000m. This difference is less than 0.1m/s on the velocity magnitude.

At the depth of -140 m and -500 m (not shown), velocity magnitude is low, around 0.2 m/s, and reaches at maximum 0.4m/s, in both TELEMAC-3D and PSY4V2R1. Flow directions at this level of intensity are highly variables and show some discrepancies between TELEMAC-3D and PSY4V2R1.

In summary, the methodology used in the regional TELEMAC-3D model provides a realistic representation of the water mass flow, similar to what is provided from outputs of a database of the circulation in the southern Atlantic Ocean. More specifically, the variation of currents intensity between the various depths, and spatial variations of the surface current and direction are in agreement in both models.

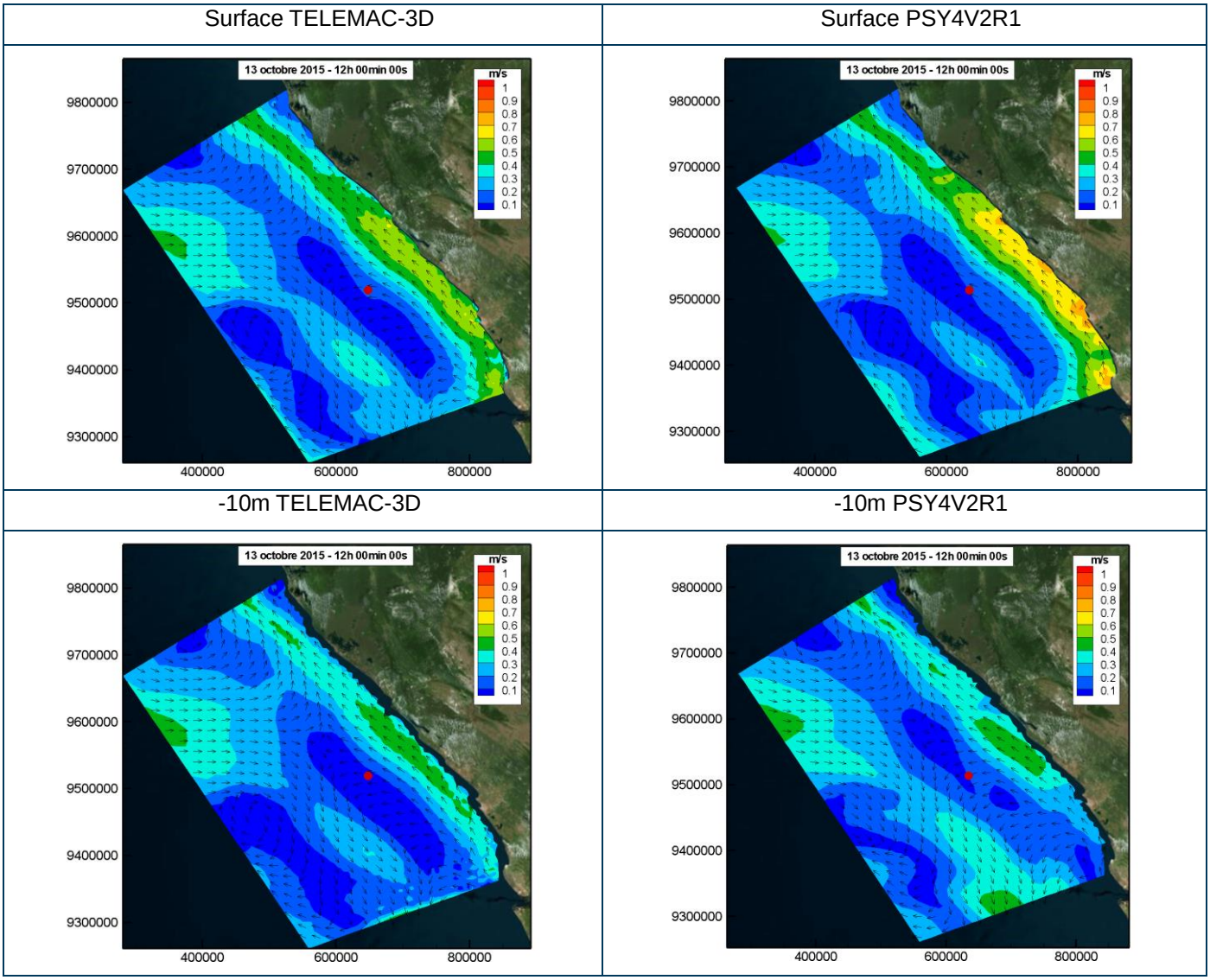

Figure 3. *Comparison of the velocity field 13 days after the beginning of the simulation between PSY4V2R1 and the regional model based on TELEMAC oil spill model for the surface and the depth of -10m.*

III. ACCIDENTAL SPILL DUE TO A VESSEL COLLISION

A. Input data

Simulation of the vessel collision is done with the following hypothesis (Tab. 1):

- Instantaneous release of the content of the vessel;
- Volume based on the vessel capacity;
- Location of the accident: drilling location ;
- Content of the discharge: 100% of marine diesel fuel oil;
- Release of 7500 m^3.

Parameter	***Value***	***Unit***	***Assumption***
Volume	4769	m^3	-
Duration	instantaneous	-	-
Release depth	0	m	surface
Percentage of oil	100	%	-
Oil density	981	kg/m^3	Marine intermediate fuel oil
Oil viscosity	25	mm^2/s	Marine intermediate fuel oil

TABLE 1. SUMMARY TABLE OF INPUT DATA FOR THE VESSEL COLLISION

B. *Methodology*

Oil discharged is assumed to be composed with only unsoluble components, as information on HAP compounds in the oil are not available. The oil slick generated by the accident is represented as particles drifting at the surface. 625 particles are released from 1October 2015 onwards (1st case) and from 26th December 2015 onwards (2nd case). The 2nd case shows more variations in the direction of the currents compared with the 1st case. It also includes a significant unfavourable period of time (from 10 to 15 January 2015) when surface currents are orientated towards the coast.

Oil beaching on the shoreline is not activated as the model aims at modelling the oil slick at large scale, and oil beaching would require detailed bathymetric features along the shore. Therefore, each particle is subject to drifting, spreading, advection, and evaporation. In the numerical model, the oil is considered as a sum of 12 petroleum pseudo-components, each characterised by a boiling temperature and fraction. The pseudo-components have been calculated from the distillation curve of the marine intermediate fuel oil, available from the ADIOS-2 software library. The law of Stiver and Mackay [5] is used for evaporation of each component of the petroleum. The water temperature used for the evaporation law is constant and set to 25°C. The determination of the spreading area is calculated from the Migr'hycar model [6].

C. *Results*

Results are analysed using maps of particles distribution over the whole domain. The percentage of initial mass remaining in each particles is displayed, indicating the percentage of oil evaporated (percentage of oil evaporated=100-percentage of initial mass).

In the first case (Fig. 4 and Fig. 5), the oil slick travels south-eastwards from 1st to 8th October. 7 days after the release, oil particles are distributed off Pointe Noire, and remains off the -50m isobath. The evaporated mass represents only 10% of the initial mass. Particles start to leave the modelled domain 7 days after the vessel collision.

In the second case (Fig. 6 to 10), the oil slick travels eastwards, in the direction of the coast. 7 days after the release, oil particles reach the -50m isobath. Then in a second phase, the oil particles travel southwards, at short distance from the coastline, until they reach Pointe-Noire 14 days after the release. 12 days after the vessel collision, the coastline is impacted between Mayumba and Pointe-Noire. The evaporated mass represents only 10% of the initial mass, as in the1st case.

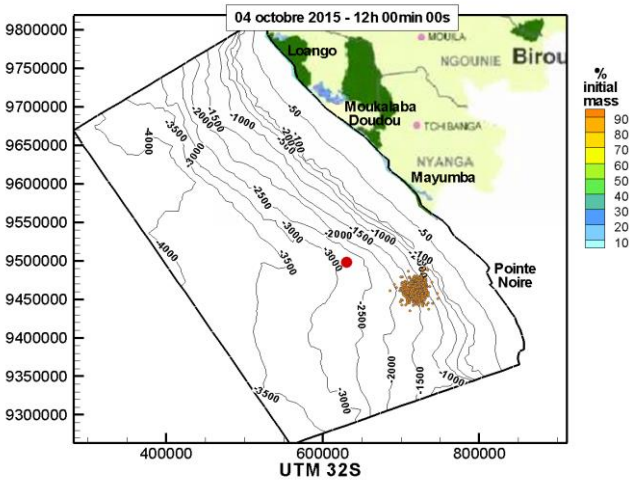

Figure 4. *Oil Slick 3 days after the vessel collision (1st case)*

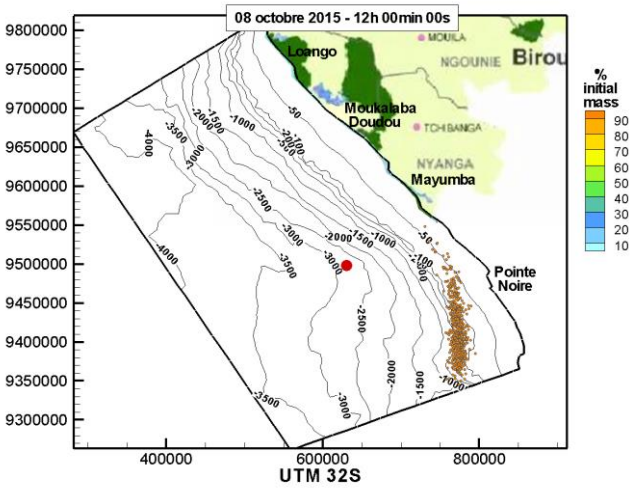

Figure 5. *Oil slick 7 days after the vessel collision (1st case)*

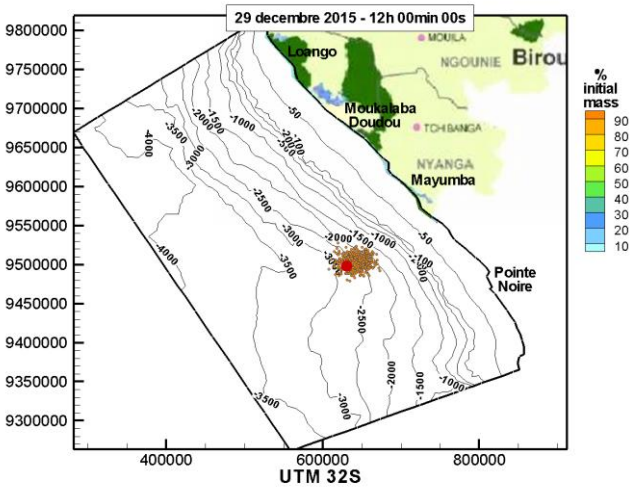

Figure 6. *Oil Slick 3 days after the vessel collision (2nd case)*

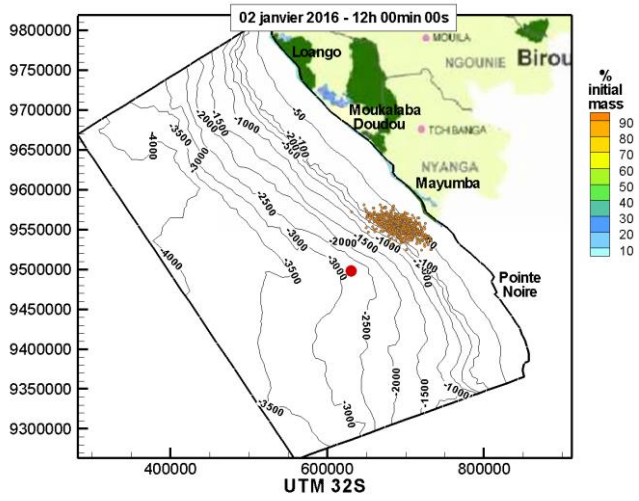

Figure 8. *Oil Slick 7 days after the vessel collision (2nd case)*

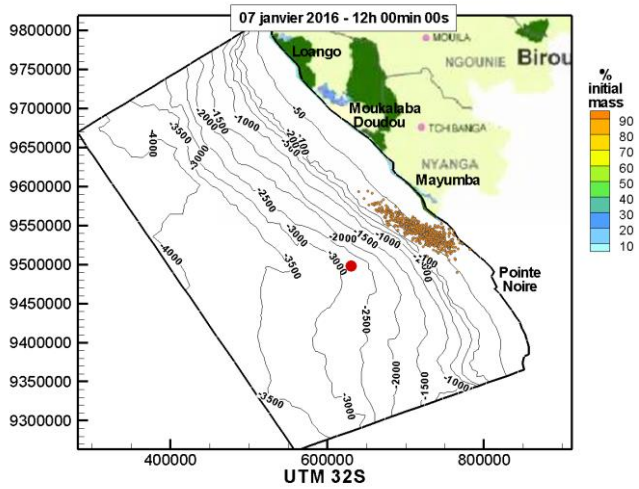

Figure 9. *Oil Slick 12 days after the vessel collision (2nd case)*

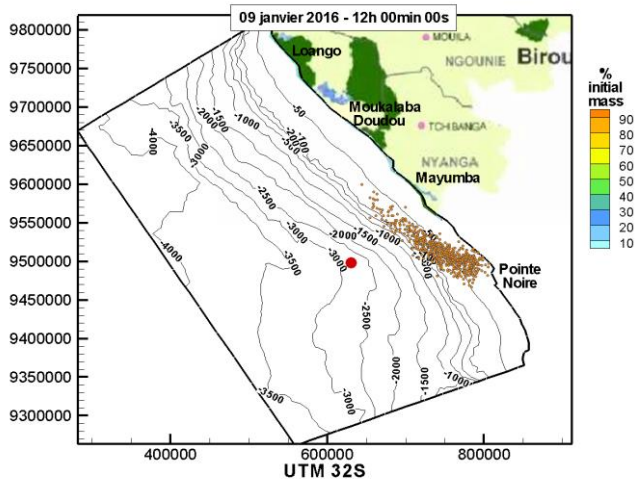

Figure 10. *Oil Slick 14 days after the vessel collision (2nd case)*

IV. ACCIDENTAL SPILL DUE TO A SURFACE BLOWOUT

A. *Input data*

Simulation of the surface blowout is done with the following hypothesis (Tab. 2):

- Location of the accident: drilling location;
- Content of the discharge: 100% of light crude oil type Lucina marine;
- Release of 4769 m^3 during 21 days.

parameter	***Value***	***Unit***	***Assumption***
volume	4769	m^3	-
duration	21	days	-
Release depth	0	m	Surface
Percentage of oil	100	%	-
Oil density	848	kg/m^3	Lucina marine
Oil viscosity	16	mm2/s	Lucina marine

TABLE 2. SUMMARY TABLE OF INPUTS DATA FOR THE SURFACE BLOWOUT

B. *Methodology*

The period from 26 December 2015 to 15 January 2015 has been selected for the simulation (2nd case in previous section), as it shows more variations in the direction of the currents compared with other period of time. Oil discharged is assumed to be composed with only unsoluble component in the oil slick, as information on HAP compounds in the oil are not available. The oil slick generated by the accident is represented as particles drifting at the surface. 21 Particles are released every 24 hours during 21 days from the 26 December onwards, to mimic the constant release of oil at the surface during 21 days. The processes modelled are identical to the vessel collision simulation (i.e. paragraph III B).

C. *Results*

The evolution of the particle distribution with time is mapped on Fig. 11 to 14. During the first phase of the surface blowout, which lasts approximately 10 days, oil particles tend to drift in the North-East direction, towards the coastline. The results show that the oil slick reaches the isobath -50m 7 days after the beginning of the surface blowout.

In a second phase, the oil slick drifts towards the South-East along the coast, under the influence of the coastal currents. The oil slick tends to expands with oil particles covering a larger surface. The monitoring of the oil particles modelled stops at day 22, when particles leave the model domain. Oil is likely to be deposited on the coast from the south of Mayumba to the Congo River.

The oil tends to evaporate more rapidly at the beginning, during the first days in the seawater. Then the percentage of evaporation stabilises around 60% of the initial mass discharged at the drilling site, which means that 40% is evaporated 22 days after the beginning of the surface blowout.

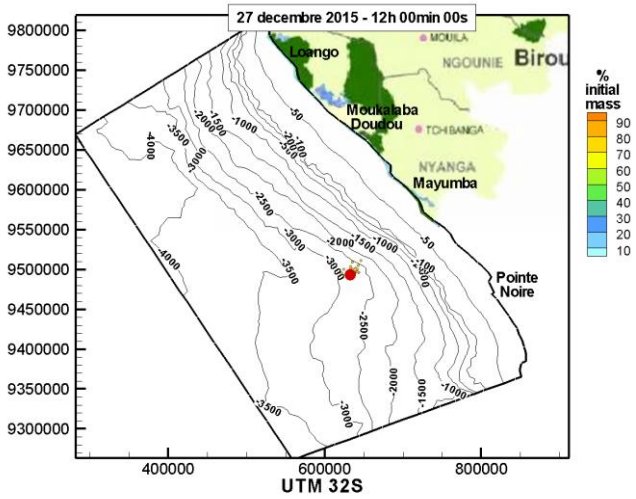

Figure 11. *Oil Slick 24 hours after the surface blowout*

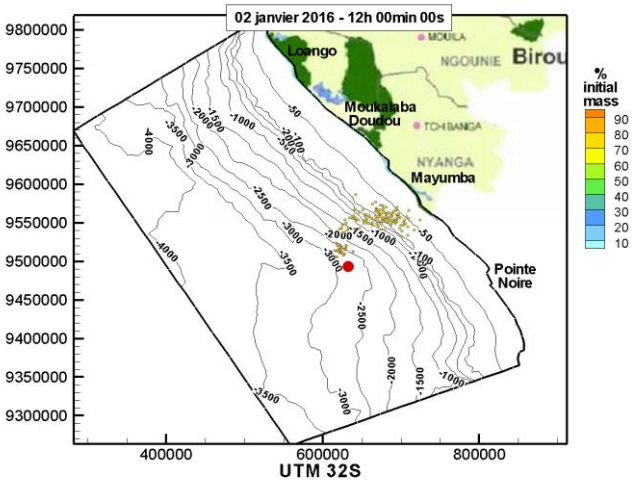

Figure 12. *Oil Slick 7 days after the surface blowout*

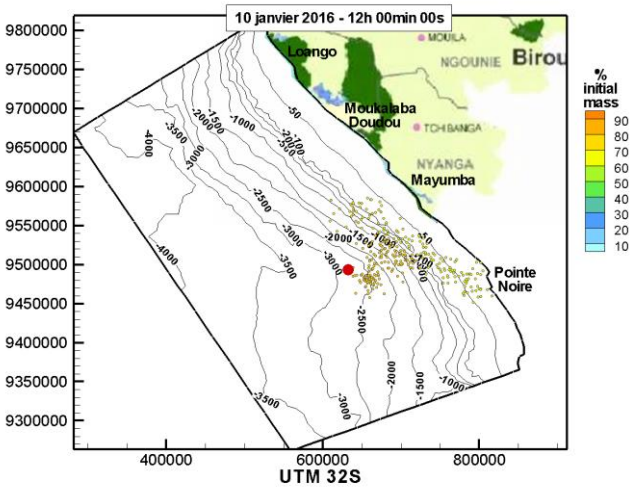

Figure 13. *Oil slick 15 days after the surface blowout*

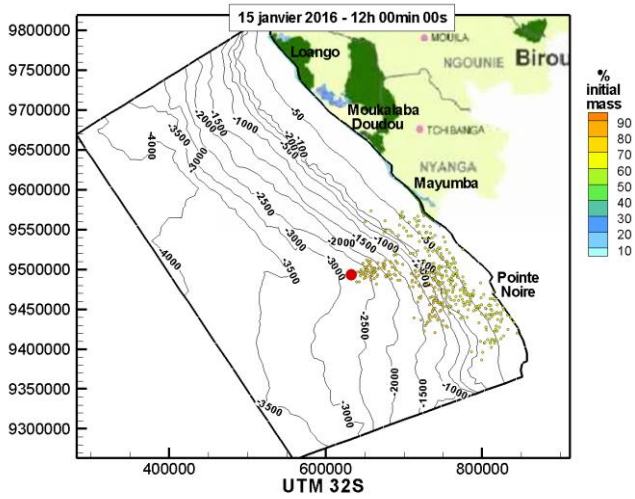

Figure 14: *Oil slick 20 days after the surface blowout*

V. CONCLUSION

A numerical model of the Gabon Sea has been constructed, based on the TELEMAC-MASCARET suite. It covers the coastline from the Congo River mouth at the South to Cap Lopez at the North. Its offshore boundary is situated approximately at a distance of 320 km from the coast. The model is able to reproduce the ocean current. A stratification representative of the period of time simulated is accounted for. The main forcings are the river Congo, the tide and the wind, and the currents in the Gulf of Guinea extracted from the outputs of a global ocean model.

The oil spill module included in the TELEMAC-MASCARET suite is used to simulate the oil slick generated by a vessel collision and a subsurface blowout. It represents the oil slick, its transport by currents and wind, oil spreading, and oil evaporation. Two types of oil are selected: Lucina marine for the subsurface blowout and marine diesel fuel oil in the case of the vessel collision. Results show the displacement of the oil slick depending on the meteocean conditions prevailing during the scenario. The oil slick migrates towards the coast under the influence of the westerly trade winds. Evaporation is higher in the case of the surface blowout. This difference is due to the hydrocarbon released: the density and viscosity of the oil are lower than the marine diesel fuel oil.

REFERENCES

[1] A. Bentamy "Product User Manual for Wind product WIND_GLO_WIND_L4_NRT_OBSERVATIONS_012_004" Issue 1.2 , Copernicus Environment Monitoring Service, 2016. Ref:CMEMS-OSI-PUM-012-004

[2] L. Nouel "Product User Manual for the GLOBAL Ocean Sea Physical Analysis and Forecasting Products GLOBAL_ANALYSIS_FORECAST_PHY_001_024". version 2.0, Copernicus Environment Monitoring Service, 2016, Ref:CMEMS-GLO-PUM-001-024.

[3] L. Carrere, F. Lyard, M. Cantet, A. Guillot., L. Roblou. "FES2012: A new global tidal model taking advantage of nearly 20 years of altimetry" proceedings of meeting "20 years of Altimetry",Venice 2012.

[4] A. Rebai, F. Gandilhon, A. Levasseur, D. Le Bris, O. Bertrand, "Study of ocean circulation by coupling with global ocean model".

Proceedings of the XXIIIrd TELEMAC-MASCARET user conference, 11-13 October 2016, Paris, France.

[5] C. Stiver, D. Mackay, “Evaporation rate of spills of hydrocarbons and petroleum mixtures”. Environmental science and technology, 18(11):834-840,1984.

[6] C. Goeury, J.-M. Hervouet, I. Baudin-Bizen, F. Thouvenel. “A lagrangian/eulerian oil spill model for continental waters” Journal of Hydraulic Research, 52:1,pp 36–48, 2014.

The Rance Tidal Power Plant Model

Christophe Cochet, Malo Lambert
Hydro Engineering Centre, EDF
Le-Bourget-du-Lac, FRANCE
christophe.cochet@edf.fr

***Abstract*— La Rance tidal power plant (in North Brittany, France) has been operating since 1966 and the plant operations can influence the hydrodynamics of the tidal flow (water levels, current velocities), in the estuary as well as on the downstream (sea) side of the plant: flow rates can evolve quickly and reach up to 15 000m^3/s, leading to velocities higher than 5m/s.**

To better understand the hydrodynamics linked to the plant operations, a TELEMAC model of the area (estuary + local coastline) was developed: the plant operations are closely represented with a specific subroutine used to call input data from the plant industrial optimization software and to impose flow rate conditions up- and down-stream of the plant; local ADCP measurements were used for calibration.

Several scenarios, based on real operational conditions, were tested and analysed with regards to a list of safety aspects (impact on boats, swimmers/divers, fishermen, or flood risks) and criteria based on water levels and velocities (maximum value, temporal and spatial gradients). The scenarios to be presented are:

- **Study of current velocities upstream and downstream of the plant when filling and emptying the estuary, and evaluation of the risk for drifting boats;**
- **Study of water levels in case of rapid variations of flow rate when stopping the plant, and evaluation of the propagating surge impact.**

The workflow includes the use of Blue Kenue for setting up the model, of Matlab for post-processing result files and of Qgis for generating maps and visualising results.

I. INTRODUCTION

La Rance Tidal Power Plant (TPP) is located on the Emerald Coast in North-East Brittany, where tide ranges can reach 13.5 meters. Forming a road bridge between Saint-Malo and Dinard since 1966, the plant has an installed capacity of 240MW and generates around 500GWh annually. At every tide cycle, the estuary (20km long, 180Mm^3 in volume) is filled and emptied, with the circulation of around 100 Mm^3 of water. Flow rates can reach up to 15 000m^3/s, and velocities exceed 5m/s. As the estuary is shared by many users, it is important for EDF, operator of the plant, to guarantee the safety of all users, by either adapting the plant operations or by informing the public of dangerous zones or periods of operation.

After 50 years of operation, the plant is undergoing a major refurbishment program, which includes the renovation of the complete automatic control system running the plant 24 hours per day, and 7 days a week, along with the tides. This renovation has led to the update of operating phases and transitions between phases.

In order to better understand the hydrodynamic behaviour of the estuary and guarantee the safety of all users, a TELEMAC-2D model was developed, calibrated, and used to test different operation scenarios.

The present article will describe how the plant was modelled and how the tested scenarios lead to better knowledge of the local hydrodynamics.

II. INPUT DATA AND MODEL CONSTRUCTION

Bathymetric data and mesh construction

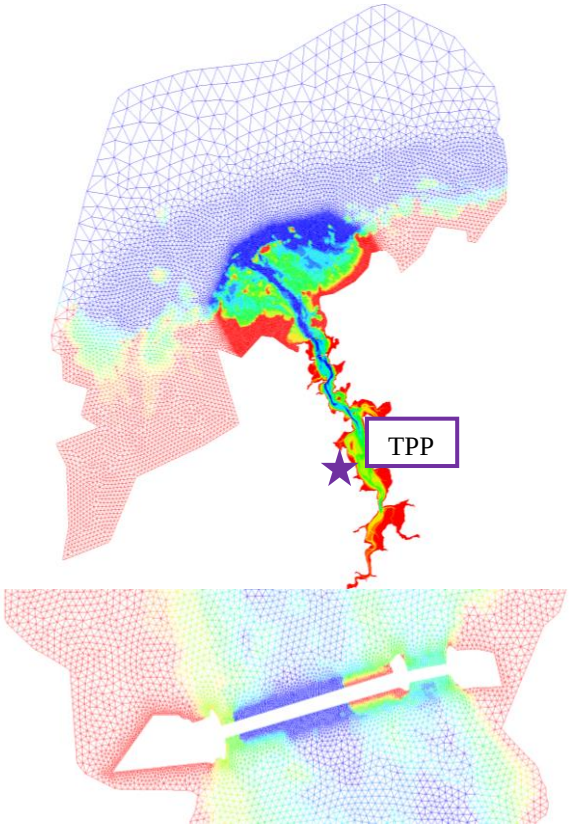

Figure 1. *Representation of the model meshed bathymetry and close-up view of the TPP*

The bathymetric data used to build the mesh was obtained by a Lidar campaign run in 2011. The mesh has been built using BlueKenue (2D interpolator tool with linear interpolation). The grid size is chosen to be 5 meters in "strategic" areas (near the plant and in the upper (i.e. narrower) part of the estuary) and 20 meters in the rest of the estuary. The mesh grid becomes larger when heading out towards the sea boundary. This leads to a mesh with 201 075 nodes and 393 065 elements (Fig. 1).

Tide data

As sea boundary condition, we use standard TPXO tide conditions (*(u,v)* velocity components and the water level) from the 2008 European Shelf database, and the corresponding TELEMAC module.

Boundary conditions

The data given on the sea side are the velocity components and the water level so the boundary is of the 5-6-6 type.

The river Rance entering the estuary at Ecluse du Chatelier is modelled with a constant flow rate (boundary 4-5-5). NB: As the flow rate from the river is small in comparison with the flow rate through the plant, a constant value was considered an acceptable assumption.

The plant is modelled as an island in the mesh and its equipment (24 bulb-unit turbines and 6 sluice gates) is represented as weirs (calling modified subroutines LECSNG and CLSING – see §0).

The code was developed using version 6.3 and small adaptations had to be made to the TPXO module in order to make it compatible with the use of weirs. Version 7.1 should have solved this issue although no test was performed.

Workflow

Any required pre-processing (bathymetry correction, plant input data preparation…) is completed using Matlab (MathWorks, R2016b). BlueKenue (CHC) is used for the mesh and boundary files construction. Post-processing of result files is achieved with Matlab scripts before importation and visualisation under Qgis (using Artelia's PostTelemac Qgis plugin).

Model calibration

ADCP recordings – data from 3 ADCP located close to the plant - were used to calibrate the Strickler coefficient, assumed constant on the domain. The model error (RMSE) obtained was considered satisfying, with values below 10cm for the water levels in the basin and below 20cm/s for the velocities (see Fig. 2 and Tab. 1).

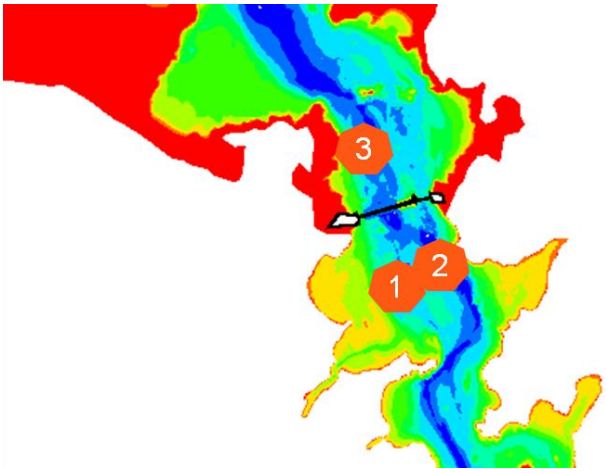

Figure 2. *Location of the 3 ADCP used for the model calibration.*

RMSE	ADCP 1	ADCP 2	ADCP 3
Water level	0.07 m	0.07 m	0.19 m
Current velocity	0.11 m/s	0.17 m/s	0.18 m/s

TABLE 1. ESTIMATED ROOT MEAN SQUARE ERROR ON WATER LEVELS AND CURRENT VELOCITIES BETWEEN MODEL AND ADCP MEASUREMENTS

III. TECHNICAL ASPECTS FOR MODELLING THE TPP AND ITS SURROUNDINGS.

Plant operations and control

La Rance tidal power plant usually generates electricity when the basin is emptying (although the turbines can also be operated in "reverse"mode); when filling the basin, the turbines are open but not active and the sluice gates are open; once the basin level has reached the sea level, the turbines operate in pump mode to continue filling the basin. This operating mode – pumping at low head – is very efficient as the water pumped will be released later at a much higher head, thus generating much more power.

For the turbines, there are in total 5 operating modes:

- Direct turbining (generating power with flow from basin to sea),
- Reverse turbining (generating power with flow from sea to basin),
- Direct pumping (consuming power with flow from sea to basin),
- Direct orifice mode (powerless with flow from basin to sea),
- Reverse orifice mode (powerless with flow from sea to basin).

For the first 3 modes, the flow rate through the turbine is determined by interpolation using the turbines hill chart, the head between basin and sea and the blade incidence, which is computed by the optimisation algorithm and recorded in the predicted operation program (input of LECSNG routine, see hereafter). For the 2 powerless modes, the flow rate is computed using an analytical formula of the form given in (1), where Q is the flow rate, C a discharge coefficient and h_{Basin} and h_{Sea} the water levels.

$$Q = C\,(h_{Basin} - h_{Sea})^{1/2}. \quad (1)$$

For the sluice gates, the flow rate is controlled by the water levels of the basin and the sea for both flow directions, as well as the downstream water level (sea or basin depending on flow direction); (2) is an example for a flow from sea to basin, where *A* and *B* are discharge coefficients.

$$Q = (A.\,h_{Basin}^{1/4} - B).(h_{Basin} - h_{Sea})^{1/2}. \quad (2)$$

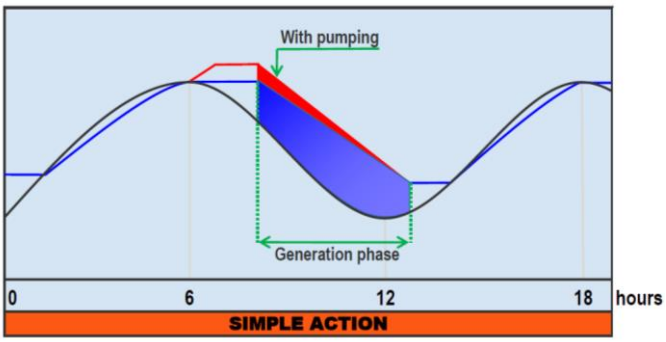

Figure 3. *Graphical representation of the water levels (sea in black, basin in blue) during a standard operating cycle*

Modelling of plant

LECSNG is a subroutine read only once during the calculation. The subroutine is used to define physically the characteristics of the weirs. In our case, the weirs describe, on one side, the 24 bulb units and, on the other side, the 6 sluice gates. We use a specific input file to define the associated boundary nodes as well as control nodes (i.e. nodes from which the water levels (estuary and sea) are read for the plant control) and some operation parameters (units starting/stopping phase duration, gates opening sequences,…). Also integrated in this subroutine are the turbine performance hill charts (output power and blade incidence as a function of head and flow rate).

A second input file read by LECSNG is the plant operation program, as generated by the optimizing software (based on a 0-D hydraulic model) which is the input data for the plant automated controls system. This file is generated each week depending on predicted tide conditions and plant configuration (number of available units and sluice gates). It gives the operating modes, the number of bulbs and gates available for the operations and the planned water levels.

Using this program file as input allows a very realistic representation of the plant operations.

CLSING uses the data previously loaded by LECSNG in order to simulate the water transfers between the two sides of the weir (turbines and sluice gates). The turbines flow rate is computed using the real turbine hill charts while the sluice gates flow rate is computed based on water levels using an analytical formula (see (2)).

At every time step (30 seconds in the model), the water levels computed by TELEMAC are compared to the predicted water levels (from the 0-D optimizing software) and the instructions are updated to achieve optimal control of the plant. Depending on the activated mode, the direction, the rate of the flow and the number of units or gates may vary. All these particularities are controlled by CLSING and may change at every time step

The implemented control system allows to test and adjust multiple parameters, including opening sequences of sluice gates or bulb units, in order to control the impact of these parameters on the flow gradient and flow velocities. For example, the gates opening sequence is defined by a 6-element vector indicating time offsets for opening each of the 6 sluice gates. Associated to this vector are the detection of the gates status (closed/opening/open/closing) and the adjustment of the gates flow rate depending on the opening ratio of each gate.

The routines have been coded so that they remain compatible with the parallel computing capabilities offered by TELEMAC-2D.

In particular, the flow rate through the turbines and sluice gates is a function of water levels measured at points located a few hundred meters upstream and downstream of the plant; thus, when the mesh is split into several sub-domains, these nodes may be separated from the plant itself. The solution was to use TELEMAC native functions "*global_to_local_point*", "*P_DMAX(X)" and "P_DMIN(X)*".

Fig. 4 shows the computation time for a one-week simulation, as a function of the number of processors used: asymptotically, 15 minutes are required to simulate one week.

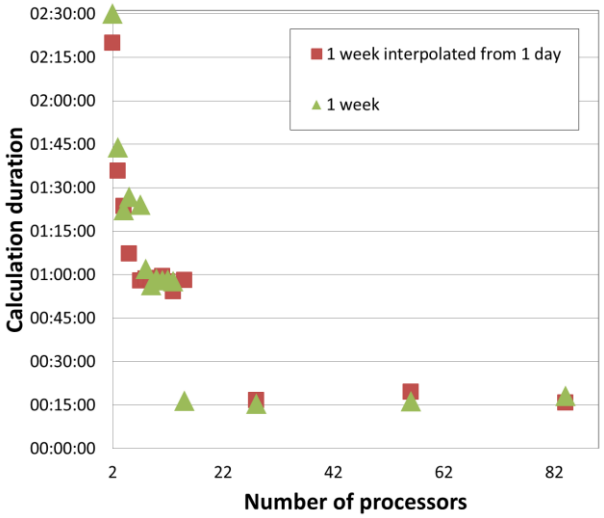

Figure 4. *Computation time as a function of the number of processors used*

IV. OPERATIONAL SAFETY: GOALS AND RESULTS

One of the goals of the model is to simulate correctly the new operating phases of the power plant in order to evaluate their impact on the local hydrodynamics. We focus on different criteria:

- The instant maximum velocities around the TPP,
- The flow and water level gradients during the transitory phases,
- The drifting time of a non-manoeuvring craft.

High current velocities and potential impacts

Some phases can generate high velocity flows around the TPP, with potential impacts to navigators, divers, swimmers, fishermen and moored boats.

The surface velocity was estimated using the model results and a logarithmic law (3) relating the depth-averaged velocity (V_{moy}), the water depth (H) and a bottom friction coefficient (z_0).

$$V(z) = V_{moy} \frac{\ln(\frac{z}{z_0})}{\ln\left(\frac{H}{z_0}\right) - 1} \quad (3)$$

Maps of the maximum velocity field for the different phases were generated in Qgis and shared with the plant operator to identify zones/activities potentially at risk.

The example given on Fig. 5 shows that the highest velocities are located inside the protected zone (identified by the safety lines represented in pink). Outside of this zone, the the velocities remain limited and do not exceed the values which were observed before the construction of the plant.

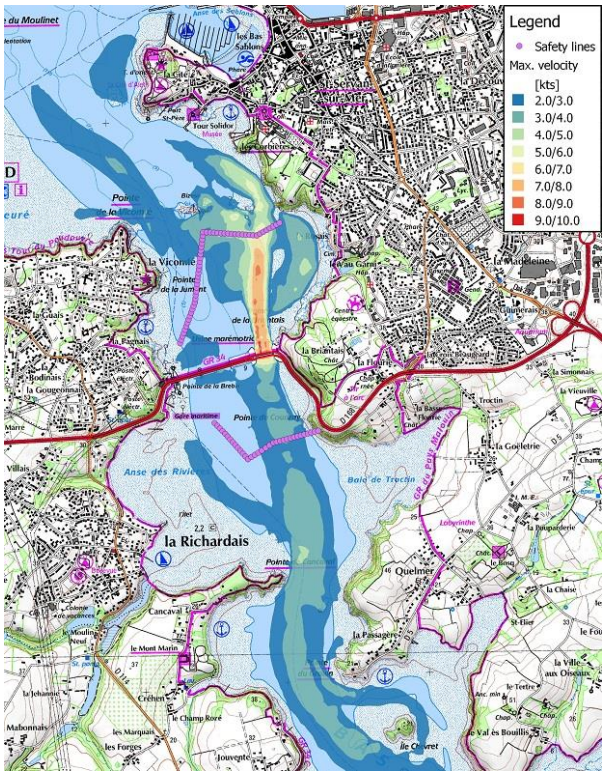

Figure 5. *Maximum velocity field when emptying the basin – close up view of the TPP surroundings*

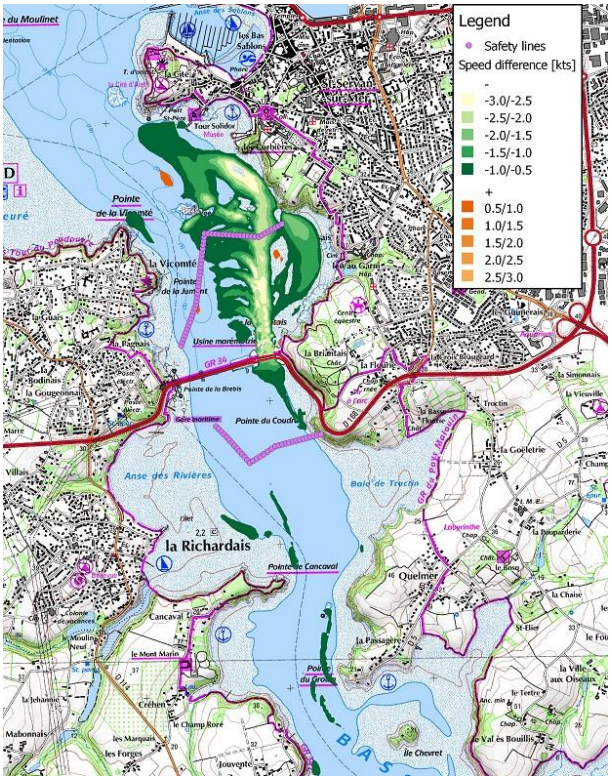

Figure 6. *Maximum velocity difference between two sequences: a significant reduction is observed, even outside of the zone protected by the safety line*

Rapid turbine stop and potential surge

The stop of the plant turbines in case of emergency can lead to rapid water levels variations, or surge wave, propagating upstream towards the estuary end. These waves are amplified as they progress towards the estuary tail because of the decreasing depth. A 30-cm high wave at the plant can transform into a 150-cm high wave at the Chatelier Lock (end of the estuary); its long period (around 40 min) limits the risks to navigators.

The simulations were compared with good accuracy to real life tests undertaken in the 1960s. Given the complexity of organising such tests, the numerical model is of great help to re-evaluate risk associated to these events.

Influence of sluice gates opening sequences

The opening of the sluice gates – which are 10m high by 15m wide - can lead to high flow gradients. The opening sequence (the gates open successively with a given time offset) can be adjusted to limit the safety risks. Sensitivity studies were realized for the different opening phases/flow directions and for a set of opening sequences by analysing the flow rate, flow rate gradient, basin water level gradient, and velocity field of each scenario. If significant differences can be observed in terms of velocity field (see Fig. 6), it appears that all the sequences tested are compatible with the current regulatory limits (fixed in terms of water level gradient). The results also highlighted the fact that a quicker opening sequence does not always lead to higher maximum velocities: it is sometimes preferable to open all the gates quickly to limit

the head increase (for longer sequences, the basin can fill more slowly than the sea is rising, thus leading to an increasing water level difference).

This study also provided some information on the impact of the sequence choice on the final basin water level (i.e. at the end of the filling phase), which is an indication of how much energy will be extracted during the following turbining phase.

Drifting times

Navigation on the estuary is subject to caution when the plant is operating as the strong currents can quickly drag a small boat towards the plant. Although there exists a safety line preventing the boats from coming too close to the plant, drifting times – i.e. duration to reach the plant from a given location, for a given operation phase – were evaluated and helped define the right emergency procedures.

A first approach was to use the algae transport module, but its application to a drifting boat was considered unnecessarily complex. Instead we chose to the following approach:

i. compute the trajectory of fluid particles by integrating the local velocity,
ii. compute the trajectory of a drifting boat (motor or sailing) using the fluid particles trajectory and hydrodynamic and aerodynamic forces (drag) applied on the boat.

These steps were integrated in the post-processing phase and allowed for a more complete analysis: several operating phases and tide conditions were studied without needing to re-run the simulations and the influence of drifting start time(s) and node(s) was tested in order to identify the most critical situations. Fig. 7 represents the "drift duration" map obtained for filling and emptying phases during an average amplitude tide. Wind conditions (constant force and direction) were also included in the parameters; its influence could be studied further by taking into account real conditions and their statistical distributions.

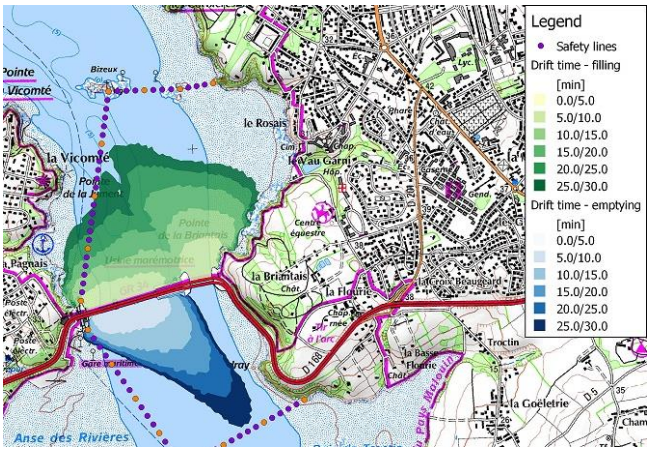

Figure 7. *Drifting times for both emptying (blue) and filling (green) phases, for a tide of average amplitude (coefficient 70)*

To validate these calculations, a real-life test was undertaken on site: a kayak, equipped with a GPS, was positioned about 700m upstream of the plant during a direct turbining phase and released in the flow. It was safely recovered after a short drift time. The GPS trajectory was analysed and compared to the theoretical trajectory (from the TELEMAC computation results): Fig. 8 shows the two trajectories and Fig. 9 the estimated drift times. Although the trajectories present slight differences (probably due to local turbulence/wave effects and kayak hull shape), a good correlation – slightly conservative - is observed in terms of "drift time to plant". More real-life tests are planned to further validate the simulation results.

V. CONCLUSION AND PERSPECTIVES

The model implemented allows a large freedom to simulate virtually any scenario one can imagine. It has already been used to address key safety issues as presented in this article. Further development is now considered, with 2 possible (non-exclusive) perspectives:

- A Sisyphe-coupled model to study the hydro-sediment processes at play in the estuary (work to be coordinated with EDF R&D),
- Implementing and completing a sensitivity analysis on water levels and/or velocities to quantify the model uncertainty (TELEMAC-OpenTurns coupling).

ACKNOWLEDGEMENT

The authors thank Denis Aelbrecht, hydraulics expert at EDF Hydro Engineering Center, for his constant support and wise advice in the studies on tidal power plants, and in particular, on La Rance tidal power plant.

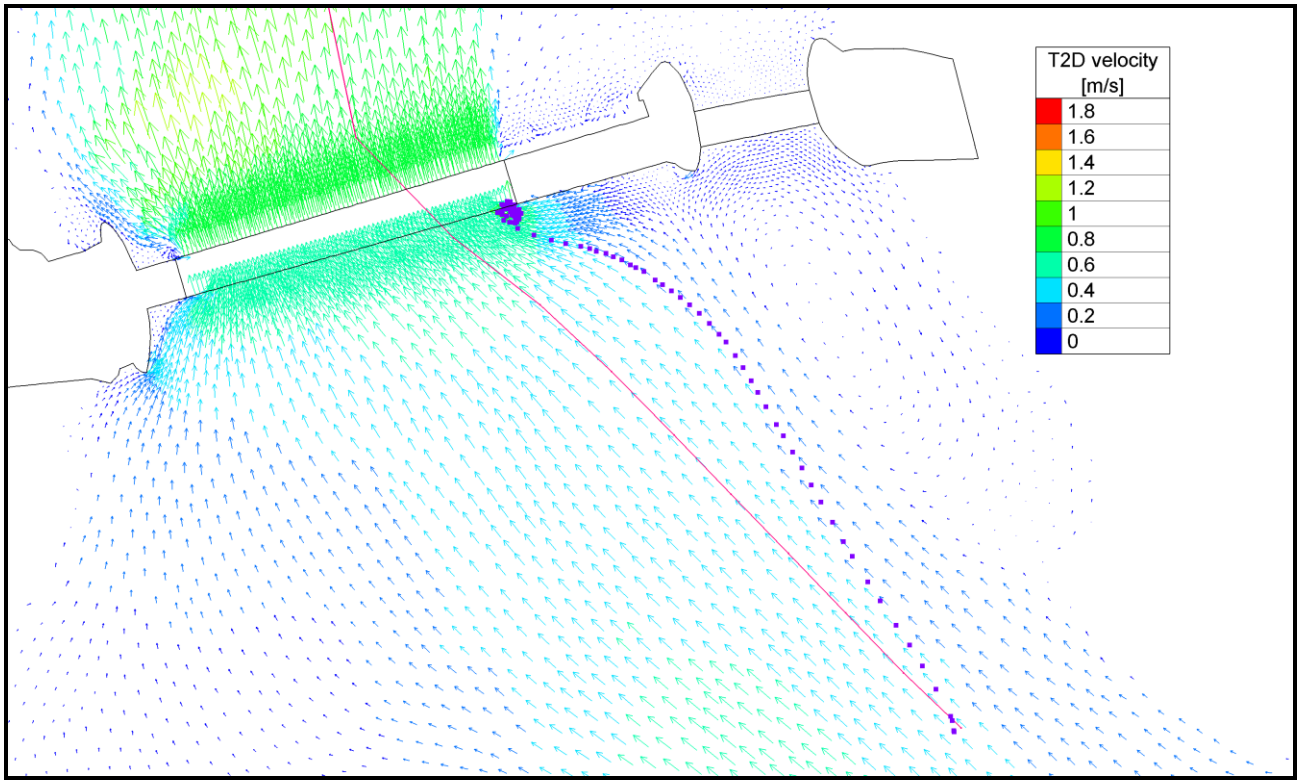

Figure 8. *Trajectories of a drifting kayak during the direct turbining phase: real-life test (purple dots) and numerical simulation (magenta line). The flow velocity field is represented as a coloured vector field*

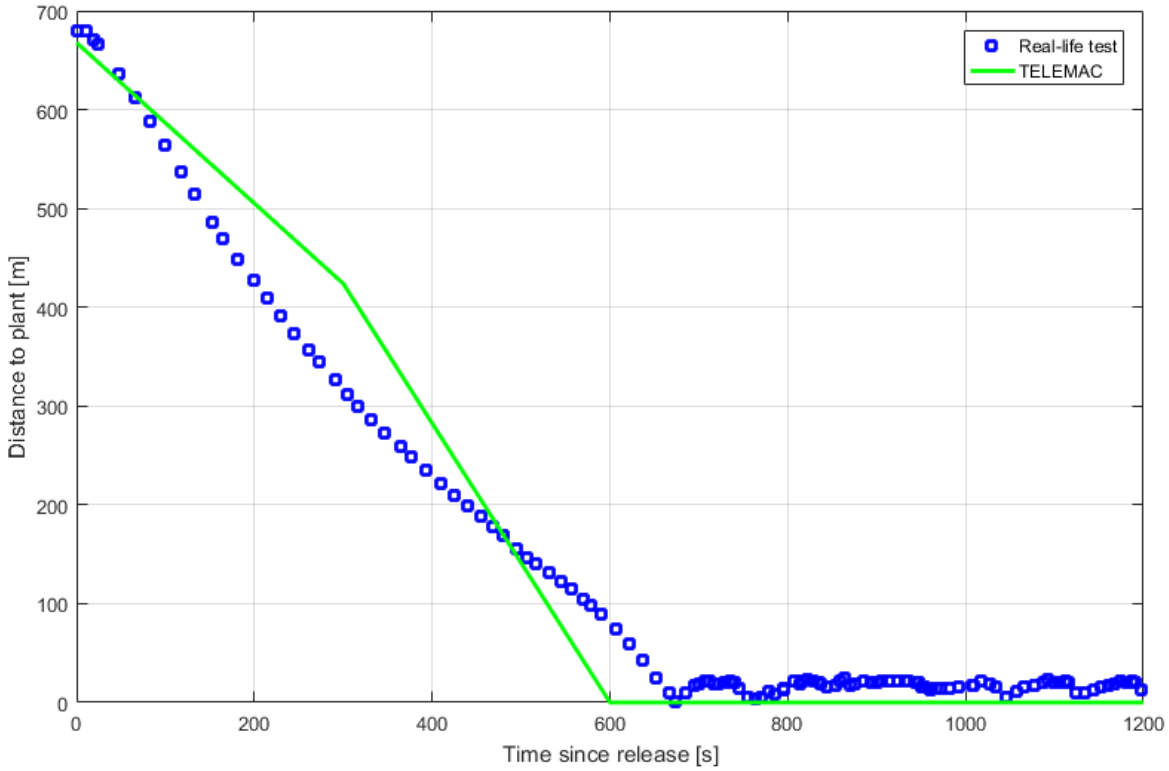

Figure 9. *Drift duration of a drifting kayak during the direct turbining phase: real-life test (blue dots) and numerical simulation (green line)*

3D modelling of the Lilla Värtan Bay in Stockholm to assess the impacts of an on-water housing project

Pierre-Louis Ligier, Anders Söderström
Sweco Energuide AB
Hydropower and Dams Department
Stockholm, Sweden
pierre-louis.ligier@sweco.se

***Abstract*—The county of Stockholm in Sweden has one of the highest immigration rate of Europe and is facing challenges to provide enough accommodations mainly due to its complex geography (islands, protected areas). Hence, the development of new housing projects are often technical challenges. The City of Stockholm is now creating a new district called Norra Djurgårdsstaden located in the North-East of the city centre where buildings of the "Kolkajen project" are planned to be built on the water in the Lilla Värtan Bay. This project is of high technical complexity due to the need to build the buildings on submerged piled decks anchored on the bedrock, to manage the loose and polluted sediments and to ensure a minimal impact on a heating power plan pumping and releasing process water within the project area. Sweco, who provide consulting services to the City of Stockholm as part of the Environmental Impact Assessment study, has developed a three-dimensional hydrodynamic model of the Lilla Värtan Bay in TELEMAC-3D (v7p1) in order to assess the impacts of the projects on the environment and on the heating power plant production. The Lilla Värtan Bay is located at the beginning of the Stockholm Archipelago and belongs to the Baltic Sea. Apart from the classical meteorological phenomena, the local flow conditions are influenced by the fresh water release from the Mälaren Lake and by the natural stratification characterized by large variations of both water temperature and salinity in depth and in time but also by the heating power plant which releases cooled and aerated water directly within the project area. This article presents the development of the TELEMAC-3D hydrodynamic model and its calibration against flow and water temperature measurements. The calibration was obtained by including a simple deaeration function in order to take into account the time dependent increasing density of the water released by the power plant. The article also presents the simulations performed with the project geometry in which the submerged piled decks has been modelled in order to assess the impact of the project on the heating power plant production. Finally, a presentation of the ongoing modelling work being performed regarding three-dimensional sediment transport and dispersion during the construction phase is presented.**

I. Introduction

The county of Stockholm in Sweden has one of the highest immigration rate of Europe and is facing challenges to provide enough accommodations mainly due to its complex geography (islands, protected areas). The population in the Stockholm county has increased by approx. 37,600 persons in 2016 which represents 1.65% of the county's population [1]. A similar population change rate has been observed during the last decade. For the year 2016, the new comers in Stockholm's county also account for 26% of Sweden's total population change.

Hence, several new housing projects are ongoing around the city. This article presents the hydrodynamic modelling work performed as part of the Environmental Impact Assessment study of the Kolkajen housing project, part of the Norra Djurgårdsstaden development in the North-East of Stockholm. This project is particular since it consists of two new housing areas entirely built onto the sea in the Lilla Värtan Bay with buildings and streets constructed on the top of piled decks. In an early phase of the project it was required to assess if the Kolkajen project could have an impact on the production of a heating power plant which pumps and releases water within the project area.

This article starts by presenting the study area with the new housing project, the flow conditions in the Lilla Värtan Bay and the heating power plant. Then, a description of the TELEMAC-3D model developed is given before describing the calibration process. Finally, the article presents the methodology followed for modelling the piled decks and the assessment of the impact of the structure on the heating power plant production.

II. Presentation of the Study Area

A. Housing project

The Norra Djurgårdsstaden district under development is located in the North-East of the city centre of Stockholm, between the Lilla Värtan Bay in the East, the Östermalm district in the West and the Norra Djurgården national city park with protected green areas in the North (see Fig. 1). The Norra Djurgårdsstaden project is designed for over 12,000 new housing apartments and for offices with a total capacity of 35,000 places by 2030 [2]. The project will be one of Stockholm's new environmental friendly district (see Fig. 2). The main areas on which housings and offices are to be constructed are located on an earlier industrial area used for gas production amongst other. The Kolkajen project is located at the North-Eastern end of the Norra Djurgårdsstaden district, and is to be built on the water in the Lilla Värtan Bay.

B. Flow conditions in the Lilla Värtan Bay

The Lilla Värtan Bay is oriented South-East to North-West between Stockholm and the Lidingö island. The bay is located near the Western end of the Stockholm Archipelago which marks the beginning of the Baltic Sea. The separation between the Baltic Sea in the East and the Mälaren Lake in the West is located around the Old Town of Stockholm where gates are used to manage the

Figure 1. *Location of the Kolkajen housing project.*

Figure 2. *Artistic illustration of the Kolkajen housing project. Illustration: Adept & Mandaworks.*

release of fresh water into the sea. The flow in the Lilla Värtan Bay is then mainly governed by the sea level changes in the Baltic Sea which propagates into the Stockholm Archipelago, by the fresh water discharge from the Mälaren Lake which mainly takes place during spring and summer when snow melts as well as contributions from smaller local catchments.

The local flow patterns are also affected by the intense ferry traffic as two major ferry terminals are located in the Lilla Värtan Bay (Värtahamnen and Frihamnen). At the location of the Kolkajen project, flow patterns are also influenced by the process water used by a heating power plant which pumps and releases cooled water inside the project perimeter. One of the goals of the hydrodynamic modelling study was to assess if the Kolkajen project will have negative impacts on the power plant production and propose possible mitigation measures.

The water depths in the Bay can reach up to 30 m and its stratification is mainly governed by a salinity gradient between the surface and a depth of about 25 m. The salinity near the surface shows a seasonal variation which corresponds with the fresh water releases from the Mälaren Lake during spring and summer. The water temperature varies a lot during the year with surface water temperature as low as 1 °C during winter up to 17 °C during the summer. The halocline ranges from the water surface down to approx. 20-25 m deep. The thermocline reaches somewhat deeper waters with temperature variations observed down to approx. 30-40 m while the stronger gradients are observed in the upper 15-20 m of the water column. Monthly average values for salinity and temperature are presented in Fig. 3.

C. *Heating power plant*

The heating power plant located just South of the Kolkajen project is pumping warm water from the Lilla Värtan Bay in an intake tower at different depths (near the water surface during summer and near the bottom during winter). After heat extraction, the cooled water is released into the Lilla Värtan Bay via an outlet structure composed of 20 openings divided in two groups with 10 openings on each side of the diffusor structure located just below the water surface. The power plant can pump and release up to 15 m^3/s of water. An illustration of the heating power plant is presented in Fig. 4. The released water is approx. 2 °C cooler than the pumped water and retains its salinity. Furthermore, air is inserted into the processed water and deaeration is not fully completed when the water is released into the Lilla Värtan Bay. The flow conditions downstream of the outlet structure are then strongly dependent on the density difference between the released water and the density of the water released by the heating power plant. Since the power plant is operated mainly during winter

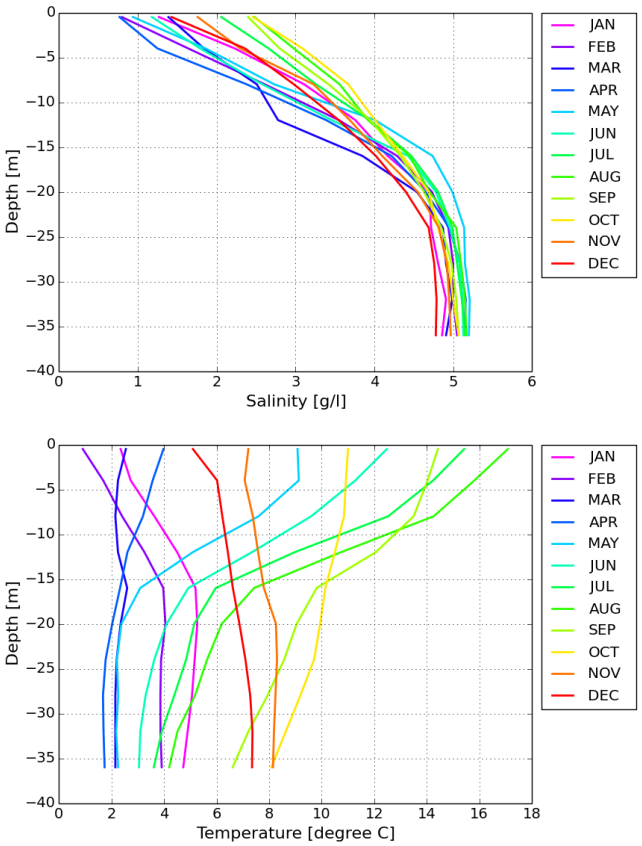

Figure 3. *Monthly average of salinity (top) and temperature (bottom) during the period 2005-2016.*

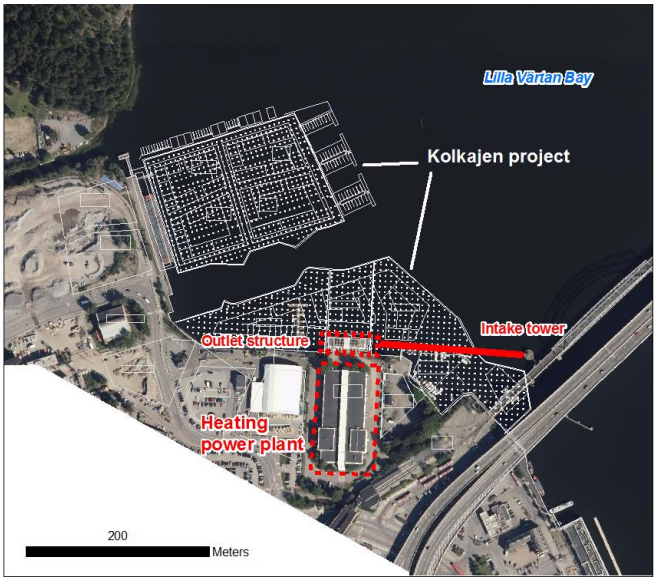

Figure 4. *Location and main components of the heating power plant. The footprint of the Kolkajen project is depicted as white lines.*

months, the density of the released water is then greater than the surrounding water mainly due to the larger salinity observed in depth.

III. Development of the TELEMAC-3D Hydrodynamic Model of the Lilla Värtan Bay

A. Model domain and bathymetry

The TELEMAC-3D hydrodynamic model covers approx. 5.3 km of Lilla Värtan Bay from the Frihamnen pier in the South and up to the North of the Tranholmen island with two boundaries located in the sounds towards Stocksundet in the North-West and towards the Stora Värtan Bay on the North-East, see Fig 5.

Figure 5. *Model domain.*

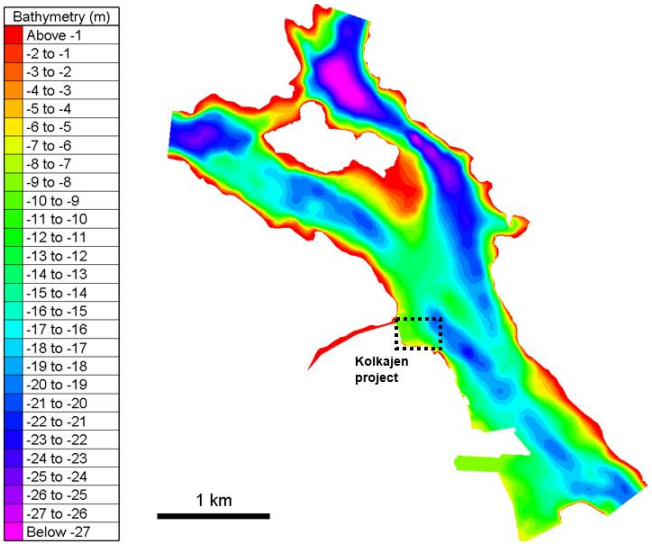

Figure 6. *Digitalized elevations within the model domain.*

A digital elevation model was created using depth information available on sea charts and a bathymetrical survey performed within the Kolkajen project area, see Fig. 6.

B. Computational mesh

The computational domain is composed of a two-dimensional horizontal unstructured triangular mesh that has been duplicated 21 times along the vertical to create a three-dimensional mesh. The lowest plane describes the bathymetry and the highest plane corresponds to the computed water surface. The two-dimensional horizontal mesh representing the current state was created with BlueKenue and contains approx. 228,500 elements while the three-dimensional mesh contains approx. 4,570,000 elements. The mesh size varies from 0.5 m at the location of the planned structures (piled decks), 10 m along the shorelines and up to 50 m in the middle of the bay. The vertical mesh has been defined with horizontal planes using a spacing of 1 m between the water surface and a depth of 19 m.

C. Boundary conditions and stratification

The model has three open boundaries with two inlets (Southern and North-Western boundaries) and one outlet with prescribed water level (North-Eastern boundary). The prescribed discharges have been defined as the average of yearly lowest flow values in order to minimize their influence on the flow patterns in the vicinity of the heating power plant outlet structure. The water level has been set to observed values of mean sea level.

The heating power plant intake tower has been modelled by a simple source with a negative discharge placed at its actual depth (2 and 17 m deep in summer and winter respectively). The outlet structure has been modelled in a fine version of the model in order to obtain the outflow characteristics. In the final version of the model, the structure has been removed and the outflow has been modelled using 8 sources, 4 on each side of the outlet structure. Discharge and velocity components of the exiting jets was obtained from the finer model.

The model has been ran for several wind scenarios corresponding to mean conditions in several directions.

Stratification has been defined for both salinity and temperature in the whole domain. It has been assumed that the

initial stratification is kept constant at the two inlet boundaries during the whole simulation with a constant prescribed value at each plane along the vertical axis.

D. Numerical settings

Bottom friction was modelled using a Strickler coefficient of 50 $m^{1/3}/s$. The bottom friction has been tested using several friction formulations and coefficients but showed very limited influence on the hydrodynamics in the area of interest.

The hydrodynamic model has been ran with TELEMAC-3D (v7p1) in non-hydrostatic mode. Turbulence has been modelled with the k-ε model. The advection scheme chosen for velocities, k-ε and tracers is the explicit MURD scheme without tidal flats treatment.

E. Deaeration function

The deaeration of the water released by the heating power plant was modelled with a tracer, representing air concentration, decaying with time. The air concentration values at each time step was then used in the computation of the water density. It has been assumed that the decay of air concentration is homogeneous within the aerated fluid. This is of course a simplification since this approach does not take into account the actual physical processes occurring during flow deaeration which depends on the water depth (air bubbles migrate upwards).

A first order decay function has been used, see the equation (1):

$$\frac{dA(t)}{dt} = -k.A(t) \text{ or } \frac{dA(t)}{A(t)} = -k.dt \quad (1)$$

Where *A(t)* is the air concentration at time *t* and *k* the decay coefficient. After integration, we obtain the equation (2):

$$ln\left(\frac{A(t)}{A(t=0)}\right) = -k.dt \quad \text{or} \quad A(t) = A(t=0) \cdot e^{-k.dt} \quad (2)$$

Where *dt* is the time between *t* and *t = 0*. Two parameters, *DECAYDAY* and *DECAYRATE* are then introduced to define the decay process as proposed by Sébastien Bourban (HR Wallingford) [3]:

$$A(t + DECAYDAY) = (1 - DECAYRATE).A(t) \quad (3)$$

Where *DECAYDAY* corresponds to the time, expressed in seconds, after which the initial concentration has decreased by a factor *DECAYRATE*, defined between 0 and 1. Rewriting (3) as:

$$ln\frac{A(t+DECAYDAY)}{A(t)} = ln(1 - DECAYRATE) \quad (4)$$

and identifying for *k* using (2) yields:

$$k = -\frac{ln\,(1-DECAYRATE)}{DECAYDAY} \quad (5)$$

The tracer decay can then be introduced in the subroutine `source_trac.f` using the explicit source terms for tracers S0TA:

$$S0TA = \frac{dA(t)}{dt} = -k \cdot A(t) = A(t) \cdot \frac{ln\,(1-DECAYRATE)}{DECAYDAY} \quad (6)$$

The water density *ρ(t)* is then computed in subroutine `drsurr.f` using equation (7):

$$\rho(t) = \rho_{ref} \cdot \{1 - [7 \cdot (T(t) - T_0)^2 - 750 \cdot S(t)] \cdot 10^{-6}\} \cdot [1 - A(t)] \quad (7)$$

Where ρ_{ref} is the reference water density (999.972 kg/m^3), *T(t)* is the local water temperature (°C), T_0 is the reference water temperature (4 °C) and *S(t)* is the local salinity (g/l) [4].

IV. Flow Measurements and Model Calibration

A. Flow measurements

Flow measurements have been performed by the firm VDM AB in February 2016 during two days using an ADCP profiler (TRDI RioGrande 1200 MHz) from boat. Currents have been measured along five profiles, see Fig. 7. Surface water temperature was also measured. Due to the local water temperature and suspended concentrations measurements were limited to the upper ten meters of the water column.

B. Model calibration

The model has been set up with the following boundary conditions:

- Release from the heating power plant: 13.7 m^3/s.
- Surface water temperature (power plant data): 1.7 °C.
- Water temperature at the intake depth (17 m deep, power plant data): 4.8 °C.
- Water temperature of the released water (power plant data): 2.5 °C.
- Wind: 5 m/s from 250 (WSW).
- Water level: 0.08 m above mean sea level.

The water temperature gradient has been defined in the model assuming a linear transition of water temperatures between the water surface and the intake depth. Since the surface water temperature as measured by the heating power plant is influenced by the warmer released water, the surface water temperature used in the simulations was iteratively reduced to 1.25 °C in order to obtain a similar surrounding surface water temperature of 1.7 °C

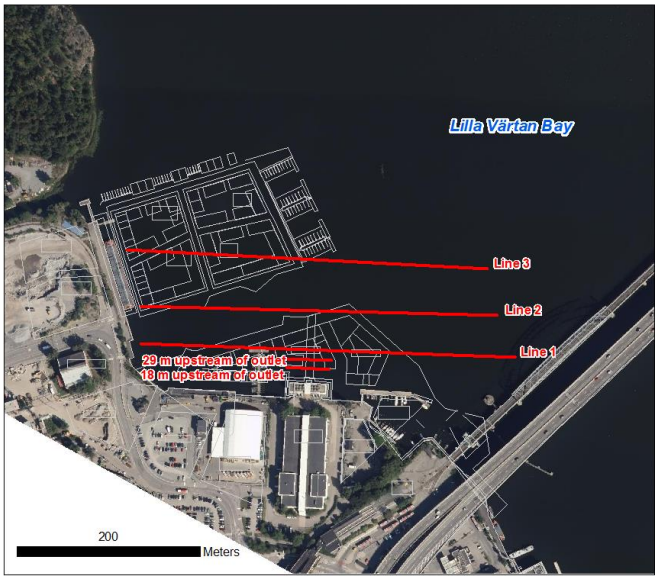

Figure 7. *Location of the ADCP profiles.*

outside of the outlet structure as confirmed by surface water temperature measurements. No salinity data during the flow measurement period was available. Hence, the salinity gradient has then been defined with values corresponding to a mean February month (see Fig. 3) with a concentration of 0.8 g/l at the surface and of 4.1 g/l at the intake depth (17 m).

Using (7), the density of the surface water is 1000.50 kg/m^3 whereas the density of the water at the intake depth is 1003.04 kg/m^3. The released water was defined with a water temperature of 2.5 °C and a salinity of 4.1 g/l, which corresponds to a density of 1003.02 kg/m^3 (without air).

The prescribed discharges at the model open boundaries were set to low values in order remove any possible influence on flow conditions at the outlet structure. This is a valid assumption since the release of fresh water from the Mälaren Lake is very low during winter and that no quick sea level change occurred during the period preceding the flow measurements.

First simulations with the above set-up showed that the released jets were abruptly plunging towards the sea bottom due to the larger density of the released water compared with the surrounding water which did not correspond with the measurements, see Fig. 8.

This result indicates that the deaeration of the released water is not completed when it enters in the Lilla Värtan Bay. Hence, a deaeration function had to be implemented in order to reproduce the actual flow conditions as accurately as possible. Unfortunately, none of the parameters needed to define the process was known since no air concentration measurements are performed by the power plant staff and that is was not possible to know how quick the natural deaeration process is (decay parameters). The methodology used was to assign the initial air concentration so that the density of the released water would be in the same range than the natural water density in the vicinity of the outlets. This assumption is compatible with observations from flow measurements since the outlet jets are not plunging immediately after release but stay somewhat near the water surface in the vicinity of the outlet structure. The initial air concentration A_0 was then set to 0.002 which means that the initial density of the released water is 1001.02 kg/m^3. The two decay parameters, *DECAYDAY* and *DECAYRATE*, have then been defined iteratively until the behaviour of the outlet jets was as close as possible from the observations. Best match was obtained

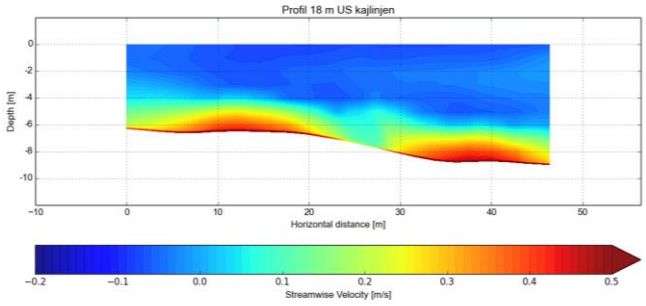

Figure 8. *Vertical velocity profile 18 m upstream of the outlet structure (see Fig. 7 for location). Calibration case without air concentration. Positive values indicate that current is oriented towards the North (out from outlet). This profile can be compared with the top image from Fig.10 (calibration case with air concentration).*

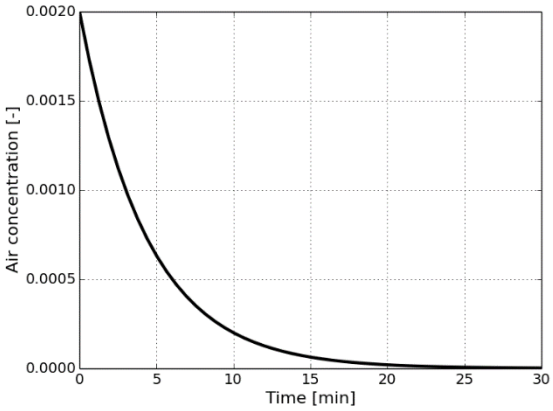

Figure 9. *Deaeration function used for the calibration case.*

with *DECAYDAY* = 30 minutes and *DECAYRATE* = 0.999 corresponding to a decay of air concentration of 99.9% after 30 minutes (Fig. 9).

Comparison between model results and the flow measurements are presented in Fig. 10. Results show that the outlet jets are progressively plunging in depth due to its increasing density, induced by the decay of air concentration, down to a depth of approx. 10 m where the density of the released water becomes equal to the surrounding water's density. Some salt dispersion occurs between the outlet and the Line 3 meaning that the pumped and then released water cannot plunge back to the intake depth due to the salt dispersion process which reduces the density of the released water in the upper part of the water body.

The maximal flow velocities are generally correctly reproduced by the model excepted at Line 2 where they are slightly underestimated (approx. -0.1 m/s).

Flow measurements show that an eddy takes places within the project area with a back current located along the Western quay. This eddy is not clearly reproduced by the model but this has no impact on the density driven currents and especially on the plunging behavior of the jets.

Fig. 11 presents the evolution of salinity and relative density as computed by the model at profile 29 m upstream of the outlet structure and at Line 1 and 3.

Comparison between surface water temperature measurements and the model results along Lines 1 to 3 are presented in Fig. 12. At Line 1, the model reproduces well the maximal observed temperature but underestimates the lateral dispersion. Results further away from the outlet (Lines 2 and 3), even if more smoothened than the measurement, show that the warmer released water is circulating along the Western quay (left side of the graphs) highlighting the presence of an eddy in that zone.

In conclusion, the model reproduces well the flow conditions as well as the thermal dispersion at the water surface as observed from the measurements. During winter months, the outflow from the heating power plant, having a greater density than the surface water once deaerated, progressively plunges in depth. Salt dispersion occurring in the upper part of the water body between the released water (high salinity) and the surrounding water (low salinity) means that the plunging jets' behavior is stopped after some distance from the outlet at approx. 10 m deep and hence cannot reach the intake depth (17 m).

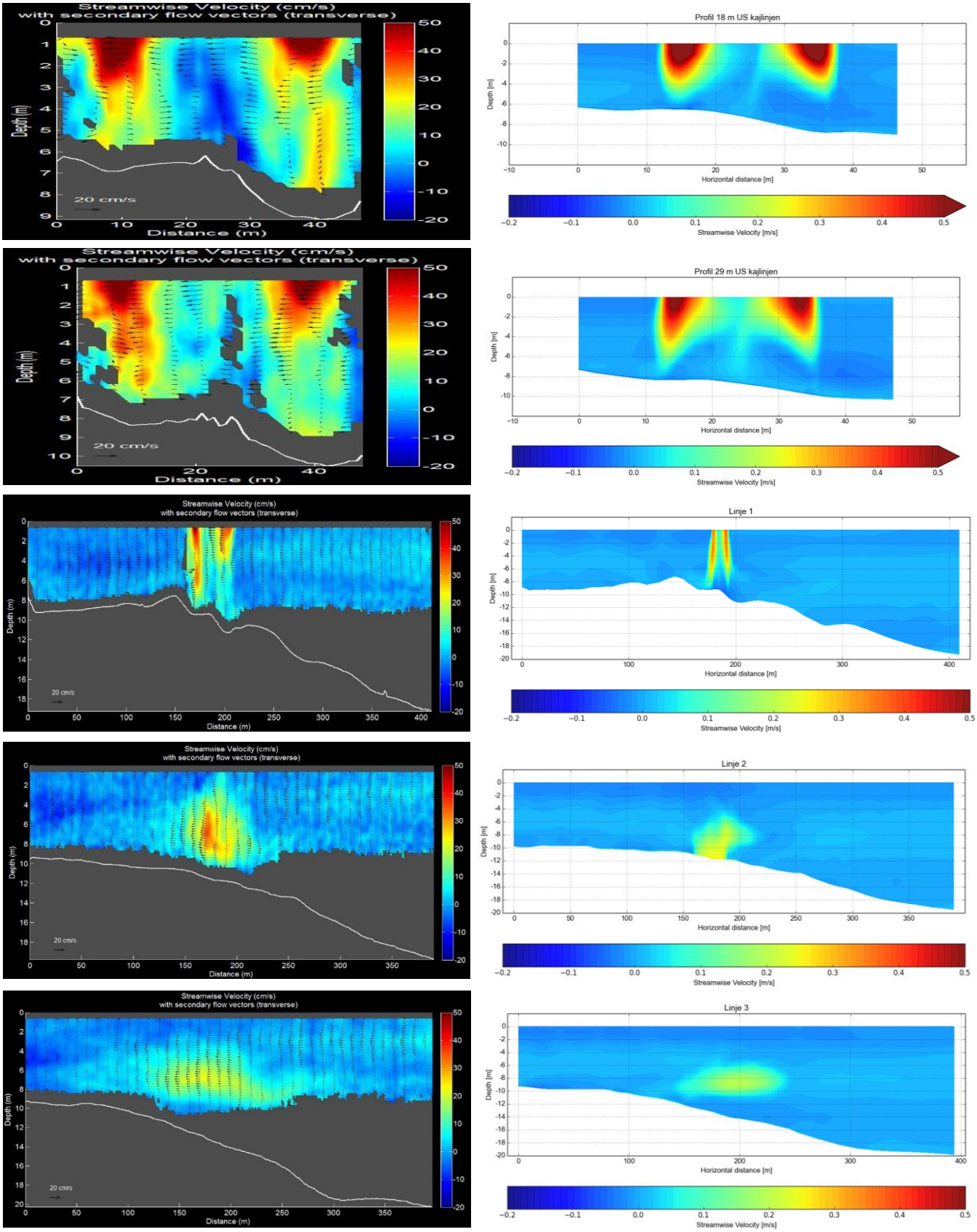

Figure 10. *Comparison between flow measurements (left column) and model results (right column) at the locations depicted in Fig. 7. Positive values indicate that current is oriented towards the North (out from outlet).*

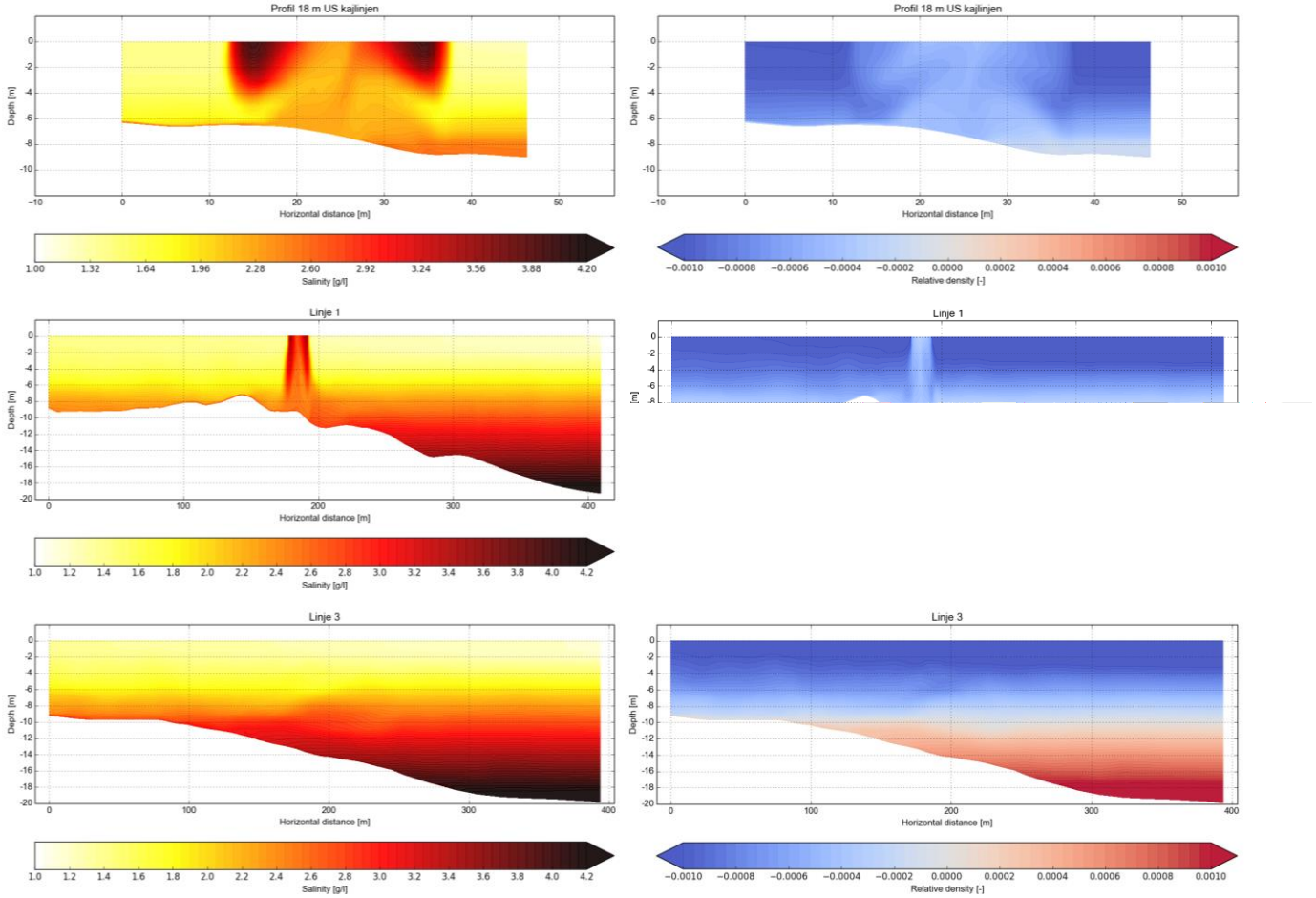

Figure 11. *Salinity (left column) and relative density (right column) evolution at profile located 29 m upstream of outlet structure and at Line 1 and 3.*

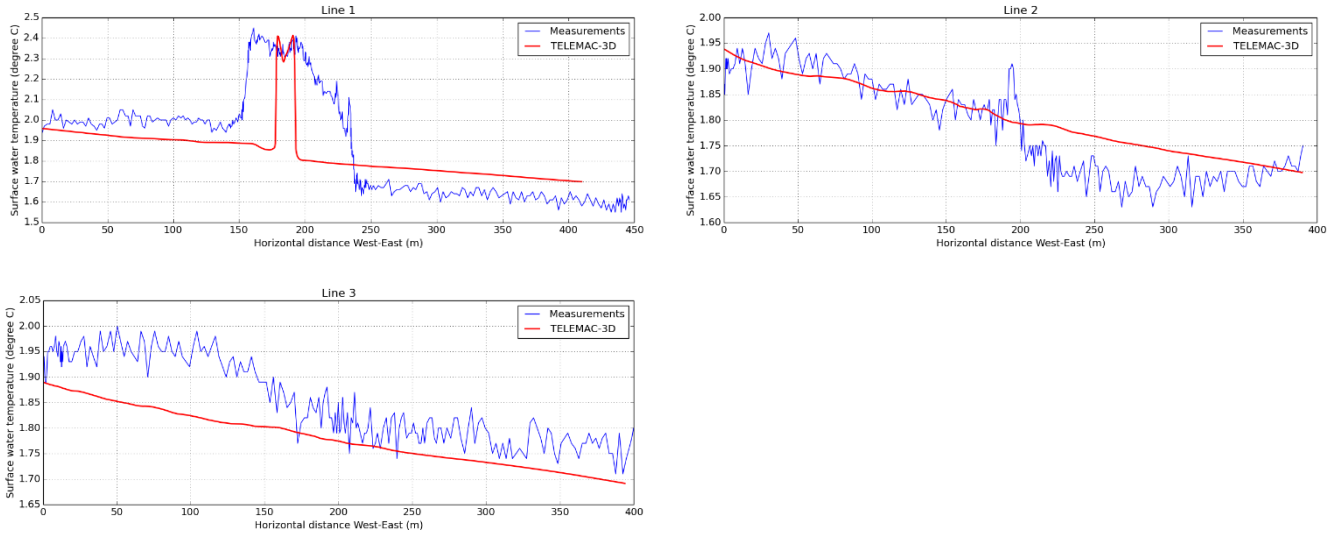

Figure 12. *Comparison between surface water temperature measurements and model results along Lines 1 to 3. Temperature measurements were not exactly performed along the same lines as the ADCP profiles which explains the slight shift between the two curves.*

V. MODELLING OF THE SUBMERGED PILED DECKS

A. Piled decks characteristics

The planned housing project will be built on two piled decks in the small bay North of the heating power plant (see Fig. 4). The piled deck alternative has been chosen for technical and environmental reasons mainly due to the presence of a layer of polluted loose sediments that can reach more than 10 m within the project area. Piles founded on the bedrock was a better technical solution and allows to avoid settlement problems in the loose sediments. It also allows to keep the sediment in place as removing it would lead to possible risk for dispersion of polluted particles. The concrete slab will be located 2.3 m below the main sea level in order to offer more space for apartments' cellars except in front of the heating power plant outlet structure where the slab will be located 0.9 m above the main sea level in order to allow the organic foam produced during process at certain periods of the year to be released freely into the Lilla Värtan Bay, see Fig. 13. The piles have a total diameter of 1.2 m and the distance between them is 6 m.

B. Computational mesh

The computational mesh used for the geometry with the piled decks is similar to the one used for the current state except within the project area where the 1426 piles were included as islands with a discretization of 0.3 m, see Fig. 14. The concrete slabs were defined using polygons with a discretization of 0.5 m in order to obtain rectilinear interfaces. The two-dimensional mesh is composed of approx. 355,800 elements while the three-dimensional mesh contains approx. 7,120,000 elements.

C. Modelling assumptions

An increased air pressure has been defined at the location of the concrete slab in order to lower the water surface 2.2 m below the main see level except in front of the heating power plant outlet using equation (8):

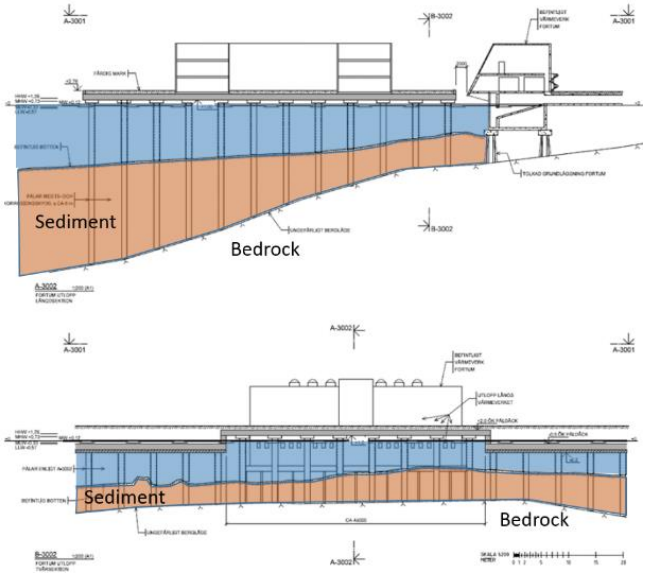

Figure 13. *Piled deck structure in front of the heating power plant outlet structure. Top: North-South cross section with the outlet structure on the right. Bottom: East-West cross section viewing towards the Southern quay with the 20 outlet openings visible just below the deck slab.*

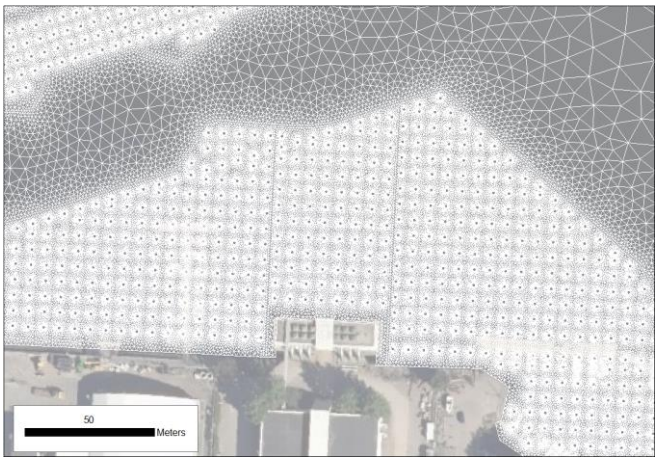

Figure 14. *Zoomed view of the piled decks mesh in the vicinity of the heating power plant.*

$$P = P_{atm} + \rho g(Z_{sea} - Z_{slab}) \quad (8)$$

Where P is the total air pressure (Pa), P_{atm} is the atmospheric pressure (10^5 Pa), ρ is the water density (kg/m^3), g is the gravitational acceleration (9.81 m/s^2), Z_{sea} is the water surface level (m) and Z_{slab} is the level of the bottom face of the concrete slab (m). The increased air pressure has been applied in combination with the keyword FREE SURFACE GRADIENT COMPATIBILITY set to 1.0 to ensure a perfect balance between the free surface gradient and the computed velocities [4, 5] to avoid triggering erroneous currents at the interface between the free and lowered water surface [6]. Surface friction at the interface between the water surface and the concrete slab was not modelled since the slab is not located below the mean sea level in front of the outlet structure where the highest flow velocities are concentrated. Furthermore, surface friction has been tested in a previous version of the model in which the slab was located entirely below the sea level and it did not show significant influence on flow conditions. An illustration of the lowered water surface after applying the increased air pressure is presented in Fig. 15.

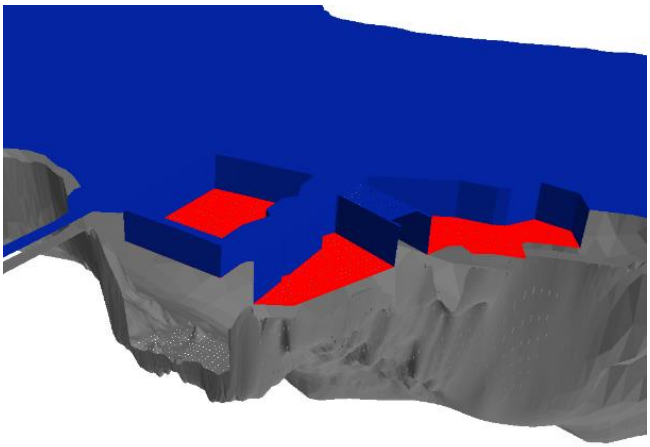

Figure 15. *Illustration of the lowered water surface (red) to model the concrete slab located below the mean sea level (blue). The bottom is depicted in grey.*

D. *Influence of the piled decks on the flow conditions and temperature dispersion*

A requirement of the project was to estimate if the Kolkajen project and more specifically the piled decks could have a negative impact on the power plant production. The model was then used to assess if there was a risk that the extra flow resistance induced by the piled decks could lead more cooler water towards the intake thus reducing the power plant's efficiency. The heating power plant owner required that simulations were performed corresponding to a mean March month with full pumping capacity (15 m^3/s). The model has then been set up with salt and temperature gradients corresponding to a mean March month in accordance with data from Fig. 3, which corresponds to very similar conditions compared with the calibration case. Salinity concentration of the released water was taken equal to the data from mean March month at 17 m depth, 4.2 g/l, while the salinity at water surface was 0.9 g/l. The temperature of the released water was set to 0.01 °C (just above the freezing point) while the natural temperature at 17 m depth is 1.97 °C for a mean March month and the natural surface temperature was 1.31 °C. The deaeration parameters were identical to the ones defined during the calibration step. The model has been run for different wind scenarios.

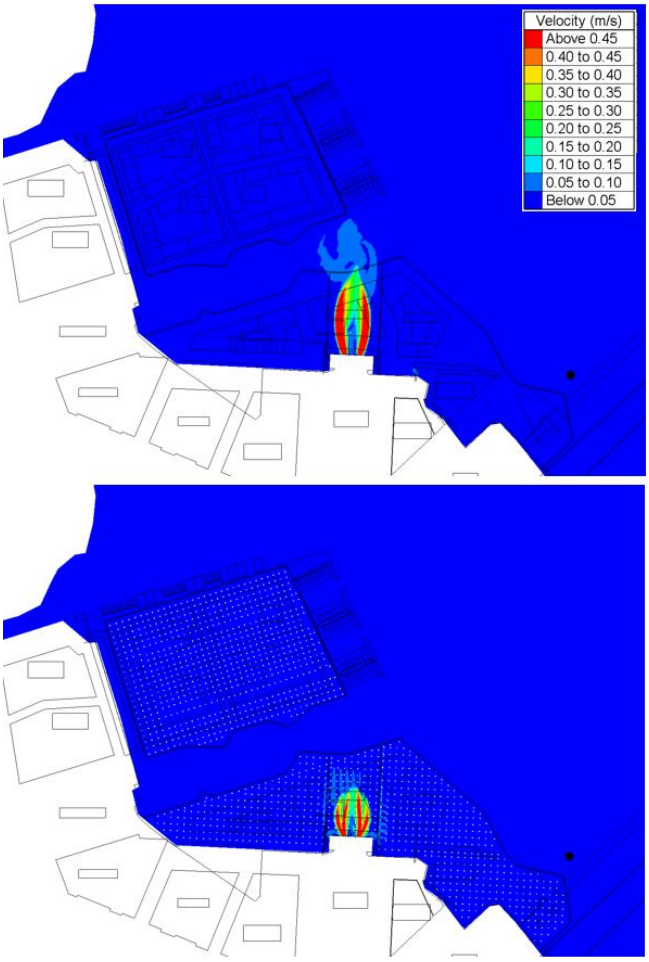

Figure 16. *Surface current in current state (top) and with piled decks included (bottom) for a mean March month with full pumping capacity. The location of the Kolkajen project is depicted on both figures for comparison purposes. The black dot located in the lower right corner of the pictures indicates the intake tower location (located 17 m deep in this configuration).*

The influence of the piled decks on the surface current is presented in Fig 16. It is visible that the flow velocities are reduced due to the extra resistance generated by the structure. The lateral dispersion and 3D flow mixing are increased. The results concerning the temperature dispersion showed, as it could be expected from the calibration case, that the released water could not reach its initial water depth (17 m) due to salt dispersion and the temperature change at the intake location after construction of the piled decks was negligible. Hence, the Kolkajen project should not affect the heating power plant production.

VI. Conclusion and Ongoing Modelling Work

The work presented in this article has been realized in a first stage of the Environmental Impact Assessment study process with focus on feasibility conditions associated with the interaction with the heating power plant. The results have shown that the Kolkajen housing project should not have negative impacts on the power plant production.

The modelling work has recently resumed with focus on sediment dispersion. The sediment, heavily polluted within the project area, is monitored with sedimentation measurements performed twice a year. The upcoming modelling work will focus on assessing the long-term impact of the Kolkajen project on sediment dispersion conditions in the Lilla Värtan Bay where areas of high ecological values are present and to help defining possible mitigation measures. Another goal of the modelling work will be to assess the risk of sediment dispersion during the construction phase during which removal and piling operations will be performed.

Acknowledgement

The work presented in this article has been performed for and funded by the City Development Office (Exploateringskontoret) of the City of Stockholm.

References

[1] Statistics Sweden (SCB). http://www.scb.se/en/finding-statistics/statistics-by-subject-area/population/population-composition/population-statistics/. Date 2017-08-07.

[2] City of Stockholm. http://vaxer.stockholm.se/projekt/hjorthagen-kolkajen/. Date 2017-08-07.

[3] Sébastien Bourban, HR Wallingford. www.opentelemac.org, forum post #855 and personal correspondence.

[4] EDF R&D, TELEMAC-3D Software, Release 7.0, Operating manual, January 2016.

[5] J-M. Hervouet, Hydrodynamics of free surface flows, John Wiley & Sons, Ltd, 2007.

[6] P-L. Ligier, A. Söderström, C. Bohlin, Ø. Lier, "Modelling complex vertical structures with TELEMAC-3D", Proceedings of the XXIIIrd TELEMAC-MASCARET User Conference, Published by HR Wallingford, June 2017.

Turbine array interactions and performance in TELEMAC-3D

Enda Murphy[1], Julien Cousineau[1], Mitchel Provan[1]
National Research Council Canada / Conseil national de recherches Canada
1200 Montreal Road
Ottawa, Canada
enda.murphy@nrc.ca, julien.cousineau@nrc.ca, mitchel.provan@nrc.ca

***Abstract*— River hydrokinetic energy (RHE) turbines for electric power generation are generally deployed in an array or farm configuration to benefit from economies of scale. To support resource assessments and decision making, RHE developers need to be able to quantify the total power that can be generated within a river reach using an array (or arrays) of RHE turbines. The total extractable power for a given site depends on (i) the drag and power characteristics of individual turbine devices, (ii) turbine wake hydrodynamics and wake interactions within arrays, and (iii) macro scale river hydrodynamics, which may be altered by the presence of turbine arrays. Quantifying total extractable power therefore requires the ability to simulate hydrodynamics at both river reach (macro) and turbine/array (micro) scales simultaneously. In this paper, we present modifications of the TELEMAC-3D source code, implemented as a first step in facilitating estimation of the total extractable power for arrays of RHE turbines. The methodology is based on the assumption that the locations, geometry and performance characteristics of individual turbines are known *a priori* (e.g. from CFD simulations or physical model tests). Preliminary work to validate the methodology, by comparing the results of numerical flume tests for cylinders and simplified turbines with numerical and physical modelling data, is presented. Limitations, and future research needs to enable a unified approach to RHE resource assessment, are identified.**

I. INTRODUCTION

Identifying suitable sites for river hydrokinetic energy (RHE) development requires the ability to quantify not only the potentially available (i.e. theoretical) resource within a river reach, but also the maximum portion of that resource that can be exploited using presently available RHE turbine technology. This is frequently an optimization exercise, balancing the number and configuration of RHE turbines against the impacts on river hydrodynamics to determine the maximum harvestable or extractable power. It is widely accepted that failing to incorporate the potential impacts of energy extraction on hydrodynamics can significantly overestimate the extractable resource [1].

The impacts of RHE turbine arrays on river hydrodynamics may include areas of increased and reduced flow speeds and water levels at the reach scale (hundreds of metres to kilometres). At the array scale (tens to hundreds of metres), the wake hydrodynamics of individual turbines and turbine-wake interactions are dependent on river stage and flow conditions, turbine size and geometry, and the spacing and configuration of turbines within an array. Both the reach scale hydrodynamics and array scale hydrodynamics influence the power that can be extracted by individual turbines within an array, and therefore, the optimal array configuration and total extractable power for a river reach. For example, downstream devices in an array may experience lower flow velocities than those at the leading edge of the array, because of the velocity reduction in the wakes of the upstream devices. The turbulence generated by the wake of an upstream device or drag element may also alter the drag or thrust imparted by a downstream turbine [2] [3]. Effective resource assessment and optimization for RHE turbine farms therefore requires the ability to analyse coupling and interactions between hydrodynamics at the river reach (macro) and array (micro) scales.

As explained above, turbine-wake interactions within an array depend on the wake characteristics of individual turbines (i.e. device-scale hydrodynamics). In general, drag and wake characteristics for specific devices are known *a priori* for a range of flow conditions based on computational fluid dynamics (CFD) simulations or physical model testing, which are suited to resolving the high frequency motions and complex device geometries at turbine scales. Consequently, analyses of device-scale hydrodynamics can typically be decoupled from the reach- and array-scale assessments. The results of CFD modelling or physical modelling may be used to characterize wake hydrodynamics at the scale of an individual turbine, for input to separate analyses of hydrodynamics within a turbine array and / or the river reach.

This paper presents preliminary work and findings from a multi-phase research project, which will combine physical modelling, CFD modelling, and numerical hydrodynamic modelling techniques to support the development of new and improved methodologies and guidelines for RHE resource assessment.

II. STUDY BACKGROUND

The National Research Council (NRC), Natural Resources Canada and Université Laval are conducting collaborative research to improve methodologies for RHE resource assessment at river reach scales. The research programme consists of three phases: 1) laboratory physical modelling and

experiments; 2) developing new and enhanced numerical techniques to simulate turbine-turbine and turbine-river interactions; and 3) developing guidelines for turbine technology selection, optimizing turbine array configuration, and total extractable power estimation.

Physical model testing will be carried out in a laboratory flume setting for multiple turbine array configurations (side-by-side, in-line and staggered). Flow, turbulence characteristics, and other key parameters will be measured and recorded using Acoustic Doppler Velocimeters (ADV) and shear probes. The physical model test results will provide detailed information on flow and wake characteristics at individual turbine scales and within arrays of turbines.

Results from the laboratory physical model testing will be used to develop new or enhanced CFD and numerical modelling approaches to support resource assessments for large-scale RHE turbine arrays. This will facilitate: accurate assessments of drag coefficients, power coefficients and wake characteristics for individual turbines (momentum deficit and recuperation length scales); an improved understanding of confinement effects and turbine-wake interactions to enable estimates of total power extraction from large-scale turbine arrays; and analysis of the impacts of RHE turbine arrays on river hydraulics (water levels and velocities).

The numerical and physical modelling will be used to support the development of new guidelines for turbine array configuration planning/design and estimating total extractable power for river reaches. These guidelines and new/enhanced methodologies for RHE resource assessment for river-scale projects will be used as the basis for providing recommendations for the International Electrotechnical Commission Technical Standard TS 62600-301 – River Resource Assessment.

III. Hydrokinetic Turbines in TELEMAC

The TELEMAC system has been successfully used for hydrokinetic energy resource assessments at both tidal and riverine sites, with and without modelling the interactions between hydrodynamics and turbines [4] [5] [6] [7] [8] [2] [9] [10]. However, the majority of previous studies either: (i) do not consider turbine-wake interactions within arrays of devices; or (ii) neglect three-dimensional flow effects; both of which may be important in characterizing the extractable resource at a given site and assessing impacts.

Recent releases of TELEMAC-2D (such as v7p2r1) offer the possibility to model the effects of sub-grid scale structures (through the VERTICAL STRUCTURES keyword and DRAGFO subroutine) via a drag parameterization. This method may be applied to simulate the thrust imparted by a hydrokinetic turbine in the form of an equivalent drag force (e.g. [11] [8]). For depth-integrated models, such as TELEMAC-2D, this method amounts to increasing the bed friction coefficient. Depending on the proportion of the total water depth occupied by turbines (which can vary by location and with stage), this depth integrated approach misrepresents the drag and velocity profiles in the vertical dimension, neglecting important phenomena such as flow bypassing [12]. With advances in computing power, three-dimensional hydrodynamic models are increasingly being used for hydrokinetic energy resource assessments. Thus, recent research has focused on incorporating the effects of turbines in three-dimensional hydrodynamic models [4] through a drag force parameterization applied as a source term in the momentum equations.

In this paper, we elaborate on the concepts presented by Bertrand el al. [4], and extend the methodology of Joly et al. [8] from TELEMAC-2D to TELEMAC-3D. Initial work to validate the methodology is presented (including comparisons with measurements from physical model tests). The source code modifications have been disseminated to the openTELEMAC-MASCARET community via the online web forum (post #20808).

IV. Turbine Drag and Power Relationships

A typical vertical axis (or cross-flow) RHE turbine consists of a series of blades oriented perpendicular to the flow, free to rotate in a horizontal plane about a central (vertical) shaft or hub, which is typically fixed to the river bed (Fig. 1) or supported by a barge. The frontal area (i.e. perpendicular to the flow) swept by the blades, A, is equivalent to the length of the blades multiplied by the diameter of the turbine, D.

Extracting energy from the river flow requires a reduction in the momentum of the fluid passing through the turbine. The force (or thrust) required to achieve this reduction in momentum can be parameterized as a drag force (e.g. [13]):

$$F_D = \frac{1}{2}\rho A C_D U_r |U_r| \qquad (1)$$

where ρ is the density of water, C_D is a drag coefficient, and U_r is a reference velocity at a defined location upstream of the turbine. The drag coefficient is specific to a given RHE device, and is generally a function of the flow speed. The coefficient is intrinsically linked to the reference velocity location, which is typically chosen sufficiently far upstream that the flow is not disturbed by the device.

The average power extracted by a turbine over one turbine revolution is given by:

$$P = \frac{1}{2}\rho A C_p U_r^2 |U_r| \qquad (2)$$

where C_P is a device-specific power coefficient, determined through design and testing, which defines the ratio of extractable to available power. Power extraction typically only occurs when a minimum threshold (cut-in) velocity is exceeded.

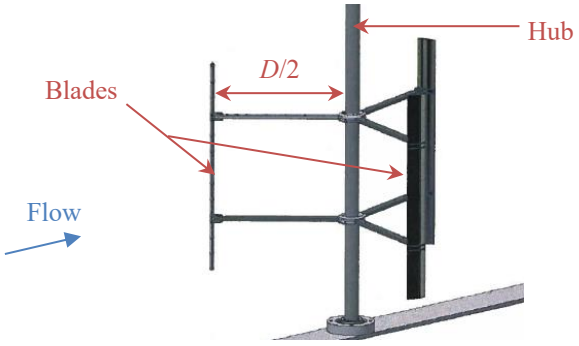

Figure 1. *Vertical axis turbine (image source: [14])*

If the power coefficient, turbine geometry, device availability, and temporal velocity distribution at a reference location upstream of the device are all known or predictable, the energy production for an individual turbine can be determined. However, in order to predict the reference velocity distribution, it is necessary to incorporate the effects of adjacent or upstream turbines on the hydraulics within the array and river reach. The approach taken here is to apply the drag force presented in equation (1) as a source term in the three-dimensional Navier-Stokes equations to simulate the impact of an individual device on the computed hydrodynamics. Hypothetically, this approach can be implemented for multiple devices within an array to simulate the impacts on both array-scale and river-reach scale hydrodynamics. Power extraction for each device is then computed as a function of the modified flow field within the array and summed to provide the total extractable power for the array.

V. Implementation in TELEMAC-3D

The method of implementing the impact of turbines on hydrodynamics in TELEMAC-3D (v7p2r1) presented here follows the approach of Joly et al. [8] for tidal energy converters (TECs) in TELEMAC-2D. A logic flow chart summarizing the key steps in the algorithm, as implemented by modifications to the source code, is shown in Figs. 2 and 3 and described as follows.

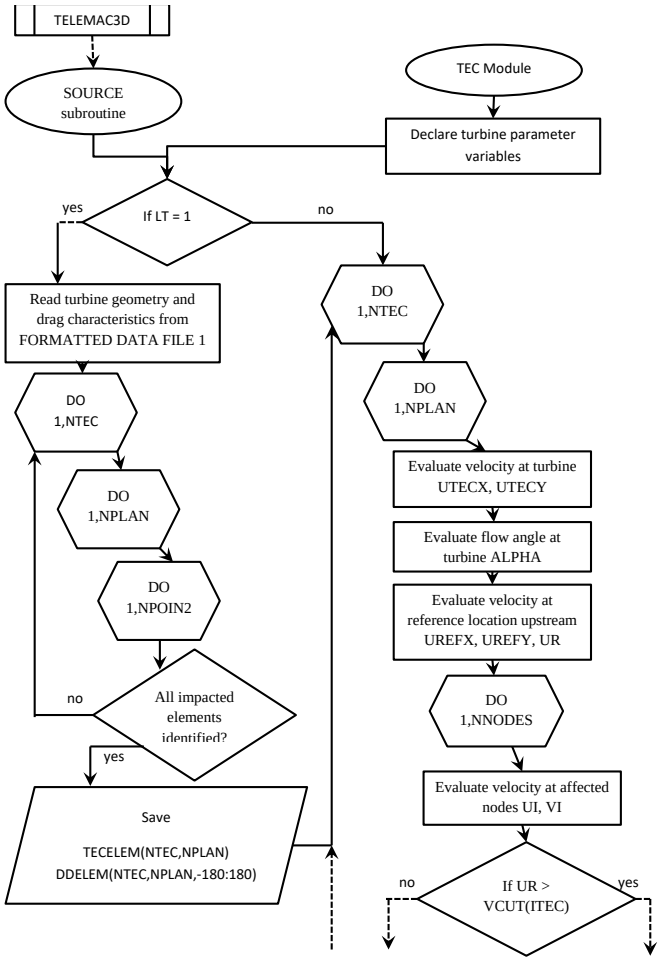

Figure 2. *Pseudocode for implementation of the TELEMAC-3D source code modifications (part 1 of 2).*

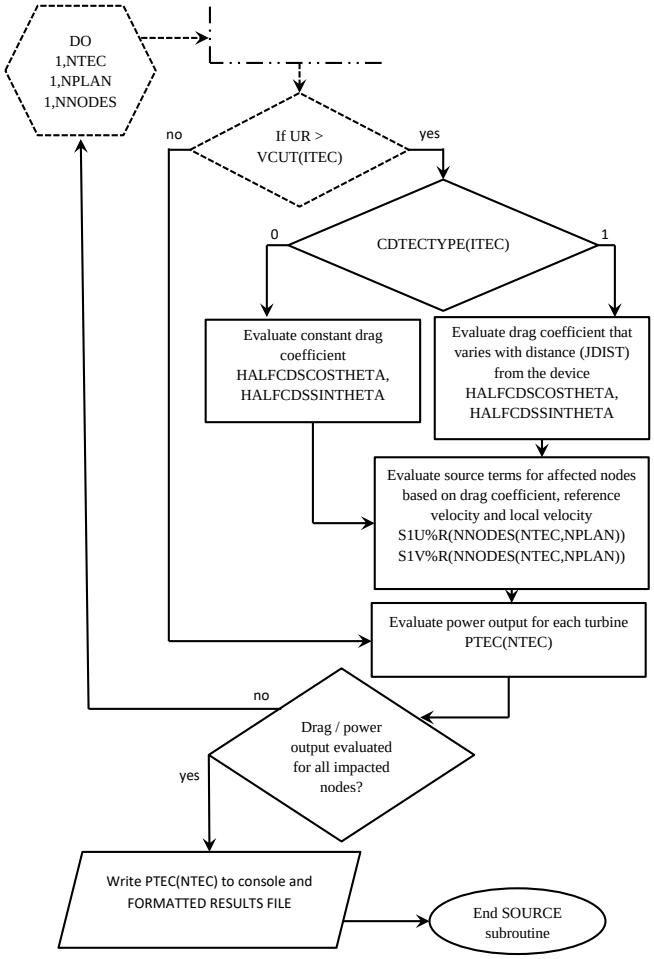

Figure 3. *Pseudocode for implementation of the TELEMAC-3D source code modifications (part 2 of 2).*

First, parameters and variables specific to the turbine geometry are defined within the TEC_PARAM module for dynamic allocation at runtime. The remaining modifications to the source code are made within the SOURCES subroutine, which is called by the main TELEMAC-3D subroutine at each time step.

At the first time step in a simulation (LT = 1), the geometry and drag characteristics of each turbine are read from the FORMATTED DATA FILE 1, specified by the user within the simulation steering file. For each user-specified device, up to the total number of devices (NTEC) the subroutine loops through the model mesh to identify mesh elements encompassed by the turbine geometry. Elements at the user-specified reference velocity distance surrounding the device are also identified and saved in an array (DDELEM).

At all subsequent time steps, the subroutine loops through the model mesh and evaluates the horizontal reference velocity components and magnitude (UREFX, UREFY and UR) upstream of the device (based on the flow direction at the device). Assuming the reference velocity exceeds the cut-in velocity for the device (VCUT), the drag force to be applied is evaluated from eqn. (1) based on the drag coefficient and drag distribution for each device given by the user in the FORMATTED DATA FILE 1. For simplicity, Fig. 3 shows two

options: (i) a uniform drag distribution over the frontal area of the device and (ii) a spatially varying drag distribution. However, any number of drag distributions could easily be added to capture the drag characteristics of specific devices.

The computed drag forces are applied as implicit source terms in the *U*- and *V*- momentum equations (S1U%R and S1V%R, respectively) since the flow approaching an individual turbine is expected to be predominantly horizontal. However, a similar source term could easily be applied to the vertical momentum equation, if desired. Finally, the power output for each turbine (PTEC) is evaluated based on eqn. (2) and written to a FORMATTED RESULTS FILE at each time step.

VI. Benchmarking and Validation – Surface-piercing Cylinder

A. Methodology

A series of numerical tests were conducted to verify that the modifications of the TELEMAC-3D source code described in Section V performed as intended, in terms of modifying the velocity distribution in the downstream wakes of individual drag (turbine) elements.

The first series of tests involved simulating the hydrodynamic response to a 1 m diameter surface-piercing (emergent) cylinder in a steady flow, modelled using four different approaches (numerical simulations listed as A01 to A04 in Tab. 1).

The objective of these simulations was to (a) establish general consistency between the 2D and 3D approaches to drag parameterization, and identify any differences, and (b) to assess the effectiveness of the parametric approaches (in 2D and 3D) in capturing wake velocity distributions downstream of a drag element (cylinder).

The simulations were carried out in a 50 m long by 10 m wide numerical flume, with a horizontal mesh resolution of 0.2 m, decreasing to 0.1 m in the immediate vicinity of the cylinder for simulations where it was fully resolved (A01 and A03).

Table 1. Summary of Validation Runs – vertical Cylinder

Run ID	Simulation Type	Description
A01	TELEMAC-2D	Cylinder fully resolved (i.e. represented as a land boundary in the mesh)
A02	TELEMAC-2D	Cylinder drag forces parameterized using the DRAGFO subroutine activated using the VERTICAL STRUCTURES keyword
A03	TELEMAC-3D	Cylinder fully resolved
A04	TELEMAC-3D	Cylinder drag forces parameterized using the source code modifications described in Section V

For the non-hydrostatic TELEMAC-3D simulations, nine fixed planes were specified at elevations of 0.0 m, 0.5 m, 1.0 m, 1.5 m, 2.0 m, 2.5 m, 3.0 m, 3.5 m and 4.0 m above the bottom. All simulations incorporated identical bed friction (uniform Strickler coefficient of 40 $m^{1/3}/s$), turbulence parameters (constant eddy viscosity of 1 x 10^{-6} m^2/s) and numerical parameters (default). The water depth was initialized to 4.0 m and fixed at the downstream boundary. The discharge at the upstream boundary was increased linearly from 0.0 m^3/s to an arbitrary value of 10.0 m^3/s over a period of 400 s and kept constant for the remainder of the simulation to reach approximately steady state conditions. The total duration of each simulation was 2,000 s. The depth-averaged velocity upstream of the cylinder was approximately 0.25 m/s, corresponding to a Reynolds' number, Re = 2,500 (cylinder diameter length scale). This corresponds to a subcritical, laminar wake regime (e.g. p.349,[15]).

For simulations A01 and A03, the cylinder was centred in the flume at a location 10D downstream of the inlet, where D is the cylinder diameter for this series of tests. For simulations A02 and A04, which involved parametric (drag force) approaches to modelling the cylinder, a drag coefficient C_D =1 was applied within a square of side D centred on the same location. C_D = 1 is based on the following curve fit from White (p.210, [16]):

$$C_D = 1 + 10.0Re^{-2/3}, \quad 1.0 < Re < 2 \times 10^5 \qquad (3)$$

which is accurate for an infinitely long cylinder. For the three-dimensional simulation (A04), the local drag coefficient was doubled for the surface and near-bed layers, to account for observed free and fixed end effects on local drag coefficients (e.g. [6] [17]).

B. Results and discussion

The computed depth-averaged velocity ratios (the ratio of the local depth-averaged velocity magnitude to the value in the absence of the modelled cylinder) are shown in Fig. 4 for Simulations A01 to A04. Grid lines in Fig. 4 are at intervals of 2D. The wake velocity distributions for two-dimensional and three-dimensional simulations where the cylinder was fully resolved (A01 and A03) are broadly in agreement. Velocity gradients in the transverse direction (perpendicular to the flow) are somewhat higher and persist further downstream (i.e. slower wake recovery) in the TELEMAC-3D simulation (A03). It is noteworthy that simulation A03 was the only run to exhibit unsteady vortex shedding in the wake of the cylinder. The results for run A03 shown in Fig. 4 are therefore based on a temporal average of the last 18 minutes of the simulation, or 3T, where T is the observed period of vortex passage. For all other simulations, the results are based on the final time step of the simulation.

For simulations A02 and A04, the depth-averaged velocity ratio is overestimated along the flume centreline at distances less than 10D downstream of the cylinder (Fig. 5). This is not surprising since the displacement of fluid owing to the presence of the cylinder cannot be captured by the drag parameterization approach [18]. The velocity distribution will therefore be inaccurate in the immediate vicinity (within

10-15*D* according to [19]) of the cylinder. At downstream distances greater than 10*D*, the two-dimensional drag parameterization (A02) continues to overestimate the velocity ratio by 8-10 %. In this region, the three-dimensional drag parameterization (run A04) more closely captures the centreline depth-averaged wake velocity distribution and the velocity ratio is generally within 3-4 % of the value for the simulation with a fully resolved cylinder (A03). A limited number of tests indicated the modelled velocities are sensitive to mesh resolution. For example, increasing the horizontal mesh resolution to 0.1 m for run A04 resulted in a 9% decrease in the centreline velocity ratio at a distance 30*D* downstream. Predicted velocities are also likely sensitive to drag coefficients, turbulence parameters, *Re* regime, and advection schemes. On a relative basis, the results demonstrate that the new TELEMAC-3D drag parameterization is comparable and consistent with the drag parameterization in TELEMAC-2D.

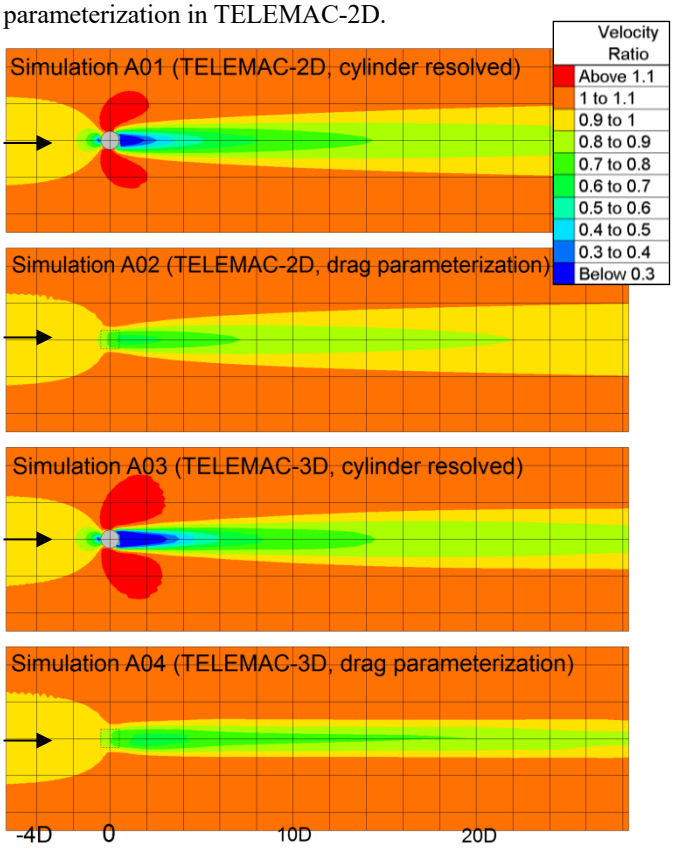

Figure 4. *Depth average velocity ratio for simulations A01 to A04.*

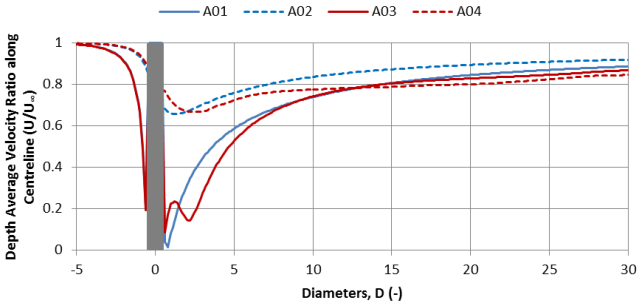

Figure 5. *Depth average velocity ratio along the centreline of the flume for simulations A01 to A04.*

Depth-averaged velocity gradients across the flume (normal to the direction of flow) in the downstream wake are higher for the TELEMAC-3D simulations compared to the TELEMAC-2D simulations. Since this applies to both the fully resolved cylinder and parametric drag scenarios, we hypothesize that this result may be sensitive to turbulence parameters. It is expected that higher eddy viscosities in the numerical model would result in smoother velocity gradients in the wake region, and shorter wake recovery distances.

VII. Benchmarking and Validation – Physical Model of Simplified Turbine (Porous Plates)

A. *Methodology*

Two numerical tests were conducted using the drag parameterization implemented in TELEMAC-3D (Section V), for comparison with physical model (laboratory) test results.

The physical model testing, described in the following section, involved using simplified model turbines (porous plates) in a flume to investigate wake velocity distributions under an imposed steady current. The flume geometry (0.05 m horizontal mesh resolution and 9 fixed, evenly spaced layers) and physical model scenarios were numerically replicated using TELEMAC-3D, wherein the porous plates were represented as drag elements. A drag coefficient of C_D = 1.2 was assigned to the porous plates, based on the experimentally determined relationship between C_D and plate porosity presented in Castro [20]. The horizontal drag force associated with the porous plates was then calculated based on C_D and U_r (evaluated at 5*D* upstream) and applied locally at model nodes within the area occupied by the plates (i.e. following the approach described in Section V). Several turbulence closure schemes and parameter values were tested in the numerical model, including Smagorinsky, constant viscosity and mixing length models.

B. *Physical model test set-up*

A physical model of a simplified turbine and a turbine array was constructed in the 97 m long by 2 m wide Large Wave Flume (LWF) at the National Research Council of Canada's laboratory in Ottawa (Fig. 6). Using information provided by project partners, the dimensions of common cross-flow turbines at prototype scale, as well as river dimensions and flow speeds, were scaled to suit the geometry of the LWF. The LWF is equipped with a current generation system comprised of 12 electrically-powered variable speed thrusters installed in a tunnel below the flume sub-floor. When activated, the thrusters generate a steady circulation within the tunnel and in the open space above the sub-floor. The current speed and direction is regulated by adjusting the rotation speed of the thrusters.

Porous plates were used to represent a simplified RHE turbine in the physical model. The porous plate extracts energy from the flow through small scale turbulence caused by the water flowing through the holes in the plate, to simulate extraction of energy by a rotating turbine. The porous plate used in the model was 0.3 m wide (transverse direction in the flume) and 0.2 m tall (vertical dimension)

and had a porosity of approximately 40 % (i.e. holes comprised 40 % of the total area of the plate). For this phase of the testing, the model represented a typical turbine at a geometric scale of approximately 1:20.

A total of 48 holes of 0.025 m diameter were drilled into the 12 mm thick PVC plate to create the simplified turbine. The plate was mounted to a support made from 2.6 mm sheet metal. The plate support was designed to minimize interference with the flow and the downstream wake field emanating from the simplified model turbine. The support (Fig. 7) was 0.69 m tall and 0.15 m long and included a 0.05 m wide by 0.3 m high gap immediately upstream of the plate. This gap allowed the flow to travel unobstructed around the sides of the porous plate. The upstream edges of the plate supports were grinded into knife edge profiles to minimize flow disturbance by the support itself. The support was levelled and anchored into the bottom of the flume, and stabilized with wires connected to the side of the flume. The resulting structure was stiff and exhibited minimal vibration during testing.

The simplified turbine models were placed in two arrangements: (i) Configuration B01 – a single turbine approximately 28.5 m downstream of the flow inlet and centred within the flume (Fig. 7); and (ii) Configuration B02 – two turbines side by side and separated by a distance of 0.3 m (Fig. 8).

The simplified turbine models were subjected to steady flow conditions (undisturbed streamwise depth-averaged velocity of approximately 0.7 m/s and water depth of approximately 0.75 m). A series of velocity measuring devices were used to characterize the velocity distribution in the wake of the porous plate. The instrumentation included one Valeport 2-axis electromagnetic current meter (ECM) and five Vectrino 3-axis acoustic Doppler velocimeters (ADVs). Velocities were measured on a pre-determined grid extending up to 40D downstream of the simplified turbines (where D = 0.2 m).

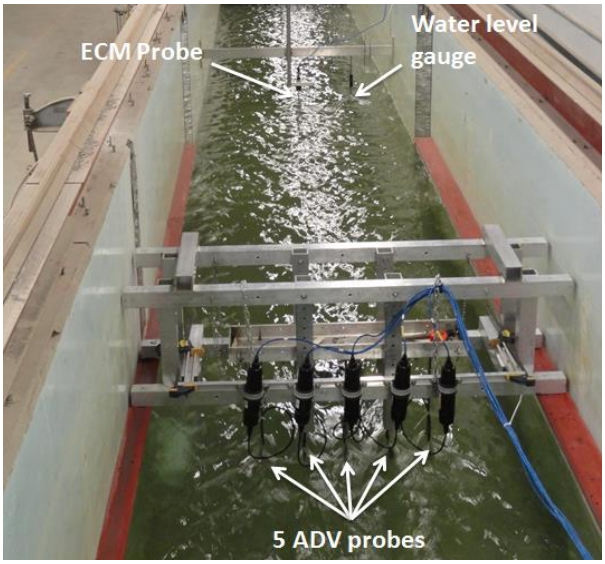

Figure 6. *Longitudinal view of the large wave flume at NRC's Ottawa laboratory.*

Figure 7. *Simplified model turbine consisting of porous plate and supports.*

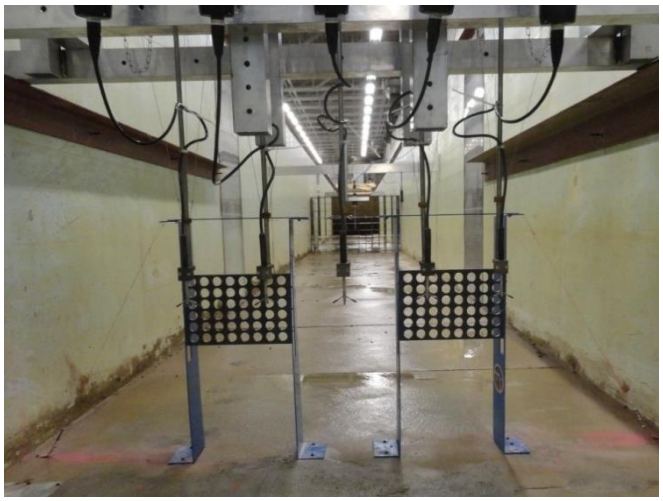

Figure 8. *Configuration B02 – two simplified model turbines.*

This experimental data will be used in future phases of the research project to calibrate and validate a CFD model of the simplified turbines, followed by physical and CFD modelling of more realistic cross-flow turbines.

C. *Results and discussion*

Contour plots showing measured (from physical model tests) and modelled (TELEMAC-3D) velocity ratios downstream of the porous plates at an elevation of 0.45 m above the bottom are shown in Fig. 9 (Configuration B01 – one porous plate) and Fig. 10 (Configuration B02 - two porous plates). This elevation represents approximately the

mid-height of the porous plates. The results shown in Fig. 9 and Fig. 10 are for the turbulence parameters that gave best overall agreement (from visual assessment) with measured wake velocity distributions. This corresponded to a Prandtl mixing length model for vertical turbulence and a constant horizontal eddy viscosity of 1 x 10^{-3} m^2/s.

Measured and modelled velocity ratios along the centreline of the flume at an elevation of 0.45 m above the bottom are shown in Fig. 11 (Configuration B01 – one porous plate) and Fig. 12 (Configuration B02 - two porous plates). Modelled velocity ratios are shown for the "best fit" turbulence parameters described above, and for simulations incorporating constant horizontal and vertical eddy viscosities of 1 x 10^{-6} m^2/s. The downstream wake recovery predicted by TELEMAC-3D is sensitive to the applied turbulence parameters. During physical model testing, it was observed that the measured wake recovery is strongly dependent on ambient turbulence in the flume (controlled by introducing roughness elements upstream), and that higher turbulence intensities resulted in shorter wake recovery distances. This observation is consistent with the delayed wake recovery observed in the TELEMAC-3D model results for simulations with relatively low, constant eddy diffusivities. Higher diffusivities in the numerical model result in smoothing of velocity gradients in the wake of the plates, and shorter wake recovery distances (in some cases leading to overshoot, as shown in Fig. 12).

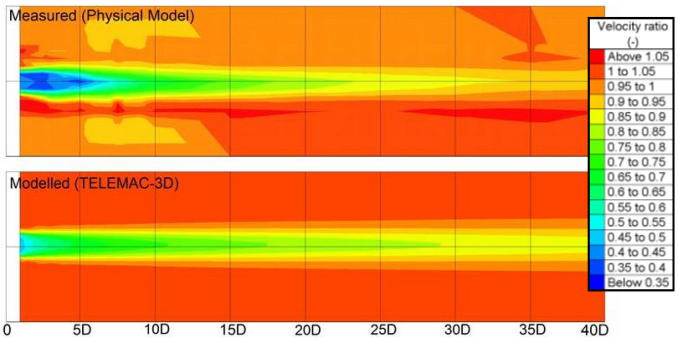

Figure 9. *Velocity ratios at elevation z = 0.45 m downstream of the single porous plate (Configuration B01).*

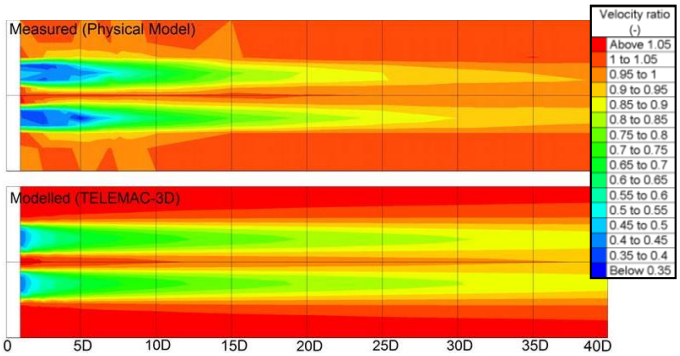

Figure 10. *Velocity ratios at elevation z = 0.45 m downstream of the two porous plates (Configuration B02).*

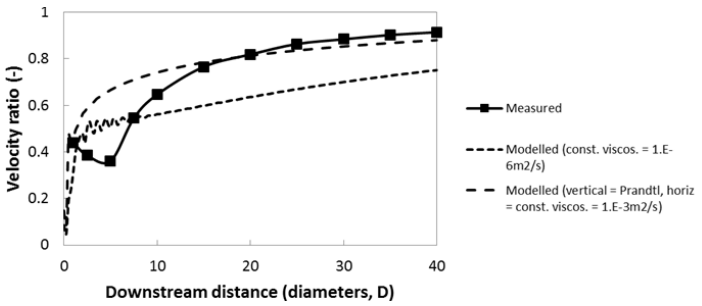

Figure 11. *Flume centreline velocity ratios at elevation z = 0.45 m downstream of the single porous plate (Configuration B01).*

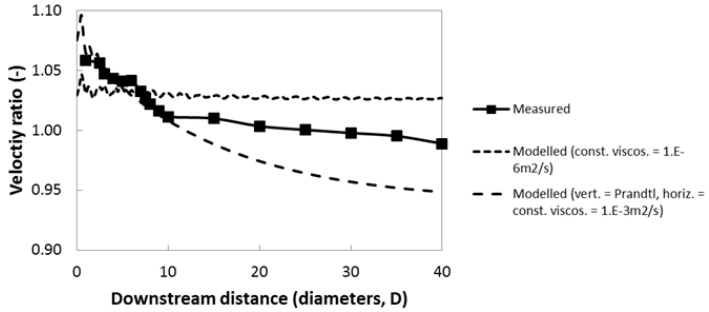

Figure 12. *Flume centreline velocity ratios at elevation z = 0.45 m, midway between and downstream of the two porous plates (Configuration B02).*

VIII. Concluding Remarks

A drag parameterization in TELEMAC-3D was implemented and described, with preliminary validation using: (i) numerical model results for an emergent cylinder in steady flow; and (ii) physical model test data for simplified hydrokinetic turbines (porous plates) in steady flow. The methodology shows some promise in capturing RHE turbine wake velocity distributions at distances of 10 to 15 turbine diameters downstream from the device. However, a number of limitations and issues remain to be addressed before the approach can be successfully integrated in RHE resource assessments. Some of the key limitations are described as follows.

A. *Blockage, drag coefficients and reference velocities*

For a specific device, power and drag coefficients are intrinsically linked to the location where the reference velocity, U_r, is specified or calibrated. The reference velocity location is typically chosen sufficiently far upstream that the flow is not disturbed by the presence of the turbine device (i.e. such that U_r is the free-stream or undisturbed flow speed). This approach is expected to be valid for a single device or row of devices where the cumulative blockage area for all turbines is less than 5 % of the channel cross-sectional area within the project site. Such conditions are not unusual for in-stream tidal energy projects. However, RHE turbine farms generally require multiple rows of turbines and/or the channel blockage may exceed 5 %. The concept of a free-stream flow velocity is therefore unlikely to be valid for most RHE projects. This is perhaps the most significant limitation of the methodology described in this paper, in terms of its usefulness for evaluating power extraction and wake velocity distributions at potential RHE generation sites.

The drag parameterization approach described in this paper cannot accurately predict wake velocity distributions in the

immediate vicinity of turbines (within about 10-15*D*), which sets a minimum distance between turbines in an array for the methodology to remain valid. Allowing for an additional buffer distance upstream of each device (corresponding to the distance to the reference velocity location), the turbine spacing limit at which the approach is valid may be prohibitively large at some sites. Modifications of the parameterization in TELEMAC-3D could be explored to partially address this limitation, such as the introduction of porosity in the momentum equations (e.g. p. 43, [18]).

In closely packed arrays of turbines, accurately modelling turbine wake velocities, turbulence, and turbine-wake interactions becomes more important [11]. In densely packed arrays, a simple extrapolation of the results for isolated turbines is not appropriate. CFD and laboratory studies combining multiple turbines in different array configurations are needed to provide a unified description of drag and power at scales ranging from individual drag elements (turbines) to river reaches. Previous research investigating hydrodynamics, drag, and wake interactions in arrays of aquatic vegetation may offer valuable insight ([21] [22], and references therein).

Recent research [19] suggests that the average flow speed through the turbine (aperture velocity) may offer a better alternative for the reference velocity in comparison to the free-stream velocity since this perturbed value is independent of the channel blockage. However, measuring or simulating flow velocities in the aperture of a moving cross-flow turbine to support the evaluation of drag and power coefficients is not a trivial task. Further laboratory and CFD modelling work is needed to investigate the practicality of this approach. Minor additional modifications of the TELEMAC-3D source code presented here would be needed to facilitate a change in the reference velocity. However, an understanding of the relationships between local velocities and velocities upstream of the turbine remains important to avoid mesh-dependent results [11].

B. Wake characteristics

Accurately modelling the characteristics of the turbine near-wake (velocity deficit and turbulence) is critical for optimizing turbine placement within an array. Although the results presented here indicate some promise in modelling wake velocity distributions at distances downstream of RHE turbines, some discrepancies in the predicted wake recovery distances were identified as discussed. It is anticipated that further calibration or tuning of turbulence closure models and mesh sensitivity testing would lead to improved results. Correction terms could be added to turbulence closure models to account for the turbulent kinetic energy production by turbines [1]. Recent research [19] suggests that the implementation of spatially and temporally varying drag coefficients could also facilitate improved predictions of turbine wake characteristics. The TELEMAC-3D source code posted on the openTELEMAC-MASCARET web forum includes an example where the drag coefficient can optionally be specified as having a Gaussian distribution in space. The addition of alternative spatial distributions or Reynolds number-dependent drag coefficients would require trivial programming effort.

ACKNOWLEDGEMENTS

The authors gratefully acknowledge funding and contributions to this work received from Natural Resources Canada, the National Research Council of Canada, Marine Renewables Canada, Mavi Innovations, Inc., and Université Laval. Sean Ferguson's helpful editorial comments on the draft manuscript are appreciated by the authors.

REFERENCES

[1] T. Roc, D. Greaves, K. M. Thyng, and D. C. Conley, "Tidal turbine representation in an ocean circulation model: Towards realistic applications," Ocean Engineering, 78, pp.95-111, 2014.

[2] C. Moulinec, C. Denis, C. T. Pham, D. Rougé, J.-M. Hervouet, E. Razafindrakoto, R. W. Barber, D. R. Emerson, and X. J. Gu, "TELEMAC: An efficient hydrodynamics suite for massively parallel architectures," Computers & Fluids, 51(1), pp.30-34, 2011.

[3] B. M. Sumer, "Hydrodynamics Around Cylindrical Structures," Advanced Series on Ocean Engineering, vol. 26, World Scientific, 2006.

[4] O. Bertrand, L. Duron, C. Girard, J. Zanette, and F. Dominguez, "Numerical modelling of vertical-axis and transverse-flow hydrokinetic turbine in the river Loire," E-proceedings of the 36th IAHR World Congress, 2015.

[5] S. E. Bourban, N. D. Durand, T. T. Coates, L. Gill, M. Harper, and R. Stephen, "Modelling tidal energy resource and extraction," Coastal Engineering Proceedings, 1(32), 2011.

[6] J. R. Chaplin, and P. Teigen, "Steady flow past a vertical surface-piercing circular cylinder," Journal of Fluids and Structures, 18(3), pp.271-285, 2003.

[7] A. Cornett, N. Durand, and M. Serrer, "3-D Modelling and assessment of tidal current resources in the Bay of Fundy, Canada," in Proc. 3rd Int. Conf. on Ocean Energy, 2010.

[8] A. Joly, C.-T. Pham, M. Andreewsky, S. Saviot, and L. Fillot, "Using the DRAGFO subroutine to model Tidal Energy Converters in Telemac-2D," Proc. 22nd Telemac & Mascaret User Club, October 2015.

[9] A. Pérez-Ortiz, J. Pescatore, and I. Bryden, "A systematic approach to undertake tidal energy resource assessment with Telemac-2D," in 10th European Wave and Tidal Energy Conference (EWTEC), 2013.

[10] C. T. Pham, and V. A. Martin, "Tidal current turbine demonstration farm in Paimpol-Brehat (Brittany): tidal characterisation and energy yield evaluation with Telemac," in Proceedings of the 8th European Wave and Tidal Energy Conference, vol. 710, 2009.

[11] S. C. Kramer, and M. D. Piggott, "A correction to the enhanced bottom drag parameterisation of tidal turbines," Renewable Energy, 92, pp.385-396, 2016.

[12] G. Sutherland, M. Foreman, and C. Garrett, "Tidal current energy assessment for Johnstone strait, Vancouver island," Proceedings of the Institution of Mechanical Engineers, Part A: Journal of Power and Energy, 221(2), pp.147-157, 2007.

[13] T. Roc, D. C. Conley, and D. Greaves, "Methodology for tidal turbine representation in ocean circulation model," Renewable Energy, 51, pp.448-464, 2013.

[14] G. W. Rawlings, "Parametric Characterization of an Experimental Vertical Axis Hydro Turbine," MSc. Thesis, University of British Columbia, Vancouver, 2009.

[15] P. K. Kundu, and I. M. Cohen, "Fluid Mechanics, 3rd ed., Elsevier, 2004, 759 pp".

[16] F. M. White, "Viscous Fluid Flow, McGraw-Hill, 1974".

[17] D. Poggi, A. Porporato, L. Ridolfi, J. D. Albertson, and G. G. Katul, "The effect of vegetation density on canopy sub-layer turbulence," Boundary-Layer Meteorology, 111(3), pp.565-587, 2004.

[18] J.-M. Hervouet, "Hydrodynamics of free surface flows: modelling with the finite element method," John Wiley & Sons, 2007.

[19] V. Klaptocz, J. Cousineau, G. Dumas, and T. Kinsey, "Quantifying extractable power in a stretch of river using an array of MHK

turbines.," Report prepared for Marine Renewables Canada, March 2016.

[20] I. P. Castro, "Wake characteristics of two-dimensional perforated plates normal to an air-stream," J. Fluid Mech., 46, pp. 599-609, 1971.

[21] H. M. Nepf, "Drag, turbulence, and diffusion in flow through emergent vegetation," Water resources research, 35(2), pp.479-489, 1999.

[22] M. Luhar, and H. M. Nepf, "From the blade scale to the reach scale: A characterization of aquatic vegetative drag," Advances in Water Resources, 51, pp.305-316, 2013.

SCIENCE ▪ PASSION ▪ TECHNOLOGY

TU Graz

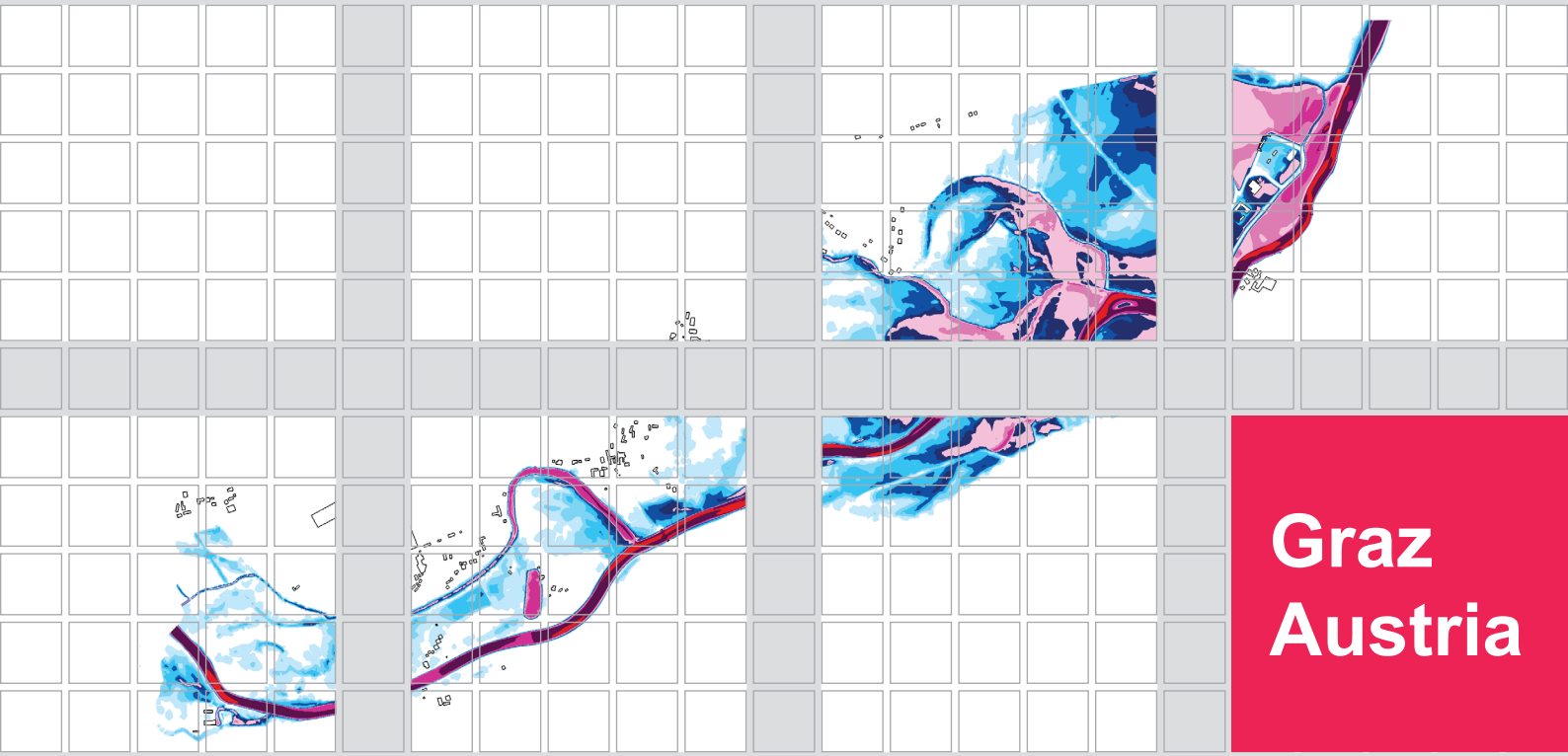

Graz Austria

Graz University of Technology
Institute of Hydraulic Engineering and Water Resources Management
Stremayrgasse 10/II, 8010 Graz, Austria
T: +43(0)316/873-8361
hydro@tugraz.at
► www.tugraz.at

ISBN 978-3-85125-544-7
DOI 10.3217/978-3-85125-544-7

sponsored by flussbau iC Verbund flussbüro hydro engineering research